THE

PHYSICAL REVIEW

VOLUME 95 SECOND SERIES NUMBER 1

JULY 1, 1954

Published for the

AMERICAN PHYSICAL SOCIETY

by the

AMERICAN INSTITUTE OF PHYSICS

Lancaster, Pa. and Grand Central Terminal, New York 17, N. Y.

THE
PHYSICAL REVIEW

A journal of experimental and theoretical physics established by E. L. Nichols in 1893

SECOND SERIES, VOL. 95, NO. 1 JULY 1, 1954

Dimensional Relations in Magnetohydrodynamics*

WALTER M. ELSASSER
Department of Physics, University of Utah, Salt Lake City, Utah
(Received January 15, 1954)

An analysis of the dimensional relations characteristic of electromagnetic phenomena in fluids of large dimensions is carried out. Most dimensionless quantities are found to be exceedingly small, or large, compared to unity, with resultant simplifications of the theory. We find that, in the absence of instabilities, the conditions for the acceleration of particles to the higher cosmic-ray energies are favorable only when the linear dimensions of the fluids involved are very large.

SYMBOLS

COSMIC fluids are as a rule highly turbulent. This entails the necessity of dimensional order-of-magnitude considerations preceding, and often even replacing, a more rigorous dynamical theory. We shall here use the symbol $\{a\}$ to designate the order of magnitude of a physical quantity a. In particular, $\{\lambda\}$ will designate a representative length and $\{\omega\}$ will designate a representative reciprocal time. We shall use the rationalized mks system of units, whence $\mu\epsilon=c^{-2}$ with the usual meaning of these, and other, electromagnetic symbols. For simplicity it will be assumed that the electrical conductivity σ is constant throughout the fluid; ϵ and μ will be assumed constant throughout space.

FIXED FRAME OF REFERENCE

In large-scale electrodynamics the electromagnetic effects arising from the difference in mass of the positive and negative carriers might not always be negligible. We shall here ignore this type of effect and assume that all the effects considered can be described *classically*, namely, by a combination of Maxwell's equations with the hydrodynamic equations. Hence $\mathbf{V}$ will designate, throughout, the material velocity of the fluid in a given frame of reference. As a general rule this velocity is small compared to the velocity of light, that is

$$\{\beta\}\ll 1. \tag{1}$$

If a conductor moves across a magnetic field, there appears an induced electric field of magnitude $\mathbf{V}\times\mathbf{B}$. From the electromagnetic field equations we then have

$$\mu^{-1}\nabla\times\mathbf{B}=\mathbf{J}=\epsilon\partial\mathbf{E}/\partial t+\sigma\mathbf{E}+\sigma\mathbf{V}\times\mathbf{B}+\eta\mathbf{V}. \tag{2}$$

The terms on the right represent in turn, the displacement current, the conduction current, the induction current, and the convection current. The convection current appears owing to the fact that (as we shall see later) $\mathbf{E}$ cannot in general be assumed divergence-free and hence there is a space-charge density η in the fluid.

The ratio of displacement current to conduction current is of the order

$$\{\omega\epsilon/\sigma\}=\{\gamma\}. \tag{3}$$

This nondimensional quantity is well known from the electromagnetic theory of metals. To estimate it here we remember that ω now represents frequencies of the macroscopic motion of the fluid. Let us take $\omega=10^{-4}$, corresponding roughly to periods of a day. Cosmic fluids are as a rule excellent conductors, of metallic order. For the earth's core the conductivity has been estimated to be a factor of 10–100 below that of iron.[1] The material of stars is highly ionized and the conductivities are again of metallic order.[2] Clouds of ionized gases near stars or in interstellar space show as a rule appreciable ionization; they are then again comparable to metallic conductors. (This results from the fact that while the number density of ions becomes small, the mean free path becomes large in the same proportion). Taking as an example $\sigma=10^7$, the con-

* Supported by the U. S. Office of Naval Research.

[1] W. M. Elsasser, Revs. Modern Phys. **22**, 1 (1950).
[2] T. G. Cowling, Monthly Notices Roy. Astron. Soc. **105**, 166 (1945).

ductivity of ordinary iron, we have $\gamma=10^{-22}$ which is small indeed.

From the field equations we have $\{\eta\}=\{\epsilon\lambda^{-1}E\}$, and hence the ratio of convection current to conduction current is

$$\{\eta\mathbf{T}V/\sigma E\}=\{\epsilon\lambda^{-1}V/\sigma\}=\{\gamma\}, \tag{4}$$

and the convection current is also negligible; (2) reduces to

$$\nabla\times\mathbf{B}=\mu\mathbf{T}=\mu\sigma\mathbf{E}+\mu\sigma\mathbf{V}\times\mathbf{B}. \tag{5}$$

We next compare the induction current to the net current. The ratio is

$$\{\mu\sigma VB\}/\{\lambda^{-1}B\}=\{\mu\sigma\lambda V\}=\{R_m\}, \tag{6}$$

where R_m is a nondimensional quantity which will be designated as the magnetic Reynolds number. To elucidate the physical meaning, or one physical meaning, of this quantity we notice that if a current flows in a *rigid* conductor of linear dimensions λ and conductivity σ the period of free decay, in the absence of an impressed emf, is of the order

$$\{\omega_{\text{dec}}^{-1}\}=\{\mu\sigma\lambda^2\}. \tag{7}$$

Again, the periods of the material motion of the fluid are of the order $\{\omega_{\text{vel}}\}=\{V\lambda^{-1}\}$. Hence

$$\{R_m\}=\{\omega_{\text{vel}}/\omega_{\text{dec}}\}. \tag{8}$$

This relation indicates that R_m is a measure of the coupling between the mechanical motion and the electromagnetic field: As we shall see, the presence of the term $\mathbf{V}\times\mathbf{B}$ in (5) implies that, in the absence of free decay, the fluid carries the magnetic field along in its motion. The decay phenomena may be visualized as a "diffusion" of the field across the conductor. Strong coupling, including the important case of amplification of the field, requires that the transport of the field by the motion exceeds the rate of diffusion. The distinctive property of cosmic magnetohydrodynamics becomes evident: in the laboratory R_m is always small; in problems of cosmic hydrodynamics R_m is, as a rule, very large. The relation of laboratory phenomena to cosmic phenomena of magnetohydrodynamics is, in a rough analog, that of Poisseuille flow to the large-scale eddy motions in a star or cosmic cloud. Here, we shall essentially confine ourselves to the cosmic case, that is to large numerical values of the magnetic Reynolds number, and shall not enter into a discussion of the laboratory experiments[3] on the interaction of sound waves with a magnetic field. In order to estimate R_m for the earth's core we take, say $\sigma=10^6$, $V=10^{-3}$ m/sec from observations of the secular magnetic variations,[1] and $\lambda=10^6$ meters, giving $R_m=10^3$. For extra-terrestrial phenomena λ and V are larger by many powers of ten and R_m is correspondingly larger.

Returning now to (5), we see that the *net* current is negligibly small in large-scale fluids; we have a balance

$$\mathbf{E}\approx-\mathbf{V}\times\mathbf{B} \tag{9}$$

in an excellent approximation. It must not, however, be concluded from (5) that $\nabla\times\mathbf{B}$ is negligible in other connections; we shall see for instance that the ponderomotive forces exerted by the field, which depend on $\nabla\times\mathbf{B}$, are by no means small.

A further dimensionless quantity of interest is the ratio of the electric to the magnetic energy density. This is

$$\{\epsilon E^2/\mu^{-1}B^2\}=\{E^2/c^2B^2\}=\{\beta^2\}, \tag{10}$$

as may be seen from the field equation

$$\nabla\times\mathbf{E}=-\partial\mathbf{B}/\partial t, \tag{11}$$

or else directly from (9).

Taking the curl of (5) we obtain by virtue of (11)

$$\partial\mathbf{B}/\partial t=\nabla\times(\mathbf{V}\times\mathbf{B})+\nu_m\nabla^2\mathbf{B}, \tag{12}$$

where the quantity

$$\nu_m=(\mu\sigma)^{-1} \tag{13}$$

will be designated as the magnetic viscosity. We have $R_m=\lambda V/\nu_m$ which shows that the magnetic Reynolds number is obtained from the ordinary hydrodynamic Reynolds number by replacing ν, the kinematic viscosity, by the magnetic viscosity ν_m. It will appear more clearly later that ν and ν_m correspond to analogous physical effects.

The integration of (12) is as a rule prohibitively difficult. The physical meaning is brought out more clearly by a corresponding integral theorem,[4]

$$\frac{d}{dt}\int\mathbf{B}_n ds=-\sigma^{-1}\int\mathbf{J}\cdot d\mathbf{L}, \tag{14}$$

where the surface integral on the left is thought of as moving bodily with the fluid. The contour integral on the right becomes small as R_m becomes large; in the limit of infinite conductivity we obtain the well-known result that the magnetic lines of force are "frozen" in the fluid and are carried along with its motion.

From (9) we may infer that the electrical space charge does not in general vanish,[5] since

$$\eta/\epsilon=\nabla\cdot\mathbf{E}=\mathbf{V}\cdot\nabla\times\mathbf{B}-\mathbf{B}\cdot\nabla\times\mathbf{V}. \tag{15}$$

The ratio of the electric to the magnetic components of the electromagnetic stress tensor is, however, given by (10) and the electrostatic forces are negligible. Furthermore, it may be shown that the irrotational part of the current (5) is small compared to the divergence-free part so that the *magnetic* effects corresponding to a nonvanishing η are also likely to be in general negligible. We have from the equation of continuity for the

[3] S. Lundquist, Phys. Rev. **76**, 1805 (1949).

[4] See for instance W. M. Elsasser, Phys. Rev. **72**, 821 (1947).

[5] S. Lundquist, Arkiv Fysik **5**, No. 15 (1952).

current, on using (15),

$$\nabla\cdot\mathbf{J}=-\dot{\eta}=\{\omega\epsilon E/\lambda\}=\{\omega\epsilon VB/\lambda\}=\{\omega^2\epsilon B\},$$

and, on the other hand,

$$\nabla\times\mathbf{J}=\mu^{-1}\nabla\times\nabla\times\mathbf{B}=\{B/\mu\lambda^2\}.$$

Hence it follows that

$$\{\nabla\cdot\mathbf{J}/\nabla\times\mathbf{J}\}=\{\omega^2\lambda^2\mu\epsilon\}=\{V^2\mu\epsilon\}=\{\beta^2\},\qquad(16)$$

which is small. This relation suggests that for large magnetic Reynolds numbers we may, without loss of the essential dynamical features, disregard η, an assumption which can most conveniently be expressed by introducing a vector potential while dropping the corresponding scalar potential; thus,

$$B=\nabla\times\mathbf{A},\quad \mathbf{E}=-\partial\mathbf{A}/\partial t,\quad \nabla\cdot\mathbf{A}=0,\qquad(17)$$

which would transform (5) into

$$\partial\mathbf{A}/\partial t=\mathbf{V}\times(\nabla\times\mathbf{A})+\nu_m\nabla^2\mathbf{A}.$$

In this form, however, the last equation is inconsistent because, by (17), the left-hand side and the second term on the right have vanishing divergence whereas the divergence of the first term on the right does not vanish, according to (15). A correct equation is

$$\partial\mathbf{A}/\partial t=[\mathbf{V}\times(\nabla\times\mathbf{A})]_{tr}+\nu_m\nabla^2\mathbf{A},\qquad(18)$$

where the index tr signifies that only the "transverse" (divergence-free) part of the bracket is to be taken. It is well known that the decomposition of a vector field into the sum of a transverse and a longitudinal (irrotational) component is unique under suitable boundary conditions (e.g., vanishing at infinity). In applications one uses Fourier transforms or spherical eigenfunctions,[4] which make the decomposition automatic. The physical meaning of this simplification is this: By (16) the contribution which the longitudinal part of $\mathbf{E}$ makes to the ponderomotive force is negligible; thus, although the transverse and longitudinal components of $\mathbf{E}$ may be of the same order of magnitude, the longitudinal component does not significantly affect the transfer of energy between fluid motion and field; hence it can be omitted to advantage in problems where the interest does not center on the electric field as such.

LORENTZ TRANSFORMATION

In view of (1) we may neglect all terms of the order of β^2 and higher terms. Texts on relativity[6] indicate that σ must be considered as an invariant; this follows from its connection with thermodynamical quantities which are invariant. To within terms linear in β, the Lorentz transformation from an unprimed system to a primed system moving with velocity $\mathbf{U}$ reduces to

$$\mathbf{R}'=\mathbf{R}-\mathbf{U}t,\quad t'=t,\quad \nabla'=\nabla,\quad \partial/\partial t'=\partial/\partial t+\mathbf{U}\cdot\nabla.\qquad(19)$$

[6] M. von Laue, *Die Relativitätstheorie* (F. Vieweg, Braunschweig, 1921).

Furthermore, in this approximation,

$$\mathbf{J}'=\mathbf{J}+\eta\mathbf{U},\quad \eta'=\eta,$$

but the convection current may be neglected if $\{U\}=\{V\}$. The field vectors transform in the same approximation as

$$\mathbf{E}'=\mathbf{E}+\mathbf{U}\times\mathbf{B},\quad \mathbf{B}'=\mathbf{B}-\mathbf{U}\times\mathbf{E}/c^2,$$

but the last term in the equation for B' is by (9) of the order β^2 and hence negligible. The transformation equations for the electromagnetic quantities thus reduce to

$$\mathbf{E}'=\mathbf{E}+\mathbf{U}\times\mathbf{B},\quad \mathbf{B}'=\mathbf{B},\quad \mathbf{J}'=\mathbf{J},\quad \eta'=\eta.\qquad(20)$$

We have been brief in this deduction, but it should be emphasized that, as closer consideration shows, all terms linear in β have indeed been included.

We see from (5) that if we transform to a frame of reference in which a given fluid particle is at rest, then the "local" electric field becomes small compared to the average value of E over the fluid, for which (9) gives $\{E\}=\{VB\}$. This latter relation, by the way, permits a convenient observational evaluation of the field, since $\mathbf{V}$ and $\mathbf{B}$ are quite directly measurable, $\mathbf{B}$ being also Lorentz-invariant to within terms of the order of β. The actual current referred to a "local" system of reference is therefore small, as R_m^{-1}, compared to the current in, say an engineering dynamo. In such a machine the current is $\{\sigma E\}=\{\sigma VB\}$. Considerable semantic difficulties are bound to arise when one speaks uncritically of the "electric currents" producing the magnetic fields of the earth, of sunspots, etc. It has been suggested in the literature[7] that since at "neutral" points (points at which $\mathbf{B}$ vanishes in the "local" frame of reference) charged particles do not travel in spirals as they do elsewhere, phenomena of the type observed in gas discharges might occur which would lead to the acceleration of particles. The extreme smallness of the "local" electric field makes this conclusion unlikely.

MECHANICAL MOTION; SYMMETRIZATION

The density of the ponderomotive force which the field exerts upon the fluid is

$$F=\mathbf{J}\times\mathbf{B}=-\mu^{-1}\mathbf{B}\times(\nabla\times\mathbf{B})$$
$$=\mu^{-1}(\mathbf{B}\cdot\nabla)\mathbf{B}-(2\mu)^{-1}\nabla(\mathbf{B}^2).\qquad(21)$$

Here, the electrostatic forces produced by the space charges have been neglected since they are small by (10). The work done on the fluid by these forces per unit time and unit volume is $\mathbf{V}\cdot\mathbf{F}$; it may be shown[4] by obtaining the energy integral from (5) and (11) that this is indeed the negative of the work done by the fluid on the field.

In writing down the equations of motion we shall for simplicity assume that the fluid is incompressible. The equations of motion are

$$\partial\mathbf{V}/\partial t+(\mathbf{V}\cdot\nabla)\mathbf{V}=-\nabla\psi+(\mu\rho)^{-1}(\mathbf{B}\cdot\nabla)\mathbf{B}+\nu\nabla^2\mathbf{V},\qquad(22)$$

[7] J. W. Dungey, Phil. Mag. 44, 725 (1953).

where

$$\rho\psi = p + u + (2\mu)^{-1}\mathbf{B}^2,$$

and u is the gravitational potential. Equations (12) and (22) together are the fundamental equations of field-motion of magnetohydrodynamics. They can be put into a remarkably symmetrical form.[8,5] Letting

$$\mathbf{P} = \mathbf{V} + (\rho\mu)^{-\frac{1}{2}}\mathbf{B}, \quad \mathbf{Q} = \mathbf{V} - (\rho\mu)^{-\frac{1}{2}}\mathbf{B},$$

$$\nu_1 = \nu + \nu_m, \qquad \nu_2 = \nu - \nu_m,$$

and remembering that for an incompressible fluid,

$$\nabla\times(\mathbf{V}\times\mathbf{B}) = (\mathbf{B}\cdot\nabla)\mathbf{V} - (\mathbf{V}\cdot\nabla)\mathbf{B},$$

we can rewrite (12) and (19) as

$$\begin{aligned} \partial\mathbf{P}/\partial t + (\mathbf{Q}\cdot\nabla)\mathbf{P} &= -\nabla\psi + \nabla^2(\nu_1\mathbf{P} + \nu_2\mathbf{Q}), \\ \partial\mathbf{Q}/\partial t + (\mathbf{P}\cdot\nabla)\mathbf{Q} &= -\nabla\psi + \nabla^2(\nu_2\mathbf{P} + \nu_1\mathbf{Q}), \end{aligned} \tag{23}$$

where now

$$\psi = p/\rho + u/\rho + (\mathbf{P}-\mathbf{Q})^2/8. \tag{24}$$

It should be noted that the symmetrized equations hold only for an incompressible fluid; no corresponding symmetrical formalism has as yet been found for the compressible case. The equations suggest strongly that if magnetohydrodynamics is considered from a *statistical* view point, as seems appropriate for turbulent fluids, the vectors $\mathbf{V}$ and $(\mu\rho)^{-\frac{1}{2}}\mathbf{B}$ should play comparable roles. Energy transfer is possible both from and to the fluid. Many authors have therefore inferred that *equipartition* of the energy as between the kinetic energy of the fluid and the magnetic field energy might be assumed to hold in a first approximation:

$$\{\rho V^2\} = \{B^2/\mu\}. \tag{25}$$

Batchelor[9] has, however, pointed out that if the statistical theory of turbulence is applied to magnetohydrodynamics, the magnetic field energy should be less than the equipartition value (25), at least for the largest eddies. The author hopes to show elsewhere that under certain conditions the field energy can also exceed the value given by (25). For rough estimates, however, (25) should be useful. An equivalent statement is clearly that in (22)

$$\{(\mathbf{V}\cdot\nabla)\mathbf{V}\} = \{(\mu\rho)^{-1}(\mathbf{B}\cdot\nabla)\mathbf{B}\}; \tag{26}$$

the ponderomotive forces are in the mean comparable to the inertial forces. Schlüter and Biermann[10] have pointed out that if the "frictional" term in (12) is neglected, this equation is of the type

$$\{\partial B/\partial t\} = \{\lambda^{-1}V\}\{B\},$$

and that the solutions of this equation are of the general form

$$\{B\} = \{B_0\}\{\exp(\lambda^{-1}V)t\}.$$

Therefore, if a small magnetic stray field exists in a conducting fluid, it will in the average be amplified at an exponential rate until some statistical equilibrium value near (25) is reached.

DISSIPATION

The quantity

$$\nu/\nu_m = R_m/R = \mu\sigma\nu, \tag{27}$$

where R is the conventional Reynolds number, measures the ratio of the generation of heat by viscous friction in the fluid to the generation of Joule's heat by the electromagnetic field. Unless this ratio happens to be close to unity, one form of dissipation will predominate. This form of dissipation will also determine the cutoff of the turbulence spectrum at the side of the smallest eddies.

We can obtain an estimate of (27) for the case of an ionized gas. From kinetic theory[11] we have $\nu = v_0 l_p/3$ and $\sigma = \alpha e^2 N l_p/2mv$, where l_p is the mean free path, α the degree of ionization, N the number density, m and v are mass and mean velocity of the electrons, v_0 mean velocity of the molecules. Since $l_p = (\pi N\delta^2)^{-1}$, where δ is the collision diameter, and $v_0/v = (m/m_0)^{\frac{1}{2}}$, we can write this:

$$\mu\sigma\nu = \frac{\alpha\mu e^2}{6\pi^2}\left(\frac{m_0}{m}\right)^{\frac{1}{2}}\rho^{-1}\delta^{-4}. \tag{28}$$

Consider hydrogen and let (mks units) $\delta = 10^{-10}$ m; then

$$\mu\sigma\nu = 2\times10^{-4}\alpha/\rho. \tag{29}$$

This result shows that in interstellar gas clouds where ρ is very small (10^{-21} mks) the dissipation is entirely caused by mechanical friction, whereas in the interior of stars where ρ is in excess of unity the dissipation is entirely electromagnetic; the transition domain, $\{\mu\sigma\nu\} = 1$, occurs near the density values obtaining in the photospheres of stars.

One should emphasize that even when the electromagnetic dissipation is numerically large, the quantity $\nu_m = (\mu\sigma)^{-1}$ is not in itself a measure of the rate at which the field is dissipated. Since cosmic fluids are highly turbulent, the actual transport or dissipation of any quantity is determined, not by the molecular coefficients of diffusion but by the corresponding eddy diffusivities which are as a rule very much larger than the former. This applies to scalar properties such as heat as well as to vectorial properties such as momentum, and clearly must apply to the magnetic field in the fluid.[9] The calculation of the free decay for a body as large as the sun[2] yields decay times longer than the age of the universe. This amounts in essence to a computation of the magnetic Reynolds number; there can be little doubt that the general result of turbulence observations applies to the magnetic diffusivity; the larger the Reynolds number, the more the eddy diffusivity exceeds the molecular diffusivity in order of magnitude. The disappearance of sunspot magnetic fields in the course of a few days or weeks is certainly a matter of eddy diffusion.

[8] W. M. Elsasser, Phys. Rev. **79**, 183 (1950).
[9] G. K. Batchelor, Proc. Roy. Soc. (London) **201**, 405 (1950).
[10] A. Schlüter and L. Biermann, Z. Naturforsch. **5a**, 65, 237 (1950).
[11] For instance *Heat*, by J. M. Cork (John Wiley and Sons, Inc., New York, 1942), p. 131.

ELECTROMAGNETIC POTENTIALS

We shall now make some applications of our results to the acceleration of individual particles in conducting fluids. It must be assumed that the particles have a certain initial velocity such that the increase of their kinetic energy by electromagnetic accelerations can exceed the average losses by ionization, collision processes, and radiation; in other words we must assume that an "injection" process[12] exists. Let us inquire into the electromagnetic potentials that accompany magnetohydrodynamic phenomena. On account of the very high energies encountered in cosmic-ray particles it is often presumed that there exist special mechanisms which increase the field strengths, e.g., self-amplificatory plasma oscillations. From the viewpoint of magnetohydrodynamics we might classify as instabilities any processes leading to electrical potentials very much in excess of those found in ordinary conducting fluids. Such processes, as well as the cyclotron or betatron mechanisms where a particle circulates in the same field many times, are open to the criticism that on purely statistical grounds they are not likely to be sufficiently widespread or effective: Given the relatively large energy density of the cosmic radiation, one is prejudiced in favor of processes that can be counted upon to occur regularly in large volumes of cosmic space.

Here, we shall abstract from all processes except those directly related to the *average* conditions of cosmic magnetohydrodynamics. The electrical potential ϕ between two points of space is by (9) of the order

$$\{\phi\} = \{\lambda E\} = \{\lambda V B\}. \tag{30}$$

If we assume that equipartition prevails, this becomes, by (25),

$$\{\phi\} = \{(\mu\rho)^{\frac{1}{2}}\lambda V^2\}. \tag{31}$$

These relations must be interpreted with some care. The potentials are, of course, to be understood as line integrals $\int E d\lambda$ along some possible trajectory. The particles spiral along the magnetic lines of force, but these lines of force are not in general closed[13] and the particles will not in general follow the lines accurately owing to collisions and accelerations. Everything depends on the measure (in a set-theoretical sense) of trajectories that actually yield potential differences of the order indicated. If this measure is not too small some particles will be accelerated provided they have the required injection velocities. The above formulas do not discriminate between the nondivergent and the irrotational part of **E**, the two being of comparable order.

If the region where the acceleration occurs is highly inhomogeneous we may apply (30): In the envelope of a star the density changes very rapidly with height and the magnetic field will as a rule not be of local origin but will emanate from the lower layers of the star. If we can estimate $\{B\}$ from other data, (30) gives an estimate of the order of magnitude of the accelerating potentials. It is well known that at the occasion of solar flares the sun has ejected numerous particles with energies of the order of 10^8 ev. The acceleration of particles in stellar envelopes has been extensively discussed and we may be satisfied to refer to the literature.[14] With $\lambda = 10^9$ m, $V = 10^4$ m/sec, and $B = 10^{-2}$ ($= 100$ gauss), we obtain $\phi = 10^{11}$ volts. Apart from possible phenomena of instability, it is not likely that magnetohydrodynamic processes in the neighborhood of stars will lead to potentials exceeding this value by several powers of ten.

If we next consider the gaseous interstellar medium, we may assume that the equipartition formula (25) applies, as has been done by a number of authors;[12,14] we may then use (31). The variations in V admissible here are rather limited; $V = 10$ km/sec should be reasonably close to an upper limit. Extremely high voltages could be produced by increasing λ. If we assume one proton per cm^3 in the average over the galaxy, that is (in mks units) $\rho = 10^{-21}$, take $V = 3 \times 10^6$ and $\lambda = 10^{20}$ (comparable to the dimensions of the more condensed parts of the galaxy) we obtain $\phi = 10^{14}$ volts. We can increase this value by increasing λ still further. Chandrasekhar and Fermi[15] suspect the presence of magnetic fields in the spiral arms of the galaxy. Parker[16] has studied the formation of galaxies from an intergalactic gaseous medium and concludes that turbulent velocities of the order of 40 km/sec ought to be present in this medium. If there is also some magnetic field in these dimensions, it seems possible to account quantitatively for the presence of extremely energetic particles by acceleration over sufficiently large linear dimensions.

If the galactic magnetic field is of the order given by the equipartition formula (25), the particles circulate in the galaxy for a very long time and they will acquire their high energies by *multiple* interaction with the irregular magnetic field of the gas. The mechanism proposed by Fermi[12] represents a specific model where the magnetohydrodynamic field takes the form of statistical motions of individualized gas clouds. If from the above figures we compute the energy density of the galactic medium, it is found to be slightly in excess of 10^{-13} erg/cm^3. Given the roughness of the data, this is very close to the energy density of the cosmic radiation estimated[14] as 10^{-12} erg/cm^3. It is likely, therefore, that the cosmic radiation is nearly in dynamical equilibrium with the galactic magnetic fields and hence also with the motions of the gas, a conclusion which has been reached by a number of previous authors.[17]

[12] E. Fermi, Phys. Rev. **75**, 1169 (1949).
[13] K. McDonald, Am. J. Phys. (to be published).
[14] L. Biermann, Ann. Rev. Nuclear Sci. **2**, 335 (1953).
[15] S. Chandrasekhar and E. Fermi, Astrophys. J. **118**, 113 (1953).
[16] E. N. Parker, Astrophys. J. (to be published).
[17] *Note added in proof.*—See also the recent paper by Morrison, Albert, and Rossi, Phys. Rev. **94**, 440 (1954).

Electron Straggling in Thin Foils*

E. T. HUNGERFORD,† *Physics Department, University of Tennessee, Knoxville, Tennessee*

AND

R. D. BIRKHOFF, *Oak Ridge National Laboratory, Oak Ridge, Tennessee, and Physics Department, University of Tennessee, Knoxville, Tennessee*

(Received March 18, 1954)

A recent experimental investigation of electron straggling distributions reports disagreement with the distribution half-widths of the Landau-Blunck-Leisegang theory. Additional experimental work has been performed in which the angle of incidence of radiation on the foil has been more carefully controlled and a different method of comparison of theory and experiment has been employed. Discrepancies noted in the previous work with light elements are no longer found.

INTRODUCTION

THE theory of the processes by which electrons lose energy in penetrating matter has been reviewed recently.[1] In general, the energy distributions obtained by allowing a monoenergetic electron beam to impinge on a foil and then examining the resultant radiation with a beta spectrometer have agreed well with the theories of Landau[2] and Blunck-Leisegang[3] as regards the displacement of the peak of the distribution, i.e., the most probable energy loss. The shapes and, in particular, the widths of the distributions at half-maximum have also been measured and here the agreement has been less certain. Such measurements are critically dependent on at least three considerations: the energy spread of the initial radiation must be small compared to the spread obtained after passage of the beam through the foil; such initial variation in energy as does exist must be carefully taken into account before theory and experiment are compared; the geometry of the source-foil arrangement must be such as to insure that electrons which have suffered large-angle scatterings are not counted.

In the present work the above three factors have been carefully considered in the design of source-foil geometry and in the treatment of the data.

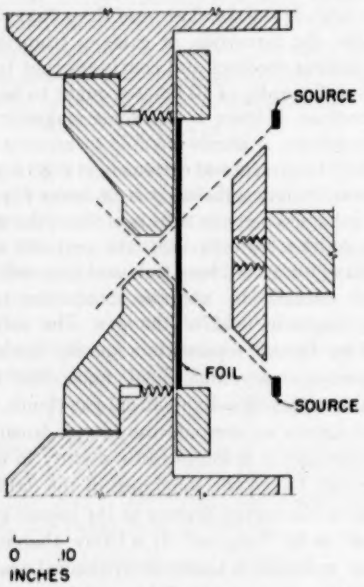

FIG. 1. Cross-sectional view of source and foil geometry.

APPARATUS

The spectrometer used has been described previously.[1] In the preceding experiment the approximately monoenergetic radiation from the K-conversion line of Cs^{137} was allowed to strike the foil through an angular range from 0 to 90°, whereas only the radiation leaving at $45°\pm0.8°$ was accepted by the spectrometer. The source foil geometry in the present experiment is shown in cross section in Fig. 1. Calculations show that the angles of incidence with this arrangement lie between 45° and 55° with the exit angles defined as before. The new system possesses the additional advantage that the radiation must pass through a circular aperture of size calculated from the spectrometer theory[4] before entering the spectrometer, thus eliminating any ambiguity in the size of the source disk as seen by the spectrometer. That is, in the first experiment scattering of radiation in the foil could have been equivalent to a larger source due to the finite distance between source and foil. It will be noted from Fig. 1 that an annular ring source is required with the new arrangement. Source and backing thicknesses were such that the incident distribution had a momentum width of 0.98 percent, 0.98 percent, and 1.9 percent for the three sources used. These compare rather unfavorably with the theoretically obtainable resolution of 0.1 percent,

* Submitted by E. T. H. in partial fulfillment of the requirements for the degree, Doctor of Philosophy, at the University of Tennessee.

† Now with Shell Development Company, Houston, Texas.

[1] F. Kalil and R. D. Birkhoff, Phys. Rev. **91**, 505 (1953).

[2] L. Landau, J. Phys. (U.S.S.R.) **8**, 201 (1944).

[3] O. Blunck and S. Leisegang, Z. Physik **128**, 500 (1950).

[4] J. W. M. DuMond, Rev. Sci. Instr. **20**, 160, 616 (1949).

but the large source thicknesses were necessary to provide sufficient activity to permit reasonable counting rates on the energy loss distributions.

CALCULATIONS

The data as taken from the spectrometer consisted of a table of count rate minus background *versus* magnet current for the initial distribution, and for the energy loss distribution. Both curves were converted to energy distributions and plotted against energy.

Next the Blunck-Leisegang distribution was plotted against energy under the assumption of a monoenergetic incident beam. This distribution was then integrated numerically over the incident distribution and plotted, the integration being greatly simplified because the Blunck-Leisegang curve shape is essentially independent of a small variation in the incident beam energy. That is, the only effect of varying the incident energy was to shift the Blunck-Leisegang curve along the energy axis without altering its shape.

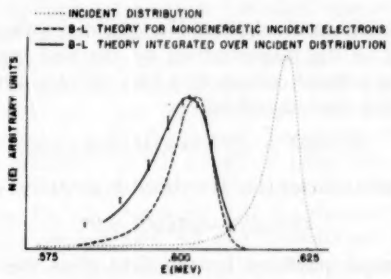

FIG. 2. Theoretical and experimental straggling distributions for 15.1 mg/cm² aluminum foil.

The experimental data were then compared with the integrated theoretical distribution. In the case of the very thick foils (−50 mg/cm²) the *L*-conversion line straggling distribution was calculated by reducing all ordinates in the experimental straggling curve by the *K*- to *L*-conversion ratio and shifting the curve upward in energy an amount equal to the difference in *K*- and *L*-binding energies. The resultant curve was added to the theoretical integrated distribution, whereupon comparison with experiment was made.

This method of treating the data differs considerably from that used previously, wherein the incident distribution was considered to be a Landau distribution and the foil thickness necessary to give this curve was added to the actual foil thickness. Unfortunately, the initial energy distribution could not be approximated very well by a Landau curve so this calculation method was abandoned in favor of the one above.

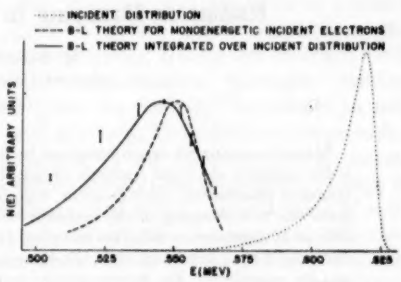

FIG. 3. Theoretical and experimental straggling distributions for 54.5 mg/cm² aluminum foil.

RESULTS

Principal disagreement with theory was found previously for the light elements. A typical straggling distribution for aluminum is shown in Fig. 2 as representative of the data taken with restricted angles of incidence and calculated as indicated. Given are the initial distribution, the theory assuming monoenergetic incident energy, this theory integrated over the initial distribution, and the experimental data. The foil thickness specified is the actual thickness multiplied by $\sqrt{2}$ to account for the oblique angles of incidence and of departure from the foil. Similar agreement between experiment and theory was found for the following foils: Al, 28.2 mg/cm²; Cu, 11.9, 28.0 mg/cm²; Ag, 14.8, 31.0 mg/cm²; Au, 29.0 mg/cm².

Figure 3 illustrates the departure from theory obtained when foil thickness is increased beyond the value permitted by the theory which neglects scattering and assumes that the cross section for a given energy loss in a single encounter is independent of the variation in energy of the electron as it passes through the foil. Agreement is still found for the high-energy side of the distribution, whereas there are many more low-energy electrons than predicted by the theory. Curves similar to this were found for Cu, 56.5 mg/cm²; and Au, 51.3 mg/cm². It is thought that the large increase in path length due to multiple scattering of the electrons in these thick foils is primarily responsible for the disagreement between theory and experiment in these cases.

CONCLUSIONS

Straggling distributions have been measured for a number of foils of various thicknesses and atomic numbers, and these distributions have been compared with the Landau-Blunck-Leisegang theory integrated over the initial energy distribution. Agreement within experimental error is found in all cases where foil thickness is kept within the limits set by the theory.

Radiation Damping in Magnetic Resonance Experiments

N. BLOEMBERGEN AND R. V. POUND
Harvard University, Cambridge, Massachusetts
(Received March 22, 1954)

Magnetic resonance experiments can be described by analogy to a coupled pair of circuits, one of which is the ordinary electrical resonant circuit. The other circuit is formed by the rotating magnetization. For transient phenomena, such as occur, e.g., in the pulse techniques of free nuclear induction, the coupling gives rise to a damping of the magnetic resonance by the electric circuit. Such damping can also be considered as spontaneous radiation damping. It is shown that in certain cases of nuclear induction this radiation damping is more important than the damping from the spin-spin and the spin-lattice relaxation mechanisms usually considered. For ferromagnetic materials at microwave frequencies the radiation damping can become very large.

I. FREE MAGNETIC INDUCTION

BY way of introduction, consider a system of volume V with a uniform macroscopic magnetization per unit volume $\mathbf{M}_0$, which precesses with an angular frequency

$$\omega_0=\gamma H_0=g\beta h^{-1}H_0 \tag{1}$$

around a constant magnetic field H_0, parallel to the z axis. Here g is the gyromagnetic ratio, β the Bohr magneton. The angle between $\mathbf{M}_0$ and $\mathbf{H}_0$ is θ_0. Assume that the magnetization can precess freely, $M_x=M_0\cos\theta\sin\omega t$, $M_y=M_0\cos\theta\cos\omega t$, and $M_z=M_0\sin\theta$ and neglect for the time being any internal damping of the magnetic system. When we introduce a pickup coil, tuned by a condenser to the frequency ω_0, in the x-y plane, a periodic voltage is induced in this coil by the precessing magnetization. If the coil has n turns of cross section A, this induction signal is given by

$$V_s=-nA\eta\frac{4\pi}{c}\frac{dM_x}{dt}=nA\frac{4\pi\omega}{c}\eta M_0\sin\theta\cos\omega_0 t, \tag{2}$$

where η is a filling factor, equal to unity if the coil is completely immersed in the magnetic material, or otherwise

$$\eta=\frac{\int\mathbf{M}\cdot(\mathbf{H}_c/i_c)dV}{\mathbf{M}_0\cdot\int(\mathbf{H}_c/i_c)dV}, \tag{3}$$

where $\mathbf{M}$ is the magnetic moment per unit volume and $\mathbf{M}_0$ its average value, allowing the extension to a sample of nonuniform magnetization. Each point in the integration over the space coordinates is weighted by the field $\mathbf{H}_c/i_c$ which a unit current through the coil would produce at that point.

A current in phase with the induced voltage will flow in the tuned circuit, and the Joule heat dissipated per unit time is $V_s^2/2R$. The energy source which generates this power is the magnetic energy of the magnetized sample in the field H_0. The energy of the permanent magnet $\mathbf{M}_0V$ is

$$W=M_0VH_0(1-\cos\theta). \tag{4}$$

As the current flows the angle θ will gradually decrease to zero. The equation of motion can be written as the requirement of conservation of energy,

$$dW/dt=M_0VH_0\sin\theta(d\theta/dt)=V_s^2/2R. \tag{5}$$

The motion can also be found by considering the torque exerted on the magnetization by the field connected with the induced current. In a long coil of n turns over a length l, the induced field is

$$H_x=4\pi V_s n/clR=4\pi\eta QM_0\sin\theta\cos\omega_0 t.$$

The quality factor Q of the circuit is given by

$$Q=\omega L/R=\omega 4\pi n^2A/Rlc^2.$$

The torque produced by this field gives rise to the equation of motion:

$$dM_z/dt=-\gamma M_yH_x,$$

or

$$d\theta/dt=-2\pi\eta M_0Q\gamma\sin\theta. \tag{6}$$

Equation (5) can easily be reduced to this same form. The solution of Eq. (6) for the special case that $\theta=\pi/2$ at $t=0$ is

$$\tan(\tfrac{1}{2}\theta)=\exp(-2\pi M_0Q\eta\gamma t), \tag{7}$$

and the amplitude of the induction signal Eq. (2) decreases proportional to $\operatorname{sech}(2\pi M_0Q\eta\gamma t)$. A damping time constant due to the reaction of the induced field on the magnetization can be defined as

$$\tau_R=(2\pi\eta M_0Q\gamma)^{-1}. \tag{8}$$

Suryan[1] has first called attention to the importance of this type of damping without giving a detailed quantitative discussion. We shall give the pertinent circuit equations, from which the above result can be derived as a special case, in the next section. The relation of this damping to magnetic relaxation processes will be discussed in a final section, where, also, a comparison will be made with the natural line width of optical spectral lines. This radiation damping has an

[1] G. Suryan, Current Sci. (India) **18**, 203 (1949).

appreciable magnitude because of the coherence between the individual spins producing the magnetization. These coherence effects have been discussed from a fundamental quantum mechanical point of view by Dicke.[2] The fact that it is possible by radiospectroscopy techniques to produce states with definite coherent phase relations between the individual elements, allows for a classical discussion of the problem in terms of one macroscopic magnet as first introduced by Bloch[3] in his classical theory of nuclear induction. We shall illustrate now with a few examples that the damping described by Eq. (8) is frequently not negligible.

a. The Proton Resonance in Water in a Field of 7000 gauss

In thermal equilibrium the protons acquire a magnetization per unit volume in this field given by

$$M_0=\chi_0 H_0=[N_0\gamma^2\hbar^2 I(I+1)/3kT]H_0,$$

where χ_0 is the nuclear paramagnetic volume susceptibility. At room temperature the static magnetization is about 2×10^{-6} oersted in a field of 7000 oersteds. A short radiofrequency pulse[4,5] at the resonance frequency and of amplitude H_{rf} and duration t such that $\gamma H_{rf}t=\frac{1}{2}\pi$, will turn this magnetization into the plane perpendicular to H_0. A coherent "superradiant" state is thus produced. At the end of the pulse free nuclear induction will occur which is damped in a time τ_R given by Eq. (8). Assuming that the resonant circuit has a $Q=100$ and $\eta=1$, we find $\tau_R=0.03$ sec. This is much shorter than the damping from spin-spin and spin-lattice relaxation mechanisms in pure water. The fact that spin-echo pulses can be obtained after times much longer than τ_R is explained by the absence of this radiation damping when the nuclear spins are out of phase in the inhomogeneous field. To make the radiation per echo negligible the inhomogeneity ΔH should satisfy the inequality $\gamma\Delta H\tau_R\gg1$. This allows detection of fine structures with separations much smaller than the inverse damping time given by Eq. (8).

When the initial magnetization is reversed by a 180° pulse, an unstable radiationless state is established. The magnetization will change only due to the spin-lattice relaxation mechanism, the angle θ remaining 180°.

b. The Proton Resonance in Water in the Earth's Magnetic Field

Recently Packard and Varian have observed the proton resonance in the earth's field at 2185 cps.[6] The radiant state was produced by magnetizing the sample in a field H_0' of about 100 gauss perpendicular to the earth's field. The field H_0' is reduced to a field H_0'' of a few gauss in a time short compared to the spin lattice relaxation time. During this adiabatic demagnetization the magnetization $M_0=\chi_0 H_0'$ remains unchanged. Then the field H_0'' is reduced to zero in a time t' such that $\gamma H_0''t'\ll1$. During this process, which is nonadiabatic in the Ehrenfest sense, the magnetization vector has no time to reorient. Thus, a radiant state is constructed with a magnetization $M_0\approx3\times10^{-8}$ oersteds precessing with a frequency of 2185 cps in the plane perpendicular to the earth's field. The radiation damping time τ_R, assuming $\eta=1$, is about $200Q^{-1}$ sec. For sufficiently high Q, this could explain the observation that the duration of the signal was shorter than the known relaxation times in pure water. It is interesting to note that in this sense a spectral line in the audiofrequency range of the electromagnetic spectrum has a "natural width."

c. A Small Ferrite Sphere in a Microwave Cavity

Assume that a ferrite with a volume magnetization of 300 gauss cm^{-3} has a g value equal to that of a free electron and is placed in a cavity with $Q=2000$. For a sphere of 0.2 mm in diameter in a cavity of 10 cc, the filling factor η is of the order of 10^{-6}. Then we find that τ_R 10^{-8} sec. This time is inversely proportional to the filling factor or roughly to the volume of the ferrite sample.

It seems as if the radiation damping would be able to broaden the line so much as to wipe out the resonance completely for larger spheres. When the time τ_R becomes shorter than the characteristic time of the electrical circuit Q/ω, the analysis of this introductory paragraph is not valid. We shall therefore proceed with a more accurate description of the coupling.

II. THE COUPLING BETWEEN THE RESONANT CIRCUIT AND THE MAGNETIZATION

The equations of motion describing the complete system consisting of the magnetic material in a constant field H_0 in the z direction and two crossed coils parallel to the x and y direction, respectively, are

$$\frac{dM_{x,y}}{dt}=\gamma(\mathbf{M}\times\mathbf{H})_{x,y}-\frac{M_{x,y}}{T_2},$$

$$\frac{dM_z}{dt}=\gamma(\mathbf{M}\times\mathbf{H})_z-\frac{M_z-M_0}{T_1},$$

$$-K_x\frac{dM_x}{dt}+L_x\frac{di_x}{dt}+R_x i_x+\frac{1}{C_x}\int i_x dt=V_{x,\text{app}},$$

$$-K_y\frac{dM_y}{dt}+L_y\frac{di_y}{dt}+R_y i_y+\frac{1}{C_y}\int i_y dt=V_{y,\text{app}},$$

$$H_x=K_x' i_x,\quad H_y=K_y' i_y,\quad H_z=H_0.$$

[2] R. H. Dicke, Phys. Rev. **93**, 99 (1954).
[3] F. Bloch, Phys. Rev. **70**, 460 (1946).
[4] E. L. Hahn, Phys. Rev. **80**, 580 (1950); **88**, 1070 (1952).
[5] H. Y. Carr, and E. M. Purcell, Phys. Rev. **94**, 630 (1954).
[6] M. Packard and R. Varian, Phys. Rev. **93**, 941 (1954).

In general there are five simultaneous nonlinear differential equations connecting the three components of magnetization and the two currents. The first three equations are the familiar Bloch equations.[3] The transverse field components H_x and H_y are now, however, related to the magnetization by the last two equations and must not be considered as impressed constants. The phenomenological damping terms for the spin-spin and spin-lattice relaxation are responsible for the fact that the magnetization has now in general not a constant magnitude M_0. Frequently there will be only one coil, and the number of equations is consequently reduced by one. In writing the relations between the transverse components of the field and the currents we have assumed that demagnetizing and anisotropy fields are zero. The K and K' are geometrical factors. They are related to each other by $KK'=4\pi L\eta$. The symmetrical arrangement of two crossed coils with identical circuit constants has the advantage that rotating fields can be produced. If the x and y components of the driving force are the real and imaginary parts of one complex function $V_{\text{app}}{}^{+}=V_{x,\text{app}}+jV_{y,\text{app}}$ the solutions for $M^{+}=M_x+jM_y$, $i^{+}=i_x+ji_y$ can be found from a set of only three differential equations:

$$-K\frac{dM^{+}}{dt}+L\frac{di^{+}}{dt}+Ri^{+}+\frac{1}{C}\int i^{+}dt=V_{\text{app}}{}^{+}, \tag{9}$$

$$\frac{dM^{+}}{dt}=-j\gamma M^{+}H_0-\frac{M^{+}}{T_2}-j\gamma M_xK'i^{+}, \tag{10}$$

$$\frac{dM_x}{dt}=\text{Im}(\gamma K'M^{+*}i^{+})-\frac{M_x-M_0}{T_1}. \tag{11}$$

We first give the steady-state solution, when the circuit is driven by a harmonic rotating potential $V_{x,\text{app}}+jV_{y,\text{app}}=V_{\text{app}}\exp(-j\omega t)$. A solution with $dM_x/dt=0$ and the other components varying with the frequency ω is obtained, $M^{+}=M_1\exp(-j\omega t)$, $i^{+}=i\exp(-j\omega t)$.

$$M_x=\frac{1+(\Delta\omega T_2)^2}{1+(\Delta\omega T_2)^2+\gamma^2H_1{}^2T_1T_2}M_0, \tag{12}$$

$$M_1=\chi H_1=\chi K'i=-\frac{j|\gamma|M_xT_2}{1+j(\omega_0-\omega)T_2}K'i, \tag{13}$$

$$i=[j\omega L(1+4\pi\eta\chi)+R+(j\omega C)^{-1}]^{-1}V_{\text{app}}. \tag{14}$$

This solution is identical with those usually given for the stationary state.[7] The effect of the rotating magnetization can be described by a complex susceptibility χ. The over-all impedance of each circuit is given by the expression between square brackets in Eq. (14). There is no additional radiation damping of the magnetic resonance in this case. The z component of the magnetization is constant. The generator supplies a current which exactly balances the effect of the radiation damping. The steady-state response of a circuit should be analyzed in terms of the impedance given by Eq. (14). Under suitable steady-state conditions it is possible to resolve fine structure lines of nuclear magnetic resonance in liquids which are only a few cycles apart, although these lines under conditions of free nuclear induction would be damped in a time short compared to their inverse spacing. The same situation prevails in ferromagnetic resonance experiments. Ordinary resonance lines are observed under steady-state conditions, although the freely precessing magnetization would radiate with a time short compared to the inverse line width.

The expression for the impedance for small H_1, allowing M_z to be taken equal to M_0, can be seen to be identical to that of a double tuned coupled circuit. It is therefore apparent that a condition of critical or more than critical coupling can be established and that a resonance detector that uses the electrical circuit as the frequency determining element of oscillation[8] is subject to frequency pulling in a discontinuous manner, sometimes called a "drag link" effect.

For transient phenomena the Eqs. (10) and (11) for the magnetization cannot be considered independently from the circuit Eq. (9). The solution in the introductory section is obtained as an approximation by dropping the last two terms in Eq. (10) and the last term in Eq. (11). The damping time τ_R is found to be half as long as given by Eq. (8) because of the presence of two crossed coils creating a rotating reaction field.

A general solution cannot be obtained since nonlinear terms containing products M_xi^{+} and $M^{+*}i^{+}$ occur. For small values of θ, we can, however, replace M_z in Eq. (10) by M_0. Equations (9) and (10) then represent two coupled linear circuits. In the absence of a driving force we obtain a third degree equation for the proper frequencies of the system. If we assume that the electric circuit is tuned to the precession frequency of the magnetization $\omega_0{}^2LC=\gamma^2H_0{}^2LC=1$ and neglect terms of the order $\Delta\omega/\omega_0$, we obtain a quadratic equation for the complex proper frequencies $\omega=\omega_0+\Delta\omega$ of the system, with the solution

$$\Delta\omega=\frac{j}{2}\left(\frac{\omega_0}{2Q}+\frac{1}{T_2}\right)\pm\left\{-\frac{1}{4}\left(\frac{\omega_0}{2Q}+\frac{1}{T_2}\right)^2+\frac{\omega_0}{Q}\left(\frac{1}{\tau_R}+\frac{1}{T_2}\right)\right\}^{\frac{1}{2}},$$

where τ_R is given by Eq. (8).

For negligible spin-spin damping, we can consider the following two limiting cases:

Case I, $1/\tau_R\ll\omega_0/Q$. The solutions are $\Delta\omega=j\omega_0/2Q$ or $\Delta\omega=2j/\tau_R$. The first solution corresponds to the damping of the mode with the electric circuit excited,

[7] N. Bloembergen, thesis, Leiden, 1948.

[8] R. V. Pound and W. D. Knight, Rev. Sci. Instr. **21**, 219 (1950).

the second to the damping of the magnetization. This last solution corresponds to the examples of nuclear induction of Sec. I. In example **b** there is no current flowing at $t=0$. We must take a linear combination of the two solutions, and initially no damping. Only after a time Q/ω_0 when the electric circuit has been excited, is the damping given by the characteristic time τ_R.

Case II, $1/\tau_R \gg \omega_0/Q$. The solutions are now

$$\Delta\omega \approx j\omega_0/4Q \pm (\omega_0/Q\tau_R)^{\frac{1}{2}}.$$

The energy swings back and forth between the electric circuit and the magnet system with a frequency $(\omega_0/Q\tau_R)^{\frac{1}{2}}$ until the energy is eventually dissipated in the resistance of the electric circuit. This situation can be realized by ferrites in a microwave cavity. The energy is never dissipated faster than is permitted by the Q of the cavity,[9] so long as $1/T_2$ is negligible. It is quite possible, however, that the magnetization of the ferrite at the end of a microwave pulse will return to its position parallel to H_0 in a time short compared to both relaxation times T_1 and T_2. This observation does not alter the interpretation of the data in reference 9 since the relaxation times were evaluated from the power absorbed in the steady-state existing for the duration of the microwave pulse. The relaxation times thus obtained are independent of the size of the sample or the filling factor.

In the third mode of the system $\omega \approx -\omega_0$, the electrical circuits are excited at the same frequency but produce a field rotating in the opposite direction. This mode is only very slightly perturbed by the presence of the magnetization.

III. SPONTANEOUS EMISSION AND THERMAL RELAXATION MECHANISMS

The transition probability for spontaneous emission of a quantum $h\nu=\gamma hH_0$ by a single spin $I=\frac{1}{2}$ is given by the well-known formula of radiation theory,[10]

$$W=16\pi^3\gamma^2 h\nu^3 c^{-3}. \tag{15}$$

Substituting numerical values, we find for the lifetime of a single free proton in a field of 10^4 oersted the astronomical value $T_1=10^{25}$ sec. In the earth's magnetic field the lifetime against spontaneous radiation would be $T_1 \approx 10^{38}$ sec. How can this result be consistent with the radiation damping of the order of one second calculated in Sec. I? This discrepancy is resolved by considering two factors. One is the coherence which exists between the individual proton spins, the other is the increase in the density of the radiation field in the tuned circuit over that in free space.[11]

In the situation of interest, the spins of protons have such phase relations that they create a macroscopic magnetic dipole which is N times as large as that of a single one. Since the emitted radiation is proportional to the square of the dipole moment, the transition probability is increased by a factor N^2. Dicke[2] has given a quantum mechanical analysis of the coherent state and also arrives at this result. The damping is, however, not increased simply by a factor N^2, but by a factor N. The quantum levels of our macroscopic system are all equally spaced. We must not consider a single transition but the damping of an N-fold excitation with coherence between all possible transitions. The same problem arises in calculating the lifetime of an excited harmonic oscillator.[12] Classically, the factor N is immediately obvious, as the radiation rate is proportional to N^2 and the stored energy proportional to N. The factor N is related to the magnetization introduced earlier by

$$N=M_0V_m/\gamma h. \tag{16}$$

Here V_m is the volume of sample.

The magnetic radiation density in the coil of volume V_c of a resonant circuit is increased over the density in free space by a factor

$$Q\lambda^3/8\pi^2V_c. \tag{17}$$

Note that this factor increases with increasing wavelength, cancelling the decrease predicted by Eq. (15). Multiplying Eq. (15) by Eqs. (16) and (17) we find a radiation damping time τ_R which is identical with Eq. (8), provided we multiply by a factor $\frac{1}{2}$ to take account of the fact that only one of the two circularly polarized modes in the coil is effective.

The interaction of a single spin with a thermal radiation field leads to induced emission and absorption. The transition probability for these processes is obtained by multiplying Eq. (15) by the Bose-Einstein factor,

$$[\exp(h\nu/kT)-1]^{-1} \approx kT/h\nu \gg 1, \tag{18}$$

for the frequency range of interest in magnetic resonance. The damping for the radiation from a single spin is consequently increased by this rather large factor.[13]

This factor should, however, not be added to Eq. (8). The influence of the thermal radiation field in the case of coherent spins in a resonant circuit can best be discussed in a classical manner. The classical analog of the magnetic thermal radiation field is the field produced in the coil by the thermal noise current $i(t)$. This current produces a fluctuating torque on the magnetization, leading to the equation of motion:

$$d\theta/dt=\gamma H_{th}(t). \tag{19}$$

Since $\langle H_{th}(t)\rangle_{Av}=0$, there is on the average no change in θ, due to the noise current. There are only fluctuations

[9] N. Bloembergen and S. Wang, Phys. Rev. **93**, 72 (1954).
[10] W. Heitler, *Quantum Theory of Radiation* (Oxford University Press, London, 1943).
[11] E. M. Purcell, Phys. Rev. **69**, 681 (1946).
[12] V. Weisskopf and E. Wigner, Z. Physik **65**, 18 (1931).
[13] V. Weisskopf, Z. Physik **34**, 1 (1933).

in θ. The mean square deviation of θ after a time t' is

$$\langle \theta_{t'}{}^2 \rangle_{Av} = \gamma^2 t' \left\langle \int_0^\infty H_{1k}(t) H_{1k}(t+t'') dt'' \right\rangle_{Av}$$

$$= \gamma^2 \langle H_{1k}{}^2 \rangle_{Av} \frac{L}{R} t' = \gamma^2 \frac{L}{R} \frac{4\pi kT}{V_c} t'.$$

The average rate of change in the stored energy due to the interaction with the thermal noise field is

$$\langle (dW/dt)_{\text{noise}} \rangle_{Av} = \tfrac{1}{2} M_0 V H_0 \cos\theta (d\langle\theta^2\rangle_{Av}/dt)$$

$$= 2\pi kT \gamma Q \eta M_0 \cos\theta, \quad (20)$$

and the average thermal damping is consequently

$$\left\langle \frac{1}{\tau_{1k}} \right\rangle_{Av} = 2\pi\gamma Q M_0 \frac{kT}{M_0 H_0 V_c} \frac{\cos\theta}{(1-\cos\theta)}. \quad (21)$$

Apart from the angular dependence, this is smaller than Eq. (8) by a factor equal to the thermal energy kT over the total magnetic energy of the system. It is very small for a large coherent magnetization, but reduces properly to the result of increased damping for an individual spin. One might put the result Eq. (21) in words by saying that there is no coherence between the rotating magnetization and the thermal field, while there is between the rotating magnetization and its own reaction field.

The relaxation or damping discussed here refers only to the approach to equilibrium energy of orientation of the classical precessing magnet that corresponds to the given coherent state. Changes in the over-all magnetization of the system that lead toward a true equilibrium state of magnetization can only occur through the mechanisms leading to T_2 and thus cannot occur in times shorter than T_2. Thus, a spin temperature is defined only after the time T_2, the spin-spin relaxation time, has elapsed. It is not correct to say that after a radiofrequency pulse which has turned the magnetization through an angle between 90° and 180°, the spin system has assumed a negative temperature. Immediately after the pulse there are certain phase relations between the spins, which change to a situation of internal thermal equilibrium[14] only after a time T_2. The radiation processes which do not change the coherence relations among the spins, do not contribute to the spin-spin relaxation mechanism.

A significant remark may be made about the conditions under which τ_R may be expected to be as short as T_2. In a rigid lattice, T_2 is of the order of magnitude of $r^3/\gamma^2\hbar$ where r is the interspin distance. Since r^3 is approximately $1/N_0$, for magnetization described by Curie's law, $(\tau_R/T_2) \sim kT/\omega\hbar\eta Q$. Thus, unless ηQ is quite large, only under the condition $\omega\hbar \gtrsim kT$, leading to saturation magnetization, would $\tau_R \lesssim T_2$. The liquid narrowing, in the example of proton resonance, and the exchange effect, in the ferromagnetic case, are essential to the presence of a significant radiative effect.

Finally, we wish to stress the fact that a coherently radiating state can only be produced after a certain macroscopic magnetization has been established. It is still necessary that a relaxation mechanism produces a thermal distribution over the various energy levels of the individual spins, which are initially incoherent. A homogeneous magnetic field, such as exists in the coil and in general in a system which has dimensions small compared to the wavelength of the radiation, will never produce the initial thermal relaxation. The Hamiltonian for the interaction energy with a homogeneous magnetic field commutes with the total angular momentum or magnetization of the sample, which is therefore a constant of the motion. Radiation damping discussed in this paper does therefore not represent a spin-lattice relaxation mechanism in the usual sense. To establish a magnetization in thermal equilibrium with the surroundings, the inhomogeneous internal or local fields[7] are essential. The inhomogeneity of the rf field in the coil was explicitly taken into account in the definition of the filling factor η. This results in a complication that the total magnetization is not rigorously a constant of the motion. The gist of the statement, however, that the radiation field in the coil does not provide a microscopic thermal relaxation mechanism is still valid.

[14] E. M. Purcell and R. V. Pound, Phys. Rev. **81**, 279 (1951).

Thermomagnetic Properties of Thin Metallic Films*

F. J. BLATT
Department of Physics, University of Illinois, Urbana, Illinois
(Received March 15, 1954)

The calculation of Sondheimer on the galvanomagnetic effects in thin metallic films is extended so as to permit the evaluation of the Nernst, Ettinghausen, and Leduc-Righi coefficients (A_N, A_E, A_L). It is assumed that the conduction electrons are quasi-free and that a relaxation time exists. General expressions are derived for A_N, A_E, and A_L and the asymptotic forms are given in the limit of the ratio of film thickness to mean free path much less than unity. As this ratio approaches zero, A_N and A_L vanish whereas A_E becomes infinite.

I. INTRODUCTION

FUCHS,[1] in 1938, calculated the electrical conductivity of thin metallic films, assuming that the electrons behave as though free and that a relaxation time existed for the bulk metal. Sondheimer[2] extended the calculation of Fuchs to the case in which the film is introduced into a magnetic field whose direction is normal to the plane of the film. These calculations assumed vanishing temperature gradients, a situation rarely achieved in practice, and it is, therefore, of interest to extend the work to include the nonisothermal cases. A generalization of Fuch's calculation in this direction has been carried out by Justi, Kohler, and Lautz.[3] In the present paper a similar generalization of Sondheimer's work is carried out. In Sec. II we give the Boltzmann equation and its solution for conduction electrons in a thin film which is in electric and thermal gradients in the plane of the film and in a magnetic field normal to the plane of the film. In Sec. III the general expressions for the electric and thermal currents are obtained. The expressions for A_L, A_N and A_E are given in Sec. IV together with the simplified forms which one obtains in the limits of vanishing magnetic field and very thin films (i.e., film thickness much less than the mean free path of conduction electrons). The derived expressions are for diffuse surface scattering. The extension to partially specular surface scattering is straight-forward and is very briefly indicated.

II. THE BOLTZMANN EQUATION AND ITS SOLUTIONS

We consider a metallic film of thickness a with surfaces parallel to the xy plane. We shall assume that the conduction electrons in the metal are quasifree in the sense that the energy ϵ is related to the wave vector $\mathbf{k}$ through

$$\epsilon=(\hbar^2|\mathbf{k}|^2)/2m^*=(m^*|\mathbf{v}|^2)/2,$$

where m^* is the effective mass and $\mathbf{v}$ is the velocity of the conduction electrons.

Let the distribution function of the conduction electrons be

$$f(\mathbf{r},\mathbf{v})=f_0(x,y,v)+f_1(z,\mathbf{v}). \tag{1}$$

In (1), f_0 is the Fermi distribution function

$$\{\exp[(\epsilon-\epsilon')/kT]+1\}^{-1}$$

which in the case of nonvanishing temperature gradients $\partial T/\partial x$ and $\partial T/\partial y$ is a function of position. The distribution function of conduction electrons in an external electric field $(E_x,E_y,0)$ and an external magnetic field $(0,0,H)$ is given by (1). To obtain the steady-state distribution one must solve the Boltzmann equation

$$-(e/m^*)[\mathbf{E}+(\mathbf{v}\times\mathbf{H})/c]\cdot\mathrm{grad}_v f+\mathbf{v}\cdot\mathrm{grad}_r f=-(f-f_0)/\tau, \tag{2}$$

where e is the absolute value of the electronic charge and τ is the relaxation time.

If second-order terms are neglected, (2) can be put into the form

$$\frac{\partial f_1}{\partial z}+\frac{f_1}{\tau v_z}-\frac{\mu}{v_z}\left(v_y\frac{\partial f_1}{\partial v_x}-v_x\frac{\partial f_1}{\partial v_y}\right)=\frac{e}{m^*v_z}\left(E_x\frac{\partial f_0}{\partial v_x}+E_y\frac{\partial f_0}{\partial v_y}\right)-\frac{v_x}{v_z}\frac{\partial f_0}{\partial x}-\frac{v_y}{v_z}\frac{\partial f_0}{\partial y}, \tag{3}$$

where $\mu=(eH/m^*c)$.

We assume a solution of the form

$$f_1=(v_xc_1+v_yc_2)\partial f_0/\partial v, \tag{4}$$

and obtain

$$\partial g/\partial z+g/\tau v_z+i\mu g/v_z=e\mathcal{E}/m^*vv_z+Q\mathcal{T}/m^*vv_z, \tag{5}$$

where

$$g\equiv c_1-ic_2,\quad \mathcal{E}\equiv E_x-iE_y,\quad \mathcal{T}\equiv\frac{\partial T}{\partial x}-i\frac{\partial T}{\partial y},$$

$$Q=\frac{\epsilon'}{T}+T\frac{d}{dT}\left(\frac{\epsilon'}{T}\right).$$

Equation (5) is identical to Eq. (7) of Sondheimer's paper[2] except for the additional term $Q\mathcal{T}/m^*vv_z$. The

* Work supported by U. S. Department of Naval Research.
[1] K. Fuchs, Proc. Cambridge Phil. Soc. **34**, 100 (1938).
[2] E. H. Sondheimer, Phys. Rev. **80**, 401 (1950).
[3] Justi, Kohler, and Lautz, Z. Naturforsch. **6a**, 544 (1951).

solution of (5) is

$$g=\frac{\tau}{(1+i\mu\tau)m^*v}[e\mathcal{E}+Q\mathcal{T}]$$
$$\times\{1+F(\mathbf{v})\exp[-(1+i\mu\tau)z/\tau v_z]\}, \quad (6)$$

where $F(\mathbf{v})$ is an arbitrary function of v and v_z and is determined by the boundary conditions at the surfaces of the film. The boundary conditions which are used depend on the scattering at the film surfaces, and we shall assume that the scattering is entirely diffuse, so that the distribution function for the electrons leaving the surface must be independent of the direction of motion.[4] To fulfill these conditions we must have

$$F(\mathbf{v})=-1 \quad \text{for} \quad v_z>0;$$
$$F(\mathbf{v})=-\exp[(1+i\mu\tau)a/\tau v_z] \quad \text{for} \quad v_z<0. \quad (7)$$

Equations (4), (6), and (7) completely determine the correct steady-state distribution (1).

III. THE ELECTRIC AND THERMAL CURRENTS

Having obtained a solution of the transport equation, one can immediately write the expressions for the components of the electric and thermal currents, J_x, J_y and W_x, W_y.

$$J_x=-\frac{2e}{a}\left(\frac{m^*}{h}\right)^3\int_0^a\int v_z f dv dz=-\left(\frac{2\pi e}{a}\right)\left(\frac{m^*}{h}\right)^3$$
$$\times\int_0^a\int_0^\infty\int_0^\tau v^4\sin^3\Theta c_1\frac{\partial f_0}{\partial v}d\Theta dv dz, \quad (8)$$

$$W_x=\frac{m^*}{a}\left(\frac{m^*}{h}\right)^3\int_0^a\int v_z v^2 f dv dz=\frac{\pi m^*}{a}\left(\frac{m^*}{h}\right)^3$$
$$\times\int_0^a\int_0^\infty\int_0^\tau v^6\sin^3\Theta c_1\frac{\partial f_0}{\partial v}d\Theta dv dz. \quad (9)$$

The currents in the y direction are given by expressions identical to (8) and (9) except that v_x is replaced by v_y and c_1 by c_2. We follow Sondheimer and define complex currents

$$\mathcal{J}=J_x-iJ_y; \quad \mathcal{W}=W_x-iW_y.$$

Upon integration over Θ and z, and changing the variables of integration from v to ϵ, Eqs. (8), (9), and the corresponding expressions for J_y and W_y reduce to

$$\mathcal{J}=-Dea\left\{e\mathcal{E}R_1+\left[T\frac{d}{dT}\left(\frac{\epsilon'}{T}\right)\right]\mathcal{T}R_1 + (1/T)\mathcal{T}R_2\right\}, \quad (10)$$

$$\mathcal{W}=Da\left\{e\mathcal{E}R_2+\left[T\frac{d}{dT}\left(\frac{\epsilon'}{T}\right)\right]\mathcal{T}R_2+(1/T)\mathcal{T}R_3\right\}, \quad (11)$$

where $D=16\pi m^*/3h^3$ and

$$R_n=R_{nr}+iR_{ni}=\int_0^\infty \epsilon^n q(s)\frac{\partial f_0}{\partial\epsilon}d\epsilon. \quad (12)$$

In Eq. (12)

$$q(s)=[\phi(s)]^{-1}=\frac{1}{s}-\frac{3}{8s^2}+\frac{3}{2s^2}\int_1^\infty\left(\frac{1}{t^3}-\frac{1}{t^5}\right)e^{-st}dt, \quad (13)$$

$$q(s)=q_r(s)+iq_i(s), \quad \phi(s)=\phi_r(s)+i\phi_i(s),$$

and $s=(a/l)+i(a/r)=\kappa+i\beta$. Here l is the mean free path, $l=v\tau$, and r is the Larmor radius, $r=(m^*vc/eH)$.

From Eqs. (10) and (11) all the thermomagnetic effects may be derived. Since our interest is in metallic films, for which the conduction electron distribution is nearly completely degenerate, the Nernst, Ettinghausen and Leduc-Righi coefficients have been calculated using only the first nonvanishing terms of the well-known expansion[5] of integrals of the type of Eq. (12):

$$\int_0^\infty\gamma(\epsilon)\frac{\partial f_0}{\partial\epsilon}d\epsilon = -\left\{\gamma(\epsilon')+\frac{\pi^2}{6}(kT)^2\left[\frac{\partial^2\gamma}{\partial\epsilon^2}\right]_{\epsilon=\epsilon'}+\cdots\right\}. \quad (14)$$

IV. THE THERMOMAGNETIC EFFECTS

The defining equations for the Leduc-Righi (A_L), isothermal Nernst (A_N) and Ettinghausen (A_E) coefficients are

$$A_L\equiv-\mathrm{Im}(\mathcal{T})/H\,\mathrm{Re}(\mathcal{T}); \quad \mathcal{J}=\mathrm{Im}(\mathcal{W})=0, \quad (15)$$

$$A_N\equiv-\mathrm{Im}(\mathcal{E})/H\,\mathrm{Re}(\mathcal{T}); \quad \mathcal{J}=\mathrm{Im}(\mathcal{T})=0, \quad (16)$$

$$A_E\equiv-\mathrm{Im}(\mathcal{T})/H\,\mathrm{Re}(\mathcal{J}); \quad \mathrm{Im}(\mathcal{W})=\mathrm{Im}(\mathcal{J})=\mathrm{Re}(\mathcal{T})=0, \quad (17)$$

where Re and Im signify the real and imaginary parts, respectively, of the quantity in parenthesis.

From (15), (10), (11), and (14) one readily finds that

$$A_L=\frac{1}{H}\cdot\frac{q_i(s)}{q_r(s)}=-\frac{1}{H}\frac{\phi_i(s)}{\phi_r(s)}, \quad (18)$$

and making use of the relations derived by Sondheimer,[2]

$$\sigma/\sigma_0=\kappa/\phi_r(s), \quad A_H/A_{H0}=\phi_i(s)/\beta,$$

and the expression for the Leduc-Righi coefficient in the bulk metal, $A_{L0}=-\beta/\kappa H$, one obtains

$$\frac{A_L}{A_{L0}}=\frac{A_H}{A_{H0}}\cdot\frac{\sigma}{\sigma_0}. \quad (19)$$

The classical relation[6] $A_L=A_H\sigma$ is thus seen to be valid also for thin films.

[4] The extension to partially specular surface scattering imposes no essential difficulties and is indicated at the end of Sec. IV.

[5] F. Seitz, *Modern Theory of Solids* (McGraw-Hill Book Company, Inc., New York, 1940), p. 148.

[6] A. Sommerfeld and N. H. Frank, Revs. Modern Phys. 3, 1 (1931).

In the limit $\kappa=a/l\ll1$, and for vanishing magnetic field, i.e., $l/r\ll1$, one has

$$A_L/A_{L0}=\{\log(l/a)\}^{-1}. \tag{20}$$

For the isothermal Nernst coefficient, one obtains the expression

$$A_N=\frac{\pi^2}{3}\frac{k^2T}{eH}q_r(s)\phi_r(s)\left[\frac{\partial}{\partial\epsilon}\left(\frac{\phi_i(s)}{\phi_r(s)}\right)\right]_{\epsilon=\epsilon'}, \tag{21}$$

which, in the limit $\kappa\gg1$ and $l/r\ll1$ reduces to the bulk expression

$$A_{N0}=\frac{\pi^2k^2T}{3m^*c}\left(\frac{\partial\tau}{\partial\epsilon}\right)_{\epsilon=\epsilon'}.$$

In the limit $|s|\ll1$, i.e., $(\kappa^2+\beta^2)\ll1$,

$$q(s)\cong\tfrac{3}{4}(1-\gamma)-\tfrac{3}{4}\log(s)+\cdots, \tag{22}$$

where γ is Euler's constant.

Making use of (22) one obtains for A_N/A_{N0} in the limit $\kappa\ll1$, $l/r\ll1$,

$$A_N/A_{N0}=\{\log(l/a)\}^{-1}=A_L/A_{L0}. \tag{23}$$

The Ettinghausen coefficient A_E is most conveniently obtained from the relation

$$\sigma_tA_E=TA_N, \tag{24}$$

where σ_t is the thermal conductivity. Equation (24) can be derived from very general considerations.[7] One can easily verify by means of (10) and (11) that in our case the Wiedemann-Franz Law holds, i.e.,

$$\sigma_t/T\sigma=\tfrac{1}{3}\pi^2(k/e)^2=L_0.$$

Thus

$$A_E=(1/L_0\sigma)A_N, \tag{25}$$

and the Ettinghausen coefficient can be obtained from the results of Sondheimer, $\sigma=\sigma_0(k/\phi_r(s))$, and Eq. (21); thus

$$A_E=\frac{T}{nc}q_r(s)[\phi_r(s)]^2\frac{1}{\beta}\left[\frac{\partial}{\partial\epsilon}\left(\frac{\phi_i(s)}{\phi_r(s)}\right)\right]_{\epsilon=\epsilon'}. \tag{26}$$

In the limit $\kappa\ll1$, $l/r\ll1$,

$$\frac{A_E}{A_{E0}}=\frac{4}{3}\frac{l}{a}\left\{\log\left(\frac{l}{a}\right)\right\}^{-2}. \tag{27}$$

The results which have been given are valid only if the scattering at the surfaces of the film is diffuse. If p, the fraction of electrons which suffer specular reflection at the surface, does not vanish, the function $F(v)$ of Eq. (6) is no longer determined by Eq. (7) but must be modified so as to satisfy the new boundary conditions. The procedure is as discussed by Fuchs and Sondheimer, and the only change which must be made in the results is the replacement everywhere of $q(s)$ and $\phi(s)$ by $q_p(s)$ and $\phi_p(s)$, where

$$q_p(s)=1/\phi_p(s)=\frac{1}{s}-\frac{3}{2s^2}(1-p)\times\int_1^\infty\left(\frac{1}{t^3}-\frac{1}{t^5}\right)\frac{1-e^{-st}}{1-pe^{-st}}dt;\quad 0\leqslant p\leqslant1.$$

Equations (20) and (23) are independent of p, while Eq. (27) becomes

$$\frac{A_E}{A_{E0}}=\frac{4}{3}\frac{1-p}{1+p}\frac{l}{a}\left\{\log\left(\frac{l}{a}\right)\right\}^{-2}. \tag{28}$$

V. CONCLUSION

A solution of the Boltzmann equation for quasifree electrons in thin metallic films under the influence of an electric field and a transverse magnetic field and of temperature gradients has been obtained under the assumption of a bulk relaxation time. From this solution expressions for the various thermomagnetic coefficients have been deduced.

In the limit of vanishing magnetic fields ($l/r\ll1$) and very thin films ($a/l\ll1$) the Nernst and Leduc-Righi coefficients approach zero as $[\log(l/a)]^{-1}$. In this limit the Ettinghausen coefficient behaves as the Hall coefficient, increasing as $(l/a)[\log(l/a)]^{-2}$ as a/l is decreased to very small values.

Also, in the above limit, the corresponding asymptotic expressions for the Nernst and Leduc-Righi coefficients are independent of the fraction of conduction electrons which suffer specular reflections at the surfaces of the film, whereas the Ettinghausen coefficient does depend upon the scattering at the surfaces. The difference in the behavior in this respect between the Nernst and Leduc-Righi and the Ettinghausen coefficients is of no fundamental significance but may be traced to the asymmetry of the defining equations. The Nernst and Leduc-Righi coefficients are defined as ratios of gradients, thermal and electric; on the other hand, the Ettinghausen coefficient as well as the Hall coefficient and the electric and thermal conductivities are defined by ratios of currents and gradients.

[7] H. Callen, Phys. Rev. 85, 16 (1952).

Photovoltaic Effect in *p-n* Junctions

ROBERT L. CUMMEROW
Knolls Atomic Power Laboratory, Schenectady, New York*
(Received March 1, 1954)

The relations between the incoming radiant energy and the outgoing electrical energy are developed in terms of the experimentally measurable constants of the semiconducting material. These results are applied to germanium by making use of constants found in the literature. The high efficiencies calculated for power conversion are strong indication that the *p-n* junction may be a practical device for the direct utilization of solar energy.

I. INTRODUCTION

A *p-n* junction exists in a semiconducting material in the region where the impurity content changes from an acceptor type (*p* type) to a donor type (*n* type). These junctions may be formed, for example, by the diffusion of impurity atoms into the surface of a crystal[1] or the segregation of impurities during crystal growth.[2] Single-crystal germanium, the most common material used for such junctions, contains two electronic bands which are involved in conduction processes. These are the valence band which is almost filled with electrons and the almost empty conduction band, which lies about 0.72 electron volt above the valence band. The Fermi energy for the intrinsic material is about in the center of the gap or forbidden region between these bands. For *p* material it lies within the gap, but below the center; for *n* material, above the center.[3]

Figure 1 shows the energy levels in the junction region at equilibrium. At equilibrium, the Fermi energy throughout the material must be the same. In order to fulfill this requirement in the junction region, a charge double layer and accompanying electrostatic potential are set up. The height of this electrostatic barrier is equal to the difference between the position of the gap in the *n* material and the *p* material. The Fermi energy and hence the barrier height vary with the temperature and the impurity concentration.[3]

A hole or unoccupied level in the valence band may diffuse for some distance in *n* material before it combines with an electron. The average distance it travels before combining is called the diffusion length for holes in *n* material. An analogous quantity is defined for electrons in *p* material.

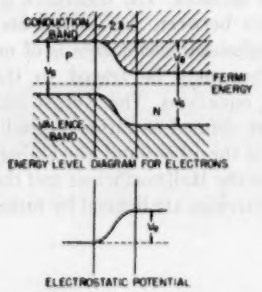

FIG. 1. Energy levels for electrons and the electrostatic potential in the transition region of a *p-n* junction.

II. MODEL OF *p-n* JUNCTION TO BE USED

The junction model which we shall use in discussing the photovoltaic effect is the one on which the usual theory is based. We define it precisely by the following assumptions:

(1) The junction or transition region itself is negligibly small compared with the extent of the *p* or *n* material and the diffusion lengths of holes in *n* material or electrons in *p* material. (We consider here the one-dimensional problem only.) Consequently, there is negligible recombination or generation of holes and electrons in the junction region.

(2) The electrostatic field is confined entirely to the narrow junction region. Even under nonequilibrium, steady-state conditions, we assume that there is no field outside this region. The rate-controlling process in current flow is, therefore, the diffusion of holes in the *n* material and electrons in *p* material. Consequently, in order to insure this field-free diffusion process, the nonequilibrium concentration of holes in *n* material or electrons in *p* material must always be much smaller than the equilibrium concentration of electrons or holes.

(3) The donor or acceptor impurity concentrations are always small enough so that Boltzmann statistics may be used instead of Fermi statistics.[4]

III. THE JUNCTION EQUATIONS

In accordance with our model defined above, we represent the junction as a narrow region of width 2δ at $x=0$ (Fig. 2). The distance 2δ is negligible compared with any other dimension of the junction and the figure is not to scale. As we traverse this region in the x direction (from *p* material to *n* material), the electrostatic potential increases by an amount V_e.

The difference in electrostatic energy in electron volts between the *p* and *n* material is then eV_e, where e is the electronic charge and V_e is the equilibrium electrostatic potential difference between the *n* and *p*

* Operated by the General Electric Company for the U. S. Atomic Energy Commission.

[1] R. N. Hall and W. C. Dunlap, Jr., Phys. Rev. **80**, 467 (1950).

[2] Teal, Sparks, and Buehler, Phys. Rev. **81**, 637 (1951).

[3] W. Shockley, *Electrons and Holes in Semiconductors* (D. Van Nostrand Company, Inc., New York, 1950), Chap. 10.

[4] V. A. Johnson and K. Lark-Horovitz, *Semiconducting Materials* (Academic Press, Inc., New York, 1951), p. 70.

regions. Then, the concentrations of holes on opposite sides of the barrier are related in the following way:

$$p_n = p_p \exp(-eV_c/kT), \tag{1}$$

where p_n is the equilibrium concentration of holes in the n material, p_p that in the p material, k the Boltzmann constant, and T the absolute temperature. With diffusion rate limiting, we may write the quasi-equilibrium equation

$$p(0) = p_p \exp[-e(V_c - V)/kT], \tag{2}$$

where $p(0)$ is the nonequilibrium value of $p(x_r)$ in the n material at $x=\delta$ or $x_r=0$, where $x_r = x-\delta$, and V is a voltage applied to the junction which changes the height of the equilibrium barrier. (In the following, all variables applying to the material to the right of the barrier are functions of x_r; those to the left, of x_l.) This voltage change may be accomplished by the use of a battery, or by the generation of nonequilibrium charge concentrations near the barrier by means of radiation. Combining Eqs. (1) and (2), we have

$$p(0) = p_n \exp(eV/kT). \tag{3}$$

We have analogous relations for electrons in p material. We shall continue to develop equations for holes in n material and write the analogous equations for electrons in p material in the appropriate places.

We consider a small volume of n material. Within this volume, holes are being generated thermally or by other means and are recombining with electrons. In addition, holes are entering and leaving this volume by diffusion. Under equilibrium conditions (thermal generation only), holes and electrons recombine at the same rate they are generated within this small volume. Shockley and Read have worked out[5] a theory of recombination of holes and electrons postulating the existence of trapping centers where recombination can occur much more readily than in a direct collision of a hole and an electron. This postulate is necessary to account for the short measured lifetime of holes in n material. Using Eqs. (3.8), (3.9), (4.4), and (5.4) of this reference and assuming that we are dealing with an n-type sample with sufficiently high donor concentration, we may write for the equilibrium thermal generation of holes:

$$g_p = p_n/\tau_p, \tag{4}$$

where τ_p is the lifetime of a hole in seconds in n material. From these same equations in reference 4 we write for the nonequilibrium recombination rate

$$r_p = p/\tau_p, \tag{5}$$

where p is the nonequilibrium concentration of holes. If we have generation of holes because of light quanta or other radiation, we may designate this by $g(x)$. The

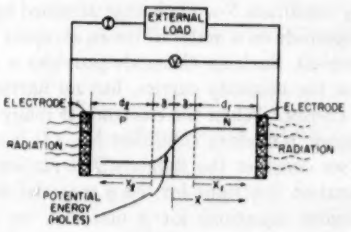

FIG. 2. Model of p-n junction used for calculations.

total net generation is then:

$$g_p + g(x) - (p/\tau_p). \tag{6}$$

This net generation rate must equal the net rate at which holes leave the small volume. This is just

$$e^{-1} \times \text{divergence of hole current density} = e^{-1}\partial I_p/\partial x.$$

We have then from (6):

$$g_p + g(x) - (p/\tau_p) = e^{-1}\partial I_p/\partial x. \tag{7}$$

Since we are dealing only with diffusion current,

$$I_p = -eD_p(\partial p/\partial x), \tag{8}$$

where D_p is the diffusion constant for holes in n material. Combining with (7),

$$g_p + g(x) - (p/\tau_p) + D_p\partial^2 p/\partial x^2 = 0. \tag{9}$$

The function, $g(x)$ can be written down by referring to Fig. 2. Let us consider first the case in which the light quanta fall on the surface of the p material. We specify that the hole-electron pair generation at the junction due to photons is g_0. The generation in the n material (to the right of the junction) is then:

$$g(x_r) = g_0 \exp(-x_r/L_\lambda) \tag{10}$$

where $(L_\lambda)^{-1}$ is the absorption coefficient for photons of wavelength λ. To the left of the junction,

$$g(x_l) = g_0 \exp(x_l/L_\lambda), \tag{11}$$

where $x_l = -(x+\delta)$ and at the surface on which the photons are incident,

$$g_s = g_0 \exp(d_l/L_\lambda).$$

If we have H_s photons/cm^2 sec of wavelength λ incident on the surface (after the incident beam has suffered reflection by the electrode or the semiconductor), then, assuming unit quantum efficiency,[6]

$$g_s = H_s/L_\lambda \quad \text{and} \quad g_0 = (H_s/L_\lambda)\exp(-d_l/L_\lambda). \tag{12}$$

The boundary conditions to be used with Eq. (9) are

(1) at $x_r = 0$, $p = p_n \exp(eV/kT)$; (13)

(2) at $x_r = d_r$, $\partial p/\partial x = 0$; (14)

(3) as $d_r \to \infty$, $p \to p_n$ for all large x_r. (15)

[5] W. Shockley and W. T. Read, Jr., Phys. Rev. **87**, 835 (1952).

[6] F. S. Goucher, Phys. Rev. **78**, 816 (1950).

Boundary condition No. (2) is that attained by putting a donor electrode on n material (or an acceptor electrode on p material). Such an electrode provides a reflecting barrier for the minority carrier, but no barrier for the majority carrier.[7] When the electrode is many diffusion lengths away, boundary condition No. (3) is used.

When we consider the differential equation and the pair generation functions for the n material along with the analogous equations for p material, we find that there are four cases of practical interest: (1) Irradiation of p material with junction near the surface; n material extends to infinity. (2) Same as 1, except n material is finite. (3) Irradiation of n material with junction near the surface; p material extends to infinity. (4) Same as 3, except p material is finite. The solutions corresponding to case 1 are

$$p=\tau_p g_p[\exp(eV/kT)-1]\exp(-x_r/L_p)+\frac{\tau_p g_0}{a_p^2-1}[\exp(-x_r/L_p)-\exp(-x_r/L_\lambda)]+\tau_p g_p, \quad (16)$$

$$n=\tau_n\left\{g_n[\exp(eV/kT)-1]+\frac{g_0}{a_n^2-1}\right\}\times\frac{\cosh[(d_l-x_l)/L_n]}{\cosh(d_l/L_n)}+\frac{\tau_n g_0}{a_n^2-1}\left[a_n\exp(d_l/L_\lambda)\times\frac{\sinh(x_l/L_n)}{\cosh(d_l/L_n)}-\exp(x_l/L_\lambda)\right]+\tau_n g_n, \quad (17)$$

where $a_p=L_p/L_\lambda$, $a_n=L_n/L_\lambda$ and L_p is the diffusion length for holes in n material $[L_p=(D_p\tau_p)^{\frac{1}{2}}]$ and L_n is the analogous quantity for electrons in p material. The electron current density and the hole current density at the junction constitute the total current density. For Case (1),

$$I_p(0)=-eD_p(\partial p/\partial x)_0=eg_pL_p\times[\exp(eV/kT)-1]-eg_0L_p/(a_p+1), \quad (18)$$

$$I_n(0)=-eD_n(\partial p/\partial x)_0=eg_nL_n[\exp(eV/kT)-1]\times\tanh(d_l/L_n)-\frac{eg_0L_n}{a_n^2-1}[a_n\exp(d_l/L_\lambda)\times\operatorname{sech}(d_l/L_n)-a_n-\tanh(d_l/L_n)]. \quad (19)$$

For Case (2),

$$p=\tau_p\left\{g_p[\exp(eV/kT)-1]+\frac{g_0}{a_p^2-1}\right\}\times\frac{\cosh[(d_r-x_r)/L_p]}{\cosh d_r/L_p}-\frac{\tau_p g_0}{a_p^2-1}\left[a_p\exp(-d_r/L_\lambda)\times\frac{\sinh(x_r/L_p)}{\cosh(d_r/L_p)}+\exp(-x_r/L_\lambda)\right]+\tau_p g_p. \quad (20)$$

n is the same as Case (1).

$$I_p(0)=eg_pL_p[\exp(eV/kT)-1]\times\tanh(d_r/L_p)-\frac{eg_0L_p}{a_p^2-1}[a_p-a_p\times\exp(-d_r/L_\lambda)\operatorname{sech}(d_r/L_p)-\tanh(d_r/L_p)]. \quad (21)$$

$I_n(0)$ is the same as Case (1). Case (3) is obtained by interchanging the letters n and p in Case (1). Case (4) is obtained by interchanging the letters n and p in Case (2). For any of these cases, the total current density is $I=I_p(0)+I_n(0)$. We may write this expression

$$I=e[\exp(eV/kT)-1]\times(g_pL_p'+g_nL_n'-eg_0(L_1+L_2), \quad (22)$$

where L_p', L_n', L_1, and L_2 are the appropriate coefficients of the corresponding terms in such expressions as Eq. (21). This current is in the direction conventionally called "reverse" in rectifier nomenclature. For convenience, we shall change the signs in the right-hand side of Eq. (22) so that we have

$$I=eg_0L-egL'[\exp(eV/kT)-1], \quad (23)$$

where $L=L_1+L_2$ and $gL'=g_pL_p'+g_nL_n'$. Solving Eq. (23) for V, we obtain

$$V=\frac{kT}{e}\log\left(1+\frac{eg_0L-I}{egL'}\right). \quad (24)$$

The power delivered to an external resistor R connected to the electrodes is

$$P=IV=I\frac{kT}{e}\log\left(1+\frac{eg_0L-I}{egL'}\right). \quad (25)$$

TABLE I. Values of constants used in the calculation of power conversion efficiency for germanium p-n junctions.

Resistivity ρ (ohm-cm)	D_p (cm²/sec)[a]	D_n (cm²/sec)[a]	τ_p (μsec)[b]	τ_n (μsec)	L_p (cm)	L_n (cm)	p_p (cm^{-3})[c]	p_n (cm^{-3})	n_n (cm^{-3})[c]	n_p (cm^{-3})	L_λ (cm)	λ (cm)
1.4	44	94	80	500	0.059	0.22	1.5×10^{15}	6.3×10^{11}	1×10^{15}	4.2×10^{11}	1.7×10^{-3}	1.5×10^{-4}
0.014	44	94	50	500	0.047	0.22	1.5×10^{17}	6.3×10^{9}	1×10^{17}	4.2×10^{9}	1.7×10^{-3}	1.5×10^{-4}

[a] Pearson, Haynes, and Shockley, Phys. Rev. 78, 295 (1950).
[b] See reference 9.
[c] Reference 3, pp. 16–17.

[7] R. N. Hall (private communication).

Setting $dP/dI=0$, we find that the current for maximum power output is

$$I_m=\frac{egL'(1+g_0L/gL')eV_m/kT}{1+eV_m/kT}, \tag{26}$$

and V_m, the voltage for maximum power is given by

$$\exp(eV_m/kT)=\frac{1+g_0L/gL'}{1+eV_m/kT} \tag{27}$$

Hence, the maximum power P_m is

$$P_m=I_mV_m=\frac{egL'(1+g_0L/gL')eV_m/kT}{1+eV_m/kT}V_m. \tag{28}$$

The load resistance for maximum power is

$$R_m=V_m/I_m. \tag{29}$$

The open-circuit voltage is

$$V_0=(kT/e)\log(1+g_0L/gL'). \tag{30}$$

The short-circuit current is

$$I_s=eg_0L. \tag{31}$$

Equations (30) and (31) are useful in determining the quantities gL' and g_0L experimentally from which the maximum power output to be expected can be calculated.

IV. DISCUSSION AND NUMERICAL EXAMPLES

The equations given above can be used to calculate the efficiency of a p-n junction as a power converter. The input power with monochromatic radiation of wavelength λ and intensity H_s photons/cm² sec is

$$P_i=H_s(hc\times10^{-7}/\lambda)(\text{watts/cm}^2), \tag{32}$$

where h is Planck's constant in erg-sec, c is the velocity of light in cm/sec and λ is the wavelength in cm. The efficiency of the junction as a power converter is

$$\text{Eff.}=P_m/P_i, \tag{33}$$

where P_m is given by Eq. (28). To obtain a curve of the efficiency as a function of any of the quantities in Eq. (28), it is necessary to solve Eq. (27) numerically for a series of values and plot the resulting points.

We consider the efficiency of junctions made of approximately 1 ohm-cm material and those made of approximately 0.01 ohm-cm material. The experimental constants needed for these calculations were taken from the current literature. In the following calculations, we have taken $\lambda=1.5$ microns. We have assumed that the absorption coefficient for 1 ohm-cm material and 0.01 ohm-cm material is the same as that measured[8] in 48 ohm-cm n germanium, since we are dealing for the most part with absorption in the fundamental band

[8] H. B. Briggs, J. Opt. Soc. Am. **42**, 686 (1952).

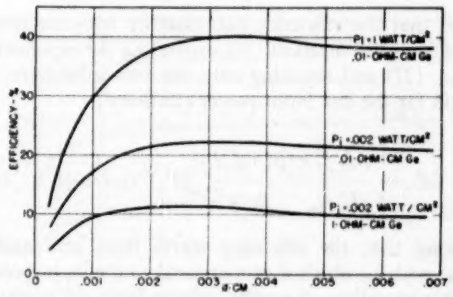

FIG. 3. Efficiency of power conversion as a function of the distance from electrode to junction.

which involves the breaking of valence bonds and does not depend on the concentration of holes or electrons. The values of the mean lifetimes of minority carriers for the 1 ohm-cm material have been found by experiment;[9] those for the 0.01 ohm-cm material are extrapolated from the same experimental results. Table I gives the experimentally-determined constants used in the calculations.

Figure 3 shows the efficiency of power conversion *versus* the thickness d of the p material and that of the n material (the total thickness is $2d$). We have taken $d_r=d_l=d$ and have assumed the n material is irradiated (Case 4). For all regions of the curves, the maximum nonequilibrium concentration of the minority carrier is never greater than one-tenth the equilibrium concentration of the majority carrier in accord with the assumptions listed above under No. (2). It will be noted that all three curves rise rapidly in the region where the material is so thin that it is transparent. This region is probably of little practical importance, since such thin sections would be too difficult to prepare. As the thickness increases and the material becomes opaque, the efficiency rises to a maximum and gradually decreases. This gradual decrease results from the increase in the total recombination rate with thickness. This increase is not very fast since the thickness is in all cases small compared with the diffusion length. Thus it is possible to make the assembly considerably thicker than the optimum without an excessive loss in efficiency. This is an important point, since it means that the thicker, more easily realizable assemblies are useful.

The 0.01 ohm-cm material, because it has a higher equilibrium concentration of majority carriers, can be used with power inputs up to 2 watts/cm² at 300°K before the concentration of minority carriers becomes so great that the theory is not valid. The corresponding limit for the 1 ohm-cm material is 0.004 watt/cm² for the optimum thickness. Figure 4 shows the variation of efficiency for input power in the 1 ohm-cm material and Fig. 5 that for the 0.01 ohm-cm material. It will be

[9] Burton, Hull, Morin, and Severiens, J. Phys. Chem. **57**, 853 (1953).

noted that the efficiency rises sharply with the power input and then levels off. By expanding the exponential in Eq. (27) and retaining only the first-order term, we obtain for the low input-power efficiency:

$$\text{Eff.}=\frac{1}{4}\frac{g_0L}{gL'}\frac{L}{L_\lambda}\frac{\exp(-d/L_\lambda)}{hc/\lambda}kT, \quad (g_0L\ll gL'), \quad (34)$$

showing that the efficiency starts from zero and is linear with g_0, which is proportional to the input power. Such a variation, of course, follows from the variation of the output power for low intensities:

$$P_m=\tfrac{1}{4}[(g_0L)^2/gL']kT. \quad (35)$$

This variation is obtained because, initially, both the current and the voltage increase linearly with input power. The variation gradually changes from a square law to an almost linear relation at high input power, because, for large g_0,

$$I_m\rightarrow eg_0L, \quad (36)$$

$$V_m\rightarrow\frac{kT}{e}\log\frac{g_0L}{gL'}, \quad (37)$$

and

$$P_m=I_mV_m\rightarrow kTg_0L\log(g_0L/gL'), \quad (38)$$

giving an approximately linear variation of the output power with input power. The efficiency at high input power is consequently

$$\text{Eff.}=\frac{P_m}{P_l}=\frac{L}{L_\lambda}\frac{\exp(-d/L_\lambda)}{hc/\lambda}kT\log\left(\frac{g_0L}{gL'}\right). \quad (39)$$

It is interesting to consider the effect of temperature on the efficiency of power conversion. We must know the temperature variation of the quantities listed in Table I. Shockley[3] (p. 288) gives results which indicate that the variation of mobility resulting from both temperature and impurity scattering

$$\mu\sim T^{-b}, \quad (40)$$

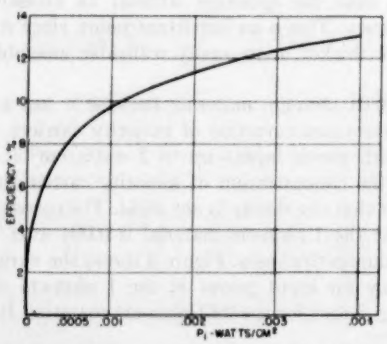

FIG. 4. Efficiency of power conversion as a function of power input for 1 ohm-cm germanium at 300°K, $d=2.5\times10^{-3}$ cm.

where b is between zero and 1. The Einstein relation[8] shows that

$$D=(kT/e)\mu, \quad (41)$$

which makes D almost temperature-independent. The diffusion length L is given by

$$L=(D\tau)^{\frac{1}{2}}, \quad (42)$$

where τ is the mean lifetime of an excess minority carrier. Shockley and Read[4] state that for highly doped material τ is insensitive to temperature. Therefore, L itself is quite insensitive to temperature.

In the temperature range in which all donor or acceptor impurities are ionized, the concentration of the majority carrier does not change with temperature. The minority carrier concentration, however, changes exponentially with temperature and therefore, in accord with Eq. (4),

$$g_p=p_n/\tau_p, \quad (4)$$

the thermal generation rate does likewise. By using the relation developed by Shockley[3] (p. 245) it is easily shown that

$$gL'=2.33\times10^{31}T^3\exp(-eV_g/kT)\left[\frac{L_p'}{n_n\tau_p}+\frac{L_n'}{p_p\tau_n}\right] \quad (43)$$

so that the thermal generation rate varies exponentially with temperature with an activation energy of eV_g, where V_g is the potential difference between the valence band and the conduction band in the semiconductor. Thus, the low-intensity efficiency [Eq. (34)] decreases exponentially as the temperature increases. The limiting high-intensity efficiency [Eq. (39)] does not decrease so rapidly as the low-intensity efficiency, but still has a negative slope. In Fig. 4 curves of efficiency *versus* input power are shown for the 0.01 ohm-cm material for three different temperatures, *viz.*, 200°K, 300°K, and 400°K. These curves were calculated from the exact expression (28) and Eq. (43) and conform in general with our approximate analysis above.

We see that the p-n junction is potentially a useful device for the conversion of light energy to electrical energy. Under our assumption of unit quantum efficiency, we may calculate the total number of charges created per second, the fraction of this total that passes through the external circuit, and hence the fraction that is lost by recombination. For example, at 300°K in the 0.01 ohm-cm material with a power input of 0.1 watt/cm² we have 7.55×10^{17} photons/cm² sec incident on the surface. Potentially the charge generation is 7.55×10^{17} charges/sec. However, because a small fraction of the photons is transmitted through the material, the charge generation is 7.43×10^{17} charges/sec. The number per unit time passing through the external resistor is 6.76×10^{17} charges/sec. The number lost by recombination is 0.67×10^{17} charges/sec. Thus, 89.4 percent of the possible charges generated pass through the external resistor; 1.6 percent are not

generated because of photon transmission, and 9 percent do not pass through the external circuit because of recombination. The potential energy obtained per charge is 0.305 electron volt. The potential energy expended in creating each charge is 0.825 ev (the energy per photon). Thus, each charge gives up only 37 percent of the energy used to create it giving the power conversion efficiency of 33 percent as plotted on the curve. From this analysis it is apparent that this device would be efficient in using the charges created, but that the potential energy per charge available for useful work is the limiting factor in power conversion efficiency. If we consider the same material with the same power input at 200°K, we find that transmission through the material is still about zero.[10] The number of charges/sec passing through the external resistor is 7.1×10^{17}. This is 94 percent of those potentially available or 95.6 percent of those created, leaving only 4.4 percent lost by recombination. The potential energy per charge delivered externally is 0.453 ev. This is 54.8 percent of the energy expended in creating a charge. The power conversion efficiency is thus 0.94 $\times$54.8 percent = 51.5 percent as plotted on the curve.

For greatest power conversion efficiency, it is thus apparent that the following conditions must be met: (1) The energy per photon must be nearly equal to the band gap (it must not be less, of course). (2) The potential barrier height in the junction should be as close to the band gap as possible. (3) The whole assembly should be short compared with the diffusion lengths of the minority carriers, but great enough in extent so that the incident radiation will be absorbed.

Condition (1), in the practical case of a fundamental power source, would be applied to the solar spectrum. Since we are not dealing with monochromatic radiation, a semiconductor with a gap energy somewhere near the photon energy characteristic of the peak of the solar spectrum, i.e., 2 ev would be required.

[10] H. Y. Fan and M. Becker, *Semiconducting Materials* (Academic Press, New York, 1951), p. 138.

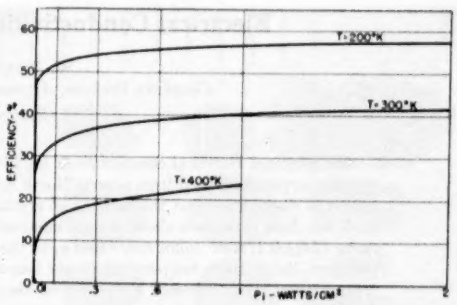

FIG. 5. Efficiency of power conversion as a function of power input for 0.01 ohm-cm germanium for three different temperatures, $d=3.5\times10^{-3}$ cm.

Our analysis shows that Condition (2) can be met by using material with the doping as high as possible and by keeping the temperature as low as possible. In addition, materials with band gaps larger than germanium and the same resistivity have potential barriers greater relative to the band gap.

Condition (3) can be readily met in practice, since the diffusion lengths of the minority carriers are reasonably long.

In practice, some provision for cutting down surface reflection would have to be made. The reflection coefficient for germanium is of the order of 50 percent. Using a germanium junction with a band gap of 0.72 ev and solar radiation and sufficient cooling, one might expect to realize an efficiency of 10 or 12 percent (assuming a reflection loss of $\frac{1}{3}$) for power conversion. The feasibility and engineering details of such a system would have to be determined by examining the over-all economy of this method of power production.

ACKNOWLEDGMENTS

It is a pleasure to acknowledge many fruitful discussions with Dr. J. W. Moyer. Helpful conversations were also held with Dr. R. P. Ruth. The interest and encouragement of Mr. C. Mannal are greatly appreciated.

Electrical Conductivities of Natural Graphite Crystals

W. PRIMAK AND L. H. FUCHS
Chemistry Division, Argonne National Laboratory, Lemont, Illinois
(Received March 4, 1954)

The principal electrical conductivities (σ_a in the basal plane and σ_c perpendicular to the basal plane) of graphite crystals isolated from several North American marbles were studied. By means of measurements of potential distributions on the surfaces of crystals carrying electric current, it was conclusively shown that σ_a/σ_c for these crystals is about several hundred at room temperature. By direct measurement σ_a was found to be $(2.6\pm0.2)\times10^4$ (ohm cm)$^{-1}$ and σ_c to vary from 150 to 230 (ohm cm)$^{-1}$ (±20 percent) at room temperature. Below room temperature it was found for two crystals that σ_a increased slowly to liquid nitrogen temperatures, then followed a T^{-1} law to about 15°K, and again slowly increased in the region 15°K to 4.2°K. Two other crystals for which σ_c was measured at low temperatures did not behave alike. For both, σ_c decreased as the temperature was lowered, reached a minimum above liquid nitrogen temperatures, and then started increasing, the one showing a T^{-1} behavior, the other increasing more slowly. For both, the rate of increase declined markedly in the region 15°K to 4.2°K.

INTRODUCTION

A NUMBER of determinations of the electrical conductivities of graphite have been reported.[1–10] The list of references is not intended to be exhaustive, and some of the determinations were incidental to other work.

The large anisotropy of the electrical conductivities of graphite was noted by Washburn,[3] who found the conductivity in the basal plane to be about 200 times the conductivity perpendicular to the basal plane. The principal conductivities of graphite will here be designated σ_a parallel to the basal plane and σ_c perpendicular to the basal plane (their reciprocals, ρ_c, ρ_a) and the square root of their ratio $(\sigma_a/\sigma_c)^{\frac{1}{2}}$ as τ. The distribution of potentials V in such a conductor in the steady state is

$$\sigma_a[(\partial^2V/\partial x^2)+(\partial^2V/\partial y^2)]+\sigma_c(\partial^2V/\partial z^2)=0.$$

If the substitution $\zeta=\tau z$ be made, then

$$(\partial^2V/\partial x^2)+(\partial^2V/\partial y^2)+(\partial^2V/\partial \zeta^2)=0,$$

the potential distribution being similar to that in an isotropic body of the same dimensions in the directions of the basal plane, but τ-fold larger perpendicular to it. Since most graphite crystals available for measurement are perhaps 1/10 to 1/20 as thick as their average diameter, their equivalent isotropic bodies are small blocks. The usual assumptions in electrical conductivity measurements, that the current is spread uniformly in the region between the potential probes, may not here be justified, and the proper method of determining the electrical conductivities is to study the potential distributions on the surfaces of crystals conducting current and to apply the appropriate solution of Laplace's equation.

GRAPHITE CRYSTALS

Recently Krishnan and Ganguli,[7] and later Dutta,[8] have reported measurements indicating $\tau^2\cong10^4$. Since their results are quite different from the results reported by others working with different specimens, it is considered desirable to carefully describe the crystals which were used in the present measurements and to give their source. All of the crystals used in the present measurements were isolated from graphite-bearing marbles. One specimen of marble collected from the Ticonderoga, New York area was furnished by Professor C. Palache (Harvard University). Another specimen was supplied by Mr. H. S. Spence (Department of Mines and Resources, Canada) and was labelled Bouthillier Township, Labelle County, Quebec. A specimen from Crown Point, New York was secured from Ward's Natural Science Establishment, Rochester, New York. Most of the elongated crystals on which σ_a was measured were isolated from a boulder found by the authors at the Lead Hill Mine, Ticonderoga, New York, a fortunate find in the mine tailings, most of which were of a different character.

The crystals were isolated in the following manner. The calcite was dissolved in dilute hydrochloric acid. The insoluble residue was then treated alternately with concentrated hydrochloric and hydrofluoric acids on a steam bath for some weeks until all the minerals but graphite were rendered soluble and washed away with distilled water.[11] Some of the crystals were loaded into a graphite capsule and heated to 3000°C in a graphite tube furnace swept with helium which in some runs, during part of the heating, bore CCl_4 vapor. Typical spectrochemical analyses before and after such heatings

[1] D. E. Roberts, Ann. Physik (4) **40**, 453 (1913); Phil. Mag. **26**, 159 (1913).
[2] J. Koenigsberger and J. Weiss, Ann. Physik **35**, 2 (1911).
[3] G. E. Washburn, Ann. Physik (4) **48**, 236 (1915).
[4] W. J. de Haas and P. M. Van Alphen, Proc. Natl. Acad. Amsterdam **34**, 70 (1931).
[5] Meissner, Franz, and Westerhop, Ann. Physik **13**, 555 (1932).
[6] E. Ryschkewitz, Z. Elektrochem. **29**, 474 (1923).
[7] K. S. Krishnan and N. Ganguli, Nature **144**, 667 (1939).
[8] A. K. Dutta, Phys. Rev. **90**, 187 (1953).
[9] Grisdale, Pfister, and Van Roosbroeck, Bell System Tech. J. **30**, 292 (1951).
[10] G. H. Kinchin, Proc. Roy. Soc. (London) **A217**, 9 (1953).

[11] This method of treatment was devised by G. Hennig of this laboratory.

are given in Table I. No difference in the electrical conductivities between heated and unheated crystals was noted.

From among a very large number of graphite crystals, most of them too imperfect to use, there were found a few suitable for the measurements described here. The appearance of some of these crystals is shown in Fig. 1. The prominent striae are reflections from zones twinned in the manner described by Palache.[12] Since the crystals are continuous across the twin plane, and since the zones are large compared to the mean free path of electrons in a solid, it is assumed that the gross twinning would have only a small effect on the electrical conductivities. The more circular crystals were used for determining σ_c and in one method of determining τ, while the elongated ones were used in determining σ_a and in another method for determining τ.

TABLE I. Typical spectrum analysis of natural graphite crystals before and after purification.

Element analyzed for	Before purification (ppm)	After purification (Case I—without CCl_4) (ppm)	After purification (Case II—with CCl_4) (ppm)
Ag	<0.1	<0.1	<0.1
Al	1000	<5	<10
As	100	<20	<10
B	20	3	1
Ba	10	<2	<5
Be	<0.5	<0.5	<0.5
Bi	<0.2	<0.2	<0.5
Ca	100	<2	<10
Co	<2	<2	<5
Cr	<1	<1	<1
Cu	10	<1	<1
Fe	2000	<1	2
Hg	<5	<5	<1
K	<10	<10	<20
Li	<1	<1	<1
Cd	<100	<100	
Mg	2000	<0.5	<0.5
Mn	0.5	<0.1	<0.2
Na	50	<2	5
Ni	10	<1	<2
P	<50	<50	<20
Pb	15	<0.5	<1
Sb	<1	<1	<1
Si	30	<2	<5
Sn	10	<5	<5
Sr	<10	<10	<10
Ti	<1	<1	<2
V	<1	25	<2
Zn	<20	<20	<20
Zr	<10	<10	<5

The dimensions of a crystal were determined by measuring the area of the basal plane with a binocular microscope fitted with a net reticule ocular calibrated against a stage micrometer. The crystal was then weighed and its mean thickness computed from its area and an assumed density of 2.265. The densities of a number of crystals were determined by a flotation method and found to vary between 2.262 and 2.268.[13]

[12] C. Palache, Am. Mineralogist **27**, 713 (1941).

[13] We are indebted to Paul Day of this laboratory for making these measurements.

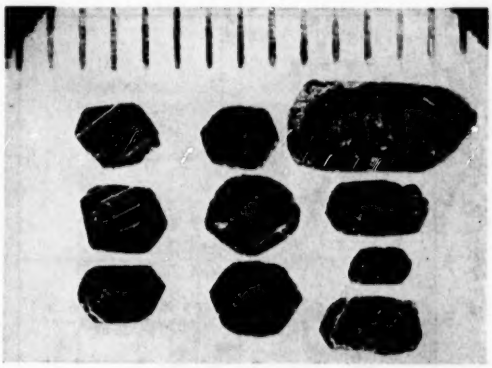

FIG. 1. Photomicrograph of typical graphite crystals of the sort used in the measurements described here. The scale is millimeters.

Some of the thicknesses were checked using a microscope fitted with a filar micrometer.

ELECTRICAL MEASUREMENTS

The methods used in making the electrical measurements were the following. Two sets of contacts were established to the crystal, current electrodes and potential probes, which were not in contact with each other. Thus, in all cases, the potential drops which were measured were potential drops on the surface of the graphite and did not include potential drops across contact resistances. The current was measured by the potential drop across a standardized resistor in series with the current contacts. Since both the current and potential drop were measured in succession with the same potentiometer, the use of a carefully calibrated standard cell was obviated. The potential drops across the standard resistor were large, hence no correction for contact potentials was necessary. The potential drops across the potential probes were often small, necessitating such a correction. It was occasionally made by subtracting the potential drop with the current off

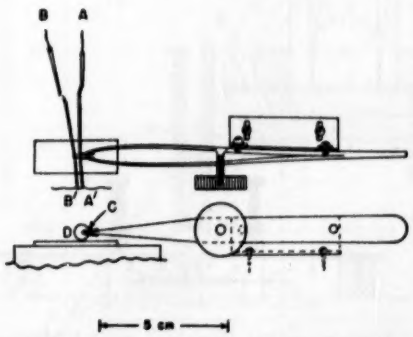

FIG. 2. Apparatus used to determine τ shown with mercury-filled capillaries for electrodes and probes. A and A' are the current electrodes; B and B' are the potential probes (they were held with micromanipulators); C are insulating pads of mica held to the forceps with glyptal varnish; D is the graphite crystal.

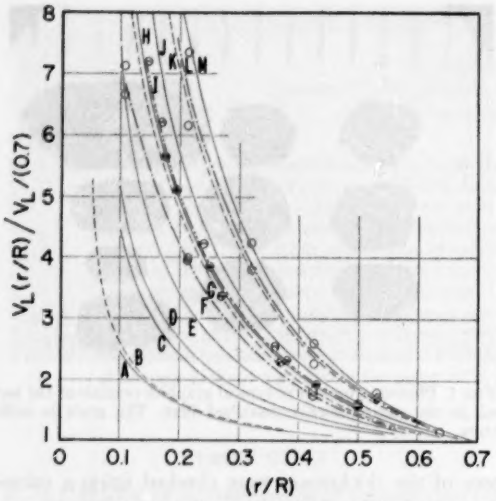

FIG. 3. Graphs of $V_L(r/R)/V_L(0.7)$. The solid curves are calculated for R/L: $A=0.159$, $C=0.333$, $D=0.385$, $E=0.556$, $H=0.714$, $J=0.769$, $M=1.00$. The dashed curves are measured for isotropic bars of R/L: $B=0.172$, $G=0.694$, $K=0.917$. The heavy dot-dash curves are results for: F, graphite crystal $23R$, I, crystal $6R$, L, crystal $20R$.

from the potential drop with the current on, or occasionally by reversing current and potentiometer leads and taking the average of the two potential drops. The correction was found to be about the same by either method, usually about 2 to 10 microvolts. Three types of apparatus were used and are shown in Figs. 2, 4, and 9. The first was used to measure $\mathfrak{r}$, the second to measure $\mathfrak{r}$ and σ_a, the third to measure σ_c.

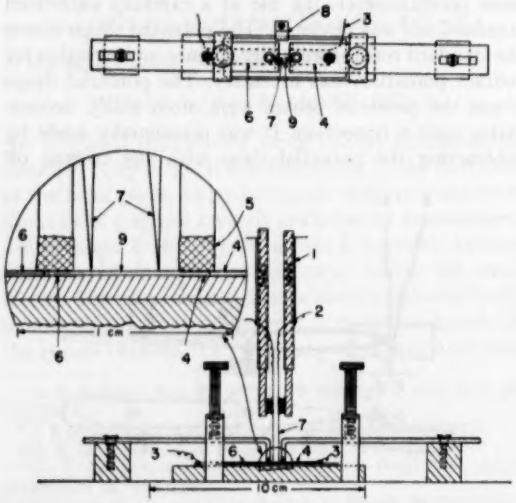

FIG. 4. Apparatus used to determine σ_a and $\mathfrak{r}$. 1. Micromanipulator support arm. 2. Potential lead. 3. Current lead. 4. Movable gold foil current electrode (attached to movable glass plate). 5. Rubber foot. 6. Fixed gold foil current electrode (attached to plastic base). 7. Tungsten wire potential probe. 8. Clamp for glass plate. 9. Graphite crystals.

The Determination of $\mathfrak{r}$

The arrangement of the apparatus is shown in Fig. 2 and is essentially that of a finite cylinder carrying electric current to which contact is made by means of small electrodes placed at the center of the bounding circular faces. Laplace's equation for the equivalent isotropic body is here

$$\frac{\partial^2 V}{\partial r^2}+\frac{1}{r}\frac{\partial V}{\partial r}+\frac{\partial^2 V}{\partial \zeta^2}=0,$$

where r is the radius variable. The boundary conditions and the solution for this case are discussed by Gray *et al.*[14] The potential at any point in the equivalent isotropic cylinder (radius R; length λ) is

$$V=\frac{S}{\pi\sigma_a(\lambda/2)}\sum_{n=1}^{\infty}\sin\frac{n\pi}{2}\sin\frac{n\pi\zeta}{\lambda}\times\left[K_0\left(\frac{n\pi r}{\lambda}\right)+\frac{K_1(n\pi R/\lambda)}{I_1(n\pi R/\lambda)}I_0\left(\frac{n\pi r}{\lambda}\right)\right],$$

where S is the current and $V=0$ at the midplane. In this experiment the potential probes were located at $\zeta=\pm\lambda/2$ and moved so that they were at equal distances from the respective current electrode on that face. The potential drop measured V_L was thus twice the value obtained by setting $\zeta=\lambda/2$. Remembering that the thickness of the crystal $L=\lambda/\mathfrak{r}$,

$$V_L=\frac{4S}{\pi L\mathfrak{r}\sigma_a}\sum_{n=1}^{\infty}\sin^2\frac{n\pi}{2}\left[K_0\left(n\pi\frac{R}{\mathfrak{r}L}\frac{r}{R}\right)+\frac{K_1\left(n\pi\frac{R}{\mathfrak{r}L}\right)}{I_1\left(n\pi\frac{R}{\mathfrak{r}L}\right)}I_0\left(n\pi\frac{R}{\mathfrak{r}L}\frac{r}{R}\right)\right].$$

The function $V_L(r/R)$ was computed for a number of values of $R/\mathfrak{r}L$. In Fig. 3 is plotted $kV_L(r/R)$, the constant k being chosen to make the function unity at $r/R=0.7$. These curves are shown by the solid lines on the graph. The potentials similarly adjusted across the faces of a number of metal bars (presumed isotropic, $\mathfrak{r}=1$) of various dimensions, whose R/L varied from 1.09 to 34.9, were determined and were found to match the computed curves very nicely. The results for three Monel bars whose respective radii/length ratios were 1.743/1.901, 1.745/2.508, and 1.745/10.16 are shown in the figure as dashed lines; another, 1.745/5.09, fell so close to one of the computed curves, $R/L=0.333$, that

[14] Gray, Mathews, and Macrobert, *Bessel Functions* (Macmillan and Company, Ltd., London, 1931), pp. 143, 146, and 147.

it is omitted. The adjusted potentials obtained for three of the graphite crystals which were measured are plotted in the figure as circles and are joined by a heavy dot-dash line. From the position of one of these curves on the graph, the value of $R/\tau L$ for the crystal can be read off; and by introducing its dimensions, τ is obtained directly. To insure comparable experimental potentials, the current was measured at each setting of the potential probes, and the potentials chosen for adjustment were the measured potentials divided by the measured currents.

For the machined bars, the current electrodes were machined pins or fine needles, and the potential probes were fine needles. Their positions were measured with comparators reading to 0.01 mm. The measurements on the crystals could not be made as precisely. Here mercury drops held by capillary tubes or on amalgamated copper wires seemed to make the best electrodes and probes. The sizes of the electrodes and probes were relatively much larger than those used for the bars.

TABLE II. Determination of τ by the ratio apparatus.

Crystal	Radius (cm)	Thickness (L) (cm)	τ
2*R* (Quebec)	0.163	0.013	20
6*R* (Quebec)	0.210	0.014	21
7*R* (Crown Point)	0.126	0.0086	19
8*R* (Crown Point)	0.118	0.0045	25
12*R* (Quebec)	0.136	0.0088	21
20*RC*	[a]	0.0104	25
24*RC*	[a]	0.0133	20–25
26*RC*	[a]	0.0243	14–17
27*RC*	[a]	0.0166	13–17
29*RC*	[a]	0.0117	~17

[a] These crystals were cut with a sand blast to form a circular disk of radius 0.241 cm.

The potential probe positions were measured with binocular microscopes fitted with micrometer reticule eyepieces. The crystals were somewhat irregular in shape and sometimes nonuniform in properties; hence the curve V_L for them was usually determined along several different radii. The potential curves given by some of the crystals crossed several of the family of curves shown in the figure. This might be expected very close to the electrodes. It was presumed that when it occurred some distance away, the conductivities in these crystals were not uniform and the data were therefore discarded. Several crystals were cut into a nearly perfect cylindrical shape by holding them between two metal cylinders and removing the protruding edges with a sand blast from a dental drill. The results for a number of uncut and cut crystals are given in Table II.

Confirmatory evidence for values of τ in this range was obtained with the use of the apparatus shown in Fig. 4 using some of the elongated crystals. For the arrangement shown here the variables of Laplace's equation are separable in Cartesian coordinates. For

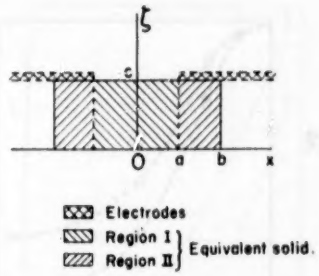

FIG. 5. Half of the equivalent isotropic solid in which the potential distribution is analyzed.

the equivalent isotropic solid

$$(\partial^2 V/\partial x^2)+(\partial^2 V/\partial \zeta^2)=0.$$

The arrangement analyzed is that of Fig. 5. In the experimental arrangement, each electrode covered about $\frac{1}{4}$ of the crystal face, and there were electrodes on both the upper and lower surfaces of the crystal. The potential drop was measured for various separations (symmetrical) of the potential probes on the upper surface (Case I). The upper electrodes were then insulated from the crystal by inserting strips of paper, and the potential drops again measured on this face (Case II). The results for two crystals are shown in Fig. 6. It is seen that in both cases the potential drop as a function of separation was linear up to distances as close to the electrodes as could be measured. What was determined in effect was $(\partial V/\partial x)$ on the upper surface and in the central plane of a hypothetical crystal of double thickness with electrodes attached at similar positions. The

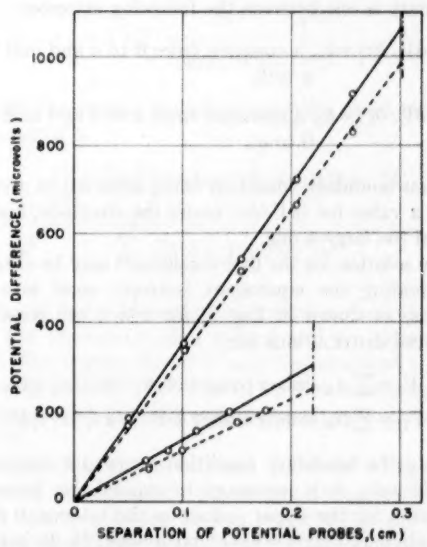

FIG. 6. Potential distribution on the faces of graphite crystals for a current of 0.098 amp. Upper curves, *AX*-2. Lower curves, *AX*-1. ———— Case I; - - - - - - - Case II; — — — — separation of current electrodes.

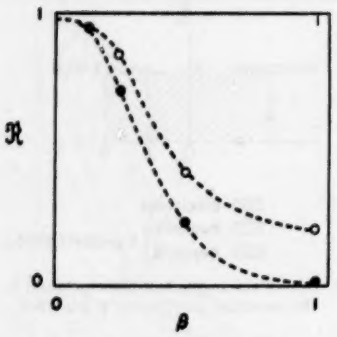

FIG. 7. $\Re$ as a function of β. ○ First boundary condition; ● second boundary condition.

appropriate boundary conditions for the planes $x=\pm b$ and $\zeta=0$ are obvious; for $\zeta=c=\lambda/2$ it is not quite clear. Potential drops were measured along the gold foils in one case and found to be about 25 μv/mm for the currents which were employed. For a 2-mm overlap this is small compared to the potential drops in the surface of the graphite between the electrodes, which were between several hundred and over 1000 μv, hence the potential along the electrode was essentially constant. However, it cannot be assumed that this is true for the graphite under the electrode since the contact resistances were high: in several cases the potential drops from the gold to the graphite adjacent to the electrode were measured and found to be several thousand microvolts and were found to change for some hours after contact was established. It thus seems reasonable to believe that the correct condition for this boundary is one between the following extremes:

(1) $(\partial V/\partial x)=k_1$, a constant from 0 to a and null from a to b,

(2) $(\partial V/\partial\zeta)=k_2$, a constant from a to b and null from 0 to a;

the first boundary condition being expected to give too small a value for $(\partial V/\partial x)$ under the electrode, and the second too large a one.

The solution for the first condition[15] may be obtained by dividing the equivalent isotropic solid into two regions, as shown in Fig. 5, for which the respective potential distributions are,

$$V_{\mathrm{I}}=\sum A_n \sinh\alpha x\cos\alpha\zeta+A_0 x \quad (0\leqslant|x|\leqslant b),$$
$$V_{\mathrm{II}}=\sum B_m \sinh\beta x\cosh\beta\zeta+B \quad (a\leqslant|x|\leqslant b).$$

Since the boundary condition at $x=\pm b$ requires m be *odd only*, it is necessary to expand the boundary condition for the upper surface in the interval 0 to $2b$. It is obvious that $\alpha=n\pi/c$ and $\beta=m\pi/2b$. It is found that

$$B_m=(8k_1b/m^2\pi^2)(\sin\beta a/\cosh\beta c).$$

[15] This solution is due to O. C. Simpson of this laboratory.

At $x=a$, $(\partial V_{\mathrm{I}}/\partial x)=(\partial V_{\mathrm{II}}/\partial x)$; hence,

$$\sum_n \alpha A_n\cosh\alpha a\cos\alpha\zeta+A_0=\sum_{\text{modd}}\beta B_m\cos\beta a\cosh\beta\zeta.$$

The final result desired, $(\partial V_{\mathrm{I}}/\partial x)$, is obtained by expanding

$$\cosh\beta\zeta=\sum_n D_n\cos\alpha\zeta+D_0/2,$$

when it is found that

$$D_n=(2m/\pi)\{(2b/c)\cos n\pi/[m^2+n^2(2b/c)^2]\}\sinh\beta c.$$

Thus,

$$\sum\alpha A_n\cosh\alpha a\cos\alpha\zeta+A_0=\sum_{\text{modd}}\sum_n\beta B_m\cos\beta a D_n^m\cos\alpha\zeta.$$

Hence,

$$A_0=\sum_{\text{modd}}\frac{2k_1}{m^2\pi^2}\frac{2b}{c}\sin\beta a\tanh\beta c\equiv\frac{2k_1}{\pi^2}\frac{2b}{c}\Sigma_1.$$

Thus,

$$2k_1=\pi^2(c/2b)(A_0/\Sigma_1),$$

and

$$A_n=\frac{2c\cos n\pi}{\pi\cosh\alpha a}\frac{A_0}{\Sigma_1}\sum_{\text{modd}}\frac{\sin 2\beta a\tanh\beta c}{m^2+n^2(2b/c)^2}$$
$$\equiv\frac{2c\cos n\pi}{\pi\cosh\alpha a}\frac{A_0\Sigma_2}{\Sigma_1}.$$

Since $\mathrm{grad}V=(\partial V_{\mathrm{I}}/\partial x)$ at $x=0$, the half-current S is

$$S=(\sigma/\mathfrak{r})\int_0^c(\partial V_{\mathrm{I}}/\partial x)_{x=0}dy,$$

where σ is σ_a multiplied by the depth of the crystal, and where the factor $1/\mathfrak{r}$ appears because it is necessary to pass an $\mathfrak{r}$-fold greater current in the equivalent isotropic body to maintain the same potential drop as in the graphite crystal. Then

$$S=\sigma A_0 c/\mathfrak{r}\quad\text{and}\quad A_0=\sigma S\mathfrak{r}/c.$$

Finally,[15]

$$\frac{(\partial V_{\mathrm{I}}/\partial x)}{S}=\frac{1}{\sigma c/\mathfrak{r}}\left[1+\sum_n\frac{2n\cos n\pi}{\cosh(n\pi a/c)}\times\frac{\Sigma_2}{\Sigma_1}\cosh\frac{n\pi x}{c}\cos\frac{n\pi\zeta}{c}\right].$$

TABLE III. Approximate values of $\mathfrak{r}$ from a-axis apparatus.

Crystal[a]	Length ($2b$) (cm)	Half-thickness ($L/2$) (cm)	$\Re$ (experimental)	Boundary condition 1 $\frac{1}{2}\lambda/2b$	Boundary condition 1 $\mathfrak{r}$	Boundary condition 2 $\frac{1}{2}\lambda/2b$	Boundary condition 2 $\mathfrak{r}$
AX-1	0.61	0.050	0.83	0.27	33	0.21	26
AX-2	0.57	0.0045	0.91	0.22	28	0.17	22
AX-3	0.325	0.00377	0.92	0.20	17	0.16	14

[a] These were all Ticonderoga crystals collected by the authors.

Then for Case I and Case II, respectively,

$$[(\partial V_{\rm I}/\partial x)/2S]_{\rm I}=(\mathfrak{r}/\sigma\lambda)\left[1+\sum_n \frac{2n}{\cosh(n\pi 2a/\lambda)}\frac{\Sigma_2(\lambda/2)}{\Sigma_1(\lambda/2)}\right],$$

$$[(\partial V_{\rm I}/\partial x)/S]_{\rm II}=(\mathfrak{r}/\sigma\lambda)\left[1+\sum_n \frac{2n\cos n\pi}{\cosh(n\pi a/\lambda)}\frac{\Sigma_2(\lambda)}{\Sigma_1(\lambda)}\right].$$

The ratio $\Re=[(\partial V_{\rm I}/\partial x)/S]_{\rm II}/[(\partial V_{\rm I}/\partial x)/2S]_{\rm I}$ can be used to determine λ and hence $\mathfrak{r}$.

The solution for the second boundary condition follows in a much simpler manner. The boundary conditions are satisfied by

$$V=\sum_{\rm modd} C_m \cosh\beta\zeta \sin\beta x,$$

where the boundary condition for the upper surface is again expanded in the interval 0 to $2b$ and it is found that

$$C_m=(8bk_2/m^2\pi^2)(\cos\beta a/\sinh\beta c),$$

where $k_2=(\partial V/\partial y)$ under the electrodes. The half-current is

$$S=(\sigma/\mathfrak{r})\sum C_m \sinh\beta c,$$

and for this boundary condition

$$\left[\frac{(\partial V/\partial x)}{2S}\right]_{\rm I}=\frac{\mathfrak{r}}{\sigma}\frac{\pi}{4b}\sum_{\rm modd}\frac{1}{m}\frac{\cos(m\pi a/2b)}{\tanh(m\pi\lambda/4b)}\Big/\sum_{\rm modd}\frac{1}{m^2}\cos(m\pi a/2b),$$

$$\left[\frac{(\partial V/\partial x)}{S}\right]_{\rm II}=\frac{\mathfrak{r}}{\sigma}\frac{\pi}{2b}\sum_{\rm modd}\frac{1}{m}\frac{\cos(m\pi a/2b)}{\sinh(m\pi\lambda/2b)}\Big/\sum_{\rm modd}\frac{1}{m^2}\cos(m\pi a/2b).$$

For most of the measurements a/b was about $\frac{1}{2}$. Using this value, $\Re$ was computed for several values of $0.5\lambda/2b$. The function is sketched in Fig. 7. Since $\lambda=\mathfrak{r}L$, a determination of $\Re$ experimentally can, with this curve, give an approximate value of $\mathfrak{r}$. The results for three crystals are given in Table III.

TABLE IV. Values of σ_a/δ for graphite crystals.

Crystal	Thickness (L) (cm)	Depth (cm)	Length ($2b$) (cm)	Current ($2S$) (10^{-3} amp)	$\partial V/\partial x$ (10^{-6} volt/cm)	σ_a/δ (10^4 (ohm cm)$^{-1}$)
AX-1	0.0101	0.326	0.61	9.86	200/0.144	2.16
AX-2	0.00445	0.257	0.53	9.83	723/0.205	2.49
AX-3	0.00743	0.095	0.33	9.80	604/0.115	2.65
2*A*	0.016	0.185	0.33	9.69	158/0.134	2.8
3*A*	0.00433	0.285	0.41	9.68	370/0.120	2.6
4*A*	0.0127	0.28	0.51	9.72	184/0.188	2.8
8*A*	0.0110	0.356	0.51	9.70	152/0.164	2.7
9*A*	0.0057	0.185	0.46	9.62	691/0.213	2.8
10*A*	0.0136	0.206	0.443	9.93	219/0.170	2.69
12*A*	0.0122	0.210	0.426	9.80	571/0.169	2.50
13*A*	0.0171	0.200	0.378	9.93	223/0.178	2.41
17*A*	0.0062	0.215	0.619	9.77	880/0.298	2.42

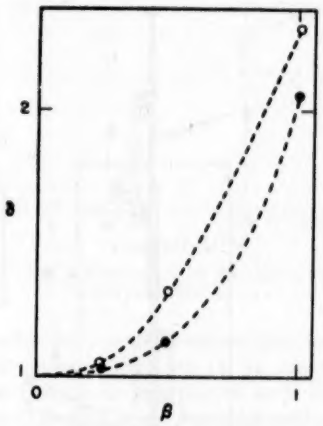

FIG. 8 δ as a function of β. ○ First boundary condition; ● second boundary condition.

The Value of σ_a

If electrodes were placed on the faces of the graphite crystal corresponding to $x=\pm b$ (Fig. 5), the potential gradient along x divided by the half current would be

$$(\partial V/\partial x)/S=2/\sigma L=\mathfrak{r}/\sigma c.$$

With the experimental arrangement used in the preceding experiment Case I, according to the first boundary condition, the potential gradient per unit half-current at $\zeta=c$, $x=0$ is greater than this by the factor δ_1,

$$\delta_1=1+\sum_n \frac{2n}{\cosh(n\pi a/c)}\frac{\Sigma_2(c)}{\Sigma_1(c)},$$

while for the second boundary condition it is greater by the factor δ_2,

$$\delta_2=\frac{\pi c}{2b}\frac{\sum_{\rm modd}(1/m)[\cos(m\pi a/2b)/\tanh(m\pi c/2b)]}{\sum_{\rm modd}(1/m)[\cos(m\pi a/2b)]}.$$

The factors were computed for several values of $c/2b$ under the assumption that $a/b=\frac{1}{2}$ and are shown in Fig. 8. The correct factor δ may be presumed to lie between δ_1 and δ_2. The value of σ_a/δ was determined for a number of crystals, and the results are given in Table IV.

For crystals *AX*-1, *AX*-2, and *AX*-3 the value of δ was in fact determined by the determination of $\Re$ and $0.5\lambda/2b$ and by referring to Fig. 8 it can be seen that for these crystals $\delta<1.03$. For the thickest crystals, 2 A, 13 A, 10 A, and 12 A, δ would not be larger than 1.15. It is therefore concluded that for these crystals $\sigma_a\cong 2.6(10^4)$ (ohm cm^{-1}) within 10 percent.

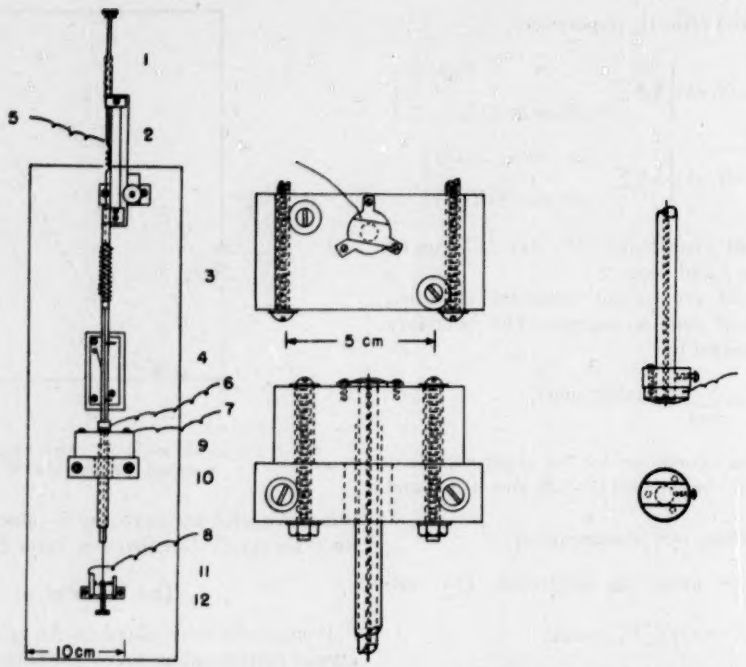

FIG. 9. Apparatus used to determine σ_c. 1. Friction adjustment for upper potential probe. 2. Rack and pinion adjustment for upper current contact. 3. Spring to regulate current contact pressure. 4. Alignment block for upper current contact. 5. Potential lead. 6. Upper current contact lead. 7. Lower current contact lead. 8. Lower potential lead. 9. Lower current contact block. 10. Support platform for current contact block. 11. Cantilever spring for lower potential probe. 12. Withdrawing screw for lower potential probe. Details of upper and lower contacts are shown.

The Determination of σ_c

The apparatus shown in Fig. 9 was used to determine σ_c. A plastic mask prepared for each crystal served to prevent the gold foils from overlapping the edges of the crystal. Potential probes of 2-mil gold wire were brought to the crystal faces through a No. 80 hole (0.014 in.) drilled through the rubber and the gold foil. In the early measurements, the gold foils were strips to which contact was made at one end. It was observed that an appreciable potential drop occurred along these strips. In the apparatus shown here the gold foils are cut in the form of a disk and soldered to a heavy copper ring at a number of points to minimize this effect. The arrangement should give rise to a nearly linear current flow through the crystal. The only question which arises concerns the distribution of potential about the hole. The problem is complicated by the large and somewhat variable contact resistance between the gold and the graphite, perhaps some tenfold greater than the resistance of the crystal itself. It was therefore considered desirable to explore these potentials experimentally.

An apparatus was constructed in which a crystal was clamped between gold foils in a manner similar to that in the apparatus shown in Fig. 9, but with a hole drilled only in the upper plate. This hole was 0.112 cm in diameter, about $3\frac{1}{2}$ times the diameter of the hole in the apparatus used to measure σ_a. The potential drop from the center of the hole to close to the edge of the

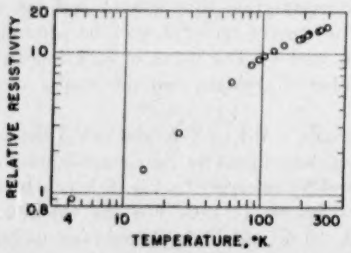

FIG. 10. Effect of temperature on the a-axis resistivity of crystal *LTA*-2.

TABLE V. The determination of σ_c (current about 0.1 amp).

Crystal	Resistance (10^{-5} ohm)	Area (cm^2)	Thickness (cm)	σ_c ((ohm cm)$^{-1}$)
31	222	0.0563	0.0190	156
32	165	0.0816	0.0282	215
25	126	0.0714	0.0177	167
26	109	0.0870	0.0197	193
27	232	0.0387	0.0191	226
28	167	0.0677	0.0221	175
29	163	0.0620	0.0221	224
30	140	0.0642	0.0200	229
33	124	0.0502	0.0123	203

hole was measured in several directions, and the largest drop found was 4 microvolts for a current of 0.10 amp. Since the potential drops measured for most of the crystals were about 100 microvolts, it was assumed that the error introduced by the smaller hole of the σ_c apparatus was small. The results of measurements with the σ_c apparatus are given in Table V. All the measurements were made with a current of about 0.1 amp. The resistance given is the average of 6 to 10 measurements, for each of which the crystal was reinserted into the apparatus. The extreme deviations among these measurements were $\pm$(10–15) percent.

Several reasons are suggested as contributing to the large deviations in the measurements of individual crystals. The crystals do not seem to have a uniform resistance over their entire area. In some cases it was observed that the thickness was not uniform. The contact resistances of the electrodes are high, much greater than the resistance of the crystal. If this contact resistance is not uniform, it would contribute to making the bounding planes nonequipotential. However, the

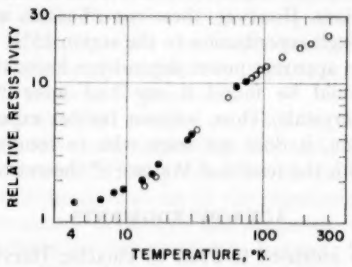

FIG. 11. Effect of temperature on the a-axis resistivity of crystal *LTA*-3. ○ Run 1; ● Run 2.

average of a number of determinations of a crystal seem quite reproducible. Some 42 sets of measurements on Crystal 31 made over several years, each set consisting of 8 to 10 measurements, deviate by only some 10 percent from the results of the first set, quoted here. Some evidence has accrued which indicates that σ_c does in fact vary somewhat from one crystal to another.

The Effect of Temperature on σ_a and σ_c

Apparatus similar to that shown in Figs. 4 and 9 but much more compact were constructed[16] and suspended at the ends of long Monel tubes in a meter-long 10-cm diameter Dewar which was cooled with liquid helium. After the liquid helium had evaporated, the temperature was permitted to rise slowly, and measurements of the resistances of the crystals were continued. In this manner the resistances of the crystals were determined at various temperatures from liquid helium temperature to room temperature. The temperatures were read on a copper-constantan thermocouple, the liquid helium and liquid nitrogen temperatures being taken as calibration

[16] The pads which were used to press the gold foils into contact with the crystals were made of polyvinyl chloride plastic, which seemed to behave better than rubber at low temperatures.

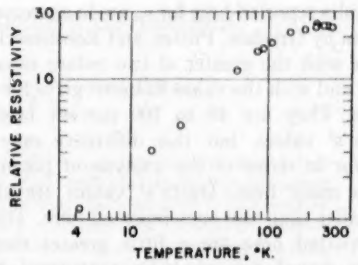

FIG. 12. Effect of temperature on the c-axis resistivity of crystal *LTC*-4.

points. Results for 2 a-axis crystals and for 2 c-axis crystals are shown in Figs. 10, 11, 12, and 13, where the relative resistivities are plotted as a function of temperature. The first power dependence of ρ_a on temperature from about 15°K to about 80°K seems characteristic. From these two results it would seem that ρ_c is more variable, but the maximum somewhat below room temperature seems characteristic although it seems to appear at different temperatures for different crystals. Further measurements at low temperatures are in progress.

DISCUSSION

The values found here for τ determined directly from relative potential distributions are larger than the ratio of the separate measurements of $(\sigma_a)^{\frac{1}{2}}$ to that of $(\sigma_c)^{\frac{1}{2}}$ by a factor of about 1.5. It was shown that for the crystals measured here, σ_a could not have been greater by 5 percent than the values reported. It does not seem possible that σ_c could be in error by the factor required to produce agreement, 2 or 3. It must therefore be concluded that there may be small errors in σ_a and σ_c; perhaps 5 percent in σ_a and perhaps as much as 20 percent in σ_c; but that most of the error is in τ and may reside in the large electrodes used in the first method and the irregular shape of the crystals in the second. In the first method the large electrodes would cause the potential to spread more uniformly over the surface and not to rise so high near the electrode; both these effects would move the potential curve to the left on adjustment, leading to a high value for τ. A detailed discussion of the second method is hardly necessary; in fact a/b was never exactly $\frac{1}{2}$ as assumed, and the crystals were not exactly rectangular in the xy plane, so that the dimensions used were not exact. However, although these direct determinations do not give exact values of τ, they prove conclusively that for these crystals σ_a/σ_c lies in the range 10^2 to 10^3.

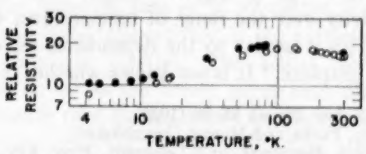

FIG. 13. Effect of temperature on the c-axis resistivity of crystal *LTC*-5. ○ Run 1; ● Run 2.

The results reported here for σ_a are in agreement with those given by Grisdale, Pfister, and Roosbroeck.[9] They also agree with the greater of two values reported by Kinchin[10] and with the value Roberts[1] gives for his best specimens. They are 40 to 100 percent larger than Washburn's[3] values, but this difference may be accounted for in terms of the analysis of potential distributions made here. Dutta's[8] values are about 2½ times smaller than the ones reported here. The values for σ_c reported here are a little greater than those Washburn found for what he considered his best samples, and they are about twice as great as his average value and the value reported by Grisdale, Pfister, and Roosbroeck but are some 200 times greater than Dutta's values for σ_c. It is therefore considered that the results reported here are in agreement with the results found by others except for those of Dutta[8] and the similar fragmentary earlier report by Krishnan and Ganguli.[7] It is difficult to assess their work from the information they have published since they have not given a sufficiently detailed description of their crystals. However, several comments can be made on the basis of experiments performed by the authors and others. Ott[17] claimed that even the agitation of the acid during solution of the rock was sufficient to alter the diffraction patterns. Cleaving and cutting crystals, such as Dutta did, may be expected to affect them severely. Attempts were made by one of the authors, in collaboration with Hennig and Montet,[18] to copperplate some graphite crystals. It was found that under some conditions, the graphite swelled enormously or blistered, which was interpreted as being caused by the interlamellar penetration of protons which combine to form hydrogen gas between the planes. It was therefore concluded that copperplated graphite crystals would have to be very carefully examined before any results with them could be trusted. It further must be demonstrated that (a) copperplatings provide an equipotential surface, for an appreciable potential drop may occur along a thin copperplate, and (b) that there is no appreciable contact resistance between such a plate and the graphite surface.

It may be expected that imperfections in the crystal will introduce scattering centers and decrease the mean free path. This effect would become especially noticeable in measurements at low temperature. However, since imperfections might trap electrons or create holes, the argument is not conclusive. It was found that introducing imperfections by means of fast neutron irradiation decreased both σ_a and σ_c and both then developed a slightly negative temperature coefficient of resistivity over the range of temperatures 4.2°K to 300°K. This is similar to the dependence reported for artificial graphite.[19] It is not known whether the imperfections introduced by fast neutrons produce the same effects as those which may be found in graphite crystals. However, it may be significant that Washburn[3] found that his best specimens showed higher values for σ_c. Thus, if the measurements made by Krishnan and Ganguli and by Dutta are correct, it may be that their crystals contain more imperfections. It is unfortunate that Dutta's measurements of the effect of temperature on σ_a and σ_c have not been carried into the significant region below 90°K. However, if his data are plotted on the graphs presented here, his curve for σ_a falls somewhat above the data shown here, and this is interpreted as indicating more scattering in his crystals. If the minimum found here in the temperature variation of σ_c is general, his results for σ_c are entirely deceptive.

There is not enough information to interpret the few low-temperature data reported here for natural graphite crystals. The temperature dependence of the resistivity found here must involve a contribution from scattering by imperfections and possibly impurities. It seems likely that much of the a-axis resistance found below 10°K, where the power dependence decreases, is due to these contributions. However, these contributions must also make enough contribution to the region 15°K to 70°K to give an apparent power dependence lower than that which would be found if one had more "perfect" graphite crystals. Thus, without further experimental information, it does not seem wise to compare these results with the results of Wallace's[20] theoretical study.

ACKNOWLEDGMENTS

We are indebted to Prof. C. Palache, Harvard University; Mr. L. H. Bauer, Franklin, N. J.; Dr. W. F. Foshag, U. S. National Museum; and Dr. H. S. Spence, Department of Mines and Resources, Canada; among others, for furnishing samples from which were isolated graphite crystals which were employed in our studies. We also express our appreciation to Dr. J. G. Broughton, New York State Geological Survey, and to Mr. C. V. Lonergan, Ticonderoga, New York, for the assistance they rendered us in our collections in the field. The method of cutting crystals with a sand blast was suggested by Mr. V. D. Carver, formerly of this laboratory; it was through the kindness of Dr. Leonard Boke, Berwyn, Illinois, who permitted us the use of his dental equipment for the purpose, that the technique was employed.

We are indebted to O. C. Simpson of this laboratory for one of the solutions to Laplace's equation used here and for general encouragement and advice. We are also indebted to G. Hennig for several discussions and to G. Hennig and G. Montet of this laboratory for their collaboration in copperplating graphite crystals and to D. Osborne of this laboratory for assistance and advice in making the measurements at liquid helium temperatures.

[17] H. Ott, Ann. Physik **85**, 86 (1928).
[18] Hennig, Fuchs, and Montet (unpublished).
[19] Reynolds, Hemstreet, and Leinhardt, Phys. Rev. **91**, 1152 (1953).
[20] P. R. Wallace, Phys. Rev. **71**, 634 (1947).

Theory of the Galvanomagnetic Effects in Germanium

B. ABELES AND S. MEIBOOM
Department of Applied Mathematics, The Weizmann Institute of Science, Rehovot, Israel

(Received January 26, 1954)

In this paper a simple anisotropic theory of the galvanomagnetic effects in germanium is presented. It is assumed that the energy as a function of momentum has a number of extrema; near the extrema the energy is approximated by a quadratic function of momentum, and the relaxation time is assumed to be a function of energy only. Equations for the galvanomagnetic coefficients in any crystallographic direction are derived. The dependence of the coefficients on magnetic field strength is calculated and an expression for the ratio between Hall mobility and conduction mobility is obtained. The calculated values of the magnetoresistance are compared with measurements of Pearson and Suhl. The agreement between the calculated and the observed values is satisfactory in *n*-germanium, but not in *p*-germanium.

I. INTRODUCTION

SYSTEMATIC measurements of the magnetoresistance coefficients in germanium have been published by Estermann and Foner[1] and by Pearson and Suhl.[2] Their results show that the magnetoresistance in *n*-germanium is highly anisotropic and that the longitudinal effect is of the same order of magnitude as the transverse effect. In *p*-germanium the transverse effect is nearly isotropic, while the longitudinal effects are much smaller. Clearly, a simple isotropic theory cannot explain the behavior of germanium.

Seitz[3] has discussed a model in which the relaxation time is a function with cubic symmetry and the energy surfaces are spherical. As pointed out by Pearson and Suhl,[2] Seitz's theory does not fit the experimental data for *n*-germanium. Shockley[4] has suggested that the energy surfaces are degenerate; he has not, however, published explicit calculations.

In this paper an attempt will be made to explain the observed magnetoresistance effects by assuming a simple anisotropic model, in which the energy surfaces in momentum space have a number of extrema. Around an extremum, the energy surface will not, in the general case, have cubic symmetry. The whole set of energy surfaces, of course, should have the cubic symmetry of the crystal.

II. THE PHYSICAL MODEL

In order to carry out quantitative calculations, specific assumptions must be made as to the shape of the energy surfaces near the extrema and the dependence of the relaxation time on the momentum $\mathbf{P}$. The simplest assumptions are:

1. The energy $\mathcal{E}$ can be approximated by a quadratic function of momentum $\mathbf{P}$ near each extremum; with appropriate choice of the coordinate system we can write

$$\mathcal{E}=\pm[(P_1^2/2m_1)+(P_2^2/2m_2)+(P_3^2/2m_3)]. \quad (2.1)$$

2. For the case of thermal scattering, the relaxation time τ is assumed to be given by

$$\tau=l/\mathcal{E}^{\frac{1}{2}}, \quad (2.2)$$

where l depends on temperature only.

Theoretical calculations of τ as function of $\mathbf{P}$ become very complicated in the case of ellipsoidal energy surfaces and, to our knowledge, have not been carried out. Assumption (2.2) has been adopted because it is the simplest one which will give the right dependence of τ on energy, in a fixed direction in $\mathbf{P}$ space (compare Shockley[5]). This assumption will be discussed in Sec. VI.

3. It is assumed that in the relaxation process only transitions between states belonging to the same extremum take place. In other words, transitions between states belonging to different extrema are neglected. With this assumption, each extremum can be treated independently, the total current being given as the sum of the contributions from each extremum.

4. According to assumption (1) the energy surfaces near an extremum are sets of ellipsoids, given by Eq. (2.1). Each set is characterized by one of its ellipsoids; for the sake of brevity, we shall, therefore, refer to a set as an ellipsoid. As mentioned in the Introduction, a number of these ellipsoids must be so arranged in the Brillouin zone as to obtain cubic symmetry. The two simplest models which fulfill this requirement are:

(a) Three or six ellipsoids of revolution ($m_1=m_2\neq m_3$), the main axes of which are directed along the cubic axes of the reciprocal lattice.

(b) Four or eight ellipsoids of revolution, the main axes of which are directed along the body diagonals of the cubic unit cell of the reciprocal lattice.

These models will have three and four ellipsoids, respectively, if the extrema are situated either on the faces of the Brillouin zone or at its center. They will have six and eight, respectively, if the extrema are at some intermediate position. The actual position is immaterial as far as the theory given here goes, provided of course that assumptions 1 to 3 are valid.

[1] I. Estermann and A. Foner, Phys. Rev. **79**, 365 (1950).
[2] G. L. Pearson and H. Suhl, Phys. Rev. **83**, 768 (1951).
[3] F. Seitz, Phys. Rev. **79**, 372 (1950).
[4] W. Shockley, Phys. Rev. **78**, 173 (1950).
[5] W. Shockley, *Electrons and Holes in Semiconductors* (D. Van Nostrand Company, Inc., New York, 1950), p. 493.

More complicated models involve a greater number of ellipsoids, not necessarily of revolution.

It will be shown that the experimental results for n-germanium can be explained on the basis of model (b) for the conduction band. Model (a) results in zero longitudinal magnetoresistance effect in the (100) direction, but the observed longitudinal effect is of the same order as the transverse effect.[2] The experimental results for p-germanium indicate that model (a) applies to the valence band.

III. THEORY FOR WEAK MAGNETIC FIELDS

We shall first give the theory based on the series expansion of the distribution function in powers of H, neglecting terms in H^3 and higher. This theory is a special case of the more general theory, given in Sec. IV, which will not be restricted to weak magnetic fields, and from which the saturation effects can be computed. The theory for weak magnetic fields is given first, however, because it shows the main features of the treatment, and because the general theory, which gives rather cumbersome equations, can then be treated in a more schematic way.

It is well known (e.g., Wilson,[6] or Davis[7]), that the current in the presence of electric and magnetic fields is given by

$$\mathbf{I}=(e/4\pi^3\hbar^3)\int \operatorname{grad}\mathcal{E}(\partial f_0/\partial\mathcal{E})\phi dV, \tag{3.1}$$

where

$$\phi=-e\{\tau\mathbf{E}\cdot\operatorname{grad}\mathcal{E}-(e/c)\tau\mathbf{H}\cdot\boldsymbol{\Omega}(\tau\mathbf{E}\cdot\operatorname{grad}\mathcal{E}) +(e/c)^2\tau\mathbf{H}\cdot\boldsymbol{\Omega}[\tau\mathbf{H}\cdot\boldsymbol{\Omega}(\tau\mathbf{E}\cdot\operatorname{grad}\mathcal{E})]+\cdots\}, \tag{3.2}$$

and

$$\boldsymbol{\Omega}\equiv\operatorname{grad}\mathcal{E}\times\operatorname{grad}. \tag{3.3}$$

Here $\mathbf{I}$ is the current density, $\mathbf{E}$ the electric field, $\mathbf{H}$ the magnetic field, $\mathcal{E}$ the energy, f_0 the Fermi distribution function, dV volume element in momentum space. The other symbols have their conventional meaning.

It is convenient to use tensor notation. Equation (3.3) is written as

$$\Omega_i\equiv\epsilon_{ikl}\frac{\partial\mathcal{E}}{\partial P_k}\frac{\partial}{\partial P_l}. \tag{3.4}$$

The convention of summing over repeated indices is used, and the tensor ϵ_{ikl} is defined as usual,

$$\begin{aligned}&\epsilon_{123}=\epsilon_{231}=\epsilon_{312}=+1,\\ &\epsilon_{213}=\epsilon_{132}=\epsilon_{321}=-1,\end{aligned} \tag{3.5}$$

all other components being zero.

We shall first calculate the current contribution of one ellipsoid. Because, in semiconductors, $\partial f_0/\partial\mathcal{E}$ decreases exponentially with energy, and because Eq. (2.1) will be substituted in (3.1), the integration in (3.1) can be taken over the whole momentum space. On inserting Eq. (3.2) into (3.1), and retaining only terms up to H^2, we obtain for the contribution to the current density from one ellipsoid

$$i_i=\sigma_{ik}E_k+\sigma_{ikl}E_kH_l+\sigma_{iklm}E_kH_lH_m, \tag{3.6}$$

where

$$\sigma_{ik}=-a\int\tau\frac{\partial f_0}{\partial\mathcal{E}}\frac{\partial\mathcal{E}}{\partial P_i}\frac{\partial\mathcal{E}}{\partial P_k}dV, \tag{3.7}$$

$$\sigma_{ikl}=ab\int\tau\frac{\partial f_0}{\partial\mathcal{E}}\frac{\partial\mathcal{E}}{\partial P_i}\frac{\partial\mathcal{E}}{\partial P_r}\frac{\partial}{\partial P_s}\left(\tau\frac{\partial\mathcal{E}}{\partial P_k}\right)\epsilon_{lrs}dV, \tag{3.8}$$

$$\sigma_{iklm}=-ab^2\int\tau\frac{\partial f_0}{\partial\mathcal{E}}\frac{\partial\mathcal{E}}{\partial P_i}\frac{\partial\mathcal{E}}{\partial P_r}\frac{\partial}{\partial P_s}\left[\tau\frac{\partial\mathcal{E}}{\partial P_t}\frac{\partial}{\partial P_u}\left(\tau\frac{\partial\mathcal{E}}{\partial P_k}\right)\right]\epsilon_{mrs}\epsilon_{ltu}dV, \tag{3.9}$$

$$a=e^2/4\pi^3\hbar^3,\quad b=e/c. \tag{3.10}$$

When τ is a function of $\mathcal{E}$ only, it can easily be shown that in the above equations terms involving derivatives of τ give zero contribution. Also, if we choose the momentum coordinates along the principal axes of the energy ellipsoid, it is seen that, with our assumptions, τ and $\mathcal{E}$ are even functions of $\mathbf{P}$, and accordingly $\partial\mathcal{E}/\partial P$ is odd. It follows that on these coordinates

$$\begin{aligned}&\sigma_{ik}\neq0 \text{ only when } i=k,\\ &\sigma_{ikl}\neq0 \text{ only when } i\neq k\neq l\neq i,\\ &\sigma_{iklm}\neq0 \text{ only when the indices are equal in pairs.}\end{aligned} \tag{3.11}$$

The integrals (3.7), (3.8), and (3.9) can be computed by integrating first over a constant energy surface and then over the energy

$$dV=dSd\mathcal{E}/|\operatorname{grad}\mathcal{E}|, \tag{3.12}$$

where dS is an element of the constant energy surface. By using (2.1), (2.2), (3.11), and (3.12), Eq. (3.7) becomes

$$\sigma_{ik}=-\frac{al}{m_i^2}\int_0^\infty\mathcal{E}^{-\frac{1}{2}}\frac{\partial f_0}{\partial\mathcal{E}}d\mathcal{E}\times\int\frac{P_i^2dS}{[(P_1/m_1)^2+(P_2/m_2)^2+(P_3/m_3)^2]^{\frac{1}{2}}}. \tag{3.13}$$

The surface integral can easily be computed for an ellipsoid of revolution ($m_1=m_2$) by introducing cylindrical coordinates. If this integral is denoted by D_i, the result is

$$\begin{aligned}&D_1=D_2=2^{7/2}3^{-1}\pi m_1^2m_3^{\frac{1}{2}}\mathcal{E}^{\frac{1}{2}},\\ &D_3=2^{7/2}3^{-1}\pi m_1m_3^{\frac{1}{2}}\mathcal{E}^{\frac{1}{2}}.\end{aligned} \tag{3.14}$$

The integral over the energy becomes

$$\int_0^\infty\mathcal{E}(\partial f_0/\partial\mathcal{E})d\mathcal{E}=-2^{\frac{1}{2}}\pi^{\frac{1}{2}}\hbar^3(kT)^{-\frac{1}{2}}nm_1^{-1}m_3^{-\frac{1}{2}}=A. \tag{3.15}$$

[6] A. H. Wilson, *The Theory of Metals* (Cambridge University Press, Cambridge, 1953), second edition, p. 225.
[7] L. Davies, Phys. Rev. 56, 93 (1939).

The above result is for the nondegenerate case: i.e., f_0 has been approximated by the Boltzmann distribution,

$$f_0=\exp[-(\mathcal{E}-\mathcal{E}_F)/kT],$$

and $\mathcal{E}_F$ has been expressed in terms of the number of electrons per unit volume n and the effective masses m_1 and m_3.

Inserting (3.14) and (3.15) into (3.13) we obtain

$$\begin{aligned}\sigma_{11}&=\sigma_{22}=uK,\\ \sigma_{33}&=u,\end{aligned}\tag{3.16}$$

where

$$u=2^2 3^{-1}\pi^{-\frac{1}{2}}e^2(kT)^{-\frac{1}{2}}lnm_3^{-1},\tag{3.17}$$

$$K=m_3/m_1.\tag{3.18}$$

The integrals (3.8) and (3.9) yield, again, the surface integrals D_1 and D_3 (3.14), while the integrals over the energy become, respectively,

$$\int_0^\infty \mathcal{E}^{\frac{1}{2}}(\partial f_0/\partial\mathcal{E})d\mathcal{E}=2^{-1}\pi^{\frac{1}{2}}(kT)^{-\frac{1}{2}}A,\tag{3.19}$$

$$\int_0^\infty (\partial f_0/\partial\mathcal{E})d\mathcal{E}=(kT)^{-1}A,\tag{3.20}$$

where A is the expression defined in (3.15).

Taking all factors together, the nonzero terms of (3.8) and (3.9) become

$$\begin{aligned}&\sigma_{123}=-\sigma_{213}=-2^{-1}\pi^{\frac{1}{2}}uvK^2,\\ &\sigma_{231}=\sigma_{312}=-\sigma_{132}=-\sigma_{321}=-2^{-1}\pi^{\frac{1}{2}}uvK,\\ &\sigma_{1122}=\sigma_{2211}=-uvK^2,\\ &\sigma_{1133}=\sigma_{2233}=-uv^2K^3,\\ &\sigma_{3311}=\sigma_{3322}=-uv^2K,\\ &\sigma_{1212}=\sigma_{2121}=\sigma_{2323}=\sigma_{3232}=\sigma_{3131}=\sigma_{1313}=uv^2K,\end{aligned}\tag{3.21}$$

where

$$v=c^{-1}el(kT)^{-\frac{1}{2}}m_3^{-1}.\tag{3.22}$$

We now have to sum the current density contributions from each ellipsoid. If we denote the total current density by **I**, we can write

$$I_i=\Sigma_{ik}E_k+\Sigma_{ikl}E_kH_l+\Sigma_{iklm}E_kH_lH_m,\tag{3.23}$$

where each Σ tensor is the sum of the corresponding σ tensors, belonging to differently oriented ellipsoids.

For model (a) (three ellipsoids along the main crystallographic directions) we obtain

$$\begin{aligned}\Sigma_{ik}&=(\sigma_{11}+\sigma_{22}+\sigma_{33})\delta_{ik}=u(2K+1)\delta_{ik},\\ \Sigma_{ikl}&=(\sigma_{123}+\sigma_{231}+\sigma_{312})\epsilon_{ikl}\\ &=-2^{-1}\pi^{\frac{1}{2}}uvK(K+2)\epsilon_{ikl},\end{aligned}\tag{3.24}$$

$$\begin{aligned}\Sigma_{iklm}&=\sigma_{1122}+\sigma_{1133}+\sigma_{3322}=-uv^2K(K^2+K+1),\\ &\qquad i=k\neq l=m\\ &=\sigma_{1212}+\sigma_{1313}+\sigma_{3232}=3uv^2K^2,\quad i=l\neq k=m\end{aligned}$$

where δ_{ik} is the Kronecker symbol.

All components not given above are zero.

In the case of model (b) (four ellipsoids along the body diagonals of the cubic unit cell) the components of the σ tensors are first transformed to a coordinate system along the cubic axes. The transformation matrix is

$$A_{i'}{}^{i}=(1/2\sqrt{3})\begin{vmatrix}1+\sqrt{3} & 1-\sqrt{3} & 2\\ 1-\sqrt{3} & 1+\sqrt{3} & 2\\ -2 & -2 & 2\end{vmatrix}\tag{3.25}$$

and the new components are

$$\begin{aligned}\sigma_{i'k'}&=(1/3)(2\sigma_{11}+\sigma_{33})\delta_{i'k'},\\ \sigma_{i'k'l'}&=(1/3)(\sigma_{123}+\sigma_{231}+\sigma_{312})\epsilon_{i'k'l'},\\ \sigma_{i'k'l'm'}&=(2/9)(2\sigma_{1111}+\sigma_{1133}+\sigma_{3311}+2\sigma_{1313}),\\ &\qquad i'=k'=l'=m'\\ &=(1/18)(7\sigma_{1122}+4\sigma_{1133}+4\sigma_{3311}-3\sigma_{1212}),\\ &\qquad i'=k'\neq l'=m'\\ &=(1/18)(\sigma_{1122}-2\sigma_{1133}-2\sigma_{3311}+15\sigma_{1212}),\\ &\qquad i'=l'\neq k'=m'\\ &=(1/18)(\sigma_{1122}-2\sigma_{1133}-2\sigma_{3311}-3\sigma_{1212}),\\ &\qquad i'=m'\neq k'=l'.\end{aligned}\tag{3.26}$$

The tensors for the three other ellipsoids are obtained by successive rotations of the coordinate system about one of the cubic axes.

Generally, there are nonzero components not given in (3.26). However, calculation shows that these components cancel out after summation over the four ellipsoids, while for the components given above, the summation reduces to multiplication by 4. Dropping the primes on the indices, we obtain

$$\begin{aligned}\Sigma_{ik}&=(4/3)u(2K+1)\delta_{ik},\\ \Sigma_{ikl}&=-(2/3)\pi^{\frac{1}{2}}uvK(K+2)\epsilon_{ikl},\\ \Sigma_{iklm}&=-(8/9)uv^2K(K-1)^2, && i=k=l=m\\ &=-(4/9)uv^2K(2K^2+5K+2), && i=k\neq l=m\\ &=(4/9)uv^2K(K^2+7K+1), && i=l\neq k=m\\ &=(4/9)uv^2K(K-1)^2, && i=m\neq k=l.\end{aligned}\tag{3.27}$$

It can be proved by symmetry considerations that all components not given above are zero, not only for the model discussed but for all cubic crystals.

In order to obtain the galvanomagnetic coefficients in accordance with their usual definition, Eq. (3.23)

must be inverted

$$E_i=\Lambda_{ik}I_k+\Lambda_{ikl}I_kH_l+\Lambda_{iklm}I_kH_lH_m. \quad (3.28)$$

If (3.28) is inserted in (3.23), and terms of the same order are equated, we obtain

$$\begin{aligned}&\Lambda_{ik}=(1/\sigma_0)\delta_{ik},\\ &\Lambda_{ikl}=-(1/\sigma_0)^2\Sigma_{ikl}\equiv -R_0\epsilon_{ikl},\\ &\Lambda_{iklm}=(1/\sigma_0)^2[-\Sigma_{iklm}+(1/\sigma_0)\Sigma_{iam}\Sigma_{akl}],\end{aligned} \quad (3.29)$$

where the conductivity σ_0 is given by

$$\Sigma_{ik}=\sigma_0\delta_{ik}, \quad (3.30)$$

and R_0 is the Hall constant.

From (3.28) it is seen that $\Lambda_{1111}\sigma_0$ and $\Lambda_{1122}\sigma_0$ are, respectively, the longitudinal and the transverse magnetoresistance coefficients for directions parallel to the cubic axes of the crystal. By transforming Λ_{iklm} to other coordinates, the coefficients in any direction can be found.

The above results complete the formal theory. However, for comparison with the measurements of Pearson and Suhl,[2] we will need explicit expressions for the coefficients in specified crystallographic directions. For model (b), we obtain from (3.29), by insertion of (3.30), (3.21), (3.22), and (3.17),

$$\begin{aligned}&R_0=(3\pi/8)[3K(K+2)/(2K+1)^2](1/Nec),\\ &M_{100}/H^2=(8/3\pi)R_0^2\sigma_0^2(2K+1)(K-1)^2/K(K+2)^2,\\ &M_{100}^{010}/H^2=(1/3\pi)R_0^2\sigma_0^2[K^2(16-3\pi)\\ &\qquad +K(16-6\pi)+4]/K(K+2),\\ &M_{110}=(1/2)M_{100},\\ &M_{110}^{1\bar{1}0}=(1/2)M_{100}+M_{100}^{010},\\ &M_{110}^{001}=M_{100}^{001},\end{aligned} \quad (3.31)$$

where R_0 denotes the Hall coefficient; σ_0 the conductivity; $N=4n$ the total number of electrons in the conduction band; $M_{ikl}/H^2=(\sigma_0-\sigma)/\sigma H^2$ the longitudinal magnetoresistance coefficient in the (ikl) direction of the crystal; and $M_{ikl}^{mnp}/H^2=(\sigma_0-\sigma)/\sigma H^2$ the transverse magnetoresistance coefficient, **I** being in the (ikl) direction, and **H**, in the (mnp) direction of the crystal.

We will also need equations for model (a) for the case of impurity scattering. The theory can easily be adapted to this case if the relaxation time is assumed to be given by

$$\tau=l\mathcal{E}^{\frac{1}{2}}. \quad (3.32)$$

In Eqs. (3.15), (3.19), and (3.20), $\mathcal{E}$ now appears to the power 3, $4\frac{1}{2}$, and 6, respectively. In the final results only the numerical coefficients differ from those in the equations for thermal scattering. We obtain for model (a)

$$\begin{aligned}&R_0=(3\pi/8)1.64[3K(K+2)/(2K+1)^2](1/Nec),\\ &M_{100}=0,\\ &M_{100}^{010}/H^2=R_0^2\sigma_0^2\{[1.58(2K^3+3K^2+3K+1)/\\ &\qquad K(K+2)^2]-1\},\\ &M_{110}/H^2=R_0^2\sigma_0^2[0.79(2K^3-3K^2+1)/K(K+2)^2],\\ &M_{110}^{1\bar{1}0}=M_{100}^{010}-M_{110},\\ &M_{110}^{001}=M_{100}^{001}.\end{aligned} \quad (3.33)$$

IV. STRONG-FIELD THEORY

The series (3.2) for ϕ can be written in closed form if τ is a function of energy and if the energy surfaces are quadratic. The expression for ϕ, which is a generalization of the one given by Wilson,[8] is

$$\begin{aligned}\phi=&-(e\tau/m_1)\{P_1+(e\tau/c)[(P_2H_3/m_2)-(P_3H_2/m_3)]\\ &+(e\tau/c)^2(H_1/m_2m_3)(P_1H_1+P_2H_2+P_3H_3)\}\\ &\times\{1+(e\tau/c)^2[(H_1^2/m_2m_3)+(H_2^2/m_3m_1)\\ &+(H_3^2/m_1m_2)]\}^{-1}E_1+(\text{two other terms obtained}\\ &\text{by cyclic permutation of the indices}),\end{aligned} \quad (4.1)$$

where the momentum coordinates are chosen along the principal axes of the ellipsoid. Inserting Eq. (4.1) in Eq. (3.1), we obtain for the current density **i**

$$i_i=s_{ik}(\mathbf{H})E_k, \quad (4.2)$$

where the components of $s_{ik}(\mathbf{H})$ are integrals over **P** space and are functions of **H**. If τ is given by Eq. (2.2), the integrals can be computed, similarly as in Sec. III, by integrating first over a constant-energy surface and then over the energy. The integrals over equal-energy surfaces are of the type (3.14). The three integrals over energy[9] are now more complicated than in Sec. III and are given by

$$\begin{aligned}&\int_0^\infty\frac{\partial f_0}{\partial\mathcal{E}}\frac{\mathcal{E}^2}{\mathcal{E}+kTw^2}d\mathcal{E}=-A\alpha(w),\\ &\int_0^\infty\frac{\partial f_0}{\partial\mathcal{E}}\frac{\mathcal{E}^{\frac{1}{2}}}{\mathcal{E}+kTw^2}d\mathcal{E}=-(kT)^{-\frac{1}{2}}A\beta(w),\\ &\int_0^\infty\frac{\partial f_0}{\partial\mathcal{E}}\frac{\mathcal{E}}{\mathcal{E}+kTw^2}d\mathcal{E}=-(kT)A\gamma(w),\end{aligned} \quad (4.3)$$

where

$$w=vK^{\frac{1}{2}}(H_1^2+H_2^2+KH_3^2)^{\frac{1}{2}}, \quad (4.4)$$

$$\alpha(\xi)=1-\xi^2+\xi^4\exp(\xi^2)E(\xi^2), \quad (4.5)$$

$$\beta(\xi)=(\pi)^{\frac{1}{2}}[\tfrac{1}{2}-\xi^2+(\pi)^{\frac{1}{2}}\xi^3\exp(\xi^2)F(\xi)], \quad (4.6)$$

$$\gamma(\xi)=1-\xi^2\exp(\xi^2)E(\xi^2), \quad (4.7)$$

[8] Reference 6, page 210.

[9] J. W. Harding, Proc. Roy. Soc. (London) **A140**, 205 (1933), obtained the same integrals in the treatment of the isotropic case.

and A is given by (3.15); K by (3.18); and v by (3.22). $E(x)$ is the integral-logarithm function and $1-F(x)$ is the error function,

$$E(x)=\int_x^\infty (e^{-t}/t)dt,$$
$$F(x)=1-(2/\sqrt{\pi})\int_0^x \exp(-t^2)dt. \tag{4.8}$$

Using Eqs. (4.3) and (3.14) we obtain for s_{ik}

$$\begin{aligned}
s_{11}&=uK[\alpha(w)+v^2H_1^2K\gamma(w)],\\
s_{22}&=uK[\alpha(w)+v^2H_2^2K\gamma(w)],\\
s_{33}&=u[\alpha(w)+v^2H_3^2K^2\gamma(w)],\\
s_{12}&=vuK^2[-\beta(w)H_3+vH_1H_2\gamma(w)],\\
s_{23}&=vuK[-\beta(w)H_1+vH_2H_3K\gamma(w)],\\
s_{31}&=vuK[-\beta(w)H_2+vH_3H_1K\gamma(w)],\\
s_{ik}(\mathbf{H})&=s_{ki}(-\mathbf{H}),
\end{aligned} \tag{4.9}$$

where u is given by (3.17).

For model (b) (four ellipsoids), $s_{ik}(\mathbf{H})$ must be transformed to the new coordinate system along the cubic axes. This must be performed in two steps, since $s_{ik}(\mathbf{H})$ is not a true tensor. First, the components of $\mathbf{H}$ are regarded as parameters; $s_{ik}(\mathbf{H})$ then transforms as a tensor and its new components are obtained by applying transformation (3.25). The components of the transformed $s_{ik}(\mathbf{H})$ are obtained, however, for a magnetic field which has not the original direction but has been rotated along with the coordinate system. The second step, therefore, consists in replacing $\mathbf{H}$ in the transformed $s_{ik}(\mathbf{H})$ by the original magnetic field referred to the new coordinate system. The s_{ik}, for the other three ellipsoids are obtained by three successive rotations about one of the cubic axes. Denoting by S_{ik} the sum over the four different s_{ik}, we obtain for the total current $\mathbf{I}$

$$I_i=S_{ik}E_k, \tag{4.10}$$

where

$$\begin{aligned}
S_{11}&=u\sum_{j=1}^{4}[\tfrac{1}{3}(2K+1)\alpha(w_j)+v^2H_1^2K^2\gamma(w_j)],\\
S_{12}&=u\sum_{j=1}^{4}[\tfrac{1}{3}(K-1)(-1)^j\alpha(w_j)-\tfrac{1}{3}vKq_j\beta(w_j)\\
&\qquad +v^2H_1H_2K^2\gamma(w_j)],\\
S_{ik}(\mathbf{H})&=S_{ki}(-\mathbf{H}),
\end{aligned} \tag{4.11}$$

$$\begin{aligned}
w_1&=3^{-\frac{1}{2}}vK^{\frac{1}{2}}[(K+2)(H_1^2+H_2^2+H_3^2)\\
&\qquad +2(K-1)(H_1H_2+H_2H_3+H_3H_1)]^{\frac{1}{2}},\\
w_2&=3^{-\frac{1}{2}}vK^{\frac{1}{2}}[(K+2)(H_1^2+H_2^2+H_3^2)\\
&\qquad +2(K-1)(-H_1H_2-H_2H_3+H_3H_1)]^{\frac{1}{2}},\\
w_3&=3^{-\frac{1}{2}}vK^{\frac{1}{2}}[(K+2)(H_1^2+H_2^2+H_3^2)\\
&\qquad +2(K-1)(H_1H_2-H_2H_3-H_3H_1)]^{\frac{1}{2}},
\end{aligned} \tag{4.12}$$

$$\begin{aligned}
w_4&=3^{-\frac{1}{2}}vK^{\frac{1}{2}}[(K+2)(H_1^2+H_2^2+H_3^2)\\
&\qquad +2(K-1)(-H_1H_2+H_2H_3-H_3H_1)]^{\frac{1}{2}},\\
q_1&=(K-1)H_1+(K-1)H_2+(K+2)H_3,\\
q_2&=(K-1)H_1-(K-1)H_2+(K+2)H_3,\\
q_3&=-(K-1)H_1-(K-1)H_2+(K+2)H_3,\\
q_4&=-(K-1)H_1+(K-1)H_2+(K+2)H_3.
\end{aligned} \tag{4.13}$$

The other components of S_{ik} are obtained by cyclic permutation of the indices of H_i in Eqs. (4.11), (4.12), and (4.13).

The galvanomagnetic effects for specified crystallographic directions are obtained by inserting in Eq. (4.10) the appropriate values of $\mathbf{I}$ and $\mathbf{H}$, and then solving for $\mathbf{E}$. In the equations that follow, the results are given for the directions measured by Pearson and Suhl:[2]

$$\begin{aligned}
R_{100}^{010}&=[vK(K+2)/(2K+1)](\beta/\alpha\sigma_{100}^{010}),\\
M_{100}&=\{(2K+1)(K+2)/[9K+2(K-1)^2\alpha]\}-1,\\
M_{100}^{010}&=\{\alpha/[\alpha^2+3\xi^2\beta^2K(K+2)/(2K+1)^2]\}-1,\\
R_{110}^{001}&=R_{100}^{001},\\
R_{110}^{1\bar{1}0}&=[vK/(2K+1)][3\beta_1+(2K+1)\beta_2]/\\
&\qquad [(\alpha_1+\alpha_2)\sigma_{110}^{1\bar{1}0}],\\
M_{110}^{001}&=M_{100}^{001},\\
M_{110}^{1\bar{1}0}&=2(\alpha_1+\alpha_2)\{(\alpha_1+\alpha_2)^2\\
&\qquad +(\alpha_2^2-\alpha_1^2)(K-1)/(2K+1)\\
&\qquad +v^2H^2K^2[3\beta_1/(2K+1)+\beta_2]^2\}^{-1}-1,\\
M_{110}&=\{(2K+1)^2/[3K(K+2)+\alpha_2(K-1)^2]\}-1,
\end{aligned} \tag{4.14}$$

where $v=2\pi^{-\frac{1}{2}}\sigma_0R_0(2K+1)/K(K+2)$; α and β are given by (4.5) and (4.6) for $\xi=3^{-\frac{1}{2}}vHK^{\frac{1}{2}}(K+2)^{\frac{1}{2}}$; α_1 and β_1 are given by (4.5) and (4.6) for $\xi=vHK^{\frac{1}{2}}$; α_2 and β_2 are given by (4.5) and (4.6) for $\xi=3^{-\frac{1}{2}}vHK^{\frac{1}{2}}(2K+1)^{\frac{1}{2}}$; R denotes the Hall coefficient and $M=(\sigma_0-\sigma)/\sigma$ the relative change of resistance. The upper and lower indices of R, M, and σ indicate the direction of the magnetic field and of the electric current, respectively. For the longitudinal effect the two directions are the same and only the lower index is written. R_0 and σ_0 are the Hall coefficient and the conductivity, respectively, for zero magnetic field strength. The expression for v, given in terms of R_0, σ_0, and K, is obtained from Eq. (4.14) for R_{100}^{010} by letting $H\to 0$. We have then $\alpha\to 1$, $\beta\to\frac{1}{2}\sqrt{\pi}$, and R_{100}^{010} becomes R_0.

The saturation values are readily obtained by inserting in Eqs. (4.14) the expansions for large ξ of the functions (4.5) and (4.6). We have $\alpha(\xi)\to 2/\xi^2$ and $\beta(\xi)\to 3(\pi)^{\frac{1}{2}}/4\xi^2$ as $\xi\to\infty$.

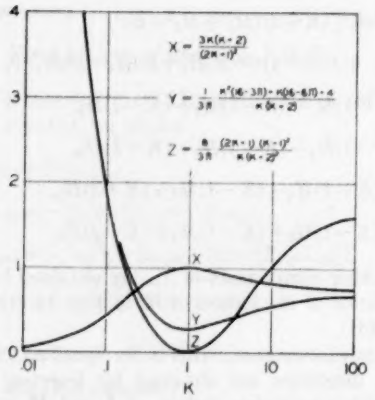

FIG. 1. Behavior of the galvanomagnetic coefficients as a function of K for model (b). K is the ratio of the effective masses characterizing the energy ellipsoids. The functions X, Y, and Z are the coefficients in Eqs. (3.31) and refer to the Hall effect, the transverse and the longitudinal magnetoresistance effects, respectively.

V. COMPARISON WITH EXPERIMENT

(A) *n*-Germanium

The observed values of the galvanomagnetic coefficients given in the paper of Pearson and Suhl[2] will be used here. These values were obtained on single crystals in specified directions at 300°K and 77°K and are therefore best suited for our purpose.

Their *n*-type sample has almost pure thermal scattering at room temperatures, while at 77°K, thermal scattering still predominates. This can be seen from the dependence of magnetoresistance on temperature (their Fig. 7), and from values of the resistivity. The resistivity is low enough for the conductivity contribution of the holes to be neglected.

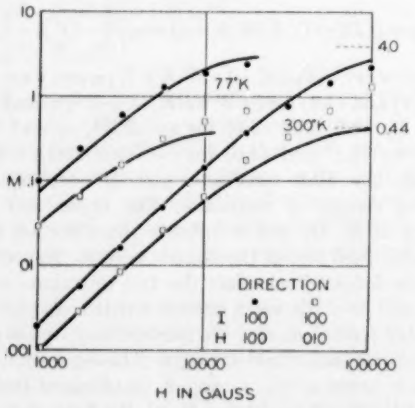

FIG. 2. Comparison of measured and calculated magnetoresistance for *n*-germanium. The directions of current and of magnetic field are indicated in the figure. The solid lines give the theoretical curves calculated from Eqs. (4.14), for $K=20$. The points indicate observed values, taken from Fig. 4 of Pearson and Suhl's paper. The numbers on the right give the theoretical saturation values for $H=\infty$.

As mentioned in Sec. II, model (b) applies to the conduction band of germanium. The final equations to be used are, therefore, those of (3.31), where K is taken as an adjustable parameter.

In Fig. 1 the factors involving K in Eqs. (3.31) are given as function of K. Satisfactory agreement with experiment is obtained for $K=20$, corresponding to prolate energy ellipsoids with a ratio of axes of $1:\sqrt{20}$. A comparison of the calculated and measured coefficients is given in Table I. The measured values are taken from Table I of Pearson and Suhl's[2] paper, while R_0 and σ_0 are taken from their Table II.

From the first of Eqs. (3.31) a theoretical value for the ratio of Hall mobility to conduction mobility can be obtained. The Hall mobility is defined as $\mu_H=R_0\sigma_0\mathcal{C}$, and the conduction mobility is $\mu_\sigma=\sigma_0/Ne$. We obtain, accordingly,

$$\mu_H/\mu_\sigma=(3\pi/8)3K(K+2)/(2K+1)^2.$$

For $K=20$ this becomes

$$\mu_H/\mu_\sigma=0.79(3\pi/8)=0.93.$$

TABLE I. Comparison between measured and calculated magnetoresistance coefficients (in gauss^{-2}) of *n*-germanium at low magnetic field strengths.

Direction		$(\sigma_0-\sigma)/\sigma H^2$			
I	H	300°K calc[a]	300°K exp[b]	77°K calc[a]	77°K exp[b]
100	100	1.91×10^{-9}	1.92×10^{-9}	87.2×10^{-9}	88×10^{-9}
100	010	0.91	0.90	41.4	28.5
110	001	0.91	1.03	41.4	31.5
110	$1\bar{1}0$	1.86	1.68	85.0	75
110	110	0.95	0.99	43.6	58

[a] Calculated for thermal scattering with $K=20$ and values of R_0 and σ_0 as found by Pearson and Suhl (reference 2) for their *n*-type sample.
[b] Measurements of Pearson and Suhl (reference 2) on above sample.

An experimental value of 1.05 for this ratio is quoted by Morin[10] although Fig. 2 of his paper seems to indicate a value of about 1.00, independent of temperature between 25 and 300°K.

From the equations given in Sec. IV the magnetoresistance can be calculated as a function of magnetic field H. The results are indicated in Figs. 2 and 3 by the solid lines, while the points in these figures indicate experimental values, taken from Fig. 4 of Pearson and Suhl's paper. It will be seen that the agreement is as good as can be expected from this treatment.

It should be noted that, for strong magnetic fields, the Hall coefficient depends on the magnetic field strength and is not isotropic. The pertinent equations are given in (4.14). It is found that with increasing magnetic field, the Hall coefficient first decreases, reaching a minimum, and then increases, approaching a limiting value for $H\to\infty$ which is slightly higher than the value at zero magnetic field. Apparently, no experimental values of the Hall coefficient at strong magnetic fields are available to check this prediction.

[10] F. J. Morin, Phys. Rev. **93**, 62 (1954).

(B) *p*-Germanium

For the *p*-type sample measured by Pearson and Suhl, the longitudinal magnetoresistance effect in the (100) direction is much smaller than the one in the (110) direction[11] and has probably no significance for our theory. It may arise from higher-order terms in the equation for the energy surfaces or from the angular dependence of the relaxation time. Assuming that we can disregard this effect, model (a) applies to the valence band.

From the resistivity values of the *p* sample measured by Pearson and Suhl, it can be concluded that impurity scattering is predominant at 77°K, while at room temperature both thermal and impurity scattering are important. Table II gives a comparison of measured and calculated values, the latter computed for impurity scattering and for $K=0.6$. It should be noted that $K=1.6$ gives nearly the same values. The agreement at 77°K is satisfactory, but at 300°K the measured values are much greater than the calculated ones. At higher temperatures, thermal scattering should also be taken into consideration, but it appears from the work of Johnson and Whitesell[12] that this cannot explain the discrepancy.

TABLE II. Comparison between measured and calculated magnetoresistance coefficients (in gauss^{-2}) of *p*-germanium at low magnetic field strengths.

Direction		$(\sigma_0-\sigma)/\sigma H^2$			
I	*H*	300°K calc[a]	300°K exp[b]	77°K calc[a]	77°K exp[b]
100	100	0	0.04×10^{-9}	0	0.14×10^{-9} [c]
100	010	0.24×10^{-9}	1.3	25.4×10^{-9}	30.4
110	001	0.24	1.3	25.4	32.2
110	$1\bar{1}0$	0.21	1.3	22.8	27
110	110	0.02	0.21	2.6	2

[a] Calculated for impurity scattering with $K=0.6$ and values of R_0 and σ_0 as found by Pearson and Suhl (reference 2) for their *p*-type sample.
[b] Measurements of Pearson and Suhl (reference 2) on above sample.
[c] See reference 11.

Measurements of the cyclotron resonance[13] and of the ratio of Hall-to-drift mobility[10] also indicate that our model for the valence band is not satisfactory.

VI. DISCUSSION

Considering the simple assumptions on which the theory is based, the good agreement with experiment for *n*-germanium is remarkable. From this it does not, however, necessarily follow that the assumptions made are a good approximation of the actual physical situation. The assumption for the relaxation time for thermal scattering,

$$\tau=l\mathcal{E}^{-\frac{1}{2}},$$

probably gives a satisfactory approximation for the dependence of τ on energy, in a fixed direction of momentum space (Shockley),[5] but in general l will be a function of direction. It is conceivable that if this is the case, the anisotropy of l has, in our theory, been absorbed into the anisotropy of the energy surfaces. The K, as found, would then be an effective value and would not represent the true ellipticity of the energy surfaces.

The theory for weak magnetic fields can be adapted to other assumptions for τ, and in fact we have obtained expressions for the σ tensors for the more general assumption,

$$\tau=A\,\mathcal{E}_p v^q,$$

where $v=\text{grad}\,\mathcal{E}$ and A, p, and q are arbitrary constants. In the present state of the theory of relaxation time, however, it does not seem worth while to engage in the rather elaborate numerical computations involved.

Our basic assumption that the energy surfaces in momentum space are degenerate and have a number of extrema, accords qualitatively with the results of computations by Herman and Callaway.[14] The figures given in their paper suggest, however, that model (a) would apply both to the valence band and to the conduction band; the latter in our theory must be described by model (b).

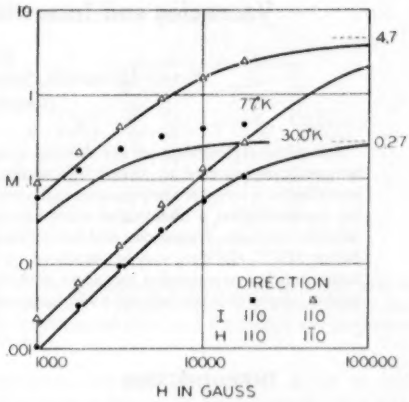

FIG. 3. Comparison of measured and calculated magnetoresistance for *n*-germanium. Details as for Fig. 2.

ACKNOWLEDGMENT

We are grateful to Dr. C. Herring for discussion of the manuscript.

[11] See Figs. 3 and 9 of Pearson and Suhl's paper (reference 2). The captions of their Figs. 8 and 9 have been interchanged by mistake, as can easily be seen by comparison with other figures. There also seems to be an error in the right-hand part of Fig. 5, where the points indicated by open circles should be about a factor of 10 lower; compare their Figs. 3 and 9. A corresponding error seems to be in Tables I and II.

[12] W. A. Johnson and W. S. Whitesell, Phys. Rev. **89**, 941 (1953).

[13] Dresselhaus, Kip, and Kittel, Phys. Rev. **92**, 827 (1953).

[14] F. Herman and J. Callaway, Phys. Rev. **89**, 518 (1953).

Vacancies and Interstitials in Heat Treated Germanium

SUMNER MAYBURG
Physics Laboratories, Sylvania Electric Products, Bayside, New York
(Received February 23, 1954)

Annealing experiments on the thermal acceptors quenched into germanium by rapid cooling from high temperatures are used to deduce information about vacancies and interstitials in germanium. Annealing is studied at a series of temperatures and a critical temperature is found at 516°C. Above 516°C, the annealing curves suggest a bimolecular recombination process implying that the heat treatment produces comparable numbers of vacancies and interstitials (Frenkel defects) which disappear by mutual annihilation. Below 516°C, the data can be explained by a model in which interstitials are trapped near dislocations before much recombination can occur with vacancies. As a result of these experiments and their interpretation, interstitials are believed to be more mobile than vacancies below, and possibly above, 516°C.

I. INTRODUCTION

THE introduction of defects into germanium by heat treatment was tried by many workers using a variety of heating furnaces, heating atmospheres, and quenching baths.[1] These workers found that the material becomes p-type after such heat treatment and the concentration of acceptors was usually in the range 10^{14} to 10^{17} per cm^3, being higher the higher the heat treatment temperature. At first glance, the "p" nature of the material was assumed to be caused by vacancies; however, the work of several groups at Bell Laboratories[2] established that by and large the "p" nature of the germanium was caused by extraneous copper which entered the germanium as an impurity during the heat treatment process. An experiment by Finn[3] demonstrated that copper can be evaporated from germanium in sufficiently good vacuum. We have been using evaporation quite successfully in order to purify the germanium before our heat treatment experiments are performed on the sample. Without such purified germanium the following studies on vacancies and interstitials would not have been possible.[4]

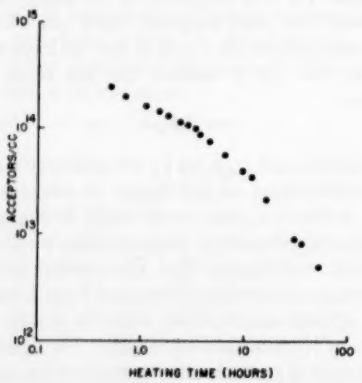

FIG. 1. The loss in acceptor concentration as a function of heating time at 636°C. These data were obtained on a sample immediately after its introduction into the vacuum system. This irreversible loss of acceptors indicates evaporation of an impurity most likely copper.

II. EXPERIMENTAL TECHNIQUES AND PROCEDURES

In a previous letter to the Editor, we briefly described the techniques used to study defects in germanium.[5] The central idea is the use of joule heating of the germanium in as good a vacuum as is conveniently obtainable which in our experiment was less than 4×10^{-7} mm of Hg. In Fig. 1, we show the evaporation of an impurity, most likely copper, from a sample immediately after its introduction into the vacuum system. This specimen was heated for various times at 636°C and quenched. In Fig. 1, we plot the number of acceptors so quenched into the germanium. We see that over a period of 40 hours at 636°C the concentration of acceptors decreases from 2×10^{14}/cm^3 to 6×10^{12}/cm^3. The evaporation from another sample where the initial heating in vacuum was performed at 750°C, took place so rapidly that it was not observed. Using evaporation we have reduced the concentration of impurity acceptors to below 3×10^{12}/cm^3 before starting our heat treatment and annealing studies.

The sample is typically a rectangular slab of germanium of dimensions 1 mm×3 mm×2 cm. The current is introduced into the germanium through tantalum leads which are welded directly to the germanium ends. Voltage probes for resistivity measurements are made of tantalum and are held by pressure contact to the narrow surface of the germanium as shown in Fig. 2. The tantalum current leads are used as supports for the germanium and they are welded to the Kovar leads in a standard vacuum tube header. The tube is attached to a kinetic vacuum system in

[1] H. C. Theuerer and J. H. Scaff, J. Metals **189**, 59 (1951); Fuller, Theuerer, and Van Roosbroeck, Phys. Rev. **85**, 678 (1952); W. E. Taylor, Phys. Rev. **86**, 642 (1952); Colman Goldberg, Phys. Rev. **88**, 920 (1952); and G. Esaki, Phys. Rev. **89**, 1026 (1953).

[2] C. S. Fuller and J. D. Struthers, Phys. Rev. **87**, 526 (1952); W. P. Slichter and E. D. Kolb, Phys. Rev. **87**, 527 (1952).

[3] G. Finn, Phys. Rev. **91**, 754 (1953).

[4] In a recent publication, R. A. Logan [Phys. Rev. **91**, 757 (1953)] suggests certain chemical treatments of the Ge to reduce the Cu contamination. However, we are always able to purify our samples satisfactorily by evaporating the Cu.

[5] S. Mayburg and L. Rotondi, Phys. Rev. **91**, 1015 (1953).

such a way that various constant temperature baths can be brought around the tube. The resistivity measurements used to determine the lattice defects are always taken at 195°K (dry ice and alcohol) unless otherwise specified. From the mobility data of Prince,[6] we are able to determine the concentration of acceptors minus the concentration of donors ($N_A - N_D$) as a function of heat treatment.

Once a germanium slab is mounted in the tube and the tube is attached to the vacuum system, there is no need to disassemble the sample in the course of the whole series of heat treatment studies. The germanium is heated by sending a direct current through it and for a sample of the dimensions mentioned, a current of about 12 amperes is sufficient to raise the temperature to near the melting point. The temperature of the germanium can be measured by measuring the resistivity of the germanium or by use of an optical pyrometer. We have used both and find it in general more convenient and more accurate to use the resistivity measurement to determine the temperature.[7]

The uniformity with which the sample is heated is very good. This results from the high thermal conductivity of germanium, from the low amount of power required to heat the germanium in vacuum to near its melting point (5 watts), and because the conductivity of germanium depends on temperature in such a way that a drop in temperature in a certain region results in an increase of the joule heating in that region and thus a restoration of the original temperature. In order to cut down heat losses from the specimen, it is necessary that the tantalum leads be as hot or slightly hotter than the germanium.

Stray chemical impurities present in the apparatus have little effect on the measurements reported here. The tantalum is the only foreign body in the vacuum which is raised to the temperature of the germanium. We have spectroscopically analyzed the tantalum for impurities and have not found copper or other acceptor type impurity present; we have heated tantalum strips in a good vacuum to much higher temperatures than were used in these heat treatment experiments and have found no tantalum deposited on the walls of the vacuum chamber, which is consistent with the high heat of vaporization of tantalum. Using the ideas on ionic radii, we find that tantalum will not fit interstitially into the germanium lattice; its diffusion in germanium must be substitutional.[8] The low diffusion rate of substitutional impurities makes it impossible to envision the tantalum diffusing from the welds to the probes and thereby affecting the measurements.

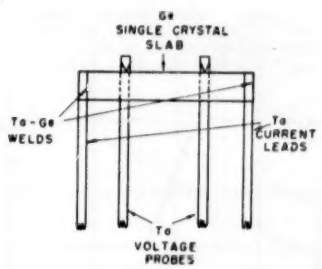

FIG. 2. The germanium single crystal specimen with tantalum current leads and voltage probes. The current leads are welded directly to the germanium and the probes are pressure contacts.

Furthermore, an impurity would enter or leave the material irreversibly during the experiments and would thereby be detected and could be accounted for. We have detected a minor effect of this sort which seems to result from the building up of an oxide layer on the germanium.

The quenching of the germanium is attained merely by switching off the heating current and allowing the germanium to cool by radiation. The cooling rate at any temperature can be estimated by noting that the power required to maintain equilibrium is equal to the radiation losses. Therefore, the cooling rate dT/dt at any temperature is equal to the power required to maintain the piece at equilibrium at that temperature divided by the heat capacity. For the samples of the dimensions mentioned above, cooling rates of 100° per second are found for temperatures near the melting point. This cooling rate is fast enough[9] to quench in the defects in the germanium.

After the sample is heated long enough to remove the copper impurity to a negligible level, the sample is heated to 830°C and quenched in order to introduce about 2×10^{14} acceptors/cc, which is the equilibrium solubility for that temperature. See Fig. 3. The sample is then annealed at a lower temperature and the change in acceptor concentration is studied as a function of time at various fixed temperatures.

III. POSSIBLE ANNEALING MECHANISMS

Before discussing the experimental results it may be helpful to speculate as to possible annealing mechanisms. There has been considerable work done on the defects produced by fast particle bombardment on crystals in general and germanium in particular. James and Lark-Horovitz[10] find that the results of neutron bombardment on germanium can be explained by

[6] M. B. Prince, Phys. Rev. **91**, 271 (1953).

[7] We have measured the intrinsic resistivity of single crystal Ge as a function of temperature, and find that a consistent error of 10°C exists in the data of Keyes (see reference 5) which we originally used. In Fig. 3, we plot the solubility of thermal acceptors as measured by Mayburg and Rotondi (see reference 5) as a function of the properly corrected quench temperature.

[8] L. W. Strock (personal communication).

[9] If the quenching rate were not fast enough, the solubility of acceptors as a function of the reciprocal of the quench temperature (Fig. 3) would show a maximum at the temperature for which the quenching rate was no longer fast enough. In the temperature range pertaining to our experiments, we observed no such maximum.

[10] H. M. James and K. Lark-Horovitz, Z. Physik. Chem. **198**, 107 (1951).

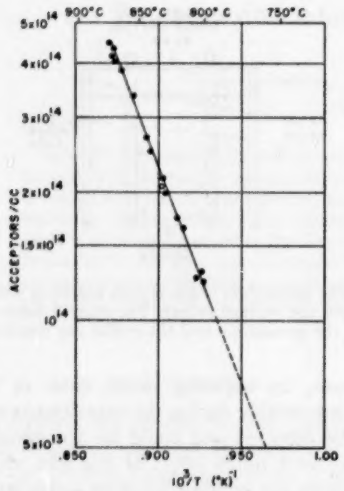

FIG. 3. The solubility of thermal acceptors in germanium as a function of the reciprocal of the heat treatment temperature from Mayburg and Rotondi (reference 5). These data have been corrected for a more accurate determination of temperature (reference 7) and are shown by the dots. The circle represents a measurement on a second specimen. The second specimen is the one used for all annealing experiments. The equation giving the concentration of acceptors, A, which are believed to equal the concentration of Frenkel defects is $A=3\times10^{25}e^{-2.01ev/kT}(\text{cm}^{-3})$.

assuming that the bombardment produces vacancies and interstitials in roughly equal numbers and that the vacancy acts as an electron trap while the interstitial germanium atom acts as an electron donor. They further suggest that around room temperature the vacancy should trap two electrons while the interstitial would donate but one electron. Brown, Fletcher, and Wright,[11] bombarding with 3-Mev electrons, find that the vacancy-interstitial pair created in the germanium by the electron bombardment gives rise to one acceptor per pair in agreement with the suggestion of James and Lark-Horovitz.

While interstitials clearly arise as a result of particle bombardment, there is no *a priori* reason to expect that the heat treatment produces interstitial germanium. However, through studies of the annealing curves it is possible to determine whether in fact there are interstitials created by heat treatment, because the mechanism of loss of acceptors would be entirely different with or without interstitials.

If the acceptors we observe are lattice vacancies alone, the annealing process should be described by the simple diffusion of the excess vacancies out of the slab of material, either by diffusion to the surface or by diffusion to dislocations.

Esaki[12] has solved the problem of acceptor centers diffusing to the surface of a slab of material of thickness $2L$. He finds, after the early stages of annealing,[13] that the acceptor concentration, A, can be represented by the equation

$$A=A_f+(A_i-A_f)(8/\pi^2)\exp(-\pi^2Dt/L^2), \qquad (1)$$

where A_i is the initial concentration of acceptors, A_f is the final concentration of acceptors which is the equilibrium concentration at the annealing temperature, and D is the diffusion constant for the acceptors.

If the acceptors are vacancies they can be absorbed on dislocations. Actually the only place along a dislocation where a single vacancy or interstitial can lose its identity is at a "jog".[14] Any place else along the body of the dislocation the defect retains its identity and must be annihilated by the opposite defect. As we shall see later, it appears unlikely that at high temperatures the body of the dislocation can even trap the defects.

Let us now see the effect of the absorption of vacancies at jogs on the diffusion process. Suppose the concentration of jogs per cc is j. The recombination of vacancies with jogs will proceed with a rate per unit volume

$$(1/\tau)(j/N)(n-n_f),$$

where τ is the jump time for a vacancy, j/N is the probability that a vacancy is making a jump will land on a jog instead of on the other N-j lattice points, n is the concentration of vacancies, and n_f is the equilibrium concentration at the annealing temperature. Under these circumstances the usual diffusion equation becomes:

$$D\partial^2n/\partial x^2-(1/\tau)(j/N)(n-n_f)=\partial n/\partial t. \qquad (2)$$

The solution to Eq. (2) is identical with Eq. (1), except the time dependence becomes

$$\exp[-(\pi^2D/L^2+j/\tau N)t].$$

Thus, if we include the effect of the jogs on dislocations in annihilating vacancies, Eq. (1) can be written in the form,

$$\log(A-A_f)=-(\pi^2D/L^2+j/\tau N)t+\text{const.} \qquad (3)$$

Therefore, if only vacancies are present as a result of the heat treatment, the acceptor concentration should vary with time according to Eq. (3) during the annealing process. All "monomolecular" processes have the same time dependence as Eq. (3).

An appreciably different time dependence from that given by Eq. (3) can be obtained for the acceptor concentration only if there are a number of interstitials comparable with the number of vacancies. (This situation corresponds to a bimolecular process.) For

[11] Brown, Fletcher, and Wright, Phys. Rev. 92, 591 (1953).
[12] G. Esaki, Phys. Rev. 89, 1032 (1953).

[13] Neglect of the "higher modes" in the solution of the diffusion equation amounts to an error of 22 percent in acceptor concentration at $t=0$. This error is negligible when compared with the annealing curves which show changes of acceptor concentration of factors of 10 and 100.
[14] F. Seitz, Acta Metallurgica 1, 365, (1953).

the purpose of this argument let us assume that the high-temperature heat treatment produces Frenkel defects, i.e., equal numbers of interstitials and vacancies. The recombination of interstitials with vacancies will now determine the annealing process. The measured acceptor concentration, A, which is the number of holes contributing to the conductivity, is the difference between the number of acceptors N_A and the number of donors N_D; i.e.,

$$A=N_A-N_D.$$

As was mentioned previously, from the analysis of the bombardment experiments by James and Lark-Horovitz we know that each Frenkel defect gives rise to one acceptor. Hence, A is the concentration of vacancies or of interstitials if Frenkel defects are the sole defects or impurities present.

The annealing of Frenkel defects has been studied extensively in connection with radiation damage experiments.[15] For our purpose, the rate of loss of defects can be expressed by the equation

$$dA/dt=-(A^2-A_f^2)/\bar{\tau}N, \qquad (4)$$

where A_f is the equilibrium concentrations of vacancies or interstitials at the annealing temperature, N is the concentration of lattice positions, and $\bar{\tau}$ is an appropriate average jump time for the defects. In the case when only one of the defects is mobile, τ represents the jump time for that defect.

Equations (3) and (4) represent two different simple mechanisms for annealing. In the next section we shall see which mechanism best describes the experimental annealing curves.

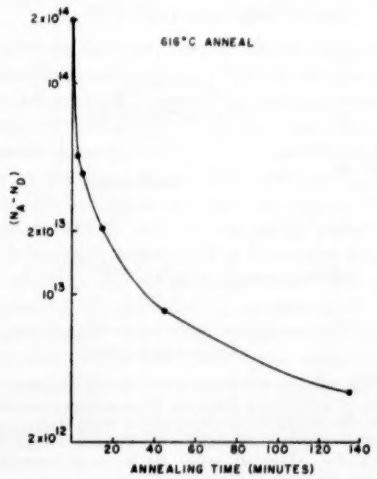

FIG. 4. The concentration of acceptors, N_A-N_D, as a function of annealing time at a temperature 616°C. The initial concentration of acceptors was 2×10^{14}/cc. Notice the extremely fast initial drop in acceptor concentration.

[15] A. W. Overhauser, Phys. Rev. **90**, 393 (1953); R. C. Fletcher and W. L. Brown, Phys. Rev. **92**, 585 (1953).

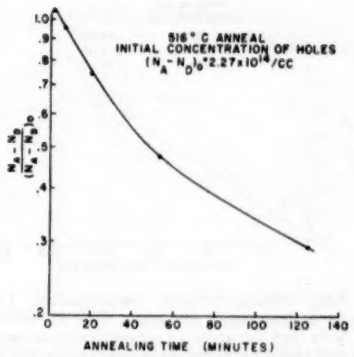
516° C ANNEAL
INITIAL CONCENTRATION OF HOLES
$(N_A-N_D)_0=2.27\times10^{14}$/CC
$\frac{N_A-N_D}{(N_A-N_D)_0}$
1.0 .9 .8 .7 .6 .5 .4 .3 .2
0 20 40 60 80 100 120 140
ANNEALING TIME (MINUTES)

FIG. 5. The relative concentration of acceptors $(N_A-N_D)/(N_A-N_D)_0$ as a function of annealing time at a temperature of 516°C. For convenience, the concentration has been normalized to one at the start of the annealing process ($t=0$). Note the initial increase in acceptor concentration in the first minute of the annealing process.

IV. COMPARISON OF EXPERIMENTAL RESULTS WITH THEORY

In Fig. 4, a typical annealing curve taken at 616°C is presented. We have plotted as a function of time the net number of holes, which is equal to the number of ionized acceptor centers, N_A, minus the number of ionized donor centers N_D. The data are plotted on the semilog scale.

Notice the extremely fast drop in concentration at the beginning of the annealing process. In the first 2.5 minutes, the concentration of holes has decreased by a factor of more than 4. These data, which are representative of many such annealing curves, cannot be represented by Eq. (3) which describes the simple diffusion mechanism. If they were representable by Eq. (3), Fig. 4 would be a straight line. Rather, Eq. (4) gives a far better description of Fig. 4. For let $A\gg A_f$. Then Eq. (4) becomes

$$d\ln A/dt=-A/\bar{\tau}N,$$

and we see immediately that $-d\ln A/dt$ is large when A is large and is small when A is small, in agreement with Fig. 4. It therefore seems highly plausible that the heat treatments have introduced comparable numbers of vacancies and interstitials into the germanium (in other words, Frenkel defects).

A strikingly different annealing behavior is obtained if the annealing temperature is lowered to 516°C or below. Instead of the fast drop in the hole concentration as typified by Fig. 4, there is a rise in hole concentration and then a drop. Data taken at 516°C, 490°C, 447°C, and 402°C are typical of this stage of the annealing process and are presented in Figs. 5 and 6. A possible mechanism to explain the difference in anneal ing behavior above and below 516°C can be found in Cottrell's ideas concerning the strain energy interaction

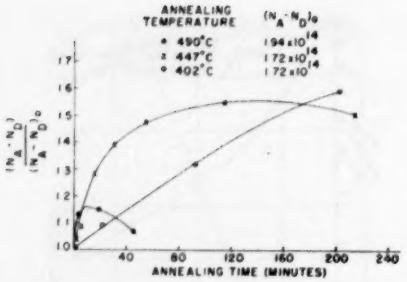

FIG. 6. The relative acceptor concentration $(N_A-N_D)/(N_A-N_D)_0$ as a function of annealing time at 490°C, 447°C, and 402°C. Note that the acceptor concentration increases before it decreases and that the maximum occurs earlier the higher the temperature.

between impurity atoms and dislocations.[16] The Cottrell argument depends on the fact that the impurity atoms strain the lattice in their neighborhood. The region around an edge dislocation is one of both lattice expansion and lattice contraction. Therefore, the dislocation will act as an attractive center for any atom which strains the lattice. The interaction energy between the impurities and the dislocation varies inversely with distance and has been estimated to be of the order of tenths of electron volts.[16] This interaction has no clear cut range but can be felt over large regions of the crystal depending on the temperature. According to the Cottrell model, a critical temperature occurs which is essentially the temperature at which kT becomes comparable to the elastic strain energy, u, of interaction between the impurity atoms and the dislocation. Below this critical temperature the impurity atoms form a condensed atmosphere around the dislocation with a distribution of concentration, C, according to the equation

$$C=C_0e^{u/kT}.$$

Above the critical temperature the impurity atoms are little influenced by the strain attraction u and therefore they are free to move throughout the crystal lattice. The dislocation is freed of its atmosphere, and far less force is required to move it.

Cottrell's ideas have been applied to the problem of impurities in germanium by Kurtz and Kulin[17] at the Lincoln Laboratory. They have focused their interest on the interaction between the dislocations in germanium and impurity atoms such as copper in order to explain phenomena similar to that originally found by Theuerer and Scaff[18] who reported that copper acceptors could be annealed out of germanium at 500°C or below while above that temperature the copper atoms remained as acceptors.

Plastic deformation in germanium is found to be critically dependent on temperature.[19] Deformation does not become important until 500°C. Seitz[20] has discussed these experiments and suggests that the Cottrell type of mechanism must be used in order to make a start toward explaining the experiments.

In order to have Cottrell's mechanism operative for a lattice defect rather than an impurity atom, all that is required is that the defect create a region of strain in the lattice surrounding it. And once such a region of strain is created there automatically will be an attractive force between the defect and the dislocation. However, this attractive force which arises from the strain energy, u, is only operative if we are below some critical temperature T_c such that u is greater than kT_c. Our annealing experiments display such a critical temperature, and our results can be explained by assuming that below this critical temperature the dislocations are able to trap interstitial germanium atoms before the interstitials have been able to make sufficient jumps to alter appreciably the concentration of vacancies. It is reasonable to expect that the dislocations prefer to trap interstitials than vacancies because in general the strain introduced in the lattice by an interstitial is larger than that produced by a vacancy and hence u will be larger for interstitials than vacancies.[21] Also, since we notice that the acceptor concentration increases in these low-temperature annealing experiments, we expect that the donor, not the acceptor, is leaving the bulk of the material.

In this connection, it is important to realize that the accumulation of the interstitials at the dislocations does not mean an annihilation of the interstitials.

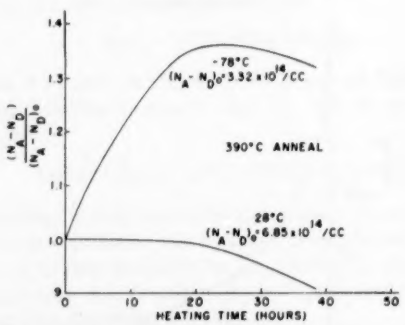

FIG. 7. The relative acceptor concentration measured both at −78°C and at 28°C as a function of annealing time at 390°C. Notice that the acceptor concentration at room temperature does not increase as does the acceptor concentration measured at dry ice temperatures. However, after 20 hours of annealing both curves show a decrease in concentration.

[16] For a general discussion and other references see A. H. Cottrell, *Dislocations and Plastic Flow in Crystals* (Oxford University Press, London, 1953), p. 134.
[17] A. D. Kurtz and S. A. Kulin, Acta Metallurgica **2**, 354 (1954).
[18] H. C. Theuerer and J. H. Scaff, J. Metals **189**, 59 (1951).
[19] G. J. Gallagher, Phys. Rev. **88**, 721 (1952).
[20] F. Seitz, Phys. Rev. **88**, 722 (1952).
[21] G. J. Dienes, Phys. Rev. **86**, 228 (1952), has shown that in copper the interstitial copper atom strains the lattice and contributes far more toward increasing the elastic constants than the vacancies.

In Fig. 7 we have compared annealing curves similar to those shown in Fig. 6, where we have measured the change in acceptor concentration at room temperature as well as at dry ice temperature. The interesting result from this experiment is that very little change in the room temperature concentration occurs while the interstitials are moving toward the dislocations. Thus the room temperature concentration stays initially constant while the dry ice concentration increases by a considerable amount. Not until we reach the maximum in the dry ice concentration curve do we see any appreciable decrease in the room temperature concentration curve.

These data must mean that in moving to the dislocations the interstitials do not annihilate any vacancies, as otherwise we could expect a change in the room temperature concentration. Therefore the difference between the room temperature and dry ice concentrations must arise from changes in electrical properties of interstitials clustered around dislocations, such changes being detectable at dry ice temperatures but not at room temperature. When we reach the peak in the dry ice concentration curve, we have reached the point where the vacancies are beginning to diffuse out of the bulk toward the dislocations. In the process, some of these vacancies will begin to recombine with the interstitials which are congregated around the dislocations. The recombination involves a direct annihilation of the acceptor center and the donor center. We therefore reasonably may expect that both the dry ice concentration and the room temperature concentration should decrease at this stage of the annealing process.

V. THE CRITICAL EXPERIMENT

In order to test the idea of interstitials segregating at dislocations, we performed the following experiment. The sample had quenched in it an original concentration of about 1.7×10^{14} acceptors per cc. It was then annealed for several days at 370°C. The concentration of acceptors at dry ice temperatures was thereby increased to 4.1×10^{14} acceptors per cc. The sample was then annealed at 585°C and the annealing curve is shown in Fig. 8. For comparison, in Fig. 8 we show an annealing curve taken at the same temperature with an initial concentration of quenched in acceptors of 1.8×10^{14}. As we readily see from Fig. 8, within the first minute of annealing the interstitials have been evaporated back into the bulk of the material from the dislocations. Thereafter, the annealing curve obtained is essentially the same as the annealing curve obtained with no anneal at 370°C. The fact that the first annealing curve lies below the second at long times can be explained because the starting point was slightly lower and because, even during the 370°C anneal, a few of the vacancies were annihilated by the interstitials. If the dislocations were not acting as storage places for interstitials, but rather as a place for the annihilation of the interstitial, the nature of the annealing curves with and without the 370°C anneal would have been entirely different.

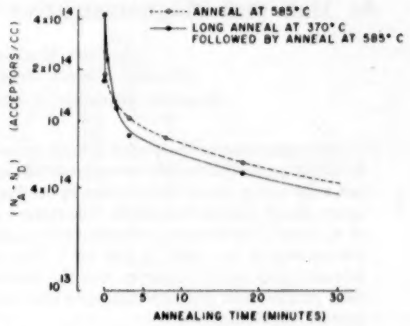

FIG. 8. The acceptor concentration as a function of annealing time at 585°C. The solid curve represents a treatment in which the sample was annealed at 370°C before being annealed at 585°C. The dashed curve represents an anneal in which the sample received no previous treatment after the initial non-equilibrium number of acceptors were quenched in. Notice that, after the early stages of annealing, the two annealing curves have the same essential features.

VI. CONCLUSIONS

In the foregoing discussion we have established certain qualitative conclusions about the nature of the defects produced in germanium by heat treatment.

1. The defects are most likely Frenkel defects, i.e., equal numbers of vacancies and interstitials.

2. Below a temperature of 516°C, the dislocations begin to preferentially trap the interstitials before the interstitials are annihilated by direct recombination with vacancies. Above 516°C, the direct recombination of interstitials with vacancies determines the annealing behavior.

3. Up to 585°C, the interstitials are more mobile than the vacancies. Above 585°C, we have no data to show which defect is more mobile.

The author wishes to thank his many colleagues, especially E. N. Clarke, E. M. Conwell, D. R. Frankl, and L. W. Strock for many helpful discussions during the course of the work.

Ac Hall and Magnetostrictive Effects in Photoconducting Alkali Halides

J. Ross Macdonald* and John E. Robinson
Chemistry Division, Argonne National Laboratory, Lemont, Illinois
(Received November 16, 1953; revised version received March 15, 1954)

This paper reports the results of room-temperature measurements of the Hall and magnetoresistive effects for single-crystal potassium bromide containing a low concentration of F centers. Measurements were carried out with strong steady illumination in the F-absorption band by means of a new ac technique which avoids space-charge polarization effects. The current carriers were found to be negative in sign with a Hall mobility of 12.5 cm^2/volt-sec and are undoubtedly electrons photoexcited from F centers. Their maximum concentration was of the order of 10^{10} cm^{-3}. The mobility was found to be substantially independent of light intensity and signal frequency over the limited ranges investigated. Transverse magnetoresistive effects of both positive and negative sign were also observed. Finally, a phenomenological discussion of the experimental results is given.

I. INTRODUCTION

MEASUREMENT of the mobility of charge carriers in photoconductors by means of the Hall effect presents difficulties not encountered in similar measurements on metals and most semiconductors. These difficulties arise from the high impedance level of the photoconducting material and from the fact that it is not always possible to employ ohmic current electrodes with such materials. When the electrodes are not ohmic, space-charge effects within the photoconductor may so distort the electric field that most of the potential drop takes place near the electrodes. In the region between the Hall electrodes, halfway between the current electrodes, the electric field will then be very small and little Hall effect will be observed.

Using an electrometer, Lenz[1] has observed the Hall effect in photoconducting diamond and zinc sulfide. His measurements were greatly simplified by the fact that substantially ohmic electrodes could be employed. Evans[2] has attempted without success to measure the Hall effect in photoconducting alkali halide single crystals containing F centers. Using about 500 volts dc applied to crystals about 7 mm long and containing about 5×10^{16}/cm^3 F centers, and a magnetic field of 12 200 oersteds, he was unable to observe any appreciable effect with either a steady or a pulsed light source. Since few, if any, electrons can pass from metal electrodes into the conduction band in alkali halides at room temperature because of the potential hill between the conduction band levels and the Fermi energy in the metal,[3] large space-charge effects are observed when a dc voltage is applied to an illuminated crystal. By using 0.1-sec flashes of light, Evans hoped to measure the Hall effect before this space-charge distribution could be set up. However, as one of us has shown elsewhere,[4] with strong illumination the space-charge distribution can usually be established in less than 0.01 sec; thus, Evans' negative results are not surprising.

In the present work it was decided to make Hall and magnetorestistive measurements using a steady light source and ac rather than dc electric fields. Measurements of the photocapacitative effect on KBr single crystals[4] interpreted by means of a theory of space-charge polarization[5] had shown that space-charge effects were negligible in strongly illuminated crystals above 50 to 500 cps. The use of ac also largely eliminates undesired thermoelectric and galvanomagnetic effects present in a dc method of measurement.

The impedance level for illuminated crystals of convenient size was found to be between 10 and 100 megohms. A further decrease in impedance level by means of an increase in light intensity was not practical because of the appearance of heating and bleaching of the crystals with stronger light intensity. Therefore, in order to obtain meaningful measurements of the mobility in these crystals, an ac Hall voltage detector having an input impedance considerably greater than 100 megohms to above 10^3 cps was necessary. The principal limitation on input impedance is imposed at these frequencies by input capacitance between Hall leads. At 10^3 cps, one $\mu\mu$f has a reactance of only about 160 megohms, so that the input capacitance had to be reduced below even this value. The requirement of exceedingly low input capacitance together with variable frequency operation make the 24-cps Hall apparatus described by Pell and Sproull[6] unsuitable for the present application. We shall consider first the experimental techniques and results of the present investigation, then the theoretical interpretation and implications of these results.

II. SPECIMENS, APPARATUS, AND METHOD OF MEASUREMENT

Most of the crystals used in this work were KBr obtained from the Harshaw Chemical Company. They

* Then on leave to Argonne National Laboratory from Armour Research Foundation. Now at Texas Instruments, Inc., 6000 Lemmon Avenue, Dallas.

[1] H. Lenz, Ann. Physik **77**, 449 (1925); **82**, 775 (1927).

[2] J. Evans, Phys. Rev. **57**, 47 (1940). Further references to the older literature are given in this paper.

[3] N. F. Mott and R. W. Gurney, *Electronic Processes in Ionic Crystals* (Clarendon Press, Oxford, 1948), second edition, p. 169.

[4] J. R. Macdonald, Phys. Rev. **85**, 381 (1952); **90**, 364 (1953).

[5] J. R. Macdonald, Phys. Rev. **92**, 4 (1953).

[6] E. M. Pell and R. L. Sproull, Rev. Sci. Instr. **23**, 548 (1952).

were either additively colored with sodium or U centered,[7] then irradiated with Co^{60} gamma rays to produce a uniform distribution of F centers. In both cases, the concentration of F centers employed was not greater than $10^{16}/cm^3$. Most of the significant measurements were obtained on initially U centered crystals because, as discussed later, bleaching was much slower for such crystals than for additively-colored crystals and the impedance level for equal light intensity was about a factor of ten lower for the former. Current electrodes were formed by painting air-drying silver paint on the crystals. For Hall and magnetoresistance measurements, the crystals were supported on a polystyrene slab containing movable copper tabs which could be advanced to make firm pressure contact to the current electrodes. In order to reduce the Hall voltage impedance level as much as possible, knife edge rather than point Hall electrodes were employed. These line electrodes were parallel to the magnetic field and extended across the thickness[8] dimension of the crystals. Note than in an ac measurement, small errors in positioning the line Hall electrodes exactly perpendicular to the longitudinal electric field will cause no first-order effect on the measured Hall voltage. One of these electrodes was embedded in the polystyrene with only about 0.2 mm projecting above the surface. The other electrode was supported by means of a movable polystyrene framework exactly above and parallel to the bottom electrode. Both electrodes were of phosphor bronze. A crystal for measurement was positioned so that the Hall electrodes were midway between the current electrodes, then the top frame was screwed down tightly enough that the top and bottom knife edges left small scratches across the thickness of the crystal.

The magnetic field employed in these measurements was supplied by an electromagnet operated from storage batteries bridged across a selenium rectifier. Pole faces were 4 in. in diameter, separated by 2 in. The maximum field obtainable was about 10^4 oersteds. The field was calibrated *vs* magnet current to better than ± 1 percent using a fluxmeter. For the maximum field strength the field direction could be reversed in about 20 sec.

Light in the F-absorption band of the crystals was supplied by a 750-watt slide projector. The entire light output was focused on an area of about 14 cm^2 containing the crystal to be illuminated. A glass heat filter[9] was usually used in the measurements and the light intensity in the F band could be further reduced when desirable by means of accurately calibrated, perforated metal filters. When the projector was operated from the ac line, undesirable 120-cps modulation was found to be present which made Hall measurements difficult. Therefore, the projector was supplied from a 120-volt storage battery bank.

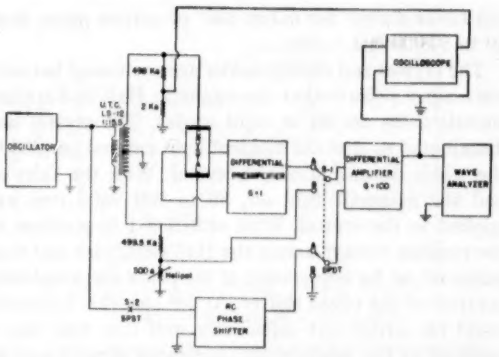

FIG. 1. Circuit diagram for Hall effect measurements.

Since it is, in general, impossible to position the Hall electrodes of a high impedance sample exactly on an equipotential line, some means is necessary for balancing out the resulting residual signal which is almost always greater than the desired Hall signal. The block diagram of the Hall apparatus with which such balancing was accomplished is shown in Fig. 1.[10] It was desired not to have to rely on the constancy of the gain of amplifiers in the circuit or of the calibration of the output meter in these measurements; therefore the circuit is arranged so that a quantity proportional to the Hall voltage ratio V_H/V_0 may be read directly on a helipot dial. Here V_H is the Hall voltage and V_0 the applied voltage across the current electrodes. The oscillator drives a step-up transformer whose output is applied push-pull to the crystal. The voltage at the Hall electrodes is applied to the very-high-input-impedance differential preamplifier. This preamplifier employs an input circuit which has already been described[11] and has a gain of unity heavily stabilized by negative feedback. Through the use of an active feedback path, it has an in-phase rejection ratio exceeding 10^3 over the frequency range of interest. The input leads of the preamplifier are double-shielded and the inner shields driven in phase with the input voltage as described previously.[11] The capacitance to ground at the input to either of the shielded leads is about 0.2 $\mu\mu f$ to above 50 kcps, and the input resistance is above 4×10^9 ohms below 4700 cps. The shields of the Hall leads are extended to within 1 mm of the Hall electrodes to which the shielded center conductor is soldered.

The single-phase output of the preamplifier is applied to one of the inputs of a Textronix differential amplifier of gain 100. The other amplifier input is connected to the output of an RC phase shifter. This phase shifter has coarse and fine adjustment for both output amplitude and phase, and by a means of switched capacitances

[7] Reference 3, p. 147.

[8] By definition, the length, L, of the crystal is the separation between current electrodes, the width, W, the separation between Hall electrodes, and the thickness, T, the remaining dimension.

[9] Corning, number 3961 or 3962.

[10] All leads shown in this diagram were shielded; for greater clarity, such shielding is omitted from this diagram.

[11] J. R. Macdonald, Rev. Sci. Instr. **25**, 144 (1954).

can cover almost the entire 360° of output phase from 50 to 50 000 cps.

The crystal and crystal holder are positioned between the magnet poles so that the magnetic, Hall, and applied electric fields are all at right angles. The crystal was illuminated so that the incident light entered parallel to the width dimension of the crystal. With the light on and the magnetic field off, 50 to 100 volts rms was applied to the crystal. With switch S-1 in position A, the residual voltage across the Hall electrodes was then balanced out by adjustment of the phase and amplitude controls of the phase shifter. At 10^3 cps, this balancing could be carried out sufficiently well that less than a millivolt of the fundamental frequency signal could be measured at the amplifier output.

When the magnetic field was turned on, a voltage proportional to the Hall voltage could be read on the wave analyzer. In practice, several readings of this voltage were taken for each magnetic field direction and these readings averaged. Such averaging largely eliminates the effect of differences in Hall voltage for the two field directions arising from deviations of the Hall electrodes from an exact equipotential. Then S-1 was switched to position B. The voltage measured on the wave analyzer in this position was proportional to V_0, the voltage applied to the crystal. This voltage was varied by means of the helipot voltage divider until the wave analyzer output reading was equal to the averaged Hall readings. This adjustment made the helipot dial reading proportional to the desired Hall ratio V_H/V_0. Finally, the apparent mobility μ_a could be obtained from the measured value of V_H/V_0 by means of the formula

$$\mu_a=\frac{10^8(V_H/V_0)}{H(\chi W/L)}(\text{cm}^2/\text{volt-sec}). \qquad (1)$$

H is the magnetic field strength in oersteds, W/L the ratio of width to length, and χ a geometrical factor to correct for possible shunting effects of the current electrodes.[12] The real Hall mobility, μ_H, of the current carriers is only equal to μ_a at frequencies where neither space-charge field effects nor capacitative loading of the Hall electrodes are important.

In order to determine the sign of the current carriers, the Hall output voltage was used, as shown in Fig. 1, to produce a Lissajou figure on the oscilloscope. The figure was a straight line of slope ± 1 or an ellipse of high axial ratio. The sign of the slope of the line or of the ellipse major axis always reversed on reversing the magnetic field. The sign of the current carriers was determined by comparing the slope of the Hall ellipse for known direction of magnetic field with the ellipse formed by connecting current electrodes individually to Hall electrodes and using a very small input voltage. Such sign determination always showed that the majority current carriers in these crystals were of negative sign.

No difficulty with 60-cps pickup was experienced with this apparatus in spite of the extremely high impedance levels encountered. The 60-cps signal measured at the amplifier output with the wave analyzer never exceeded 3 mv. On the other hand, considerable difficulty was experienced with low-frequency noise arising from the preamplifier input tubes. This noise depended on the input impedance level and roughly decreased with increasing frequency inversely proportional to frequency. With the preamplifier input leads shorted, the equivalent input noise level was essentially frequency independent and less than 10 μv. On the other hand, with the input leads connected to ground through resistances of 40 megohms, the equivalent 1000-cps input noise level was 20 μv, and the level measured with a wide-band vacuum-tube voltmeter was 300 μv. This low-frequency flicker noise was considerably greater than any internally generated crystal noise and limited the accuracy of the measurements at low frequencies. Above 100 cps, Hall measurements could be repeated to better than ± 2 percent for Hall voltages greater than 10 mv. It is estimated that the absolute accuracy of the measurements carried out with this apparatus is better than ± 5 percent.

Magnetoresistance measurements were made with much the same apparatus. No Hall electrodes were employed, and the driving voltage was applied to the crystals single phase. The low potential end of the crystal was connected to ground through a 3×10^4-ohm resistor. The voltage across this resistor, proportional to the current through the sample, was measured using the differential preamplifier with one input grounded. With the crystal illuminated and no magnetic field applied, the preamplifier output voltage was balanced by means of the phase shifter, with S-1 in position A. On turning on the magnetic field, the wave analyzer then read a quantity proportional to the change of current through the sample caused by the magnetic field. As soon as this reading was carried out, the magnetic field was turned off and the phase input removed with switch S-2. Since the resulting wave analyzer reading is proportional to the current, the ratio $\Delta I(H)/I(0)=\Delta\sigma(H)/\sigma(0)$ may be obtained from these two readings. Since the magnetic field was perpendicular to the current, the transverse magnetoresistive effect was investigated in this experiment.

III. EXPERIMENTAL RESULTS

As discussed above, space-charge effects may be expected to make the apparent mobility decrease at low frequencies and capacitative loading make it decrease at high frequencies. Before discussing the experimental results, it is of interest to consider the curve shapes to be expected from these processes. At sufficiently high frequencies, the impedance of the crystal between Hall electrodes will be purely resistive; when

[12] Isenberg, Russell, and Greene, Rev. Sci. Instr. 19, 685 (1948).

the capacitative reactance of any shunt capacity, C, present between these electrodes becomes comparable to the internal resistance, R, the measured Hall voltage will begin to decrease with frequency. The resulting decrease in apparent mobility is shown on a log-log plot in Fig. 2. The normalized frequency for the capacitative curve is $RCf/10$.

At low frequencies where space-charge effects become important, most of the potential drop across the crystal occurs near the current electrodes, and the electric field in the length direction at the Hall electrodes is very small. The Hall voltage is, to first order, directly proportional to this longitudinal field and hence will be abnormally small at low frequencies. The apparent mobility determined experimentally from Eq. (1) will therefore decrease at low frequencies in the same way as the longitudinal field at the center. This frequency dependence may be obtained, at least approximately, from the space-charge theory of one of the authors.[5] This theory shows that the absolute magnitude of the longitudinal field at the center (in the absence of a

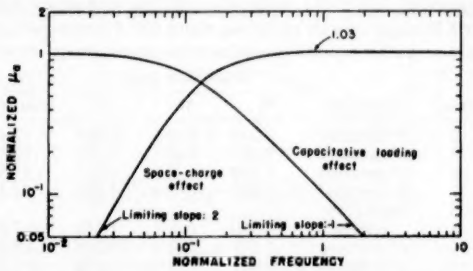

FIG. 2. Theoretical dependence of normalized apparent mobility on frequency arising from space-charge and capacitative-loading effects.

magnetic field) decreases proportionally to frequency at low frequencies, whereas the real part of the field decreases proportionally to the square of frequency. The field is complex because of the space-charge effects. It is not possible to decide definitely which of the above functions of the field will be most nearly effective in producing the Hall voltage without solving the pertinent two-dimensional boundary value problem with magnetic field present. This is an extremely complicated problem and its solution has not been obtained; instead, in Fig. 2, we have plotted the low-frequency dependence of μ_a, normalized to unity at high frequencies, which would arise from the real part of the longitudinal field since it is this result which agrees best with experiment. The normalized frequency for this curve is $2\pi fC_g/G_\infty$, where C_g is the ordinary geometric capacitance/cm^2 between current electrodes and G_∞ is the ordinary ohmic conductance/cm^2 between the electrodes in the absence of space charge.[5] Note that the field contribution in Fig. 2 overshoots its high-frequency value slightly. An experimental determination of μ_a should yield a frequency dependence made up of the two curves of Fig. 2,

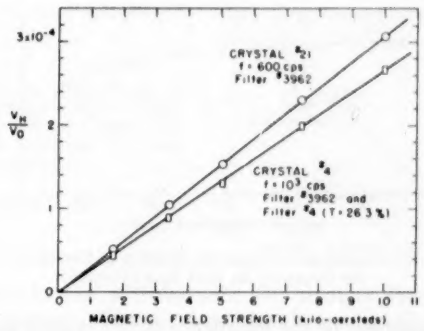

FIG. 3. Dependence of Hall voltage ratio, V_H/V_0, on magnetic field strength for fixed frequency and light intensity.

possibly separated by a flat plateau between. The value of μ_a at the plateau should be the true value of the Hall mobility. Note that if the curves of Fig. 2 overlap sufficiently, no true plateau will be observed and the correct Hall mobility will not be obtained.

Equation (1) indicates that the Hall ratio V_H/V_0 should depend linearly on magnetic field strength provided the Hall mobility is independent thereof. Figure 3 shows the dependence on field strength of this ratio for two different crystals at different frequencies and light intensities. The dependence was linear within experimental error for all crystals for which it was measured. For all crystals the carriers were found to be negatively charged, as one would expect for electrons near the bottom of the conduction band. Free holes should not be present in any of the crystals measured.

Typical frequency response curves for different light intensities are presented in Fig. 4 for crystal No. 4. The dimensions and the treatment of this and other crystals are summarized in Table I. As expected, the high-frequency decrease in μ_a is inversely proportional to frequency. Further, reducing the light intensity increases the source resistance of the Hall voltage and causes the high-frequency decrease to occur at lower frequencies the lower the light intensity. From the absence of a low-frequency decrease in μ_a for these curves, one can conclude that space-charge effects were practically negligible in the frequency range covered. In this range, possible space-charge effects at the Hall electrodes themselves will also be negligible. A rough

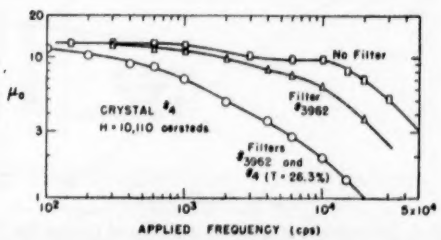

FIG. 4. Dependence of apparent mobility on Crystal No. 4 on frequency and light intensity.

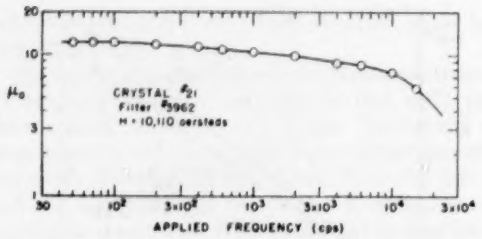

FIG. 5. Dependence of apparent mobility of Crystal No. 21 on frequency for fixed light intensity.

measurement of the impedance of this crystal showed in fact that with the highest light intensity, space-charge parallel capacitative susceptance was negligible above about 30 cps compared with the normal conductance of the crystal. The upper curve in Fig. 4 shows the presence of two plateaus. Such behavior, or a very slow rise in μ_a with decreasing frequency to a final limiting plateau was generally observed. The increase observed is too large to be accounted for by the small overshoot in the real part of the longitudinal field discussed in connection with Fig. 2. The theory from which this curve is taken is based on the assumption that the electrodes are blocking for all carriers, however. It is shown in another paper by one of the authors[13] that the acutal electrodes used in this work, silver paint directly on the crystal, are only rectifying for electrons. The dependence on frequency of the current within the crystals with rectifying electrodes is considerably different from that with blocking electrodes, and it is possible that such difference may lead to a sufficiently large overshoot in the actual longitudinal field to explain the results. Unfortunately, no Hall measurements have been made with blocking electrodes. These circumstances make the real value of the Hall mobility somewhat ambiguous. It seems likely, however, that the final low-frequency plateau value of μ_a is the Hall mobility, since practically all crystals measured yield the same value for this quantity.

Figures 5 and 6 show the dependence of μ_a on frequency and light intensity for another sample. The measurements presented in Fig. 5 could not be extended to sufficiently low frequencies to detect an appreciable drop in μ_a because of the increase of flicker

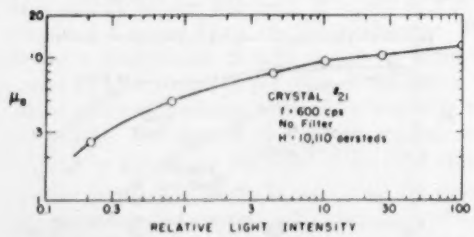

FIG. 6. Dependence of apparent mobility of Crystal No. 21 on light intensity for fixed frequency.

[13] J. R. Macdonald (submitted to J. Chem. Phys.).

noise level with decreasing frequency. Figure 6 shows that the apparent mobility at a fixed frequency decreases with a decrease in light intensity because of the resulting increase in impedance level which leads to greater capacitative loading. This curve does not show a clearly-defined saturation in the value of μ_a at high light intensities because at 600 cps a relative intensity slightly greater than 100 would have been required to reach saturation. At lower frequencies, similar curves for this and other crystals did show such saturation even for smaller light intensities. Thus, for sufficiently low frequencies and high light intensities, the apparent mobility is independent of light intensity.

Figure 7 shows the frequency dependence of μ_a for the one crystal found which did show a clearly-defined decrease in μ_a at low frequencies. This decrease is proportional to frequency squared. Since the apparent plateau of thic curve gives a value of μ_a considerably below that obtained for all other U-centered crystals, it seems likely that there was too much overlap between the low- and high-frequency curves shown in Fig. 2 to allow the true Hall mobility plateau to be reached for this crystal.

TABLE I. Summary of treatment, dimensions, and Hall mobility for KBr single crystals containing about 10^{16} F centers per cm^3.

Crystal	Treatment	Dimensions (cm)			μ_H cm^2/volt-sec
		L	W	T	
2	U centered	1.240	0.463	1.020	12.4
3	U centered	1.685	0.495	1.098	12.5
4	U centered	1.278	0.476	1.017	12.5
7	U centered	1.422	0.196	1.020	12.3
8	Additively colored	1.556	0.363	1.050	>7.5
14	U centered	1.039	0.382	0.757	12.8
16	U centered	1.041	0.333	0.732	>7.5
21	U centered	1.696	0.479	1.040	12.3

Figure 8 shows the results of measurements on an additively-colored KBr crystal. Measurements on this crystal were difficult because even with maximum light intensity its impedance level was many times higher than that of similar U-centered crystals containing the same F-center concentration. Further, it was necessary to use considerably less than maximum light intensity to reduce its bleaching rate sufficiently that negligible change occurred during the course of a measurement. This necessity increased the impedance level even further. The result of the impedance level of several hundred megohms is shown by the loading apparent in the figure. It was impossible to carry out measurements to sufficiently low frequencies that a plateau could be reached. Even at the lowest frequencies for which accurate results could be obtained, capacitative loading was still dominant.

There is no reason to believe that the Hall mobility of electrons in additively-colored crystals should be appreciably different from that of electrons in U-centered crystals. The U-center concentration, about

$10^{18}/cm^3$, is so small relative to the normal ionic concentration that additional impurity scattering from U centers should be entirely negligible. Therefore, it is likely that the final plateau value of the curve of Fig. 8 is the same as that obtained for U-centered crystals. Certainly, it is not greatly less. Similar measurements were carried out for an additively-colored potassium iodide crystal, and, although a Hall effect could be detected, capacitative loading reduced μ_a even further for this crystal. Results for the Hall mobility of a number of crystals are summarized in Table I.

For a substance exhibiting electronic conduction, the relative change in conductivity due to a magnetic field, provided that electrons from only one energy band are appreciably involved, should follow[14] for low fields,

$$\frac{\sigma(0)-\sigma(H)}{\sigma(0)}=\frac{\Delta\sigma}{\sigma(0)}=BH^2. \qquad (2)$$

This quantity is plotted *vs* H^2 in Fig. 9 and it is evident that such proportionality is fairly good. Note that a field of 10 kilo-oersteds causes a 7 percent decrease in

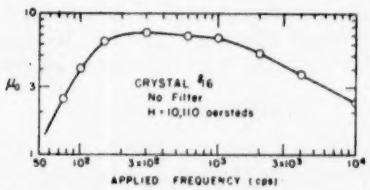

FIG. 7. Dependence of apparent mobility of Crystal No. 16 on frequency for fixed light intensity.

current. Two other crystals gave similar results and a check of frequency response at this field strength indicated no appreciable dependence between 10^2 and 10^3 cps. Measurements of this nature must be carried out within a frequency range where the current is almost entirely conductive, or spurious results will be obtained. At low frequencies a large part of the current will arise from parallel space-charge capacitance whereas at high frequencies where such capacitance may be negligible the geometrical capacitance of the crystal will begin to account for a large share of the observed current. Rough impedance measurements were carried out preparatory to making magnetoresistance measurements to establish that the current at the operating frequency was, in fact, largely conductive. While it was true that three crystals were found that gave results similar to those presented in Fig. 9, all other crystals which were measured gave very anomalous magnetoresistive results. With 10 kilo-oersteds applied, the maximum change in conductance observed for these crystals was not greater than 1 percent and apparently corresponded to an increase in conductance, rather

[14] F. Seitz, *Modern Theory of Solids* (McGraw-Hill Book Company, Inc., New York, 1940), p. 184.

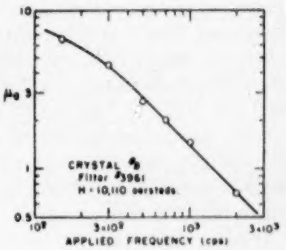

FIG. 8. Dependence of apparent mobility of additively-colored Crystal No. 8 on frequency for fixed light intensity.

than a decrease with magnetic field strength. No difference between the Hall mobilities of the crystals which gave high or low magnetoresistance values could be detected. The reason for the magnetoresistive discrepancy could not be determined in the limited time available for this work.

IV. DISCUSSION

Interpretation of the experimental results is complicated not only by the limitations on the data imposed by the time available but also by the well-known shortcomings of the theory of electronic transport properties in polar crystals. Accordingly, a complete discussion is not possible at present.

For discussion purposes, the electric and magnetic fields are assumed homogeneous over that part of the crystal in which are to be found the electrons with whose properties we are concerned. Any conceivable relaxation time for electrons is negligibly small compared to the period of the applied fields; thus, it is permissible to treat the fields as time-independent.

Because of the low density of centers from which electrons are excited, it seems reasonable to expect the electrons in the conduction band to have approximately thermal velocities and a Maxwellian distribution. So far as the authors are aware, no satisfactory theoretical treatment has been given which can be applied to the present case in discussing either the energy states of the conduction electrons or their scattering by the longitudinal optical lattice vibrations. The field theoretic approximational procedures of Frohlich,

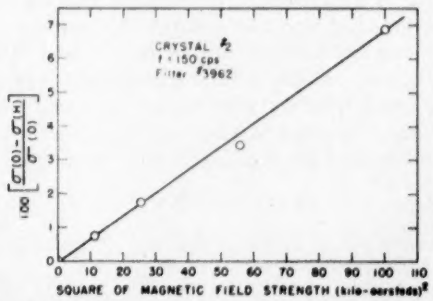

FIG. 9. Dependence of percentage relative change in conductance of Crystal No. 2 on the square of magnetic field strength; fixed frequency, fixed light intensity.

Pelzer, and Zienau,[15] of Lee, Low, and Pines,[16] and of Low and Pines[17] break down for electrons of kinetic energy comparable to $h\nu$, where ν is the frequency of the logitudinal optical modes of greatest wavelength; and for KBr, $(kT/h\nu)\approx(T/250)$ is of order unity at room temperature. As discussed by several authors,[15–17] the coupling between the electrons and the longitudinal optical modes is too strong to be treated properly as a small perturbation.

Failing the apparatus for a detailed calculation, it is of interest to see if the present data can be brought in any simple way within a familiar phenomenological structure by making an educated guess at the energy spectrum of the conduction electrons and at the energy dependence of their relaxation time. It seems reasonable to assume in the present instance that an electron excited to the conduction band has a constant effective mass and a kinetic energy of thermal magnitude which is an isotropic function of crystal momentum. With regard to the relaxation time, it cannot be supposed that the theoretical results derived by low temperature approximations could nevertheless be usefully applied here if the polarization waves were the only important scatterers. Both perturbation theory[18] and field theory[15,17] methods give a relaxation time independent of electron (or polaron) kinetic energy; and for a constant relaxation time, there is no change of resistance in a magnetic field as long as the energy surfaces are spherically symmetric. For scattering by the optical modes at high temperatures we adopt

$$\tau(\epsilon)=(\pi^{\frac{1}{2}}/2)(\epsilon/kT)^{\frac{1}{2}}\tau_0, \tag{3}$$

where ϵ is the kinetic energy and τ_0 the average of this $\tau(\epsilon)$ over the occupied energy states. Such an energy dependence is indicated by the Boltzmann transport equation for the case of weak electron-phonon coupling at elevated temperatures, and corresponds to a $(1/v)$ scattering cross section. For scattering by the acoustic modes, we take as valid the constant mean free path found, e.g., by the method of deformation potentials and write

$$\tau(\epsilon)=(\pi^{\frac{1}{2}}/2)(kT/\epsilon)^{\frac{1}{2}}\tau_a, \tag{4}$$

where τ_a is the average of (4) over the filled states.

The formal theoretical expressions appropriate under the above assumptions may all be obtained directly from Wilson's treatise.[19] The magnetic fields employed in the measurements were always sufficiently small that only the leading terms of expansions in powers of H^2 need be retained. We have, for the Hall angle,

$$\theta(H)=(K_2/K_1)\omega, \tag{5}$$

and for the relative change of resistance,

$$\frac{\rho(H)}{\rho(0)}-1\doteq\left[\frac{K_3K_1}{K_2^2}-1\right]\theta^2(H), \tag{6}$$

where $\omega=(eH/mc)$, $m=$effective electronic mass, e is the absolute value of the electronic charge, and

$$K_r\equiv\frac{4ne^2}{3\pi^{\frac{1}{2}}m}\int_0^\infty\tau^r(xkT)x^{\frac{1}{2}}e^{-x}dx,$$

with n the number of conduction electrons per cm^3. The coefficient of $\theta^2(H)$ in Eq. (6) would be 0.085, if only the optical phonons were significant and would be 0.27 for purely acoustical scattering. In either case, the change of resistance computed by using the observed Hall angles is too small by a factor of 10^6. No conceivable single-term power-law expression for the relaxation time can reduce the discrepancy much. With so few electrons in the conduction band, it is hard to believe that re-entrant energy surfaces can be invoked as for semiconductors to account for the magnitude of the effect of Fig. 9. Clearly something more drastic than adjustment of an empirical effective mass and of a single relaxation time will be required to correlate the Hall and magnetoresistance effects in KBr.

V. NUMERICAL RESULTS

From the measured resistivities and Hall angles we can estimate the number of electrons excited to the conduction band under strong illumination. It is of the order of 10^{10} cm^{-3} or less for all U-centered crystals herein reported. As discussed elsewhere by one of the authors,[13] not only negative ion vacancies but also other traps for electrons are important in determining the conduction band population, and the situation is sufficiently complex to preclude estimates of recombination times without further data.

If we ignore any difference between Hall and microscopic mobilities and assume the effective mass to be equal to the free electron mass, we find that a Hall mobility of 12.5 cm^2/volt-sec gives a mean relaxation time of 6×10^{-15} sec. Allowing for an effective mass of between one and four electron masses, we can conclude that the mean relaxation time lies between 10^{-14} and 10^{-15} sec. Assuming thermal velocities for the electrons, one then finds mean free paths which to order of magnitude are greater than 10^{-8} cm and less than 10^{-7} cm. These values are in conformity with what one would expect from other evidence.[20]

ACKNOWLEDGMENTS

The authors wish to thank Elson Hutchinson for aid in making the measurements. One of us (J.R.M.) is greatly indebted to the Argonne National Laboratory for a visiting appointment.

[15] Frohlich, Pelzer, and Zienau, Phil. Mag. **41**, 221 (1950).
[16] Lee, Low, and Pines, Phys. Rev. **90**, 297 (1953).
[17] F. E. Low and D. Pines, Phys. Rev. **91**, 193 (1953).
[18] H. Frohlich and N. F. Mott, Proc. Roy. Soc. (London) **A171**, 496 (1939).
[19] A. H. Wilson, *The Theory of Metals* (Cambridge University Press, Cambridge, 1953), second edition, Secs. 8.51 and 8.64.
[20] Reference 3, p. 104; reference 14, p. 558.

Some Properties of p-Type Gallium Antimonide between 15°K and 925°K

H. N. LEIFER AND W. C. DUNLAP, JR.
General Electric Research Laboratory, Schenectady, New York

(Received March 1, 1954)

Gallium antimonide has been produced by direct combination of gallium and antimony under hydrogen. The product was zone refined and pulled in single crystal form using the Czochralski technique. The product was p type, with resistivities in the range 0.08–0.1 ohm cm. Hall coefficient and resistivity were measured in the temperature range 15–925°K. The slope of the Hall curve at low temperatures yielded the value 0.024 ev for the ionization energy of the carriers. It has been shown necessary to assume an additional acceptor level at 0.037 ev. The room temperature mobility of several samples was about 800 cm²/volt sec. The Hall mobility varied as $T^{-0.87}$ in the temperature range below room temperature, but the slope changed at about room temperature, and shifted nearly to a T^{-1} law in the higher temperature range. The Hall coefficient changed sign at 357°C, as the sample became intrinsic. The mobility ratio was determined from the ratio of the extrapolated extrinsic resistivity and the actual resistivity at the Hall inversion temperature. The value was about 5. The effective mass and intrinsic band gap were estimated from the resistivity data and infrared measurements. The best values were estimated to be $0.20m$ for the effective mass of electrons, $0.39m$ for holes, and 0.80 ev for the intrinsic band gap at 0°K. The best value for room-temperature band gap was taken to be 0.71 ev; the coefficient of band gap with temperature 3×10^{-4}/°C.

INTRODUCTION

THE properties of semiconducting intermetallic compounds have become of increasing interest during the last several years. Work on Mg_2Sn,[1] for example, indicated that intermetallic compounds could be semiconductors. The work of Welker[2] has focused attention on the intermetallic compounds of the third and fifth column elements. Recently, there have been a number of publications[3–7] dealing, in particular, with the properties of aluminum, gallium, and indium antimonide.

It is the object of the present work to present results on the temperature variation of some of the conduction properties of single crystals of gallium antimonide, in the temperature range 15°K to close to the melting point (about 700°C). The results are preliminary in the sense that they deal only with p-type material of rather high carrier density.

PREPARATION OF GALLIUM ANTIMONIDE SINGLE CRYSTALS

Purest available commercial antimony and gallium were used as starting materials and zone refining[8] was employed for additional purification of the antimony metal. The compound was prepared by direct combination of the two elements. Gallium metal was brought to a temperature of approximately 750°C in a crucible at the bottom of a quartz tube in an atmosphere of dry hydrogen. Antimony metal, at room temperature, was contained in a side arm connected to the main body of the tube through a ground joint. Antimony could thus be introduced into the molten gallium in small amounts making it possible to keep the temperature up to 750°C. This method insures intimate mixing and minimizes the evaporation of antimony.

The compound was subsequently zone refined and used for the production of single crystals ($\frac{1}{2}$ in. diam. $\times 3$ in.) by the Czochralski technique, using seed crystals obtained from the zone-refined compound. Quartz crucibles and a hydrogen atmosphere were used.

EXPERIMENTAL MEASUREMENTS

Gallium antimonide is remarkably similar to germanium in appearance and many of its physical properties. Etching of the samples was accomplished with diluted $HF-HNO_3$, a standard etchant for germanium. As for p-type germanium, indium was found to make quite satisfactory nonrectifying contacts.

The low-temperature measurements were made on rectangular plates (1 cm×0.5 cm×0.2 cm) on which six contacts were indium-soldered for the Hall effect and resistivity measurements. The samples were mounted inside a low-temperature cryostat and a calibrated copper-constantan thermocouple was used for the temperature measurements. The reversal of the field could be made by rotation of the permanent magnet through 180°. All the voltage measurements were made with a Rubicon Type-B low-impedance potentiometer.

For the high-temperature measurements, the samples were cut in a form[9] such that the probes were all narrow projections from the sample itself. The samples were mounted inside a special high-temperature vacuum

[1] W. D. Robertson and H. H. Uhlig, Trans. Am Inst. Mining Met. Engrs. **180**, 345 (1949). See also B. I. Boltaks, J. Tech. Phys. (U.S.S.R.) **20**, 180 (1950).
[2] H. Welker, Z. Naturforsch. **7a**, 744 (1952); **8a**, 248 (1953).
[3] Breckenridge, Hosler, and Oshinsky, Phys. Rev. **91**, 243 (1953); see also Phys. Rev. **90**, 488 (1953).
[4] Willardson, Beer, and Middleton, Phys. Rev. **91**, 243 (1953); see also Phys. Rev. **93**, 912 (1954).
[5] M. Tanenbaum and G. L. Pearson, Phys. Rev. **91**, 244 (1953); Phys. Rev. **93**, 912 (1954).
[6] M. Tanenbaum and J. P. Maita, Phys. Rev. **91**, 1009 (1953).
[7] D. A. Jenny, AIEE–IRE Semiconductor Devices Conference, Pennsylvania State College, July, 1953 (unpublished).
[8] W. G. Pfann, J. Metals **4**, 747 (1952).
[9] Dunlap, McMillan, and Brooks, Phys. Rev. **93**, 911 (1954).

furnace and chromel-alumel thermocouples were used for temperature measurements. This furnace was found to give almost complete freedom from errors arising from temperature inhomogeneity in the furnace and from the thermoelectric voltages arising therefrom. The sample was held in a quartz holder with graphite contacts to prevent chemical action between sample and contacts. A vacuum of better than 10^{-4} mm Hg was maintained in the system during heating and measurement.

In both the low- and the high-temperature measurements, it is necessary to restrict values of sample current in order that ohmic heating may not change the sample temperature and thus change the observed properties. At all temperatures the samples were found to obey Ohm's law satisfactorily.

RESULTS

The results on a typical sample are shown in Fig. 1 as the logarithm of both the Hall effect and resistivity *versus* the reciprocal temperature. It is seen that the Hall coefficient increases continuously as the temperature is lowered from room temperature, whereas the resistivity goes through a minimum and then increases. The slope of the Hall curve, although not quite constant, is used to estimate an ionization energy of about 0.024 ev, based upon the equation

$$1/R \propto n = n_0 \exp(-\Delta E/kT).$$

Both the Hall coefficient and the resistivity curves tend to flatten out at the lowest temperatures. This tendency was confirmed by a resistance measurement in liquid helium which showed that the resistance at

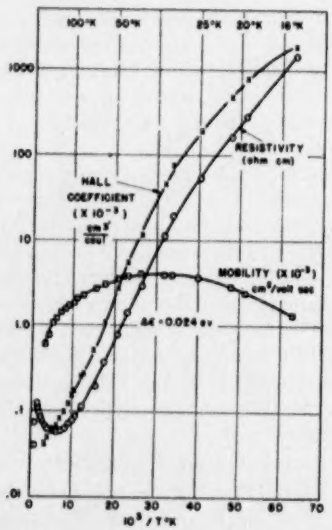

FIG. 1. Results of Hall effect and resistivity measurements on gallium antimonide single crystals at temperatures from 298°K down to 15°K.

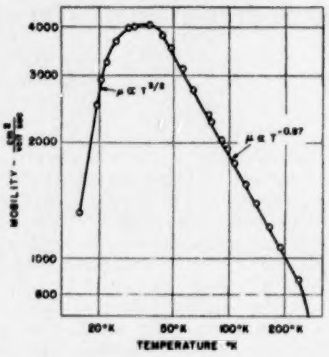

FIG. 2. Plot of log mobility *versus* log$T$ for a sample of gallium antimonide in the low temperature range. The maximum occurs at about 33°K.

4°K was about 20 times that at 20°K. Thus there is evidence of a conductivity, in parallel with that of 0.024 ev ionization-energy carriers, which limits the resistance attainable on cooling. The present information is insufficient to determine whether this low-temperature conductivity is a bulk or surface effect.

The nature of the p-type centers in gallium antimonide has not been determined. They may be impurities, or they may be an excess of one of the constituents. In most cases studied to date, the carrier density at room temperature, as determined from the Hall data, was about $10^{17}/cm^3$.

The room temperature mobility varied somewhat from sample to sample, ranging from 700 to 850 cm^2/volt sec. Below room temperature, we see from Fig. 2 that the mobility increases with decreasing temperature, until 33°K is reached. Below this temperature, the mobility drops off.

Below the temperature of the maximum in Fig. 2, the mobility very nearly follows a $T^{\frac{3}{2}}$ law, as predicted for impurity scattering. However, employing the theory of Conwell and Weisskopf[10] and using the density of carriers at 33°K, one finds for the mobility due to impurity scattering $\mu_I \simeq 5\times10^5$ cm^2/volt sec. Since this value is large compared to the actual mobility, it appears that the drop in mobility below 33°K is determined by factors other than the charged impurity ions present. Possible factors could include effects of neutral impurities, imperfections and space-charge barriers in the material.

Above the temperature of the maximum in Fig. 2, the mobility obeys a $T^{-0.87}$ law. Since this temperature range is the region of deionization of carriers, it is necessary to consider scattering by charged and neutral impurities (with possibly comparable cross sections and differing temperature dependence). This makes interpretation difficult.

Figure 3 shows the mobility variation above room

[10] E. Conwell and V. F. Weisskopf, Phys. Rev. **77**, 388 (1950).

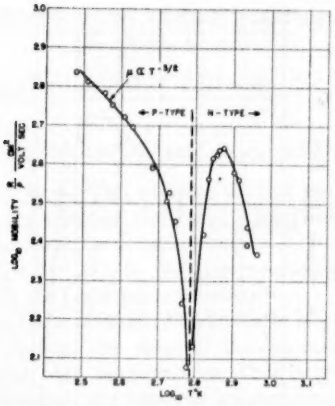

FIG. 3. Plot of log mobility *versus* log$T$ for the high-temperature region.

temperature on a logarithm mobility *versus* logarithm temperature scale. The beginnings of a change in mobility temperature dependence could be seen in Fig. 2 above 200°K. The straight line portion of the curve of Fig. 3 above room temperature and before the temperature at which intrinsic conduction begins indicates that the hole mobility follows very nearly a $T^{-\frac{3}{2}}$ law. We assume that this theoretical lattice scattering law ($T^{-\frac{3}{2}}$) is obeyed in the high-temperature range.

Figure 4 shows results of Hall and resistivity measurements on several samples of gallium antimonide, in the temperature range between 25°C and 650°C. The Hall coefficient changed sign at 357°C. It is seen that not all of the impurity centers become ionized until the temperature rises well above room temperature. This condition of the Hall coefficient continuously increasing as the temperature decreases will be considered in the next section.

Because of the low melting point (700°C) and the high impurity content, the sample never reached the condition that the number of intrinsic carriers greatly exceeded the number of impurity centers. For this reason, interpretation of the intrinsic resistivity line in terms of the theoretical band gap of the gallium antimonide lattice becomes more difficult than is usually the case. The detailed analysis is given in the next section.

DISCUSSION

Acceptor Level Model

The experimental shape of the Hall coefficient curve from about 30°K to the inversion temperature, cannot be justified on the assumption of a single acceptor level or one acceptor level plus donor levels. A model of two acceptor levels will, however, quite satisfactorily fit the experimental data. Calculations indicated that, in this model, donor levels play no part in the observed properties. The two acceptor levels needed to fit the data are at $E_{A1}=0.024$ ev and $E_{A2}=0.037$ ev and have a density of $N_{A1}=1.1\times10^{16}/\text{cm}^3$ and $N_{A2}=1.7\times10^{17}/\text{cm}^3$, respectively, for the particular samples studied here.

The Hall data provide the hole density and Fermi level at any temperature plus the experimental value of E_{A1}, as 0.024 ev. The charge neutrality condition is

$$p+p_{A1}+p_{A2}=N_{A1}+N_{A2}$$

where p is the hole density in the valence band, p_{A1} is the hole density in acceptor level A_1 whose density is N_{A1}, and p_{A2} is the hole density in acceptor level A_2 whose density is N_{A2}. At low temperatures (e.g., 50°K), A_2 may be neglected and N_{A1} determined. At higher temperatures (e.g., 100°K), these values are used to determine E_{A2} and N_{A2} which are interdependent. Since the ratio of acceptor-level densities is ten, it seems unlikely that they may both be attributed to a single imperfection.

Determination of the Mobility Ratio b

From an analysis of the Hall and resistivity data, one can determine the mobility ratio b for electrons and holes. The method essentially involves the determination of the actual resistivity and the extrapolated extrinsic resistivity, at the temperature of inversion of the Hall coefficient. For the sample studied most intensively, this temperature (T') was 357°C.

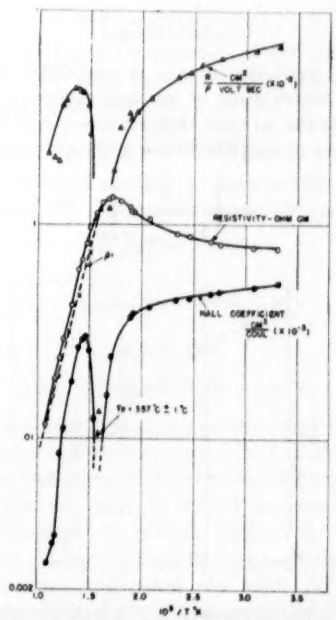

FIG. 4. Results of Hall effect and resistivity measurements on gallium antimonide single crystals at temperatures from 298°K up to 925°K.

At the inversion temperature, the Hall coefficient is zero, and the Hall formula,[12]

$$R=\frac{3\pi}{8e}\frac{nb^2-p}{(nb+p)^2}, \tag{1}$$

reduces to

$$n_{T'}b^2=p_{T'}. \tag{2}$$

Since $p=n+p_0$, where p_0 is the hole concentration arising from complete ionization of the impurity centers,

$$n_{T'}=p_0/(b^2-1). \tag{2a}$$

Likewise, the conductivity $\sigma=e(n\mu_n+p\mu_p)$ is given by

$$\sigma=e[n(\mu_n+\mu_p)+p_0\mu_p)], \tag{3}$$

and this yields

$$n=(\sigma-ep_0\mu_p)/e(\mu_n+\mu_p). \tag{3a}$$

Combining (2) and (3), we find

$$b=\left[\frac{1}{1-(ep_0\mu_p/\sigma)}\right]_{T'}. \tag{4}$$

It is thus possible to determine b by using the extrapolated value of μ_p at T', assuming a $T^{-\frac{1}{2}}$ law, and solving for p_0 using Eq. (1), which for the extrinsic range becomes

$$R=3\pi/8ep_0. \tag{5}$$

This method is quite sensitive to small errors in the determination of μ_p and p_0. It is, therefore, preferable to use the extrapolated extrinsic conductivity σ_{ext} where

$$(\sigma_{ext})_{T'}=(ep_0\mu_p)_{T'}. \tag{6}$$

This extrapolation of σ_{ext} is considered to be valid since the contribution of intrinsic carriers at temperatures below the intrinsic temperature is seen from Fig. 5 to be orders of magnitude below the value of p_0. Thus,

$$b=\left[\frac{1}{1-\sigma_{ext}/\sigma}\right]_{T'}. \tag{7}$$

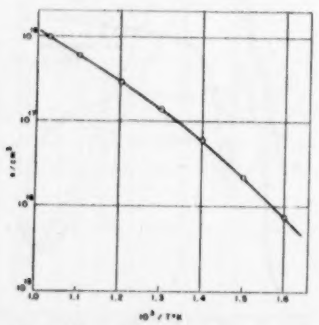

FIG. 5. Plot of ln$n$ *versus* $1/T$. n is the theoretically calculated density of electrons.

[12] See W. Shockley, *Electrons and Holes in Semiconductors* (D. Von Nostrand Company, Inc., New York, 1950), Chap. 8.

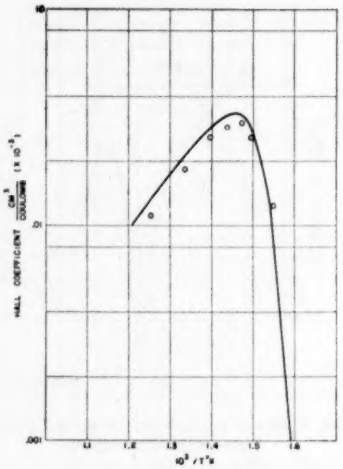

FIG. 6. Comparison of theoretically calculated Hall coefficient with experimental results, in intrinsic range of temperature above 357°C.

Using the data of Fig. 4, $\{(\sigma_{ext})_{T'}=6.9$, $\sigma_{T'}=8.7$ ohm^{-1} cm$^{-1}\}$, a value of 5.0 for the mobility ratio is then found from Eq. (7).

Determination of the Impurity Carrier Concentration

For the determination of p_0, the density of carriers when ionization is complete, the Hall coefficient for the extrinsic region was extrapolated to a temperature of 600°K.

Equation (5) yields $p_0=1.85\times10^{17}$/cm^3. From Eq. (6) $\mu_p)_{T'}=230$ cm^2/volt sec, and thus $\mu_n)_{T'}=1150$. From (2a) or (3a), $n)_{T'}=7.7\times10^{15}$/cm^3, and thus $p)_{T'}=1.9\times10^{17}$/cm^3.

Analysis of the Intrinsic Region

a. The calculation of the intrinsic Hall curve

Figure 5 shows a plot of ln$n$ *vs* $1/T$, determined from Eq. (3a) assuming a $T^{-\frac{1}{2}}$ law for the mobilities. It is helpful in calculations involving n and p at any temperature.

The theoretically determined Hall coefficient for the intrinsic region above T' [obtained from Eq. (1) using calculated values of n, p, μ_n, and μ_p] is shown in Fig. 6 as the solid curve. The circles indicate the experimental Hall coefficient values. This comparison, it is believed, demonstrates the degree of consistency between the conductivity data (used to determine b, n, and p) and the Hall data. The degree of agreement also indicates that for gallium antimonide there may be little or no difference between "Hall mobility" and "conductivity" or "drift" mobility.[13]

[13] See reference 12, p. 206.

b. Determination of the intrinsic band gap E_g and the effective masses

Consider the theoretical expression for a simple model

$$(np)^{\frac{1}{2}}=2(2\pi mk/h^2)^{\frac{3}{4}}(m^*)^{\frac{3}{4}}T^{\frac{3}{2}}\exp[-(E_0-\alpha T)/2kT], \quad (8)$$

where $m^*=(m_nm_p)^{\frac{1}{2}}/m$; m_n and m_p are the effective masses of the electron and hole, respectively, m the free-electron mass.

Also, $E_g=E_0-\alpha T$ is the temperature-dependent band gap, E_0 the band gap at absolute 0.

Normally, in a pure semiconductor it is possible to determine E_0 from the slope of the log resistivity *vs* $1/T$ curve at high temperatures. This is so since at high temperatures the impurity carrier concentration is usually negligible in comparison to the intrinsic carrier concentration ($n\simeq n_i$) and ρ is an excellent approximation to ρ_i. In the present case, however, the impurity concentration is high enough—and the melting point of the compound low enough—that at 50° below the melting point the density of electrons n is only about three times the impurity density p_0. Thus, for p-type material, the measured slope of the intrinsic conductivity curve *vs* $1/T$ can be equal to, greater than, or less than that for intrinsic material, depending upon the temperature range chosen. Since the number of electrons is always less than that for intrinsic material and the actual and intrinsic resistivities are equal at the inversion temperature, (for $b>1$), it follows that the resistivity curve overshoots that for intrinsic on the high temperature side and at much higher temperatures the slope returns to the same value as that for intrinsic material.

For n-type material, on the other hand, the intrinsic resistivity always exceeds the actual resistivity, and there is no overshoot.

Therefore, to obtain E_0 it is necessary to calculate ρ_i or $(np)^{\frac{1}{2}}/T^{\frac{3}{4}}$ as a function of temperature. Logarithm ρ_i and $(np)^{\frac{1}{2}}/T^{\frac{3}{4}}$ *versus* reciprocal temperature are shown in Figs. 4 and 7, respectively. These plots are, of course, not independent of each other.

The slope of either curve yields the value

$$E_0=0.80 \text{ ev}.$$

Unpublished infrared transmission data on gallium antimonide, by Newman of this laboratory, at 298°K and 77°K indicate a temperature dependence of the band gap. It can be seen from Eq. (8) that this dependence may be accounted for by adjustment of two parameters, namely m^* and α. With no other evidence available, we have chosen α so as to yield a band gap agreeing with the room-temperature infrared transmission results. From this value of α, using Eq. (8), a value for m^* may be determined.

Because of the lack of sharpness at the absorption edge, the band gap determined from infrared data will depend upon an arbitrary choice of absorption coefficient. The value of room-temperature band gap selected (0.71 ev) corresponds to an absorption coefficient of 100 cm^{-1}.

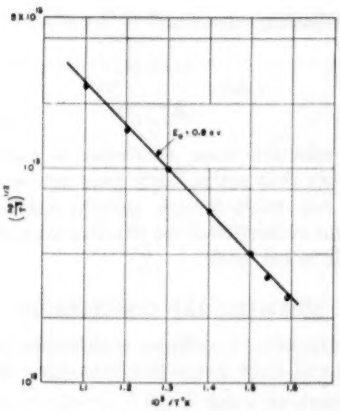

FIG. 7. Plot of $(np)^{\frac{1}{2}}/T^{\frac{3}{4}}$ *versus* $1/T$ for gallium antimonide. This method is used instead of the actual resistivity *versus* $1/T$ because of the effects of high impurity content.

A band gap of 0.71 ev dictates a temperature coefficient α of 3×10^{-4} ev/°K. These values plus the data of Fig. 7 yield a value of $m^*=0.28$.

From this value of m^* and the ratio of electron to hole mobility, it is possible to calculate a reasonably significant value of the separate effective masses of holes and electrons. According to Shockley, the mean free path of either carrier depends reciprocally upon the square of the effective mass:[14]

$$l=\pi h^4C_{ll}/(E_{1n}{}^2kTm_n{}^2), \quad (9)$$

where C_{ll} and E_{1n} are parameters of the lattice, independent of the effective mass. Also, the mobility depends upon mean free path according to the law:

$$\mu=4el/3(2\pi m_nkT)^{\frac{1}{2}}. \quad (10)$$

Thus, the ratio of electron to hole mobility depends upon $(m_n/m_p)^{-5/2}$. Solving the two equations:

$$(m_nm_p)^{\frac{1}{2}}=0.28m,$$

and

$$(m_n/m_p)^{-5/2}=5,$$

one finds

$$m_n=0.20m,$$

$$m_p=0.39m.$$

An independent evaluation of the effective mass of holes is available from the value of the ionization energy of the holes, determined from the low-temperature data, namely 0.024 ev. Now, it should be noted that the source of carriers in gallium antimonide is as yet unidentified. However, tentatively assuming a hydrogen-like system, and using the value 14.0 for the dielectric constant of K gallium antimonide,[15] one finds

[14] See reference 12, p. 278.

[15] Briggs, Cummings, Hrostowski, and Tanenbaum, Phys. Rev. **93**, 912 (1954).

from the following equation:[16]

$$\Delta E=\frac{13.56\,m_p}{K^2\ m}\text{ev} \qquad (11)$$

that the effective mass for holes is about $0.35m$. These values thus are in fairly good agreement. Since we have not made n-type gallium antimonide, no independent evaluation of the effective mass of electrons is available in our work.

SUMMARY AND CONCLUSIONS

Single crystals of gallium antimonide have been prepared, and their properties have been determined over a wide range of temperature. These properties have been found to fit well with the present theory of semiconductors. Of special interest among the results are the large ratio of electron to hole mobility (about five), the rather large intrinsic band gap (0.8 ev). Also, it is necessary to assume two acceptor levels in the energy scheme to fit the Hall data. A value of the hole effective mass has been estimated from the infrared absorption data, and from the electrical properties.

[16] See reference 12, p 224.

ACKNOWLEDGMENTS

We should like to thank Dr. R. Newman for the use of his infrared absorption data, and for fruitful discussions. We should also like to thank Dr. W. W. Tyler for growing the single crystals.

PHYSICAL REVIEW VOLUME 95, NUMBER 1 JULY 1, 1954

Theory of Secondary Electron Cascade in Metals

P. A. WOLFF
Bell Telephone Laboratories, Murray Hill, New Jersey
(Received March 5, 1954)

A study is made of the cascade process which describes the diffusion, energy loss, and multiplication of secondary electrons within a metal. The secondaries interact mainly with conduction electrons through a screened Coulomb potential. For low secondary energy (<50 ev) the resultant scattering is nearly spherically symmetric and the transport equation which governs the cascade process can be approximately solved. The velocity distribution turns out to be spherically symmetric for low secondary energy. Energy distributions are in agreement with experiment for metals to which the theory is applicable. Calculations are also made of the rate of change of yield with work function and the results are in accord with observed values. Finally, rough estimates are made of the total yield and the theory is shown to be consistent with the observed values.

I

THE phenomenon of secondary electron emission[1] can be thought of as occurring in two distinct steps. First of these is the production of internal secondaries by collisions between fast primaries and electrons bound in the metal. The second is the subsequent cascade process in which these secondaries diffuse through the solid, multiplying and losing energy en route, until they either sink back into the sea of conduction electrons or reach the surface with sufficient energy to emerge as true secondary electrons. These two steps pose two separate problems, each of considerable complexity, which must be solved before one can understand the various phases of SE. To date, most of the theoretical work[2] in the field has concentrated on the first of these and treated the second in a radically simplified way. Usually the whole second step is lumped into an effective absorption coefficient α for the internal secondaries. Calculations using this approach have given fair agreement with the shapes of observed total yield *versus* primary energy curves, but they cannot predict the absolute magnitude of the yield since, without solving the diffusion problem, there is no way of estimating α.

Other aspects of SE probably depend even more critically on the details of the internal electron cascade. For example, the energy distribution of secondaries is observed to be independent of primary voltage. This suggests that the cascade process is almost entirely responsible for the shape of the spectrum and that the method of production of the internal secondaries is relatively unimportant. The aim of the present work is to investigate this internal electron cascade and to verify to what extent this hypothesis is correct. The picture of SE which will arise from this study turns out to be a reasonable and consistent one which accounts for a number of the experimental results.

To solve the problem of the internal cascade one must, of course, know the elementary interactions by which electrons lose energy within the metal. This

[1] Hereafter abbreviated as SE.

[2] For a review and bibliography of work performed prior to 1948 see K. G. McKay's article in *Advances in Electronics* (Academic Press, Inc., New York, 1948). Other, more recent, articles are E. M. Baroody, Phys. Rev. **78**, 780 (1950); A. J. Dekker and A. van der Ziel, Phys. Rev. **86**, 755 (1952); J. F. Marshall, Phys. Rev. **88**, 416 (1952).

subject, which is clearly a critical one in the theory, will be discussed in the next section. Following that, the remainder of the paper will be devoted to a study of the transport equation whose solution provides the energy distribution of secondaries. Various methods of attacking this problem will be investigated and, finally, a comparison will be made between theory and the results obtained experimentally.

II

For an electron to escape from a metal and be observed as a secondary it must have an energy of about ten volts or more relative to the bottom of the conduction band.[3] In this energy range, where the exclusion principle does not operate strongly, the main way it loses energy is by collision with conduction electrons in the metal. Electron-phonon interactions also undoubtedly occur, but the fact that SE from metals is independent of temperature indicates that they play only a minor role in the slowing down process. They will be neglected here and only electron-electron collisions considered in calculating energy loss. Furthermore, in discussing these collision processes the electrons will be treated as free; no attempt will be made to include the effect of the crystal field on the scattering. The validity of this approximation depends to a large extent upon the material being studied, but for simple, monovalent metals such as the alkalis and noble metals it probably is reasonably close to the truth.

The potential U which causes electron-electron scatterings is the Coulomb field, screened by the plasma of conduction electrons. Probably the best calculation of the effect of the screening is that of Pines and Bohm[4] who found

$$U=\sum_{\mathbf{k},k<k_c}\left[\frac{4\pi e^2 e^{i\mathbf{k}\cdot\mathbf{r}}}{k^2}\right]. \tag{1}$$

Other potentials have also been used. For example, Mott[5] in his paper on impurity scattering employs a screened potential of the form

$$U=e^2e^{-qr}/r, \tag{2}$$

where

$$q=\frac{4me^2}{\hbar^2}\left(\frac{3p_0}{\pi}\right)^{\frac{1}{3}}. \tag{3}$$

Fortunately, for the present purpose the form of U is rather unimportant. The crucial point is that in all these potentials the cut-off distance is small; for a typical metal the values of k_c used by Pines[6] correspond to lengths of about 1A and the $1/q$ values used by Mott are considerably smaller. With such short range potentials the scattering is spherically symmetric (s wave) over a considerable range of electron energies. By way of illustrating this point, Table I gives the s- and p-wave phase shifts for an $(e^2/r)\exp(-r/\lambda_D)$ potential, with λ_D taken as 0.75A and 1.00A. These values were obtained by numerically integrating the appropriate Schrödinger equation; from them it is clear that s-wave scattering predominates for low energies and that even at 50 ev it constitutes about one-half of the total scattering cross section. Below 50 ev, therefore, the scattering is roughly spherically symmetric (in the center of mass system) which means that, on the average, an electron loses about half its energy at each collision. This is in marked contrast to the behavior of faster electrons which suffer typical Rutherford scattering and lose only a small fraction of their energy at each impact. In solving the transport equation, therefore, the correct electron-electron cross section to use is one that is spherically symmetric for small electron energy but which develops more and more of a forward peak as the energy increases, eventually approaching the Coulomb cross section. Unfortunately, with such a general interaction the transport equation, which gives the spatial and energy distributions of internal secondaries, is far too difficult to solve. Therefore, in order to get at least a semiquantitative idea of how these internal electrons behave, the electron-electron scattering will be assumed to be spherically symmetric up to an energy W (about 100 ev), beyond which it will be described by Rutherford's formula. This is a very rough approximation but, fortunately, it should not have a great effect on the shapes of the SE spectra, since they are almost entirely determined by the behavior of electrons with energies below about 40 ev. As a consequence of this fact, the spectra also turn out to be quite insensitive to the choice of W. The value of 100 ev given above is hardly more than an intelligent guess based on experience gained in evaluating the phase shifts for the screened Coulomb field, but a variation in it by 50 percent in either direction would only change the energy distribution by a few percent in the low-energy region. Thus, even with the crude approximation outlined above, the theoretical spectra should be fairly accurate in the 0–40 ev range where most of the secondaries fall. For higher energies,

TABLE I. Phase shifts for scattering from screened Coulomb potential.

E (Rydbergs)	δ_0 (s-wave phase shift)	δ_1 (p-wave phase shift)
	$\lambda_D=0.75$A	
2	−24°	−1° 20′
4	−24° 40′	−5° 40′
6	−25°	−5° 40′
	$\lambda_D=1.00$A	
2	−31°	−8° 30′
4	−32°	−9°

[3] In this paper all energies will be measured from the bottom of the conduction band.
[4] D. Pines and D. Bohm, Phys. Rev. **85**, 338 (1952).
[5] N. F. Mott, Proc. Cambridge Phil. Soc. **32**, 281 (1936).
[6] David Pines (private communication).

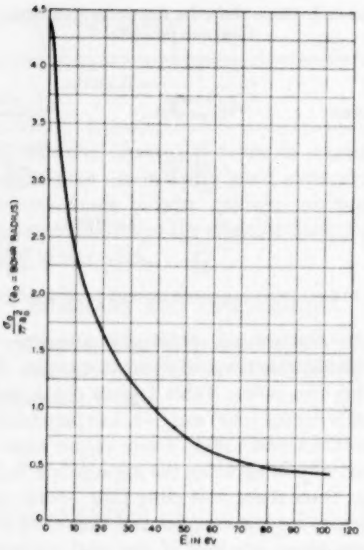

FIG. 1. Electron scattering cross section *versus* electron energy.

of course, the formulas are much less reliable and could give large errors in the number of secondaries.

For low electron energy, the numerical value of the electron-electron cross section is given by the usual formula[7]

$$\sigma = (4\pi/k^2)\sin^2\delta_0,$$

where the values of δ_0 are taken from Table I. Figure 1 shows the σ *vs* E curve obtained in this manner using a cut-off distance of 0.75A. Of course, this cross section still has to be corrected for the effect of the exclusion principle since scatterings in which either of the electrons winds up with energy less than the Fermi energy are forbidden. For the time being, however, this point will be neglected; it will be considered in detail at a more convenient point in the later discussion of the transport equation.

III

The equation describing the electron cascade process within the metal is the same as that given by Marshak[8] for neutron slowing down, namely,

$$\frac{\partial N}{\partial t}(\mathbf{r},\boldsymbol{\Omega},E,t)+\mathbf{v}\cdot\operatorname{grad}N(\mathbf{r},\boldsymbol{\Omega},E,t) = -\frac{vN(\mathbf{r},\boldsymbol{\Omega},E,t)}{l(E)}+S(\mathbf{r},\boldsymbol{\Omega},E,t)+\int dE' \times\int\frac{d\Omega' v' N(\mathbf{r},\boldsymbol{\Omega}',E',t)}{l(E')}F(\boldsymbol{\Omega},E;\boldsymbol{\Omega}'E'). \quad (5)$$

[7] See, for example, N. F. Mott and H. S. W. Massey, *Theory of Atomic Collisions* (Oxford Press, London, 1933).
[8] R. E. Marshak, Revs. Modern Phys. **19**, 185 (1947).

Here $N(\mathbf{r},\boldsymbol{\Omega},E,t)$ is the number of electrons between $\mathbf{r}$ and $\mathbf{r}+d\mathbf{r}$, $\boldsymbol{\Omega}$ and $\boldsymbol{\Omega}+d\boldsymbol{\Omega}$, E and $E+dE$ at time t, where $\mathbf{r}$ represents space coordinates, $\boldsymbol{\Omega}$ is a unit vector in the direction of the electron velocity, $\mathbf{v}$ is the electron velocity, and E the energy. $l(E)$ is the mean free path and $F(\boldsymbol{\Omega},E;\boldsymbol{\Omega}'E')$ the probability that, given an electron at $\boldsymbol{\Omega}'E'$, one will be found at $\boldsymbol{\Omega}$, E after a scattering. $S(\mathbf{r},\boldsymbol{\Omega},E,t)$ is a source term representing the density of internal secondaries produced by the primary bombardment. It should be emphasized that the factor $F(\boldsymbol{\Omega},E;\boldsymbol{\Omega}'E')$ takes into account two types of electrons: those which scatter down in energy from $\boldsymbol{\Omega}'$, E' to $\boldsymbol{\Omega}$, E; and those which are knocked up from the conduction band to $\boldsymbol{\Omega}$, E. Thus, this term specifically includes the electron multiplication and is not normalized to unity as in Marshak's paper. Indeed, if the effect of the exclusion principle on the scattering is neglected, the correct normalization factor is twice his

$$\int_0^{E'} dE\int d\Omega(F(\boldsymbol{\Omega},E;\boldsymbol{\Omega}',E')=2. \quad (6)$$

This equation expresses the fact that for each electron in the cascade which scatters, there are two present after the collision.

The most common geometry in SE experiments is one in which the primary electrons are incident normally on a plane surface. With this configuration the problem is one-dimensional and has azimuthal symmetry, which means that Eq. (5) simplifies greatly. For the steady state ($\partial N/\partial t=0$) it contains three variables; z, the distance normal to the surface; θ, the angle that the velocity of the secondary electron makes with the normal; and the energy E. Following the usual procedure (see Marshak's paper, for example) N, F, and S are expanded into spherical harmonics

$$\begin{aligned} N(z,\cos\theta,E)&=(1/4\pi)\textstyle\sum_l(2l+1)N_l(z,E)P_l(\cos\theta),\\ S(z,\cos\theta,E)&=(1/4\pi)\textstyle\sum_l(2l+1)S_l(z,E)P_l(\cos\theta),\\ F(\boldsymbol{\Omega},E;\boldsymbol{\Omega}'E')&=F(\cos\Theta;E,E')\\ &=(1/4\pi)\textstyle\sum_l(2l+1)F_l(E,E')P_l(\cos\Theta), \end{aligned} \quad (7)$$

where Θ is the angle between the vectors $\boldsymbol{\Omega}'$ and $\boldsymbol{\Omega}$. With the abbreviation $\psi_l=vN_l/l(E)$ the following set of simultaneous integro-differential equations in z and E is obtained

$$\psi_l=l(E)\left[\left(\frac{l}{2l+1}\right)\frac{\partial\psi_{l-1}}{\partial z}+\left(\frac{l+1}{2l+1}\right)\frac{\partial\psi_{l+1}}{\partial z}\right] +\int_E^\infty dE'F_l(E,E')\psi_l(z,E')+S_l(z,E). \quad (8)$$

These are the equations which govern the cascade process for the simple geometry under consideration. Most of the remainder of this article will be devoted to various approximate ways of solving them.

Since Eqs. (8) are quite complicated it is important to examine them in various special cases. One of great interest is that in which ψ_l is independent of z. This corresponds to a situation in which the internal secondaries are produced uniformly deep inside a metal (away from the influence of the surface). Although this is rather a far cry from the usual experimental situation in which secondaries are observed as they leave the surface, the fact that observed secondary electron spectra are almost entirely independent of primary energy suggests that the depth of penetration of the primaries (and hence the distance the cascade develops from the surface) is relatively unimportant and that calculations of this type may give reasonably good expressions for the energy distributions. This expectation is actually borne out by later work which correctly includes the space variation for a particular choice of F in Eq. (5). For the time being, therefore, consider the case in which ψ_l is independent of z. Equations (8) then reduce to a set of uncoupled integral equations,

$$\psi_l=\int_E^\infty dE' F_l(E,E')\psi_l(E')+S_l(E). \tag{9}$$

These will be solved first with a simplified expression for $F_l(E,E')$. The results of this calculation will then be used as a guide in treating the problem with a more realistic choice of F_l. F_l is determined by inverting Eq. (7)

$$F_l(E,E')=\int d\Omega F(\cos\Theta;\,E,E')P_l(\cos\Theta). \tag{10}$$

In line with the arguments of Sec. II, F is taken to be spherically symmetric. The simplification mentioned above comes in also assuming that the conduction electrons are moving slowly compared to those in the cascade. This means that the energy of an electron after scattering is determined uniquely by the scattering angle and its initial energy (hence the delta function in the formula below). Under these conditions F is given by

$$F(\cos\Theta;\,E,E')=\frac{2}{4\pi}\delta[E-E'\cos^2\Theta]4\cos\Theta, \tag{11}$$

where the factor $4\cos\Theta$ is the Jacobian of the transformation from center of mass to laboratory angles.

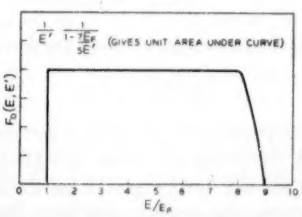

FIG. 2. $F_0(E,E')$ *versus* E/E_F for $E'=9E_F$.

$F_l(E,E')$ can now be obtained from Eq. (10),

$$F_l(E,E')=\frac{2}{E'}P_l\left(\sqrt{\frac{E}{E'}}\right). \tag{12}$$

The factor two which appears here takes care of the electron multiplication and is the same as that appearing in the normalization of F [Eq. (6)]. The integral equations now read

$$\psi_l=2\int\frac{dE'}{E'}P_l\left(\sqrt{\frac{E}{E'}}\right)\psi_l(E')+S_l(E). \tag{13}$$

The homogeneous equations have solutions of the form

$$\psi_l\sim E^{\alpha_l}, \tag{14}$$

where the values of α_l are obtained from the formula

$$1=2\int_1^\infty x^{(\alpha_l-1)}P_l\left(\sqrt{\frac{1}{x}}\right)dx. \tag{15}$$

For the first three spherical harmonics the α_l's turn out to be $\alpha_0=-2$, $\alpha_1=-\frac{3}{2}$, $\alpha_2=-\frac{1}{2}\pm\frac{1}{2}i\sqrt{3}$. With these functions the complete solution of Eq. (13) is obtained by integrating over S_l. It is readily verified (by substitution) that ψ_l is given by

$$\psi_l=-\int_E^\infty\left(\frac{E}{E'}\right)^{\alpha_l}\frac{\partial S_l}{\partial E'}dE'. \tag{16}$$

Electron multiplication clearly plays an important role in determining the α_l values given above. Neglecting it [by replacing the factor two in Eq. (13) by unity] gives, for example, $\alpha_0=-1$ instead of -2. Thus, it strongly emphasizes the singularity at zero in the energy distribution. Another important feature is also apparent from these figures; namely that in going towards larger l values the order of the singularity at zero energy decreases rapidly. Physically this is very reasonable since a high spherical harmonic represents a complicated and special angular distribution which is easily smeared out by scattering. The net effect is that at low energies the internal electron velocity distribution is nearly spherically symmetric since the electrons have made enough collisions to wash out any angular variation. Of course, this argument is hardly correct for the p wave ($l=1$), but it will not be highly excited in any case since the secondaries are mainly produced at right angles to the primary beam which means a small $P_1(\cos\theta)$ component in S.

The above conclusions have been obtained by using a special form for $F(\mathbf{\Omega},E;\Omega,E')$, a form which gives a unique relation between E, E', and cos. In the actual case the formula

$$E=E'\cos^2\Theta \tag{17}$$

will only give the average energy after a scattering—there will always be a spread around this value because

interactions are not with stationary particles (as was assumed previously) but with moving conduction electrons. This effect strengthens the conclusion that for small energies the electron distribution is spherically symmetric. It furnishes another source of averaging so that angular variations are wiped out even sooner than the values of α_l given above suggest. Thus, the high harmonics are only important for large E and are soon overwhelmed by ψ_0, which grows very rapidly as $E\to 0$ and determines the shape of the energy distribution. For this reason, attempts to improve the approximate solutions discussed above will concentrate on the spherically symmetric part of ψ.

IV

The expression for ψ_0 given in the previous section [Eq. (14)] is inaccurate because the F_0 used in the integral equation takes no account of either the exclusion principle or motion of the conduction electrons. The correct F_0 is given by

$$F_0=\int d\Omega F(\cos\Theta; E,E') \tag{18}$$

and is just the total probability of scattering from energy E' to E, irrespective of angle. For S-wave scattering from a degenerate Fermi gas this quantity has been evaluated by Goldberger.[9] An examination of his analysis shows that F_0 is unaffected by the motion of the electrons, but is changed through the exclusion principle. The resultant F_0, instead of being flat as a function of E, has the form shown in Fig. 2. The differences between this curve and the previous F_0 have a clear physical interpretation. Below $E=E_F$ (E_F = Fermi energy) there is a gap because no electron may wind up with less energy than E_F. For $E'>E>E'-E_F$ the curve tails off because collisions are impossible unless the target electron is within $E'-E$ of the surface of the Fermi sphere. Within this range, therefore, the number of conduction electrons available for scattering is decreasing, approaching zero at $E=E'$.

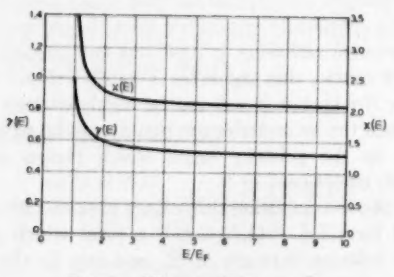

FIG. 3. $\gamma(E)$ and $x(E)$ *versus* E.

[9] M. L. Goldberger, Phys. Rev. **74**, 1269 (1948). Goldberger's calculation is made for a cross section which is constant in energy. This is not strictly true in the present case, but the variation of σ is slow enough that his formula is a good approximation.

Besides changing F_0, the exclusion principle reduces the total scattering cross section. This effect has also been considered by Goldberger who finds

$$\sigma_{eff}=\sigma_0(1-7E_F/5E), \tag{19}$$

where this formula, as well as the curve given for F_0, are valid for $E>2E_F$. This gives a mean free path

$$l(E)=\frac{1}{n_e\sigma_0(E)(1-7E_F/5E)} \tag{20}$$

to be used in calculating N_0 from ψ_0. In this formula the energy dependence of the two factors, $\sigma_0(E)$ and $(1-7E_F/5E)$, is in the opposite sense so that the mean free path is roughly constant (to within 25 percent) over the energy range 10–50 ev.

With the new $F_0(E,E')$ the integral equation [Eq. (13)] is no longer solved by a ψ_0 which is a simple power of E. As is clear from Fig. 2, the main effect of the exclusion principle on F_0 is to increase the average energy after scattering. This can be expressed by writing

$$\bar{E}=\alpha(E')E', \tag{21}$$

where E' is the energy before scattering, $\bar{E}$ the average energy afterwards, and $\alpha(E')=\frac{1}{2}$ for $E/E_F\ll 1$, but gradually rises as E' decreases. A rough idea of how this effect influences the energy distribution can be gained by assuming that the energy after collision is always given by the average energy of Eq. (21). This method gives the correct $1/E^2$ distribution for large E, and will also be right for small $E(E\sim E_F)$ since there, because of the exclusion principle, the energy spread around $\bar{E}$ is small. This method should, therefore, give a satisfactory interpolation between high and low E. With it the integral equation reads

$$\psi_0(E)=2\int\delta[E-E'\alpha(E')]\psi_0(E')dE'. \tag{22}$$

Since there is a one-to-one relation between $\bar{E}$ and E' (according to Eq. (21)) one can also write

$$\bar{E}=\gamma(\bar{E})E'. \tag{23}$$

The integral in Eq. (22) can now be performed directly, giving

$$\psi_0(E)=\frac{2}{\gamma(E)}\psi_0\left[\frac{E}{\gamma(E)}\right]. \tag{24}$$

This equation has a solution of the form $\psi\sim 1/E^s$, where

$$2[\gamma(E)]^{s-1}=1. \tag{25}$$

In Fig. 3, $\gamma(E)$ and $x(E)$ are plotted as functions of E. As expected, $x(E)$ has the value two for large E and rises slowly as the energy gets smaller. At $E=2E_F$, which is where the energy spectrum begins to be dominated by the effect of the escape probability

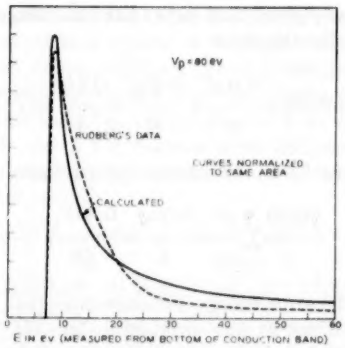

FIG. 4. Energy distribution of secondary electrons from Li.

$[P(E)$ of Eq. (27)$]$, $x(E)$ has only reached 2.3. Thus, the effect of exclusion on F_0 does not change the spectrum greatly and this rough way of taking it into account is probably adequate. Using this approximation, the current is given by

$$j=Nv=\frac{\psi_0}{l(E)}=P(E)\frac{1}{n_c\sigma_0(E)(1-7E_F/5E)}\left(\frac{E_0}{E}\right)^x. \quad (26)$$

Here $x(E)$ is taken from Fig. 2, and $P(E)$ is a geometrical factor which gives the probability that an electron with energy E that strikes the surface will have a large enough normal velocity to overcome the work function and escape. For a spherically symmetric distribution, $P(E)$ is given by

$$P(E)=1-[(\varphi+E_F)/E]^{\frac{1}{2}}, \quad (27)$$

where φ is the work function.

V

According to the assumption of Sec. II, Eq. (26) is valid when $E_0<W$. Therefore, when the primary electron energy is less than 100 ev the spectrum of secondaries can be obtained directly from Eq. (26) by replacing E_0 by V_p. A simple metal that has been studied for bombarding energies in this range is lithium, which was investigated by Rudberg.[10] In Fig. 4 a comparison is made between theory and his results in this case. Of particular interest is the fact that both the theoretical and experimental spectra have very small half-widths—widths which are smaller by a factor of three than those observed in Au or Ag. This happens because the work function of Li is smaller, in comparison to its Fermi energy, than those of Au or Ag. Therefore, in units of E_F, the vacuum level in lithium lies considerably closer to the Fermi level than it does in the other two metals. Near the Fermi level, however, the internal energy distribution is falling steeply from the infinity at $E=E_F$. The external distribution, which is a product of the internal distribution and the escape probability of Eq. (27), is therefore quite narrow since the rapidly falling internal distribution cuts off the spectrum very sharply on the high energy side. For Au or Ag, on the other hand, the work function is considerably larger and the SE spectra are placed higher relative to E_F. The part of the internal distribution which determines the spectrum is, therefore, much flatter than for Li which means a broader and smoother energy distribution.

For bombarding energies greater than W, Eq. (26) cannot be used as simply as above. Electrons with energy greater than W must be followed individually, their rate of energy loss and secondary production being calculated from Rutherford's formula, until they reach energy W where they can be described by Eq. (26). These fast electrons produce secondaries, by small-angle Coulomb scattering, which are distributed in energy according to a $1/E^2$ law. For $E_0<W$, this distribution function can be used directly in Eq. (16). In addition, there are also a few secondaries produced with energy greater than W. For the bombarding energy of 155 ev used by Rudberg[11] on Cu, Ag, and Au they are quite few in number, however, and can be neglected in analyzing his data. Thus, of the 155-ev primary energy, 55 ev goes into a $1/E_0^2$ energy distribution extending up to W and the rest is accounted for by the fast electron which ultimately winds up with 100 ev and there joins the cascade described by Eq. (26). The complete source distribution to be used in the integral of Eq. (16) therefore consists of one electron with energy W plus a $1/E_0^2$ distribution containing the rest of the primary energy. This source function turns out to be $S=(0.1W/E_0^2)+\delta(W-E_0)$ if the maximum impact parameter, which determines the minimum value of E_0, is taken equal to the screening radius. In Fig. 5 the theoretical curve obtained using it is plotted along with Rudberg's data on silver. As in the case of Li, the theoretical curve is somewhat sharper than the experimental. However, the overall agreement is good and, in

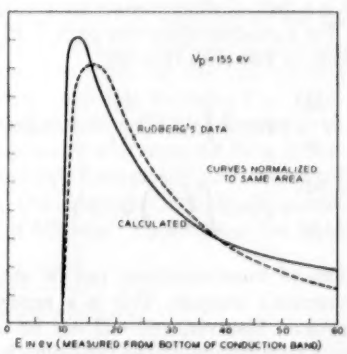

FIG. 5. Energy distribution of secondary electrons from Ag.

[10] Erik Rudberg, Kgl. Svenska Vetenskapsakad. Handl. No. **7**, (1929).

[11] Erik Rudberg, Phys. Rev. **50**, 138 (1936).

particular, the half-width is correct to about 15 percent. As one would expect from examining the φ and E_F values for Ag and Au, the spectrum obtained from gold is almost identical to that from silver. In copper the φ/E_F ratio is smaller than for Au or Ag, which explains the fact that it has a somewhat narrower energy distribution than the other two metals.

When the energy of bombarding electrons is appreciably larger than W, the above treatment must be modified to take account of the secondaries produced with energies greater than W. However, the argument given in Sec. II indicates that for low electron energy the shape of the SE spectrum should be relatively unaltered since it is mainly determined by the behavior of electrons at energies near or below about 50 ev. Thus, one would expect to obtain energy distributions like those in Figs. 4 and 5 for all values of the primary energy.

VI

In the two previous sections Eq. (5) was solved under the assumption that N was independent of z. An argument based on the fact that electron spectra are independent of primary energy was then used to suggest that this solution corresponds closely to the observed energy distribution. That this is actually the case will be demonstrated by solving Eq. (5), including the space variation of N, for the geometry discussed in Sec. III.

For this geometry the surface of the metal is taken to be the plane $z=0$ and the source function is chosen as

$$\begin{aligned} &S_l=0 && (l\neq 0),\\ &S_0=A\delta(E-E_0) && z>0,\\ &S_0=0 && z<0. \end{aligned} \tag{29}$$

This is a reasonable choice for S_l provided the primary electrons are fast enough not to lose an appreciable fraction of their energy in a distance equal to the range of a typical secondary. With this S, the transport problem becomes almost identical with one solved by Weymouth.[12] His method consists in neglecting all but the first two spherical harmonics in the expansion of N. The result is a pair of simultaneous integro-differential equations. For a constant mean free path $[l(E)=l_0]$ and the F_l's given in Eq. (12), they are

$$\begin{aligned} &l_0\frac{\partial\psi_1}{\partial z}+\psi_0=2\int\psi_0(E')\frac{dE'}{E'}+S_0(z,E),\\ &\frac{l_0}{3}\frac{\partial\psi_0}{\partial z}+\psi_1=2\int\left(\frac{E}{E'}\right)^{\frac{1}{2}}\psi_1(E')\frac{dE'}{E'}. \end{aligned} \tag{30}$$

The solutions of these equations can be obtained by using Weymouth's analysis. This is a purely mathematical problem, however, and will not be treated in detail here; a brief outline of the procedure is given in Appendix A. The result of these calculations is that $\psi_0(0,E)$ and $\psi_1(0,E)$ turn out to have an energy dependence given by the series

$$\frac{1}{E}\left[0.54+0.48\mu+\frac{0.46\mu^2}{2!}+\frac{0.46\mu^3}{3!}+\frac{0.43\mu^4}{4!}+\cdots\right], \tag{31}$$

where $\mu=\ln(E_0/E)$. This series approximates closely to

$$\frac{0.50}{E}\sum_n\frac{\mu^n}{n!}=\frac{0.50e^\mu}{E}=\frac{0.50E_0}{E^2}, \tag{32}$$

which is the same energy distribution as that given by Eq. (14). Thus, as was surmised in Sec. III, inclusion of the spatial variation of ψ has only a slight effect on the spectrum of secondary electrons.

VII

The energy distribution of secondary electrons is not the only quantity which gives direct information about the internal electron cascade in metals. The variation of total yield with work function also determines, to a considerable extent, the form of the internal energy distribution. This is so because the yield is proportional to the integral of the probability of escape [Eq. (27)] times the internal energy distribution [Eq. (26)] and thus depends on the shape of the latter. That is

$$\delta\sim\int^\infty E_F+\varphi\, l\frac{P(E)dE}{E^x}. \tag{33}$$

For the time being, the energy dependence of l will be neglected in accordance with the remark after Eq. (20). This expression can then be simplified by making use of the fact that P is a function of $(E/E_F+\varphi)$ and using this quantity as a new variable of integration. δ is then proportional to

$$\frac{1}{(E_F+\varphi)^{x-1}}\int_1^\infty P(y)\frac{dy}{y^x}, \tag{34}$$

if x is assumed constant. The integral is now independent of the work function and a simple differentiation gives the desired result,

$$\partial(\ln\delta)/d\varphi=\frac{1-x}{(E_F+\varphi)}. \tag{35}$$

This formula is correct to within about 10 percent in the range where $l(E)$ changes slowly.

Experimental measurements of the change in yield with work function have been made by a number of workers.[2] The technique used consists in covering the surface of a high work function metal (tungsten) with a thin layer of low work function material such as sodium. By varying the thickness of the Na layer (from zero to one monolayer) it is possible to obtain surfaces having work functions ranging from about 2.2 to 4.5 ev. In this method the amount of low work function metal deposited is exceedingly small so that the bulk properties

[12] John Weymouth, Phys. Rev. **84**, 766 (1951).

of the material are unchanged and the internal energy distributions remain typical of the high work function base. Under these conditions the only change in yield comes through the change in φ and should, therefore, be calculable from Eq. (35). Using for x its value at a point 2 ev above the vacuum level (estimated most probable velocity of secondaries), one obtains for tungsten the values:

$$\partial(\ln\delta)/\partial\varphi=-0.12 \text{ ev}^{-1} \quad \text{at} \quad \varphi=4.5 \text{ ev},$$

and

$$\partial(\ln\delta)/\partial\varphi=-0.14 \text{ ev}^{-1} \quad \text{at} \quad \varphi=3.5 \text{ ev}.$$

These numbers compare well with the experimental values of -0.12 and -0.15 ev^{-1}, respectively. At very low work functions the assumption $l(E)=$ constant is no longer valid so that Eq. (35) should not apply. In this range $l(E)$ increases rapidly as E approaches E_F. Just such behavior is evident in McKay's data where, below $\varphi=3$ ev, the value of δ increases much faster than it does for higher values of the work function. At 2.5 ev, for example, $\partial(\ln\delta)/\partial\varphi$ has reached about -0.5 ev^{-1}. A crude theoretical estimate, made by evaluating the integrand of Eq. (33) numerically for two adjacent values of the work function, gives $\partial(\ln\delta)/\partial\varphi=-0.35$ ev^{-1} at $\varphi=2.5$ ev, again in reasonably good accord with the observed value. Thus the theory of the internal electron cascade predicts in a fairly detailed way the course of the $\partial(\ln\delta)/\partial\varphi$ *versus* φ curve. As a matter of fact, the agreement is probably partly fortuitous since one would not expect a theory based on a free electron model to apply to a metal as complicated as tungsten. Nevertheless, it is evident that the change of work function with yield provides an important tool for investigating internal energy distributions and it is to be hoped that further experiments along this line will be carried out. In particular, it would be very useful to have measurements of $\partial(\ln\delta)/\partial\varphi$ for a metal to which one could apply the free electron model with real confidence in its validity.

VIII

The preceding sections of this paper have dealt with the problem of the shapes of electron energy distributions. In them no attempt was made to calculate the absolute yield of secondary electrons. Indeed, any such calculation is bound to be quite difficult since, as was pointed out in the introduction, it depends critically on both of the fundamental steps in the SE process. On the other hand, the mechanism proposed above to explain the SE spectra is a rather explicit one and it is important to know whether or not it is at least consistent with the observed values of total electron yield. In this section, therefore, an estimate will be made of the total yield which, though not good enough to give quantitative values of δ, will show that the picture of SE developed in the earlier part of this article is a reasonable one in this respect.

The total yield values are obtained by solving the transport equations [Eq. (30)] with a source function that takes account of the fact that primaries have only a finite depth of penetration into the metal. The simplest function which includes this finite range is

$$\begin{aligned} S_0&=A\delta(E-E_0), \quad (0<z<z_0),\\ S_0&=0, \qquad\qquad (z<0, z>z_0), \end{aligned} \tag{36}$$

where both z_0 and A are functions of the bombarding energy V_p. Even with this simple form for S_0, the complete solution of the equations is very difficult, but an asymptotic formula (for large z_0) can be obtained fairly readily and it will be used in subsequent calculations. The asymptotic form, which is derived in Appendix B, is

$$\psi_1(0,E)\cong\frac{AE_0}{2E^2}\left[1-\frac{40}{3\pi}\frac{l}{z_0}\right]. \tag{37}$$

The necessary value of A and the energy dependence of z_0 are obtained from Bohr's[13] formula for the rate of energy loss by fast electrons moving through matter. They are

$$A=\frac{\pi n_0 e^4}{V_p}\frac{1}{E_0^2}J_0, \tag{38}$$

and

$$z_0\sim V_p^2.$$

Here V_p is the bombarding energy, J_0 the primary current, and n_0 the number of electrons per cubic centimeter in the metal which are bound loosely enough to contribute to secondary emission. The total yield δ is now obtained by integrating over E and E_0. In calculating δ, the variation of $\sigma_{eff}(E)$ with energy, as well as the cut-off factor $P(E)$, will be neglected. The effects of these two factors are not large, and in addition they tend to cancel one another, so that for the crude sort of estimate being made here they can be dropped. The total secondary current is then

$$J_s=\frac{\pi n_0 e^4 J_0}{2n_e\sigma_{eff}V_p}\int\int\left[1-\frac{40}{3\pi}\frac{l_0}{z_0}\right]\frac{dE}{E^2}\frac{dE_0}{E_0}, \tag{39}$$

where n_e is the density of electrons in the conduction band and σ_{eff} an average value of the electron-electron cross section. The limits on the two integrations are $\varphi+E_F<E<E_0$ and $\varphi+E_F<E_0<V_p$. This assumes that the energy distribution is proportional to $1/E^2$ up to $E=V_P$. Actually, of course, the form of the distribution changes when E reaches W, but the contribution to the integral from electrons with $E>W$ is small, so the error made is not large. The result of the integration is

$$\delta=\frac{J_S}{J_0}=\frac{\pi n_0 e^4}{2n_e\sigma_{eff}V_P(\varphi+E_F)}\times\left[1-\frac{40}{3\pi}\frac{l_0}{z_0}\right]\left[\ln\left(\frac{V_P}{\varphi+E_F}\right)-1\right]. \tag{40}$$

[13] N. Bohr, Phil. Mag. **24**, 10 (1913).

This formula is most conveniently tested by maximizing δ and comparing the calculated δ_{max} values with those obtained experimentally. Using the form given in Eq. (38) for the energy dependence of z_0 one obtains

$$\delta_{max}=\frac{4}{3}\left(\frac{\pi a_0^2}{\sigma_{eff}}\right)\left(\frac{n_0}{n_e}\right)\frac{(Ry)^2}{(\varphi+E_F)V_P(\max)}\times\left[\ln\left(\frac{V_P(\max)}{\varphi+E_F}\right)-1\right], \quad (41)$$

where a_0 is the Bohr radius. In evaluating δ_{max} the values of $V_P(\max)$ will be taken from experiment. In principle, of course, $V_P(\max)$ could also be calculated provided one knew the constant of proportionality in Eq. (38). However, with the somewhat oversimplified source function that is being used it is rather hard to know what value to choose for this constant. The present method avoids the difficulty by using only the energy dependence of z_0 in calculating δ_{max}.

Before using Eq. (41) to obtain δ_{max} some method must be found for evaluating n_0/n_e. For low $V_P(\max)$ (Li, for example) n_0/n_e is equal to unity since all but the conduction electrons have a binding energy which is of the order of $V_P(\max)$ and hence cannot contribute appreciably to the SE. At higher bombarding energies the electrons in lower shells begin to play a role. An approximate idea of how important they are can be obtained by including a binding energy correction in the integral of Eq. (39). The effect of the binding is to move each internal electron cascade down in energy by just the binding energy. The integral then becomes

$$\int\int\frac{(E_0-E_B)}{E^2}\frac{dE_0dE}{E_0^2}, \quad (42)$$

where E_B is the binding energy and the limits now are $\varphi+E_F<E<E_0-E_B$ and $E_B<E_0<V_P$. The result of the integration is approximately

$$\frac{1}{(\varphi+E_F)}\left[\ln\left(\frac{V_P}{E_B}\right)-1\right], \quad (43)$$

whereas without the binding energy this term is

$$\frac{1}{(\varphi+E_F)}\left[\ln\left(\frac{V_P}{\varphi+E_F}\right)-1\right]. \quad (44)$$

TABLE II. Total yield values.

Element	δ_{max} (calc)	δ_{max} (obs)
Al	0.7	1.5
Cu	1.3	1.3
Li	0.6	0.5
Ag	1.1	1.5
K	1.3	0.7

Thus the effectiveness of the bound electrons is measured by the ratio:

$$\frac{\ln(V_P/E_B)-1}{\ln[V_P/(\varphi+E_F)]-1}. \quad (45)$$

The number of bound electrons in each shell will be multiplied by the appropriate factor of this type to obtain the effective number of electrons contributing to n_0. Tabulated in Table II[14] are δ_{max} values obtained using this procedure. Considering the crudeness of the approximations used in deriving and evaluating Eq. (41) the agreement with experiment is satisfactory, indicating that the cascade theory of SE is at least consistent with the observed values of total yield.

In calculating the δ_{max} values for Table II, σ_{eff} was taken equal to πa_0^2. Actually, in elements such as K or Na it should be considerably larger since the density of conduction electrons in these metals is quite low. Conversely, in Al or Be the correct values of σ_{eff} are probably somewhat lower than πa_0^2 since these metals have an especially high electron density. Inclusion of this effect would give better agreement between theory and experiment but, since really good values of δ_{max} could only be obtained by a considerably more refined approach than that given above, it was not deemed worth while to perform the extra calculations necessary to incorporate it into the table.

IX

The theory presented in this article predicts the shapes of secondary electron spectra from monovalent metals by investigating the behavior of the electronic cascade process within the solid. The agreement with experiment that is obtained suggests that this is a valid and useful way of picturing the second stage of SE. Probably it could be applied with equal success to study SE from more complicated metals. However, in such cases the conduction and secondary electrons could no longer be treated as being free so that, before the cascade process could be investigated, one would have to understand how electron-electron scattering is modified by the presence of a strong crystal field.

In conclusion the author would like to express his indebtedness to Dr. K. G. McKay who, through a number of stimulating conversations, has contributed greatly to his insight into the whole problem of SE. He would also like to thank Conyers Herring for helpful comments and discussion on the topics discussed here.

APPENDIX A

Equations (30) of the text are most simply solved[15] by Laplace transforming with respect to z and Mellin transforming with respect to E. The result is the

[14] Experimental values here are the work of various authors. They are all taken from McKay's review article.

[15] The analysis culminating in Eq. (8a) is essentially the same as Weymouth's. For a more detailed exposition, see his paper.

following pair of algebraic equations:

$$\left(\frac{s-1}{s+1}\right)\psi_0(y,s)+yl_0\psi_1(y,s)=l_0\chi_1(s)+S_0(y,s),$$
$$\frac{yl_0}{3}\psi_0(y,s)+\left(\frac{s-\frac{1}{2}}{s+\frac{3}{2}}\right)\psi_1(y,s)=\frac{l_0}{3}\chi_0(s). \tag{1a}$$

Here

$$\psi_0(y,s)=\int_0^\infty dze^{-ys}\int_0^\infty dEE^s\psi_0(z,E),$$
$$\psi_1(y,s)=\int_0^\infty dze^{-ys}\int_0^\infty dEE^s\psi_1(z,E),$$
$$\chi_0(s)=\int_0^\infty dEE^s\psi_0(0,E), \tag{2a}$$
$$\chi_1(s)=\int_0^\infty dEE^s\psi_1(0,E),$$

and

$$S_0(y,s)=\int_0^\infty dze^{-ys}\int_0^\infty dEE^sS_0(z,E)=AE_0^s/y. \tag{3a}$$

The solutions of these algebraic equations are easily obtained; for example,

$$\psi_0=\begin{vmatrix} l_0\chi_1+S_0 & yl_0 \\ \frac{1}{3}l_0\chi_0 & (s-\frac{1}{2})/(s+\frac{3}{2}) \end{vmatrix} \Bigg/ \left[\frac{(s-1)(s-\frac{1}{2})}{(s+1)(s+\frac{3}{2})}-\tfrac{1}{3}l_0^2y^2\right]. \tag{4a}$$

In inverting the Laplace transforms to obtain $\psi(z,s)$, there are poles at

$$y=\pm\frac{\sqrt{3}}{l_0}\left(\frac{(s-1)(s-\frac{1}{2})}{(s+1)(s+\frac{3}{2})}\right)^{\frac{1}{2}}=y^{\pm}(s), \tag{5a}$$

one of which will give an exponentially rising solution, the other a decaying one, for large positive z. Since ψ_0 and ψ_1 must remain bounded as $z\to\infty$ one of the boundary conditions is that the coefficient of the positive exponential be zero, i.e.,

$$\begin{vmatrix} l_0\chi_1+AE_0^s/y^+(s) & l_0y^+(s) \\ \frac{1}{3}l_0\chi_0 & (s-\frac{1}{2})/(s+\frac{3}{2}) \end{vmatrix}=0. \tag{6a}$$

The other boundary condition is the requirement that there be no incoming current at the metal surface; that is,

$$\int_0^1\chi_0\cos\theta d(\cos\theta)+\int_0^1\chi_1 3\cos^2\theta d(\cos\theta)=0,$$

or

$$\tfrac{1}{2}\chi_0+\chi_1=0. \tag{7a}$$

These two equations may now be solved for χ_0, χ_1, which are the quantities needed since they determine the current at the surface. For instance,

$$\chi_1(s)=AE_0^s\left[\frac{3(s-1)(s-\frac{1}{2})}{(s+1)(s+\frac{3}{2})}\right]^{-\frac{1}{2}} \times\left\{1+\tfrac{2}{3}\left[\frac{3(s-1)(s+\frac{3}{2})}{(s+1)(s-\frac{1}{2})}\right]^{\frac{1}{2}}\right\}^{-1}. \tag{8a}$$

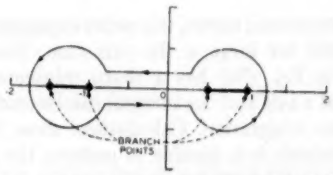

FIG. 6. Path of integration in complex plane.

The final step in the analysis is the inversion of this Mellin transform. To do this one must evaluate the integral

$$\frac{1}{2\pi i}\int_{\delta-i\infty}^{\delta+i\infty}\chi_1(s)E^{-(s+1)}ds =\frac{1}{2\pi i}\int_{\delta-i\infty}^{\delta+i\infty}\frac{1}{E}e^{s\mu}\left[\frac{3(s-1)(s-\frac{1}{2})}{(s+1)(s+\frac{3}{2})}\right]^{-\frac{1}{2}} \times\left\{1+\tfrac{2}{3}\left[\frac{3(s-1)(s+\frac{3}{2})}{(s-1)(s-\frac{1}{2}}\right]^{\frac{1}{2}}\right\}^{-1}ds \tag{9a}$$

where $\mu=\ln(E_0/E)$. The path of integration, which is parallel to the imaginary axis and to the right of all singularities, may be deformed to encircle the four branch points of $\chi_1(s)$ as shown in Fig. 6. With this contour s ranges only over finite values so that for small μ the inversion can be performed by expanding $e^{s\mu}$ into a power series and evaluating it term-by-term. The nth term in this series has the form

$$\frac{1}{2\pi i}\oint\frac{1}{E}\frac{(s\mu)^n}{n!}\left[\frac{3(s-1)(s-\frac{1}{2})}{(s+1)(s+\frac{3}{2})}\right]^{-\frac{1}{2}} \times\left\{1+\tfrac{2}{3}\left[\frac{3(s-1)(s+\frac{3}{2})}{(s+1)(s-\frac{1}{2})}\right]^{\frac{1}{2}}\right\}^{-1}ds, \tag{10a}$$

where the contour of integration is the loop in Fig. 6 which encircles all the singularities in the finite plane. For $s=\infty$ the integrand has a pole; hence the value of the integral can be obtained by replacing s by $1/q$ and calculating the residue at $q=0$. When n is big the evaluation of this residue is very tedious so that for large μ the method is not practical. Fortunately, however, for SE one is only interested in values of μ up to about 2 (a factor of 10 in energy). In this case only the first 4 or 5 terms in the series are necessary. Equation (9a) is then given by

$$\frac{1}{E}\left[0.54+0.48\mu+\frac{0.46}{2!}\mu^2+\frac{0.46}{3!}\mu^3+\frac{0.43}{4!}\mu^4+\cdots\right], \tag{11a}$$

which is just Eq. (31) of the text.

As was mentioned above, this series expansion method is not useful for large μ. In this case, though, the integrand in Eq. (9a) has a sharp minimum on the positive real s axis and the integral can be evaluated by saddle point integration. Calculations show that with the two methods it is feasible to perform the inversion for all values of μ from 0 to ∞.

APPENDIX B

With a finite range source [Eq. (33)] the transport equations can be solved by the same method used in Appendix A. As a matter of fact, Eq. (8a), when rewritten in terms of S_0, gives exactly the solution desired:

$$\chi_1(s)=\frac{S_0(y^+(s),s)}{l_0}\left\{1+\tfrac{2}{3}\left[\frac{3(s+1)(s+\frac{3}{2})}{(s+1)(s-\frac{1}{2})}\right]^{\frac{1}{2}}\right\}^{-1}. \quad (1b)$$

In the present case $S_0(y^+(s),s)$ is given by

$$S_0(y^+(s),s)=\frac{AE^*l_0\{1-\exp[-y^+(s)z_0]\}}{\sqrt{3}y^+(s)}. \quad (2b)$$

Without the $\exp[-y^+(s)z_0]$ term (1b) reduces to (8a) and can be inverted by the method given there. The part of the integral involving $\exp[-y^+(s)z_0]$ is much more complicated and will only be evaluated in the limit of large z_0. It is given by the expression

$$\frac{1}{2\pi i}\int_{\delta-i\infty}^{\delta+i\infty} A\exp\left\{\frac{-z_0}{l_0}\left[\frac{3(s-1)(s-\frac{1}{2})}{(s+1)(s+\frac{3}{2})}\right]^{\frac{1}{2}}\right\}\left(\frac{E_0}{E}\right)^s ds \times\frac{}{E\left[\frac{3(s-1)(s-\frac{1}{2})}{(s+1)(s+\frac{3}{2})}\right]^{\frac{1}{2}}\left\{1+\tfrac{2}{3}\left[\frac{3(s-1)(s+\frac{3}{2})}{(s+1)(s-\frac{1}{2})}\right]^{\frac{1}{2}}\right\}}. \quad (3b)$$

For large z_0 the exponent has a sharp maximum near $s=1$. Therefore, to obtain the first term in the asymptotic expansion set $s=1$ in all slowly varying terms. The result is that Eq. (3b) becomes

$$\sim\frac{1}{2\pi i}\int_{\delta-i\infty}^{\delta+i\infty}\frac{A}{E}\frac{1}{[3(s-1)/10]^{\frac{1}{2}}} \times\exp\left\{\frac{-z_0}{l_0}\left[\frac{3(s-1)}{10}\right]^{\frac{1}{2}}\right\}\frac{E_0}{E}ds. \quad (4b)$$

Now let $s-1=it$ and integrate up the line defined by $R(s)=1$ (going to the right of the branch point at $s=1$). Equation (4b) then breaks into two integrals:

$$\frac{1}{2\pi}\int_0^\infty\frac{A}{(3/20)^{\frac{1}{2}}(1+i)t}\exp\left[-\left(\frac{3}{20}\right)^{\frac{1}{2}}\frac{z_0}{l_0}(1+i)\sqrt{t}\right] \times\frac{E_0}{E^2}dt+\frac{1}{2\pi}\int_0^\infty\frac{A}{(3/20)^{\frac{1}{2}}(1+i)t} \times\exp\left[-\left(\frac{3}{20}\right)^{\frac{1}{2}}\frac{z_0}{l_0}(1-i)\sqrt{t}\right]\frac{E_0}{E^2}dt. \quad (5b)$$

The fact that $(1+i)$ appears in the first and $(1-i)$ in the second of these integrals is due to the fact that the two integrals refer to different branches of the square root. These integrals can now be rewritten as the sum of two real ones and it is a straightforward calculation to show that this first term in the asymptotic expansion is

$$(20/3\pi)(AE_0/E^2). \quad (6b)$$

Combining this with the calculation of Appendix A, one is led directly to Eq. (37) of the text.

The Disintegration of Rh^{102}

LUIS MARQUEZ*
Institute for Nuclear Studies, University of Chicago, Chicago, Illinois
(Received January 8, 1954)

The disintegration of Rh^{102} has been investigated using a beta-ray spectrometer. It was found that it decays by the emission of a negatron of end-point energy of 1150 kev and three positrons of end-point energies of 400 kev, 760 kev, and 1240 kev. Five gamma rays were also found in its disintegration of 86 kev, 124 kev, 195 kev, 353 kev, and 475 kev.

THE disintegration of Rh^{102} has been investigated using the double magnetic lens nuclear spectrometer of Agnew and Anderson.[1] The Rh^{102} was prepared by irradiation of 20 g of Ag for three hours with full intensity and 420 Mev in the University of Chicago synchrocyclotron. The target was dissolved in HNO_3 and 2-mg carriers of Sr, Y, Zr, Nb, Mo, Ru, Rh, Pd, and Cd added. After long boiling the solution was diluted with H_2O, the Ag precipitated with HCl and filtered. The Pd was precipitated with dimethylglyoxime and centrifuged. More Pd was added, reprecipitated, and centrifuged. The supernatant was evaporated to near dryness and strongly fumed with a mixture of $HClO_4$, $NaBiO_3$, and H_3PO_4 to evaporate the Ru. The Rh was finally purified by pyridine extraction as described by Meinke.[2]

The samples for the beta-ray spectrometer were prepared three months later to allow the shorter-lived activities to decay. They were prepared as the finely divided metal by precipitation with $TiCl_3$ and when mounted had a thickness of about 0.3 mg/cm². They were mounted on a thin Zapon film, placed in the beta-ray spectrometer, and counted with a Geiger counter having a mica window of 1.5 mg/cm² as described in a previous work.[3]

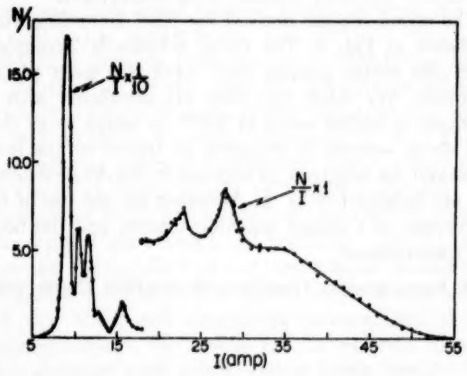

FIG. 1. The spectrum of the negatrons from Rh^{102}.

The beta-ray spectrometer was operated with a resolution of 3.5 percent and was calibrated with the conversion line of Ba^{137m} in equilibrium with Cs^{137}. The relationship between the momentum of the electrons and the current was $\eta = 5.695 \times 10^{-2} I$, where η is the momentum in units of mc and I is the current in amperes. The measurements were taken during one week and no appreciable decay occurred during the measurements. We assume that all the activity measured corresponds to Rh^{102}.

The spectrum of the negatrons is shown in Fig. 1. It is formed by seven conversion electron lines and a negatron spectrum. The conversion electrons are due to five gamma rays, the two hardest ones come from Ru^{102} and the three softest could come from either Ru^{102} or Pd^{102}, but more likely from the first one for reasons that will be seen later. So, to calculate the energies of the gamma rays we used for all of them the corresponding x-ray energies of Ru. The relevant data about the conversion electrons and the gamma rays are shown in Table I. The errors in the energies of the gamma rays are of the order of one percent. It is possible that there are more gamma rays than those listed and they were not detected due to their small conversion coefficient, particularly if they are harder than those detected. The K/L ratio for γ_1 is greater than 2.5 which places it as $M1$, $M2$, or $M3$ transition,[4] we can only place a lower limit to this ratio because below 100 kev the

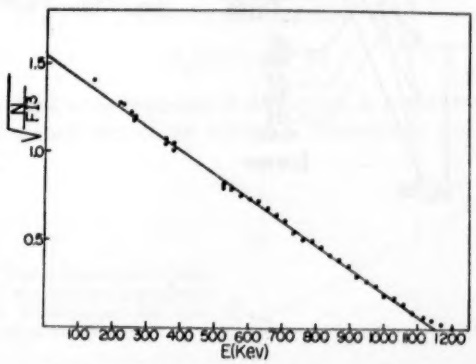

FIG. 2. The Fermi plot of the negatron spectrum of Rh^{102}, leaving out the conversion electrons.

* Now at the Centro Brasileiro de Pesquisas Fisicas, Rio de Janeiro, Brazil.
[1] H. L. Anderson and H. M. Agnew, Rev. Sci. Instr. **20**, 869 (1949).
[2] W. W. Meinke, University of California Radiation Laboratory Report UCRL-432, 1949 (unpublished).
[3] Luis Marquez, Phys. Rev. **92**, 1511 (1953).
[4] M. Goldhaber and A. W. Sunyar, Phys. Rev. **83**, 906 (1951).

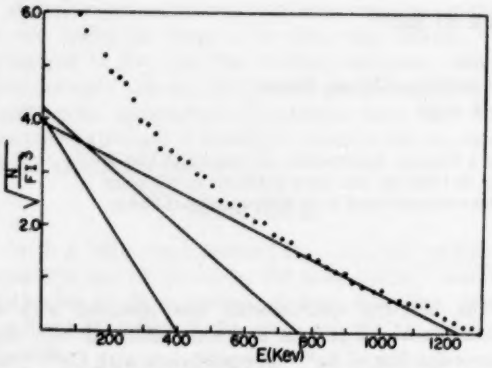

FIG. 3. The Fermi plot of the positron spectrum of Rh^{102}.

transmission decreases. The K/L ratio of γ_2 is about 7.5 which places it as $M1$ or $M2$.

The Fermi plot of the negatron spectrum, leaving out the conversion electrons, is shown in Fig. 2. There seems to be only one negatron group and to have an allowed shape. In view of the expectations that there were about it having an "unique" first forbidden shape, the spectrum was plotted using the corresponding correction factor and it was found that it gave a much worse straight line than the allowed shape. Therefore we conclude that within our experimental errors there is only one negatron group and it has an allowed shape.

The Fermi plot of the positron spectrum is shown in Fig. 3. It is complex and we were able to resolve it in the three groups shown in the figure. The hardest group was explored from the end point to the point where the second group begins to show, that is, a region of about 450 kev, and in this region the Fermi plot is compatible with an allowed shape, although a categoric statement cannot be made because the spectrum was examined without interference only in this small region. All the relevant information about the positron groups and the negatron group are given in Table II. The log ft values given were calculated using the data in the article of Feenberg and Trigg[5] to correct for the K capture.

TABLE I. The energy and the intensity of the conversion electrons from the gamma rays following the decay of Rh^{102}.

Current (amp)	Energy of conversion electron (kev)	Origin of conversion electron	Energy of gamma ray (kev)	Intensity of conversion electron ($\beta^-=100$)	Name of gamma ray
9.07	64.1	K	86.3	>66	γ_1
10.44	83.4	L	86.6	26	γ_1
11.61	101.6	K	123.7	28	γ_2
12.90	123.0	L	126.4	3.8	γ_2
15.62	172.9	$K+L$	195	10.0	γ_3
23.0	331.1	$K+L$	353	1.5	γ_4
28.1	452.7	$K+L$	475	3.0	γ_5

TABLE II. The end-point energy, intensity, and log ft of each positron and negatron group from Rh^{102}.

Group	End-point energy (kev)	Intensity ($\beta^-=100$)	Log ft
β^-	1150±20	100.0	9.8
β_1^+	400±30	3.9	8.0
β_2^+	760±30	21.3	8.7
β_3^+	1240±20	58.8	9.1

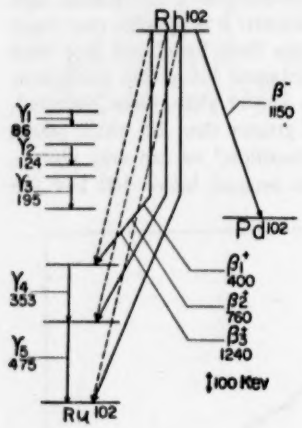

FIG. 4. The incomplete decay scheme of Rh^{102}.

These log ft values are really lower limits, but we think that they are close to the true ones, since the K captures which were not detected are probably not a large fraction of the total number of disintegrations.

The decay scheme derived for Rh^{102} from this work is shown in Fig. 4. The decay scheme is incomplete since the softer gamma rays have not been placed definitely. We think that they are associated with K captures to higher levels in Ru^{102}. It seems to us that this decay scheme is complete in regard to the positrons and the negatron, as is shown in the decay scheme.

I am indebted to H. L. Anderson for the use of the University of Chicago synchrocyclotron and the beta-ray spectrometer.

[5] E. Feenberg and G. Trigg, Revs. Modern Phys. **22**, 406 (1950).

Effect of Pressure on the Optical Absorption of the Activator System in KCl:Tl

PETER D. JOHNSON AND FERD E. WILLIAMS
General Electric Research Laboratory, Schenectady, New York

(Received March 24, 1954)

The optical absorption spectrum of thallium-activated potassium chloride has been measured at 2000 atmospheres. The absorption band corresponding to the $^1S_0 \rightarrow {}^3P_1{}^0$ transition of Tl^+ shifts 4 A to longer wavelengths at this pressure. The spectral shift is calculated theoretically from the quantitative configuration coordinate model of KCl:Tl. The occupation probabilities of accessible atomic configurations of the activator system are dependent on pressure, whereas the transition energy for a particular configuration is independent of pressure. The pressure is considered to act hydrostatically on six pistons corresponding to the Cl^- nearest neighbors. The theoretical shift in absorption under 2000 atmospheres pressure is 5 A to longer wavelengths.

I. INTRODUCTION

A QUANTITATIVE theory of solid-state luminescence has been formulated and applied to impurity-activated ionic crystals.[1] From fundamental considerations and the properties of the constituent ions, the theoretical absorption and emission spectra of thallium-activated potassium chloride have been evaluated and found to be in satisfactory agreement with experiment. The dependence on temperature of these spectra has also been successfully computed.[2]

A single parameter, the activator—nearest-neighbor distance, was found adequate for quantitative calculation of the properties considered. By measuring the effect of pressure on the optical properties of a phosphor crystal, it is possible to affect directly this important parameter and so to subject the theory to a crucial test. In the present work, the effect of pressure on the absorption spectrum of the activator system in KCl:Tl is determined experimentally and computed theoretically.

II. EXPERIMENTAL

The absorption measurements were made using an American Instrument Company high-pressure cell No. 11–550 as the sample holder and hydraulic pump No. 406–155 to provide pressures up to 2000 atmospheres. A Bourdon gauge was used for the determination of pressure. Phillips "spectro grade" isooctane was found to be a satisfactory pressure-transmitting fluid. Particular care was exercised to eliminate from the apparatus all traces of hydrocarbons exhibiting absorption and fluorescence in the spectral region from 2400 to 2600 A. The optical path-length in isooctane was 1.5 mm. Pressure has no effect on the transmission of isooctane from 2400 to 2600 A. The KCl:0.00002 Tl crystal was 4.5 mm thick and completely covered the optical opening through the sample cell. It was held in place by a stainless steel holder with a recess machined to accommodate the crystal.

The sample cell was placed at the exit slit of an ultraviolet monochromator[3] having a LiF window at the exit slit. A 1P28 photomultiplier was used as the detector of transmitted radiation. Because of the construction of the pressure cell, the detector was approximately 12 cm from the phosphor crystal. This arrangement eliminated the necessity for making any special provision to exclude from the detector, fluorescence of the phosphor or of the fused quartz windows of the high-pressure cell. With such a long optical path between monochromator exit slit and detector, the system might be expected to be sensitive to changes in geometry of the absorption cell or of the crystal. Deliberate alteration of the geometry of sample cell and detector, and use of two different exit-slit settings corresponding to band widths of 5 A and 12 A showed no detectable effect on the results.

The shift in absorption with pressure was observed by determining the intensity of transmitted radiation at various wavelengths at approximately 330-atmosphere intervals from atmospheric to 2000 atmospheres pressure. Lack of any permanent effect on the crystal or contamination of isooctane was ascertained by also measuring the transmitted radiation as the pressure was decreased to one atmosphere. Typical experimental results for two wavelengths are shown in Fig. 1, in which the ratio of intensity I_p of radiation transmitted at pressure P to that I_0 transmitted at atmospheric pressure is plotted as a function of pressure.

This ratio is given by the expression

$$I_p/I_0 = e^{-l(k_p - k_0)}, \qquad (1)$$

where l is the thickness of the crystal, k_0 is the absorption coefficient of the crystal at atmospheric pressure

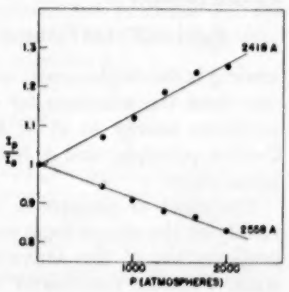

FIG. 1. Experimental data on the pressure dependence of transmission for two typical wavelengths.

[1] F. E. Williams, J. Chem. Phys. **19**, 457 (1951); J. Phys. Chem. **57**, 780 (1953).
[2] F. E. Williams and M. H. Hebb, Phys. Rev. **84**, 1181 (1951).
[3] P. D. Johnson, J. Opt. Soc. Am. **42**, 278 (1952).

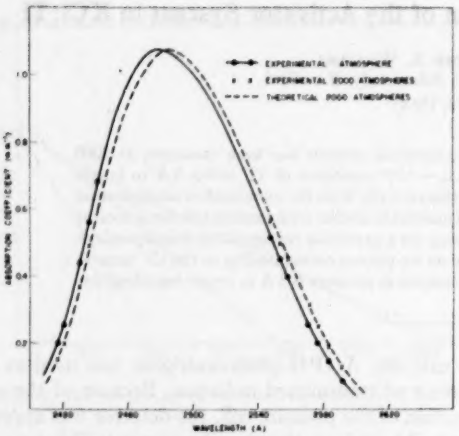

FIG. 2. Theoretical and experimental dependence on pressure of the $^1S_0 \rightarrow {}^3P_1{}^0$ absorption spectrum of KCl:Tl.

for the wavelength in question, and k_p is the absorption coefficient for this wavelength at pressure P. The quantity k_0 was determined from separate absorption measurements, using apparatus permitting accurate comparison of incident and transmitted radiation.[3]

At absorption coefficients above about 0.6 mm^{-1}, the small amount of transmitted radiation reduced the accuracy of the measurements. No strongly anomalous behavior was observed at these higher absorption values. On the more accurate portions of the curve, indicated by the experimental points, there is a substantially uniform shift of the absorption band 4 A to longer wavelengths.

III. THEORETICAL

The potential energies of the activator system in the $^1S_0$ and $^3P_1{}^0$ states of Tl^+ in KCl have been determined as a function of the symmetric radial displacement of the six nearest-neighbor Cl^- ions from the Tl^+ ion.[1] The resulting parabolic dependence of potential energy on configuration permits the calculation of luminescent spectra. Since potential energy is a markedly different function of the configuration coordinate for the different electronic states, the transition energy is strongly dependent on the configuration. The classical formula for the absorption or emission spectrum with no applied pressure is

$$Q_0(\epsilon)=(K/2\pi kT)^{\frac{1}{2}}\exp(-Kq^2/2kT)(dq/d\epsilon), \quad (2)$$

where q is the displacement in the configuration coordinate from the minimum for the initial state; ϵ is the transition energy at q, in accordance with Franck-Condon principle; and K is the force constant for the initial state.

The effect of pressure is to shift the spectrum by modifying the occupational probability of any arbitrary configuration of the activator system in the initial state. Pressure contributes the same energy to the initial and to the final states for any arbitrary configuration; hence, the net effect on the transition energy is zero. The spectrum with the applied pressure P is therefore

$$Q(\epsilon,P)=Q_0(\epsilon)e^{W/kT}, \quad (3)$$

where W is the work done on the system by the pressure in going from a reference configuration to the configuration in question and is given by the expression

$$W=-\int_{V_0}^{V}PdV=-P(V_q-V_0). \quad (4)$$

The quantity V_q is the volume of the activator system with the arbitrary configuration q, and V_0 is the volume with the reference configuration determined by normalization of $Q(\epsilon,P)$.

The volume difference (V_q-V_0) is equal to the volume displacement from the reference configuration q_0 to the configuration q of six pistons, each with cross-sectional area equal to the cross-sectional area of the nearest-neighbor Cl^-, since it is the displacement of these Cl^- ions which corresponds to q. The spectrum is therefore

$$Q(\epsilon,P)=Q_0(\epsilon)e^{-A(q-q_0)P/kT}, \quad (5)$$

where A is the total cross-sectional area of the six Cl^- ions and q_0 is the configuration corresponding to V_0. At the configuration q_0, it is evident from Eq. (5) that $Q(\epsilon,P)=Q_0(\epsilon)$. The substitution of Eq. (2) in Eq. (5) reveals that the activator system with the applied pressure P is characterized by the same force constant K but with a new equilibrium configuration q_e. The spectrum can, therefore, be written:

$$Q(\epsilon,P)=\left(\frac{K}{2\pi kT}\right)^{\frac{1}{2}}\frac{dq}{d\epsilon}\exp\left[\frac{-K}{2kT}(q-q_e)^2\right]. \quad (6)$$

The force applied to the activator system by the pressure must equal the restoring force at the equilibrium configuration,

$$PA=Kq_e. \quad (7)$$

By combining Eqs. (5) and (6) and by substituting for q_e according to Eq. (7), we obtain:

$$q_0=\tfrac{1}{2}q_e=PA/2K. \quad (8)$$

From Eqs. (5) and (8) for the absorption band corresponding to the $^1S_0 \rightarrow {}^3P_1{}^0$ transition of Tl^+, and using the experimental $Q_0(\epsilon)$, the absorption under 2000 atmospheres pressure can be calculated. A shift of absorption approximately 5 A to longer wavelengths is calculated, in excellent agreement with experiment as shown in Fig. 2.

The authors are indebted to Mr. F. L. Hughes for assistance during the early phases of this research, and to Dr. J. S. Prener for several helpful discussions.

Relativistic Thomas-Fermi Atom Model

J. J. GILVARRY
The Rand Corporation, Santa Monica, California

(Received March 24, 1954)

It is shown that an expression for the density of states derived from the Dirac wave equation for a central field removes the convergence difficulties in the usual relativistic Thomas-Fermi equation.

THE relativistic Thomas-Fermi atom model,[1-3] based on the use of a density of states derived from Schrödinger's equation, poses a number of difficulties. If the potential is assumed asymptotic to that of a point charge at the nucleus, the electron density is not normalizable and the energy diverges. For these reasons, Jensen[2] introduced a finite nuclear radius into the boundary conditions on the potential in this case. By means of a density of states based on the Klein-Gordon equation for a central field, Plaskett[4] has deduced a relativistic Thomas-Fermi equation, which yields a cut-off of the electron density at the nucleus and thus a finite energy, provided the atomic number Z satisfies the restrictive condition $Z<(2\alpha)^{-1}\sim 137/2$ in terms of the fine-structure constant α. The purpose of this note is to show that an expression for the density of states, derived by Rudkjøbing[5] from the Dirac equation for the case of a spherically symmetric potential, removes both difficulties mentioned above when applied to obtain a relativistic Thomas-Fermi model of the atom.

For the number of states $n(r,E)$ per unit volume and per unit energy range of an electron of total energy E at a point r in a spherically symmetric atom where the electrostatic potential is $V(r)$, Rudkjøbing's result yields

$$n(r,E)=\sigma_1[(E+eV)^2-m^2c^4-(redV/dr)^2]^{\frac{1}{2}}(E+eV), \quad (1)$$

in which e and m are the electronic charge and mass respectively, c is the speed of light, and $\sigma_1=8\pi/h^3c^3$, where h is Planck's constant. The corresponding number density $\rho(r)$ of electrons at the point r at temperature T, if E_m is a maximum total energy fixed by the total number of electrons and k is Boltzmann's constant, is

$$\rho(r)=\int_0^\infty n(r,E)\{\exp[(E-E_m)/kT]+1\}^{-1}dE, \quad (2)$$

which yields the relativistic form of the generalized[6] Thomas-Fermi equation when it is substituted into Poisson's equation. As $V\to Ze/r$, the density ρ is normalizable since it varies as $r^{-\frac{3}{2}}$ (as in the non-relativistic case). It is easily verified that the total energy is finite. The energy term $(redV/dr)^2$ in $n(r,E)$ is interpreted by Rudkjøbing as due to spin-orbit coupling of the electrons, since it arises from the terms in the Dirac equation which yield this effect quantum-mechanically. However, the spin-orbit correction to the energy will not vanish for values of Z corresponding to closed subshells or shells of electrons, since an integration over states of angular momentum involved in the derivation of Eq. (1) does not distinguish between the states $j=l+\frac{1}{2}$ and $j=l-\frac{1}{2}$.

The relativistic Thomas-Fermi equation for zero temperature is

$$r^{-1}d^2(rV)/dr^2=\sigma_2\{\eta+eV+[(\eta+eV)^2-(redV/dr)^2]/2mc^2\}^{\frac{1}{2}}, \quad (3)$$

where $\eta=E_m-mc^2$ and $\sigma_2=(32\pi^2/3)(2m)^{\frac{3}{2}}e/h^3$. To first-order terms in α, the right-hand side of this equation can be written

$$\sigma_2(\eta+eV)^{\frac{1}{2}}\{1+(3\mu\alpha/2e)[(\eta/e+V)^2-(rdV/dr)^2]/(\eta+eV)\}, \quad (4)$$

where μ is the Bohr magneton; in this form the spin-orbit character of the term $(\mu\alpha/e)(rdV/dr)^2$ is evident from its limiting form $-Z\mu\alpha dV/dr$ as $r\to 0$. With omission of the spin-orbit term, Eq. (3) is the one derived by Vallarta and Rosen[1] (for $\eta=0$). Since the relativistic effect should be small except for the heavier elements, Eq. (3) generally can be solved by a first-order perturbation procedure based on the usual Thomas-Fermi function ϕ. It can be shown in this case that the differential perturbation equation can be solved analytically in terms of quadratures on ϕ.

If one is willing to assume that relativistic effects affect the exchange correction only slightly and operate mainly to modify the uncorrected potential V_0, one can obtain a relativistic Thomas-Fermi-Dirac equation.[7] At zero temperature, this equation is

$$\frac{1}{r}\frac{d^2}{dr^2}(rV_0)=\sigma_2\left\{\gamma+\left[\gamma^2+\eta+eV_0+\frac{(\eta+eV_0)^2-(redV_0/dr)^2}{2mc^2}\right]^{\frac{1}{2}}\right\}^{\frac{3}{2}}, \quad (5)$$

where $\gamma=(2m)^{\frac{1}{2}}e^2/h$.

[1] M. S. Vallarta and N. Rosen, Phys. Rev. **41**, 708 (1932).
[2] H. S. Jensen, Z. Physik **82**, 794 (1933).
[3] S. Chandrasekhar, Monthly Notices Roy. Astron. Soc. **95**, 207 (1934).
[4] J. S. Plaskett, Proc. Phys. Soc. (London) **A66**, 178 (1953).
[5] M. Rudkjøbling, Kgl. Danske Videnskab. Selskab, Mat.-fys. Medd. **27**, No. 5 (1952). Rudkjøbing used his expression for the density of states to obtain a refinement of Chandrasekhar's mass-radius relation for the white dwarf stars.
[6] E. C. Stoner, Proc. Roy. Soc. (London) **A152**, 672 (1935).
[7] P. A. M. Dirac, Proc. Cambridge Phil. Soc. **26**, 376 (1930).

It is intended to apply these equations to obtain the correction to the binding energy of the Thomas-Fermi atom due to relativistic effects. At present, the relativistic effect is known only on the basis of rough numerical estimates,[8] although it represents a significant correction to the binding energy of the heavier elements. Rudkjøbing's results can be used also to obtain a relativistic analog of Hellmann's equation,[9] in which the angular momenta of the electrons enter explicitly into the electron density. The expression for the density of states corresponding to (4), suitably modified to apply to nucleons, may have application in the statistical theory[10] of the nucleus. The analog of Hellmann's equation noted above, suitably modified to apply to nucleons, may be of help in clarifying aspects of the spin-orbit coupling in the shell model of the nucleus.

The author wishes to thank Dr. A. L. Latter and Dr. R. Latter of the Rand Corporation for helpful discussions.

[8] J. M. C. Scott, Phil. Mag. 43, 859 (1952).
[9] H. Hellmann, Acta Physicochim. (U.R.S.S.) 4, 225 (1936).
[10] P. Gombas, Ann. Physik 10, 253 (1952); 12, 155 (1953); W. G. McMillan, Phys. Rev. 92, 210 (1953).

PHYSICAL REVIEW VOLUME 95, NUMBER 1 JULY 1, 1954

Approximate Hartree-Type Wave Functions and Matrix Elements for the *K* and *L* Shells of Atoms and Ions

R. E. MEYEROTT*
Argonne National Laboratory, Lemont, Illinois
(Received February 9, 1954)

Perturbation effects of electron screening on wave functions and dipole matrix elements of K and L electrons of ions or inner shells of atoms have been computed to order Z^{-1}. Some screening effects of this order have also been computed for the M shell. Some of the terms of order Z^{-2} have also been evaluated and found to be small compared with those neglected in this paper. The dipole matrix elements have been used to compute x-ray mass absorption coefficients and the comparison with the experimental values is discussed.

INTRODUCTION

FOR many problems, such as the determination of the photoelectric absorption, ionization by electron impact, stopping power for fast particles, etc., one needs to know atomic wave functions and dipole matrix elements for atoms and ions. In the case of highly ionized atoms such as found in stellar interiors, or for atoms of atomic number of 20 or greater, the wave functions of K and L shells are sufficiently "hydrogen-like" so that the effects of screening can be roughly estimated.[1] These estimates serve to give the order of magnitude of screening effects but in many cases may be off by large factors. In some problems such as that of determining the Rosseland mean opacity of matter under conditions of high temperature and pressure, one needs to be able to calculate the photoelectric cross sections for a large variety of atoms in all stages of ionization. The straightforward procedure of obtaining, say, Hartree wave functions for a sample of states of each atom for each stage of ionization, is a prohibitively long program even for high-speed computers. Since the quantities involved are nearly hydrogen-like, it is probable that such a program would be greatly overdoing the problem and that the same amount of information can be obtained with considerably less work.

A possible analytical approach to this problem might be to employ the set of approximate variational functions of Morse, Young, and Hawrwitz[2] for the bound states and Coulomb free functions using an atomic number equal to that of the nucleus, minus the number of screening electrons in the shell of the initial state and those lying inside that shell.[3] This procedure suffers from two difficulties: first, in not correctly representing the actual potential in which the optical electron moves, and second, in not obtaining the correct wave functions for even the assumed potential. Since the dipole moment is the expansion coefficient of r times the bound wave functions in terms of the wave functions of the upper state, this moment may be very sensitive to small changes in the form of the function assumed. The correction thus obtained to the hydrogen-like values may merely represent the error in the assumed solution.

In order to eliminate part of the uncertainty in the calculation, we have employed a method in which the potential is assumed but the radial wave equation and the dipole moment are solved for directly. This enables one to investigate, without ambiguity, the dependence of the dipole moment on the form of the potential assumed. The results of these computations can also be used as a basis for testing the validity of variational wave functions since they are solutions of a definite non-Coulombic problem.

The method of the present paper is to extend the

* Now with The Rand Corporation, 1700 Main Street, Santa Monica, California.
[1] H. Hall, Revs. Modern Phys. 8, 358 (1936).
[2] Morse, Young, and Hawrwitz, Phys. Rev. 48, 948 (1935); also, L. Goldberg and A. M. Clogston, Phys. Rev. 56, 696 (1939).
[3] J. A. Wheeler, Phys. Rev. 43, 258 (1933).

computations by developing the wave functions and dipole matrix elements in power series in the number of screening electrons divided by the atomic number. The validity of this expansion is investigated and an experimental verification is made using the observed x-ray mass absorption coefficient.

THE CALCULATIONAL PROCEDURE

A. Bound Wave Functions

Hartree wave functions are solutions of the central field problem. The radial wave functions R_{nl} of type nl are solutions of Schrödinger's radial equation

$$\frac{d^2R_{nl}}{dr^2}+\left[\epsilon_{nl}+\frac{2}{r}-\frac{1}{Z}\sum_{ij}{}'N_{ij}V_{ij}-\frac{l(l+1)}{r^2}\right]R_{nl}=0, \quad (1)$$

where Z is the atomic number, ϵ_{nl} is the energy parameter in units $Z^2e^2/2a_0$, and r is in units a_0/Z, where a_0 is the Bohr radius. N_{ij} is the number of screening electrons of type ij (the prime on the summation indicates that the nl term whose wave function is being computed is omitted from the summation). V_{ij} is the screening potential of a radial charge distribution of type R_{ij}.

$$V_{ij}=+\frac{2}{r}\int_0^r[R_{ij}]^2dr+2\int_r^\infty[R_{ij}]^2dr/r. \quad (2)$$

The Hartree method consists of making an initial guess of the radial wave functions $R_{ij}{}^0$, using these to compute the potential $V_{ij}{}^0$, and then solving the differential equation (1) for the resulting set of functions, say $R_{nl}{}^1$. These functions are then used in Eq. (2) to compute a new potential $V_{ij}{}^1$ which is again used in Eq. (1) to determine a new set of solutions $R_{nl}{}^2$ etc., until there is no change in the resulting wave functions. Since we are dealing with high stages of ionization and inner shells of atoms, we take hydrogenic functions as our initial guess, i.e., $R_{ij}{}^0=R_{ij}{}^H$.

Each solution of Eq. (1) will be a function of Z, the number of screening electrons in the configuration, and the particular stage of the iteration process. We express this dependence in the following example. The $2s$ radial wave function for $Z=26$, which is a solution of the differential equation (1) in the configuration $(1s)^x(2s)^y(2p)^z$ in which hydrogen-like screening functions were used in Eq. (2) for the potential, will be written as $R_{2s}{}^1[26;(1s^0)^x(2s^0)^{y-1}(2p^0)^z]$. In the next iteration the screening functions would be $(1s^1)^x(2s^1)^{y-1}\times(2p^1)^z$ so that the function would be written $R_{2s}{}^2\times[26;(1s^1)^x(2s^1)^{y-1}(2p^1)^z]$.

The method of the present paper is based on the assumption that the effect of the screening potential on any solution of Eq. (1) is given sufficiently well by a first order perturbation of the corresponding hydrogen-like wave function. Taking hydrogen-like zero-order functions, the rth iterative solution of Eq. (1) can be written as

$$R_{nl}{}^r=R_{nl}{}^H+\frac{1}{Z}\sum_{ij}{}'N_{ij}\sum_p{}'\frac{[V_{ij}{}^{r-1}]_{pl,\,nl}R_p{}^H}{\epsilon_n{}^H-\epsilon_p{}^H}, \quad (3)$$

where as before the indices i,j run over all the screening electrons, and $[V_{ij}{}^{r-1}]_{pl,\,nl}$ is the matrix element of $V_{ij}{}^{r-1}$ calculated with the hydrogen-like radial functions $R_{nl}{}^H$ and $R_{pl}{}^H$. The quantity

$$\sum_p{}'\frac{[V_{ij}{}^{r-1}]_{pl,\,nl}R_{pl}{}^H}{\epsilon_n{}^H-\epsilon_p{}^H}\equiv\Delta R_{nl}(ij^{r-1}), \quad (4)$$

which we will call the change in the radial wave function of type nl introduced by the radial wave functions of type (ij^{r-1}), is independent of the atomic number Z and of the number of screening electrons present when hydrogen-like functions are used in Eq. (2). Equation (3) can then be written

$$R_{nl}{}^r=R_{nl}{}^H+\frac{1}{Z}\sum_{ij}{}'N_{ij}\Delta R_{nl}(ij^{r-1}). \quad (5)$$

The $2s$ radial wave functions for an ion of nuclear charge Z having a full K and L shell screened by hydrogen-like screening functions would be written

$$R_{2s}{}^1[Z;(1s^0)^2(2s^0)(2p^0)^6]=R_{2s}{}^H+(2/Z)\Delta R_{2s}(1s^0)+(1/Z)\Delta R_{2s}(2s^0)+(6/Z)\Delta R_{2s}(2p^0). \quad (6)$$

Since the ΔR's are orthogonal to R^H to the approximation used here, the functions on the left-hand side of the Eqs. (5) and (6) are normalized as they stand to terms of order $(1/Z^2)\int_0^\infty(\Delta R_{2s})^2dr$.

In the second approximation when one inserts $R_{nl}{}^1$ from Eq. (5) into Eq. (2) for the potential, $V_{ij}{}^1$ can be written in a manner analogous to Eq. (5) as

$$V_{ij}{}^1=V_{ij}{}^0+\frac{1}{Z}\sum_{nl}{}'N_{nl}\Delta V_{ij}(nl^0), \quad (7)$$

if we neglect the term involving the square of ΔR. If we neglect the terms $\Delta R_{1s}(2s^0)$ and $\Delta R_{1s}(2p^0)$ as is the usual practice in the Hartree method, the $2s$ and the $2p$ radial solutions of Eq. (1) for a configuration $(1s)^x\times(2s)^y(2p)^z$ can be written

$$\begin{aligned}R_{2s}{}^2[Z;(1s^1)^x(2s^1)^{y-1}(2p^1)^z]&=(2s^0)+\frac{x}{Z}\Delta_{2s}(1s^0)\\&+\frac{x(x-1)}{Z^2}\Delta_{2s}[\Delta_{1s}(1s^0)]+\frac{(y-1)}{Z}\Delta_{2s}(2s^0)\\&+\frac{x(y-1)}{Z^2}\Delta_{2s}[\Delta_{2s}(1s^0)]+\frac{(y-1)(y-1)}{Z^2}\Delta_{2s}[\Delta_{2s}(2s^0)]\\&+\frac{(y-1)z}{Z^2}\Delta_{2s}[\Delta_{2s}(2p^0)]+\frac{z}{Z}\Delta_{2s}(2p^0)\\&+\frac{zx}{Z^2}\Delta_{2s}[\Delta_{2p}(1s^0)]+\frac{zy}{Z^2}\Delta_{2s}[\Delta_{2p}(2s^0)]\\&+\frac{z(z-1)}{Z^2}\Delta_{2s}[\Delta_{2p}(2p^0)]; \quad (8)\end{aligned}$$

$$R_{2p}{}^2[Z;\,(1s^1)^x(2s^1)^y(2p^1)^{z-1}]=(2p^0)+\frac{x}{Z}\Delta_{2p}(1s^0)$$
$$+\frac{x(x-1)}{Z^2}\Delta_{2p}[\Delta_{1s}(1s^0)]+\frac{y}{Z}\Delta_{2p}(2s^0)+\frac{xy}{Z^2}\Delta_{2p}[\Delta_{2s}(1s^0)]$$
$$+\frac{y(y-1)}{Z^2}\Delta_{2p}[\Delta_{2s}(2s^0)]+\frac{yz}{Z^2}\Delta_{2p}[\Delta_{2s}(2p^0)]$$
$$+\frac{(z-1)}{Z}\Delta_{2p}(2p^0)+\frac{(z-1)x}{Z^2}\Delta_{2p}[\Delta_{2p}(1s^0)]$$
$$+\frac{(z-1)y}{Z^2}\Delta_{2p}[\Delta_{2p}(2s^0)]+\frac{(z-1)(z-1)}{Z^2}$$
$$\times\Delta_{2p}[\Delta_{2p}(2p^0)], \quad (9)$$

where the expression $\Delta_{2s}[\Delta_{1s}(1s^0)]$ etc., the change in a $2s$ due to the change in a $1s$ by a $1s^0$, etc., are merely an extension of the notation $\Delta_{2s}(1s^0)$, etc. For simplicity in the above and following equations, the R will be suppressed whenever no confusion from this results. It is at once apparent from the point of view of perturbation theory, that the Hartree procedure is a power series expansion of the radial wave functions in essentially the number of screening electrons divided by the atomic number Z. If this expansion parameter is small, convergence is, of course, rapid. The rapid increase in the number of terms in the expression with each stage of the iteration process, as well as the fact that we have neglected terms of order $1/Z^3$ in the first iteration, make the extension of the present method past $R_{nl}{}^2$ unprofitable.

B. Free Wave Functions

The free radial wave functions result from a solution of Eq. (1) for positive values of the energy parameter $\epsilon_{nl}=\eta$. In the one-electron problem, η is, of course, the kinetic energy of the escaping electron. The expression analogous to Eq. (5) for the free function is

$$R_{\eta l}{}^1=R_{\eta l}{}^0+\frac{1}{Z}{\sum_{ij}}' N_{ij}\Delta R_{\eta l}(ij), \quad (10)$$

where we have replaced n by η as a subscript of R. Since second-order effects are likely to be unimportant for the free functions, no second-order terms are considered. We should point out that $R_{\eta l}{}^1$ in Eq. (10) is the wave function for the *same energy* ϵ_{nl} as $R_{\eta l}{}^0$.

C. Matrix Elements

Consider the matrix element $I_{nl}{}^{n'l'}$ defined as

$$I_{nl}{}^{n'l'}=\int_0^\infty R_{nl}rR_{n'l'}dr, \quad (11)$$

with R_{nl} and $R_{n'l'}$ defined as in Eq. (5):

$$I_{nl}{}^{n'l'}={}^HI_{nl}{}^{n'l'}+\frac{1}{Z}{\sum_{ij}}' N_{ij}\Delta I_{nl}{}^{n'l'}(ij), \quad (12)$$

where we neglect terms in $Z^{-2}\int_0^\infty R_{nl}r\Delta R_{n'l'}dr$. Matrix elements involving $R_{2s}{}^2$ and $R_{2p}{}^2$ can be obtained from Eqs. (8) and (9) on replacing $\Delta_{2s}(1s^0)$, $\Delta_{2s}[\Delta_{2s}(2s^0)]$, etc., by $\Delta I_{2s}{}^{n'l'}(1s^0)$ and $\Delta I_{2s}{}^{n'l'}[\Delta_{2s}(2s^0)]$, etc., respectively.

Care must be exercised in the use of Eq. (12) in computing $[I_{nl}{}^{n'l'}]^2$ as $(1/Z)\Delta I$ is not necessarily small compared to I, so that terms in $(1/Z^2)[\Delta I]^2$ must be retained.

COMPUTATIONAL DETAILS

A. First-Order Terms

In order to evaluate the first-order terms in Eqs. (8) and (9) the following computations were made:

$R_{1s}{}^1[6;\,(1s^0)]$, $R_{2s}{}^1[6;\,(1s^0)]$, $R_{2p}{}^1[6;\,(1s^0)]$,
$R_{3s}{}^1[6;\,(1s^0)]$, $R_{3p}{}^1[6;\,(1s^0)]$, $R_{3d}{}^1[6;\,(1s^0)]$,
$R_{2s}{}^1[26;\,(1s^0)(2s^0)]$,
$R_{2p}{}^1[26;\,(1s^0)^2(2s^0)]$, $R_{3s}{}^1[26;\,(1s^0)^2(2s^0)]$,
$R_{3p}{}^1[26;\,(1s^0)^2(2s^0)]$,
$R_{3d}{}^1[26;\,(1s^0)^2(2s^0)]$, $R_{2s}{}^1[26;\,(1s^0)^2(2p^0)]$,
$R_{2p}{}^1[26;\,(1s^0)^2(2p^0)]$,
$R_{3s}{}^1[26;\,(1s^0)^2(2p^0)]$, $R_{3p}{}^1[26;\,(1s^0)^2(2p^0)]$,
$R_{3d}{}^1[26;\,(1s^0)^2(2p^0)]$,
$R_{\eta s}{}^1[6;\,(1s^0)]$, $R_{\eta p}{}^1[6;\,(1s^0)]$, $R_{\eta d}{}^1[6;\,(1s^0)]$,
$R_{\eta f}{}^1[6;\,(1s^0)]$,
$R_{\eta s}{}^1[26;\,(1s^0)^2(2s^0)]$, $R_{\eta p}{}^1[26;\,(1s^0)^2(2s^0)]$,
$R_{\eta d}{}^1[26;\,(1s^0)^2(2s^0)]$,
$R_{\eta f}{}^1[26;\,(1s^0)^2(2s^0)]$, $R_{\eta p}{}^1[26;\,(1s^0)^2(2p^0)]$,
$R_{\eta d}{}^1[26;\,(1s^0)(2p^0)]$,
$R_{\eta f}{}^1[26;\,(1s^0)^2(2p^0)]$.

The free functions were computed for $\eta=0.00$, 0.25, 0.50, 1.00. The International Business Machines Card Programmed Calculator was used for this computation using the Noumerov method. A description of this method has already been given by Pratt.[4]

The free functions were computed numerically out to distances required to evaluate the matrix elements. At that point they were joined to a WKB-Jeffreys solution for purposes of normalization.

Since the method involves taking of differences, considerable accuracy was maintained throughout the

[4] G. W. Pratt, Jr., Phys. Rev. 88, 1217 (1952).

calculation. In all the work 10 decimal places were carried in the computation, and the wave functions are expected to be good to five or six places. In this approximation, the radial functions for the same Z and screening are strictly orthogonal. Our numerical functions turned to be orthogonal to about 1 part in 10^6.

In Table I are listed the energy parameters obtained in the calculation of the bound functions. A plot of the various ΔR's can be found in ANL–5008.[5] The plotting accuracy is sufficient so that if one desires first-order wave functions, they are obtainable from these graphs and a good table of hydrogen-like wave functions. In Table II are listed the intensity integrals, I, computed with these functions, and the ΔI's. For reference, a list of hydrogen-like integrals are also given. The functions $R_{\eta s}[26; (1s^0)^2(2p^0)]$ were not computed because they should be very similar to $R_{\eta s}[26; (1s^0)^2(2s^0)]$. The latter function was used to compute the intensity integral $I_{2p}{}^{\eta s}[26; (1s^0)^2(2p^0)]$. This should be permissible since these transitions are not very important in most applications. As a matter of fact, most of the free functions might have been taken as Coulomb functions for $Z=Z-N_b$ where N_b is the number of bound screening electrons. A check of this was made in one case by setting $V_{ij}=2$ in Eq. (1) for $Z=6$ and $l=1$ and computing the free wave function for $\eta=\frac{1}{4}$. The corresponding intensity integral $I_{1s}{}^{\eta p}$ was 1.26017 as compared with 1.24435 for the correct wave function, while that of $I_{2s}{}^{\eta p}$ was 1.65975 as compared with 1.65106 for the correct wave functions.

Since the first-order functions $R_{nl}{}^1$, have all been computed in the same potential, the sum rule,

$$\sum_n [I_{nl}{}^{n'l'}]^2 = \int_0^\infty R_{nl} r^2 R_{nl} dr,$$

should hold exactly. For completeness, we have also computed $\int_0^\infty R_{nl} r^2 R_{nl} dr$ for the bound states, and have included this in Table II.

A check of the over-all numerical procedure, as well as the method of normalization of the free functions, was made by computing the hydrogen-like intensity integral $I_{1s}{}^{\eta p}$ for $\eta=0.7949720$. The numerical result was 0.5120256 as compared with the result of 0.5120225 obtained on evaluating the usual formula.

B. Second-Order Terms

Second-order terms have been computed for the L shell only. The following computations were made:

$R_{2s}{}^2[6; (1s^1)]$, $R_{2p}{}^2[6; (1s^1)]$, $R_{1s}{}^2[6; (1s^1)]$, $R_{2s}{}^2[26; (1s^1)^2]$, $R_{2p}{}^2[26; (1s^1)^2]$, $R_{2s}{}^2[26; (1s^1)^2(2s^1)]$, $R_{2p}{}^2[26; (1s^1)^2(2s^1)]$, $R_{2s}{}^2[26; (1s^1)^2(2p^1)]$, $R_{2p}{}^2[26; (1s^1)^2(2p^1)]$,

[5] R. E. Meyerott, Argonne National Laboratory Report ANL–5008, 1953 (unpublished).

TABLE I. Energy parameters.[a]

$\epsilon_{1s}[6; (1s^0)]$	−0.7949720
$\epsilon_{2s}[6; (1s^0)]$	−0.1838118
$\epsilon_{2p}[6; (1s^0)]$	−0.1749160
$\epsilon_{3s}[6; (1s^0)]$	−0.080076815
$\epsilon_{3p}[6; (1s^0)]$	−0.077584471
$\epsilon_{3d}[6; (1s^0)]$	−0.077171480
$\epsilon_{2s}[26; (1s^0)^2(2s^0)]$	−0.207294688
$\epsilon_{2p}[26; (1s^0)^2(2s^0)]$	−0.201800451
$\epsilon_{3s}[26; (1s^0)^2(2s^0)]$	−0.090172552
$\epsilon_{3p}[26; (1s^0)^2(2s^0)]$	−0.088502789
$\epsilon_{3d}[26; (1s^0)^2(2s^0)]$	−0.087328213
$\epsilon_{2s}[26; (1s^0)^2(2p^0)]$	−0.206515011
$\epsilon_{2p}[26; (1s^0)^2(2p^0)]$	−0.200498725
$\epsilon_{3s}[26; (1s^0)^2(2p^0)]$	−0.089998252
$\epsilon_{3p}[26; (1s^0)^2(2p^0)]$	−0.088238438
$\epsilon_{3d}[26; (1s^0)^2(2p^0)]$	−0.087186374
$\epsilon_{1s}[6; (1s^1)]$	−0.801402423
$\epsilon_{2s}[6; (1s^1)]$	−0.184327493
$\epsilon_{2p}[6; (1s^1)]$	−0.175211915
$\epsilon_{2s}[26; (1s^1)^2]$	−0.218559937
$\epsilon_{2p}[26; (1s^1)^2]$	−0.213908925
$\epsilon_{2s}[26; (1s^1)^2(2s^1)]$	−0.207711391
$\epsilon_{2s}[26; (1s^1)^2(2s^1)]^*$	−0.206912949
$\epsilon_{2p}[26; (1s^1)^2(2s^1)]^*$	−0.201314780
$\epsilon_{2s}[26; (1s^1)^2(2p^1)]^*$	−0.206124176
$\epsilon_{2p}[26; (1s^1)^2(2p^1)]^*$	−0.199982918

[a] See footnote to Table III.

where

$$\begin{aligned} 1s^1 &= 1s^0 + (1/6)\Delta_{1s}(1s^0) \quad \text{for} \quad Z=6, \\ 1s^1 &= 1s^0 + (1/26)\Delta_{1s}(1s^0) \quad \text{for} \quad Z=26. \end{aligned} \tag{13}$$

For the R_{2s} function the $2s^1$ and $2p^1$ screening functions were taken to be, respectively,

$$\begin{aligned} 2s^1 &= 2s^0 + (2/26)\Delta_{2s}(1s^0) + (1/26)\Delta_{2s}(2s^0), \\ 2p^1 &= 2p^0 + (2/26)\Delta_{2p}(1s^0) + (1/26)\Delta_{2p}(2s^0). \end{aligned} \tag{14}$$

For the $R_{2p}{}^2$ function the $2s^1$ and $2p^1$ screening functions were taken to be, respectively,

$$\begin{aligned} 2s^1 &= 2s^0 + (2/26)\Delta_{2s}(1s^0) + (1/26)\Delta_{2s}(2p^0), \\ 2p^1 &= 2p^0 + (2/26)\Delta_{2p}(1s^0) + (1/26)\Delta_{2p}(2p^0). \end{aligned} \tag{15}$$

The functions $1s^1$, $2s^1$, and $2p^1$ used in computing the potential were normalized even though this is not assumed according to our procedure. As stated before, this is a small correction.

By mistake, the sign of the correcting terms in Eqs. (13), (14), and (15) was reversed in computing the functions used for $R_{2s}{}^2[26; (1s^1)^2(2s^1)]$, $R_{2p}{}^2[26; (1s^1)^2(2p^1)]$, $R_{2p}{}^2[26; (1s^1)^2(2s^1)]$, and $R_{2s}{}^2[26; (1s^1)^2 \times (2p^1)]$. This should not cause any trouble but merely change the sign of some of the differences. To check the consistency of the result, $R_{2s}{}^2[26; (1s^1)^2(2s^1)]$ was computed with the correct signs of the correcting terms. Any differences between the two functions are due to higher-order terms appearing in Eq. (3).

The functions computed are insufficient to evaluate all the quantities needed in Eqs. (8) and (9). We can

TABLE II. First-order intensity integrals and first-order ΔI's.

					$Z=6(1s^0)$ screening				
n^a	$I_{1s}{}^{np}$	$I_{2s}{}^{np}$	$I_{2p}{}^{ns}$	$I_{2p}{}^{nd}$	$I_{3s}{}^{np}$	$I_{3p}{}^{ns}$	$I_{3p}{}^{nd}$	$I_{3d}{}^{np}$	$I_{3d}{}^{nf}$
2	1.29559	6.1406	6.14065		1.43380	3.07338		5.61755	
3	0.586998	3.07338	1.43380	5.67155	15.1046	15.1046	12.0943	12.0943	
0	2.01835	6.25230	2.28790	7.83744	12.2526	6.13942	16.0318	2.49776	14.336
0.25	1.24435	1.65106	0.472576	1.22085	1.38188	0.474232	1.09684	0.108914	0.4587
0.50	0.843023	0.772599	0.191802	0.442043	0.542853	0.156840	0.334255	0.0268495	0.1052
1.00	0.459698	0.296261	0.0603773	0.126313	0.184924	0.0428945	0.0855735	0.00530984	0.0198
	$\int_0^\infty R_{1s}{}^2R_{1s}dr$	$\int_0^\infty R_{2s}{}^2R_{2s}dr$	$\int_0^\infty R_{2p}{}^2R_{2p}dr$	$\int_0^\infty R_{2p}{}^2R_{2p}dr$	$\int_0^\infty R_{3s}{}^2R_{3s}dr$	$\int_0^\infty R_{3p}{}^2R_{3p}dr$	$\int_0^\infty R_{3p}{}^2R_{3p}dr$	$\int_0^\infty R_{3d}{}^2R_{3d}dr$	$\int_0^\infty R_{3d}{}^2R_{3d}dr$
	3.47772	54.2062	42.3876	42.3876	277.158	256.106	256.106	181.358	181.358
					$Z=26(1s^0)^2(2s^0)$ screening				
n		$I_{2s}{}^{np}$	$I_{2p}{}^{ns}$	$I_{2p}{}^{nd}$	$I_{3s}{}^{np}$	$I_{3p}{}^{ns}$	$I_{3p}{}^{nd}$	$I_{3d}{}^{np}$	$I_{3d}{}^{nf}$
2		5.67625	5.67625		1.17940	3.07143		5.12788	
3		3.07143	1.17940	5.12788	14.1007	14.1007	11.3641	11.3641	
0		5.64602	1.84898	6.91708	11.1038	5.08199	14.0362	2.29917	12.7353
0.25		1.63509	0.447271	1.30624	1.41192	0.470139	1.19039	0.122625	0.530050
0.50		0.788399	0.191717	0.499157	0.566094	0.161080	0.382222	0.032430	0.133986
1.00		0.308216	0.0631504	0.147219	0.194954	0.0455828	0.100482	0.00624807	0.0345254
		$\int_0^\infty R_{2s}{}^2R_{2s}dr$	$\int_0^\infty R_{2p}{}^2R_{2p}dr$	$\int_0^\infty R_{2p}{}^2R_{2p}dr$	$\int_0^\infty R_{3s}{}^2R_{3s}dr$	$\int_0^\infty R_{3p}{}^2R_{3p}dr$	$\int_0^\infty R_{3p}{}^2R_{3p}dr$	$\int_0^\infty R_{3d}{}^2R_{3d}dr$	$\int_0^\infty R_{3d}{}^2R_{3d}dr$
		48.1784	35.9486	35.9486	246.428	221.810	221.810	158.939	158.939
					$Z=26(1s^0)^2(2p^0)$ screening				
n		$I_{2s}{}^{np}$	$I_{2p}{}^{ns}$	$I_{2p}{}^{nd}$	$I_{3s}{}^{np}$	$I_{3p}{}^{ns}$	$I_{3p}{}^{nd}$	$I_{3d}{}^{np}$	$I_{3d}{}^{nf}$
2		5.70630	5.70630		1.20306	3.06419		5.16505	
3		3.06419	1.20306	5.16505	14.1379	14.1379	11.3817	11.3817	
0		5.65067	1.89457	6.92050	11.1073	5.16784	14.1929	2.29723	11.9974
0.25		1.62323	0.452938	1.29846	1.41011	0.476388	1.19206	0.123010	0.610714
0.50		0.781755	0.192600	0.495770	0.562067	0.162709	0.381937	0.031506	0.102245
1.00		0.308216	0.0631504	0.147219	0.194954	0.0455828	0.100482	0.00624807	0.0345254
		$\int_0^\infty R_{2s}{}^2R_{2s}dr$	$\int_0^\infty R_{2p}{}^2R_{2p}dr$	$\int_0^\infty R_{2p}{}^2R_{2p}dr$	$\int_0^\infty R_{3s}{}^2R_{3s}dr$	$\int_0^\infty R_{3p}{}^2R_{3p}dr$	$\int_0^\infty R_{3p}{}^2R_{3p}dr$	$\int_0^\infty R_{3d}{}^2R_{3d}dr$	$\int_0^\infty R_{3d}{}^2R_{3d}dr$
		48.4672	36.3496	36.3496	247.313	223.099	223.099	159.680	159.680
					$Z=1$ hydrogen-like				
η	${}^HI_{1s}{}^{\eta p}$	${}^HI_{2s}{}^{\eta p}$	${}^HI_{2p}{}^{\eta s}$	${}^HI_{2p}{}^{\eta d}$	${}^HI_{3s}{}^{\eta p}$	${}^HI_{3p}{}^{\eta s}$	${}^HI_{3p}{}^{\eta d}$	${}^HI_{3d}{}^{\eta p}$	${}^HI_{3d}{}^{\eta f}$
0	1.53114	4.6888	1.35354	5.41416	9.18038	3.70927	11.1283	1.65892	9.95349
0.25	1.01374	1.54627	0.399246	1.26292	1.43050	0.457785	1.24844	0.131597	0.619401
0.50	0.720119	0.778912	0.183591	0.519275	0.593643	0.167183	0.425597	0.0366297	0.162317
1.00	0.416175	0.316690	0.0826810	0.163538	0.209439	0.0492777	0.116877	0.00779185	0.0330580
η	$\Delta I_{1s}{}^{\eta p}(1s^0)$	$\Delta I_{2s}{}^{\eta p}(1s^0)$	$\Delta I_{2p}{}^{\eta s}(1s^0)$	$\Delta I_{2p}{}^{\eta d}(1s^0)$	$\Delta I_{3s}{}^{\eta p}(1s^0)$	$\Delta I_{3p}{}^{\eta s}(1s^0)$	$\Delta I_{3p}{}^{\eta d}(1s^0)$	$\Delta I_{3d}{}^{\eta p}(1s^0)$	$\Delta I_{3d}{}^{\eta f}(1s^0)$
0	2.92322	9.38101	5.60613	14.5397	18.4333	14.5809	29.4210	5.03304	26.2951
0.25	1.38364	0.628750	0.439986	−0.252422	−0.29172	0.098682	−0.969600	−0.135098	−0.964206
0.50	0.737425	−0.0378835	0.0492656	−0.463391	−0.30474	−0.062058	−0.548052	−0.058621	−0.342702
1.00	0.261138	−0.122576	−0.133822	−0.223350	−0.14709	−0.038299	−0.187821	−0.0148921	−0.079548
η		$\Delta I_{2s}{}^{\eta p}(2s^0)$	$\Delta I_{2p}{}^{\eta s}(2s^0)$	$\Delta I_{2p}{}^{\eta d}(2s^0)$	$\Delta I_{3s}{}^{\eta p}(2s^0)$	$\Delta I_{3p}{}^{\eta s}(2s^0)$	$\Delta I_{3p}{}^{\eta d}(2s^0)$	$\Delta I_{3d}{}^{\eta p}(2s^0)$	$\Delta I_{3d}{}^{\eta f}(2s^0)$
0		6.12558	1.66912	9.99641	13.1423	6.52892	16.7634	6.58042	19.7369
0.25		1.05186	0.368684	1.63121	0.10036	0.12384	0.4299	0.038924	−0.394714
0.50		0.322407	0.112731	0.403703	−0.106794	−0.034562	−0.031646	0.008055	−0.051202
1.00		0.0531988	−0.231628	0.0460098	−0.072758	−0.0213466	−0.047508	−0.0227189	−0.0052422
η		$\Delta I_{2s}{}^{\eta p}(2p^0)$	$\Delta I_{2p}{}^{\eta s}(2p^0)$	$\Delta I_{2p}{}^{\eta d}(2p^0)$	$\Delta I_{3s}{}^{\eta p}(2p^0)$	$\Delta I_{3p}{}^{\eta s}(2p^0)$	$\Delta I_{3p}{}^{\eta d}(2p^0)$	$\Delta I_{3d}{}^{\eta p}(2p^0)$	$\Delta I_{3d}{}^{\eta f}(2p^0)$
0		6.24642	2.85441	10.0854	13.2333	8.76102	20.8376	6.52998	0.55146
0.25		0.743362	0.516039	1.42892	0.05330	0.286314	0.47332	0.048934	1.70255
0.50		0.149667	0.135690	0.315658	−0.211496	0.007792	−0.039056	−0.015972	−0.876468
1.00		0.0248130	−0.240153	0.0224028	−0.08243	−0.0194694	−0.050628	−0.010354	0.197248

[a] The upper state here has been labeled by the index n. When the upper state is a free state the n should be replaced by η for the n values 0.00, 0.25, 0.50, 1.00.

only evaluate

$$\Delta_{2s}[\Delta_{1s}(1s^0)],\quad \Delta_{2p}[\Delta_{1s}(1s^0)],\quad \Delta_{2s}[\Delta_{2s}(1s^0)^2(2s^0)],$$
$$\Delta_{2s}[\Delta_{2p}(1s^0)^2(2s^0)],\quad \Delta_{2p}[\Delta_{2s}(1s^0)^2(2p^0)],$$
$$\Delta_{2p}[\Delta_{2p}(1s^0)^2(2p^0)].$$

Since these second-order terms are small, we have resorted to an approximation in order to reduce the amount of computing necessary.

Inspection of Figs. 2 and 3 in ANL-5008 shows that $\Delta_{2s}(1s^0)$, $\Delta_{2s}(2s^0)$, and $\Delta_{2s}(2p^0)$ are approximately proportional, as are $\Delta_{2p}(1s^0)$, $\Delta_{2p}(2s^0)$, and $\Delta_{2p}(2p^0)$. Also, since the changes due to the $1s^0$ are considerably larger, not much error will be made if we assume those due to the $2s^0$ and $2p^0$ are strictly proportional to that of $1s^0$ for the purpose of computing the second-order terms. The proportionality constant has been chosen at the first maxima for the $2p$ function and second maxima for the $2s$ function. This is on the assumption that this region is the most important for the L-shell functions.

We then have

$$\begin{aligned}
\Delta_{2p}(2p^0)&=0.369\Delta_{2p}(1s^0),\\
\Delta_{2s}(2p^0)&=0.325\Delta_{2s}(1s^0),\\
\Delta_{2s}(2s^0)&=0.236\Delta_{2s}(1s^0),\\
\Delta_{2p}(2s^0)&=0.223\Delta_{2p}(1s^0).
\end{aligned}\tag{16}$$

The various Δ's are given by

$$\begin{aligned}
\Delta_{2p}[\Delta_{2p}(1s^0)] &= 0.4221\Delta_{2p}[\Delta_{2p}(1s^0)^2(2p^0)],\\
\Delta_{2p}[\Delta_{2p}(2s^0)] &= 0.0942\Delta_{2p}[\Delta_{2p}(1s^0)^2(2p^0)],\\
\Delta_{2p}[\Delta_{2p}(2p^0)] &= 0.1558\Delta_{2p}[\Delta_{2p}(1s^0)^2(2p^0)],\\
\Delta_{2p}[\Delta_{2s}(1s^0)] &= 0.4301\Delta_{2p}[\Delta_{2s}(1s^0)^2(2p^0)],\\
\Delta_{2p}[\Delta_{2s}(2s^0)] &= 0.1012\Delta_{2p}[\Delta_{2s}(1s^0)^2(2p^0)],\\
\Delta_{2p}[\Delta_{2s}(2p^0)] &= 0.1398\Delta_{2p}[\Delta_{2s}(1s^0)^2(2p^0)],\\
\Delta_{2s}[\Delta_{2s}(1s^0)] &= 0.4472\Delta_{2s}[\Delta_{2s}(1s^0)^2(2s^0)],\\
\Delta_{2s}[\Delta_{2s}(2s^0)] &= 0.1055\Delta_{2s}[\Delta_{2s}(1s^0)^2(2s^0)],\\
\Delta_{2s}[\Delta_{2s}(2p^0)] &= 0.1455\Delta_{2s}[\Delta_{2s}(1s^0)^2(2s^0)],\\
\Delta_{2s}[\Delta_{2p}(1s^0)] &= 0.4498\Delta_{2s}[\Delta_{2p}(1s^0)^2(2s^0)],\\
\Delta_{2s}[\Delta_{2p}(2s^0)] &= 0.1003\Delta_{2s}[\Delta_{2p}(1s^0)^2(2s^0)],\\
\Delta_{2s}[\Delta_{2p}(2p^0)] &= 0.1659\Delta_{2s}[\Delta_{2p}(1s^0)^2(2s^0)].
\end{aligned}\tag{17}$$

For a full K and L shell, substitution in Eqs. (8) and (9) gives

TABLE III. Second-order integrals.[a]

η	$I_{1s}^{\eta p}$	$I_{2s}^{\eta p}$	$I_{2p}^{\eta s}$	$I_{2p}^{\eta d}$
	$Z=6(1s^1)$ screening			
0.00	2.00996	6.22435	2.27097	7.84849
0.25	1.24534	1.65412	0.469878	1.23067
0.50	0.846387	0.776522	0.190117	0.448074
1.00	0.463290	0.298905	0.0596231	0.129059
	$Z=26(1s^1)^2(2s^1)$ screening			
η	$I_{2s}^{\eta p}$	$I_{2p}^{\eta s*}$	$I_{2p}^{\eta d*}$	
0.00	5.64154	1.86353	6.9001	
0.25	1.64003	0.448450	1.29724	
0.50	0.791521	0.191707	0.495553	
1.00	0.310500	0.0633291	0.147244	
	$Z=26(1s^1)^2(2p^1)$ screening			
η	$I_{2s}^{\eta p*}$	$I_{2p}^{\eta s*}$	$I_{2p}^{\eta d*}$	
0.00	5.65849	1.91256	6.90200	
0.25	1.62687	0.455107	1.28726	
0.50	0.778468	0.193193	0.490782	
1.00	0.306751	0.0631279	0.145772	

[a] The I's in this table marked with *, and also the E_{nl} of Table I marked with *, refer to those functions mentioned in part B of the section on Computational Details, computed using the wrong sign of the second-order potential correction.

$$\begin{aligned}
R_{2s}^2[Z;\,(1s^1)^2(2s^1)^1(2p^1)^6] &= (2s^0)+\frac{2}{Z}\Delta_{2s}(1s^0)\\
&+\frac{2}{Z^2}\Delta_{2s}[\Delta_{1s}(1s^0)]+\frac{1}{Z}\Delta_{2s}(2s^0)\\
&+\frac{1.8729}{Z^2}\Delta_{2s}[\Delta_{2s}(1s^0)^2(2s^0)]+\frac{6}{Z}\Delta_{2s}(2p^0)\\
&+\frac{9.7782}{Z^2}\Delta_{2s}[\Delta_{2p}(1s^0)^2(2s^0)],
\end{aligned}\tag{18}$$

and

$$\begin{aligned}
R_{2p}^2[Z;\,(1s^1)^2(2s^1)^2(2p^1)^5] &= (2p^0)+\frac{2}{Z}\Delta_{2p}(1s^0)\\
&+\frac{2}{Z^2}\Delta_{2p}[\Delta_{1s}(1s^0)]+\frac{2}{Z}\Delta_{2p}(2s^0)\\
&+\frac{3.6004}{Z^2}\Delta_{2p}[\Delta_{2s}(1s^0)^2(2p^0)]+\frac{5}{Z}\Delta_{2p}(2p^0)\\
&+\frac{9.058}{Z^2}\Delta_{2p}[\Delta_{2p}(1s^0)^2(2p^0)].
\end{aligned}\tag{19}$$

The second-order L-shell functions were used with the corresponding first-order free functions to evaluate the intensity integrals. These are listed in Table III. As before in $Z=26$, we have insufficient functions to evaluate all the ΔI's needed. We can evaluate

$$\Delta I_{2p}^{\eta d}[\Delta_{2p}(1s^0)^2(2p^0)],\ \Delta I_{2p}^{\eta d}[\Delta_{2s}(1s^0)^2(2p^0)],$$
$$\Delta I_{2s}^{\eta p}[\Delta_{2s}(1s^0)^2(2s^0)],\ \Delta I_{2s}^{\eta p}[\Delta_{2p}(1s^0)^2(2s^0)],$$
$$\Delta I_{2p}^{\eta s}[\Delta_{2p}(1s^0)^2(2p^0)],\ \Delta I_{2p}^{\eta s}[\Delta_{2s}(1s^0)^2(2p^0)].$$

TABLE IV. Second-order ΔI's.

η	$\Delta I_{1s}^{\eta p}[\Delta_{1s}(1s^0)]$	$\Delta I_{2s}^{\eta p}[\Delta_{1s}(1s^0)]$	$\Delta I_{2p}^{\eta s}[\Delta_{1s}(1s^0)]$	$\Delta I_{2p}^{\eta d}[\Delta_{1s}(1s^0)]$
0.00	−0.301896	−1.00654	−0.60932	+0.3978
0.25	+0.035808	+0.110054	−0.09714	+0.3534
0.50	+0.121108	+0.141244	−0.06068	+0.2171
1.00	+0.129326	+0.0951983	−0.02715	+0.09886

η	$\Delta I_{2s}^{\eta p}[\Delta_{2s}(1s^0)^2(2s^0)]$	$\Delta I_{2p}^{\eta s}[\Delta_{2s}(1s^0)^2(2p^0)]$	$\Delta I_{2p}^{\eta d}[\Delta_{2s}(1s^0)^2(2p^0)]$
0.00	−1.00976	−8.6206	+10.6743
0.25	+3.11999	−0.6028	+5.3768
0.50	+1.82818	+0.1281	+2.0019
1.00	+0.68336	+0.1551	+0.3990

η	$\Delta I_{2s}^{\eta p}[\Delta_{2p}(1s^0)^2(2s^0)]$	$\Delta I_{2p}^{\eta s}[\Delta_{2p}(1s^0)^2(2p^0)]$	$\Delta I_{2p}^{\eta d}[\Delta_{2p}(1s^0)^2(2p^0)]$
0.00	−3.27519	−10.9453	+11.711
0.25	−2.68340	−1.2717	+6.869
0.50	+1.93914	−0.2796	+2.938
1.00	+0.80006	+0.0695	+0.7803

The ΔI's corresponding to the ΔR's can be found from Eq. (17). The corresponding Δ's are given in Table IV. For atoms or ions having full K and L shells, the substitution of I for R in Eqs. (18) and (19) lead to expressions for I of the form

$$I_{nl}^{\eta l'} = {}^{H}I_{nl}^{\eta l'} + a_{nl}^{\eta l'}/Z + b_{nl}^{\eta l'}/Z^2. \qquad (20)$$

In Table V are listed the a's and b's for the case of atoms or ions having initially full K and L shells.

For ions having electrons in K and L shells only, the $I_{nl}^{\eta l'}$ are those which correspond to electrons leaving the system with kinetic energy η. It is shown in Appendix I for atoms or ions which have electrons in M or higher shells, that the intensity integral is the one for an electron leaving the system with kinetic energy $\eta+\epsilon_0$, where ϵ_0 is the change in the ionization energy due to external screening.

ACCURACY OF THE PERTURBATION APPROXIMATION

The difference between first- and second-order radial functions for the same Z and screening is due to the change in the potential. This has been computed and found to be small, as is indicated by the small change in the intensity integrals. Since this change is so small, we can compare $\Delta_{2s}(1s^1)$ or $\Delta_{2p}(1s^1)$ computed for $Z=6$, with the same quantities computed for $Z=26$ as a measure of error introduced due to neglect of further terms in Eq. (5). In Fig. 1, $\Delta_{2s}(1s^1)$ and $\Delta_{2p}(1s^1)$ are plotted for $Z=6$ and $Z=26$. To the accuracy of this graph, $\Delta_{2s}(1s^0)$ and $\Delta_{2p}(1s^0)$ computed for $Z=6$ would be coincident with $\Delta_{2s}(1s^1)$ and $\Delta_{2p}(1s^1)$ respectively computed for $Z=6$. It can be seen that the Δ's computed for $Z=6$ and $Z=26$ agree to about 10 percent, so that, since the Δ's themselves do not contribute more than about 10 percent to the total wave function, the use of either Δ would give errors of the order of 1 percent. The difference between the Δ's for $Z=6$ and $Z=26$ which is due to neglect of further terms in Eq. (5) is several times larger than the change in the Δ's because of the change in the screening potential from its hydrogen-like value.[6] Repeating the calculation for one more Z value would enable one to evaluate terms of order Z^{-2}. In that event, the Z^{-2} terms computed here due to the change in screening from its hydrogen-like value can be used and need not be recomputed.

TABLE V. Values of a and b for Eq. (20) for atoms and ions with full K and L shells.

η	${}^{H}I_{1s}^{\eta p}$	$a_{1s}^{\eta p}$	${}^{H}I_{2s}^{\eta p}$	$a_{2s}^{\eta p}$	$b_{2s}^{\eta p}$
0.00	1.5311	2.923	4.6888	62.37	−35.93
0.25	1.0137	1.384	1.5463	6.769	−20.18
0.50	0.7201	0.7374	0.77891	1.145	+22.67
1.00	0.4162	0.2611	0.31669	−0.04312	9.29

η	${}^{H}I_{2p}^{\eta s}$	$a_{2p}^{\eta s}$	$b_{2p}^{\eta s}$
0.00	1.3535	28.82	−131.4
0.25	0.39925	4.198	−13.884
0.50	0.18359	1.0022	−2.193
1.00	0.08268	−1.932	+1.1336

η	${}^{H}I_{2p}^{\eta d}$	$a_{2p}^{\eta d}$	$b_{2p}^{\eta d}$
0.00	5.4142	99.50	145.0
0.25	1.2629	9.902	82.3
0.50	0.51928	1.459	34.3
1.00	0.16354	−0.2427	8.70

THE ENERGY PARAMETER

Some problem exists regarding the interpolation of the energy parameter, ϵ_{nl}. In the first-order solutions, R_{nl}^1 contains terms of order $1/Z$, and hence the corresponding energy parameter ϵ_{nl}^2 [7] can, in principle, be determined to terms of order $1/Z^2$. To do this, we can

[6] The quantities A, B, C, D, $(1/26)\Delta_{2s}[\Delta_{1s}(1s^0)]$, and $(1/26)\times\Delta_{2p}[\Delta_{1s}(1s^0)]$ shown in ANL-5008, were computed using $\Delta_{2s}(1s^1)$ and $\Delta_{2p}(1s^1)$ from $Z=26$, and $\Delta_{2s}(1s^0)$ and $\Delta_{2p}(1s^0)$ from $Z=6$. It is evident that the functions plotted there are essentially due to the higher terms in Eq. (5) and not to the change in the potential.

[7] According to this notation, ϵ_{nl}^0 is the hydrogen-like energy parameter. ϵ_{nl}^1 is the first-order energy parameter computed with hydrogen-like functions and then ϵ_{nl}^2 would be that computed with the function R_{nl}^1.

make use of $F_0(nl,n'l')$ [8] integrals computed analytically with hydrogen-like wave functions. The first-order energy parameter for say the $2s$ function in the configuration $(1s)^x(2s)^y(2p)^z$ would be

$$\epsilon_{2s}{}^1=\epsilon_{2s}{}^0+(x/Z)F_0(1s,2s)+[(y-1)/Z]F_0(2s,2s)+(z/Z)F_0(2p,2s). \quad (21)$$

The energy parameters $\epsilon_{nl}{}^2$ given in Table I found in the first-order computation can then be used to determine the terms of order $1/Z^2$. However, when we use $R_{nl}{}^2$, this contains terms of order $1/Z^2$ so that the energy parameter should contain terms of order $1/Z^4$. We have no method for using the computed parameters $\epsilon_{nl}{}^3$ to determine the coefficients of these terms.

Fortunately, we can make use of screening constants, as was suggested by Slater. In Eq. (21), $\epsilon_{2s}{}^0=-\frac{1}{4}$, if we write Eq. (21) as

$$\epsilon_{2s}{}^1=-\frac{1}{4}\left[1-\frac{x4F_0(1s,2s)}{2Z}-\frac{(y-1)4F_0(2s,2s)}{2Z}-\frac{z4F_0(2p,2s)}{2Z}\right]^2, \quad (22)$$

we have an expression which is identical with Eq. (21) to first-order terms but includes terms of higher order. The energy parameter given by Eq. (22) compares favorably with that obtained in the second-order computations so that we have used this approximation to obtain our energy parameters. The quantities

$$\sigma_{n'l',\,nl}=\tfrac{1}{2}n^2F_0(n'l',nl) \quad (23)$$

are screening constants and turn out to be practically the same as those derived by Slater.[9] For reference, Table VI is a list of these constants taken from Harris Mayer.[10]

THE MASS ABSORPTION COEFFICIENT

If the linear absorption coefficient is denoted by μ, for matter of density ρ, then the contribution to the mass absorption coefficient μ/ρ, by transitions $nl\rightarrow\eta l'$

TABLE VI. Screening constants.

	$\sigma(nl',nl)$		
	$1s$	$2s$	$2p$
$1s$	0.6250	0.8395	0.9712
$2s$		0.6016	0.6484
$2p$			0.7266

[8] See E. V. Condon and G. H. Shortley, *The Theory of Atomic Spectra* (Cambridge University Press, Cambridge, 1950), p. 177.
[9] J. C. Slater, Phys. Rev. 36, 57 (1930).
[10] H. Mayer, Los Alamos Report LADC-464 (unpublished).

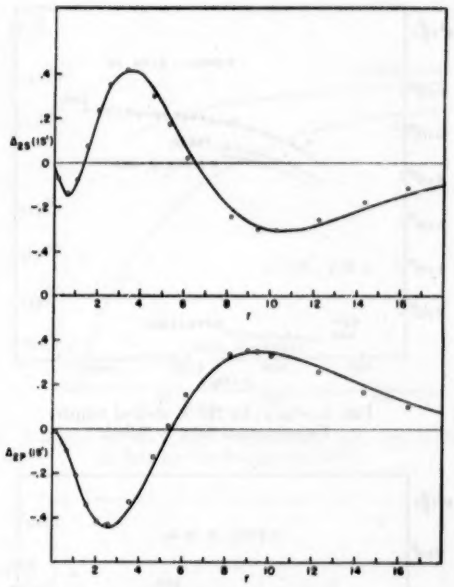

FIG. 1. $\Delta_{2s}(1s^1)$ and $\Delta_{2p}(1s^1)$ plotted as a function of r. The solid curves computed from $Z=6$, while the points indicate the same quantities for $Z=26$.

is given by

$$\mu/\rho=N_{nl}\cdot\frac{4\pi^2\alpha a_0{}^2A}{MZ^2}\cdot N_{nl}\frac{1}{3}\frac{\mathrm{Max}(l,l')}{(2l+1)}\nu[I_{nl}{}^{\nu l'}]^2$$
$$=\frac{4.8596\times10^6}{MZ^2}\cdot N_{nl}\frac{1}{3}\frac{\mathrm{Max}(l,l')}{(2l+1)}\nu[I_{nl}{}^{\nu l'}]^2, \quad (24)$$

where N_{nl} = number of electrons per atom in the state specified by nl, a_0 = radius of the first Bohr orbit, α = fine structure const., A = Avogadro's Number, M = molecular weight of the substance, and ν = frequency of radiation absorbed expressed in Rydberg units.

Equation (24) assumes product-type wave functions and neglects exchange effects as well as lack of orthogonality of the initial and final state wave functions of electrons not making the transition.

The methods discussed in the previous sections can be used with Tables II to IV to calculate the I's in Eq. (24). However, since the mass absorption coefficient varies approximately as ν^{-3}, it is important to know the value of ν with some precision. Strictly speaking, when we use the first-order wave functions and compute the I's to order $1/Z$, the energy parameter, which is taken to be the same as the ionization energy, should be taken to order $1/Z^2$. Second-order corrections in the I's are not as important as the effect of change in the frequency, ν.

For purposes of experimental comparison, the mass absorption coefficients have been computed for aluminum and copper for frequencies beyond the K absorp-

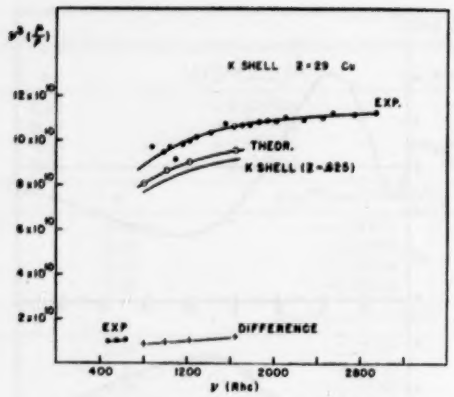

FIG. 2. $\nu^3(\mu/\rho)$ for the K shell of copper. Experimental data by Schulz.

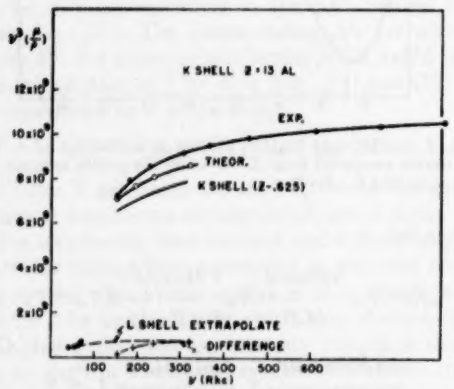

FIG. 3. $\nu^3(\mu/\rho)$ for the K shell of aluminum. The points below K edge are taken from Hill. The points above K edge are taken from Victoreen.

tion edge, and for aluminum, copper, and silver for frequencies between the L absorption edge and the K absorption edge. Since the mass absorption coefficients for the photoelectric effect vary approximately as ν^{-3}, $\nu^3(\mu/\rho)$ was plotted instead of μ/ρ. The results are shown in Figs. 2 to 6. For comparison the experimental values of the same quantities are shown. These data were taken from Landolt-Börnstein (data by Schulz, Jönsson, Andrews), Victoreen, Hill, Biermann, and Tomboulian and Pell,[11] as indicated in the figures, and have been corrected for scattering by the tables given by White.[12]

Unfortunately only the total absorption is measured and not the contribution due to the various electron shells. It is only at the absorption edges that one knows that the increase in absorption is due to a new shell. Here also, there is uncertainty since the effects of the lattice structure gives the experimental points considerable scatter.

The results of the present calculation and the magnitude of the absorption from the M and higher-lying shells can be somewhat better understood by making a comparison with the Coulomb result for some effective Z. Since $\nu^3(\mu/\rho)$ varies like Z^4 for the Coulomb problem, it seems likely that the maximum value for this quantity should be that computed for the effective $Z^*=Z$, the nuclear charge of the atom in question. For the K shell, where screening is relatively unimportant, we have shown for comparison, the Coulomb result for $Z^*=Z-0.625$ the screening constant result. It can be seen that our theoretical curve lies somewhat above this curve. The difference between the theoretical curve and the experimental curve in copper is a reasonable extrapolation of the L-shell absorption below the K edge. In the case of aluminum, the experimental data has considerable scatter so that we have used Victoreen's curve for the K absorption and Hill's experimental points for the L absorption. In this case, the difference is small but is in reasonable agreement with experiment, considering the experimental difficulties in the longer-wavelength regions.

In the region of the L shell the Coulomb result for the L shell is shown for $Z^*=Z-2$ and $Z^*=Z-6.522$, the latter being the energy screening constant result. It can be seen that in the frequency range considered, our theoretical curve starts in the neighborhood of the $Z-6.522$ curve and becomes asymptotic to the $Z-2$ curve, indicating the more or less complete screening of the two K electrons on the L shell.

It is not possible to use the mass absorption coefficient for the M shell for neutral atoms computed from Table II since the M-shell screening has not been taken into account. However, we have plotted in Figs. 7 and 8, $\nu^4 I^2$ averaged over the M shell for $Z=6$ and $Z=26$

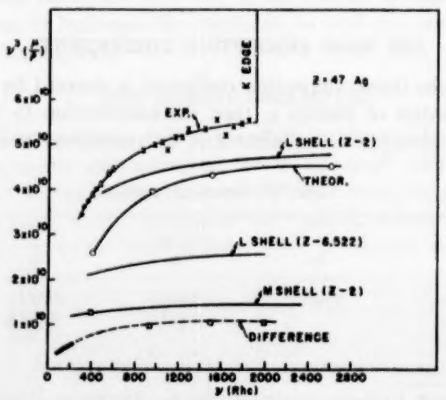

FIG. 4. $\nu^3(\mu/\rho)$ for the L shell of silver··· and the data represented by the solid curve below the L edge are from Biermann. Δ data are from Andrews. ×× data are from Schulz.

[11] H. H. Landolt and R. Börnstein, *Zalenwerte und Funktionen aus Physik, Chemie. Astronomie* (Springer Verlag, Berlin, 1950), sixth edition, Vol. I, pp. 314–316; J. A. Victoreen, J. Appl. Phys. **20**, 1141 (1949); R. D. Hill, Proc. Roy. Soc. (London) **A161**, 284 (1937); H. H. Biermann, Ann. Physik **26**, 740 (1936); D. H. Tomboulian and E. M. Pell, Phys. Rev. **83**, 1196 (1951).

[12] Gladys R. White, National Bureau of Standards Report NBSR-1003 (unpublished).

from the values given in Table II. Since in $Z=6$, there was screening by a $1s^0$ charge distribution, and in $Z=26$ screening by a $(1s^0)^2(2s^0)$ charge distribution, the Coulomb values of $\nu^4 I^2$ for $Z^*=6$ and $Z^*=5$, and $Z^*=24$ and $Z^*=23$, respectively, for $Z=6$ and $Z=26$, are also shown. In the case of $Z=6$, it can be seen that the $Z^*=5$ fits the calculations reasonably well. In $Z=26$, however, the calculation behaves at high frequency, more like $Z-2$ than $Z-3$. The L-shell screening in this limit has little effect on the M shell.

For $Z=47$ and 29 the Coulomb result of $\nu^3(\mu/\rho)$ for the M shell computed with $Z^*=Z-2$ is also shown in Figs. 4 and 5. In $Z=47$ the difference between the experimental curve and the theoretical curve extrapolate reasonably well from the experimental points below the L edge. This difference cruve lies somewhat below the M shell $Z-2$ curve and the remainder of the absorption is of the correct order of magnitude for the remaining 19 electrons in the N and higher shells. In the case of copper, the difference curve lies somewhat below the M shell $Z-2$ curve, indicating that the M shell $Z-2$ limit may not apply for that low a nuclear charge.

The first point on the difference curve seems to be too high for silver and perhaps for copper depending on how one wishes to draw the curve. This "bump" does not appear in the curves for tin as published in ANL–5008, but an error was found in the Landolt-Börnstein Tables[13] from which the data was obtained, and when one uses the original data of Biermann this "bump" also appears in tin. While there is no other data for the M shell below the L edge for elements in the neighborhood of $Z=25$, the difference curve shows the same behavior for nickel in the region of the L absorption as it does for copper.

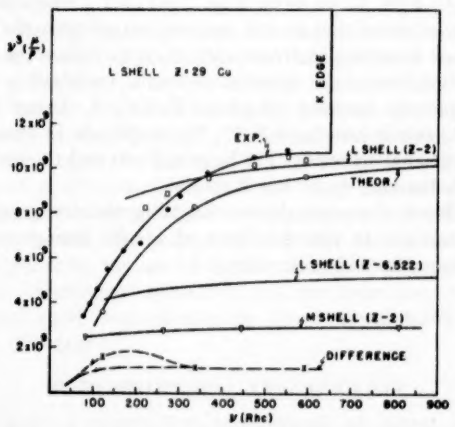

FIG. 5. $\nu^3(\mu/\rho)$ for the L shell of copper. ● ● data by Jönsson. □ □ data by Andrews. Solid curve below L edge represents 3 points taken from Hill.

[13] Apparently the measurements given by Landolt-Börnstein, page 316, from λ2.0988→λ9.8678 for Sn and Ta should be for Ag and Sn, respectively.

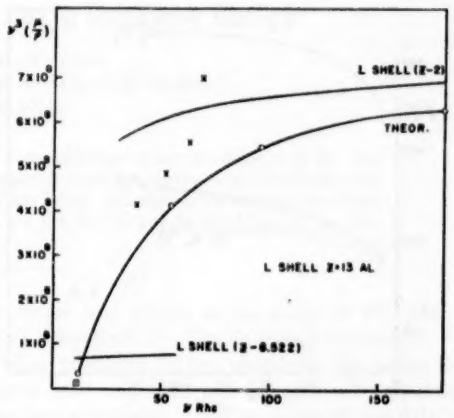

FIG. 6. $\nu^3(\mu/\rho)$ for the L shell of aluminum. ×× data by Hill. ⊡ data by Tomboulian and Pell.

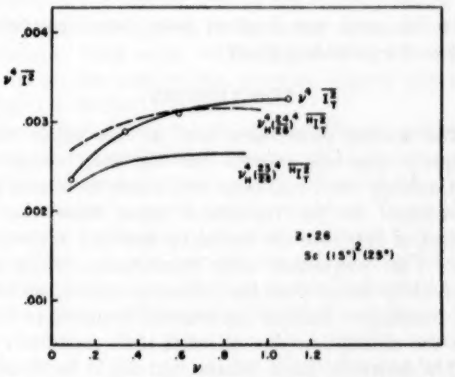

FIG. 7. $\nu^4\langle I^2\rangle_{Av}$ for the M shell for $Z=6$, with $1s^0$ screening. The curve labeled $\nu^4\langle I\gamma^2\rangle_{Av}$ was computed from the integrals in Table II.

The origin of this apparent irregularity is, of course, not known. It may be due to effects not considered in this paper, such as the neglect of the penetration of the M-shell charge distribution into the L shell, exchange effects or two-electron transitions. An estimate of the latter effect appears to amount to a correction at the edge of less than one percent. It is very likely that fault lies with the present scaling procedures and that the terms of order $1/Z^2$ in Eq. (5) contribute errors at this point where first-order corrections themselves are large.

In the case of the absorption due to the L shell of aluminum, there are very few data in this long-wavelength region, and the effects of screening are large. The ratio of the number of bound electrons to Z is 10/13 which is not a small quantity. Nevertheless, the qualitative agreement between the theoretical curve and the data is surprisingly good. The fact that the one experimental point due to Tomboulian and Pell falls on the theoretical curve is not to be taken too seriously,

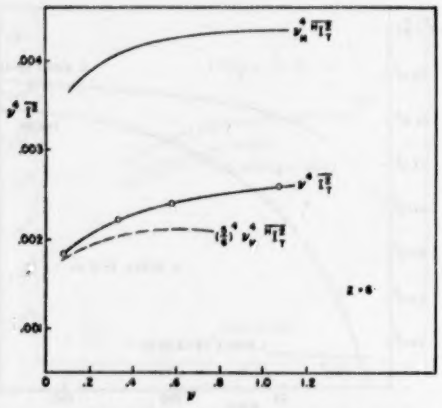

FIG. 8. $\nu^4\langle I^2\rangle_{Av}$ for the M shell for $Z=26$ screened by $(1s^0)^2(2s^0)$. The curve labeled $\nu^4\langle I_T{}^2\rangle_{Av}$ was computed from the integrals in Table II.

since this point was obtained from a small logarithmic plot in the published paper.

CONCLUSIONS

The scaling procedures used in this paper which properly take into account the first-order corrections to Coulomb wave functions and dipole moments, give corrections to the theoretical mass absorption by factors of two over the screening constant approximation. The comparison with experiments, while it is apparently better than the screening approximation, is not conclusive. Further experiments designed to measure the absorption due to each shell separately are highly desirable. Such information might be obtained by a study of the velocity distribution of the ejected photoelectrons.

The separation of the absorption by each shell might be handled theoretically by computing the dipole moments for a complete atom in the neighborhood of atomic number 30. A comparison of the K- and L-shell absorption with our scaled values would provide a further check on these numbers. The M-shell computation could be used to check the difference curve between the theory and experiment. One could then see whether the Hartree functions are good enough to explain the observed absorption or whether other effects must be taken into consideration.

ACKNOWLEDGMENTS

It is a pleasure to acknowledge the assistance of Donald A. Flanders who set up the numerical procedures used in this work, and that of Janet Sukup for programming and supervising the machine calculations. Thanks are also due to Lucille Renick for assistance in the latter parts of the work.

APPENDIX I

If there are screening electrons whose charge distribution is external to that of the optical electron, then in carrying out the integration of Eq. (1) for the charge distribution of the optical electron, $\sum_{ext.} V_{ij}$ for these external electrons according to Eq. (2) will be just

$$V_e=\sum_{\text{ext.}} V_{ij}=+2\sum_{ij}\int_0^\infty \frac{[R_{ij}]^2}{r}dr=-\epsilon_e \text{ a constant.}$$

Thus the energy parameter for these cases $\epsilon_{nl}{}^1$, plus this interaction term, $-\epsilon_0$, will have to be the same as the energy parameter without external screening, ϵ_{nl}. Hence,

$$\epsilon_{nl}=\epsilon_{nl}{}^1-\epsilon_0,$$

or

$$\epsilon_{nl}{}^1=\epsilon_{nl}+\epsilon_0. \tag{1A}$$

The energy differences are the same as before, except that the free function having energy parameter η that corresponded to an electron leaving the system with kinetic energy η, now corresponds to an electron leaving the system with energy $\eta+\epsilon_0$.

The free wave functions are still correctly normalized. For the free function, the numerical solution to Eq. (1) is continued by means of the WKB-Jeffreys solution. This solution has an amplitude factor of the form $(\epsilon_{nl}{}^1+V)^{-\frac{1}{4}}$. If we write V as $V=V_i+V_e$, where V_i is the potential due to the nuclear charge plus the internal screening electrons and, V_e is as before the potential due to the external electrons, for small r, the amplitude becomes $(\epsilon_{nl}+\epsilon_0+V_e+V_i)^{-\frac{1}{4}}$. Using Eq. (1A) this is just $(\epsilon_{nl}+V_i)^{-\frac{1}{4}}$, the amplitude in absence of external screening. For large r, $V\to 0$ and the amplitude becomes $(\epsilon_{nl}{}^1)^{-\frac{1}{4}}$ as it should.

Hence, the external screening integrals correspond to transitions to free functions of kinetic energy $\eta+\epsilon_0$ rather than of kinetic energy η.

L-Shell Ionization by Protons of 1.5- to 4.25-Mev Energy*

E. M. BERNSTEIN AND H. W. LEWIS
Department of Physics, Duke University, Durham, North Carolina
(Received March 26, 1954)

Characteristic *L*-shell x-rays produced when protons of 1.5- to 4.25-Mev energy are stopped in Ta, Au, Pb, and U have been studied with a NaI scintillator. The absolute cross sections for x-ray production are presented. By correcting these values for Auger transitions, the *L*-shell ionization cross sections have been determined. At 3 Mev, the x-ray production cross sections are 104, 74, 54, and 24 barns for Ta, Au, Pb, and U, respectively.

I. INTRODUCTION

SINCE protons, deuterons, and alpha particles stopping in matter lose their energy by ionization and excitation processes, characteristic x-rays of the absorber are emitted. Measurement of the cross section for x-ray production, and application of corrections for the Auger effect, allow the cross section for ionization to be obtained. In addition to the characteristic x-rays a small intensity of bremsstrahlung is also produced and has been detected.[1]

The most recent investigation of x-rays produced by heavy particles was made by Lewis, Simmons, and Merzbacher.[2] References to previous work are given in that article. *K*-shell x-rays produced by protons of Van de Graaff energies on Mo, Ag, Ta, Au, and Pb were studied. The measurements were made with a NaI scintillator. *K*-shell x-ray cross sections were obtained as a function of proton energy and atomic number. These were converted to *K*-shell ionization cross sections and compared with the nonrelativistic theoretical ionization cross sections calculated by Henneberg[3] in 1933. There was qualitative agreement between the experimental and theoretical values; however, significant quantitative discrepancies were noted.

Using similar techniques, but with certain experimental modifications dictated by the fact that *L* x-rays are softer than *K* x-rays we have measured the cross sections for *L*-shell ionization by protons up to 4.25 Mev in Ta, Au, Pb, and U. Thin windows were essential for the target chamber and NaI scintillator, and the use of a scintillator about 2 mm thick removed the background due to higher energy gamma and x-rays, but was still 100 percent efficient for the *L* x-rays. Furthermore, the use of the Dumont 6292 phototube, with its excellent resolution and low noise level permitted good measurements on x-rays to well below 10 kev of energy.

II. EXPERIMENTAL ARRANGEMENT

Figure 1 shows the arrangement of target and detector, and a detailed view of the NaI crystal holder. The target was placed at an angle of 45° with the proton beam from the Van de Graaff accelerator.

Pulses produced in the phototube by single x-ray photons were amplified and fed into a single-channel pulse-height analyzer. Typical curves of counting rate against pulse height, normalized to 10 μcoul, are shown in Fig. 2. The width of the peaks is due partly to the presence of the several lines of the *L* series which are not resolved, and partly to the finite resolution of the phototube. Tube noise, which begins to rise at about 5 volts on the scale shown, overlaps slightly the low-energy tail of the Ta curve.

The x-rays interact with the scintillator primarily by the photoelectric effect, thereby giving pulses corresponding to the full photon energy, provided the x-rays from iodine in the crystal are also absorbed. To calculate the number I of iodine x-rays which escape if I_0 photons are incident on the crystal, we proceed as follows. Since the beam of incident x-rays is collimated such that it strikes a small area in the center of the crystal face, and since they penetrate only a small percentage of the depth of the crystal, the NaI crystal can be con-

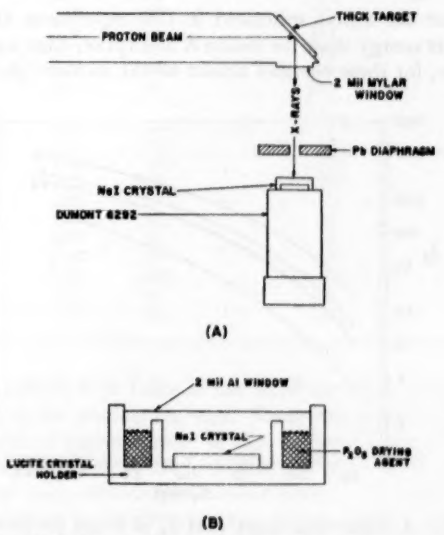

FIG. 1. (A) Arrangement of target and detector. (B) Crystal holder.

* This work was supported by the U. S. Atomic Energy Commission.
[1] Č. Zupančič and T. Huus (private communication).
[2] Lewis, Simmons, and Merzbacher, Phys. Rev. 91, 943 (1953).
[3] W. Henneberg, Z. Physik 86, 592 (1933).

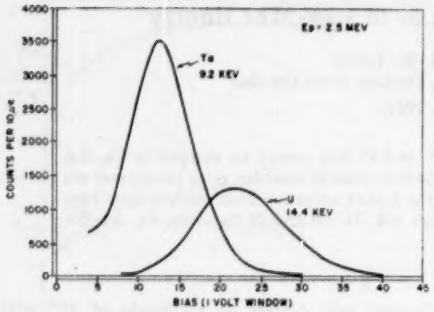

FIG. 2. Typical differential pulse-height spectra of the L-shell x-rays from Ta and U.

sidered a semi-infinite medium. Then,

$$I=\sum_j \alpha_j\beta_j \int_{x=0}^{\infty}\int I_0\mu_1 e^{-\mu_1 x}e^{-\mu_j x/\cos\theta}\frac{d\Omega}{4\pi}dx,$$

where the angle integration is over a solid angle of 2π and the summation is over all the electron shells in the iodine atom ($j=K,L,M,N,O$). α_j is the fraction of incident x-rays absorbed in the jth shell. β_j is the ratio of j-shell x-ray emission to j-shell ionization (the other atoms undergo Auger transitions). x is the distance an incident photon penetrates the crystal before it is absorbed; θ is the angle between the direction of the incident photon and the escaping iodine x-ray. μ_1 is the absorption coefficient of NaI for the incident x-rays; μ_j is the absorption coefficient of the NaI for the x-rays from the jth shell of iodine. Evaluation of the integral gives

$$I=\sum_j \tfrac{1}{2}\alpha_j\beta_j I_0[1-(\mu_j/\mu_1)\ln(1+\mu_1/\mu_j)].$$

Since the x-rays measured in this experiment are of lower energy than the iodine K absorption edge, $\alpha_K=0$. Also, for these energies almost all the incident photons

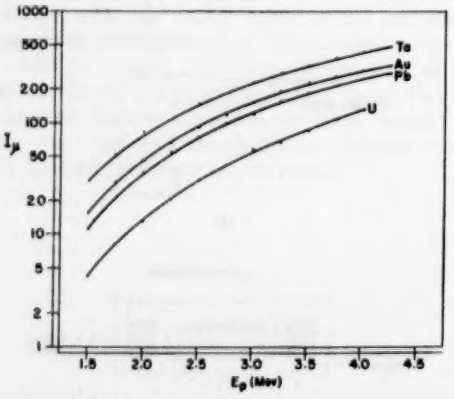

FIG. 3. Total thick target yield I_μ of x-rays per proton of initial energy E_p. I_μ is 4π times the differential yield at 90° to the proton beam, and is uncorrected for self-absorption in the target.

interact with the iodine L shell. Then, to calculate the escape intensity we assume $\alpha_L=1$ and $\alpha_M=\alpha_N=\alpha_O=0$. This assumption leads to an escape intensity slightly greater than the actual case. Now $\beta_L=0.12$, so we have

$$I=0.06I_0[1-(\mu_L/\mu_1)\ln(1+\mu_1/\mu_L)].$$

For Ta, which has the maximum escape of iodine x-rays of the elements investigated, $I=0.015I_0$. Also, due to the finite resolution of the detection apparatus, many of the degraded pulses caused by iodine x-ray escape are counted. Thus, even with the assumption made above, any effect due to escape can be neglected.

III. EXPERIMENTAL RESULTS

An angular distribution of the L x-rays from a thin Au target was taken, and found to be isotropic to at least two percent. Therefore, to obtain I_μ, the total yield of x-rays when one proton of initial energy E_p is

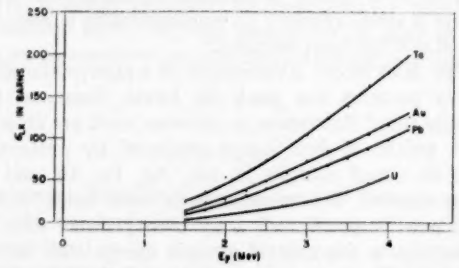

FIG. 4. X-ray production cross sections *vs* proton energy E_p.

stopped in the thick target, the following calculations must be made:

(a) Find the integrated number of counts under the counting rate *vs* bias curve, and divide by the number of current integrator counts (1.03 μcoul per integrator count). This gives the number J of photons counted per 6.42×10^{12} incident protons, listed in column 5 of Table I.

(b) Apply the solid angle correction, which was 5.5×10^{5}.

(c) Correct for the absorption of the x-radiation in the thin windows and air.

The absorption corrections for the thin windows were determined experimentally by inserting additional window material, two mils of Mylar foil and two mils of aluminum foil between the target and the scintillator. The air absorption correction was calculated, using weighted-average x-ray wavelengths and known absorption coefficients. The over-all absorption correction factors are given in column 6 of Table I. The calculated values of I_μ are given in column 7 of Table I.

To calculate the cross section for x-ray production, one must take account of the self-absorption of the target for its own radiation, and the slowing down of the proton as it penetrates the thick target. Proceeding

in the same manner as in reference 2, we obtain the following relation:

$$\sigma[E(x)]=-\frac{1}{n}\frac{dI_\mu(x)}{dE}\frac{dE}{d(\rho x)}+\frac{\mu}{n\rho}I_\mu(x).$$

This gives the cross section for x-ray production as a function of known parameters and I_μ, the total yield from a thick target. n denotes the number of target atoms per gram, dI_μ/dE is the slope of the curves given in Fig. 3, $dE/d(\rho x)$ is the well-known specific energy loss, and μ/ρ is the mass-absorption coefficient of the target for its own x-rays. The values of these absorption coefficients are rather important, since at high proton energies the second term in the cross-section relation predominates over the first. Again by using weighted averages to obtain the effective wavelength, the absorption coefficients were obtained from relations given by Siegbahn.[4] The values thus obtained were checked experimentally for Ta and Au. The computed average mass-absorption coefficients employed were:

Element	Ta	Au	Pb	U
$(\mu/\rho)_{Av}$ in cm²/g	120	107	98	79.

TABLE I. Yields of L-shell x-rays.

1 Element	2 Z	3 E_L in kev	4 E_p in Mev	5 J	6 C	7 I_μ
Ta	73	9.2	1.50	0.77×10^{9}	4.55	3.0×10^{-4}
			1.75	1.3		5.1
			2.00	2.2		8.6
			2.50	3.8		1.5×10^{-3}
			3.00	5.8		2.26
			3.25	7.3		2.8
			3.50	8.2		3.2
			3.75	9.8		3.8
			4.00	11.1		4.3
			4.25	12.3		4.8
Au	79	10.6	1.50	0.71×10^{9}	2.60	1.6×10^{-4}
			1.75	1.35		3.0
			2.00	2.1		4.7
			2.25	3.2		7.2
			2.50	4.0		8.9
			2.75	5.2		1.17×10^{-3}
			3.00	6.9		1.53
			3.25	8.5		1.9
			3.50	9.6		2.2
			3.75	11.4		2.5
			4.00	13		2.9
			4.25	14		3.1
Pb	82	11.6	1.50	0.64×10^{9}	2.12	1.16×10^{-4}
			1.75	1.16		2.1
			2.00	1.9		3.5
			2.25	2.9		5.3
			2.50	4.1		7.5
			2.75	5.5		1.0×10^{-3}
			3.00	6.5		1.2
			3.25	8.7		1.6
			3.50	10		1.8
			3.75	11.8		2.1
			4.00	13.5		2.4
			4.25	15.7		2.8
U	92	14.4	1.50	3.2×10^{9}	1.58	4.5×10^{-5}
			1.75	6.2		8.3
			2.00	9.5		1.3×10^{-4}
			2.25	1.5×10^{9}		2.0
			2.50	2.3		3.1
			2.75	3.1		4.2
			3.00	3.9		5.3
			3.25	5.0		6.8
			3.50	6.3		8.5
			3.75	7.9		1.07×10^{-3}
			4.00	9.5		1.3

TABLE II. L x-ray and ionization cross sections.

1 Element	2 E_p in Mev	3 σ_{LX} in barns	4 Auger factor	5 σ_{LI} in barns	6 σ_{KI} in barns
Ta	1.50	24	3.56	84	
	1.75	36		126	
	2.00	54		192	0.017
	2.50	74		265	
	3.00	104		370	0.10
	3.25	124		440	
	3.50	139		495	0.20
	3.75	164		584	
	4.00	177		630	
	4.25	198		705	
Au	1.50	11.6	2.74	32	
	1.75	23		63	
	2.00	27		73	
	2.25	38		103	
	2.50	48		131	0.018
	2.75	59		161	
	3.00	74		203	
	3.25	85		233	
	3.50	96		263	
	3.75	105		288	
	4.00	116		318	
	4.25	126		345	
Pb	1.50	9.1	2.51	23	
	1.75	15		38	
	2.00	24		61	0.0045
	2.25	32		81	
	2.50	42		104	0.013
	2.75	48		122	
	3.00	54		134	0.032
	3.25	68		171	
	3.50	76		191	
	3.75	87		218	
	4.00	99		248	
	4.25	115		288	
U	1.50	3.4	2.22	7.6	
	1.75	6.2		14	
	2.00	9.0		20	
	2.25	13		28	
	2.50	16.5		37	
	2.75	20		45	
	3.00	24		54	
	3.25	30		67	
	3.50	38.0		83	
	3.75	46		103	
	4.00	56		123	

In column 3 of Table II are listed the cross sections for L x-ray production, σ_{LX}. These are plotted as a function of proton energy in Fig. 4. For Au the thick-target results were supplemented by and found consistent with thin-target measurements. An analysis of the errors in the determination of the absolute values

[4] M. Siegbahn, *Spektroskopie Die Roentgenstrallen* (Verlag Julius Springer, Berlin, 1931).

of the x-ray production cross sections indicate they are correct to 20 percent or better for all four elements. The total L-shell ionization cross sections σ_{LI}, listed in column 5 of Table II, are obtained by correcting σ_{LX} for Auger transitions. The Auger factors are not too well known; those used were the ones obtained by Lay in 1934 and given by Burhop.[5]

Table II includes for comparison some K-shell ionization cross sections σ_{KI}, taken from reference 2. These are smaller than the L-shell cross sections by several orders of magnitude. The L-shell cross sections do not fit simple power laws in either proton-energy or atomic-number dependence; however, the variation is slower in both respects than the approximately E^4/Z^{12} dependence of the K shell.

We wish to thank Dr. E. Merzbacher for many helpful discussions of the theory and for his continuing interest in this work.

[5] E. H. S. Burhop, *The Auger Effect* (Cambridge University Press, Cambridge, 1952), p. 55.

PHYSICAL REVIEW VOLUME 95, NUMBER 1 JULY 1, 1954

Decay Scheme and Gamma-Gamma Correlations in B^{10}†

S. M. SHAFROTH* AND S. S. HANNA
Department of Physics, The Johns Hopkins University, Baltimore, Maryland

(Received March 18, 1954)

Gamma rays from the deuteron bombardment of beryllium were studied with two scintillation spectrometers operated in coincidence. Gamma rays of energies 2.86, 2.15, 1.43, 1.02, 0.72, and 0.41 Mev, which have previously been associated with the B^{10} nucleus, were identified in single-channel spectra. Coincidences were observed between the following pairs of gamma rays: 2.86−0.72, 2.15−1.43, 1.43−1.43, 1.43−1.02, 1.43−0.72, 1.43−0.41, 1.02−0.72, 1.02−0.41, and 0.72−0.41. The decay scheme obtained from these measurements agrees with the one proposed by Ajzenberg, except for the presence of an additional 1.43-Mev transition between the 3.58- and 2.15-Mev states of B^{10}. A survey was made of the directional angular correlations between several of these coincident radiations.

I. INTRODUCTION

THE gamma rays emitted in the $Be^9(d,n)B^{10*}(\gamma)B^{10}$ reaction have been investigated by Rasmussen *et al.*[1] with a spectrometer of high resolution. From measurements on the energies of the neutron groups, Ajzenberg[2] has determined the excitation energies of the states in B^{10} and has deduced a decay scheme which would account for all the observed gamma rays. The excitation energies have also been obtained by Pruitt *et al.*[3] and Dyer and Bird[4] from observations of the neutron groups in the same reaction, and by Bockelman *et al.*[5] from the inelastic scattering of protons and deuterons by B^{10} nuclei.

In order to establish the decay scheme directly and to investigate some of the gamma-gamma angular correlations, we have searched for coincidences between all possible pairs of gamma rays emitted by the B^{10} nucleus in the Be^9+d reaction at bombarding energies below 0.7 Mev.

II. APPARATUS

A thick target of beryllium was bombarded with deuterons from an electrostatic accelerator. The target was located at the center of a cylindrical target chamber, 3 inches in diameter. The brass wall of the chamber was $\frac{1}{32}$ inch thick.

The spectrum of the gamma radiation was studied with a scintillation spectrometer consisting of a cylindrical, sodium iodide crystal, 2 inches long, 1.5 inches in diameter, packed in magnesium oxide powder,[6] and mounted on an RCA 5819 photomultiplier tube. The pulses from the phototube passed through a cathode follower, a linear amplifier, and then were analyzed in a single channel differential analyzer.

For the coincidence work a second scintillation spectrometer was used in coincidence with the first. The second system was similar in every way to the first, except that the crystal was 1.25 inches long. The pulses from the two analyzers operated blocking oscillators which presented uniform pulses to a 6AS6 tube for coincidence analysis. Accidental coincidences were monitored with a separate coincidence circuit, which received delayed pulses from one analyzer and undelayed pulses from the other.

† Assisted by a contract with the U. S. Atomic Energy Commission.

* Now at Northwestern University, Evanston, Illinois

[1] Rasmussen, Hornyak, and Lauritsen, Phys. Rev. **76**, 581 (1949); V. K. Rasmussen, Ph.D. thesis, California Institute of Technology, 1950 (unpublished).

[2] F. Ajzenberg, Phys. Rev. **82**, 43 (1951); Phys. Rev. **88**, 298 (1952).

[3] Pruitt, Swartz, and Hanna, Phys. Rev. **92**, 1456 (1953).

[4] A. J. Dyer and J. R. Bird, Australian J. Phys. **6**, 45 (1953).

[5] Bockelman, Browne, Sperduto, and Buechner, Phys. Rev. **90**, 340 (1953); **92**, 665 (1953).

[6] C. J. Borkowski and R. L. Clark, Rev. Sci. Instr. **24**, 1046 (1953).

III. GAMMA RADIATION FROM B^{10}

The counters were calibrated with gamma rays of known energy from radioactive sources. A typical calibration is given in Fig. 1. A knowledge of the spectrum of the ThC″ gamma ray (2.62 Mev), which depends on the crystal geometry, aided in untangling the complex spectrum from the Be^9+d reactions. For the high-energy gamma rays identified in Fig. 2, the positions of the three main pair peaks and the Compton maximum are indicated. The 3.36-Mev gamma ray is attributed to Be^{16}, the 2.86, 2.15, 1.43, 1.02, and 0.72-Mev gamma rays to B^{10}.[1,7] Figure 3 shows the low energy spectrum. The structure at 0.48 Mev is

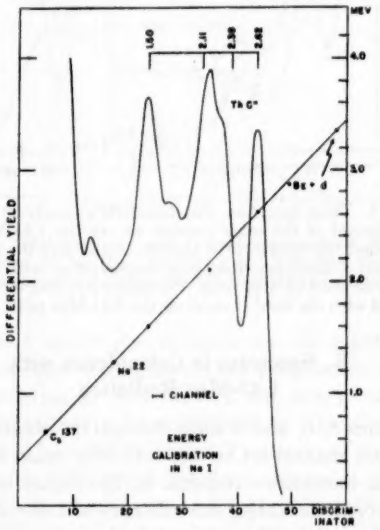

FIG. 1. Energy calibration of the 2-inch long NaI crystal and the pulse-height spectrum of the ThC″ (2.62-Mev) gamma ray. The vertical lines at the top locate the two-escape pair peak, the one-escape peak, the upper edge of the Compton distribution, and the no-escape (plus photo) peak. The one-escape pair peak is distorted by the Compton structure. The points labeled Cs^{137} and Na^{22} give the location of the photopeaks of the corresponding 0.67- and 1.28-Mev radiation. The points labeled Be^9+d show the location of the two highest recorded peaks, at 3.36 and 2.86 Mev, in the gamma-ray spectrum from Be^9+d (see Fig. 2).

attributed to the Li^7 gamma ray, the peak at 0.41 Mev to a B^{10} gamma ray. The structure in this region, however, was not very reproducible because of the presence of some annihilation radiation resulting from the bombardment of carbon impurity on the target.

IV. COINCIDENCE SPECTRA

The coincidence spectra were obtained by keeping the channel of one detector fixed on a peak in the spectrum and moving the channel of the other detector through the region of interest, while recording the

[7] The weak 3.58-Mev gamma ray is not apparent in these spectra, but no special effort was made to resolve it.

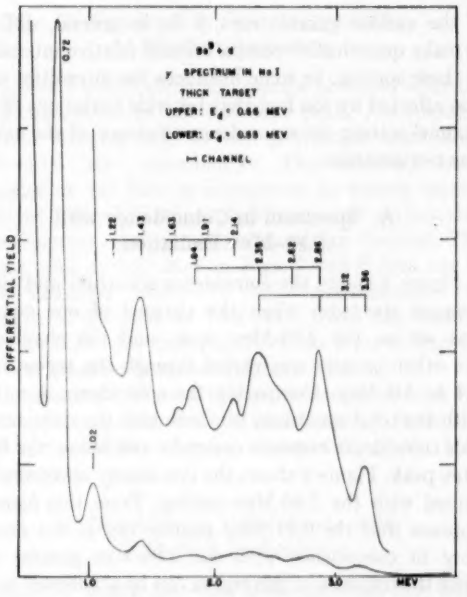

FIG. 2. Two spectra of the high-energy gamma rays from the Be^9+d reactions. The ordinates of the two curves are in the ratio of approximately 10:1. There is also a slight shift in the abscissas of the two spectra. The energy scale applies to the lower spectrum. The vertical lines locate the three pair peaks and the Compton edge of the various gamma rays. Above 3.0 Mev the energy scale is nonlinear because of overloading in the amplifier.

coincidence yield. Total yields and coincidence yields were normalized to the count in the fixed channel. In order to obtain sufficient intensity, most of the coincidence runs were made with fairly wide channels (3 to 8 volts). Because of the overlapping structure

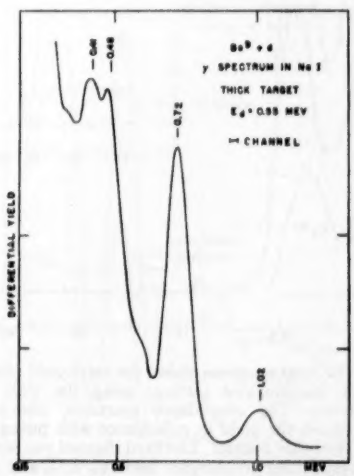

FIG. 3. Spectrum of the low-energy gamma rays from the Be^9+d reactions. In the region of 0.5 Mev there is a small contribution of annihilation radiation arising from the positron decay of N^{13} produced by deuteron bombardment of C^{12}.

of the various gamma rays, it is, in general, difficult to make quantitative comparisons of relative intensities in these spectra. In some instances the intensities were also affected by the fact that for wide variations of the channel setting the coincidence efficiency of the circuit was not constant.

A. Spectrum in Coincidence with 2.86-Mev Radiation

Figure 4 shows the coincidence spectrum and single channel spectrum when the channel of one counter was set on the 2.86-Mev peak, and the channel of the other counter was varied through the region from 0.4 to 3.0 Mev. Comparing the coincidence spectrum with the total spectrum, it is seen that the only detectable coincidence response occurs at and below the 0.72-Mev peak. Figure 8 shows the low-energy spectrum obtained with the 2.86-Mev setting. From this figure it appears that the 0.41-Mev gamma ray is not detectably in coincidence with the 2.86-Mev gamma ray, since the response in this region can be attributed to the Compton structure from the 0.72-Mev gamma ray.

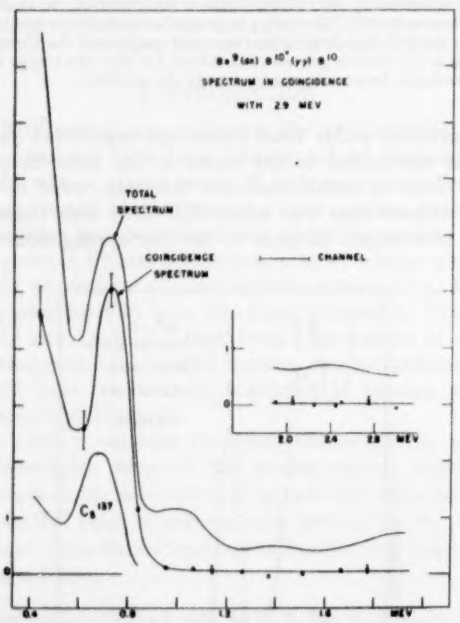

FIG. 4. The total spectrum shows the total yield obtained as a function of discriminator setting, using the wide (7.5-volt) channel shown. The coincidence spectrum, obtained simultaneously, shows the yield in coincidence with pulses in a fixed channel of the other counter. The fixed channel was set to receive pulses corresponding to energies between 2.55 and 3.05 Mev, i.e., on the 2.86-Mev peak. The energy scale was obtained from a calibration similar to Fig. 1. For comparison the Cs^{137} gamma-ray spectrum is shown, taken under the same conditions as the total spectrum. The vertical scales are arbitrary and of course different for the three spectra.

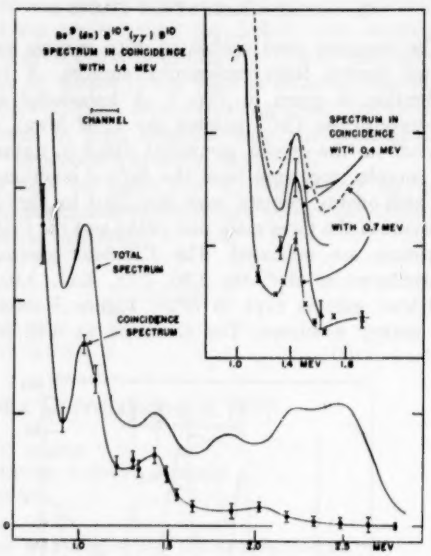

FIG. 5. Total spectrum and coincidence spectrum with the fixed channel of the other counter set on the 1.43-Mev peak. In the inset the dotted curve and the crosses give the total spectrum and coincidence spectrum, respectively, with the fixed channel on the 0.72-Mev peak. The solid curve and the dots were obtained with the fixed channel on the 0.41-Mev peak.

B. Spectrum in Coincidence with 1.43-Mev Radiation

Figures 5, 6, and 8 show the spectra obtained with the fixed channel set on the 1.43-Mev peak. In Fig. 5 a weak coincidence response in the region of 2 Mev is observed, indicating the existence of 1.43−2.15 Mev coincidences. In Figs. 5 and 6 there is evidence for 1.43−1.43 Mev coincidences, although the peak in this region can be attributed partially to 1.43−2.15 Mev coincidences. With both counters fixed on the 1.43-Mev setting, an increased response is expected, since both counters are also recording some 2.15-Mev radiation, and either gamma ray can count in either detector. At most, however, this response should be less than twice that for the 1.43−2.15 Mev setting, since 1.43 Mev does not correspond to a peak in the 2.15-Mev gamma spectrum. The pronounced 1.43−1.43 Mev response was also observed in a third run made independently.[8] It is interesting that the energies of these two coincident gamma rays are so nearly the same that they were not resolved in the work of Rasmussen *et al.*[1]

[8] In evaluating these spectra, it is also necessary to consider the effect of two 0.72-Mev pulses occurring within the resolving time of a detector to produce a 1.43-Mev pulse. It can be seen that this effect is negligible in the data in Fig. 4, and it was also investigated with radioactive sources. In the spectra presented here it was standard practice to keep the counting rates low enough so that the effect was not significant.

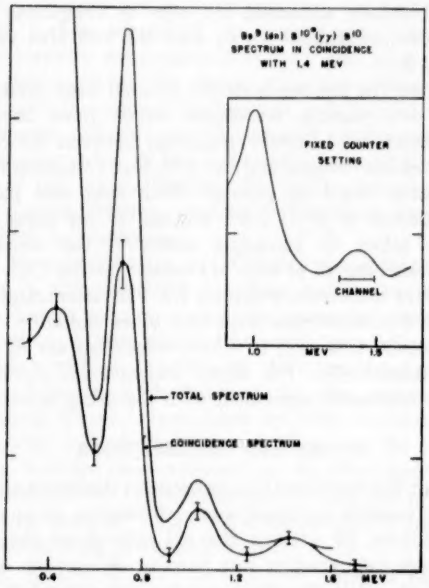

FIG. 6. Total spectrum and coincidence spectrum with the fixed channel set on the 1.43-Mev peak. The inset shows the total spectrum and fixed channel setting of the second counter.

Figures 5 and 6 give evidence for the existence of 1.43−1.02 Mev coincidences. The peak in the coincidence spectrum at 1.02 Mev is too strong and not properly located to be attributed to the Compton structure of 1.43-Mev radiation. To determine the effect of 2.15-Mev radiation in the fixed channel, a run was made with the channel set at 2.1 Mev. To within the statistical accuracy of the measurement, no 2.15−1.02 Mev coincidences were observed (i.e., the structure observed could be attributed to 2.15−1.43 Mev coincidences).

Figures 6 and 8 show a strong peak in the coincidence spectrum at 0.72 Mev. Part of this response can, of course, be attributed to 2.86−0.72 Mev coincidences, since the fixed channel is responding to some 2.86-Mev radiation. If, however, one counter is fixed on the 0.72-Mev peak, and the region around 1.4 Mev is searched with the other counter, a strong coincidence peak is obtained at 1.43 Mev, as shown in the inset in Fig. 5. In this case also, part of the response can be attributed to coincidences between 1.43-Mev gamma rays and other radiations. If there were no 1.43−0.72 Mev coincidences, however, either this peak or the one at 0.72 Mev (1.43 Mev fixed) would be expected to be weaker than observed.

In Fig. 8 the 1.43-Mev and 2.85-Mev curves are compared in the low energy region. At 0.41 Mev the 1.43-Mev curve rises above the 2.86-Mev curve, indicating the presence of 1.43−0.41 Mev coincidences.

C. Spectrum in Coincidence with 1.02-Mev Radiation

Figures 7 and 8 show the spectra obtained with the fixed channel set on the 1.02-Mev peak. The response at 1.43 Mev is due to the previously established 1.43−1.02 Mev coincidences. The relatively weak response at 1.0 Mev is interpreted as arising merely from the 1.43−1.02 Mev coincidences and the fact that either gamma ray can record in either channel. The strong peak at 0.72 Mev in Figs. 7 and 8 does not in itself establish 1.02−0.72 Mev coincidences. The strength of the peak at 1.02 Mev, when one channel is set on 0.72 Mev (see Fig. 9, or the inset in Fig. 5), however, makes these coincidences plausible.

The spectrum below 0.8 Mev is compared with the other spectra in Fig. 8. It is apparent that there is a very pronounced response from 1.02−0.41 Mev coincidences.

D. Spectrum in Coincidence with 0.72-Mev Radiation

Figure 9 shows the data obtained with the fixed channel on the 0.72-Mev peak. Comparing this curve with the curves in Fig. 8, it is seen that the rise at 0.4 Mev is significantly greater, as compared to the 0.72-Mev peak, with the fixed counter on 0.72 Mev than on any higher gamma ray, indicating the existence of 0.72−0.41 Mev coincidences. The coincidence response at 0.72 Mev in Fig. 9 is just about that which would be expected from coincidences between 0.72-Mev radiation and higher energy gamma rays (recorded in

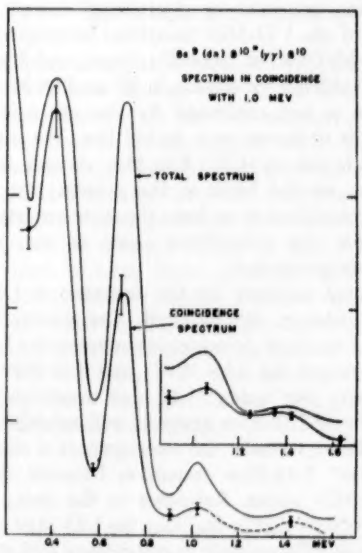

FIG. 7. Total spectrum and coincidence spectrum with the fixed channel set on the 1.02-Mev peak. The inset shows an independent run obtained with decreased gain and lower resolution.

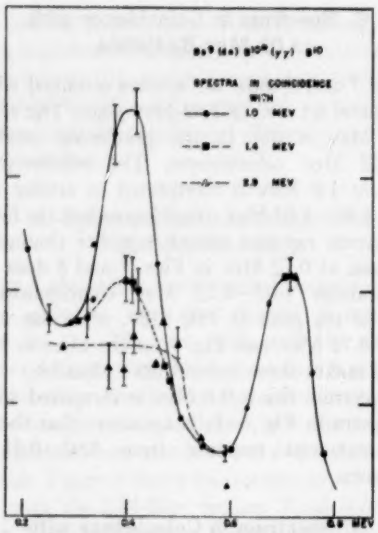

FIG. 8. Comparison of the 2.86-, 1.43-, and 1.02-Mev coincidence curves in the region of the 0.41- and 0.72-Mev peaks. These are independent runs not shown in the other figures. The 0.72-Mev curve in Fig. 9 may also be compared with these spectra, and the total spectrum in Fig. 9 is typical of the total spectra for the curves in this figure.

the 0.72-Mev channel). There is therefore no appreciable number of 0.72−0.72 Mev coincidences.

E. Decay Scheme

The decay scheme which is compatible with all these observations is shown in Fig. 10. It agrees with the scheme proposed by Ajzenberg,[2] except for the presence of the 1.43-Mev transition between the 3.58- and 2.15-Mev states. Recently, Dyer, and Bird[4] have reported evidence for a state in B^{10} at 2.86 Mev. Since this state is not confirmed by the other investigations,[2,3,5] it is shown as a dotted line. We cannot, of course, rule out an 0.72−2.86 Mev cascade involving this state, on the basis of the present work. Other possible transitions to or from the state are improbable from either the coincidence work or the observed gamma-ray spectrum.[1]

Additional evidence for the existence of 1.43−1.43 Mev coincidences can be cited. The spectra in Figs. 5, 6, and 8 establish coincidences between the 1.43-Mev gamma ray and the 2.15-, 1.02-, and 0.41-Mev gamma rays. Hence, the "upper" 1.43-Mev transition between the 3.58- and 2.15-Mev states is well established. One may, however, consider the consequences of eliminating the "lower" 1.43-Mev transition between the 2.15- and 0.72-Mev states. Reference to the decay scheme in Fig. 10 shows that in that case the 1.43-Mev radiation should be equally strongly in coincidence with 0.41- and 0.72-Mev radiation. That this is not the case can be seen from Figs. 6 and 8. It can be ruled out not only on the basis of the relative efficiency of counting 0.41- and 0.72-Mev radiation, but also by comparing the 1.43-Mev coincidence curve with the 1.02-Mev curve in Fig. 8.

Among the five states shown by solid lines, there are only two possible transitions which have escaped detection: the 1.84-Mev transition between the 3.58- and 1.74-Mev states, and the 1.74-Mev transition from the latter state to ground. With spin and parity assignments of 3^+, 1^+, 0^+, 1^+, and 2^+ for these five states taken in ascending order,[2,5,9] the observed transitions are all of type $M1$ except for the 2.15- and 0.72-Mev radiations, which are $E2$. The latter transition is not in competition with any other radiation. The unobserved 1.84- and 1.74-Mev transitions are $E2$ and $M3$, respectively. The above assignments, therefore, are in reasonable agreement with the decay scheme.

V. ANGULAR CORRELATIONS

With the experimental arrangement described above, it was possible to obtain some information on angular correlations for various channel settings of the two counters. One counter was fixed at 90° to the beam direction, while the other counter was rotated in the plane containing the first counter and the beam. Each channel setting was selected so as to maximize the response from a particular gamma ray. The experimental arrangement and equipment were tested from time to time by measuring the well-established correlation between the Co^{60} gamma rays.[10]

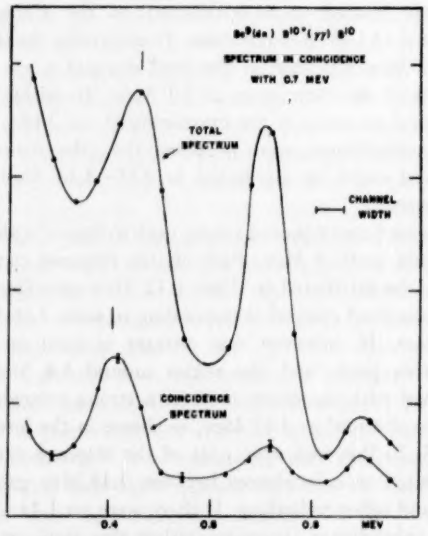

FIG. 9. Total spectrum and coincidence spectrum with the fixed channel set on the 0.72-Mev peak. The lowest peak in the total spectrum is a mixture of 0.41-, 0.48-, and 0.51-Mev radiations. Of these the coincidence spectrum selects only the 0.41-Mev gamma ray.

[9] H. T. Richards, University of Pittsburgh Conference on Medium Energy Nuclear Physics, June, 1952 (unpublished).
[10] E. L. Brady and M. Deutsch, Phys. Rev. 74, 1541 (1948).

The channel settings investigated are listed in Table I. For several of the gamma-ray pairs, the measurements were made first with one gamma-ray direction fixed and the second direction varying, and then with the roles of the gamma rays interchanged. In general different correlations will be observed in these two cases if the correlations are a function also of the beam direction. To within the accuracy of the measurements, significant differences were not observed in these cases.

In the angular data, no evidence was obtained for terms in the correlation functions higher than $\cos^2\theta$. Accordingly, after applying the necessary geometric corrections, a least square fit to each set of data was obtained with a function of the type $1+A_2\cos^2\theta$, where θ is the angle between the two gamma-ray directions. As can be seen from the table, the observed anisotropy in each case was not large, and the coefficients have not been corrected for the finite apertures of the detectors. Corrections arising from the motion of the radiating B^{10} nuclei are of the order of 1 percent or less and have not been included.

The 2.86−0.72 Mev pair is well isolated experimentally from other coincident radiations. With spin assignments of 2–1–3 to the participating states, a value of $A_2\simeq-0.08$ can be obtained theoretically

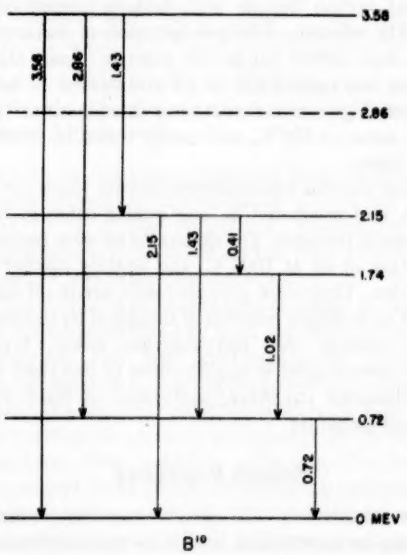

FIG. 10. The decay scheme in B^{10} which is compatible with the coincidence measurements.

TABLE I. Angular correlation coefficients. The first column indicates the channel setting of the counter fixed at 90° to the deuteron beam. The second column gives the channel setting of the other counter rotating in the plane containing the first counter and the beam. A_2 is the measured coefficient in the correlation function $1+A_2\cos^2\theta$, where θ is the angle between the counters. The errors include not only the statistical uncertainty, but also an estimate of the uncertainty arising from other sources.

Channel settings		
Fixed (Mev)	Rotating (Mev)	A_2
2.86	0.72	−0.08±0.05
0.72	2.86	−0.07±0.05
1.43	0.72	−0.08±0.07
0.72	1.43	−0.14±0.07
1.02	0.72	−0.09±0.05
0.72	1.02	−0.10±0.05
1.43	0.41	−0.13±0.07
0.41	1.02	−0.06±0.05
0.41	0.72	−0.03±0.05

if the 2.86-Mev transition is a mixture of $M1$ and $E2$ radiation. For pure $M1$ radiation, the theoretical coefficient is −0.01. For a 0–1–3 assignment one obtains $A_2=-0.10$ uniquely.

The 1.43−0.72 Mev and 1.02−0.72 Mev measurements both give coefficients about equal to −0.10. Since the former measurement provides a rough estimate of the effect of the background correlation in the latter observation, it may be concluded that the coefficient for the 1.02−0.72 Mev cascade is itself not greatly different from the measured value. The 1.43−0.72 process is complex, involving as many as three separate cascades (see Fig. 10), and the experimental measurement includes also some 2.86−0.72 Mev coincidences. For the 1.02−0.72 Mev process, however, a value of $A_2=-0.10$ is expected with the spin assignments of 0–1–3.

The final measurements on the 0.41−1.43, 0.41−1.02, and 0.41−0.72 Mev settings may be discussed on the basis of Figs. 8 and 9. In the first measurement, the coincidences are due chiefly to the 0.72−1.43 Mev process, and the coefficient obtained is not inconsistent with the value found for the 0.72−1.43 Mev setting. In the other two measurements, on the other hand, the value of A_2 is reduced. It can be seen from Figs. 8 and 9 that in both these cases the coincidences involving the 0.41-Mev gamma comprise at least 50 percent of the observed yield. The smaller values found for A_2, therefore, are consistent with the fact that both the 0.41−1.02 and 0.41−0.72 Mev correlations should be isotropic, since they involve the 1.74-Mev state, with zero spin, as an intermediate state.

Thermal Neutron Capture Cross Section of Carbon-13

G. R. HENNIG
Chemistry Division, Argonne National Laboratory, Lemont, Illinois
(Received March 22, 1954)

The thermal neutron capture cross section of C^{13} has been determined from the amount of C^{14} formed in pile-irradiated samples of graphite, barium carbonate, and carbon dioxide. Because of the impurity reaction, $N^{14}(n,p)C^{14}$, of comparatively high cross section, the results were consistent only when samples were used which were enriched in C^{13}.

The average isotopic cross section determined for the enriched samples was 1.4 ± 0.2 millibarns. The final value of the cross section in these samples corrected for the estimated residual nitrogen impurity is 0.9 ± 0.2 millibarn.

INTRODUCTION

THE total cross section of carbon for the capture of thermal neutrons has been reported[1] as 4.5 to 4.9 millibarns. The method used to determine this value does not distinguish between C^{12}, C^{13}, or residual absorption. The present investigation has been carried out to determine the extent to which this cross section is due to neutron capture by C^{13}.[2] The method entailed the irradiation of carbon-containing samples with moderated pile neutrons and the radiochemical determination of the yield of C^{14}. Extreme care was necessary to minimize the spurious production of C^{14} from nitrogen impurities by the reaction $N^{14}(n,p)C^{14}$. To ascertain the most favorable conditions for reducing this nitrogen contamination, the carbon was irradiated in several chemical forms such as graphite, barium carbonate, and carbon dioxide. Furthermore, samples were prepared in which the C^{13} isotopic concentration had been artificially enhanced to increase the yield of C^{14}. These enriched samples had to be analyzed for C^{14} even before irradiation since C^{14} is present in many natural sources of carbon dioxide and becomes concentrated even more than C^{13} during the isotope enrichment process.[3]

The samples were irradiated in the Argonne CP-3 heavy water moderated pile. The slow neutron flux was estimated in most cases by placing lead nitrate samples adjacent to the carbon samples during irradiation and determining the C^{14} produced from the nitrogen in these monitors.

[1] National Bureau of Standards Nuclear Data Group, Natl. Bur. Standards (U. S.) Circ. No. 499 (U. S. Government Printing Office, Washington, D. C., 1950).

[2] In a recent compilation of cross sections [D. J. Hughes *et al.*, U. S. Atomic Energy Commission Report AECU-2040 (Technical Information Service, Department of Commerce, Washington, D. C., 1952).], a value of 1.0 ± 0.3 mb was included for the cross section of C^{13}. It is believed that this compilation quoted the results of the determination discussed herein. This value was reported by the author in an Argonne National Laboratory Report ANL-4345, October 11, 1949 (unpublished). The difference between the earlier value of 1.0 ± 0.3 mb and the 0.9 ± 0.2 mb value reported in the present paper is due merely to the use of a more proper method of weighting the individual determinations.

[3] Anderson, Libby, Weinhouse, Reid, Kirschenbaum, and Grosse, Science **105**, 576 (1947).

EXPERIMENTAL PROCEDURES

Sample Preparation

High-purity graphite was heated in quartz tubes to 1000°C for times up to 24 hours. The samples were evacuated during this heat treatment, and were sealed into the same quartz tubes after cooling.

Samples of a $BaO-BaCO_3$ mixture were prepared from Baker analyzed barium oxide which had been degassed in quartz tubes for three hours at 900°C in vacuo. This material was reacted with twice-sublimed carbon dioxide at 400°C for 24 hours.

Barium carbonate was prepared by reacting twice-sublimed carbon dioxide with boiled, filtered barium hydroxide solution. The precipitation of barium carbonate was carried out in the absence of air, and the filtration was carried out in an atmosphere of helium. The filtered barium carbonate was dried in air at 120°C, then *in vacuo* at 500°C, and finally sealed in evacuated quartz tubes.

Carbon dioxide was sublimed several times for purification, and irradiated in long quartz tubes at nearly atmospheric pressure. The quartz tubes were pretreated by heating in air at 1000°C, and heating further after evacuation. They were provided with break-off seals at one end to facilitate removal of the gas after irradiation.

Lead nitrate was recrystallized twice. Weighed samples were placed in quartz tubes of less than 4-mm inside diameter (to insure uniformity of flux), evacuated, and sealed off.

Sample Processing

After irradiation, the quartz capsules containing solid samples were boiled in alkaline permanganate and aqua regia to remove externally deposited C^{14} and placed in a breaking device which permitted fracturing the capsules in an evacuated container. For carbonate samples, the broken fragments of the quartz tube and its contents were allowed to drop into the bottom of the breaking device which contained concentrated sulfuric acid. Reaction with the acid released carbon dioxide. For the lead nitrate samples, water and carrier carbon dioxide had been frozen into the breaking device.

On warming, these samples dissolved in the water and released C^{14} as carbon dioxide.

Graphite samples were sometimes opened in the same breaking device and burned directly in it, but this procedure was found unnecessary. Usually, the graphite samples were opened in air and transferred rapidly to a combustion tube. They were burned in oxygen and the combustion gases passed over copper oxide and lead chromate at 600°C.

Samples irradiated as carbon dioxide were frozen in their quartz container after irradiation, the container was sealed to a vacuum line and opened via the break-off seal. A small amount of carbon monoxide was added to the sample and the gases separated into carbon monoxide and carbon dioxide. It had been anticipated that some of the C^{14} formed would show up as carbon monoxide rather than carbon dioxide. A separation was accomplished by passing the gas through two traps cooled with liquid nitrogen, each containing sintered glass disks. Carbon dioxide was thus removed and remained in the traps. The carbon monoxide was then passed over hot copper oxide and the resulting carbon dioxide was condensed in a third trap. Finally the empty quartz tube in which the sample had been irradiated was filled with oxygen and carrier carbon dioxide and heated at 1000°C to oxidize substances, presumably C_3O_2 polymers, which had formed on the wall. This fraction is labeled "C_3O_2 (wall)" in Table III.

All the carbon dioxide samples obtained in this way except the flux monitors had to be converted to methane for counting. This was accomplished by adding an excess of hydrogen and cycling over a ruthenium catalyst.[4] The catalytic reduction is fairly rapid at 350°C but requires small amounts of moisture in the reacting gas mixture. After complete reduction, the methane was separated from excess hydrogen by palladium or by copper oxide at 400°C and dried. The methane was then condensed with liquid nitrogen and purified further by pumping from the trap in which it was condensed at −196°C. The methane obtained in this way was nearly always found to contain radioactive impurities. This was established by counting the methane, and subsequently reoxidizing it to carbon dioxide over copper oxide at 900°C, drying the carbon dioxide and reducing it again. Such a reconversion cycle nearly always reduced the counting rate of the methane. The process was repeated until a constant counting rate was reached. The number of such reduction cycles for each sample are listed in Tables I to III under the heading of "times converted."

The radioactive impurity could not be eliminated by pretreating the carbon dioxide prior to reduction. Repeated passages over copper oxide and lead chromate at 600°C followed by freezing and subliming at −78°C did not eliminate the impurity. However, an efficient method for removing the spurious activity was found just in time to be adopted for the last sample examined (D-32, see Table III). The sample of carbon dioxide

TABLE I. C^{13} cross section determined from a $BaO-BaCO_3$ sample.

Sample	Fraction C^{13} in carbon	Total times converted	Integral neutron flux[a] (10^{17} *nvt*)	Count rate (cpm/ 150 mm)	σ_a (cm²)	σ_i (cm²)
D-17	0.4532	1	0	297 ±5		
		2	4.94	860 ±7		
		3		854 ±6	2.06×10^{-39}	1.88×10^{-37}

[a] Estimated from pile power.

TABLE II. C^{13} cross section determined from several $BaCO_3$ samples.

Sample	Fraction C^{13} in carbon	Total times converted	Integral neutron flux (10^{17} *nvt*)	Count rate (cpm/ 150 mm)	σ_a (10^{-39} cm²)	σ_i (10^{-37} cm²)
D-1	0.011	1	4.69	176 ±2	28.4	25.8
D-21	0.011	1	7.15	1715 ±16		
		2		719 ±11		
		3		240 ±9	25.5	23.2
D-24	0.011	1	5.10	386 ±10		
		2		119 ±9		
		3		107 ±12	16.0	14.5
D-26[a]	0.0622	4	6.89	392 ±41		
		5		354 ±12	6.86	6.26
D-23[b]	0.4532	3	0	854 ±6		
		4	8.52	2930 ±13		
		5		2000 ±28		
		6		1710 ±10	1.85	1.68
D-28	0.53	1	0	322 ±4		
		2	9.73	1695 ±12		
		3		1068 ±6		
		4		1029 ±8	1.13	1.03

[a] This sample had been enriched from petroleum methane, which was assumed free of C^{14} because of its age. Therefore no pre-irradiation measurements of C^{14} content was made.
[b] This sample had previously been irradiated as barium oxide-barium carbonate (sample D-17, Table I).

TABLE III. C^{13} cross section determined from CO_2 samples.

Sample	Gas fraction	Fraction C^{13} in carbon	Total times converted	Integral neutron flux (10^{17} *nvt*)	Count rate (cpm/ 150 mm)	σ_a (10^{-39} cm²)	σ_i (10^{-37} cm²)
D-31	CO_2	0.53	2	0	322 ±4		
	CO_2	0.53	3	6.74	14740 ±10		
			4		697 ±11		
			5		621 ±3		
			6		607 ±6	0.66	
	CO	0.011[a]	1		258 ±7		
			2		113 ±6	0.26	
	C_3O_2 (wall)					(0.45)	
	Total					1.37	1.25
D-32	CO_2	0.53	2	0	322 ±4		
	CO_2	0.53	3	5.97	763 ±6		
					762 ±4	1.15	
	CO	0.011[a]	1		51 ±5	0.13	
	C_3O_2 (wall)	0.011[a]	1		199 ±6		
			2		171 ±6	0.45	
			3		182 ±4		
	Total					1.73	1.57

[a] Virtually all of this sample consisted of carrier carbon of normal C^{13} abundance, and had not been converted previously.

[4] G. R. Hennig, Argonne National Laboratory Report ANL-4080, January, 1948 (unpublished).

was precipitated with barium hydroxide in the presence of small amounts of potassium permanganate. The barium carbonate formed was filtered, dried, and reacted with concentrated sulfuric acid to regenerate the carbon dioxide. This carbon dioxide did not change its counting rate on repeated reduction and reoxidation cycles.

The source of the spurious activity which was removed in this laborious procedure is still doubtful. It was probably a soft beta emitter since it did not penetrate 2 mg/cm² of mica. Most of the radioactive impurity followed inert gases when they were added as carriers to the carbon dioxide and subsequently separated by freezing the carbon dioxide. The amount of contaminating activity increased with the size of the quartz irradiation container.

Counting Procedures[5]

Samples containing concentrations of C^{14} exceeding 10^{-7} mole per mole of carbon (e.g., flux monitors) were counted as carbon dioxide in a glass cup sealed around the window of an end-window counter. The pressure of the carbon dioxide in the counting cup did not exceed 300 mm Hg, as determined with a mercury manometer. Standardization of the apparatus was accomplished using a sample which had been accurately diluted from a mass spectrometrically analyzed sample of $C^{14}O_2$. The standardization was repeated periodically. Low concentrations of C^{14} were measured at much higher efficiency by counting as methane in internal counters. The counters, 1279 cc in volume, 23.5 inches in length, and 2 inches in diameter, were made of brass with a 0.003- inch tungsten center wire. The gas was counted at a pressure of 150 mm Hg whenever possible. A Neher-Harper quenching circuit was used. Inasmuch as the counting efficiency depended somewhat on the methane pressure and on the counting rate, appropriate correction factors were determined by standardization with a mass spectrometrically analyzed sample of C^{14}. The counting rates of the samples were of the order of and often less than the background of the heavily shielded counter. They were therefore counted for many hours or even days. The counting rate was recorded continuously to detect spuriously high counts due to atmospheric disturbances or to the proximity of sources of penetrating radiation.

Flux Determination

Carbon dioxide from the lead nitrate samples was counted in aliquot amounts. From the counting rate and the standardization of the counter, the concentration of C^{14} in the sample was calculated and was then multiplied by the number of moles of carbon dioxide, pv/RT, to obtain N, the number of moles of C^{14} formed.

[5] It should be noted that these experiments were carried out in 1948 and 1949. Therefore scintillation and other counting methods which would now be considered for these experiments were not employed.

The integral neutron flux (nvt) was calculated from the equation

$$nvt = (N \times M)/(1.78 \times 10^{-24} \times W \times 2),$$

where $M = 331.2$ is the molecular weight of the lead nitrate monitor, 1.78×10^{-24} cm² the cross section of nitrogen,[2] and W the weight of the monitor.

When samples D-31 and D-32 of carbon dioxide gas were irradiated, the containers were so long that the flux varied considerably along their length. In these cases small disks of aluminum were attached to the container at six-inch intervals and a lead nitrate monitor was attached to one end. The aluminum disks were counted on an end-window counter and the average of their counting rates was divided by the count rate of the disk adjacent to the monitor. This ratio multiplied by the flux detected by the monitor was used for the average flux in the sample. The monitor for sample D-32 broke prematurely and the flux for this sample was calculated by comparing the activity of the aluminum disks with the activity of the aluminum disks from sample D-31, which had been monitored.

For a number of irradiations in which no monitor was used the flux was estimated from the known pile power in kilowatt hours and from the relation, observed for a number of monitored samples, that the flux in the sample location used in CP-3 was 1.8×10^{13} neutrons/cm² per kw-hr with a probable error of 10 percent.

Cross-Section Calculations

The element cross section (for C^{12} and C^{13} in normal abundance), σ_e, in Tables I to III was calculated from the equation:

$$\sigma_e = \frac{C \times R \times T}{k \times nvt \times pv \times A \times e} \frac{0.011}{f},$$

where C = counts min^{-1}, R = gas constant (cc mm °K^{-1} mole^{-1}), T = temperature (°K), k = decay constant (min^{-1}), nvt = integral neutron flux (neutrons cm^{-2}), p = pressure of the counter gas (mm Hg), v = volume of counter (cc), A = Avogadro's number, e = efficiency of counting, and f = fraction of C^{13} in the carbon of the sample. Since e was determined from a sample of known C^{14} concentration, the factor e is proportional to $1/k$ and the calculated value of σ_e is independent of the decay constant of C^{14}. The isotopic cross section σ_i for C^{13} was obtained from the relationship

$$\sigma_i = \sigma_e/0.011.$$

RESULTS

Analysis of the irradiated graphite samples for C^{14} yielded results which were so inconsistent that they have not been included in the present report. However, most of the values for the isotopic cross section determined this way fell below 2.5 mb, the lowest being 1.2 mb. It is certain that the results for graphite are

high because trace amounts of nitrogen are known to remain even after graphite has been heated to 1000°C.[6]

Several $BaO-BaCO_3$ samples were prepared from carbon dioxide of normal C^{13} abundance but they are not reported here because their counting rates after irradiation and conversion to methane were very high and quite inconsistent, due to the presence of the radioactive impurity mentioned earlier. A satisfactory procedure for removal of the impurities by repeated reconversion had not been perfected at the time of this analysis. However, one enriched sample (D-17) was subjected to the purification procedure and was reconverted a sufficient number of times to reach a constant counting rate. The results of this measurement are reported in Table I.

Results obtained from barium carbonate samples are given in Table II. Analyses of enriched samples irradiated as carbon dioxide are collected in Table III. The so-called "C_3O_2 (wall)" fraction from sample D-31 was lost during reduction. As a first approximation the value for the wall fraction of sample D-32 was also used for D-31.

DISCUSSION

Inspection of Tables I to III reveals that the cross section determined from unenriched C^{13} samples varies much more than the probable error of the individual determinations. Samples highly enriched in C^{13} agree much more closely and an average cross section was calculated from them as shown in Table IV. The

TABLE IV. Average C^{13} cross section. (Samples enriched in C^{13}).

Sample	σ_a (10^{-29} cm²)	(Percent) error	
		Est. flux	Counting rate
D-17	2.06	10	2
D-23	1.85	5	2
D-28	1.13	5	2
D-31	1.37	5	11
D-32	1.73	5	14
Average	1.54		

average cross section was arrived at by weighting each determination by the inverse square of its probable error. The errors in the individual determinations are listed in the third and fourth columns. The flux determination is in error by less than 5 percent if a monitor was used, and about 10 percent if the flux was calculated from the pile power output. The errors due to counting are the sums of all pertinent errors in statistics; i.e., $D_1+D_2+2D_B$, where D_1 is the standard deviation of the count before irradiation, D_2 after irradiation, and D_B the standard deviation of the background count. Combining the individual standard deviations in Table IV, one obtains a standard deviation of 2.1 microbarns. Thus the experimental value for the contribution of the C^{13} cross section to the cross section of the element is $1.54\pm0.21\times10^{-29}$ cm².

[6] C. L. Mantell, *Industrial Carbon* (D. Van Nostrand Company, Inc. New York, 1946), p. 361.

TABLE V. Cross sections of enriched barium carbonate samples corrected for nitrogen impurities.

Sample	σ_a Measured (10^{-29} cm²)	σ_a Nitrogen correction (10^{-29} cm²)	σ_a Corrected (10^{-29} cm²)	Estimated probable error (10^{-29} cm²)
D-23	1.85	0.57	1.28	±0.18
D-28	1.13	0.49	0.64	±0.13
D-17	2.06	0.57	1.49	±0.27
Weighted average			0.96	±0.19

The results for the samples irradiated as barium carbonate show that these samples contained much nitrogen. The unenriched samples of barium carbonate, D-1, D-21, and D-24, give an average carbon element cross section of $2.3\pm0.5\times10^{-28}$ cm². This is so much larger than the value obtained from enriched samples that it can probably be attributed almost entirely to nitrogen. The amount of nitrogen calculated from this cross section is $2.3\times10^{-28}/\sigma_N$ atoms per molecule of $BaCO_3$, where $\sigma_N=1.78\times10^{-24}$ cm². This corresponds to 9.4 parts per million of nitrogen by weight. It can be assumed further that the method of preparation used always introduced approximately this amount of nitrogen into the barium carbonate. If then the contribution of this nitrogen is calculated for the enriched samples of barium carbonate, the corrected values listed in Table V are obtained.

The amount of nitrogen present in the gas samples D-30 and D-31 cannot be estimated.

CONCLUSIONS

In conclusion it can be stated that the experimental determination of the C^{13} contribution to the carbon element cross section resulted in an average value for enriched samples of $1.5\pm0.2\times10^{-29}$ cm², but that good evidence exists that the correct value is closer to $1.0\pm0.2\times10^{-29}$ cm², the average value of the corrected results on the enriched samples listed in Table V. These values correspond to a measured isotopic cross section for C^{13} of 1.4 ± 0.2 mb and to a corrected isotopic value of 0.9 ± 0.2 mb. It is thus apparent that the contribution of C^{13} to the total measured cross section of carbon is small.

ACKNOWLEDGMENT

The author wishes to thank Professor W. F. Libby for valuable advice and for one of the enriched C^{13} samples. The author is also indebted to A. French Kurs for her help in the counting and in the sample preparations, and to M. G. Inghram and D. Hess for mass spectrometer analyses of C^{13} samples.

Determination of Maximum Beta Energy in the Decay of P^{33}

B. Elbek, K. O. Nielsen, and O. B. Nielsen
Institute for Theoretical Physics, University of Copenhagen, Copenhagen, Denmark
(Received February 5, 1954)

The maximum energy of the β spectrum of P^{33} has been measured with sources prepared in two different ways. The first source was activated according to the method of Westermark. The second source was prepared in an isotope separator. The results were 252 ± 5 kev and 250 ± 5 kev, respectively.

THE maximum energy of negatrons from the 25-day phosphorus activity, which is ascribed to P^{33} from the discussions of various possible reactions, has been determined by several authors. Sheline *et al.*[1] found $E_{max}=270\pm20$ kev and Jensen *et al.*[2] 260 ± 20 kev. These values were based upon β-spectrometer measurements, but in both cases the predominance of P^{32} in the β source complicated the experiments. More recently Westermark[3] succeeded in making P^{32} activities of high isotopic purity in piles and by absorption measurements he obtained $E_{max}=246\pm5$ kev.

The present investigation was undertaken to determine more precisely the value of E_{max} from β-spectrometer measurements by using P^{33} sources of high isotopic purity. In the first experiment the source was prepared accorcing to Westermark, and in the second experiment the electromagnetic isotope separator of Koch[4,5] was employed in the source preparation. The β-spectrometer measurements were made with the instrument of Kofoed-Hansen *et al.*[6] (transmission 10 percent, resolution 2.5 percent).

In the first experiment, 20 g of sulfur were irradiated for 4 weeks in a Harwell pile at a location close to the reflector, where the flux of 5×10^{10} neutrons/cm^2 sec is predominantly thermal. The resulting phosphorus activity was about 0.1 rutherford per g of irradiated sulfur, of which 85 percent was P^{33} and the rest P^{32}. For preparing a β source, 3 g of sulfur were dissolved in CS_2, from which it was extracted by shaking with water. The active phosphorus together with 0.1 mg of carrier was concentrated on a 150-μg/cm^2 Al foil by evaporation resulting in a source strength of 8000 dis/min. A check on the half-life showed that the content of the 87-day S^{35} was very low. Figure 1 shows the Kurie plot of the β radiation from P^{33}. The upper part of the spectrum is straight, while at lower energies the counter windows (4 mg/cm^2) introduced a distortion. The resulting maximum energy is $E_{max}=252\pm5$ kev.

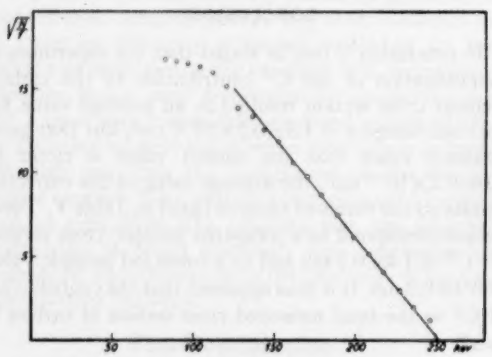

FIG. 1. Kurie plot of β radiation from P^{33}.

In the second experiment the β source was prepared in the isotope separator. To compensate for the low efficiency in the separation of phosphorus isotopes (4×10^{-4}), large starting activities were necessary. Thus, 20 g of sulfur were irradiated in the high flux at the center of the pile. The resulting phosphorus activity was a few hundred rutherford, but only 1.6 percent was due to P^{33}. For reasons given below, the active phosphorus was converted to phosphine, PH_3.[7]

Preliminary experiments demonstrated the tendency of phosphorus to form hydride ions in the source,[4,5] which would prevent the preparation of pure P^{33} samples by collecting the mass 33 beam, since $(P^{33})^+$ and $(P^{32}H)^+$ would be collected simultaneously. Most favorable conditions for collection were found by running the ion source with the gaseous compound PH_3, whereby all hydrides up to $(PH_3)^+$ were formed in large abundances; no higher hydrides, however, being observable.[8] Therefore, in the actual separation experiment, $(P^{33}H_3)^+$ was allowed to impinge on a 150-μg/cm^2 Al foil for several hours, giving a β-source strength of 5000 dis/min. This P^{33} source was, however, still contaminated with about 30 percent P^{32} (=0.2 percent of the total P^{32} activity on the collector) originating from a general background, which was possibly due to unusually high gas scattering of neighboring beams.

[1] Sheline, Holtzman, and Fan, Phys. Rev. **83**, 919 (1951).
[2] Jensen, Nichols, Clement, and Pohm, Phys. Rev. **85**, 112 (1952).
[3] T. Westermark, Phys. Rev. **88**, 573 (1952).
[4] J. Koch and B. Bendt-Nielsen, Kgl. Danske Videnskab. Selskab, Mat.-fys. Medd. **21**, No. 8 (1944).
[5] J. Koch, National Bureau of Standards Circular 522 (U. S. Government Printing Office, Washington, D. C., 1953.)
[6] Kofoed-Hansen, Lindhard, and Nielsen, Kgl. Danske Videnskab. Selskab, Mat.-fys. Medd. **25**, No. 16 (1950).
[7] After extraction with boiling nitric acid and addition of 200 mg phosphate, ordinary conversion to $Mg_2P_2O_7$ was carried out. Reduction with Mg in hydrogen yielded Mg_3P_2 which gives PH_3 with water vapor.
[8] V. Ubisch, Arkiv Fysik **2**, 517 (1951).

The assignment of the 25-day phosphorus activity to P^{33} was established beyond any doubt by the fact that the activity appeared at mass 36 ($P^{33}H_3$), but at no higher masses. The β-spectrometer investigation of this P^{33} source, in which the active atoms were distributed uniformly in a thin surface layer,[5,9] gave $E_{max}=250\pm5$ kev.

After completion of the measurements, knowledge was obtained of the latest result of Nichols *et al.*[10] who found the value 249 ± 2 kev using P^{33} resulting from neutron irradiation of enriched S^{33}.

The authors would like to express their thanks to Professor N. Bohr for the excellent working facilities, and to Dr. J. Koch for help and advice.

[9] Brostrøm, Huus, and Koch, Nature **160**, 498 (1947).

[10] R. T. Nichols and E. N. Jensen, Phys. Rev. **94**, 369 (1954).

PHYSICAL REVIEW VOLUME 95, NUMBER 1 JULY 1, 1954

Inner Bremsstrahlung in the Electron Capture Process—Ge^{71}†

BABULAL SARAF*
Bartol Research Foundation of The Franklin Institute, Swarthmore, Pennsylvania

(Received February 8, 1954)

The spectral distribution of the inner bremsstrahlung of Ge^{71} has been studied at quantum energies as low as 20 kev. It was observed that the radiation intensity at energies less than ~100 kev is much larger than is indicated by currently available theory. The absolute radiative capture probability has been measured. This latter quantity and the spectral shape are in good agreement with theoretical considerations at energies greater than ~100 kev.

THE gamma-ray continuum (inner bremsstrahlung) emitted in the course of electron capture has been under study in several laboratories. The continuous spectra of a number of different radio-nuclides have been observed, particular emphasis being placed upon obtaining an exact measurement of the energy of the spectral end point, since the disintegration energy is thus determined. The theory of the emission of inner bremsstrahlung has been given, with some restrictions and approximations, by Morrison and Schiff.[1] To obtain confirmation of the theory, most investigators have sought to demonstrate that $(N/E)^{\frac{1}{2}}$ is proportional to E (N being the number of photons per unit range of energy E), but only recently have serious efforts been made to extend comparison of theory and measurement to very low quantum energies.[2]

A source[3] of Ge^{71}, of high specific activity (30 mC/g), was obtained from the Brookhaven reactor (exposure time 15 days). After decay of Ge^{77}, As^{77} was removed by distillation of $GeCl_4$ which was converted to GeO_2. A source of uniform thickness, ~10 mg/cm², and 10 cm² in area was prepared by mixing GeO_2 powder in Formvar solution and making a film.

The spectrum was measured by using a crystal of NaI(Tl) having a diameter of 3.5 cm and thickness

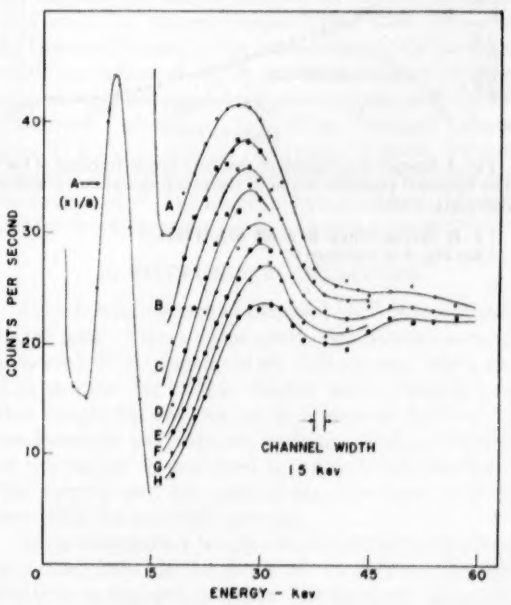

FIG. 1. Low-energy region of the continuous gamma-ray spectrum of Ge^{71} observed through various amounts of absorber. Curve *A* was obtained with 200 mg/cm² of Al and 100 mg/cm² of MgO intervening; Curves *B* through *G* with addition of successive copper absorbers each of the thickness 5 mg/cm²; Curve *H* with total thickness 40 mg/cm² of additional Cu.

† Assisted by the joint program of the U. S. Office of Naval Research and the U. S. Atomic Energy Commission.

* Research Fellow, Bartol; on leave of absence from Agra College, Agra, India.

[1] P. Morrison and L. I. Schiff, Phys. Rev. **58**, 24 (1940).

[2] The writer has previously studied the low-energy region of Cs^{131} [Phys. Rev. **94**, 642 (1954)], A^{37}, and Fe^{55} where significant deviations from theory have been noted of the same nature as those described in this paper. Subsequent discussions with Dr. Franco Rasetti have revealed that he and his associates have noted similar effects in Fe^{55}. The measurements are as yet unpublished. *Note added in proof.*—See Madansky and Rasetti, Phys. Rev. **94**, 407 (1954).

[3] Saraf, Varma, and Mandeville, Phys. Rev. **91**, 1216 (1953).

of 3.5 cm. The source to crystal distance was 1.25 cm. The crystal assembly introduced an absorption of 200 mg/cm² of Al and 100 mg/cm² of MgO. These intervening materials also served as a filter to reduce the intensity of the K x-radiation of Ga. The residual x-ray peak is shown as part of curve A in Fig. 1. The experimentally observed spectrum was corrected to take into account self-absorption in the source, absorption in Al and MgO, finite energy resolution[4] detection efficiency, and escape of x-rays of iodine. Any correction for Compton effect is negligible[5] for the energies under consideration (0 to 200 kev). The energy resolution (full width at half-maximum) was 25 percent for x-rays of Xe of energy 30 kev.

To correct for initial absorption, the low-energy portion of the spectrum below 60 kev where absorption is greatest, was observed through various thicknesses of copper. The counting rate at each channel setting is plotted as a function of copper absorber thickness in the curves of Fig. 1. In a separate figure not shown, a semilog plot of the counting rate in each channel was extrapolated to zero absorber thickness. The experimentally observed curve, corrected in all aspects, is shown in Fig. 2 where it is seen to differ considerably from the theoretically expected result. The indicated probable errors include estimates of systematic errors in the various corrections and far exceed the actual statistical probable errors. The ordinates of the experimental curve of Fig. 2 were determined in the absolute sense by dissolving the GeO_2 source in NaOH and measuring the absolute counting rate of the gallium x-rays of a known volumetric subdivision in a scintillation spectrometer. Agreement of the curves at high energies is fortuitous, since the absolute source strength determination could be in error by as much as thirty percent.

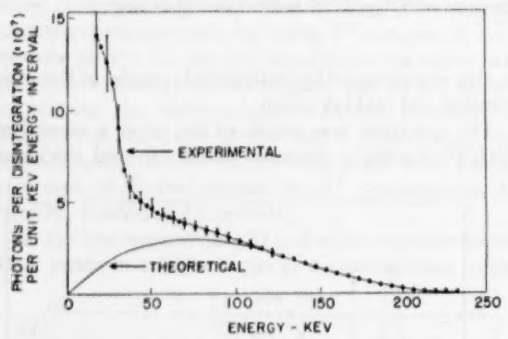

FIG. 2. Energy distribution of the inner bremsstrahlung of Ge^{71}. The indicated probable errors of the experimental curve include systematic errors.

[4] T. B. Novey, Phys. Rev. **89**, 672 (1953).
[5] See Fig. 5 of reference 2.

Cutkosky[6] has calculated the radiation probability associated with p electrons of the L shell. His expression is

$$dp_{LII}=\frac{\alpha^3Z^2}{32\pi}\frac{[3m^2-2(m-w)^2]}{4m^2w}\left(1-\frac{w}{w_0}\right)^2dw,$$

where dp_{LII} is the probability of emission of a bremsstrahlung of energy between w and $w+dw$. This quantity becomes equal to dp_K at ~40 kev. However, Marshak's formula[7] shows that p-electron capture has only about 0.2 percent of the probability of K-electron capture. It may be suggested that the additional radiation observed at low energies is bremsstrahlung associated with the magnetic moment of the neutrino. However, theoretical calculations of expected intensity of this effect are not sufficiently accurate for comparison.

The writer wishes to express his appreciation to Dr. F. R. Metzger and Dr. C. E. Mandeville for discussions in connection with this problem, and to Dr. W. F. G. Swann for his continued interest.

[6] R. E. Cutkosky, Ph.D. thesis, Carnegie Institute of Technology, 1953 (unpublished).
[7] R. A. Marshak, Phys. Rev. **61**, 431 (1942).

Gamma Radiation from Magnesium-26 under Proton Bombardment*

LEONARD N. RUSSELL,† WARREN E. TAYLOR,‡ AND JOHN N. COOPER
The Ohio State University, Columbus, Ohio

(Received March 31, 1954)

Thin targets of Mg^{26} were bombarded with protons from a Van de Graaff generator. Fifteen well-defined resonance peaks were found in the proton energy region between 300 and 1500 kev. These resonances were attributed to the reaction $Mg^{26}(p,\gamma)Al^{27}$. The maxima of the resonances occur at proton energies of 343, 450, 662, 720, 813, 840, 954, 992, 1015, 1056, 1172, 1255, 1295, 1425, and 1464 kev. Measurement of the gamma-ray energies from some of the stronger resonances indicate that the compound nuclei do not in most cases decay to the ground state by a single transition.

I. INTRODUCTION

IN 1939 Curran and Strothers[1] bombarded relatively thin targets of magnesium with protons having energies up to 1000 kev. Although their resolution was rather poor by modern standards, they detected several gamma-ray resonance peaks for protons in this energy region. The three proton capture reactions which are energetically possible in natural magnesium for protons of low (under 2 Mev) energy are:

$$(1)\quad Mg^{24}+H^1\rightarrow Al^{25*}\rightarrow \begin{cases} Al^{25}+h\nu \\ \searrow \\ Mg^{25}+\beta^+, \end{cases}$$

$$(2)\quad Mg^{25}+H^1\rightarrow Al^{26*}\rightarrow \begin{cases} Al^{26}+h\nu \\ \searrow \\ Mg^{26}+\beta^+, \end{cases}$$

$$(3)\quad Mg^{26}+H^1\rightarrow Al^{27*}\rightarrow Al^{27}+h\nu.$$

By measuring the positron yield as a function of proton energy as well as the gamma-ray yield, Curran and Strothers were able to assign gamma-ray resonances unaccompanied by positron activity to proton capture in Mg^{26}. All resonance peaks at which both gamma rays and positrons were emitted were attributed to proton capture in Mg^{25}, because the unstable isotope Al^{25} was unknown at that time and because all the half-life measurements for the positron activity gave values near to the one accepted for Al^{26}.

Hole, Holtzmark, and Tangen[2] bombarded thin targets of natural magnesium with protons in the energy region between 200 and 500 kev. Only gamma-ray resonances were measured and eight peaks were observed, all of which can now be shown to be associated with proton capture in Mg^{24} and Mg^{26}. In 1946 Tangen[3] restudied the proton capture reactions in this energy region with much improved techniques. He found several additional resonances and was able to assign each resonance to capture in the correct magnesium isotope. In particular, he reported resonances in Mg^{26} at proton energies of 290, 314, 336, 383, 430, 451, and 494 kev. In 1953 Hunt and Jones[4] observed and measured the half-widths of the $Mg^{26}(p,\gamma)$ resonances excited by protons with energies between 250 and 500 kev. They reported peaks at 314.8, 338.5, 389.4, 436.5, 454.2, and 484.0 kev.

A survey of the gamma-ray yield from proton capture in magnesium targets was made for proton energies between 700 and 1600 kev by Cooper, Taylor, Harris, and Grove.[5] They found a number of resonances, some of them overlapping. The availability of separated isotopes of magnesium suggested the possibiltiy of resolving the complex spectrum by proton bombardments of the separated isotopes. A substantial increase in yield could be expected for Mg^{25} and Mg^{26}, which are present in natural magnesium to the extent of 11.5 and 11.1 percent, respectively. Upon allocation by Isotopes Division of the Atomic Energy Commission, small quantities of highly enriched isotopes of magnesium were obtained from the Carbide and Carbon Chemicals Corporation, Oak Ridge National Laboratory. It is the purpose of this paper to report the data obtained by the proton bombardment of thin targets made from Mg^{26}. The results of bombardment of targets of Mg^{25} have been presented in an earlier paper.[6]

II. EXPERIMENTAL PROCEDURE

Fifty-five milligrams of enriched Mg^{26} were obtained in the form of magnesium oxide. The isotopes analysis indicated 95.91 percent Mg^{26}, 1.56 percent Mg^{25}, and 2.53 percent Mg^{24}. Thin targets were prepared from this sample by evaporation in a vacuum followed by condensation on tantalum backings. The preparation of the targets is described in more detail elsewhere.[7] The targets used for most of the data were 10 to 15 kev thick for one-Mev protons.

These targets were bombarded by protons which were separated from the ion beam of the electrostatic generator by a magnetic analyzer. The energy of the proton impinging on the target was determined by reading

* Supported in part by the U. S. Atomic Energy Commission through a contract with The Ohio State University Research Foundation.

† Now at Mound Laboratory, Miamisburg, Ohio.

‡ Now at Sandia Corporation, Albuquerque, New Mexico.

[1] S. C. Curran and J. E. Strothers, Proc. Roy. Soc. (London) A172, 72 (1939).

[2] Hole, Holtzmark, and Tangen, Naturwiss. 28, 399 (1940).

[3] R. Tangen, Kgl. Norske Videnskab. Selskabs, Forh. Skrifter No. 1. (1946).

[4] S. E. Hunt and W. M. Jones, Phys. Rev. 89, 1283 (1953).

[5] Cooper, Taylor, Harris, and Grove, Phys. Rev. 80, 131 (1950).

[6] Taylor, Russell and Cooper, Phys. Rev. 93, 1056 (1954).

[7] Russell, Taylor, and Cooper, Revs. Sci. Instr. 23, 764 (1952).

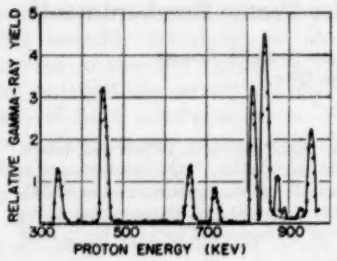

FIG. 1. The relative gamma-ray yield per incident proton from the $Mg^{26}(p,\gamma)Al^{27}$ reaction for protons with energies from 300 to 1000 kev. The peaks at 874, 890, and 935 kev are due to proton capture in a fluorine contamination in the target.

the current flowing in the coils of the analyzing magnet. This magnet current had been calibrated in terms of proton energy by use of the well-known resonance in lithium at 440 kev, and the resonances in fluorine at 486, 669, 873.5, 935.5, 1290, 1355, and 1381 kev as reported by Hornyak, Lauritsen, Morrison, and Fowler[8]

The target to be bombarded was placed at the end of a Faraday cage so that the charge carried by the proton beam could be determined. A thin-walled Geiger-Müller tube was used to detect the gamma rays emitted from the target. The gamma-ray yield per incident proton was then plotted as a function of the proton energy.

III. RESONANCES IN THE $Mg^{26}(p,\gamma)Al^{27}$ REACTION

The relative gamma-ray yield is shown as a function of the proton energy in Figs. 1 and 2. Figure 1 shows the proton energy region between 300 and 1000 kev, and Fig. 2 the region between 900 and 1600 kev. In this energy range there are fifteen resonance peaks attributed to proton capture in Mg^{26}. The proton energies corresponding to these resonance levels are 343, 450, 662, 720, 813, 840, 954, 992, 1015, 1056, 1172, 1255, 1295, 1425, and 1464 kev. The absolute energy value quoted for each of the fifteen resonance is probably correct within 10 kev, and the relative spacing

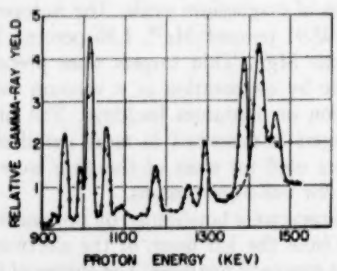

FIG. 2. The relative gamma-ray yield per incident proton from the $Mg^{26}(p,\gamma)Al^{27}$ reaction for protons with energies between 900 and 1600 kev. The peaks at 935 and 1379 kev are due to proton capture in a fluorine contamination in the target.

[8] Hornyak, Lauritsen, Morrison, and Fowler, Rev. Modern Phys. **22**, 291 (1950).

is believed to be right within 5 kev. The peaks at 343 and 450 kev agree with those reported by Tangen[3] and by Hunt and Jones[4] within the predicted errors. No effort was made to reexamine the very weak peaks under 500 kev which they reported.

In addition to the fifteen resonance peaks attributed to Mg^{26} there are shown resonances at 874, 890, 935, and 1379 kev which arise from proton capture in fluorine contamination on the target. These resonances are present in data taken with each of the three magnesium isotopes. The exact origin of this fluorine contamination is not certain.

The cross section of Mg^{26} for proton capture is low over the range of proton energies studied. Calculations for the 450-kev resonance indicate the cross section is approximately 5×10^{-27} cm^2.

IV. EXCITED STATES IN Al^{27}

The Q value for the $Mg^{26}(p,\gamma)Al^{27}$ reaction is 8.262 Mev according to the mass values presented by Li.[9] On the basis of this Q value the excitation levels in Al^{27} corresponding to the 15 proton resonance energies are listed in Table I.

TABLE I. Excitation levels in Al^{27} as determined by the proton energies at resonances.

Proton energy (kev)	Excitation energy (Mev)	Proton energy (kev)	Excitation energy (Mev)
343	8.592	1015	9.239
450	8.695	1056	9.278
662	8.899	1172	9.392
720	8.955	1255	9.471
813	9.046	1295	9.510
840	9.071	1425	9.634
954	9.180	1464	9.672
992	9.217		

In order to determine whether the excited Al^{27} nuclei went directly to the ground state by a single transition, efforts were made to measure the energy of the gamma rays emitted by two separate methods. The first method consisted of the measurement of the attenuation of the gamma rays in known thicknesses of lead and copper. The second method was the coincidence technique described by Fowler, Lauritsen, and Lauritsen.[10] Measurements were made at the 450, 813, 840, 954, and 1015-kev resonances and in every case the results indicated that the predominate mode of decay was not by a single transition to the ground state.

The indicated gamma-ray energies from resonance to resonance varied between 5.3 and 7.3 Mev. In view of the very large number[11,12] of known energy levels of

[9] C. Li, Phys. Rev. **88**, 1038 (1952).

[10] Fowler, Lauritsen, and Lauritsen, Revs. Modern Phys. **20**, 236 (1948).

[11] Reilly, Allen, Arthur, Bender, Ely, and Hausman, Phys. Rev. **86**, 857 (1952), and references.

[12] H. F. Stoddard and H. E. Gove, Phys. Rev. **87**, 262 (1952), and references.

Al^{27} below 6 Mev, it is clear that absorption techniques are not likely to be adequate to establish the decay scheme from the highly excited states produced by proton capture in Mg^{26}.

Casson[13] has measured the gamma-ray energies at the 336- and 314-kev resonances with a scintillation spectrometer. At the 336-kev resonance he found 5.8- and 2.8-Mev gamma rays, while the gamma rays from the 314-kev resonance had an energy of about 4.3 Mev. Our measurement at the 450-kev level indicated a 6.0-Mev gamma ray, a value in good agreement with the 6.2 Mev reported by Tangen.[3] These values are compatible with the possibility of an initial transition to the well-known 2.8-Mev level.

[13] H. Casson, Phys. Rev. 89, 809 (1953).

V. ACKNOWLEDGMENTS

The authors are indebted to Dr. J. C. Harris for many excellent discussions and suggestions. They wish to thank the other members of the electrostatic generator group for their assistance in many phases of this research. Both the Ohio State University Development Fund and the Graduate School gave major support which we gratefully acknowledge.

PHYSICAL REVIEW VOLUME 95, NUMBER 1 JULY 1, 1954

Decay Scheme of Co^{56}

M. Sakai, J. L. Dick, W. S. Anderson, and J. D. Kurbatov
The Ohio State University, Columbus, Ohio

(Received January 28, 1954)

The decay scheme of Co^{56} was studied by means of a magnetic lens spectrometer and a gamma-gamma coincidence scintillation spectrometer. The positron spectrum consists of two groups of maximum energies of 1.50 Mev and 0.44 Mev, relative abundance of 96 percent and 4 percent, respectively, leading to a second and third excited state of Fe^{56}. Orbital electron capture also takes place involving several other excited states. Both of the beta-ray spectra involved appear to have the "allowed" shape of the Fermi plot. The energies of the gamma rays emitted by the Fe^{56} nucleus were determined by studies of the photoelectron spectrum and scintillation spectrum. The energies determined were 0.845 Mev, 1.24 Mev, 1.75 Mev, 2.30 Mev, 2.60 Mev, and 3.25 Mev, respectively. These gamma rays were fitted into the decay scheme by means of beta spectrum analysis and gamma-gamma coincidence experiments.

INTRODUCTION

IT was first reported by Livingood and Seaborg[1] that Co^{56} had a half-life of about 72 days. Cook and McDaniel,[2] using absorption and coincidence methods, reported that the disintegration took place by K capture and a single positron emission with an upper energy limit of 1.20 Mev. The average energy for the several gamma rays present was 1.74 Mev. Elliott and Deutsch[3] using a magnetic lens spectrometer and coincidence methods, reported a positron spectrum of a maximum energy of 1.50 Mev; they found the Fermi plot to be a straight line down to 0.48 Mev. The presence of the other cobalt isotopes prevented the investigation of the spectrum beyond this point. Six gamma rays ranging in energy from 0.845 Mev to 3.25 Mev were also reported.

In the present work the aim was to study Co^{56} without interference from Co^{57} and Co^{58}. For this purpose, a sample of ferric oxide enriched in Fe^{56} (99.84 percent) was obtained from Oak Ridge National Laboratory and bombarded in the cyclotron of the University of California. The target was under bombardment by 10-Mev protons for six hours, the protons being accelerated as hydrogen molecule ions. The total irradiation was 28 microampere hours. A carrier-free sample of Co^{56} was obtained and its mode of decay was studied by both a magnetic lens type spectrometer and a gamma-gamma coincidence scintillation spectrometer.

[1] J. J. Livengood and G. T. Seaborg, Phys. Rev. **60**, 913 (1941).
[2] C. S. Cook and P. W. McDaniel, Phys. Rev. **62**, 412 (1942).
[3] L. G. Elliott and M. Deutsch, Phys. Rev. **64**, 321 (1943).

SOURCE PREPARATION

The bombarded ferric oxide was dissovled in $6N$ hydrochloric acid and treated with a few drops of bromine water, the latter acting as an oxidizing agent for the iron. The solution was evaporated to dryness and the residue dissolved in $6N$ hydrochloric acid. The solution was cooled to 5 degrees centigrade and transferred to a separatory funnel along with an equal volume of chilled ether. The two phases were shaken together and the aqueous phase containing the radioactive cobalt and some iron was extracted. The aqueous phase was then evaporated almost to dryness, diluted to 25 ml with triple distilled water, and the pH adjusted to 1.5. The solution was gently heated, then dilute ammonium hydroxide was added until the pH was approximately 4.5. After allowing 2 hours for the hydrous ferric oxide to settle, the solution was filtered, evaporated to dryness, and the ammonium chloride sublimed. The small residue remaining was dissolved in 1 ml of $0.01N$ hydrochloric acid and ammonium hydroxide added until the pH of the solution was ap-

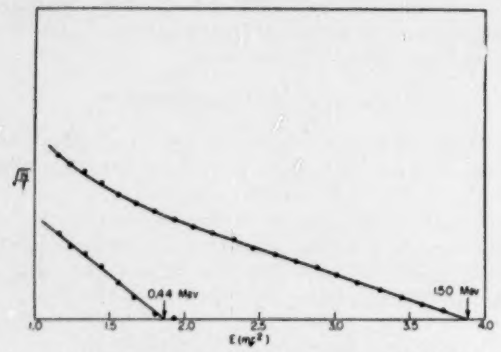

FIG. 1. Fermi plot of the positron spectrum of Co^{56} obtained with a solenoidal spectrometer.

proximately 8.5. The solution was allowed to stand several hours, filtered to remove the remaining hydrous ferric oxide, and evaporated to dryness. After volatilizing the ammonium chloride, the invisible quantity of radioactive cobalt was dissolved in hydrochloric acid and transferred to a spectrometer mount for spectroscopic studies.

THE BETA SPECTRUM

The beta spectrum was measured using a solenoidal type spectrometer. The spectrometer was equipped with a "thin window" Geiger-Müller tube. The window was made of zapon film weighing 120 $\mu g/cm^2$ and reinforced by a nylon fiber grid. The source, weighing approximately 40 $\mu g/cm^2$, was mounted on a zapon backing of 50 $\mu g/cm^2$. Figure 1 shows the Fermi plot of the positron spectrum. It can be seen that the spectrum is complex, consisting of two components with the end-point energy of the main group 1.50 Mev±0.01 Mev and that of the second group 0.44 Mev±0.03 Mev. Their relative abundances were determined to be 96 percent and 4 percent, respectively. The second beta component must be considered as requiring further experimental verification, because of the low abundance

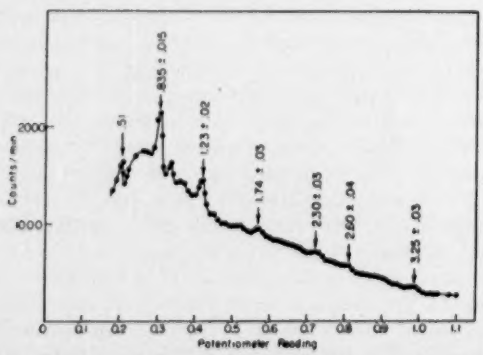

FIG. 2. Photoelectron spectrum produced in a 70-mg/cm² uranium radiator by the gamma rays of Co^{56} obtained with a spectrometer of thick-lens type with moderate resolution.

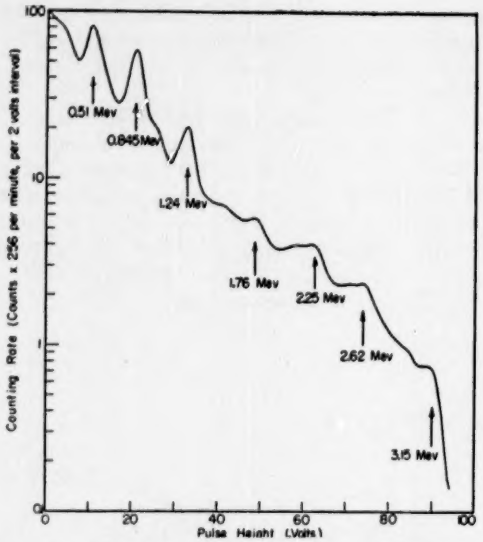

FIG. 3. Pulse-height spectrum of Co^{56} on NaI(Tl) scintillation spectrometer.

and low energy end point. The main component has an end-point energy in agreement with that previously reported.[3] The possibility of the presence of other cobalt isotopes, Co^{57} and Co^{58}, was checked by attempting to detect the presence of the conversion electron peaks at 0.119 Mev and 0.133 Mev characteristic of Co^{57} and the conversion electron peak at 0.805-Mev characteristic of Co^{58}. There was no indication that these isotopes were present. Thus, the lower-energy positron group may be attributed to the radioactive isotope Co^{56}.

THE GAMMA-RAY SPECTRUM

Figure 2 shows the spectrum of secondary electrons produced in a 70-mg/cm² uranium radiator by the gamma rays of Co^{56}. The gamma-ray spectrum was also studied using a gamma-ray scintillation spectrometer. Seven gamma rays were observed, including the 0.511-Mev positron annihilation radiation. The scintillation spectrometer was equipped with a thallium-activated sodium iodide crystal (diameter 1.0 in., length 1.0 in.). Figure 3 is a plot of the data obtained. Table I is a summary of these results and those obtained by Elliott and Deutsch.[3] The intensities of the

TABLE I. Gamma-ray spectrum of Co^{56}.

Gamma ray	Investigation: Photo-spectrum	Investigation: Scintillation-spectrum	Investigation: Selected value	Previous work*: Inten-sity	Previous work*: Photo-spec.	Previous work*: Inten-sity
1st	0.835 ±0.015	0.845 ±0.015	0.845 ±0.015	1.00	0.845	1.0
2nd	1.23 ±0.02	1.24 ±0.02	1.24 ±0.02	0.55	1.26	0.5
3rd	1.74 ±0.03	1.76 ±0.04	1.75 ±0.04	0.24	1.74	0.2
4th	2.30 ±0.03	2.25 ±0.04	2.30 ±0.03	0.12	2.01	0.1
5th	2.60 ±0.04	2.62 ±0.04	2.60 ±0.04	0.14	2.55	0.2
6th	3.25 ±0.03	3.15 ±0.05	3.25 ±0.03	0.24	3.25	0.2

* See reference 3.

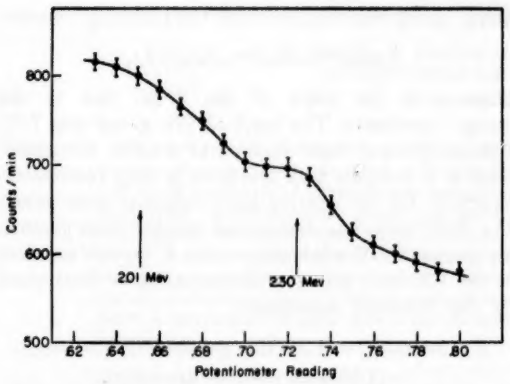

FIG. 4. Photospectrum near the region of 2.30-Mev gamma ray of Co^{56}. The energy indicated in the figure is the sum of photoelectron energy and the K binding energy of uranium.

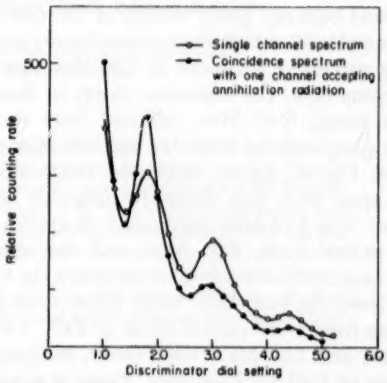
Single channel spectrum
Coincidence spectrum with one channel accepting annihilation radiation
Relative counting rate
500
0 1.0 2.0 3.0 4.0 5.0 6.0
Discriminator dial setting

FIG. 5. Single-channel and coincidence spectra of gamma rays of Co^{56}. The prominent peaks are due to gamma rays at 0.511 Mev (annihilation radiation), 0.845 Mev, and 1.24 Mev.

gamma rays were estimated from the photoelectron spectrum except for the first and second gamma rays. These were determined from the scintillation spectrum corrected for counting efficiency. This was necessary since the photopeak of the 0.835-Mev gamma ray was so distorted by the thickness of the radiator that an accurate intensity estimate was difficult. The fourth column of Table I is the value for gamma-ray energies selected by the authors. The results of scintillation-spectrum are chosen for the values of first and second gamma-ray energy, because the 70-mg/cm² radiator is too thick for precise measurement of energies about 1 Mev or less. The energy of the third gamma ray is the mean value, and the energies of the fourth, fifth, and sixth gamma rays are those from the results of the photospectrum, since it is very difficult to determine correctly many high-energy gamma rays from a complex scintillation spectrum.

The results are in good agreement with those of the previous workers with the exception of the energy of the fourth gamma ray. The authors found the energy to be 2.30 Mev. (See Fig. 4.)

COINCIDENCE MEASUREMENTS

A gamma-gamma coincidence scintillation spectrometer was used as an aid in determining the disintegration scheme. Two 5819 photomultiplier tubes mounted with thallium-activated sodium iodide crystals were arranged at 180 degrees to each other. The time constant of the coincidence circuit was measured as 5×10^{-7} second. An example of the coincidence spectrum is shown in Fig. 5. The gate of one channel was adjusted to admit the annihilation peak and the threshold of the other channel was varied throughout the energy range. It was found that the annihilation radiation was in coincidence with the 0.845-Mev gamma ray and the 1.24-Mev gamma ray. This confirms the decay scheme proposed by Elliott and Deutsch. Table II shows the results of the coincidence experiments.

TABLE III. Gamma-gamma coincidence of Co^{56}. Energies are in Mev. "O" means that a coincidence was observed, "X" that it was not.

	0.845	1.24	1.75	2.30	2.60	3.25
0.511	O	O	—	—	—	X
0.845		O	O	O	O	O
1.24			O	X	X	X

THE DISINTEGRATION SCHEME OF Co^{56}

Figure 6 shows the disintegration scheme of Co^{56} based on the beta-ray analysis, the gamma-ray measurements, and the coincidence experiments. This scheme is similar to the tentative disintegration scheme proposed by the M.I.T. group which was based on gamma-ray intensity measurements. The main beta-ray group decays to the 2.09-Mev second excited level of Fe^{56} which de-excites to the ground state, emitting successively 1.24-Mev and 0.845-Mev gamma rays.

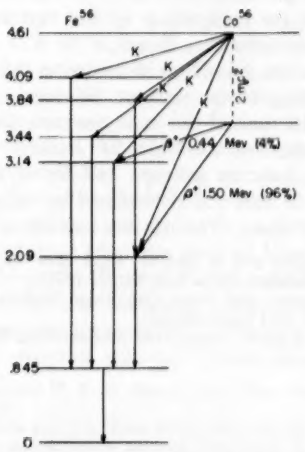

FIG. 6. Disintegration scheme of Co^{56}.

The second beta-ray group decays to the third, 3.14-Mev, excited level of Fe^{56} which de-excites to the ground state by successive emissions of 2.30-Mev and 0.845-Mev gamma rays. The maximum energy of the second positron group, 0.45 Mev, deduced from the main positron group and the 1.24-Mev and 2.30-Mev gamma rays (see Fig. 6), agrees within the range of experimental error with that found by beta-ray analysis, 0.44 Mev. The 1.75-Mev gamma-ray de-excites to the second excited level, 2.09 Mev, and the other two gamma rays, 2.60 and 3.25 Mev de-excite, to the first excited level, the 0.845-Mev level. These three gamma rays arise from three excited levels of Fe^{56}, 3.44 Mev, 3.84 Mev, and 4.09 Mev, respectively, resulting from the decay of Co^{56} by K capture. There is some possibility of decay to the 3.44-Mev level by positron emission but this may be of very low intensity because of the competition of electron capture as the available energy is small, 0.14 Mev. The confirmation of this latter positron group is outside the range of the instrument.

DISCUSSION

The 3.14-Mev excited state of Fe^{56} was established by photoelectron measurements and the analysis of the positron spectrum. This level is higher than the 2.85-Mev level found by the M.I.T. group and is also higher than the 2.98-Mev level deduced by the study of the disintegration scheme of Mn^{56} by the same group. From the present work it is difficult to state if these two levels are identical.

The comparative lifetimes of beta-ray transitions were determined by the following method. The 0.845-Mev internal conversion electron peak was measured along with the positron spectrum. Assuming the radiation to be electric quadropole according to Goldhaber's[4] empirical rule, the internal conversion coefficient of the 0.845-Mev gamma ray is given as 2.8×10^{-4} from Rose's table.[5] By using this factor, the intensity of the positron to the 0.845-Mev gamma ray can be determined from the comparison of the two areas of the spectra. This ratio was found to be 0.23. As all the gamma rays are known to de-excite to the 0.845-Mev level according to the present disintegration scheme, the partial lifetime of the main positron disintegration may be estimated as 3.12×10^{7} seconds which was determined from an average half-life of 76 days. A $\log ft$ value of 8.64 was determined by using Feenberg and Trigg's[6] chart. The relative half-life of the lower-energy group was deduced from the following formula:

$$(\tan\alpha_1)^2/(\tan\alpha_2)^2=(f_2l_2)/(f_1l_1),$$

where α is the slope of the Fermi line to the energy coordinate. The $\log ft$ of this group was 7.73. This simple and rapid method of ft-value determinations of a complex beta spectrum is very convenient, especially for the relative $\log ft$ values of each group. The K/β^+ ratio was determined roughly from gamma-ray intensities. The intensity of the K capture involved in the 1.50-Mev positron disintegration is determined by the following expression:

$$K_e\ (\text{intensity})=(1.24\text{-Mev gamma-ray intensity})-(1.50\text{-Mev positron intensity})-(1.75\text{-Mev gamma-ray intensity}).$$

The ratio of the K/β^+ is found to be 0.35. This value may be compared with the theoretical value of the allowed transition, 0.1.[6] However, it is noted that the accuracy of the intensity estimation may be no greater than 20 percent. If the intensity of the 1.24-Mev gamma ray is assumed to be 0.5 as reported by the M.I.T. group, then the K/β ratio is 0.13. The above argument is only considered as one piece of evidence for the presence of K electron capture involved in the 1.50-Mev positron transition. The K/β^+ ratio involved in the lower-energy positron transition is also deduced from the same argument by taking into account the 4 percent branching ratio determined from the analysis of the beta spectrum. The ratio was found to be 12.

Since Co^{56} may have the nuclear configuration $f_{7/2}-p_{3/2}$ from the nuclear shell model,[7] it is probable that the ground state of Co^{56} has a spin of 5 from the Nordheim empirical rule.[8] The positron disintegration appears to be l- or first-forbidden according to Nordheim's classification. If the second (2.09-Mev) excited level and the third (3.14-Mev) excited level are assumed to have spins of +4 and +6, respectively, according to Goldhaber's rule,[4] the $\Delta I=1$, $\Delta I=2$ characterisitc may be applied to both disintegrations. So far as the $\log ft$ value is concerned, the 1.50-Mev positron has, most likely, the characteristic $\Delta I=2$, yes.[8] At the present there is insufficient experimental evidence to confirm either of these.

This work was supported in part from funds granted to The Ohio State University by the Research Foundation for aid in fundamental research. The authors express their deep gratitude to The Ohio State University Development Fund for the grant which made this work possible.

[4] M. Goldhaber and A. Sunyar, Phys. Rev. **83**, 906 (1951); G. Scharff-Goldhaber, Phys. Rev. **90**, 587 (1953).
[5] Rose, Goertzel, and Perry, Oak Ridge National Laboratory Report—1023, 1951 (unpublished).
[6] E. Feenberg and G. Trigg, Revs. Modern Phys. **21**, 399 (1950).
[7] M. Mayer, Phys. Rev. **78**, 16 (1950).
[8] L. W. Nordheim, Revs. Modern Phys. **23**, 322 (1951).

Capture of Polarized Neutrons by Polarized Sm^{149} Nuclei

L. D. ROBERTS, S. BERNSTEIN, J. W. T. DABBS, AND C. P. STANFORD
Oak Ridge National Laboratory, Oak Ridge, Tennessee

(Received February 4, 1954)

The Sm^{149} nuclei in the paramagnetic salt, samarium ethyl sulfate, were polarized by use of the hyperfine structure coupling, which was known to be large from paramagnetic resonance measurements. The Sm salt was placed in a field of 11 000 gauss after being cooled by thermal contact with a sample of iron ammonium alum which was demagnetized to zero field from 15 500 gauss and 1.2°K. The nuclear polarization was observed and measured by observations on the state of polarization of the neutrons transmitted by the Sm sample. A single crystal of magnetized magnetite, set to reflect neutrons of 0.07 ev in first order from the 220 planes was used as the analyzer. A nuclear polarization of about 0.12 was deduced from the data. The observed polarization direction of the transmitted neutrons gives $J=I+\frac{1}{2}$ for the 0.094-ev resonance level in Sm^{149}. A temperature of about 0.13°K for the Sm-containing salt was deduced from the observed neutron polarization.

I. INTRODUCTION

THE polarization of nuclei by use of hyperfine structure coupling was suggested by Rose[1] and by Gorter.[2] In this method a large electron polarization is produced by subjecting a suitable paramagnetic salt to appropriate magnetic field and temperature conditions. The large effective magnetic field produced by the electrons at the nucleus serves to polarize the nuclei by means of the large electron nuclear coupling. This method of nuclear polarization has been used at the Clarendon Laboratory to study the angular distribution of γ rays emitted by polarized nuclei.[3] We have used this method[4] for polarizing Mn^{55} nuclei in the salt, manganous ammonium sulfate, at a temperature of 0.2°K, in a field of 2350 gauss. The spin dependence of the capture cross section for thermal neutrons of Mn^{55} was studied by bombarding the sample with polarized neutrons and observing the dependence of the Mn^{56} activity upon relative spin directions of incident and bombarded particles. In the Mn experiment, the final conditions of 0.2°K and 2350 gauss came about by demagnetizing the salt containing the nuclei to be polarized, from the initial conditions, 1.2°K and 15 500 gauss.

In this paper we present the results of an experiment in which the nucleus Sm^{149} in samarium ethyl sulfate was polarized through the use of hyperfine structure coupling. In this case, for reasons explained in Sec. II, the samarium ethyl sulfate was cooled indirectly by thermal contact through a copper bar with a sample of ferric ammonium sulfate which served as the paramagnetic salt refrigerant in the adiabatic demagnetization. The nuclear polarization was measured by observations on the state of polarization of the neutrons transmitted by the sample. The state of polarization of the transmitted neutron beam is interpreted in terms of the angular momentum of the 0.094-ev resonance level in Sm^{149}. The neutron effects observed serve also as a "thermometer" giving a value for the average temperature of the salt in a region of temperature well below 1°K.

II. PRODUCTION OF THE POLARIZATION OF Sm^{149} NUCLEI

Recently, Bogle and Scovil reported the results[5] of paramagnetic resonance experiments on the trivalent samarium ion in the salt samarium ethyl sulfate $Sm(C_2H_5SO_4)_3\cdot 9H_2O$, which crystallizes in hexagonal form. Their measurements were performed at 4°K where the electronic ground state was found to be a Kramers' doublet. Their results relative to Sm^{149} may be summarized in terms of the "spin" Hamiltonian $\mathcal{H}$,

$$\mathcal{H}=g_{\parallel}\beta H_z S_z+g_{\perp}\beta(H_x S_x+H_y S_y)+AS_z I_z+B(S_x I_x+S_y I_y)+\mathcal{H}_1. \quad (1)$$

Here, the spectroscopic splitting factor for the magnetic field parallel to the hexagonal axis is $g_{\parallel}=0.596$ and for the field perpendicular to this axis, it is $g_{\perp}=0.604$. In the following it is sufficiently precise to neglect this small asymmetry and take an average spectroscopic splitting factor $g=0.60$. β is the Bohr magneton. The nuclear spin I is $7\hbar/2$. H_x, H_y, and H_z are the components of the magnetic field; S_x, S_y, and S_z are the components of the electron spin operator; and I_x, I_y, and I_z are the components of the nuclear spin operator with the z direction taken along the hexagonal axis. The hyperfine structure coupling constants for Sm^{149} have the values $A=-0.0049$ cm^{-1} and $B=-0.0205$ cm^{-1}. The negative sign of the hyperfine structure coupling is obtained from the work of Murakawa and Ross[6] and from the theoretical treatment by Elliot and Stevens[7] of the samarium ethyl sulfate paramagnetic resonance measurements. The term $\mathcal{H}_1$, which includes the electron spin-spin interactions, nuclear

[1] M. E. Rose, Phys. Rev. **75**, 213 (1949).
[2] C. J. Gorter, Physica **14**, 504 (1948).
[3] Ambler, Grace, Halban, Kurti, Durand, Johnson, Lemmer, Phil. Mag. **44**, 216 (1953).
[4] Bernstein, Roberts, Stanford, Dabbs, and Stephenson, Phys. Rev. **94**, 1243 (1954).
[5] G. S. Bogle and H. E. D. Scovil, Proc. Phys. Soc. (London) **A65**, 368 (1952).
[6] K. Murakawa and J. S. Ross, Phys. Rev. **82**, 967 (1951).
[7] R. J. Elliot and K. W. H. Stevens, Proc. Roy. Soc. (London) **A219**, 387 (1953).

quadrupole coupling, and the direct interaction of the nucleus with the external field, may be expected to be small compared to the first two terms in $\mathcal{H}$ for values of the magnetic field of interest here, and is neglected.

Following our earlier report,[4] the average nuclear polarization f_N for a powder sample is

$$f_N=\frac{S(I+1)hc(A/3+2B/3)}{3kT}\tanh\frac{g\beta H}{2kT}, \qquad (2)$$

where the electron spin S is taken as $\frac{1}{2}$ to describe the doublet ground state, h is Planck's constant, c is the velocity of light, k is Boltzmann's constant, H is the magnetic field, and T is the absolute temperature. Substituting the values for the several constants we obtain

$$f_N=(0.0165/T)\tanh(2.02\times10^{-5}H/T). \qquad (3)$$

The maximum value of H available with our Weiss magnet is 15 500 gauss and the minimum temperature available by pumping on liquid helium in our nuclear polarization cryostat is about 0.9°K. For these conditions (3) gives an f_N of only 0.006 which is too small to be readily usable.

This polarization may be enhanced by a partial demagnetization as was done[4] in case of Mn^{55}. This enhancement may be estimated as follows: We assume Curie law behavior for the samarium electron moments. Also we assume that the specific heat of $Sm(C_2H_5SO_4)_3\cdot9H_2O$ is primarily due to hyperfine structure coupling and that it has a $1/T^2$ behavior. Then it follows that the optimum value for the nuclear polarization f_N' is given by

$$f_N'=\frac{1}{6[I(I+1)]^{\frac{1}{2}}}\frac{S(I+1)}{}\frac{g\beta H_i}{kT_i}\tanh\frac{g\beta H_i}{2kT_i},$$

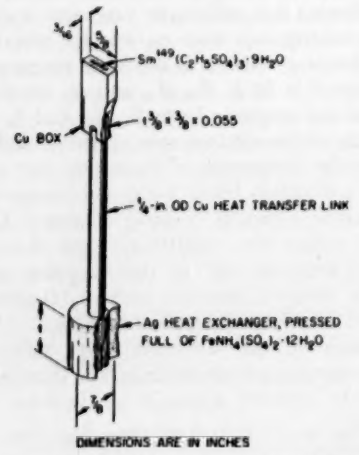
Sm149(C2H5SO4)3·9H2O
Cu BOX
¼-in. OD Cu HEAT TRANSFER LINK
Ag HEAT EXCHANGER, PRESSED FULL OF FeNH4(SO4)2·12H2O
DIMENSIONS ARE IN INCHES
AT 0.15°K AND 10⁴ GAUSS A POLARIZATION OF 11% MAY BE EXPECTED.

FIG. 1. Heat transfer arrangement.

where the subscript i refers to the initial conditions of the demagnetization. Assuming $H_i=15\,500$ gauss and $T_i=0.9$°K, this leads to an f_N' of 0.027, which is still rather small. The reason for this lies in the fact that the spectroscopic splitting factor $g=0.60$ is relatively small and correspondingly, the initial entropy removal is small.

To increase this initial entropy removal, we decided to cool the $Sm(C_2H_5SO_4)_3\cdot9H_2O$ by the adiabatic demagnetization of an additional coolant salt thermally connected to the samarium sample. In this heat transfer equipment, shown in Fig. 1, the samarium ethyl sulfate powder sample is pressed into a rectangular copper box which is connected by a copper tube to a "heat exchanger" consisting of two concentric silver tubes pressed full of $Fe(NH_4)(SO_4)_2\cdot12H_2O$. In using this equipment to polarize the Sm^{149} nuclei, the iron ammonium alum was demagnetized to a temperature[8] of about 0.043°K, but this temperature was increased to about 0.06°–0.07°K at the time the neutron observations were made, primarily by eddy-current heating effects. The samarium salt is cooled by heat conduction through the copper heat transfer link (Fig. 1) and partially by stray field adiabatic demagnetization. Finally, to produce the nuclear polarization it is necessary to apply a magnetic field exclusively to the samarium salt. This magnetic field must not be applied to the coolant salt since this would raise the temperature of the sample assembly.

Figure 2 shows a diagram of the cryostat built to perform the above operations. It consists fundamentally of two concentric Dewars containing liquid helium jacketed by liquid nitrogen. The heat transfer link shown in Fig. 1 is mounted within the sample tube on a string suspension as is customary in adiabatic demagnetization experiments. This suspension is designed to minimize vibration-induced heat leak to the sample. Heat leaks of the order of 20–40 ergs per minute to the sample assembly at temperatures below 1°K were usual. Four radiation shields recently described elsewhere[9] are inserted in the sample tube above the sample assembly. The sample tube was inserted into the cryostat through an "O"-ring seal so that this tube and the enclosed samarium heat transfer assembly could be raised and lowered. Figure 2 shows the tube in the mid-position. In a typical experiment, we began with this tube in the upper position with the coolant salt—"heat exchanger" in the magnet gap. The coolant salt was magnetized for 15 minutes with a helium exchange gas pressure of about 50μ, at an $H_i/T_i=12\,300$ gauss per degree. Then, opening valves A and B, the exchange gas was pumped for 30 minutes to a final pressure as measured at the VG1A vacuum gauge of 5×10^{-6} mm of Hg pressure. Then the Weiss magnet field was decreased slowly to zero, this process taking

[8] A. H. Cooke, Proc. Phys. Soc. (London) A62, 269 (1949).
[9] Erickson, Roberts, and Dabbs, Rev. Sci. Instr. (to be published).

of the order of 10 minutes to reduce eddy-current heating in the metal parts of the sample assembly. Valves A and B were then closed and the sample tube was slowly moved to the lower position, in which the coolant salt was surrounded by a magnetic field shield and the samarium sample was in the magnet gap. The magnetic shield, which consisted of concentric cylinders of Armco iron with inner and outer radii in geometric progression, was quite effective. A field of 10 000 gauss applied to the samarium sample produced a field, on the coolant salt 5 inches below, of less than one gauss. Storage batteries were used to excite the magnet in the lower position of the experiment in order to obtain a very steady field. This field was turned on slowly to decrease eddy-current heating. About twenty minutes after the application of this field, nuclear polarization effects were observed as described in the next section.

III. OBSERVATION OF THE NUCLEAR POLARIZATION OF Sm^{149}

The cross section of polarized nuclei for polarized neutrons is given by[1]

$$\sigma=\sigma_0\left(1+\frac{I}{I+1}f_n f_N\right), \quad J=I+\tfrac{1}{2}; \tag{4a}$$

$$\sigma=\sigma_0(1-f_n f_N), \quad J=I-\tfrac{1}{2}. \tag{4b}$$

σ_0 is the cross section in the absence of polarization. The quantity I is the spin quantum number of the polarized nuclei, f_n is the neutron polarization, f_N is the nuclear polarization. The quantity J is the angular momentum quantum number of the compound state. If an unpolarized neutron beam is incident upon a sample containing polarized nuclei, the cross section σ can be expressed as

$$\sigma=\sigma_0\pm p, \tag{5}$$

in which

$$p=\sigma_0\frac{I}{I+1}f_N \quad \text{if} \quad J=I+\tfrac{1}{2}, \tag{6a}$$

$$p=\sigma_0 f_N \quad \text{if} \quad J=I-\tfrac{1}{2}. \tag{6b}$$

For $J=I+\frac{1}{2}$, the plus sign of (5) applies to that half of the incident number of neutrons whose polarization is parallel to the nuclear polarization, the minus sign to that half whose polarization is antiparallel. For $J=I-\frac{1}{2}$, the positive sign in (5) applies to those neutrons whose spin direction is antiparallel to the spin direction of the nuclei. Because of the different cross section for the two neutron spin states, the neutron beam emerging from the sample will be polarized. Its polarization P_1 is given by

$$P_1=\tanh(Npd), \tag{7}$$

in which N is the number of nuclei per unit volume and d is the thickness of the sample. The neutron polarization produced by the sample is a measure of the amount of nuclear polarization of the sample. Since the neutron polarization produced by the sample increases with its thickness, a value of d as large as is consistent with intensity requirements is desirable.

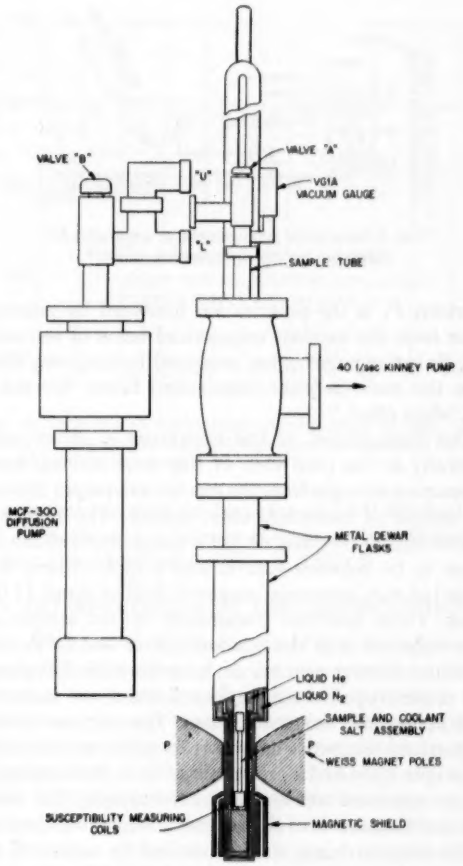

FIG. 2. Nuclear polarization cryostat.

The polarization of a beam of neutrons of a single energy (produced by a given polarizer) can be measured easily if the polarization produced by a second polarizer from the same incident unpolarized beam is known.[10] In this method the neutron beam passes from the polarizer to the analyzer (second polarizer) and then into the detector. The counting rate C_1 is measured with the magnetic field conditions along the beam arranged so that only adiabatic changes of neutron spin can take place between polarizer and analyzer. The counting rate C_2 is obtained when the polarization of the beam is brought to zero between polarizer and analyzer by transmission through a thin foil of iron placed in near-zero field in this region. Then

$$G=C_1/C_2=1+P_1P_2, \tag{8}$$

[10] Stanford, Stephenson, Cochran, and Bernstein, Phys. Rev. **93**, 374 (1954).

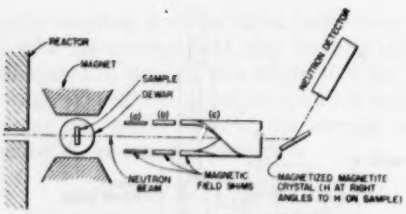

FIG. 3. Schematic arrangement of apparatus for observing nuclear polarization of Sm^{149}.

in which P_1 is the polarization produced by polarizer alone from the incident unpolarized beam of neutrons, and P_2 is the polarization produced by analyzer alone from the same incident unpolarized beam. We call G the "shim effect."

The arrangement of the apparatus is shown schematically in the plan view of Fig. 3. A thermal beam of neutrons emerges from the reactor and passes through the sample of samarium ethyl sulfate. The sample is located within the cryostat (at a temperature estimated below to be between 0.12°K and 0.15°K) where it is subjected to a horizontal magnetic field of about 11 000 gauss. Those neutrons transmitted by the sample are then reflected into the window slit of the $B^{10}F_3$ proportional counter neutron detector from the 220 planes of a single crystal of magnetite subjected to a magnetic field of several thousand gauss. The purpose of the magnetized magnetite crystal is to select neutrons of a given spin state and a given energy from the continuous energy spectrum transmitted by the sample. The direction and magnitude of the magnetic field along the path of the neutron beam were controlled by means of the parallel plate shims (a), (b), and (c). The magnetic field between the plates was adjusted according to the requirements of the two types of observation, C_1 and C_2, by bridging the distance between the plates at various points with numerous U-shaped permanent magnets. The polarization produced by the magnetite crystal is greatest when the field applied to it is perpendicular to the neutron scattering plane.[11] The field was therefore applied to the crystal in the vertical direction. The purpose of the "twister" shim (c) was to produce a slowly varying change in the magnetic field direction along the beam path from the horizontal at the Sm sample to the vertical at the magnetite crystal. Magnetic field measurements were made, and the permanent U-shaped magnets adjusted so that the conditions necessary for the neutron spin to "follow" the field obtained during the measurement of the counting rate C_1. For the measurements of C_2, the permanent magnets were adjusted so that the field was close to zero in (b). Several sheets of iron, each 0.005 in. thick, were placed in the path of the beam at the point of near-zero field to destroy the neutron polarization produced by the Sm^{149} nuclei. The depolarizing foils of iron reduce the intensity of the beam C_2 by a small amount due to scattering and capture. This decrease in intensity was compensated for by inserting the depolarizing foils in the path of the beam during measurements of C_1 at a point between the crystal and the detector, where their depolarizing action is of no consequence.

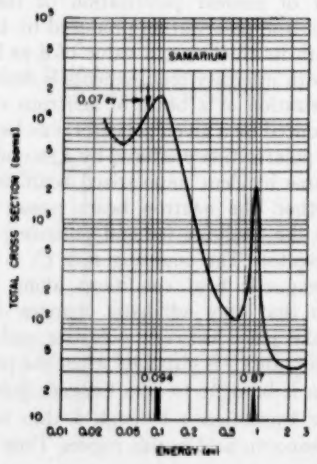

FIG. 4. Total cross section of Sm^{149} vs energy. See *Neutron Cross Sections*, Atomic Energy Commission Report AECU-2040 (Technical Information Division, U. S. Department of Commerce, Washington, D. C., 1952).

All of the data were taken with the 220 planes of the magnetite crystal set to reflect 0.07-ev neutrons in the first order. The relationship of this energy to the known resonance levels of Sm^{149} is shown in Fig. 4. The results of a single run are shown in Fig. 5, in which time is plotted along the x axis. The counting rate C_1 is shown as the dotted line, and C_2 as the solid line. The figure illustrates how the over-all counting rate repeatedly increased by about 10 percent when the neutron polarization produced by the polarized Sm^{149} nuclei was destroyed by the iron foils. The statistical standard errors in the counting rates for the one run are shown on the graph. The observed changes in intensity are 3 or 4 times as great as the statistical error in each observation.

The over-all counting rate plotted in Fig. 5 includes not only the first-order 0.07 ev neutrons but also higher-order reflected neutrons. The counts due to the higher-order reflections constitute an appreciable fraction of the total counting rate for two reasons: the Sm resonance at 0.094 ev depletes the transmitted beam of first-order neutrons; the crystal structure factor of the 440 planes of magnetite is very much larger than that of the 220 planes. The shim effect is reduced by the presence of these higher-order neutrons.[10] For example, the 440 reflected neutrons should be polarized to about 10 percent in the direction opposite to that of the 220 reflection; the 660 reflection will have the same direction

[11] O. Halpern and M. H. Johnson, Phys. Rev. 55, 898 (1939).

of polarization as 220, but will be much less because of the decrease in the magnetic form factor with increasing $(\sin\theta/\lambda)$. The effect of the higher-order reflections upon the shim effect was studied quantitatively by means of appropriate filters, and corrections to G were made.

A summary of all the data is given in Table I. The results presented are the average of four experiments. The observations of all of these experiments were in good agreement.

The shim effect G, including all orders of reflection for all runs at the low temperature was 0.882 ± 0.007. This value is corrected to the value 0.787 ± 0.024, which should have been observed if first-order neutrons only were present in the beam. The polarization P_2 produced by reflection from the 220 planes of our magnetite crystal was known to be close to 90 percent.[10] Substituting the measured values of 0.787 for G, and 0.9 for P_2 into (8), the polarization P_1 produced by transmission through the Sm sample is calculated to have the value minus 0.24 (it is opposite in direction to the polarization produced by the magnetite).

The polarization of the neutron beam transmitted by the polarized Sm nuclei should be accompanied by an increase in the transmitted intensity. This increase is related to the polarization P_1 by the expression

$$P_1=[1-(C_3/C_2)^2]^{\frac{1}{2}}, \qquad (9)$$

in which C_2 is the intensity transmitted by the sample, as defined in the foregoing, C_3 is the intensity transmitted with the Sm in zero field. Using the value $P_1=0.24$, given by the shim effect data, in (9), a value of C_3/C_2 of 0.97 should have been observed for first-order neutrons only, or a value of about 0.98 for all neutrons. A change in intensity of approximately this amount was observed, but this type of measurement was not pursued, since the shim effect is larger in size and simpler to measure reliably.

TABLE I. Shim effect G.

Temperature	Shim effect G	Beam
(0.12°–0.15°K)	0.787 ± 0.024	Includes first-order neutrons only
(0.12°–0.15°K)	0.882 ± 0.007	Includes all orders
(1.2°K)	0.986 ± 0.007	Includes all orders

Table I shows also the results obtained for a series of runs in which the sample was maintained at 1.2°K in a field of 11 000 gauss. The shim effect in this case was 0.986 ± 0.007. This value of G corresponds to a neutron polarization and nuclear polarization from about (1/9) to (1/17) times that produced at the low temperature. This ratio, calculated using best estimates of the values of T and H in the two experiments, should be (1/34). Thus the polarization of the Sm^{149} nuclei decreases with temperature roughly in accordance with theory. Agreement can be obtained by assuming that the experimental error in the value of $G=0.986$ for the high temperature is 1.5 times as large as the calculated statistical standard error shown in Table I.

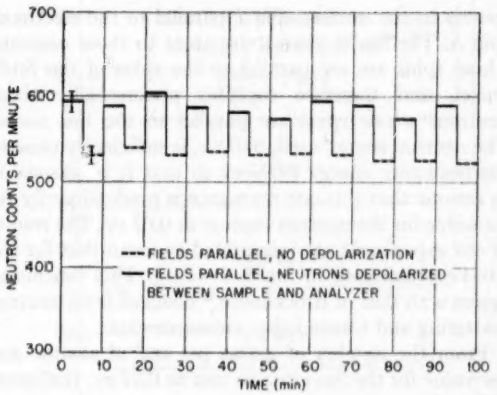

FIG. 5. Intensity of transmitted neutron beam vs time. The intensity increases when the neutron polarization produced by the polarized Sm^{149} is destroyed.

IV. INTERPRETATION OF THE OBSERVATIONS

Consideration of the relative directions of the various vector quantities involved in the interpretation of the fact that the neutron polarization P_1 produced by transmission through the polarized Sm nuclei, is opposite to the neutron polarization P_2 produced by the magnetite leads to the conclusion that the capture cross section in the sample was greater when the nuclear spin and incident neutron spin are in the same direction. The directions of the relevant vectors are sketched in Fig. 6. The fields applied to the Sm sample and the magnetite crystal can be considered to be parallel, since nonadiabatic neutron transitions were not permitted to occur. The neutron spin direction corresponding to P_2, produced by the 220 reflection, is known from theory and experiment[12] to be antiparallel to the field applied to the crystal. The neutron spin direction predominant in the beam transmitted by the Sm sample is antiparallel to P_2, or parallel to the magnetic field applied to the Sm. The negative sign of the hfs coupling means that the most densely populated hyperfine structure level in samarium ethyl sulfate is the one which corre-

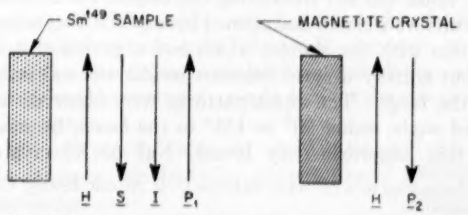

FIG. 6. Relative directions of relevant vector quantities leading to the conclusion that $J=I+\frac{1}{2}$ in 0.094-ev resonance in Sm^{149}.

[12] Sherwood, Stephenson, Stanford, and Bernstein, Bull. Am. Phys. Soc. 29, No. 1, 54 (1954).

sponds to the nuclear spin I parallel to the electronic spin S. The Sm is more transparent to those neutrons whose spins are antiparallel to the spins of the Sm^{149} nuclei, and therefore captures preferentially those neutrons whose spins are parallel to the Sm nuclei. The neutron energy used, 0.07 ev, is sufficiently close to the resonance energy 0.094 ev so that it is reasonable to assume that this one resonance is predominantly responsible for the neutron capture at 0.07 ev. The results of our experiment are interpreted to mean that for the 0.094 ev resonance in Sm^{149}, $J=I+\frac{1}{2}$. This conclusion agrees with that of Brockhouse,[13] deduced from neutron scattering and transmission measurements.

From the number of grams per cm^2 of sample and the value for the Sm cross section at 0.07 ev, the factor $(N\sigma_0 d)$ for the Sm nuclei is calculated to be about 2.5, i.e., the intensity of 0.07-ev neutrons is diminished by the factor $e^{-2.5}$ by Sm capture. The value of the nuclear polarization f_N is calculated from (6a) and (7) to be about 0.12.

Inserting $f_N=0.12$ and $H=11\,000$ oersteds into (3), a sample temperature of 0.13°K is obtained. From the uncertainty in the exact value of $(N\sigma_0 d)$ at 0.07 ev, the sample temperature is estimated to have been between 0.12°K and 0.15°K. The difference between this temperature, and the temperature of the ferric ammonium sulfate coolant salt of 0.06°–0.07°K was somewhat larger than was expected based on the heat leak and on thermal conductivity considerations.[14]

[13] B. N. Brockhouse, Can. J. Phys. 31, 432 (1953).

[14] E. Mendoza, "*Les Phenomènes Cryomagnetiques*" (College de France, 1948).

PHYSICAL REVIEW VOLUME 95, NUMBER 1 JULY 1, 1954

Beta-Alpha Correlation in the Decay of Li^8†

S. S. HANNA, E. C. LAVIER, LT. COL., U.S.A.F., AND C. M. CLASS*
Department of Physics, The Johns Hopkins University, Baltimore, Maryland
(Received February 25, 1954; revised manuscript received March 29, 1954)

The beta-alpha directional correlation in the $Li^8(\beta)Be^{8*}(\alpha)He^4$ decay has been measured for various portions of the upper end of the beta spectrum, from about 90 percent to 10 percent of the total beta spectrum. No significant departure from isotropy was observed at the higher beta energies, as reported in earlier measurements. An average of the measurements gives a value of $A_2=0.01\pm0.03$ in the correlation function $1+A_2\cos^2\theta$.

THE beta decay of Li^8 leads primarily to the formation of the Be^8 nucleus in its first excited state, which then decays into two alpha particles.[1] The directional correlation between the beta and the alpha particles has been studied, and a small angular effect of the type $1+A_2\cos^2\theta$ has been reported.[2,3] We have continued the measurements made earlier in this laboratory.

Thin targets of natural lithium were bombarded with deuterons to produce Li^8 nuclei through the $Li^7(d,p)Li^8$ reaction. The deuteron beam of energy 0.66 Mev was interrupted periodically by means of a rotating shutter, to allow observation of the decay products only when the beam was not irradiating the target. The recording circuits were closed and opened by a switch in synchronization with the shutter which had a period of 4 sec, about equally divided between irradiation and eclipse of the target. The alpha particles were observed at a fixed angle, either 90° or 135° to the beam, by means of thin (approximately 10-mil) NaI or KI crystals. The crystal, mounted inside the target chamber, was coupled optically to an external photomultiplier tube through a light pipe. A NaI crystal, 2 inches long by 1.5 inches in diameter, which gave good resolution for gamma radiation, was used as the beta particle detector. The beta particles were admitted to the crystal through a 1-mil aluminum foil. The target chamber was constructed entirely of aluminum and Lucite. For observation of the beta particles, seven windows covered with 1-mil aluminum foil were provided at intervals from 45° to 270°, as measured from the alpha detector. After amplification, the pulses from each detector were discriminated with an integral bias and then presented to a coincidence detector. Accidental coincidences were recorded with a separate circuit counting delayed coincidences.

The beta detector was calibrated with the 4.43-Mev gamma ray from C^{12} (from a Po-Be source) and the 17.6-Mev gamma ray from the $Li^7(p,\gamma)Be^8$ reaction, using differential pulse-height analysis. The resolution of the alpha detector was tested with Po alpha particles, but the counter was not calibrated directly. Instead, the beta-alpha coincidence yield from the Li^8 decay was measured as a function of the bias (or the gain) of the alpha detector. A typical curve is shown in Fig. 1.

† Supported by a contract with the U. S. Atomic Energy Commission.

* Now at Rice Institute, Houston, Texas.

[1] For additional information see the review article: F. Ajzenberg and T. Lauritsen, Revs. Modern Phys. 24, 321 (1952).

[2] C. M. Class and S. S. Hanna, Phys. Rev. 89, 877 (1953).

[3] D. St. P. Bunbury, Phys. Rev. 90, 1121 (1953).

On the plateau of this curve the observed coincidence yield per beta particle was 90–100 percent of the yield expected from a consideration of the solid angle subtended by the alpha detector.

The angular correlation was measured for various portions of the upper end of the beta spectrum. The results are shown in Fig. 2. In a typical run the average coincidence rate was of the order of 2 per sec and the accidental rate about 10 percent of the real rate. Because of the recoil velocity of the Be^{8*} nuclei following the beta decay, it is necessary to convert the observed yields from the laboratory to the center-of-mass system. This correction cannot be computed precisely, because of the continuous nature of the alpha and beta spectra and the lack of specific knowledge concerning the beta-neutrino correlation. As a result of the essential symmetry about 90° in the beta-alpha correlation, however, it is possible to obtain the correction experimentally by comparing the yields observed at θ and $\pi-\theta$. In each case, the estimated theoretical correction, having a maximum value between 5 and 10 percent, was compatible with the experimental value. As can be seen in the figure, no significant change in the correlation with beta energy is observed. An average of all the runs gives a value of $A_2=0.01\pm0.03$ in the expression $1+A_2\cos^2\theta$.

In our earlier work[2] the values of A_2 obtained when a major portion of the beta spectrum was observed are compatible with the present results. Larger values of A_2, obtained when the high end of the beta spectrum was recorded, resulted from a failure to achieve a sufficiently low bias on the alpha detector, completely below the low-energy limit of the alpha spectrum ($\sim$0.5 Mev). As discussed above, the use of thinner sources and improved resolution made it possible to include effectively the total alpha spectrum in the present investigation. The shift in the alpha energy resulting from the recoil of the Be^8 nucleus, when the beta particle is emitted parallel instead of perpendicular to the alpha particle, amounts to about 5 percent when averaged over the beta and alpha spectra. When the high end of the beta spectrum is selected, however, the shift is of the order of 15 percent at the low end of the alpha spectrum.

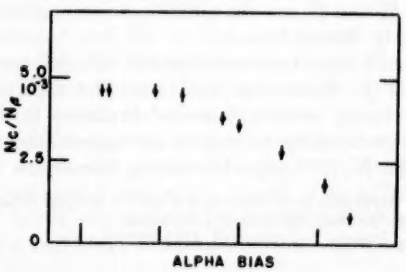

FIG. 1. Coincidence yield as a function of the integral bias on the alpha detector. The abscissa is in arbitrary units. The coincidences are normalized to the count in the beta detector, which had a fixed bias corresponding to a beta energy of 4.5 Mev.

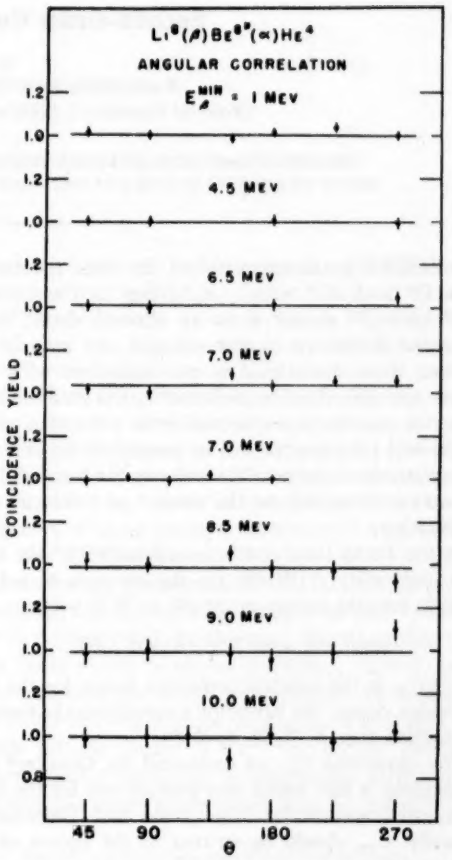

FIG. 2. Angular correlation in the $Li^8(\beta)Be^{8*}(\alpha)He^4$ decay. In all the curves, except the first, the total alpha spectrum was used. For the first curve the alpha bias corresponded to an alpha energy of about 2.5 Mev, and the data have been corrected for the change in alpha energy occurring in the laboratory system. For all the curves, except the fifth, the alpha counter was at an angle of 135° to the beam direction. For the fifth curve the angle was 90°. θ is the angle of the beta detector as measured from the fixed alpha detector. The bias on the beta detector is given for each curve in terms of the (approximately) equivalent beta energy.

As discussed by Gardner,[4] an isotropic result for the beta-alpha correlation does not serve to specify the spins of the particles, although it can be of help in eliminating certain possibilities. If the spin of Li^8 is assumed to be two, an isotropic correlation would result for either spin two or spin zero for the first excited state of Be^8.

We are greatly indebted to Mr. Richard Lee for his generous assistance in various phases of this investigation.

[4] J. W. Gardner, Phys. Rev. 82, 283 (1951).

Second-Order Corrections to Beta Spectra

P. F. ZWEIFEL
Knolls Atomic Power Laboratory, Schenectady, New York*
(Received December 1, 1953; revised manuscript received March 23, 1954)

The origin of small correction terms to beta spectra is discussed. The second-order corrections to allowed spectra are presented for both pure interactions and linear combinations.

RECENT measurements[1,2] of the beta spectra of C^{14} and Ni^{63} which, according to the nuclear shell model,[3,4] should show an allowed shape, have indicated deviations at low energies. An attempt to explain these deviations[2] is not consistent with the parity and spin changes predicted by the shell model.

In the present paper, second-order correction terms to allowed beta spectra will be presented. An attempt to explain the experimental results on the basis of these correction terms will be the subject of a future communication.

In the Fermi theory of beta radioactivity,[5] the relative probability $N(W)dW$ for the emission of a beta particle into the energy range dW at W is written

$$N(W)dW=pWK^2F_0(W,Z)C_{nx}dW, \tag{1}$$

where C_{nx} is the spectral correction factor for the nth forbidden decay, the subscript x specifying the form of interaction (i.e., S, V, T, A, or P).

The quantities C_{nx} as computed by Greuling[6] are incomplete, a fact which was pointed out for the case of allowed spectra by Konopinski and Uhlenbeck.[7] Actually, C_{nx} should be written as the square of an infinite sum

$$C_{nx}=|a_n+a_{n+2}+\cdots|^2, \tag{2}$$

where parity selection rules forbid the presence of terms involving subscripts $n+1$, $n+3$, etc.

For an allowed scalar decay, for example, $|a_0|^2 \sim |\int\beta|^2$, while $|a_2|^2 \sim |\int\beta r^2|^2$. Presumably, $|\int\beta r^2|^2$ is a fourth-order small quantity compared to $|\int\beta|^2$, and is indeed negligible. However, the cross term involving $[(\int\beta)(\int\beta r^2)^*+\text{c.c.}]$ is of second order, and may be observable, particularly if some poorly understood effect, such as l forbiddenness, decreases the size of $\int\beta$ without acting on $\int\beta r^2$.[8]

The quantities $[a_0^*a_2+\text{c.c.}]$ are given below for the allowed spectra.

Scalar:

$$-[(\int\beta r^2)^*(\int\beta)+\text{c.c.}](\tfrac{1}{6}K^2L_0+\tfrac{1}{3}KN_0).$$

Polar vector:

$$i[(\int 1)(\int\boldsymbol{\alpha}\cdot\mathbf{r})^*-\text{c.c.}](\tfrac{1}{3}KL_0-N_0)$$
$$+[(\int 1)(\int r^2)^*+\text{c.c.}](-\tfrac{1}{6}K^2L_0+\tfrac{1}{3}KN_0).$$

Tensor:

$$\tfrac{1}{2}[(\int\beta\boldsymbol{\sigma})\cdot(\int\beta\boldsymbol{\alpha}\times\mathbf{r})^*+\text{c.c.}](-\tfrac{1}{3}KL_0+N_0)$$
$$+[(\int\beta\boldsymbol{\sigma})\cdot(\int\beta\boldsymbol{\sigma}r^2)^*+\text{c.c.}](-\tfrac{1}{3}K^2L_0)$$
$$+[(\int\beta\boldsymbol{\sigma})\cdot(\int(\beta\boldsymbol{\sigma}\cdot\mathbf{r})\mathbf{r})^*+\text{c.c.}][-(1/15)KN_0].$$

Axial vector:

$$i[(\int\boldsymbol{\sigma})\cdot(\int\gamma_5\mathbf{r})^*-\text{c.c.}](\tfrac{1}{3}KL_0-N_0)$$
$$+[(\int\boldsymbol{\sigma})\cdot(\int\boldsymbol{\sigma}r^2)^*+\text{c.c.}](-\tfrac{1}{3}K^2L_0)$$
$$+[(\int\boldsymbol{\sigma})\cdot(\int(\boldsymbol{\sigma}\cdot\mathbf{r})\mathbf{r})^*+\text{c.c.}][(1/15)KN_0].$$

Although ordinarily selection rules and the transformation properties of the nuclear matrix elements preclude any linear combinations of interactions in the allowed spectra, there are second-order contributions for combinations of S with T and V with T. These are

$$ST: -i[(\int\beta)(\int\beta\boldsymbol{\alpha}\cdot\mathbf{r})^*-\text{c.c.}](N_0+\tfrac{1}{3}KL_0),$$

$$VT: -i[(\int 1)(\int\beta\boldsymbol{\alpha}\cdot\mathbf{r})^*-\text{c.c.}](R_0+\tfrac{1}{3}KP_0),$$

where R_0 and P_0 are the radial function combinations defined by Pursey.[9]

I should like to acknowledge the valuable contributions of J. Mize, who first called the experimental results to my attention, and of Professor H. Brysk. I wish particularly to express my appreciation to H. Hurwitz, Jr., for many illuminating discussions.

* Operated for the U. S. Atomic Energy Commission by the General Electric Company.

[1] J. P. Mize and D. J. Zaffrano, Phys. Rev. **91**, 210 (1953).

[2] Kobayashi, Miyamoto, and Mori, J. Phys. Soc. Japan **8**, 684 (1953).

[3] Mayer, Moskowski, and Nordheim, Revs. Modern Phys. **23**, 315 (1951).

[4] L. W. Nordheim, Revs. Modern Phys. **23**, 322 (1951).

[5] E. Fermi, Z. Physik **88**, 161 (1934).

[6] E. Greuling, Phys. Rev. **61**, 568 (1942).

[7] E. J. Konopinski and G. E. Uhlenbeck, Phys. Rev. **60**, 308 (1941). We adopt the notation of this paper.

[8] The experiments of references 1 and 2 involve decays predicted by the shell model to be l forbidden.

[9] D. L. Pursey, Phil. Mag. **42**, 1193 (1951).

Technetium Activities at Mass 97

G. E. Boyd
Oak Ridge National Laboratory, Oak Ridge, Tennessee
(Received March 1, 1954)

A technetium activity believed to be Tc^{97g} has been observed to decay with molybdenum K x-rays and to possess a half-life in the range of 10^4 to 10^5 years.

ONE of the first technetium activities to be discovered was that of a nuclear isomer of 90-day half-life.[1] The assignment of mass number 97 to this period now seems reasonably established.[2–4] As yet, however, no reports of a daughter, Tc^{97g}, activity formed in its decay have appeared. The possibility that a stable isotope may be the product has been of interest because of its relevance to the problem of the occurrence of technetium on the crust of the Earth.

Useful inferences about the properties of Tc^{97g} may be drawn from information on the radiations of 90-day Tc^{97m}. The emission of low-energy electrons (*ca* 1.4 mg Al/cm² half-thickness) has been reported using absorption methods,[5] and this is confirmed by our own observations (Fig. 1). Magnetic lens spectrograph measurements[6,7] have showed these electrons to result from the internal conversion of an 87–97 kev gamma ray, while critical absorption measurements[7] have revealed that Tc x-rays were emitted thereby establishing the 90-day period as a technetium isomer. This latter important fact is also confirmed by us (Fig. 2). Further, a precision half-life of 90.5±1.0 days has been obtained.

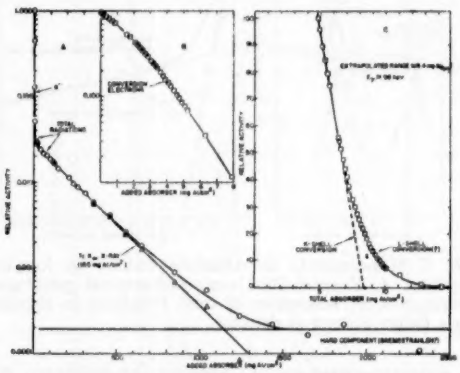

FIG. 1. Absorption in aluminum of radiations from 90.5-day Tc^{97m}: *A* Absorption of total radiations. *B* Absorption of low-energy electrons. *C* Linear range plot of absorption of low-energy electrons. Detector: mica-end-window Geiger counter.

Magnetic beta-ray spectrographic measurements have given the ratio of conversion in the K to the $(L+M)$ electron shells of technetium as 2.0,[7] 1.6±0.2[8] and 1.7±0.2 (see Fig. 3), respectively. Goldhaber and Sunyar[9] accordingly have classified the isomeric transition as $M4$ making use of this ratio, the life-time, and the fact that the total conversion coefficient is very large.[10] This multipole order assignment is in agreement with shell theory predictions[11] which indicate close lying $p_{1/2}^-$ and $g_{9/2}^+$ levels in technetium. The energy systematics of these levels is such that it may be inferred that Tc^{97g} has a spin of 9/2.

Recent energy considerations[12,13] predict that Tc^{97g} is probably slightly unstable relative to Mo^{97g} whose spin[14] is probably 5/2. In this case, the transition between them would be second forbidden, ($\Delta I=2$, no), and a long half-life would be expected. By analogy with Tc^{99g}, if a logft value of about 12.5 occurs, a half-life for the decay of Tc^{97g} by orbital electron capture of *ca* 10^5 years may be estimated. Lower limits of 15 and 250 years, respectively, may be deduced for

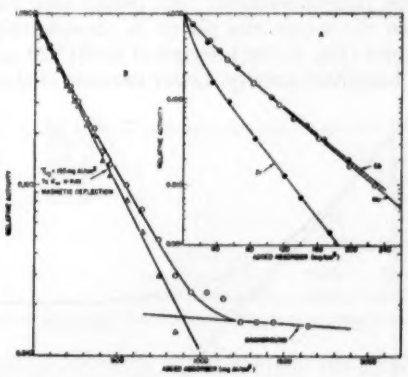

FIG. 2. Absorption of x-rays from 90.5-day Tc^{97m}: *A* Critical absorption measurements. *B* Absorption in aluminum after removal of electrons by magnetic field.

[1] B. N. Cacciapuoti and E. Segrè, Phys. Rev. **52**, 1253 (1937).
[2] Motta, Boyd, and Brosi, Phys. Rev. **71**, 210 (1947).
[3] E. E. Motta and G. E. Boyd, Phys. Rev. **74**, 344 (1948).
[4] D. T. Eggen and M. L. Pool, Phys. Rev. **74**, 57 (1948).
[5] B. N. Cacciapuoti, Phys. Rev. **55**, 110 (1939).
[6] D. C. Kalbfell, Phys. Rev. **55**, 422 (1939).
[7] A. C. Helmholtz, Phys. Rev. **60**, 415 (1941).
[8] H. Medicus and P. Sherrer, Helv. Phys. Acta **23**, 299 (1950).
[9] M. Goldhaber and A. W. Sunyar, Phys. Rev. **83**, 906 (1951).
[10] We have been unable as yet to detect any unconverted 95.8 kev gamma rays using intense sources of 90.5-day Tc^{97m} and a sodium iodide scintillation counter spectrometer.
[11] Mayer, Moszkowski, and Nordheim, Revs. Modern Phys. **23**, 315 (1951).
[12] H. Suess and J. Jensen, Arkiv. Fysik **3**, 577 (1951).
[13] K. Way and M. Wood, Phys. Rev. **94**, 119 (1954).
[14] O. H. Arroe, Phys. Rev. **79**, 212 (1950).

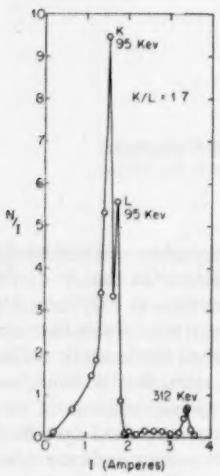

FIG. 3. Conversion electron spectrum of 90.5-day Tc^{97m} (magnetic lens beta-ray spectrometer. Measurements in collaboration with B. H. Ketelle).

the half-life of the ground state from reports[7,15] on the decay of the 90.5-day Tc^{97m}.

In our experimental work, the decay of six technetium sources of varying initial intensity was measured for periods ranging from 1800 up to 2250 days. Three of these sources were separated from molybdenum metal irradiated with 19-Mev deuterons, two were from molybdenum enriched in Mo^{97} (78 percent) irradiated with 14- and 19-Mev deuterons, respectively, and one was prepared from 25 grams of ruthenium oxide irradiated in the Oak Ridge Pile to an integrated flux, *nvt*, of 5.2×10^{18}. The decay of the latter, measured using a flow-type (argone-methane) beta proportional counter in which the source was placed in the counting gas, now shows (Fig. 4) the presence of about 320 counts/min of long-lived activity. Lesser amounts of the same activity (60, 135, and 125 counts/min were also seen in three other sources. Two sources decayed to less than 10 counts/min.

The presence of Mo *K* x-rays in the radiations emitted by the long-lived activity was established using a beryllium side-window, krypton-filled proportional spectrometer (Fig. 5*A*). Absorption of the total radiations in aluminum further showed beta rays of *ca* 0.3-Mev maximum energy (Fig. 5*B*) together with molybdenum x-rays. The beta particles presumably arise from lesser amounts of long-lived Tc^{97g} also formed in all the bombardments.

A half-life of approximately 10^4-10^5 years for the decay of Tc^{97g} has been deduced using the amounts of 90-day Tc^{97m} activity observed at the end of the bombardments to estimate the number of Tc^{97g} atoms formed, and the observed Mo x-ray counting rate corrected for geometry, absorption and Geiger counter detection efficiency. The considerable uncertainty in this estimate arises largely because the unknown relative yields of Tc^{97m} and Tc^{97g} produced in the deuteron irradiations of molybdenum. The branching to form these isomers in the decay of 2.9-day Ru^{97} is also not sufficiently known to permit more than a rough estimate of the total number of Tc^{97g} atoms in the sources measured.

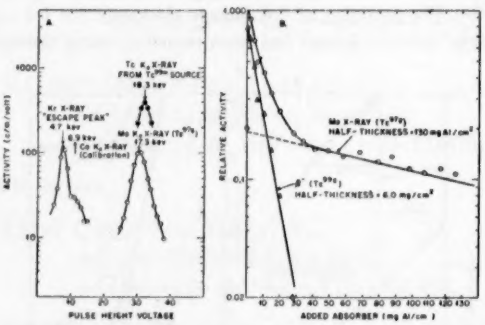

FIG. 5. Measurements on radiations emitted by long-lived technetium. *A*. Krypton-filled x-ray proportional spectrometer measurements. *B*. Absorption of total radiations in aluminum using a Geiger counter as detector.

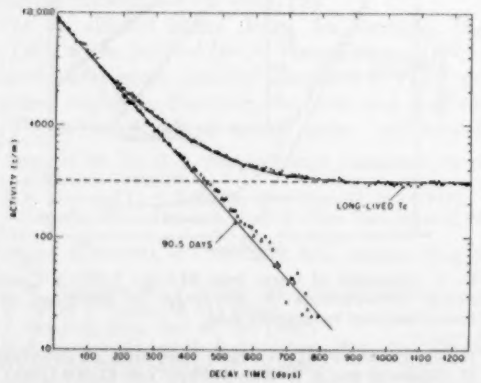

FIG. 4. Decay of total radiations from a 90.5-day Tc^{97m} source separated from neutron-irradiated ruthenium (observed with an internal beta-proportional flow counter). Plot of decay starts 714 days after bombardment.

It is believed that the foregoing observations may exclude the possibility that Tc^{97g} will be found in terrestrial, or in meteoritic materials. However, the possible occurrence of minute amounts of the odd-odd isotope, Tc^{98}, has not been eliminated. In a forthcoming publication[16] we shall report additional searches for technetium in various ores and meteorites, as well as new information supporting the view[17] that Tc^{98} must possess a very long half-life.

[15] J. E. Edwards and M. L. Pool, Phys. Rev. **72**, 384 (1947).

[16] Boyd, Larson, and Cobble, 1952 (unpublished researches).

[17] G. E. Boyd, Record Chem. Progr. (Kresge-Hooker Sci. Lib.) **12**, 67 (1951); see also, E. Segré, Nuovo cimento **9**, 1008 (1952).

Further Study of the Decay Scheme of Ir^{192}

R. W. Pringle, W. Turchinetz, and H. W. Taylor
Physics Department, University of Manitoba, Winnipeg, Canada

(Received March 15, 1954)

Scintillation spectrometer studies have revealed four high-energy gamma-ray components at 788, 883, 1080, and 1210 kev, with the possibility of a fifth component near 920 kev. The $Ir^{192}-Pt^{192}$ ground-ground state transition energy has been measured as 1490±20 kev. Level schemes are proposed for Pt^{192} and Os^{192}, the product nuclei upon the beta decay of Ir^{192}.

DECAY schemes for the disintegration of Ir^{192} have been proposed on the basis of several earlier investigations.[1-3] In the present work the gamma-ray spectrum has been studied carefully in the high-energy region,[3] and new measurements have been made. The spectrum was obtained with a scintillation spectrometer of improved resolution, utilizing a 1½ in.×1½ in. NaI(Tl) cylinder, DuMont K 1186 photomultiplier, and sliding channel differential discriminator. The resolution of the device was 7 percent for the 662-kev gamma ray from Cs^{137}.

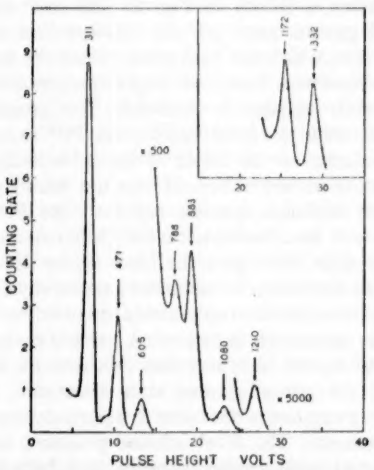

FIG. 1. Scintillation spectrometer pulse-height distribution for the gamma rays from Ir^{192}, showing four new high-energy components at 788, 883, 1080, and 1210 kev. An additional component at approximately 920 kev is inferred from a study of pulse-height distribution photographs, but is not resolved here. The inset shows the 1172- and 1332-kev lines from Co^{60}, used for calibration.

Figure 1 is the pulse-height distribution obtained with Ir^{192}, and the inset shows the 1172- and 1332-kev lines for Co^{60}, used for calibration of the high-energy components. The measurements were made with the source and detector in a 3-inch lead castle to reduce background. The feature at 311 kev is due to three unresolved gamma rays at 296, 308, and 316 kev (see Table I); the peak at 471 kev is the sum of the 468- and 485-kev lines with an intimation of the 415-kev line in the trough between 311 kev and 471 kev. At 605 kev is a peak due to two unresolved gamma rays at 605 and 613 kev. These energies were obtained using the 662-kev gamma ray from Cs^{137} for calibration. The high-energy radiation is of very low intensity as may be seen from the change in counting rate scale by a factor of 500 in Fig. 1, followed by a change to a factor of 5000. Four high-energy components are well resolved at 788 (0.9), 883 (1.9), 1080 (0.4), and 1210 (0.07) kev. Corrected gamma-ray intensities are given in parenthesis, and indicate percentage of the intensity of the unresolved group formed by the 605- and 613-kev gamma rays. An analysis of a number of long-exposure oscillograms of the pulse-height spectrum verified the presence of the four well-resolved components, and encouraged the belief that a further weak component existed close to 920 kev.

TABLE I. Comparative list of gamma rays from Ir^{192}. Energies in kev.

Cork	Muller	Roulston and Pringle	Present investigation	Energies used for level scheme
135.9	136.331			136
150				
173				173
201.1	201.306			201 *K*
205.7	205.376			205 *K*
283				283(*K*)
294.9	295.949			296
307.7	308.454			308
316.1	316.462			316
396				396 *K*
415.1				415
438				
467.4	467.984			468
484	484.75			485 *K*
588.6	588.40			588
603.7	604.53			605
611.2	612.87			613
		775	788	788
		870	883	883
		further unresolved radiations up to 1200	*ca* 920 1080 1210	921 1080 *K* 1210

In order to be sure that these high-energy components were due to true cross-over transitions (see Fig. 2), and not due to "pileup," i.e., to chance coincidences

[1] Cork, LeBlanc, Stoddard, Childs, Branyan, and Martin, Phys. Rev. **82**, 258 (1951).
[2] Muller, Hoyt, Klein, and DuMond, Phys. Rev. **88**, 775 (1952).
[3] K. I. Roulston and R. W. Pringle, Phys. Rev. **87**, 930 (1952).

in the phosphor between gamma rays of energies to provide these lines as sums, the source-crystal distance was increased threefold, and the distribution was obtained again. If the lines were genuine they would have been reduced in the same proportion, due to the reduction in solid angle. Any spurious lines would have been reduced in proportion to the (solid angle)^2 since the probability for the occurrence of such an event is the product of the probabilities for the occurrence of each constituent event and these are proportional to the solid angle subtended by the crystal at the source. Since all the features in Fig. 1 were reduced in the same proportion it was concluded that the high-energy lines were due to genuine cross-over transitions. The low-energy features of the gamma-ray spectrum were obtained in a short time, but the high-energy required very long counting times, up to several hours on each point, in order to insure adequate statistics. A slight long-term drift in the energy scale was detected during these observations, and it became necessary to monitor the energy scale after each count.

Table I is a comparative list of gamma rays from the work of Cork *et al.* (beta-ray spectrometer), Muller *et al.* (crystal diffraction spectrometer), Roulston and Pringle (scintillation spectrometer), and the present investigation. The last column gives the best energy values, to the nearest kev, as they have been selected for use in the level scheme of Fig. 2. The association of a gamma ray with the K-capture process to Os^{192} is designated by K. This is done on the basis of Cork's beta-spectrometer measurements, for all but the 1080-kev component (see below).

A measurement of the $Ir^{192}-Pt^{192}$ ground-ground state transition energy was made to clarify the decay scheme. This was accomplished by measuring the integral bias end point for the beta-ray plus gamma-ray distribution due to a fine powder source of Ir^{192} immersed in a liquid scintillator consisting of xylene with 0.1 g/l diphenyloxazole and 4.0 g/l terphenyl.[4] The end point thus obtained was compared with the beta-ray-gamma-ray end point for a Cs^{137} source, using the end point for the Co^{60} gamma-ray distribution to correlate the two sets of measurements. The result of this measurement gave 1.49 ± 0.02 Mev for the $Ir^{192}-Pt^{192}$ ground-ground state transition energy. This is lower than an earlier reported value,[3] where the measurement was taken under less favorable circumstances with an Ir^{192} source external to a sodium iodide crystal, before efficient liquid scintillators were available.

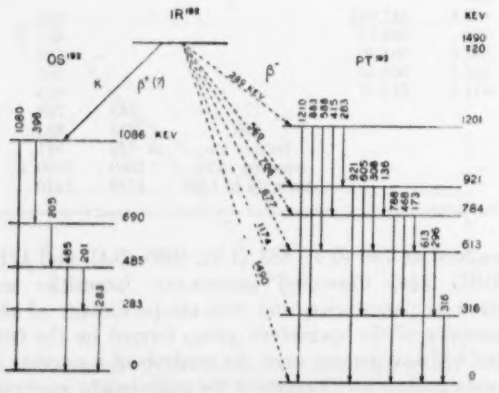

FIG. 2. Proposed level schemes for Pt^{192} and Os^{192}, following beta emission from Ir^{192}. The gamma-ray energies are the selected measured values (see Table I), the level values give the best fit to these, the $Ir^{192}-Pt^{192}$ ground-ground state transition energy is that obtained by direct measurement (see text), and the negatron partial components are those required to fit this transition energy and the proposed level scheme. There is evidence for the existence of five of these components (see reference 5).

The gamma rays listed in the last column of Table I made it possible to construct a decay scheme which was self-consistent and which made use of all but two of the gamma rays reported by Cork, without introducing any gamma rays that have not been observed directly either by Cork's group or in this laboratory. This scheme is shown in Fig. 2. The two unaccommodated gamma rays are the 150-kev line and the 438-kev line, which are both weak. Since the existence of these lines was based on single features of Cork's curves, their validity is doubtful. The ground-state transition from the level 921 kev in Pt^{192} is included in the scheme on the basis of the admittedly weak evidence mentioned above. It was not found possible to fit the 1080-kev gamma ray into the Pt^{192} level scheme, and its allocation to the Os^{192} scheme seems most plausible. In Fig. 1 the level values are chosen to give the best fit to the measured gamma-ray energies. The negatron partial components required to fit the Pt^{192} level scheme are indicated. A private communication from Kyles[5] indicates that whereas he has not observed the ground-ground state transition, he has evidence in support of the other five partial components of this scheme. The level scheme proposed for Pt^{192} is consistent with gamma-gamma[3] and beta-gamma[5] coincidence investigations. Gamma-gamma angular correlation studies will be undertaken to determine uniquely the spins of the excited levels of Pt^{192}.

To sum up, Ir^{192} decays by negatron emission to form Pt^{192} in five possible excited states, with no evidence for the ground-ground state transition; and by orbital electron capture to form Os^{192} in at least one excited state. While the possibility of positron emission cannot be ruled out, the absence of any features in the 511-kev region of the distribution, which would be the result of annihilation quanta, indicates that this mode of decay is very rare.

Our thanks are due to the National Research Council of Canada for the support of this work, and for the award of a Fellowship to one of us (H.W.T.).

[4] Pringle, Black, Funt, and Sobering, Phys. Rev. **92**, 1582 (1953).

[5] J. Kyles, University of Edinburgh (private communication).

Angular Distribution and Cross Section of $Li^6(n,\alpha)H^3$ for Neutrons of 1.1, 1.5, and 2.0 Mev*

JAMES B. WEDDELL† AND JAMES H. ROBERTS
Northwestern University, Evanston, Illinois

(Received March 29, 1954)

The angular distribution of $Li^6(n,\alpha)H^3$ has been determined for 1.1, 1.5, and 2.0 Mev neutrons by track measurements in 100-micron Ilford *C2* and *E1* lithium-six loaded emulsions. The triton yield function has been expressed as a finite series of spherical harmonics in the center-of-mass system. The s and p components of the neutron wave appear to predominate in the reaction, but the data are not sufficiently accurate to exclude the possibility of contributions from higher angular momentum components.

The cross section was also determined for the reaction at neutron energies of 1.5 and 2.0 Mev relative to that at 0.60 Mev. This was done by exposing the same plate to 0.60-, and to 1.5- or 2.0-Mev neutrons; a long counter was used to measure the neutron flux at each energy. Tracks were selected in a suitable cone so as to resolve the two energy groups. Ther esults were 0.32 ± 0.06 and 0.27 ± 0.04 barn at 1.5 and 2.0 Mev, respectively.

1. INTRODUCTION

MEASUREMENTS on the angular distribution of $Li^6(n,\alpha)H^3$ at neutron energies of 200, 270, 400, and 600 kev have been previously reported.[1] In order to extend to higher energies the range of usefulness of this reaction for neutron spectroscopy, and to obtain more data of theoretical interest, measurements have been performed at neutron energies of 1.1, 1.5, and 2.0 Mev. Measurements have also been made at these energies of the cross section of the reaction. Preliminary results were reported previously.[2]

The technique in the angular distribution measurements is essentially the same as that used at the lower energies.[1] Ilford *E1* and *C2* plates loaded with enriched Li^6 were exposed to unidirectional monoergic neutrons. The cross section of the reaction is determined, relative to that at 600 kev,[3] by exposing the same plates to measured fluxes of this energy and of one of the higher energies. The sums of ranges, $\sum R$, of tracks having neutron-triton angles ϕ less than selected values, fall into two groups associated with the two exposures. From the relative numbers of tracks in these two groups, and the angular distributions at the two energies, the cross sections at 1.1, 1.5, and 2.0 Mev are calculated.

2. EXPOSURE AND PROCESSING OF PLATES

The 100-micron Ilford *C2* and *E1* plates loaded with enriched Li^6 were exposed to neutrons from $Li^7(p,n)Be^7$ at the large electrostatic generator of the Oak Ridge National Laboratory. The exposure geometry is shown in Fig. 1. Each plate was in a cadmium box. The long-counter was calibrated with a Po–Be source placed as close as possible to the Li target. To reduce attenuation of the neutron beam in the emulsion, the neutrons were incident at an angle $\nu=8°$ to the emulsion plane.

The proton energies were chosen so that the neutron energies would peak at the desired values. The target for the 600-kev exposure had a thickness of 18 ± 3 kev; for the higher energies a target 57 ± 5 kev thick was used. At 600 kev the flux at the center of each plate was 7.0×10^8 neutrons/cm^2; at the higher energies it was 8.5×10^8 neutrons/cm^2.

The plates were processed essentially as before.[1] All were restored to their original thickness, at the time of exposure, by soaking in an aqueous solution of glycerin.

3. TRACK MEASUREMENTS

Track measurements[1] and observer training[4] have been discussed previously. Some tracks were difficult to interpret correctly. A misinterpreted track, in which the triton direction had been reversed, could often be identified from its length;[5] such identification rested upon the assumption that the track was produced by a neutron of full energy coming directly from the target. No doubt some tracks were caused by neutrons scattered in the laboratory. Since the

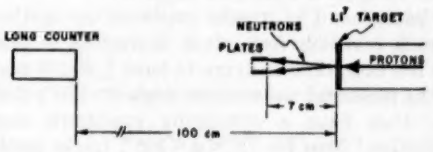

FIG. 1. Exposure geometry.

* This work was supported by a U. S. Atomic Energy Commission contract. It formed the subject of a dissertation submitted to the Graduate School of Northwestern University by James B. Weddell in partial fulfillment of the requirements for the degree of Doctor of Philosophy, June, 1953.

† Now at Westinghouse Research Laboratories, East Pittsburgh, Pennsylvania.

[1] J. H. Roberts and H. M. Mann, Phys. Rev. **83**, 202 (1951); W. O. Solano and J. H. Roberts, Phys. Rev. **89**, 892 (1953); Darlington, Haugsnes, Mann, and Roberts, Phys. Rev. **90**, 1049 (1953).

[2] J. B. Weddell and J. H. Roberts, Phys. Rev. **89**, 891 (1953); Phys. Rev. **93**, 924 (1954).

[3] J. M. Blair and R. Holland, cited in Neutron Cross-Sections, Atomic Energy Commission Report 2040 (Office of Technical Services, Department of Commerce, Washington, D. C., 1952).

[4] J. Haugsnes and J. H. Roberts, Los Alamos Scientific Laboratory Report LA-1303, Los Alamos (unpublished).

[5] G. R. Keepin, Jr., and J. H. Roberts, Rev. Sci. Instr. **21**, 163 (1950).

number of questionable tracks was generally about 10 percent of the total number measured, no attempt was made to correct for these misinterpretations. On the average, errors resulting from misinterpretation tend to cancel. As the neutron energy is increased, the difference in length increases for tracks having neutron-triton angles ϕ and $(180°-\phi)$, as measured in the laboratory system. This fact enabled the observers to reduce the fraction of misinterpreted tracks below that experienced in work at lower neutron energies.

In the determination of the reaction cross section, ϕ was restricted to $\leq 30°$ in the plate exposed at 600 and 1100 kev, and to $\leq 60°$ at the other pairs of energies. This is necessary in order that the groups of tracks associated with the two exposures be adequately resolved on the basis of the sum of ranges, $\sum R$.

4. GEOMETRICAL AND BACKGROUND CORRECTIONS

For a track of given $\sum R$ and ϕ, there is a certain probability P that it satisfy the geometrical selection criteria. These criteria were that the vertical projection of a track not exceed 25 microns and that no part of a track lie less than 3 microns from either emulsion surface. These restrictions refer to a plate which has had its emulsion thickness restored to the value which existed at the time of exposure. If one end of the track (e.g., the alpha) is at least 25 microns from either surface, the triton end will lie on a circle of radius $\sum R \sin\phi$; P is the fraction of the circumference of this circle less than 25 microns above or below the alpha end. Consequently,

$$\frac{1}{P}=\frac{\pi/2}{\sin^{-1}(25/\sum R \sin\phi)}. \tag{1}$$

If the alpha end is at a distance $\gamma<25$ microns from the emulsion surface toward which the triton has traveled,

$$\frac{1}{P}=\frac{\pi/2}{\sin^{-1}(\gamma/\sum R \sin\phi)}. \tag{2}$$

These formulas must be corrected for the fact that the angle of incidence of the neutrons with respect to the emulsion plane is not zero, but 8°. The correction is small and is treated in detail elsewhere.[6] Each track is then assigned a statistical weight $1/P$.

A background of tracks produced by epithermal neutrons resulting from room scattering is present. With few exceptions such tracks have $\sum R<49$ microns and the measured alpha-triton angle $\theta>170°$; furthermore, they have a spherically symmetric angular distribution.[1] Now for $75°\leq\phi\leq 105°$, tracks produced by neutrons of energy greater than 1 Mev have $\sum R>55$ microns and $\theta<170°$; within this range of values of ϕ, the epithermal background tracks can usually be identified. From the number of these tracks in that interval, and their isotropic distribution in ϕ, the total number of epithermal background tracks is determined. The corrections for such tracks were small, their number never exceeding 7 percent of those measured.

Be^7 has an excited state at 430 kev.[7] The threshold for the production of the group of neutrons associated with this state in $Li^7(p,n)$ is not attained until the neutrons associated with the ground state have an energy of 660 kev. In the energy region which concerns us, the group of neutrons associated with this excited state is about 10 percent as abundant as the main group, and the two groups emitted in the forward direction differ in energy by about 480 kev.[7] Since the angular distribution and cross section were measured for neutron energies differing by about this amount, it was possible to correct for the presence of this secondary group of neutrons.

5. DATA AND RESULTS

In order to determine the angular distribution, the tracks were grouped in 10° intervals of ϕ. Each track was assigned its statistical weight P^{-1}, and $\sum P^{-1}$ was determined for the tracks in each interval. After the background corrections were made, the results were transformed to the center-of-mass system and expressed in terms of equal 10° intervals of ϕ_0, the neutron-triton angle in this system. The results are shown in Table I. The results are normalized so that the sum of the weighted numbers of tracks in all ϕ_0-intervals is numerically equal to the capture cross section σ_c in barns, at each neutron energy. At each

TABLE I. Relative number of tritons per 10° interval in the center-of-mass system. (Sum normalized to cross section.)

ϕ_0 interval (degrees)	Neutron energy (Mev) 1.1	1.5	2.0
0–10	0.006	0.006	0.004
10–20	0.019	0.017	0.008
20–30	0.019	0.021	0.014
30–40	0.025	0.023	0.013
40–50	0.030	0.028	0.019
50–60	0.028	0.025	0.025
60–70	0.029	0.026	0.030
70–80	0.029	0.032	0.024
80–90	0.024	0.033	0.027
90–100	0.017	0.028	0.019
100–110	0.014	0.020	0.021
110–120	0.013	0.016	0.017
120–130	0.012	0.014	0.016
130–140	0.007	0.011	0.009
140–150	0.004	0.008	0.010
150–160	0.002	0.006	0.007
160–170	0.001	0.004	0.004
170–180	0.001	0.001	0.001
0–180	0.28[a]	0.32	0.27

[a] This value was taken from the data of F. L. Ribe (private communication).

[6] J. B. Weddell, dissertation, Northwestern University (University Microfilms, Inc., Ann Arbor, 1953).

[7] Johnson, Laubenstein, and Richards, Phys. Rev. 77, 413 (1950).

energy, the total number of measured tracks was from 1400 to 1500.

To determine σ_e for $Li^6(n,\alpha)$, about 400 tracks were measured for $\phi_0 \leq 68°$ in a plate exposed to 600-kev neutrons alone. About 400 tracks were also measured for $\phi_0 \leq 68°$ in the plates exposed at both 600 kev and 1100, 1500, or 2000 kev. Tracks in this same forward cone were selected from the angular distribution data obtained from the plates exposed only at 1100, 1500, or 2000 kev. (The forward cone was $\phi_0 \leq 33°$ for the work at 1100 kev.) The neutron flux to which each plate was exposed was determined by a long-counter placed 1 meter from the target of the electrostatic generator (Fig. 1).

Figure 2 shows the number of tracks, weighted by P^{-1}, plotted as a function of $\sum R$ for the three plates used to determine σ_e at 2000 kev. From the reaction kinetics, the range-energy relationships for the emulsions, and straggling, about 90 percent of the tracks from 2.0-Mev neutrons in $0° \leq \phi_0 \leq 68°$ should have $\sum R$ in the range from 72 to 105 microns. The corresponding values for 0.6 Mev are from 48 to 66 microns. After adjusting the area under curve (c) to that under curve (b), the tracks in the region from 48 to 66 microns resulting from the higher energy exposure can be subtracted. The tracks remaining in this region are then attributed to 0.6-Mev neutrons with $0° \leq \phi_0 \leq 68°$. The ratio of the longer group of tracks to the shorter, adjusted to equal neutron fluxes, gives the ratio of $\int_0^{68°} (d\sigma_c/d\Omega_0) 2\pi \sin\phi_0 d\phi_0$ for 2.0 and 0.6 Mev, where $d\Omega_0$ is the solid angle between ϕ_0 and $(\phi_0 + d\phi_0)$ in the center-of-mass system, after small corrections are made for the presence of neutrons associated with the 430-kev state of Be^7. From these measurements and the data in Table I, the relative values of σ_e are determined at these two energies. Using 0.45 barn as the value of σ_e at 0.6 Mev, from the data of Blair and Holland,[3] the values of σ_e at 1.5 and 2.0 Mev are 0.32 ± 0.06 barn and 0.27 ± 0.04 barn, respectively. Our measurement of σ_e at 1.1 Mev gave 0.19 barn, but this is believed to be less reliable because of poorer resolution and statistics. Our data in Table I at 1.1 Mev are therefore normalized to 0.28 barn, as reported by Ribe.[8]

TABLE II. Coefficients of the triton yield function in barns per steradian. (± gives statistical accuracy only.)

Neutron energy (Mev)	a_0	a_1	a_2
0.20	0.167±0.004	0.102±0.007	0.156±0.009
0.40	0.095±0.003	0.049±0.005	0.078±0.006
0.60	0.040±0.001	0.012±0.002	0.019±0.002
1.10	0.022±0.001	0.022±0.001	0.006±0.002
1.50	0.026±0.001	0.017±0.002	0.003±0.002
2.00	0.022±0.001	0.008±0.001	0.001±0.001

[8] F. L. Ribe, Phys. Rev. 87, 205 (1952); also private communication.

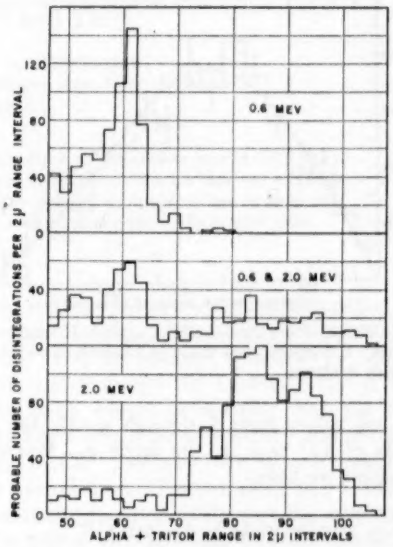

FIG. 2. Weighted numbers of tracks in each 2 micron interval of ΣR. Upper curve, plate exposed to 0.6-Mev neutrons alone. Middle curve, plate exposed to 0.6-Mev and 2.0-Mev neutrons. Lower curve, plate exposed to 2.0-Mev neutrons alone.

6. YIELD FUNCTION

We assume that the yield function $Y(\phi_0)$ can be expanded into spherical harmonics:

$$Y(\phi_0) = \sum_{i=0}^{\infty} a_i P_i(\phi_0), \tag{3}$$

and furthermore that the yield function can be adequately approximated by the finite series

$$Y(\phi_0) = \sum_{i=0}^{2} a_i P_i(\phi_0), \tag{4}$$

where $P_0(\phi_0) = 1$, $P_1 = \cos\phi_0$, and $P_2 = \frac{3}{2}\cos^2\phi_0 - \frac{1}{2}$. The coefficients a_i are obtained by a numerical integration from

$$a_i = (i + \tfrac{1}{2}) \int_0^{\pi} 2\pi Y(\phi_0) P_i(\phi_0) \sin\phi_0 d\phi_0, \tag{5}$$

or, if written as a summation,

$$a_i = 2\pi(i + \tfrac{1}{2}) \sum_{k=1}^{n} P_{ik}(\phi_0) Y_k(\phi_0) (\Delta \cos\phi_0)_k, \tag{6}$$

where P_{ik} is the mean value of P_i in the kth 10° interval of ϕ_0, and Y_k is the mean value of Y in the same interval.

Now in our measurements we have determined

$$Y_k(\phi_0)(\Delta \cos\phi_0)_k = (\textstyle\sum P^{-1})_k, \tag{7}$$

normalized such that

$$\sigma_e = \int_0^{\pi} 2\pi Y(\phi_0) \sin\phi_0 d\phi_0, \tag{8}$$

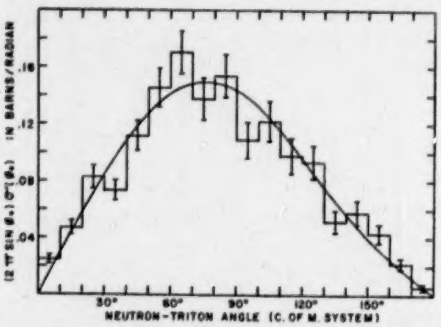

FIG. 3. Weighted number of tracks in each 10° interval of ϕ_0 (histogram). Integrated yield function (smooth curve). Data are for 2.0-Mev neutrons.

and k has values from 1 through $n=18$, for the 18 intervals of 10° each in the angle ϕ_0. Making this substitution, we have

$$a_i=2\pi(i+\tfrac{1}{2})\sum_{k=1}^{n}P_{ik}(\phi_0)(\textstyle\sum P^{-1})_k. \tag{9}$$

The standard deviation of $(\sum P^{-1})_k$ is equal to $(\sum P^{-1})_k/\sqrt{N_k}$, where N_k is the actual measured number of tracks in the kth interval; N_k is of the order of 50 to 100 for most intervals. Let a'_{ik} be the standard deviation of the contribution to a_i from the kth interval:[9]

$$a_{ik}'=(i+\tfrac{1}{2})P_{ik}(\phi_0)(\textstyle\sum P^{-1})_k/\sqrt{N_k}. \tag{10}$$

Therefore the standard deviation of a_i is given by

$$a_i'=(i+\tfrac{1}{2})\{\sum_{k=1}^{n}[(\textstyle\sum P^{-1})_k^2/N_k]P_{ik}^2(\phi_0)\}^{\frac{1}{2}}. \tag{11}$$

Table II gives the values of a_0, a_1, and a_2 as calculated from Eq. (9), not only for the neutron energies studied in this paper, but also for the energies previously investigated in this laboratory.[1] The variations given after the values of a_i are the values a_i' as found from Eq. (11). The yield function, including only the first three coefficients, is therefore

$$Y(\phi_0)=a_0+a_1P_1(\phi_0)+a_2P_2(\phi_0), \tag{12}$$

which can also be written as

$$Y(\phi_0)=A+B\cos\phi_0+C\cos^2\phi_0, \tag{13}$$

where $A=a_0-\frac{1}{2}a_2$, $B=a_1$, and $C=\frac{3}{2}a_2$. The values of these coefficients as thus determined for the lower neutron energies agree within their statistical accuracy with those previously reported.[1]

It should be noted that, from Eq. (5) and the orthogonality of the spherical harmonics, the first three terms of Eq. (12) are independent of the possible existence of terms of higher order, but in the power series (13) in $\cos\phi_0$ this is not so. The statistical accuracy is not adequate at any of the neutron energies definitely to exclude the existence of terms of higher order in (12) arising from d, f, etc., components of the neutron wave. But if the given series are complete, only the s and p components enter into the reaction; in any case these appear to be the predominant components.

The smooth curve in Fig. 3 is a plot of $2\pi Y(\phi_0)\sin\phi_0$ including terms through a_2 for $E_n=2.0$ Mev. The agreement with the histogram of the data is satisfactory in view of the statistical accuracy of the latter. Figure 4 shows a plot of $Y(\phi_0)$ at neutron energies of 1.1, 1.5, and 2.0 Mev.

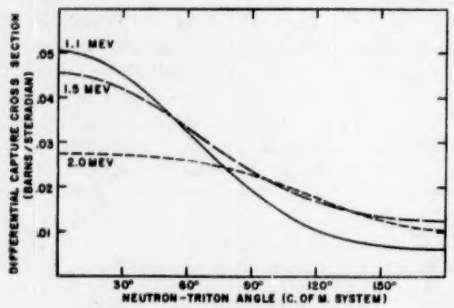

FIG. 4. Normalized yield functions *vs* ϕ_0.

7. ACKNOWLEDGMENTS

The authors wish to express their appreciation of the work of those who participated in the previous investigations: Lillian E. Darlington, Jack Haugsnes, and Harry M. Mann. They also wish to thank H. B. Willard, J. K. Bair, and others at the Oak Ridge National Laboratory for their assistance in exposing the plates; F. L. Ribe for an advance copy of his results regarding the reaction cross section; H. B. Billington for developing the plates; Jack Haugsnes for preparing the figures and Lillian Darlington for help with the calculations; and especially Mrs. Margaret Steele, Jerome Green, Richard Leach, William Meltzer, Bernard Turbow, and Daniel Wilson, who for long hours faithfully measured tracks and performed routine calculations.

[9] P. M. Endt, Physica 18, 421 (1952).

Decay Schemes of Cd^{114} and Te^{125}

D. C. Lu, W. H. Kelly, and M. L. Wiedenbeck
Randall Laboratory of Physics, University of Michigan, Ann Arbor, Michigan

(Received March 8, 1954)

Using the scintillation-crystal summing technique, coincidences between the gamma rays of Cd^{114} and of Te^{125} were studied. In the case of Cd^{114} no indications were seen of the existence of a 1.3-Mev and a 576-kev gamma ray previously reported. In the case of Te^{125}, the 176-kev gamma ray appeared not to be in coincidence with any other gamma rays. It must, therefore, end in a metastable state or the ground state.

COINCIDENCE studies have been made on the γ rays emitted following orbital electron capture of In^{114} and the β decay of Sb^{125}, using the single scintillation crystal summing technique described in a previous letter.[1] This method consists of introducing the nuclear samples at the center of a NaI(Tl) crystal. Coincidences are then revealed by the appearances of new peaks in the γ spectrum whose positions correspond to the sums of the individual energies of the coincident γ rays.

The result for In^{114} is shown in Fig. 1. The upper curve represents the ordinary γ-ray spectrum taken with the sample six inches outside the crystal; a weak peak appears at 1.28 Mev. The lower curve, taken with the sample inside the crystal, shows a marked strengthening of the 1.28-Mev peak. This is interpreted as being due to the coincidences between the 552-kev and the 725-kev γ rays. No indication is noticed, however, of a sum peak representing the coincidence between the 1.3-Mev and the 552-kev γ rays as is required by the decay shown in Fig. 1. This decay scheme was taken from the table of isotopes compiled by Hollander, Perlman, and Seaborg.[2] The 1.3-Mev γ ray, if it exists, must be much weaker in intensity than has been reported.[3] The strong β activity of In^{114} and the 22.6-kev K x-rays of Cd^{114} produced from electron capture were mostly cut off by a 2.5-mm copper shield and therefore essentially do not interfere with the measurements.

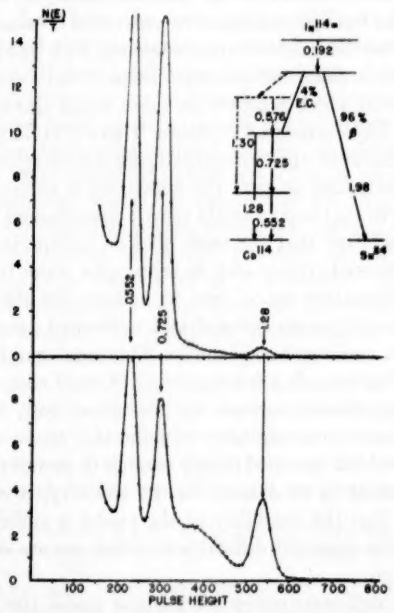

FIG. 1. γ-ray spectra of Cd^{114}. Energies in Mev indicated at the top of peaks.

The γ rays of Te^{125} following β decay from Sb^{125} have been studied by previous investigators.[4,5] Figure 2 shows the results of the present investigation and the decay scheme proposed by Siegbahn and Forsling.[4] The dotted curve represents the ordinary γ-ray spectrum with the sample outside, the solid curve with the sample inside. The shift in positions of the 425-kev and the 601-kev peaks are interpreted as an indication of their being in coincidence with the 27-kev K x-ray from the very highly internally converted 35-kev transition. The decay scheme also indicates that the 176-kev γ ray is in cascade with the 425-kev and the 35-kev transitions. In view of the relatively high efficiency of the crystal for the low-energy 176-kev γ ray and the 27-kev x-ray, this cascade should be clearly revealed,

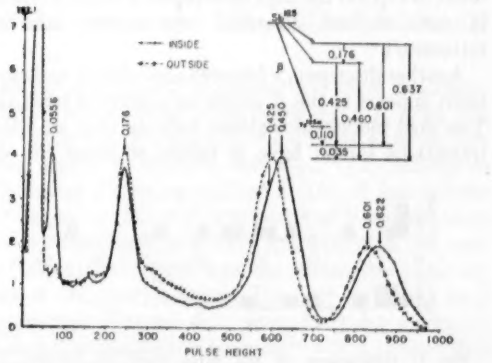

FIG. 2. γ-ray spectra of Te^{125} dotted curve with sample outside crystal, solid curve with sample inside. Energies in Mev indicated at the top of peaks.

[1] D. C. Lu and M. L. Wiedenbeck, Phys. Rev. **94**, 501 (1954).

[2] Hollander, Perlman, and Seaborg, Revs. Modern Phys. **25**, 469 (1953).

[3] Johns, Cox, Donnelly, and McMullen, Phys. Rev. **87**, 1134 (1952).

[4] K. Siegbahn and W. Forsling, Arkiv. Fysik **1**, 505 (1949).

[5] Kern, Mitchell, and Zaffarano, Phys. Rev. **76**, 94 (1949).

when the sample is inside, by (a) a shift to the right of the position of the 176-kev peak as a result of its coincidence with the 27-kev x-rays; and (b) a marked increase in intensity for the peak at 622 kev due to the coincidence between the 176-kev and the 425-kev γ rays. Such indications, however, are definitely lacking here. If the good energy fitting of this decay scheme is to be preserved, one must assume that the energy level at 470 kev is metastable with a half-life longer than several microseconds. However, γ rays originating in this level have been reported to have low e/γ factors. An alternative solution is to place the 176-kev transition elsewhere. This would require a fourth β transition from Sb^{125}, which has not been reported.

PHYSICAL REVIEW VOLUME 95, NUMBER 1 JULY 1, 1954

A β-Decay Matrix Element for a Deformed Core Model*

MARTIN G. REDLICH† AND EUGENE P. WIGNER
Palmer Physical Laboratory, Princeton University, Princeton, New Jersey
(Received March 29, 1954)

The *ft* value for an allowed unfavored β transition, calculated on a deformed core+single-particle model, is $\lesssim 3$ times the single-particle value and about 4 percent of the observed value. The deformations of initial and final states were based on their quadrupole moments. The calculation indicates that for this model core orthogonality generally does not account for the difference between allowed favored and unfavored *ft* values.

I. INTRODUCTION

THERE exist many nuclei whose quadrupole moments are much larger than can be expected from the shell model. For example, the quadrupole moments of two In ($Z=49$) isotopes and two Sb ($Z=51$) isotopes, which, according to that model, have single-hole and single-particle proton configurations, are approximately three times the theoretical values. It is noteworthy, however, that the signs of quadrupole moments are quite generally (as for In and Sb) those predicted by shell theory, and further, that no anomalous quadrupole moments appear for those nuclei which have both closed neutron and closed proton shells±one nucleon. In order to explain the high quadrupole moments observed in some regions, deformed core models have been introduced.[1]

Another discrepancy between shell theory and experiment appears in the *ft* values for allowed β transitions. The shell model calculations indicate that all allowed transitions should have *ft* values of about the same order of magnitude.[2] Actually, nearly all *ft* values for allowed transitions fall into two groups: Favored, $\log ft = 2.9$ to 3.6, and unfavored, $\log ft = 4.5$ to 6.0. Empirically, it appears that only transitions between states which, according to the supermultiplet theory, should belong to the same supermultiplet, are favored. Nearly all of these transitions appear for light nuclei (with mass number $A<40$). On the other hand, nearly all allowed transitions for heavier nuclei, as well as many for the light nuclei, have unfavored *ft* values. It is for the heavier nuclei that anomalously high quadrupole moments appear, and one might suspect that a deformed core model which accounts for these would also account for the high unfavored *ft* values. There is no indication at all, however, that substantial core deformations exist for light nuclei, so that the unfavored *ft* values which appear in that region would remain unexplained. It will be seen below that the most obvious interpretation of the deformed core model, in terms of a wave function in configuration space, fails to account for the whole difference between favored and unfavored transitions even in medium heavy nuclei. This need not be considered as a conflict between the deformed core models and experiment because the deformed core model's wave function in ordinary configuration space has not hitherto been specified closely enough to permit definite conclusions to be drawn. On the contrary, it may be hoped that the flexibility of the model is sufficient to avoid the apparent difficulty to which we are drawing attention.

In a deformed core+one particle model (for odd-*A*

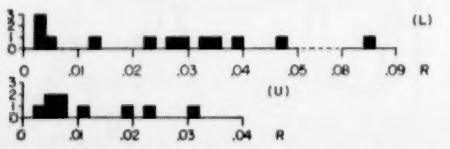

FIG. 1. Histograms of the ratio $R=[(ft)_{sp}]/[(ft)_{exp}]$ for allowed unfavored transitions of the like-core (L) and unlike-core (U) types.

* This work was supported in part by the U. S. Atomic Energy Commission and the Higgins Scientific Trust Fund.
† Hercules Fellow, 1952–1953.
[1] J. Rainwater, Phys. Rev. **79**, 432 (1950); D. L. Hill and J. A. Wheeler, Phys. Rev. **89**, 1102 (1953); A. Bohr and B. R. Mottelson, Kgl. Danske Videnskab. Selskab, Mat.-fys. Medd. **27**, No. 16 (1953).

[2] E. P. Wigner, Proceedings of the Harwell Nuclear Physics Conference (Ministry of Supply, Harwell, Berks., 1950). Also, I. Talmi, Phys. Rev. **91**, 122 (1953).

nuclei) β transitions fall into two groups.[3] The like-core transitions, for which the neutron and proton numbers, N_c, Z_c, of the initial core equal the ones of the final core, and the others, unlike-core transitions. An example of the like-core type is the following transition:[4]

$$\begin{array}{lcll} \mathrm{Ge}^{75} & \beta^- \longrightarrow & \mathrm{As}^{75} & ft=160\,000 \\ N,Z=43,32 & & 42,33 & \\ J=\tfrac{1}{2}\ \text{(from shell theory)} & & J'=\tfrac{3}{2}\ \text{(measured)} & \end{array} \quad (1)$$

$$Q=(0.3\pm0.2)\times10^{-24}\ \mathrm{cm}^2.$$

The core for both nuclei has $N_c,Z_c=42,32$. Both the ft value and Q are typical for this region. The assumption of a single particle β transition ($p_{1/2}\rightarrow p_{3/2}$) leads to $\Sigma\mathbf{G}^*\cdot\mathbf{G}=8/3$, and $(ft)_{\mathrm{sp}}=1990$. $\mathbf{G}$ is the Gamow-Teller matrix element, and the summation is over final states with different components J_z' of total angular momentum. $(ft)_{\mathrm{sp}}$ is based upon constants[5] obtained for transitions between nuclei which, according to the shell model, have single-particle and -hole configurations. The calculated ft value is too small by a factor of 80. Ge^{75} has $Q=0$ if its spin is 1/2. In the present calculation, its core will be assumed to be spherically symmetric. Spin 1/2, corresponding to a $p_{1/2}$ single-particle state, is predicted by the simple coupling rules for 43 odd nucleons. Spins 5/2 and 3/2, corresponding to $f_{5/2}$ and $p_{3/2}$, have not been observed for any nucleus in this shell with more than 37 odd nucleons.

As an illustration of an unlike-core transition, let us consider $Ga^{73}(\beta^-)Ge^{73}$. For the initial nucleus, $N,Zs=42,31$; for the final one, 41,32. The initial core thus has $N_c,Z_c=42,30$; the final one has 40,32. One might expect that the core factors in β-decay matrix elements (see Sec. II) would differ for the two types of cores.

All data[4] for the set of ground state to ground state transitions between odd-A nuclei in the regions where, according to the shell model, allowed transitions may appear were examined. There are 22 such transitions with definitely known ft values and $4.5<\log ft<6.0$. Two additional transitions, which may have $\Delta J=0$ or 1 and no change in parity, probably are of the l-forbidden type; they are $Ni^{63}(\beta^-)Cu^{63}$ and $Ni^{65}(\beta^-)Cu^{65}$. Their ft values both equal 3.6×10^6; the initial spins are not known. The remaining transitions in this set are of the favored type with $\log ft<4.0$.

The ratio $R=(ft)_{\mathrm{sp}}/(ft)_{\mathrm{exp}}$ of the theoretical single-particle ft value divided by the experimental one, was calculated for the 22 allowed unfavored transitions. Histograms of R of these transitions, divided into like-core (L) and unlike-core (U) groups, are given in Fig. 1. R is proportional to the square of the matrix element. It is plain that the matrix element is, on the average, larger for the L transitions; the average value of R for these is 2.3 times that for the U transitions. However, the difference seems to be much smaller than we would have expected on the basis of a deformed core model with only one particle outside the core. The ratio R was also calculated for the favored transitions in this set. This time there are ten transitions each of the L and U types. The average of R for the L transitions is 1.02 times that for the U transitions. This is consistent with the generally accepted hypothesis that the core plays at most a very slight role in the favored transitions.

It may seem surprising that there are, in fact, four transitions among the like-core ones with $0.002\leq R\leq0.006$. (See Fig. 1.) Two of these transitions are $O^{19}(\beta^-)F^{19}$ and $Si^{31}(\beta^-)P^{31}$. The single particle has been assigned an $s_{1/2}$ state for both transitions; this leads to an especially low R. Probably a several-particle configuration would describe the situation better. No reason for the low R's of the other two transitions, $Ca^{45}(\beta^-)Sc^{45}$ (with single-particle transition $f_{7/2}\rightarrow f_{7/2}$) and $Te^{127}(\beta^-)I^{127}$ (with $d_{3/2}\rightarrow d_{5/2}$), seems apparent.

II. MATRIX ELEMENTS FOR THE DEFORMED CORE MODEL

Let us calculate the matrix element for a like-core transition on the following model: $A-1$ particles are contained in a box, which is a sphere for the undeformed core, and an ellipsoid for the deformed one. The last nucleon is in a state with angular momenta j and l in a system fixed in the core (strong coupling). If x_k denotes the space and spin coordinates of the kth particle in the laboratory system, and ξ is the set $(x_1,\cdots,x_{A-1})$ and further, $x_A=x$, then the wave function is

$$\Psi_{Mn}{}^{Jj}(\xi,x)=a(J,j,\mathfrak{n})\int\mathfrak{D}^J(R)_{nM}\psi_n{}^j(Rx)\Phi(R\xi)dR. \quad (2)$$

Φ and $\psi_n{}^j$ are core and single-particle wave functions; $\mathfrak{D}^J(R)_{nM}$ is a representation coefficient;[6] R is an element of the rotation group; a is a normalization factor. It can readily be checked that $\Psi_{Mn}{}^{Jj}(\xi,x)$ belongs to M'th line of the representation $\mathfrak{D}^J(R)$. Ψ has definite parity equal to that of ψ. The parity of Φ is even, since there are two particles to each space state in the core. The integration is taken over the parameters of all elements of the rotation group. The core state may be a superposition of states with several angular momenta, $J^{(c)}$, but it is assumed to have $J_{z_c}{}^{(c)}=0$. z_c is the z axis in the core system, and $J_{z_c}{}^{(c)}$ is the component of core angular momentum along this axis.

The matrix element of the ν component of an irreducible tensor operator T^k of order k which operates only on the coordinates and spin x of the outer particle

[3] L. W. Nordheim, Report on the Indiana Conference on Nuclear Spectroscopy and the Shell Model (University of Indiana, Bloomington, 1953).

[4] Data are taken from: King, Dismuke, and Way, Oak Ridge National Laboratory Report No. 1450, 1952 (unpublished), and P. F. A. Klinkenberg, Revs. Modern Phys. 24, 63 (1952).

[5] G. L. Trigg, Phys. Rev. 86, 506 (1952). Also, A. Winther and O. Kofoed-Hansen, Kgl. Danske Videnskab. Selskab, Mat.-fys. Medd. 27, No. 14 (1953).

[6] See, e.g., E. P. Wigner, *Gruppentheorie und ihre Anwendung auf die Quantenmechanik der Atomspektren* (F. Vieweg und Sohn, Braunschweig, 1931).

can readily be calculated. It is

$$\langle J'M'j'n'|T_\nu^k|JMjn\rangle = \int\int \Psi'_{M'n'}{}^{J'j'}(\xi,x)^* \, T_\nu^k \, \Psi_{Mn}{}^{Jj}(\xi,x)d\xi dx, \quad (3)$$

where the integration includes a summation over spin components. Then, with Φ and Φ' wave functions of the spherical and deformed cores,

$$\frac{\langle J'M'j'n'|T_\nu^k|JMjn\rangle}{a'(J',j',n')^* a(J,j,n)} = \int dR \int dS \mathfrak{D}^{J'}(R)_{n'M'}{}^* \mathfrak{D}^J(S)_{nM} \cdot \int \psi_{n'}{}^{j'}(Rx)^* T_\nu^k \psi_n{}^j(Sx)dx \cdot \int \Phi'(R\xi)^* \Phi(S\xi)d\xi. \quad (4)$$

$\psi_n{}^j$ belongs to the nth line of $\mathfrak{D}^j$:

$$\psi_n{}^j(Sx) = \sum_\nu \mathfrak{D}^j(S)_{n\nu}{}^* \psi_\nu{}^j(x). \quad (5)$$

Substitution of (5) into (4) and the transformation $R\xi = \eta$ lead to

$$\int dR \mathfrak{D}^{J'}(R)_{n'M'}{}^* \sum_{\nu'} \mathfrak{D}^{j'}(R)_{n'\nu'} \cdot \int dS \mathfrak{D}^J(S)_{nM} \sum_\nu \mathfrak{D}^j(S)_{n\nu}{}^* \cdot \int \psi_{\nu'}{}^{j'}(x)^* T_\nu^k \psi_\nu{}^j(x)dx \cdot \int \Phi'(\eta)^* \Phi(SR^{-1}\eta)d\eta. \quad (6)$$

The orthogonality relation for the representation coefficients is, with $h = \int dR$,

$$\int dR \mathfrak{D}^k(R)_{ab}{}^* \mathfrak{D}^{k'}(R)_{a'b'} = \frac{h}{2k+1}\delta(k,k')\delta(a,a')\delta(b,b'). \quad (7)$$

Φ is spherically symmetric, so that (6) and (7) lead to

$$\langle J'M'j'n'|T_\nu^k|JMjn\rangle = a'(J',j',n')^* a(J,j,n) \cdot \frac{h^2}{(2j'+1)(2j+1)} \int \psi_{M'}{}^{j'}(x)^* T_\nu^k \psi_M{}^j(x)dx \cdot \int \Phi'(\eta)^* \Phi(\eta)d\eta \cdot \delta(J',j')\delta(J,j). \quad (8)$$

The matrix element equals 0, unless $J=j$ and $J'=j'$. The first condition is obvious: Since Φ is spherically symmetric, it describes a core state with angular momentum $J^{(c)}=0$, and the nucleon's j coupled to it can give only $J=j$. The second condition follows from an expansion of Φ' in terms of core functions with definite angular momenta, $\chi[J^{(c)}]$. The core integral equals 0 unless $\chi(0)$ appears in this expansion. This will occur only if $J'=j'$.

$|a(j,j,n)|^2$ may be calculated from (4) and (8) by substitution of $J'=J=j$, $T_\nu^k = T_0^0 = 1$ and $\Phi'=\Phi$. Then $|a(j,j,n)|^2 = (2j+1)^2 h^{-2}$. The expression for $|a'(j',j',n')|^2$ is more complicated. From (4) and (6), with $V=SR^{-1}$,

$$\frac{1}{|a'(j',j',n')|^2} = \frac{h}{2j'+1}\int dV |\mathfrak{D}^{j'}(V)_{n'n'}|^2 \cdot \int \Phi'(\eta)^* \Phi'(V\eta)d\eta. \quad (9)$$

An upper limit to the integral in η is 1 for all V. Then $|a'(j',j',n')|^2 \geq (2j'+1)^2 h^{-2}$. It should be noted that only this lower limit, not $a'(j',j',n')$ itself, is independent of n'. Substitution in (8) gives:

$$|\langle J'M'j'n'|T_\nu^k|JMjn\rangle|^2 \geq \left|\int \psi_{M'}{}^{j'}(x)^* T_\nu^k \psi_M{}^j(x)dx\right|^2 \cdot \left|\int \Phi'(\eta)^* \Phi(\eta)d\eta\right|^2. \quad (10)$$

The lower limit of the factor in the matrix element due to the core thus has absolute value $|\int \Phi'(\eta)^* \Phi(\eta)d\eta|$.

III. A CALCULATION OF THE CORE FACTOR

In order to obtain an orientation concerning the magnitude of the core matrix element, we have chosen the previously mentioned Ge^{75} transition as an example. Cube-shaped and parallelopiped-shaped boxes of equal volume were substituted for the spherical and ellipsoidal ones. It is most likely that the matrix element between the last two states does not differ substantially from the one to be calculated here. The edge

TABLE I. States for a cube-shaped box.

$n_x^2+n_y^2+n_z^2$	n_x	n_y	n_z	Number of states for one particle type (spin ½)	Cumulative number
18	1	1	4	6	46
17	2	2	3	6	40
14	1	2	3	12	34
12	2	2	2	2	22
11	1	1	3	6	20
9	1	2	2	6	14
6	1	1	2	6	8
3	1	1	1	2	2

TABLE II. $I(n,m;\xi)$ for $m\neq n$. ($\epsilon=1.0275$).

(n,m)	(1,3)	(3,1)	(2,4)	(4,2)
$I(n,m;\epsilon)$	−0.020	−0.021	−0.035	−0.038
$I(n,m;\epsilon^2)$	−0.038	−0.043	−0.066	−0.078

of the cube (state α) will be taken as $d=2\epsilon a$. The parallelopiped (state β) has a square base with edges $2a$ and height $2\epsilon^3 a$.

The wave functions are products of those for a one-dimensional square well with infinitely high walls at $x=d$ and $x=-d$:

$$u_n(x)=\frac{1}{\sqrt{d}}\,t\left(\frac{n\pi x}{2d}\right), \quad |x|\leq d, \tag{11}$$

$$=0, \qquad |x|>d,$$

where

$$t\left(\frac{n\pi x}{2d}\right)=\begin{cases}\cos(n\pi x/2d), & \text{if } n \text{ is odd}\\ \sin(n\pi x/2d), & \text{if } n \text{ is even.}\end{cases} \tag{12}$$

The states for the three-dimensional cube-shaped box are given in Table I. Three quantum numbers n_x, n_y, n_z determine each state, and its energy is given by $(n_x^2+n_y^2+n_z^2)\cdot\hbar^2\pi^2/8md^2$.

The deformation, ϵ, can be calculated from the contribution to Q by the core of As^{75}. This contribution will be assumed equal to 0.67×10^{-24} cm^2, a value about twice the largest observed in the region around As. The operator is

$$Q=\sum_{j=1}^{Z_c}(2z_j^2-x_j^2-y_j^2), \tag{13}$$

where the summation is over protons only. The total wave function is the antisymmetrized product of single-particle wave functions, and application of a well-known formula[7] leads to

$$\langle\beta\{n\}|Q|\beta\{n\}\rangle=\sum_{j=1}^{Z_c}\langle\beta n_j|2z_j^2-x_j^2-y_j^2|\beta n_j\rangle, \tag{14}$$

where the j's denote proton coordinates and $Z_c=32$. $n_j=(n_{jx}, n_{jy}, n_{jz}, s_{jz}, t_{j\xi})$; it denotes the quantum numbers of a single-particle state. s_{jz} and $t_{j\xi}$ are spin and isotopic spin components. $\{n\}$ is the set $n_1, \cdots, n_{A-1}$, with $A-1=74$. β denotes the deformed state. From the volume of the cube-shaped state,

$$8d^3=(4\pi/3)\cdot74\cdot1.4^3\times10^{-39}\text{ cm}^3, \tag{15}$$

d is calculated as 4.74×10^{-13} cm. Substitution of the assumed Q and of d into (14) leads to $\epsilon=1.0275$.

The integral of the wave functions of the two core states will be calculated next:

$$\int\Phi'(\eta)^*\Phi(\eta)d\eta\approx\langle\alpha\{n\}|\beta\{n\}\rangle=\prod_{i=1}^{A-1}\langle\alpha n_i|\beta n_i\rangle$$

$$+\text{terms containing at least one factor}$$

$$\langle\alpha n_i|\beta n_k\rangle\langle\alpha n_k|\beta n_i\rangle, \text{ with } i\neq k. \tag{16}$$

Each scalar product for one particle is a product of three integrals:

$$\langle\alpha n_i|\beta n_k\rangle=I(n_{ix},n_{kx};\epsilon)I(n_{iy},n_{ky};\epsilon)$$
$$\times I(n_{iz},n_{kz};\epsilon^2)\delta(s_{iz},s_{kz})\delta(t_{i\xi},t_{k\xi}). \tag{17}$$

The I's are defined as follows. Let $2d=$ a particular edge for one state, and $2\xi d$ the corresponding edge for the other state. Then

$$I(n,m;\xi)=\frac{1}{d\sqrt{\xi}}\int_{-d}^{d}t\left(\frac{n\pi x}{2\xi d}\right)t\left(\frac{m\pi x}{2d}\right)dx, \tag{18}$$

which depends only upon the ratio ξ of the two edges and on n and m. From parity considerations, $I(n,m;\xi)=0$ if $n-m$ is odd, and direct integration for $n-m\neq0$ and even gives

$$I(n,m;\xi)=\frac{4}{m\pi\sqrt{\xi}}\cdot\frac{(-1)^{\nu/2}}{(n/m\xi)^2-1}\,t\left(\frac{n\pi}{2\xi}\right), \tag{19}$$

where $\nu=m$, if m is even, and $\nu=m+1$, if m is odd. Numerical results are given in Table II. $\xi=\epsilon$ for the x and y directions and $\xi=\epsilon^2$ for the z direction.

For $n=m$, the integral can be calculated as a series in $\delta=\xi^{-1}-1$, which is a small quantity. One can expand, with $v=n\pi x/2d$,

$$\sin\left(\frac{n\pi x}{2\xi d}\right)=\sin(1+\delta)v=\sin v+\delta v\cdot\cos v$$
$$-\frac{(\delta v)^2}{2}\sin v-\frac{(\delta v)^3}{6}\cos v+\cdots. \tag{20}$$

A similar expansion can be made for $\cos(n\pi x/2\xi d)$. Simple integrations lead for both even and odd n to

$$I(n,n;\xi)=1-\tfrac{1}{3}\delta^2(1+\tfrac{1}{3}n^2\pi^2)+\tfrac{1}{5}\delta^3-\cdots. \tag{21}$$

Table III contains numerical values of $1-I(n,n;\xi)$.

From the results of Tables I to III it follows that the first term in (16) equals 0.584, and the sum of terms containing just two integrals $I(n,m;\xi)$ with $n\neq m$ equals −0.025. The remaining terms contain more factors of these integrals and their sum is much smaller. Therefore,

$$|\langle\alpha\{n\}|\beta\{n\}\rangle|^2=(0.559)^2=0.31. \tag{22}$$

TABLE III. $[1-I(n,n;\xi)]\times10^4$. ($\epsilon=1.0275$).

$n=$	1	2	3	4
$[1-I(n,n;\epsilon)]\times10^4$	4	13	27	48
$[1-I(n,n;\epsilon^2)]\times10^4$	15	49	107	187

[7] See, for example, 6[6](9), of E. U. Condon and G. H. Shortley, *The Theory of Atomic Spectra* (Cambridge University Press, Cambridge, 1951), p. 171.

IV. CONCLUSION

From (10) and (22), by using the constants of reference 5,

$$(ft)_{\text{core+sp}} \leq 1990/0.31 = 6420.$$

This calculation yields an upper limit only ~3 times the single-particle *ft* value, despite the fact that it was based upon a quadrupole moment equal to about twice the observed one. The experimental *ft* value for Ge^{75} is 25 times larger than this upper limit. It is evident from the nature of the calculation that the result for other like-core nuclei in this mass region will be similar. For lighter nuclei, the core matrix element $\langle\alpha\{n\}|\beta\{n\}\rangle$ will be still larger, even though the measured *ft* values for unfavored transitions are not substantially lower.

Formula (8) indicates that, in fact, the matrix element equals 0 if $J' \neq j'$. A modification of the model in which at least one of the core states contains a large admixture of states with $j' \neq J'$ could therefore yield an arbitrarily small matrix element. A regularity found by Kopfermann,[8] however, seems to indicate that, for several isotope pairs at least, the single particle appears in just one state: On graphs of quadrupole moment *vs* magnetic moment, the two experimental points for odd-*A* isotopes and the theoretical point for the pure single-particle model are approximately collinear. Another possibility of explaining the large *ft* values within the framework of the deformed core model would be by assuming that both the initial and final cores are deformed. The core functions would have to be substituted in formula (6). It does not appear, however, that this would change our result drastically. It should be mentioned, finally, that the results of calculations[9] based upon the collective model in the form given by Bohr and Mottelson, a form which assumes that both cores are deformed, are of the same magnitude as the one obtained here.

An alternate explanation of the unfavored *ft* values for allowed transitions in terms of the original shell model would postulate instead the predominance of different configurations in the initial and final states. The fact that all the allowed transitions between nuclei with double closed shells±one nucleon fall into the favored group is consistent with this explanation. It is not clear, however, how to explain the grouping of the allowed *ft* values which is observed. (There are very few with $3.6 < \log ft < 4.5$.)

[8] H. Kopfermann, Naturwiss. **38**, 29 (1951).

[9] S. Suekane, Progr. Theoret. Phys. Japan **10**, 480 (1953).

PHYSICAL REVIEW VOLUME 95, NUMBER 1 JULY 1, 1954

Energy Distributions of Fragments from Fission of U^{235}, U^{238}, and Pu^{239} by Fast Neutrons*

JOHN S. WAHL†‡
University of California, Los Alamos Scientific Laboratory, Los Alamos, New Mexico
(Received March 17, 1954)

The energies of fragments from fission of U^{235}, U^{238}, and Pu^{239} by 14-Mev neutrons, from fission of U^{238} by 2.5-Mev neutrons, and from fission of U^{235} and Pu^{239} by thermal neutrons have been measured in a single Frisch grid ionization chamber. The energy distributions for fast neutrons are similar to those previously obtained for fission by thermal neutrons. The most probable energies of the light and heavy fragments for fission by 14-Mev neutrons do not change significantly from their values for slow-neutron induced fission. The valley between peaks is higher for fission induced by 14-Mev neutrons than for low-energy neutron-induced fission.

A double Frisch grid chamber has been used to measure simultaneously the energies of both fragments from fission of U^{235} by 14-Mev neutrons. The main change in the distribution of fission modes from that for thermal-neutron-induced fission is the increased probability for symmetrical fission.

INTRODUCTION

SINCE the first work of Frisch[1] many measurements of the energy distributions of fission fragments have been made, on a number of fissionable isotopes, and at various neutron energies.[2] The purpose of the present work was to make measurements at a neutron energy of 14 Mev for comparison with measurements at other energies.

The experiments reported fall into two classes: (a) measurements of the energy of one of the fragments

* Work done under the auspices of the U. S. Atomic Energy Commission.

† Submitted in partial fulfillment of the requirements for the degree of Doctor of Philosophy in the Graduate College of the State University of Iowa.

‡ Present address: Schlumberger Well Surveying Corporation, Ridgefield, Connecticut.

[1] O. R. Frisch, Nature **143**, 276 (1939).

[2] See, for example, (a) J. L. Fowler and L. Rosen, Phys. Rev. **72**, 926 (1947); (b) D. C. Brunton and G. C. Hanna, Can. J. Research **A28**, 190 (1950) and Phys. Rev. **75**, 990 (1949); (c) D. C. Brunton and W. B. Thompson, Can. J. Research **A28**, 498 (1950) and Phys. Rev. **76**, 848 (1949); (d) J. Jungerman and S. C. Wright, Phys. Rev. **76**, 1112 (1949).

from a fission event, obtained from the ionization produced in a single ionization or Frisch grid chamber; (b) simultaneous measurement of the energies of both fragments from a fission event in two chambers placed on opposite sides of the fission foil. These two classes will be referred to as single- and double-chamber experiments, respectively.

In the evaluation of fission fragment energies from the measured ionization, it has been customary to assume that w, the ratio of kinetic energy to ionization produced, is the same for fission fragments as for alpha particles. It is now known that this is not correct,[3] and also that the ratio varies for different fission fragments. Leachman[4] has estimated that $w_L/w_H=0.96$, where L and H refer to the most probable light and heavy fragments. From a direct measurement of the velocities of fission fragments[5] it has been inferred that about 5.7 and 6.7 Mev (these corrections are called ionization defects) should be added to the energies of the most probable light and heavy fragments, respectively, to take account of energy not observed as ionization in argon. In the present work nitrogen was used as a chamber filling. No corrections for ionization defects have been made to the measured energies.[6]

APPARATUS AND EXPERIMENTAL METHODS

Fast neutrons were obtained from the Los Alamos Cockcroft-Walton accelerator. The reaction $T(d,n)\alpha$ gave neutrons with a mean energy of 14.1 Mev and a spread, due to target thickness and finite solid angle subtended by the foil of fissionable material, which in the worst case was about ± 0.5 Mev. Neutrons of energy 2.52 Mev were obtained from the reaction $D(d,n)He^3$; the energy spread was about ± 0.3 Mev. Thermal neutron measurements were made by placing both the chamber and a Po-α-Be neutron source in a graphite pile.

In the fast neutron measurements some of the neutrons seen by the fissionable material are low-energy neutrons arising from inelastic scattering and $(n,2n)$ reactions in the chamber walls. An estimate has been made for the 14-Mev case, on the assumption of isotropic angular distribution of the scattered neutrons, and using the inelastic cross sections of Phillips *et al.*[7] Recent measurement by Graves[8] have shown that the extra neutrons contributed by $(n,2n)$ reactions roughly compensate for those lost to other reactions. It is calculated that in the single-chamber measurements about four percent of the neutron flux incident upon the foil is due to low-energy neutrons. For the double-chamber measurements the figure is nine percent. Nearly all of these neutrons are below about 3 Mev.[7,9]

A measurement of fission rates with and without cadmium surrounding the single chamber showed that about 2 ± 1 percent of the fissions in the 14-Mev measurements on U^{235} and Pu^{239} were due to thermal neutrons. This figure should also apply to the double-chamber measurements.

The chamber used for the single-fragment measurements was similar to that used by Fowler and Rosen.[2] No collimator was used to limit the angular range over which fission fragments were observed. The foil-to-grid spacing was about 2 cm, and the chamber pressure of about two atmospheres of nitrogen was sufficiently high that all tracks of alpha particles and fission fragments were contained in this region. The calculated shielding efficiency of the grid[10] was 96 percent in the U^{235} measurements, and 98 percent in those on U^{238} and Pu^{239}.

The double chamber consisted of two Frisch grid chambers back to back, with a common high voltage electrode and foil. The foil was mounted on Zapon and supported on a brass collimator 0.017 in. thick with about five thousand 0.032-in. diameter holes. The foil-to-grid spacing in this chamber was one inch. The grid shielding efficiency was more than 99 percent.

The chambers were filled with nitrogen which was purified continuously by allowing it to circulate through an oven containing calcium metal at 150°C. After purification, saturation for fission fragments was obtained at a chamber potential of about 8 kv. Measurements were made at 10 or 14 kv. It was verified that the shape of the fission fragment spectrum did not change with chamber potential above the saturation point. Attempts to use argon, with or without CO_2, failed because it was not possible to obtain voltage saturation for fission fragments. This may be due to the use of higher chamber pressures than were required by previous investigators.

Signals received by the collector plate of a chamber were amplified by a Model 101 preamplifier and amplifier and clipped to produce roughly rectangular pulses 3 to 4 microseconds long. Energy distributions were obtained with the use of a ten-channel pulse-height analyzer.[11] Energy calibrations were obtained from measurements of natural alpha particles whose energies are known[12] (U^{234}: 4.76 Mev; U^{238}: 4.18 Mev; Pu^{239}: 5.16 Mev). Pulse heights due to fission fragments were compared with those from a generator of artificial pulses. Then alpha-particle pulse heights were compared with

[3] Knipp, Leachman, and Ling, Phys. Rev. **80**, 478 (1950).
[4] R. B. Leachman, Phys. Rev. **83**, 17 (1951).
[5] R. B. Leachman, Phys. Rev. **87**, 444 (1952).
[6] Recently ionization defects of various gases (including nitrogen) relative to argon have been measured by L. O. Herwig, thesis, Iowa State College, Ames, Iowa (unpublished).
[7] Phillips, Davis, and Graves, Phys. Rev. **88**, 600 (1952).
[8] E. R. Graves (to be published).
[9] E. R. Graves and L. Rosen, Phys. Rev. **89**, 343 (1953); B. G. Whitmore and G. E. Dennis, Phys. Rev. **84**, 296 (1951); P. H. Stelson and C. Goodman, Phys. Rev. **82**, 69 (1951).
[10] Bunemann, Cranshaw, and Harvey, Can. J. Research **A27**, 191 (1949).
[11] W. C. Elmore and M. Sands, *Electronics, Experimental Techniques* (McGraw-Hill Book Company, Inc., New York, 1949).
[12] Way, Fano, Scott, and Thew, *Nuclear Data*, National Bureau of Standards Circular 499 (U. S. Government Printing Office, Washington, D. C., 1950).

artificial pulses of the same size, but passed through a 20–1 attenuator. Thus the energy measurement depends on the attenuation factor of the attenuator. This factor was obtained from measurements of the resistances of which the attenuator was composed. It is estimated that inaccuracies in the measurement of the ionization energies of the fission fragments do not exceed two percent.

For the double-chamber measurements, the amplified rectangular pulses due to the two fragments from a fission event were placed on the horizontal and vertical plates of an oscilloscope tube, whose intensifier was gated on for about one microsecond when the pulses were at their peak values. Thus two coincident fragments were represented on the oscilloscope tube by a well-defined bright spot whose horizontal and vertical distances from the position of the undeflected beam were proportional to the ionization energies of the two fragments.

The oscilloscope tube was photographed and the energies of the fragment pairs obtained from calibration marks placed on each frame by a pair of pulse generators. The energies of the fragments passing through the Zapon foil backing and the collimator is lower than the energy of fragments going into the uncollimated chamber. It was found that energy distributions from the two chambers could be made to agree when 2.5 Mev was added to the energy of the fragments in the collimated chamber. This correction was applied to the measured energies of this chamber.

The foils of fissionable material used in the single chamber measurements were prepared on 0.005-in. platinum sheet by painting on uranyl nitrate or plutonium nitrate with a brush.[13] The uranium foils were heated to convert the nitrate to oxide. Heating of plutonium foils showed apparent diffusion of the active material into the backing, and final measurements were made on unheated foils. The foil for the double chamber measurement consisted of a Zapon backing 12 $\mu g/cm^2$ thick, on which was sprayed 10–20 $\mu g/cm^2$ of uranyl nitrate. Energy losses for fission fragments in the foil materials were calculated from their compositions and weights. The initial energy loss of fission fragments was taken as: $dE/dx = kZ^{-1}$ with $k = 148$ kev/$\mu g/cm^2$. This equation can be derived from published measurements of stopping power and initial energy loss of fission fragments.[14] In the single-chamber measurements, the energy losses of fragments passing through the active material and normal to the plane of the foil are, for U^{235}, 0.84 Mev; for U^{238}, 1.2 Mev; and for Pu^{239}, 0.01 Mev. The single-chamber energy distributions have not been corrected for foil losses; however, the energies of the peaks of the distributions given in the text and in Table I are corrected. The energy loss of a fragment passing through the foil used for the double-chamber measurements is 0.7 Mev. Since the maximum angle of fragments is limited by the collimator to about 60° to the normal, a well-defined average energy loss exists in this case. The energies of the double-chamber distributions have been corrected for energy loss in the foil.

RESULTS

The energy distribution of fragments from fission of U^{235} by thermal neutrons was obtained as a check on the over-all operation of the equipment. The resulting spectrum is shown in Fig. 1A. The shape of the spectrum is in good agreement with previous measurements.[2,15] The peak energies, corrected for energy loss in the foil, are 91.1 and 58.8 Mev, about three percent lower than those obtained by Brunton and Hanna[2] or by Deutsch and Ramsey,[16] when the latter are corrected by ½ percent for energy loss in the foil.

The spectrum of fragments obtained from fission of U^{235} induced by 14-Mev neutrons is shown in Fig. 1B. The rise below 20 Mev is due to background from reactions in the chamber gas. The spectrum agrees with that of Friedland,[16] for fission of U^{235} by 14-Mev neutrons, when account is taken of the poorer resolution occasioned by his greater foil thickness.

A spectrum for fragments from fission of U^{238} by 2.5-Mev neutrons is shown in Fig. 1C. Because of the low neutron flux available at this energy, 5-Mev channel widths were used, and the statistical accuracy is poor. Another measurement differed somewhat from the spectrum shown, but the two agreed within their statistical errors, and the peak energies agreed to within 2 Mev. The spectrum is not in agreement with the measurement of Kanner and Barschall,[17] who used 2.8-Mev neutrons, or that of Jentschke,[18] who used Ra-Be neutrons. Their energies are about eight percent higher than the present results. The spectral shape of Kanner and Barschall differs considerably from that given here, while that of Jentschke is similar to that of Fig. 1C.

A spectrum for fission fragments from 14-Mev neutron bombardment of U^{238} is shown in Fig. 1D. Another measurement agreed with these results within about 1 Mev on the average.

Spectra for fragments from fission of Pu^{239} by thermal and 14-Mev neutrons are shown in Figs. 1E and 1F. The thermal measurement was made to permit comparison with previous work, and the agreement with spectra of Deutsch and Ramsey[15] and of Brunton and

[13] The author is indebted to John Povelites and Jane Evans for preparation of the foils.

[14] F. Suzor, Compt. rend. **226**, 795 (1948); E. Segrè and C. Wiegand, Phys. Rev. **70**, 808 (1946); D. West, Can. J. Research **A26**, 115 (1948); N. O. Lassen, Phys. Rev. **68**, 230 (1945); R. Scherr and R. Peterson, Rev. Sci. Instr. **18**, 567 (1947); K. W. Allen and J. T. Dewan, Phys. Rev. **82**, 527 (1951).

[15] M. Deutsch and M. Ramsey, Atomic Energy Commission Report MDDC-945, 1946 (unpublished).

[16] S. S. Friedland, Phys. Rev. **84**, 75 (1951).

[17] M. H. Kanner and H. H. Barschall, Phys. Rev. **57**, 372 (1940).

[18] W. Jentschke, Z. Physik **120**, 165 (1943).

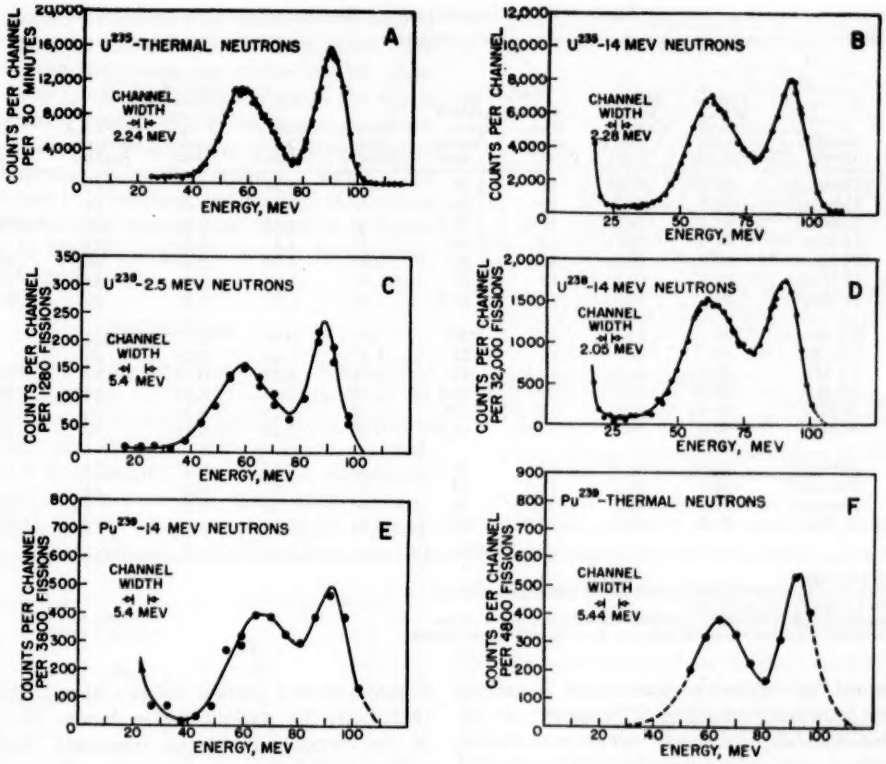

FIG. 1. Single-chamber energy distributions of fission fragments.

Thompson[2] is satisfactory. The valley between the peaks, which is about 30 percent higher in the present work than in the published spectra, indicates somewhat poorer resolution.

In all three cases the spectra for 14-Mev neutron bombardment are similar to those for low-energy neutrons. The peak energies change only by amounts of the order of 1 Mev. In view of the experimental errors this is not considered significant. In each case the valley between the peaks is higher at 14 Mev than at the lower neutron energies, and this may well be due to an increase in the probability of symmetrical fission. However, no quantitative data on this point can be deduced from the single-chamber measurements.

The observation that there is no significant change in fragment energies with change in energy of the incident neutron is in agreement with predictions of the fission theory of Fong.[19] In this theory, the main contribution to fragment kinetic energies is considered to arise from Coulomb repulsion.

In Table I are given data on the spectra obtained in this work, together with a selection from previously published spectra. The energies have been corrected for foil losses except where noted. In addition, the data of this paper for fast-neutron fission include a correction for center-of-mass motion. The purpose of this correction is to convert the measured energies (which are for fragments going into the forward hemisphere with respect to the incident neutron) to the energy averaged over all fragment directions. It is not known whether such corrections have been applied to the other fast-neutron data.

The double-chamber data all refer to fission of U^{235} by 14-Mev neutrons. In Fig. 2 are shown the energy distributions of fragments entering the collimated side of the chamber (C circuit) when the coincident fragments (T circuit) are restricted to energy bands 3 Mev wide, centered on the value given with each curve. All ordinates are normalized to the same number of fissions taking place in the foil. A comparison of these spectra with those obtained by Brunton and Hanna[2] for thermal neutron induced fission of U^{235} shows that the main change in going to 14 Mev is the large increase in the probability of symmetrical fission, most of which appears as a tail on the low energy side of the light fragment peak. Figure 3 shows the variation of the most probable energy of the spectra of Fig. 2, as a function of the energy of the coincident fragments. In Fig. 4 are given the derived single fragment energy distributions which were obtained by summing over all energies of the coincident fragments.

[19] P. Fong, *A Theory of Nuclear Fission* (unpublished).

TABLE I. Fission fragment energy distributions.

Nuclide	Neutron energy	Position of high-energy peak (Mev)	Position of low-energy peak (Mev)	Width at half-maximum, (Mev) High-energy peak	Width at half-maximum, (Mev) Low-energy peak	Ratio of peak energies	Ratio of peak heights	Ratio of height of minimum to height of high-energy peak	Nominal foil thickness $\mu g/cm^2$	Reference
U^{235}	Thermal[a]	94.5[b]	60.3[b]	12	19	1.56	1.37	0.12	<12	15
	Thermal[a]	94.5	60.2	12	20	1.57	1.49	0.13	14	2(b)
	Thermal	91.1	58.8	12.6	20.3	1.55	1.43	0.16	40	This paper
	14 Mev	91[c]	59[c]	15[d]	26[d]	1.54	1.1	0.57	140	16
	14 Mev[e]	89.9	62.1	14.7	24	1.45	1.14	0.42	40	This paper
	14 Mev	91.1	60.7	16	25	1.50	1.17	0.39	40	This paper
	14 Mev[a]	89.5	59.9	14.3	23.2	1.49	1.22	0.32	20	This paper
U^{238}	2.8 Mev	98	65	29[d]	19[d]	1.51	0.89	0.50	120	17
	Ra–Be	97	66	14	22	1.47	1.43	0.13	40	18
	2.5 Mev[e]	90.0	61.8	13.5	19	1.46	1.24	0.31	50	This paper
	2.5 Mev	89.0	60.0	12.8	26.5	1.48	1.49	0.30	50	This paper
	14 Mev	89.8	61.1	17[d]	27[d]	1.47	1.16	0.50	50	This paper
	14 Mev	89.6	59.7	17.8[d]	28.8[d]	1.50	1.15	0.51	50	This paper
Pu^{239}	Thermal[a]	93.5[b]	65.3[b]	12.5	20.5	1.43	1.50	0.21	<12	15
	Thermal[a]	94.6	65.2	13.6	24	1.45	1.47	0.23	14	2(c)
	Thermal	92.8	64.5	14.5	24	1.44	1.42	0.30	1.4	This paper
	14 Mev	91.0	64.7	19.6[d]	32[d]	1.41	1.23	0.59	1.4	This paper

[a] Double-chamber data.
[b] Energies have been increased ½ percent to correct for energy loss in the foil.
[c] Uncorrected for energy loss in the foil.
[d] Widths estimated from extrapolated curves for the light and heavy peaks.
[e] This measurement has lower statistical accuracy than the other measurements.

Data obtained by summing either over fragments entering the collimated chamber (*C* channel) or the uncollimated chamber (*T* channel) are given and show good agreement with each other. To avoid confusion, the data for the dashed curves which define the energy distributions of the light and heavy fragments separately have not been plotted. The uncertainties of these curves are about the same as for the data shown.

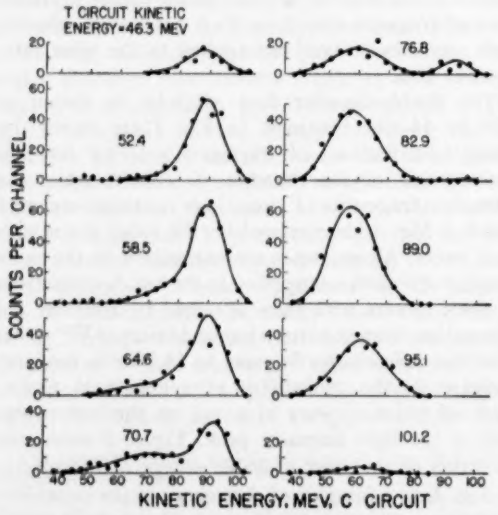

FIG. 2. Energy distributions of fragments from fission of U^{235} by 14-Mev neutrons, when the energy of the coincident fragments is fixed.

Figure 5 gives a contour diagram showing the relative probability for various fission modes as a function of the energies of the two fragments. Auxiliary coordinates give the ratio of energies of the fragments, as well as their masses, with the assumption that no neutrons are emitted from the fragments. Figure 6 gives the distribution in mass of the fragments, again with the assumption that no neutrons are emitted. In this figure a curve has also been plotted to show approximately the effect of including the ionization defect. The values given by Leachman for argon[6] have been used for the most probable light and heavy fragments, and it has been assumed that the ionization defect varies linearly with fragment energy. Some data on mass yields obtained radiochemically by Spence[20] have been shown in the same figure. His

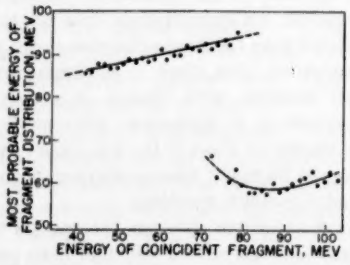

FIG. 3. Most probable energy of fragment energy distributions as a function of the energy of the coincident fragments.

[20] R. W. Spence, Brookhaven National Laboratory Report BNL-C-9, 1949 (unpublished).

fragment masses are masses after emission of secondary neutrons from the fragments, and thus a direct comparison of these data with the curves of this paper does not have much significance except in the region of symmetrical fission, where the latter is almost unaffected either by consideration of neutron emission from fragments, or by the ionization defect. The agreement here is satisfactory, and confirms the increase in the probability of symmetrical fission by a factor of 100 at 14 Mev as compared to that for thermal-neutron-induced fission.

DISCUSSION

The measured fission fragment energy distributions differ somewhat from the energy distributions of the fragments in the center-of-mass system of the fissioning nucleus, and before the emission of secondary neutrons. The effects to be considered are a spread in the energies of fragments which have the same initial energy, together with a shift in the mean energy of these fragments. The causes of these distortions are, (a)

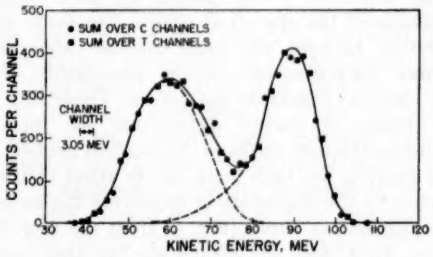

FIG. 4. Energy distribution of the light and heavy fragments from fission of U^{235} by 14-Mev neutrons.

"inherent" effects, including motion of the center of mass, emission of secondary neutrons, and the ionization defect and ionization straggling; (b) statistical errors; and (c) instrumental errors, such as use of finite channel widths, energy loss in the foil, foil nonuniformity, noise and background, and errors in pulse-height measurement.

Calculations have been made of the change in fragment energy, based on a fission model in which fission occurs before the compound nucleus has lost any energy, either kinetic or internal. It is assumed that the fragments are emitted isotropically in the center-of-mass system.[21] Secondary neutrons are assumed to be emitted from the fragments with isotropic angular distribution in the frame of reference of the moving fragment and before the fragment has been slowed down.

On the basis of this model, it is found that the mean energy, $\langle E_\nu \rangle$, of fragments in the laboratory system

[21] W. C. Dickinson and J. E. Brolley, Phys. Rev. **90**, 388 (1953) have recently measured an anisotropy in the angular distribution of fragments from fission induced by 14-Mev neutrons.

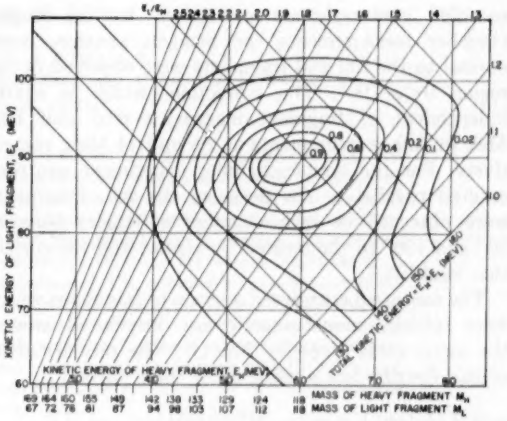
KINETIC ENERGY OF LIGHT FRAGMENT, E_L (MEV)
KINETIC ENERGY OF HEAVY FRAGMENT, E_H (MEV)
MASS OF HEAVY FRAGMENT M_H
MASS OF LIGHT FRAGMENT M_L

FIG. 5. Contour diagram of fission modes for fission of U^{235} by 14-Mev neutrons.

and after the emission of ν neutrons[22] is given very nearly by

$$\langle E_\nu \rangle = (E_1+Q)(1-\nu m_n/m)(M-m)/M + [E_1 Q m (M-m) m_n]^{\frac{1}{2}} M^{-1}(1+E_1/2Q)\langle \cos\phi \rangle. \quad (1)$$

Here E_1 is the energy of the incident neutron, Q is that portion of the energy of fission which is released as kinetic energy of the primary fragments, and M, m, and m_n are masses of the compound nucleus, of the fragment before neutron emission, and of a neutron, respectively. In obtaining this expression averages have been taken over the angle of emission of the fragments, over the angles and energies at which secondary neutrons may be emitted, and over a distribution in the number of neutrons emitted, whose mean value is ν. The second term in the equation involves an average over the angle ϕ between the incident neutron and the fragment. This term is the

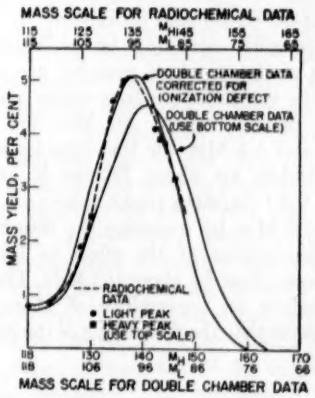
MASS SCALE FOR RADIOCHEMICAL DATA
DOUBLE CHAMBER DATA CORRECTED FOR IONIZATION DEFECT
DOUBLE CHAMBER DATA (USE BOTTOM SCALE)
MASS YIELD, PER CENT
RADIOCHEMICAL DATA
LIGHT PEAK
HEAVY PEAK (USE TOP SCALE)
MASS SCALE FOR DOUBLE CHAMBER DATA

FIG. 6. Mass distribution of fragments from fission of U^{235} by 14-Mev neutrons.

[22] Note that, contrary to general usage, ν gives the number of neutrons emitted by a *single* fragment.

so-called center-of-mass correction. In the single-chamber measurements the incident neutrons were normal to the foil and fragments were observed in the region $0<\phi<90°$. The correction, which is nearly independent of fragment masses, is 0.65 and 1.54 Mev for the measurements at 2.5 and 14 Mev, respectively. For the double-chamber experiment neutrons entered parallel to the plane of the foil. Fragments were observed in each chamber at angles between 30° and 150° to the incident neutrons, and the correction vanishes.

The measured energies of a group of fragments which were initially monoenergetic are distributed around the mean value given by Eq. (1). The rms deviation of this distribution is made up of three parts:

$$\sigma_0=2[(E_1Qm(M-m)m_n/M^3)(\langle\cos^2\phi\rangle-\langle\cos\phi\rangle^2)]^{\frac{1}{2}}\times(1+E_1/2Q), \quad (2)$$

due to motion of the center of mass;

$$\sigma_1=2[E_0\langle E_n\rangle\nu m_n/3m]^{\frac{1}{2}}, \quad (3)$$

due to the emission of ν neutrons of mean energy $\langle En\rangle$; and

$$\sigma_2=E_0m_n\sigma_\nu/m, \quad (4)$$

due to the distribution in ν, with rms deviation σ_ν. E_0 is the energy of a fragment before neutron emission.

Estimates were made of the effect which small pulses due to natural alpha particles from the foil and due to the reactions in the chamber gas have on the spectrum. It was found that no observable distortion should result, except possibly in the case of gas reaction background. Experimental checks were performed on the effect of the gas background pulses by taking fission fragment spectra at various neutron flux strengths ranging from one-tenth to three times the flux used in the final measurements. No changes in spectral shape with neutron flux were found.

The over-all dispersion introduced in the fission fragment energies can only be estimated roughly, since some of the numbers required are not known. Even for the unreasonably large value $\nu=5$ the rms dispersions do not exceed 2.6 Mev for the heavy fragments and 3.4 Mev for the light fragments. The measured widths are about 25 and 16 Mev for the heavy and light fragment peaks. These are reduced to 24.2 and 13.8 Mev by removing the dispersions given above. Consideration of the effect of foil thickness further reduces these by about 0.3 Mev. The statistical errors introduce an uncertainty of about 0.5 Mev. Thus it appears that the distortions of the experimental spectra from their true shapes, although appreciable, are not serious.

The rms dispersions given above, when converted to widths of distributions at half-maximum, become 6 and 8 Mev, respectively. These may be compared with an estimate[4,5] of 8 Mev for the instrumental spread in ionization chamber measurements. This estimate referred, however, to measurements made with thermal neutrons. Since one would expect a smaller energy dispersion for thermal neutron measurements than for those at 14 Mev, it may well be that there exist other sources of dispersion, such as ionization straggling, which have not been taken into account.

Estimates have been made of the corrections to be applied to the measured spectra to account for fission fragments produced by low-energy neutrons. It is found that, for fission of U^{235} by 14-Mev neutrons, the measured ratios of peak heights, 1.16 and 1.22, found in the single chamber and double chamber measurements, should be reduced to 1.15 and 1.20 and the measured ratios of the height of the valley to that of the high-energy peak, 0.40 and 0.32, should be increased to 0.41 and 0.34. These changes are of the order of magnitude of the statistical errors. The cause of the differences between the single-chamber and double-chamber measurements, which presumably should yield identical results, is not known. There may be a real change in energy distribution for fragments emitted at different angles to the incident neutron.

An analysis has been made of the effect of neutron emission by the fragments in modifying the measured mass distribution curve (Fig. 6) from the true distribution. To a good approximation the true curve is obtained by shifting the fragment masses by

$$\Delta m_H=-\Delta m_L=m_n(m_H\nu_H-m_L\nu_L)/M, \quad (5)$$

where m_H and m_L refer to the masses of the heavy and light fragments before neutron emission.

The rms instrumental deviation in the mass distribution, as computed from the rms deviations in fragment energies given above, is 3.2 mass units. The experimentally observed distribution has a width at half-maximum of about 19 mass units, and this is reduced to about 17.5 units by removing the instrumental spread. Thus the observed distribution reproduces the main features of the true mass distribution. However, a fine structure peak, such as has been observed by Glendenin *et al.*[23] for fission of U^{235} by thermal neutrons, would not be detected with the resolution obtained here.

[23] Glendenin, Steinberg, Inghram, and Hess, Phys. Rev. **84**, 860 (1951).

Disintegration of I^{126}†

M. L. Perlman and Joan P. Welker
Chemistry Department, Brookhaven National Laboratory, Upton, New York

(Received March 26, 1954)

The radiations from I^{126} have been investigated with a scintillation coincidence spectrometer; β-γ, γ-γ, and x-γ events were studied. In a fraction of the electron-capture disintegrations, a gamma ray of energy 0.74 Mev was found to occur in cascade with the previously known 0.65-Mev gamma ray. The crossover transition also was observed. In a fraction of the negative beta-decay processes, a gamma ray of energy 0.48 Mev occurs in cascade with the previously known 0.38-Mev gamma ray; in addition, the crossover transition was observed. The maximum energy of the positron spectrum and the relative intensities of all gamma transitions and of the annihilation radiation were measured. The intensity information, combined with the previously measured ratio of electron-capture probability to beta-decay probability and with the ratio of the intensities of the 0.85-Mev and 1.24-Mev beta rays, is sufficient to give the abundances of all observed transitions in the decay scheme. Both the *ft* values and the measured ratio of electron-capture probability to positron-emission probability for the ground-state transitions indicate that I^{126} has spin 2 and negative parity. The shell structure assignments, neutron $h_{11/2}$ and proton $g_{7/2}$, are the only ones which can couple to give the resultant spin 2 and negative parity.

IT has been known that I^{126} decays to stable Xe^{126} by negative beta emission and to stable Te^{126} by both electron capture and positron emission.[1–3] Recently, Marty, Langevin, and Hubert,[3] by a method based on a knowledge of the conversion coefficient of the Cs^{137} gamma ray, measured the ratio of the electron-capture probability to the beta-decay probability; their result, 1.1 ± 0.15, is in agreement with the value, 1.26 ± 0.13,[4] obtained earlier by absolute counting techniques.[2] The negative beta spectrum has been investigated several times;[1–3] the measurements, which are all in agreement, show the existence of two beta groups with energies 1.24 ± 0.02 Mev and 0.85 ± 0.03 Mev. The results of coincidence experiments[2,3] prove that the 1.24-Mev beta group, which is 1/2.6 times as abundant as the lower energy group, represents the transition to the ground state of Xe^{126}; moreover, the 0.85-Mev beta group was found to be in coincidence with the difference gamma ray of energy 0.382 ± 0.004 Mev. The 0.65-Mev gamma ray has been proved[2,3] to be in the electron-capture branch. A small fraction of the decay of I^{126} takes place by emission of positrons[2,3] with maximum energy 1.21 ± 0.05 Mev.[3]

The gamma-gamma coincidences observed by Perlman and Friedlander,[2] not accounted for in the decay scheme of Marty *et al.*,[3] indicate the existence of gamma rays other than the 0.65-Mev and 0.38-Mev radiations. The results presented in this paper make clear the origin of these coincidences and reveal previously unknown electron-capture and negative beta transitions.

EXPERIMENTAL METHODS AND RESULTS

Source Preparation and Purity

The I^{126} used in these experiments was made by the reaction $I^{127}(n,2n)I^{126}$. Small amounts of I^{125} were simultaneously produced by the reaction $I^{127}(n,3n)I^{125}$. Solid potassium iodate was irradiated with fast neutrons produced by (d,n) reaction on beryllium. Two irradiations were carried out, one with a maximum neutron energy of 26 Mev and the other with 19-Mev neutrons, in order to vary the yield of I^{126} relative to that of I^{125}. After the addition of a few milligrams of iodide carrier, the I^{126} activity was concentrated by means of a Szilard-Chalmers separation. Several extraction cycles served to purify the activity, which was finally deposited onto thin copper foils in the form of cuprous iodide.[5]

The decay of a fraction of the material produced with 26-Mev neutrons was followed for approximately 90 days. Counting measurements were made with a proportional counter, the window of which was approximately 1.2 mg/cm² thick. Rates were observed with and without a beta-stopping beryllium absorber. The usual semi-log plot of the data taken without absorber is a straight line showing a half-life of 13.3 ± 0.1 days. With absorber the count rate was only a few percent of the rate without absorber; and the plot begins to deviate from a straight line after approximately 45 days, because of the presence of a small amount of 60-day I^{125}. The experiments described in this paper were completed before the contribution of I^{125} to the radiation intensity of the samples became appreciable. Moreover, the well-established decay scheme of I^{125}, electron capture followed by the emission of a single highly converted gamma ray, is such as

† Research performed under the auspices of the U. S. Atomic Energy Commission.

[1] Mitchell, Mei, Maienschein, and Peacock, Phys. Rev. **76**, 1450 (1949).

[2] M. L. Perlman and G. Friedlander, Phys. Rev. **82**, 449 (1951).

[3] Marty, Langevin, and Hubert, J. phys. et radium **14**, 663 (1953).

[4] In calculating their published value, 1.44 ± 0.15, Perlman and Friedlander used a K-fluorescence yield value for Te of 0.75. The value 1.26 ± 0.13 is obtained by use of the better fluorescence yield figure of 0.86 as given by Broyles, Thomas, and Haynes, Phys. Rev. **89**, 715 (1953) and by E. H. S. Burhop in his book *The Auger Effect* (Cambridge University Press, Cambridge, 1952).

[5] G. Friedlander and W. C. Orr, Phys. Rev. **84**, 484 (1951).

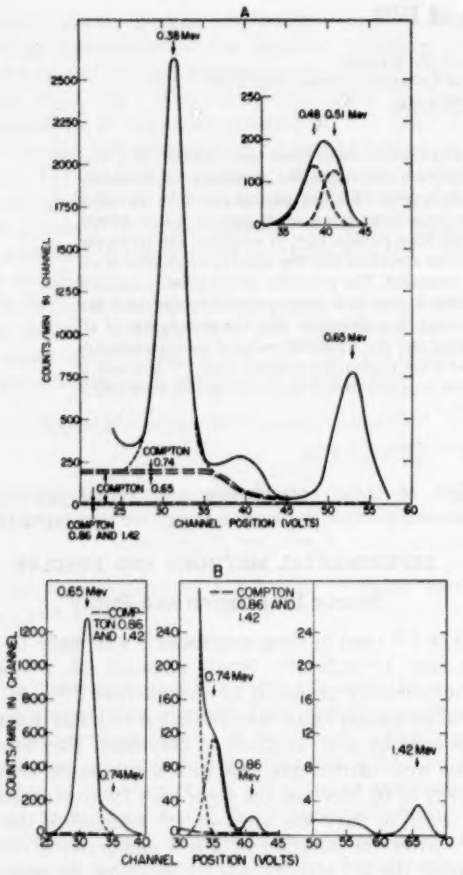

FIG. 1. Gamma rays emitted in the decay of I^{126}. Pulse-height distribution measured with a scintillation spectrometer. A (high gain); B (low gain).

not to make the interpretation of the results for I^{126} ambiguous.

Energies and Intensities of Gamma Rays

A scintillation spectrometer with a DuMont K1186 photomultiplier tube and a NaI(Tl) detector, 1.5 inches in diameter and 1 inch long, was used to measure the energies and intensities of the gamma rays emitted in the decay of I^{126}. An examination with a gray-wedge pulse-height analyzer[6] of the radiations which were transmitted through a beryllium absorber (600 mg/cm²) showed the existence of photopeaks at energies 0.74, 0.86, and 1.42 Mev in addition to the expected lines at 0.027 (K x-ray), 0.38, 0.51, and 0.65 Mev. Observation of the relative photopeak intensities at various source-to-detector distances demonstrated that the peaks at 0.74, 0.86, and 1.42 Mev represent nuclear gamma transitions and not the summation in the detector of two coincident gammas of lower energies. The pulse-height spectrum shown in Fig. 1 was obtained with the detector described above and a single-channel analyzer; the I^{126} source was that produced by irradiation with 19-Mev neutrons. A source-to-detector distance of 2 inches was chosen after it had been established that at this distance the contribution of summation pulses was negligibly small. Beta-stopping absorbers were placed in contact with both sides of the source; the annihilation quanta and the nuclear gamma rays were thus detected in the same geometry.

The energy scale in Fig. 1 was calibrated by the use of gamma-ray standards:[7] Na^{22}(1.28, 0.51 Mev), Mn^{54}(0.84 Mev), Cs^{137}(0.662 Mev), and Be^{7}(0.48 Mev). Each photopeak area in the curves of Fig. 1 was evaluated after a subtraction had been made from the observed pulse-height spectrum of the contributions due to Compton processes. A method of curve analysis similar to that of McGowan[8] was used. The evaluation of the Compton contributions was based on the observed pulse-height spectra of the gamma-ray standards. The analysis of the maximum in the region of 0.5 Mev (Insert, Fig. 1A) involved coincidence experiments discussed in the next section. In Table I are listed the energies and relative intensities of the gamma rays emitted in the decay of I^{126}.

Coincidence Studies

The coincidence investigations were carried out with pairs of scintillation detectors appropriate for the various radiations and a gray-wedge coincidence spectrometer.[9] With this spectrometer it is possible to display and photograph pulses representing events in one detector which occur in time coincidence with events of selected amplitude in a second detector.

TABLE I. Energies and relative intensities of the gamma rays emitted in the decay of I^{126}.

(1) Energy (Mev)	(2) Photopeak efficiency[a] (arbitrary units)	(3) Photopeak area (count-volts/min)	(4) Intensity [col. (3)/col. (2)]
0.382±0.004[b]	309	8700	28 ±3
0.482±0.015	202	550	2.7 ±0.4
0.510[c]	185	445	2.4 ±0.4
0.651±0.010	135	3680	27 ±3
0.740±0.020	111	358	3.2 ±0.4
0.862±0.020	91	47.0	0.52±0.07
1.420±0.030	40	12.1	0.30±0.04

[a] The relative photopeak efficiencies are taken from the data of B. Kahn and W. S. Lyon, reference 11. A small correction has been applied to take into account the fact that measurements were made at a source-to-detector distance of 2 inches rather than 1 inch. This correction, amounting to ~4 percent maximum, was evaluated from unpublished curves of P. R. Bell.
[b] See reference 2.
[c] Annihilation radiation.

[6] Bernstein, Chase, and Schardt, Rev. Sci. Instr. **24**, 437 (1953).

[7] *Nuclear Data*, National Bureau of Standards Circular 499 and Supplements (U. S. Government Printing Office, Washington, D. C., 1950).

[8] F. K. McGowan, Phys. Rev. **93**, 167 (1954).

[9] Chase, Bernstein, and Schardt, Phys. Rev. **90**, 353 (1953); R. L. Chase, Brookhaven National Laboratory, Report BNL 263 (T-42) (unpublished).

A coincidence resolution time of 0.1 microsecond was used. The geometrical arrangement of the detectors and source and the nature of the absorbers used were varied to suit the individual experiments. In Table II are summarized the results of these experiments.

The number of x-x coincidences per K x-ray observed from the I^{126} sources was considerably in excess of the number expected from conversion of any of the gammas associated with the electron-capture decay. A careful search of the events in coincidence with x-rays failed to reveal the existence of any highly converted gamma transitions in the energy range 70–190 kev. The results of two experiments made it evident, however, that the x-x coincidences originated mostly from a few percent I^{125} impurity in the sources. In the first, the ratio of the x-x coincidence rate to the x-ray emission rate for the source produced by irradiation with 26-Mev neutrons was found to be approximately 3.5 times as great as that for the source made with 19-Mev neutrons. This observation is in agreement with the expectation that the yield of the reaction $I^{127}(n,3n)I^{125}$, relative to that of the reaction $I^{127}(n,2n)I^{126}$, rises with increasing neutron energy. Secondly, the x-x coincidence rate from the source made with 19-Mev neutrons was found to decay with the half-life characteristic of I^{125}.

As previously noted, the photopeaks at 0.48 and 0.51 Mev were not resolvable from each other in the gamma-ray spectrum (see Fig. 1A); however, the existence of the 0.48-Mev gamma ray was established from the coincidence observations in 135° geometry. The intensity of the 0.48-Mev transition relative to that at 0.38 Mev was determined by an experiment with 135° geometry in which the 0.38-, 0.48-Mev coincidence rate per 0.38-Mev gamma was compared with the beta, 0.411-Mev gamma coincidence rate per beta from a Au^{198} source.[10] In this comparison, one of the detectors was either an anthracene scintillator for the betas of Au^{198} or a NaI(Tl) crystal and pulse-height selector, channeled at 0.38 Mev, for I^{126}. The second detector, a standard 1.5 inch by 1 inch cylindrical NaI(Tl) crystal kept in a fixed position relative to the sources, was used in conjunction with a pulse-height selector to detect, in turn, the coincident 0.411-Mev Au^{198} or 0.48-Mev I^{126} radiations. The areas under the coincident 0.411- and 0.48-Mev photopeaks were evaluated, and a correction for the ratio of the photopeak efficiencies at the two energies was applied.[11] It was calculated that the intensity of the 0.48-Mev transition is 9.6 percent of that of the 0.38-Mev transition. This result was used to evaluate the contribution of the 0.48-Mev photopeak to the maximum observed in the gamma-ray spectrum in the vicinity of 0.5 Mev. After this contribution had been subtracted from the composite area at 0.5 Mev, the difference curve was found to peak at 0.51 Mev, as shown in the Insert of Fig. 1A. The energy, 0.482 ±0.015 Mev, quoted in Table II, was determined by comparison of the position of the coincident photopeak with that from a gamma-ray standard.

TABLE II. Results of coincidence experiments with I^{126}.

Selected event	Events observed in coincidence with selected event	Remarks
K x-ray	K x-ray;[a] 0.85-Mev β spectrum; conv. e^- of 0.38-Mev γ; 0.65-, 0.74-, 1.42-Mev γ's	no conv. electrons of energy 40–160 kev in coinc.; neither 0.38- nor 0.84-Mev γ in coinc.
all β^+'s	0.39-, 0.51- (0.48-)[b] Mev γ's	
β^+'s of energy >0.96 Mev	0.51-Mev γ	no other γ in coinc.
0.38-Mev γ	0.85-Mev β spectrum; 0.48-Mev γ	135° geometry[c]
0.48-Mev γ	0.38-Mev γ	135° geometry[c]
0.51-Mev γ	1.19[d] ±0.05-Mev β^+ spectrum; 0.51-Mev γ	
0.65-Mev γ	K x-ray; 0.74-Mev γ	little or no β^+ in coinc.
0.74-Mev γ	K x-ray; 0.65-Mev γ	little or no β^+ in coinc.
0.86-Mev γ	0.38-Mev β spectrum	no x-ray in coinc; no γ in coinc.
1.42-Mev γ	K x-ray	no γ in coinc.

[a] See discussion of x-x coincidences in text.
[b] The photopeaks of the 0.51-Mev and 0.48-Mev gamma rays are not resolved from each other.
[c] A detector-source-detector angle of approximately 135° was chosen in order to eliminate 0.51-, 0.51-Mev annihilation coincidences.
[d] The end-point energy of the positron spectrum was determined directly from the photographic record of this coincidence experiment; the Au^{198} beta spectrum (0.963 Mev, see reference 7) was used to calibrate the energy scale. The result obtained is in good agreement with that of Marty *et al.*, reference 3, who reported 1.21 ±0.05 Mev. Throughout this paper the value 1.21 Mev, the result of a spectrographic measurement, will be used.

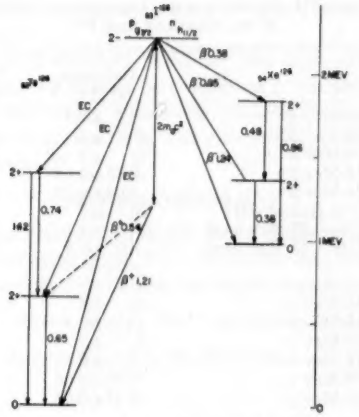

FIG. 2. Decay scheme of I^{126}.

DISCUSSION

The results of the coincidence studies show that the 0.65-, 0.74-, and 1.42-Mev gamma rays are associated with electron-capture decay and that the 0.38-, 0.48-, and 0.84-Mev radiations follow negative beta decay. On the bases of the relative gamma-ray intensities, the coincidence results, and the beta- and gamma-ray energy measurements, the level arrangements shown in Fig. 2 are firmly established. The abundances of the various transitions (Table III) were calculated from the relative intensities of the gamma rays and the

[10] The fact that only 96 percent of the beta transitions from Au^{198} are followed by unconverted 0.411-Mev gamma rays was taken into account. See reference 7.
[11] B. Kahn and W. S. Lyon, Nucleonics **11**, No. 11, 61 (1953).

TABLE III. Abundances and comparative half-lives of the radiations from I^{126}.

Radiation	Abundance (percent)	log*ft*
0.38-Mev β^-	3.7 ±0.5	7.6
0.85-Mev β^-	29 ±3	7.9[a]
1.24-Mev β^-	11 ±2	8.9[a]
0.54-Mev β^+	0.33±0.03[b]	
1.21-Mev β^+	1.04±0.25	8.5
EC to ground state	24 ±7	7.8
EC to 0.65-Mev level	27 ±3	7.5
EC to 1.42-Mev level	4.0 ±0.5	7.8
	100	
0.38-Mev γ	32 ±3	
0.48-Mev γ	3.1 ±0.5	
0.65-Mev γ	31 ±3	
0.74-Mev γ	3.7 ±0.5	
0.86-Mev γ	0.59±0.08	
1.42-Mev γ	0.35±0.05	

[a] The comparative half-lives given by Marty *et al.*, reference 3, for these transitions are in error due to an interchange of *f* values in their Table II, p. 669.

[b] Calculated from the abundance of the EC transition to the 0.65-Mev level and from the ratio, *K*-capture/β^+=75, expected for an allowed transition. See reference 13. The *L*-capture rate is estimated to be 12 percent of the *K*-capture rate. See M. E. Rose and J. L. Jackson, Phys. Rev. **76**, 437 (1949).

annihilation radiation, from the ratio (1.26) of electron-capture probability to negative beta-decay probability, and from the intensity of the 0.85-Mev beta relative to that of the 1.24-Mev beta (2.64).[3] The comparative half-lives given in Table III were calculated from the graphs of Moszkowski[12] and the tabulated abundances.

From the results in Table III, several comparisons (Table IV) may be made with the data of Marty *et al.*[3] Although these authors were unaware of the existence of the 0.48-, 0.74-, 0.84-, and 1.42-Mev gamma rays and of other associated transitions, their experimental results are in agreement with the results presented in this paper in so far as comparisons may be made.

For the ground-state transition, $I^{126} \longrightarrow Te^{126}$, the experimentally determined *K*-capture/β^+ probability ratio is 21±8. The value expected from theory,[13] if the transition were allowed, would be 4.6; and this value would not be changed significantly if the transition were first forbidden of the type $\Delta I=0$ or 1, yes.[5,14] However, when $\Delta I=2$, yes, the theoretical value is increased by a factor approximately 4 to 6.[14] In the case of this I^{126} ground-state transition, Marty *et al.*[3] have calculated from the theory of Nataf and Bouchez[15] that the value of the ratio, *K* capture/β^+, would be 18 for the condition $\Delta I=2$, yes. These arguments indicate that a spin change of 2 with parity change is involved; and since Te^{126}, an even-even nucleus, must have the ground-state assignment 0+, the designation for I^{126} should be 2−.

The designation 2− for I^{126} is in accord with several other experimental results. Stevenson and Deutsch,[16] from measurements of β-γ angular correlation, concluded that I^{126} has spin 2 and negative parity. The log*ft* values (Table III) for the β^+ and β^- ground-state transitions, 8.5 and 8.9, respectively, fall about midway in the range of observed comparative half-lives[17,18] for transitions of the class $\Delta I=2$, yes; they are out of the range for $\Delta I=0$ or 1, yes, and seem too high for $\Delta I=1$, no, $\Delta l=2$, the choice of Marty and co-workers[3] and of Nordheim.[17]

Because the first excited states of Xe^{126} and Te^{126} are expected to have spin 2 and even parity,[19,20] the beta transitions to these states should involve a spin change of zero and parity change. The log*ft* values, 7.9(Xe^{126}) and 7.5(Te^{126}), are about one unit higher than the midpoint value,[18] 6.5, for transitions of this type; however, as pointed out by King and Peaslee,[18] when the single particle spin change Δj exceeds the nuclear spin change ΔI, log*ft* is increased by approximately one unit. It is plausible that such a condition is operative in the case of these transitions to the first excited states, for which $\Delta I=0$.

The designations 2+ for the second excited states of Xe^{126} and Te^{126} may be deduced from consideration of the intensity of the 0.48-Mev gamma relative to that of the 0.86-Mev crossover and of the intensity of the 0.74-Mev gamma relative to that of the 1.42-Mev crossover. With any assignments other than 2+ or 2−, the expected intensity ratios[21] would be greatly different from those observed; and 2− appears improbable because the log*ft* values for the transitions to the second excited states, 7.6(Xe^{126}) and 7.8(Te^{126}), are larger than those found for allowed transitions. Moreover, no second excited states of even-even nuclei are definitely known to have spin 2 and negative

TABLE IV. Comparisons of some intensity ratios.

Intensity ratio	This work	Marty, Langevin and Hubert
$\frac{\text{Total } K \text{ capture}}{(0.65\text{-Mev } \gamma + 0.74\text{-Mev } \gamma)}$	1.4 ±0.2	1.35 ±0.1[a]
β^+/β^-	0.031±0.006	0.027±0.002
$\left(\frac{K \text{ capture}}{\beta^+}\right)_{\text{ground state}}$	21 ±8	12 $^{+7}_{-3}$

[a] The instrument used by these authors did not resolve the 0.65- and 0.74-Mev gammas from each other.

[12] S. A. Moszkowski, Phys. Rev. **82**, 35 (1951).
[13] E. Feenberg and G. Trigg, Revs. Modern Phys. **22**, 399 (1950).
[14] Good, Peaslee, and Deutsch, Phys. Rev. **69**, 313 (1946).
[15] R. Nataf and R. Bouchez, J. phys. et radium **13**, 190 (1952).
[16] D. T. Stevenson and M. Deutsch, Phys. Rev. **84**, 1071 (1951).
[17] Mayer, Moszkowski, and Nordheim, Revs. Modern Phys. **23**, 315 (1951); G. P. Nordheim, Revs. Modern Phys. **23**, 322 (1951). It may be noted that Nordheim, in his classification of the I^{126} ground-state beta transition, has made use of an erroneous log*ft* value, 7.6, given by Mitchell *et al.*, reference 1.
[18] R. W. King and D. C. Peaslee, Phys. Rev. **94**, 1284 (1954).
[19] In the case of the Xe^{126}, the value of the conversion coefficient of the 0.38-Mev gamma ray shows that the transition from the first excited state to ground involves a spin change of 2 and no parity change. See reference 3.
[20] G. Scharff-Goldhaber, Phys. Rev. **90**, 587 (1953).
[21] M. Goldhaber and A. W. Sunyar, Phys. Rev. **83**, 906 (1951).

parity.[20] The magnitude of these values for log ft, very little different from those for the transitions to the first excited states, may be explained by the same arguments[18] which apply to the transitions to the first excited states.

The assignment 2− for the ground state of I^{126} is readily interpretable in terms of the nuclear shell model. The only reasonable single-particle configurations[22] which can couple to give the resultant spin-parity value 2− are neutron $h_{11/2}$ and proton $g_{7/2}$.

From the spin and parity assignments for the levels in Xe^{126} and Te^{126} and from the energies of the gamma rays, it is concluded that approximately 1 percent of the total K x-ray intensity from I^{126} arises from internal conversion.[23]

A value, 0.99±0.05 Mev, for the mass difference, Xe^{126} minus Te^{126}, may be calculated from the energies of the ground-state transitions. This figure is believed to be more accurate than that now available from mass measurements.[24]

ACKNOWLEDGMENT

We would like to thank Dr. Rolfe Herber for arranging an irradiation at the MIT cyclotron, and Drs. A. W. Schardt and G. Friedlander for helpful suggestions.

[22] P. F. A. Klinkenberg, Revs. Modern Phys. **24**, 63 (1952).

[23] Rose, Goertzel, Spinrad, Harr, and Strong, Phys. Rev. **83**, 79 (1951).

[24] R. E. Halsted, Phys. Rev. **88**, 666 (1952).

PHYSICAL REVIEW VOLUME 95, NUMBER 1 JULY 1, 1954

Angular Distribution of Charge-Exchange Scattering of 40-Mev π^- Mesons by Hydrogen*

J. TINLOT AND A. ROBERTS
Department of Physics, University of Rochester, Rochester, New York

(Received March 15, 1954)

The angular distribution of the reaction $\pi^-+p\rightarrow\pi^0+n$ has been measured at a mean π^- energy of 40 Mev by detecting coincident photons corresponding to π^0 emission at approximately 0°, 90°, and 180°. The result is

$$d\sigma^0/d\Omega=(0.45\pm0.07)-(0.98\pm0.13)\cos\theta+(0.54\pm0.21)\cos^2\theta \text{ mb/sterad.}$$

The corresponding total cross section is $\sigma_t^0=7.9\pm1.8$ mb. An analysis of this result and of previous measurements on π^+ and π^- scattering at 37 Mev has been made, following the hypothesis of charge independence. It is possible to find two distinct types of solution. One type has positive $T=\frac{1}{2}$ s-wave and $T=\frac{3}{2}$ p-wave phase shifts, and negative $T=\frac{3}{2}$ s-wave and $T=\frac{1}{2}$ p-wave phase shifts. For the other type, the signs of the phase shifts are almost all reversed. Each type consists of a pair of solutions which are intrinsically indistinguishable at low energies because of the impossibility of determining the sign of the spin-flip scattering amplitude. A choice between the two types of solution is in principle possible with improved data. Predictions of the angular distributions of π^- elastic scattering are made.

I. INTRODUCTION

THE study of the scattering of pi mesons from nucleons is one of the more direct means of investigating the meson-nucleon interaction. In this connection, the simplification introduced into the interpretation of meson-nucleon scattering by the hypothesis of charge independence is of current interest. This hypothesis allows one to describe all meson-nucleon scattering processes by specifying only $2(2l+1)$ phase shifts, where l is the largest relevant orbital quantum number of the incident meson. In the energy range in which the meson wavelength is more than its Compton wavelength, it is reasonable to limit consideration to low angular momentum states, $l=0$ and 1; one therefore seeks a measure of six phase shifts.

Angell, Perry, and Barnes *et al.*[1–3] have reported on the elastic-scattering processes at an incident energy of 37 Mev, and we have previously reported[4] a measurement of the total cross section for charge-exchange scattering at a mean energy of 34 Mev. In the present paper, we present the results[5] of a measurement of the angular distribution of charge-exchange scattering at a mean energy of 40 Mev. Within the experimental errors, all of these observations can be explained in terms of the same phase shifts.

II. METHOD

In previous observations[6–8] of the angular distribution of pion-proton charge-exchange scattering, only

* This work was supported in part by the U. S. Atomic Energy Commission.

[1] C. E. Angell and J. P. Perry, Phys. Rev. **92**, 835 (1953).

[2] J. P. Perry and C. E. Angell, Phys. Rev. **91**, 1289 (1953). J. P. Perry, thesis, University of Rochester, 1953 (unpublished).

[3] Barnes, Angell, Perry, Miller, and Nelson, Phys. Rev. **92**, 1327 (1953).

[4] A. Roberts and J. Tinlot, Phys. Rev. **90**, 951 (1953).

[5] A brief report of these results was presented at the 1954 New York meeting of the American Physical Society [Phys. Rev. **94**, 766 (1954)].

[6] Anderson, Fermi, Martin, and Nagle, Phys. Rev. **91**, 155 (1953).

[7] Fermi, Glicksman, Martin, and Nagle, Phys. Rev. **92**, 161 (1953).

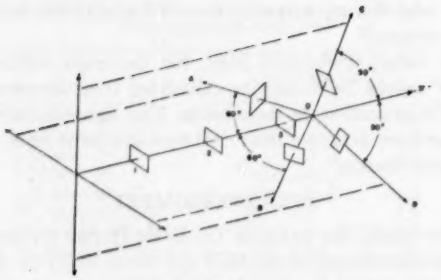

FIG. 1. Arrangement of photon detectors A, B, C, D in approximate tetrahedral geometry.

one of the two π^0 decay photons was detected. At the π^- energies involved in these experiments (60 Mev and above), a fairly strong correlation exists between the angular distributions of the photons and of the parent π^0 mesons. At 40 Mev, this correlation is very weak; therefore, it becomes necessary to detect both photons to obtain the π^0 angular distribution with reasonable accuracy.

The usable intensity of π^- mesons in our experiment was such ($\sim$1000 min^{-1} cm^{-2}) that the rate of counting charge-exchange events by observing two coincident photons was expected to be very low—of the order of 4 counts per hour—even though the photon detectors subtended rather large solid angles at the target. Thus, simultaneous measurements at several π^0 emission directions were clearly desirable. Accordingly, we took advantage of a peculiarity of π^0 decay kinematics. At the average π^- energy of 40 Mev, the minimum (and most probable) angle between the two decay photons has a value of about 110°, averaged over the range of π^0 energies. This angle is very nearly the same as that between the axes of symmetry of a regular tetrahedron (109° 28′). For this reason, four photon detectors were placed so that their axes coincided approximately with those of an imaginary tetrahedron[9] centered on the target. (See Fig. 1.) In the resulting assembly, one pair of detectors (C and D) counted neutral mesons emitted predominantly in the forward direction; another pair (A and B) those emitted backward; and the four other pairs (A, C; A, D; B, C; B, D) those emitted near 90°. The symmetry of the detectors is that of the point group C_{2v}; i.e., there is a twofold axis of symmetry and two mutually perpendicular planes of symmetry containing this axis, as in the molecule CH_2Cl_2. Since there can be no azimuthal angular dependence, the four 90° pairs are essentially identical.

The terms "backward," "forward," and "90°" are only very approximate designations of the angular definition of the detector pairs. It will be seen (Fig. 2) that each pair of detectors is sensitive over an angular range exceeding 90°.

III. APPARATUS AND PROCEDURE

(a) Experimental Arrangement

The π^- beam used in this experiment was the external 50-Mev beam of the Rochester synchrocyclotron, selected in energy and focused by the cyclotron fringing field, a "z-focusing" magnet, and a double-focusing wedge magnet. The general arrangement is shown in Fig. 3. The resulting beam traversed a counter telescope (counters 1, 2, 3) consisting of scintillators 2 in.$\times$2 in. $\times\frac{3}{16}$ in., and entered the target. A fourth scintillator (4), having the form of a hollow rectangular box open on one side, surrounded the target, as indicated in Fig. 4b. Counter 4 was in anticoincidence with the meson telescope counters and served to eliminate mesons which traversed the target without interacting,

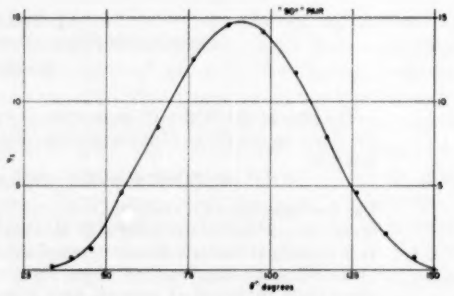

FIG. 2. The relative efficiency of a 90° pair of counters for detecting a neutral meson, as a function of angle of emission in the c.m. system.

or which produced ionizing fragments by interaction in nonhydrogenous material. Mesons elastically scattered from target nuclei could not penetrate the photon detectors, and therefore were not counted. Each of four photon detectors consisted of a $\frac{1}{4}$-in. Pb converter in front of two liquid scintillators, the first of which had dimensions 3.5 in.$\times$3.5 in.$\times$0.9 in., and the second, 4 in.$\times$4 in.$\times$0.4 in.; the two counters were separated by $\frac{1}{16}$ in. aluminum (see Fig. 4a). An 8-Mev electron could just penetrate the counters and aluminum. This threshold energy was selected to simplify the calculation of photon detection efficiency.[10]

(b) Targets

The targets used were either CH_2 or C, and had square cross sections $2\frac{1}{4}$ in.$\times 2\frac{1}{4}$ in.

The hydrogen effect was determined by taking CH_2-C differences. Approximately equal amounts of

[9] Bodansky, Sachs, and Steinberger, Nevis Cyclotron Laboratories Report No. 1, 1953, Phys. Rev. **93**, 1367 (1954).

[9] The regular tetrahedron geometry would be suitable in the meson-proton center-of-mass system. In order to compensate roughly for the center-of-mass motion (which causes forward photon pairs to have smaller angular separation than backward ones), the axes chosen were slightly distorted from those of the tetrahedron.

[10] The same criterion was used in the experiment of reference 4, and is discussed in more detail there.

data were taken using targets of equal stopping power, and targets of equal carbon content. In the first case, the surface densities of CH_2 and C were 2.06 g-cm^{-2} and 2.50 g-cm^{-2}, respectively; in the second case the CH_2 surface density was 2.92 g-cm^{-2}, and the carbon target was unchanged. The meson energy spread was 34 to 43 Mev in the "thin" CH_2 and carbon targets, and 29 to 43 Mev in the "thick" CH_2 target. In order to obtain the mean interaction energy, we weight the meson energy as a function of depth by the total cross section, as measured by Spry.[11] The mean meson energy in the "thin" CH_2 target is 40 Mev. Although the mean meson energy in the "thick" CH_2 target is somewhat lower, the results from the two target thickness can be combined, if one assumes slow variation of the angular distribution at this energy. As shown in Sec. V and VI, this is a reasonable assumption.

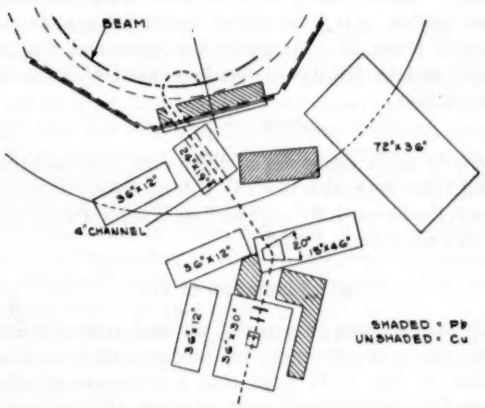

FIG. 3. Arrangement of apparatus at the cyclotron, showing the focusing magnets and some of the shielding.

(c) Shielding

The mechanical assembly of the twelve scintillators and associated photomultipliers (seven 1P21, four 6199, and one 6292) was greatly facilitated by using only enough iron and Permalloy to shield the multipliers against fields of the order of 5 to 10 gauss, instead of the 100–200 gauss cyclotron fringing field. The entire array was mounted inside the rectangular H yoke of a large magnet originally intended for cloud-chamber use; the sides of the yoke were closed with 2-in. iron plates. A 3-in. hole in one end of the yoke collimated the meson beam. The yoke served both as an adequate magnetic shield and as a shield against cyclotron radiation.

(d) Electronics

A simplified block diagram of the circuits used is shown in Fig. 5. The meson telescope triples and the anticoincidence rate (1234), which will be called M, were recorded. Coincidences MA, MB, MC, and MD

[11] W. Spry, Phys. Rev. 94, 766 (1954).

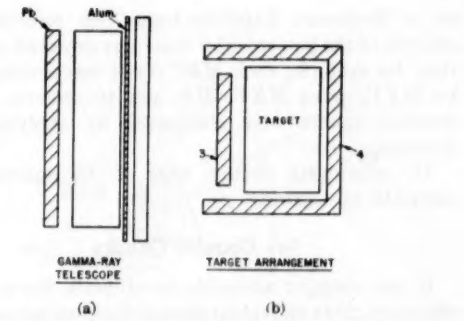

FIG. 4. (a) Detail of gamma-ray detector, showing lead converter, two liquid scintillators, and aluminum absorber between them. (b) Detail of target arrangement inside the hollow anticoincidence counter, No. 4.

of M with each photon detector were formed in a fast (20 mμsec) and a slow (0.1 μsec) circuit. The data from the slow circuit (with one input delayed) were used to compute accidental rates. The CH_2-C differences in the fast rates, after correction for accidentals, are a measure of the single photon yield from hydrogen. The results were useful as a continuing check on the operation of the photon detectors. The coincident photon rates $MAB\cdots MCD$ were obtained by forming coincidences between the six combinations of counts $MA\cdots MD$ in separate coincidence circuits. This scheme was chosen because it served to define resolving times and required relatively slow final coincidence circuits. The accidental background in the $MAB\cdots MCD$ rates was negligible. In view of the complexity of the circuitry and the low counting rates, independent instrumental checks were obtained in the following ways:

(1) A triple coincidence between M and any two photon detectors (called MXY) was formed in a combination coincidence and addition circuit. These counts were recorded directly, and also in coincidence with a 500-μsec gate which included the total time of the beam on target (about 250 μsec).

(2) The rates $MA\cdots MD$, $MAB\cdots MCD$, MXY, and gated MXY were recorded in register circuits and

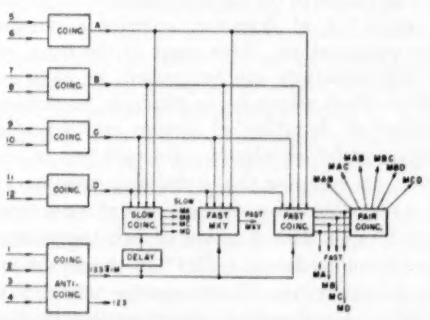

FIG. 5. Simplified block diagram of the circuits used. Not shown are the beam gating circuit and 20-channel pen recorder (see text), and sundry amplifiers, discriminators, pulse equalizers, etc.

on a 20-channel Esterline-Angus pen recorder. An analysis of the pen-recorder chart was expected to show that, for example, each MBC count was accompanied by MXY, gated MXY, MB, and MC counts. A few spurious counts were eliminated by applying this criterion.

All coincidence circuits were of the general type described by Garwin.[12]

(e) Counter Checks

It was thought advisable to calibrate the absolute efficiency of the individual photon detectors for counting single minimum-ionization particles, both before and after obtaining data. For this purpose, we used the 15 percent electron contamination in the negative meson beam. Since the electrons have the same momentum as do the mesons (130 Mev/c), their range is much greater than that of either π or μ mesons. The mesons were stopped by interposing about 2 in. of CH_2 and C. Each photon telescope was then placed between counter 3 and counter 4 (after the latter had been retracted), and the efficiency of the telescope measured by taking the ratio of 6-fold to 4-fold coincidences. The efficiencies were found to be about 90 percent. We consider this appreciable counting loss to be explained, at least in part, by the poor light collection from the large counters, particularly those viewed by 1P21 multipliers. We believe, however, that the resulting inefficiency for counting π^0-decay photons is quite negligible. The reason is that, according to Wilson,[13] the most probable numbers of conversion electrons produced in $\frac{1}{4}$ in. of Pb by a photon of energy near 100 Mev are zero or two; the probability of producing only one electron of energy greater than 8 Mev is less than 10 percent. (This is because the major interaction is pair production.) The counter efficiency for the detection of a converted high-energy photon should therefore be near 100 percent.

IV. GEOMETRICAL CALIBRATION OF THE APPARATUS

The calculation of the angular definition and effective solid angles for π^0 detection involves a number of lengthy computations. Since none of the usual small-angle approximations can be applied, we have used a procedure which allows us, in principle, to deduce the probability of detecting π^0 mesons emitted with an arbitrary angular distribution. For each pair of photon detectors, we compute the probability function $\bar{I}(\theta)d\theta$ which is the probability of detecting a π^0 meson emitted at angle θ in $d\theta$. This function is then transformed to the corresponding function $\bar{I}^*(\theta^*)$ in the meson-proton center-of-mass system. If we consider only the effects of s- and p-wave scattering, the π^0 angular distribution will have the form

$$J(\theta^*)=a+b\cos\theta^*+c\cos^2\theta^*, \tag{1}$$

and the probability η_i of detecting a π^0 meson in the ith pair of detectors will be

$$\eta_i=a\eta_{i1}+b\eta_{i2}+c\eta_{i3}=[4\pi(a+c/3)]^{-1}\int_0^\pi\langle\bar{I}^*(\theta^*)\rangle_{\text{Av}}\times(a+b\cos\theta^*+c\cos^2\theta^*)\sin\theta^*d\theta^*. \tag{2}$$

This expression is normalized to a π^0 flux of unity. The ratio R_i of detected π^0 to incident π^- mesons is then the product of η_i and the probability of production of a π^0 meson:

$$R_i=(a\eta_{i1}+b\eta_{i2}+c\eta_{i3})\kappa\rho N\sigma_t x, \tag{3}$$

in which formula ρ is the fraction of π^- mesons in the impure "meson" beam, σ_t is the total charge exchange cross section, κ is a correction factor for gamma-ray detector losses, N is Avogadro's number, and x is the target surface density. σ_t can be eliminated by using the relation

$$\sigma_t=4\pi(a+c/3), \tag{4}$$

and a, b, and c expressed as differential cross sections. With three equations like (3), corresponding to detection in the forward, 90°, and backward pairs of detectors, we can solve for a, b, and c.

(a) Calculation of $\bar{I}(\theta)$

In the following paragraphs, we shall make frequent reference to the geometry of the experiment, as illustrated in Fig. 6. Suppose that a π^--meson incident along the Z axis interacts with a proton, and a π^0 meson is emitted in a direction specified by θ and ϕ. The meson decays essentially at the point of origin into two photons whose directions of flight lie in a plane containing the π^0 direction. The orientation of the plane is specified by the angle ϕ' with an arbitrary reference plane (since all values of ϕ' are equally probable). Let us define ξ as the angle between the two photon directions, and ζ as the inclination of one of them from the π^0 direction.

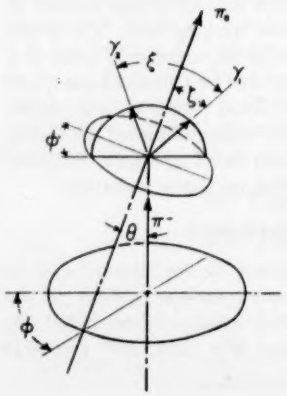

FIG. 6. Geometry of charge-exchange scattering. θ, ϕ are polar coordinates of the direction of the emitted π^0 meson. The plane of the two decay gamma rays is specified by ϕ', the angle between them by ξ, and the angle one gamma ray makes with the π^0 direction by ζ.

[12] R. L. Garwin, Rev. Sci. Instr. **21**, 569 (1950); Phys. Rev. **90**, 274 (1953).
[13] R. R. Wilson, Phys. Rev. **86**, 261 (1953).

The probability λ of detecting an event defined by the angles θ, ϕ, ξ, and $\zeta(\xi)$ is then equal to the probability that the photons strike two of the photon detectors, multiplied by the product of the intrinsic efficiencies ϵ_1 and ϵ_2 of the detectors. ϵ_1 and ϵ_2 depend on the photon energies, and therefore on the π^- energy and the angles θ, ξ. The probability that both photons strike the detectors is simply the fraction of 360° occupied by the range of ϕ' over which such space coincidence occurs. The quantity $I(\theta)$ is obtained by taking an appropriate average of λ over the variables ξ, ϕ; and $\bar{I}(\theta)$ by taking the average of $I(\theta)$ over the π^0 source position in the target. The procedure outlined above is done in the following sequence:

(1) We first compute the energy of the π^0 meson in the laboratory system for various values of θ, for π^- energies appropriate to the source positions in the target.

(2) For each value of the π^0-meson energy, we evaluate the differential correlation probability $P(\xi)d\xi$ that the angle ξ between the two photon directions lies in the range $d\xi$, and calculate the related values of ζ.

(3) We then determine the effective fractional range of ϕ' for space coincidence at a number of values of ξ, holding θ and ϕ fixed. The measurement is then repeated over the entire range of θ and ϕ.

(4) The numbers obtained in part (3) are multiplied by the corresponding product of detection efficiencies $\epsilon_1\epsilon_2$, weighted by the correlation probability $P(\xi)$, and averaged over the range of ξ.

(5) The results of steps 3 and 4 are then averaged over ϕ for each value of θ. This gives $I(\theta)$, the detection probability for a given value of θ.

(6) Finally, we repeat the procedure of steps (3), (4), and (5) for a selected number of source points in the target, and obtain a weighted average over the target. The result is the quantity $\bar{I}(\theta)$.

(7) The transformed function $\bar{I}^*(\theta^*)$ is calculated; we neglect the small variation in center-of-mass motion because of the distribution in π^- interaction energy, and transform to the system corresponding to the average interaction energy. The resulting function $\bar{I}^*(\theta^*)$ appears in Eq. (2) for the detection efficiency. The calculations in steps (1) and (2) of the above procedure involve straightforward application of the formulas for π^0 kinematics,[14] which for convenience are given in the appendix.

In performing step (4), we have, as in our previous work, used the Monte Carlo calculations of Wilson[13] to evaluate the intrinsic photon detection efficiency ϵ as a function of photon energy.

The results of steps (3)–(6) are peculiar to the experimental arrangement, and could in principle be obtained analytically. Preliminary study showed that an analytical solution would require a prohibitive effort. Accordingly, we adopted a numerical sampling method involving the use of a simple mechanical device (actually an analog computer) as an aid in performing these operations.

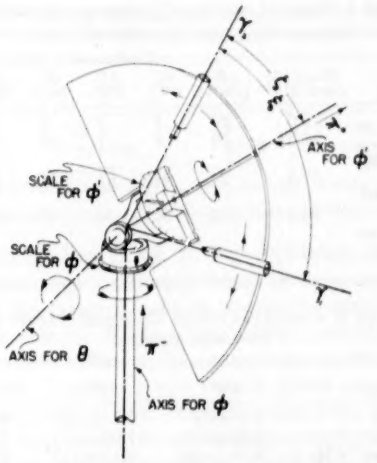

FIG. 7. The analog computer used for solid angle determinations. The angles shown are those defined in Fig. 6.

(b) The Analog Computer

The analog computer was constructed to duplicate the geometry of Fig. 6, on a scale three times actual size, with rectangular screens representing the photon detectors. A drawing of the computer is shown in Fig. 7. A swivel camera mount was modified to hold a semicircular plate, which supported two flashlights with collimated light beams. The movable axis of the mount, representing the direction of the π^0 meson, could be oriented over a wide range of directions (specified by θ and ϕ), and the plane of the light beams rotated about this axis; the relative angular position of the plane represented the variable ϕ'. The light beams were directed from the center of rotation of the mount and were inclined from the axis by angles ζ and $\xi-\zeta$. To implement the procedure of step (3), we then (a) set the center of the mount at a position corresponding to a chosen point in the target, (b) adjust the coordinates of the movable axis to particular values of θ, ϕ, (c) set the flashlight beams at appropriate angles ζ, $\xi-\zeta$, as determined in step (2), and (d) measure the range of ϕ' over which the light beams strike the two screens.

Data were obtained in this way for θ taken in 5° steps and ϕ in 30° steps in the cases of the backward and forward pairs of detectors, and for θ and ϕ both in steps of 10° for the 90° pairs. In most cases, 4 sets of values of ζ and $\xi-\zeta$ were taken for each position of the mount. It was shown that this sampling was adequate by repeating some of the measurements for seven sets of values for ζ and $\xi-\zeta$. The entire procedure was carried out for seven different source points in the

[14] Some of these are given by J. Steinberger and A. S. Bishop, Phys. Rev. **86**, 171 (1952); Panofsky, Steinberger, and Steller, Phys. Rev. **86**, 180 (1952).

TABLE I. Observed numbers of gamma-gamma coincidences.

Target	No. of 123 coinc. $\times 10^{-6}$	Total counts in pair: AB (180°)	AC (90°)	AD (90°)	BC (90°)	BD (90°)	CD (0°)
None	5.0	10	1	1	0	4	0
Carbon 2.92 g/cm³	10.03	30	9	7	14	10	3
CH_2 2.06 g/cm³	12.3	99	41	41	32	40	6
CH_2	20.4	134	56	54	45	47	6
CH_2, C, no Pb conv.	2.0	1	0	1	1	0	0

TABLE II. Counts per million 123 triples. The 90° pairs have been averaged.

Target	180°	90°	0°
A. None	2.0 ±0.7	0.3 ±0.15	0
B. Carbon	3.00±0.55	1.00±0.16	0.30±0.17
C. "Thick" CH_2	8.05±0.80	3.12±0.25	0.49±0.25
D. "Thin" CH_2	6.55±0.56	2.50±0.16	0.29±0.12

target: the center of the target and the centers of the six faces. The results were then averaged using Simpson's rule for numerical integration. Figure 2 shows the result for the "90°" pairs.

It is of course very difficult to estimate the error in $\bar{I}(\theta)$ arising from observational errors, insufficient sampling, and uncertainties in Wilson's shower theory. We believe, however, that although the uncertainly in $\bar{I}(\theta)$ may be quite large for some values of θ, the resulting relative uncertainties in the detection efficiencies η_i are probably not larger than 10 percent.

V. REDUCTION OF DATA

The individual total counts for all of the pairs of photon detectors are given in Table I, and the rates per million triple coincidences (123) are shown in Table II. The hydrogen effect (Table III) was determined in different ways for the two CH_2 targets. It is simply the CH_2-C difference in the case of the "thick" CH_2 target (equal carbon content). In the case of the thin CH_2 target, we must take into account the yield with no target. If σ is the ratio of carbon nuclei in the CH_2 and C targets, then

$$\text{Hydrogen yield} = (CH_2 \text{ yield}) - \sigma(\text{C yield}) - (1-\sigma)(\text{no target yield}).$$

The results for the two different targets were in excellent agreement for all pairs of detectors, if account was taken of the slight reduction in total cross section in the energy range 29–34 Mev, compared to 34–43 Mev. Therefore, the hydrogen effects obtained with both targets have been averaged in Table III. It will be seen that, within statistics, the four 90° pairs gave equal rates; this is to be expected, since the counter array has the above-mentioned C_{2v} symmetry about the incident π^- direction. It should also be noted that the rates with no Pb converters are very low; this result is a strong indication that (a) the phenomenon we have observed is truly the consequence of coincident photons, and (b) the accidental counting rates are negligibly small. The individual rates $MA\cdots MD$ are not given, but were in all cases equal within the experimental errors. The factor κ in Eq. (3) includes several corrections which must be applied to the data.

(a) The meson beam is attenuated by nuclear absorption in traversing the target, so that the number of 123 triples exceeds the number of effective mesons in the target. We estimate this correction as one percent.

(b) Each neutral meson decay gamma ray has a 0.7 percent probability of being internally converted;[15] if it is, counter 4 will prevent its being recorded. The correction for two gamma rays in coincidence is thus 1.4 percent.

(c) The gamma rays may be converted in the target itself or in counter 4. An accurate estimate of this effect is difficult to make because of the wide variation in path lengths in the target. We estimate 3 percent probability of conversion for each gamma ray, or 6±2 percent for both.

(d) A few π^- mesons stop in the target and are captured in hydrogen; half of these captures result in π^0 emission yielding two gamma rays. A direct measurement of this process, made by stopping the entire beam in the target, gave a two-photon coincidence rate only three times that observed with fast π^-'s. We estimate this correction as not more than one percent, and have neglected it.

The radiative capture of π^- mesons produces only one gamma ray, and is therefore not observed.

Combining all the above corrections, we find a value for κ of 0.92±0.02.

VI. CALCULATION OF ANGULAR DISTRIBUTION

As stated previously, we assume that only *s*- and *p*-wave scatterings are important at this interaction energy. Accordingly, the equations obtained in Sec. IV for the detection efficiencies are directly applicable. Substitution of the results of Table III gives the following numerical relations (with $\rho=0.72$, $\kappa=0.92$,

TABLE III. Net hydrogen and carbon effects, in counts per million 123 triples.

Datum from Table II[a]	180°	90°	0°
$C-B$	5.05±0.97	2.12±0.30	0.19±0.30
$D-0.7B-0.3A$	3.85±0.70	1.70±0.20	0.09±0.17
Average H effect	3.94±0.52	1.70±0.16	0.11±0.15
Carbon effect $(B-A)$	1.0 ±0.9	0.70±0.23	0.3 ±0.2

[a] In Table II the targets of entries *B* and *C* contain the same number of C atoms; the first entry in Table III, $C-B$, is thus the net hydrogen effect for the "thick" CH_2 target. The second entry is the hydrogen effect for the "thin" CH_2 target, containing 0.7 as many C atoms. The average in the third line is normalized to the "thin" CH_2 target, assuming the total cross section at 29–33 Mev is 0.8 times the cross section from 33–43 Mev. (See reference 11.)

[15] Lindenfeld, Sachs, and Steinberger, Phys. Rev. **89**, 531 (1953).

$x=0.294$ g/cm^2):

$$\begin{aligned}(0°):&\quad 0.117(39.3a+31.7b+26.6c) = 0.11\pm0.15,\\ (90°):&\quad 0.117(26.5a-0.69b+3.42c) = 1.70\pm0.23,\\ (180°):&\quad 0.117(19.25a-16.9b+15.1c) = 3.94\pm0.65,\end{aligned} \tag{5}$$

where a, b, and c are now in mb/sterad. The coefficients of a, b, and c are 10^3 times the values of η_1, η_2, and η_3 in Eq. (2). The errors in the counting ratios on the right-hand sides of the equations have been increased over those shown in Table III to take into account the uncertainty in the analog computations and in κ.

The solution of these equations gives the following angular distribution:

$$d\sigma^0/d\Omega = (0.45\pm0.07) - (0.98\pm0.13)\cos\theta + (0.54\pm0.21)\cos^2\theta \text{ mb/sterad}. \tag{6}$$

This distribution is strongly peaked in the backward direction, in agreement with results[6–8] at higher energies. From Eq. (4), the total cross section is found to be $\sigma_t=7.9\pm1.8$ mb, where an estimated additional error in absolute gamma-ray efficiency has been added. This number is in reasonable agreement with our previous result[3] at 34 Mev (5.5±1.5 mb), assuming the angular distribution given above, and with the more recent measurements of Spry[11] (6.9±1.2 mb at 42 Mev).

VII. ANALYSIS AND DISCUSSION OF RESULTS

(a) Evaluation of Phase Shifts

The analysis of pion-nucleon scattering is usually carried out according to the hypothesis of charge independence. Accordingly, if only s- and p-wave scattering contribute, there are six independent phase shifts, corresponding to the combinations $l=0$ or 1, $J=1\pm\frac{1}{2}$, and $T=\frac{1}{2}$ or $\frac{3}{2}$. They are conventionally denoted by α_{ij}, where $i=2T$, $j=2J$ (but is omitted for $l=0$). These six phase shifts, in suitable combinations, should describe the scattering of pions of any sort by either neutrons or protons.

The expressions of Van Hove,[16] in which the first order Coulomb terms are retained, can be written as follows for the observable cases:

$$\frac{d\sigma^+}{d\Omega}=\frac{1}{k^2}\left[\left(x_+ + y_+\cos\theta - \frac{\alpha}{2\sin^2(\theta/2)}\right)^2 + z_+^2\sin^2\theta\right], \tag{7}$$

$$\frac{d\sigma^-}{d\Omega}=\frac{1}{9k^2}\left[\left(x_- + y_-\cos\theta + \frac{3\alpha}{2\sin^2(\theta/2)}\right)^2 + z_-^2\sin^2\theta\right], \tag{8}$$

$$\frac{d\sigma^0}{d\Omega}=\frac{2}{9k^2}\frac{v_0}{v}\left[(x_0+y_0\cos\theta)^2+z_0^2\sin^2\theta\right]. \tag{9}$$

In Eqs. (7) and (8), which refer to elastic scattering from protons, α is a relativistic Coulomb phase shift discussed by Van Hove. In Eq. (9), which describes charge-exchange scattering from protons, we have inserted the factor v_0/v which is usually omitted. Here v_0 is the velocity of the neutral meson relative to the neutron, and v that of the charged meson relative to the proton. The factor v_0/v (which differs appreciably from unity only at low energies) arises from the definition of flux for the charge-exchange process, which in reality is an exothermic reaction. At 40 Mev, the value of v_0/v is 1.05. The coefficients x, y, and z are directly related to the s- and p-wave phase shifts. Their values in the small angle approximation which we adopt [$\exp(2i\alpha)-1\approx 2i\alpha$] are shown in Table IV.

TABLE IV. Relations between scattering parameters and phase shifts, in the small-angle approximation.

Scattering process	x	y	z
+	α_3	k	m
−	$\alpha_3+2\alpha_1$	$k+2l$	$m+2n$
0	$\alpha_3-\alpha_1$	$k-l$	$m-n$

$k=2\alpha_{13}+\alpha_{31}$, $l=2\alpha_{13}+\alpha_{11}$, $m=\alpha_{33}-\alpha_{31}$, $n=\alpha_{13}-\alpha_{11}$.

It is convenient to write the experimental angular distribution for charge exchange scattering in the form

$$\frac{d\sigma^0}{d\Omega}=\frac{2}{9k^2}\frac{v_0}{v}(A+B\cos\theta+C\cos^2\theta), \tag{10}$$

and to define new parameters,

$$\mu=(A+B+C)^{\frac{1}{2}}, \quad \lambda=(A-B+C)^{\frac{1}{2}}. \tag{11}$$

Combining Eqs. (9), (10), and (11), we obtain the following solutions for the parameters x_0, y_0, and z_0;

$$\begin{aligned}&x_0=\tfrac{1}{2}(\mu+\lambda), && y_0=\tfrac{1}{2}(\mu-\lambda), && z_0^2=\tfrac{1}{2}(A-C-\mu\lambda),\\ &x_0=\tfrac{1}{2}(-\mu+\lambda), && y_0=\tfrac{1}{2}(-\mu-\lambda), && z_0^2=\tfrac{1}{2}(A-C+\mu\lambda),\\ &x_0=\tfrac{1}{2}(-\mu-\lambda), && y_0=\tfrac{1}{2}(\mu+\lambda), && z_0^2=\tfrac{1}{2}(A-C-\mu\lambda),\\ &x_0=\tfrac{1}{2}(\mu-\lambda), && y_0=\tfrac{1}{2}(-\mu+\lambda), && z_0^2=\tfrac{1}{2}(A-C+\mu\lambda).\end{aligned} \tag{12}$$

There are in reality eight separate solutions, since z_0 can be either positive or negative. Upon evaluating A, B, C, μ, and λ from the values given in Eq. (6), we find that $\mu=0$, and that $(A-C)$ is negative. The latter condition would require z_0 to be imaginary, which is inadmissible since imaginary phase shifts cannot represent a pure scattering process. Within the experimental uncertainty, it is quite possible to take $(A-C)$ to be zero, in which case there are only two distinct solutions:

$$x_0=\pm\tfrac{1}{2}\lambda=\pm0.22, \quad y_0=\mp\tfrac{1}{2}\lambda=\mp0.22, \quad z_0=0. \tag{13}$$

One should in principle be able to make a choice of signs from information as to the nature of the Coulomb interference in elastic scattering, and thus select a unique solution.

The above result is not necessarily the best fit to the data, and the uncertainties cannot be deduced in any

[16] L. Van Hove, Phys. Rev. 88, 1358 (1952).

TABLE V. Acceptable solutions for phase-shift parameters of charge-exchange scattering. ω is the deviation parameter defined in the text. x_0, y_0, and z_0 are in radians, phase shifts in degrees.

Solution	x_0	y_0	z_0	x_0 $=\alpha_{13}-\alpha_{11}$	$\frac{1}{2}(y_0+z_0)$ $=\alpha_{33}-\alpha_{13}$	$\frac{1}{2}(y_0-2z_0)$ $=\alpha_{31}-\alpha_{11}$	ω
a	−0.21	0.24	0	−12.0°	4.6°	4.6°	0
b	0.21	−0.24	0	12.0	−4.6	−4.6	0
c	−0.17	0.28	0.14	−9.7	8.0	0	0.7
d	0.17	−0.28	0.14	9.7	−2.7	−10.7	0.7
e	−0.17	0.28	−0.14	−9.7	2.7	10.7	0.7
f	0.17	−0.28	−0.14	9.7	−8.0	0	0.7

simple way; furthermore, if one allows z_0^2 to have a positive value, as is quite possible within the errors, the degeneracy in the preceding solutions disappears. We have accordingly tried to fit the distribution of Eq. (6) with a number of values of the parameters x_0, y_0, and z_0, and computed the deviation from the experimental points by evaluating the quantity, $\omega=\sum_{i=1}^{3}(\delta_i^2/\Delta_i^2)$, where δ_i is the deviation of the predicted value from the observed value of the ith coefficient of the distribution, and Δ_i is the corresponding standard deviation in that coefficient. Assuming that $\omega\leqq 1.5$ defines a reasonable fit to the data, we find that acceptable solutions exist only for the values of z_0^2 between 0 and 0.03. The best values of x_0 and y_0 have been evaluated for $z_0^2=0$ and 0.02, and these results and the corresponding relations between the phase shifts appear in Table V. It may be noted that the value of ω for solutions *a* and *b* is essentially zero, indicating a perfect "fit."

(b) Comparison with Results of Elastic Scattering

The pairs of solutions *a*, *b*; *c*, *d*; and *e*, *f* correspond to opposite sign of spin-flip terms z_0; *c*, *f* comprise a "Fermi," *d*, *e*, a "Yang" pair. We now inquire as to which (if any) of these six sets can be discarded, from a comparison with the results on elastic scattering at about the same energy.

It is readily seen that no choice can ever be made between solutions differing only in the sign of z. Reversing the signs of m and n, as defined in Table IV, will obviously leave all angular distributions unchanged, since z only enters quadratically in Eqs. (7) to (9). (The individual phase shifts will in general be different in the two cases.) This conclusion is valid only at low energies, when the angles are so small that the approximate expressions of Table IV can be used. At higher energies, it may be possible to determine the sign of the spin-flip terms.

It may be hoped, however, that the results of the present experiment could be used to determine the sign of the interference term in Coulomb and nuclear scattering, and to test the hypothesis of charge independence. Since the present experiment yields only three relations among the six phase shifts, we have combined our results with those obtained from an analysis of the π^+ elastic scattering data of Perry and Angell.[2] These two experiments together give six conditions on the six phase shifts and therefore determine the possible values. The results can then be checked against the available data on π^- scattering.

A recalculation, including first-order Coulomb terms, of possible fits to the data of Perry and Angell is in progress;[17] preliminary results obtained by Noyes give two sets of scattering parameters (four sets of phase shifts, because of the spin-flip degeneracy) which fit the π^+ scattering data. Because of the limited accuracy of the data, rather wide variation of the parameters is possible. We have included in Table VI, which gives the scattering parameters for the π^+ data, the two "best" fits (solution 1–4) and a variant of each (solution 5–8).

It is now appropriate to try to fit the available π^- scattering data at 37 Mev, using combinations of solutions from Table V and VI. The available data[1,3] include the total π^- scattering cross section for angles larger than 55°, and the differential scattering cross section at 45° (laboratory angle).

From the total attenuation cross section (12.9±1.7 mb) and our measurement of the total charge exchange cross section (7.9±1.8 mb) we obtain a total elastic-scattering cross section of 5.0±2.5 mb. The 45° cross section has been measured to be 1.7±0.4 mb.

Comparison of the predicted values with the measured ones shows that there are three acceptable sets of scattering parameters; because of the spin-flip degeneracy, there are, thus, six allowed sets of phase shifts. These sets, and the corresponding predicted cross sections, are given in Table VII, and the predicted π^- elastic-scattering angular distributions are shown in Fig. 8. One of the allowed sets (labeled 7a in Table VII) is of the conventional "Fermi" type, and is nearly identical with that deduced by Perry and Angell—positive α_{33}, small negative α_3; set 8a is the corresponding "Yang" type solution. The other sets are basically different, in that α_3 is large and positive, the $T=\frac{3}{2}$ p-wave phase shifts are small and negative, and the $T=\frac{1}{2}$ p-wave phase shifts are quite large.

TABLE VI. Some possible parameters for 37-Mev π^+ angular distributions. x_+, y_+, z_+ are in radians, phase shifts in degrees. The deviation parameter in this case is $\omega=\sum_{i=1}^{5}\{[\sigma(\theta_i)-\sigma_{ih}]^2/\Delta_i^2\}$. These parameters were deduced by Noyes from data of Perry and Angell (see reference 2).

Solution	x_+	y_+	z_+	α_3	α_{33}	α_{31}	ω
1	0.14	−0.09	−0.021	8.0°	−2.1°	−0.9°	0.3
2	0.14	−0.09	0.021	8.0	−1.3	−2.5	
3	−0.09	0.13	0.08	−5.2	4.0	−0.5	0.48
4	−0.09	0.13	−0.08	−5.2	1.0	5.5	
5	0.10	−0.15	−0.095	5.7	−4.7	0.7	0.9
6	0.10	−0.15	0.095	5.7	−1.0	−6.7	
7	−0.065	0.16	0.098	−3.7	4.9	−0.7	0.46
8	−0.065	0.16	−0.098	−3.7	1.2	6.8	

[17] We are indebted to H. P. Noyes for giving us the preliminary results of this investigation.

If we limit consideration to the conventional solutions (set III), we see that the conclusion of Barnes *et al.*[3] as to the relative sign of Coulomb and meson-nucleon forces is corroborated. A unique, but different, conclusion would be reached if one chose sets I and II, which correspond to solutions found at 65 and 78 Mev by Bodansky, Sachs, and Steinberger.[8] It may be that sets I and II cannot be extrapolated in a reasonable way to explain results at energies above 78 Mev; we have not investigated this question. It is possible that improved experimental results for elastic scattering will allow one to identify the correct set of solutions; the intrinsic spin-flip degeneracy will of course remain.

It should be noted that if one makes any reasonable extrapolation of the phase shifts for any of the solutions of Table V, the form of the charge-exchange distribution changes only slightly with energy in the range 30–50 Mev. It can therefore be concluded that the general results of the present experiment are not affected by the large spread in π^- interaction energy.

(c) Precision of Phase Shifts

It is difficult to assign uncertainties to the phase shifts given in Tables V and VI without making a much more thorough study of the experimental results for all three scattering processes. One should evidently evaluate the appropriate deviation parameter as a function of the six parameters α_1, α_3, k, l, m, n, taking into account all of the experimental points at 37–40 Mev. It is clear from the foregoing that we have not attempted this. We cannot therefore consider the sets of phase shifts of Tables V and VI to be true least-square fits but only representative values for the different acceptable types of solutions.

One can obtain qualitative indications as to the probable accuracy of the phase-shift determinations by noting how the phase shifts contribute to the scattering parameters (see Table IV). For example, the $p_{\frac{1}{2}}$ phase shifts contribute only to the parameters l and n. In turn, n enters into z_0 and z_-. Since z_0 must be very near zero, and enters quadratically in the expressions

TABLE VII. Pairs of solutions which fit π^- data: $\sigma^-(45°) \geqq 0.5$ mb/sterad and $\sigma_i^-(>55°)$ between 3 and 10 mb. Labeling of solutions follows that of Tables V and VI.

Set	Solution	$\sigma^-(45°)$ mb	$\sigma_i^-(>55°)$ mb	α_3	α_1	α_{33}	α_{31}	α_{13}	α_{11}
I	1*d*	1.0	5.8	8.0°	−1.7°	−2.1°	−0.9°	0.6°	9.8°
	2*f*			8.0	−1.7	−1.3	−2.5	6.7	−2.5
II	1*f*	0.78	3.0	8.0	−1.7	−2.1	−0.9	5.9	−0.9
	2*d*			8.0	−1.7	−1.3	−2.5	1.4	8.2
III	7*a*	0.8	6.7	−3.7	8.3	4.9	−0.7	0.3	−5.3
	8*a*			−3.7	8.3	1.2	6.8	−3.4	2.2
	$7a_1$ ($z_0=0.05$)			−3.7	8.3	4.9	−0.7	−0.6	−3.4
	$7a_2$ ($z_0=0.07$)			−3.7	8.3	4.9	−0.7	−1.0	−2.7
	$7a_3$ ($z_0=0.10$)			−3.7	8.3	4.9	−0.7	−1.5	−1.5

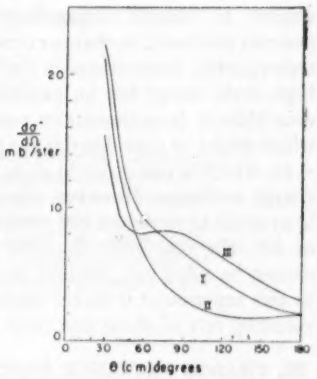

FIG. 8. Angular distributions of π^- elastic scattering predicted by the three solutions of Table VII. (Note: the ordinate scale should read 1.0, 2.0 . . . . instead of 10, 20, ...)

for the differential cross sections, the $p_{\frac{1}{2}}$ phase shifts are particularly poorly determined by the charge-exchange results. For example, consider set 7*a* of Table VII, which corresponds to $z_0=0$, and gives α_{13} and α_{11} equal to 0.3° and −5.3°, respectively. Changing z_0^2 to 0.005 (which changes the angular distribution insignificantly) results in pairs of values for α_{13} and α_{11} of 1.6° and −7.9° (for $z_0=-0.07$) or −1.0 and −2.7° (for $z_0=+0.07$). A much larger variation in z_0 would be allowed if x_0 and y_0 were readjusted to give a best fit. Three variants on solution 7*a* are given at the end of Table VII. They show that the values of α_{13} and α_{11} are not well determined.

It should, however, be remarked that the angular distributions for π^- elastic scattering are strongly affected by these changes in z_0. The predicted distributions for solutions 7*a* to $7a_3$ give cross sections at 90° differing by almost a factor of 2.

The s and $p_{\frac{1}{2}}$ phase shifts appear in parameters whose values are more strictly defined and which enters in the scattering formulas in linear and quadratic combinations. From reasoning analogous to the foregoing, we believe that these phase shifts are determined to roughly 20 percent, within each set of Table VII.

VIII. ANOMALOUS EVENTS

In the course of the experiment, a total of 589 coincident photon events were recorded with a CH_2 target. In addition six cases of triple coincidences were recorded, all of which satisfied the rather rigid criteria outlined in Sec. III. No such events were observed during the runs with carbon target and no target, when three would have been expected if the effect were independent of target material. We have considered various hypotheses as to the origin of these events. These include the internal or external conversion in the target of one of the gamma rays (detection is suppressed by anticoincidence counter 4); backscattering of a shower electron in one lead radiator to count in another gamma-ray detector (too unlikely); three-photon decay of the neutral meson (forbidden by symmetry with

respect to charge conjugation[18]); detection of the neutron produced in charge-exchange in hydrogen (too improbable); interactions in carbon (threshold rather high, little energy left for gamma ray); and accidental coincidences (experimentally ruled out). A possibility which might be considered is the reaction $\pi^-+p\rightarrow\pi^0+n+h\nu$, which is one order in e^2/hc less likely than direct charge exchange. However, the available phase space is so small as to reduce the cross section another factor of 10^3. The possibility that the effect is instrumental cannot be ruled out. Further study by the means used in this experiment is rather impractical, in view of the counting rate of about one event in four hours.

IX. CHARGE EXCHANGE SCATTERING IN CARBON

Table III shows the net counting rate of coincident photons from carbon, as well as from hydrogen. Since charge-exchange scattering in carbon is not a unique two-body process, the energy distribution of the emitted neutral mesons is unknown. Accordingly the angular distribution and cross section cannot be inferred from the observed gamma-ray coincidence rates. It may be remarked, however, that the cross section for charge-exchange scattering in carbon seems to be less than that for hydrogen.

ACKNOWLEDGMENTS

We have been materially assisted in the construction of the complicated electronic circuitry by our chief electrical engineer, Kurt Enslein, and the Electronic Shop staff under L. Braun. We are indebted to Dr. E. M. Hafner and Mr. W. Chestnut, Mr. I. Goldberg, Mr. R. Harding, Mr. R. Santirocco, Mr. S. Spital, and Mr. W. Spry for assistance in the experimental work and in the laborious computations. We wish to acknowledge the cooperation of the laboratory staff in the design, construction, and setting up of the equipment, and we are indebted to Professor H. P. Noyes for discussions concerning the evaluation of the gamma-ray detector efficiencies, and the analysis of the π^+ data.

[18] L. Wolfenstein and D. G. Ravenhall, Phys. Rev. **88**, 279 (1952).

APPENDIX

We summarize here, for convenience, the relations that govern the decay of a π^0 meson into two gamma rays.

Let the velocity of the meson be βc, its rest mass μ, its total energy $\gamma\mu$, and its direction the axis from which angles are measured. Let the angle between the two gamma rays be ξ, the angle one of them makes with the direction of the meson ζ, and their energies E_1 and E_2 (or in general E_γ).

Then the minimum angle $\xi_{\min}$ between the gamma rays is given by

$$\sin^2(\xi_{\min}/2)=1/\gamma^2,$$

and in general

$$\sin^2(\xi/2)=\mu^2/4E_1E_2.$$

If $P(\xi)d\xi$ is the probability that ξ lies between ξ and $\xi+d\xi$,

$$P(\xi)=\sin\xi/[\beta\gamma(1-\cos\xi)^{\frac{1}{2}}\{\gamma^2(1-\cos\xi)-2\}^{\frac{1}{2}}].$$

If we define

$$R=\int_{\xi_{\min}}^{\xi} P(\xi)d\xi$$

as the fraction of decays with ξ equal to or less than ξ, then

$$R=[\gamma^2-\csc^2(\xi/2)]^{\frac{1}{2}}(\beta\gamma)^{-1},$$

$$\cos\zeta=(\beta+R)(1+\beta R)^{-1},$$

$$\sin^2(\xi/2)=[\gamma^2+(1-\gamma^2)R^2]^{-1},$$

$$E_\gamma=\tfrac{1}{2}\mu\gamma(1\pm\beta R).$$

Low-Momentum End of the Spectra of Heavy Primary Cosmic Rays*†

R. A. Ellis, Jr.,‡ M. B. Gottlieb, and J. A. Van Allen
Department of Physics, State University of Iowa, Iowa City, Iowa

(Received March 8, 1954)

Measurements of the intensity of heavy primary cosmic-ray nuclei have been made above the atmosphere by means of the new Iowa balloon-launched rocket ("rockoon") technique at geomagnetic latitudes $\lambda = 56°$, 76°, and 86°. The measuring instrument was a thin-walled, pulse-ionization chamber of 15-cm diameter. The observed data, in conjunction with geomagnetic theory, demonstrate a complete or nearly complete absence of primary heavy nuclei of $Z \geq 6$ having a magnetic rigidity less than 1.5×10^9 volts ($p/mc < 0.8$), the result being the most significant for the C, N, O group. It is noted that this spectral cutoff occurs at closely the same magnetic rigidity, and distinctly not at the same velocity, as the previously reported cutoff in the spectra of primary protons and α particles.

I. INTRODUCTION

RECENT investigations[1–5] of the dependence of cosmic-ray intensity at high altitude upon geomagnetic latitude make it abundantly clear that there occurs a marked and rapid change in form of the integral number-magnetic rigidity spectrum of the primary radiation at a rigidity R (momentum-to-charge ratio pc/Ze) of about 1.5×10^9 volts. In particular,[4] there appears to be a complete or nearly complete absence of primary protons in the magnetic rigidity range 1.2×10^9 volts to 0.18×10^9 volts (kinetic energy range 590 Mev to 18 Mev), and of primary alpha particles in the magnetic rigidity range 1.2×10^9 volts to 0.37×10^9 volts (kinetic energy range 700 Mev to 72 Mev).

But because of the low relative abundance of heavy primary nuclei (atomic number $Z > 2$) these results do not make possible any significant conclusion as to their presence or absence in the low-momentum portion of their spectra.

Substantial progress has been made in the determination of the spectra of heavy primaries at rigidities greater than 1.5×10^9 volts, principally by means of balloon-borne photographic emulsions. But the available data approaching the low-rigidity end of the spectrum are in substantial disagreement. Thus, the Minnesota group[6] reports a steepening of the integral number spectrum of nuclei of $Z \geq 10$ toward low energies, whereas the Rochester group reports a flattening.[7] Indeed, the definitive investigation of the low-rigidity portion of the spectra of heavy particles is, at present, impractical by balloon methods due to the altitude limitation of balloon flights. Most of the balloon data have been obtained at residual atmospheric depths of about 15 g/cm². Even at depths as small as 10 g/cm², investigation of this matter is prevented simply by the short ionization range of those particles whose presence, or absence, it is desired to determine. The quantitative nature of this limitation is exhibited in Fig. 1.

The question of the presence or absence of low-momentum (or low-rigidity) heavy primaries is, however, a matter of keen interest in connection with the astrophysical origin of the cosmic radiation and with its propagation to the earth. Any proposed mechanism of origin, any postulated amount of interstellar material traversed, and any postulated system of magnetic fields must eventually be tested against observed data bearing on this question. It is evident from Fig. 1 that high-altitude rocket techniques are uniquely suited to this observational undertaking. To fully exploit such techniques, it is further necessary to minimize the wall thickness of the detecting apparatus and to make the flights at sufficiently high latitude as to be free of geomagnetic limitations.

The new Iowa balloon-launched rocket ("rockoon") scheme[4] makes it possible to fly 30 pounds of apparatus to some 100-km altitude at a vehicle cost less than that of a large Skyhook balloon flight.

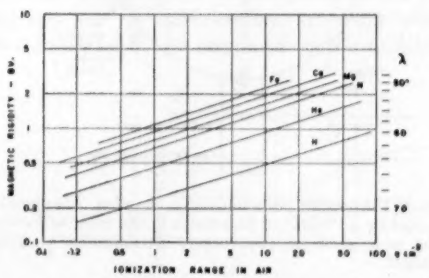

FIG. 1. Ionization range in air of representative nuclei as a function of magnetic rigidity. Curves derived from pp. 40–41 of reference 14 on assumption of complete stripping. Scale of ordinates on the right gives geomagnetic latitude at which vertical geomagnetic cutoff equals magnetic rigidity on the left.

* Based on doctoral dissertation of R. A. Ellis, Jr., February, 1954 (unpublished).

† Assisted by joint program of the U. S. Office of Naval Research, the U. S. Atomic Energy Commission, and the Navy Bureau of Aeronautics; and by the Research Corporation.

‡ Present address: Department of Physics, Tennessee Agricultural and Industrial State University, Nashville, Tennessee.

[1] J. A. Van Allen and S. F. Singer, Phys. Rev. **78**, 819 (1950); **80**, 116 (1950).
[2] J. A. Van Allen and S. F. Singer, Nature **170**, 62 (1952).
[3] Neher, Peterson, and Stern, Phys. Rev. **90**, 655 (1953).
[4] J. A. Van Allen, Nuovo cimento **10**, 630 (1953).
[5] Meredith, Van Allen, and Gottlieb, Phys. Rev. (to be published).
[6] Freier, Anderson, Naugle, and Ney, Phys. Rev. **84**, 322 (1951).
[7] Kaplon, Peters, Reynolds, and Ritson, Phys. Rev. **85**, 295 (1952).

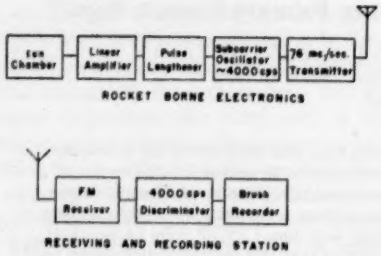

FIG. 2. Block diagram of circuitry and radio telemetering system.

It has been shown[8–10] that thin-walled pulse ionization chambers are effective detectors of heavy primaries and that it is possible to construct such chambers and associated electronic circuits which can be installed in rockets and adapted to conventional telemetering systems. The burst size distributions obtained during the time that thin-walled ionization chambers are effectively above the atmosphere are, primarily, the result of direct traversals of heavy primaries. From the analysis of such burst size distributions obtained in the geomagnetic latitude range from 56° to 90°, it is possible to determine the form of the low-momentum end of the spectra of heavy primaries over the momentum range from the vertical geomagnetic cutoff at about 56° to the cutoff due to the finite wall thickness of the apparatus.

The present report is based on data obtained in four successful rocket flights and one balloon flight (in which the rocket failed to fire) on a shipboard expedition to northerly latitudes during the summer of 1953.

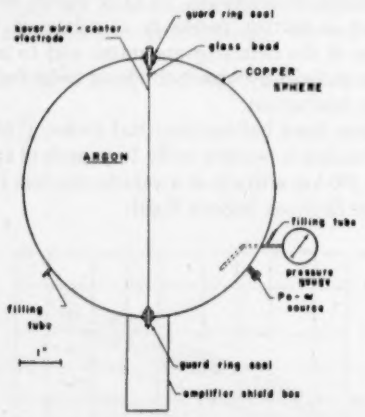

FIG. 3. Thin-walled pulse-ionization chamber. The chamber was supported by a "bowl" of Styrofoam in the extreme forward end of the nose shell of the rocket. Surrounding material was minimized.

[8] T. Coor, Jr., Phys. Rev. **82**, 478 (1951) and doctoral dissertation, Princeton University, August, 1948 (unpublished).
[9] J. A. Van Allen, Phys. Rev. **84**, 791 (1951).
[10] M. Pomerantz and G. W. McClure, Phys. Rev. **86**, 536 (1952).

II. DESCRIPTION OF APPARATUS

A block diagram of the system used in this experiment is shown in Fig. 2. The ionization chamber and the associated circuitry were mounted in the nose shell of a Deacon rocket which was carried to an altitude of about 60 000 feet by a General Mills model 551-A plastic balloon and fired by either a pressure or time switch.[11] The data were transmitted to the ship by an FM-FM telemetering system. The nose shells were aluminum and had an average wall thickness of 0.050 inch.

The ionization chambers were fabricated from copper hemispheres, six inches in diameter and 0.010-inch average wall thickness. The collecting electrode was a 0.025-inch Kovar wire which was soldered into a guard ring system made from Stupakoff seals. Figure 3 shows the details of the ionization chamber.

A fairly thin polonium alpha source was permanently mounted in each chamber to provide an absolute system calibration for burst size. These sources were prepared by a method described by Hulsizer,[12] and were mounted $2\frac{1}{4}$ mm outside the inner surface of the chamber wall such that a $\frac{1}{16}$-inch diameter hole in the wall served to collimate the beam of alpha particles. The sources chosen produced from twenty to sixty pulses per minute at the time of flight. Figure 4 is an integral number bias curve obtained from a typical chamber with an electronic pulse-height analyzer, and Fig. 5 is the same type of curve obtained from the same chamber over the complete telemetering system.

The program for filling the chambers was the following: the chambers were pumped on for twenty-four hours with a mechanical pump while they were maintained at a temperature of approximately 80°C by heat lamps; after cooling, 99.6 percent pure argon was admitted to the chambers to a pressure of about 15 psi and circulated over hot calcium (100°C) for twenty-four hours; the filling system was allowed to come to thermal equilibrium with the surroundings and the pressure was dropped to about 10 psi on a calibrated "standard" gauge just prior to sealing off the chambers with soft solder. The exact reading of the standard gauge was chosen in accordance with the ambient laboratory temperature and pressure to yield a sealed-off pressure of 1.50 atmospheres at 0°C, 760 mm of Hg. An inexpensive pressure gauge was left permanently connected to the chamber to indicate any subsequent leakage.

These chambers were operated as electron collection chambers with the center wire at high positive potential. The gas purity was considered adequate when identical integral number bias curves were obtained for the polonium alpha sources for sweeping voltages of 600 and 900 volts. Each of the chambers satisfied this criterion from the time of its initial filling until it was

[11] J. A. Van Allen and M. B. Gottlieb, Rev. Sci. Instr. (to be published).
[12] R. I. Hulsizer, dissertation, Massachusetts Institute of Technology, 1950 (unpublished).

flown about three months later. The chambers were flown with 900 volts sweeping voltage. The enclosing nose shells were sealed at sea level pressure to prevent any possibility of corona when the apparatus was at high altitudes. The counting rate of bursts larger than the bursts from the polonium source due to radioactive contamination was less than one burst per minute for each chamber.

The pulse amplifiers had a rise time of about 2 microseconds, a decay time of about 40 microseconds, and a voltage gain of about 2000. The gain of these amplifiers was not measurably different over the range 75 to 100 volts of the B^+ supply voltage.

The short-duration pulses from the amplifier were lengthened and given a characteristic shape for the purpose of satisfactory telemetering transmission and recording. The lengthened pulses had a width of about 15 milliseconds at half-height and their amplitude was accurately related, though not proportional, to the

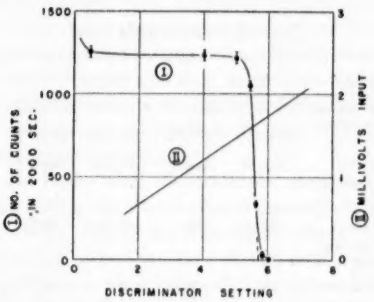

FIG. 4. Typical integral number bias curve (I) of bursts from Po$-\alpha$ particle source. Output of linear amplifier was fed to a commercial pulse-height analyzer. Ordinate scale of curve I to left. Ordinate scale of calibration curve (II) to right.

input pulse amplitude. There was no change in the performance of this circuit over a range of the supply voltage of 60 to 90 volts. Loss of counts due to finite pulse width was negligible at the maximum observed counting rate of about 2 counts/sec (due to cosmic-ray events plus calibrating Po$-\alpha$'s). The pulse lengthening circuit was modelled after one described by Elmore and Sands.[13]

Raytheon rugged subminiature tubes, such as the CK5678, were used throughout all circuits—with the exception of the telemetering transmitter, in which a 3A5 was used.

The subcarrier oscillator was a voltage-controlled frequency-modulated audio-oscillator. The nose shell and body of the rocket, which were insulated from each other, formed the arms of an asymmetrical dipole transmitting antenna.

A two-bay Yagi antenna, a Clarke Instrument Company FM telemetering receiver, an audio discriminator,

[13] W. C. Elmore and M. Sands, *Electronics* (McGraw-Hill Book Company, Inc., New York, 1949), p. 196.

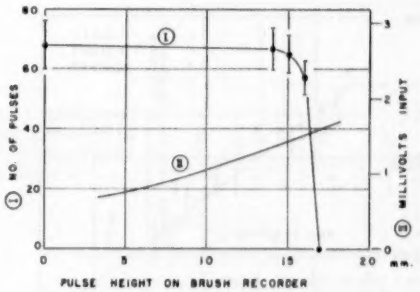

FIG. 5. Typical integral number bias curve (I) for Po$-\alpha$ source as obtained over complete telemetering system as shown in Fig. 2. Curve II is calibration curve. Scales of ordinates as in Fig. 4.

Model BL 905 Brush amplifier, and Model BL 202 Brush inking oscillograph comprised the receiving station. It was possible to record data without evidence of noise with a radio signal input to the receiver as low as 4 microvolts.

A meterological radiosonde was sent up with each flight to provide pressure-altitude *vs* time-data for the ascent to the firing altitude.

The entire instrumentation was turned on about a half-hour before release of the rockoon system from the ship. From then on it was in continuous operation during final preparations for release, during the balloon phase of the ascent and during the final free-rocket flight until eventual destructive impact with the sea.

The capacity of the batteries used was great enough to insure that the decline in voltages during the entire period of operation was slight enough to allow the application of the preflight calibration throughout, a period of not more than two and a half hours. In addition to this general provision, the built-in polonium alpha source provided an over-all system calibration throughout the balloon and rocket phases of the flight. The entire electronic system, including radio telemetering link and receiving station was also calibrated over its full range immediately before a flight by introducing step pulses of known size (from a battery and mercury switch) directly on the center wire of the ionization chamber and recording the output pulses on the Brush oscillograph in the telemetering receiving station. Figure 6 is a plot of the results of such a calibration.

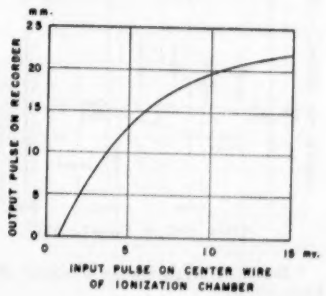

FIG. 6. Over-all calibration of complete system of Fig. 4.

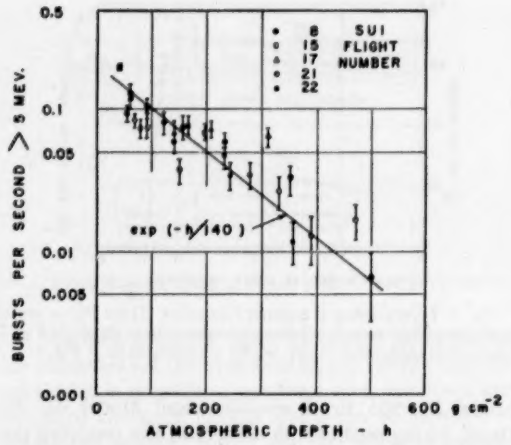

FIG. 7. Counting rates of bursts larger than 5 Mev as observed during balloon-ascent phase of Flights 8, 15, 17, 21, and 22. For comparison a curve of the form $\exp(-h/140)$ has been drawn among the observed points.

These calibration curves were reproducible to within 3 percent.

The conversion of the experimental data to an absolute scale was achieved by combining the system calibration and the pulse-height distribution due to the polonium alpha source (Figs. 4 and 5). The number of millivolts equivalent to a polonium alpha burst was taken to be the number of millivolts required to produce a pulse the size of the extrapolated integral pulse height for the polonium alpha distribution. The number of millivolts equivalent to one polonium alpha lay within a 0.1-millivolt range for each chamber for several determinations during the period between assembly and launching. This correspondence between pulse height and energy lost in the chamber is strictly true only for ion pairs produced near the wall because of the dependence of pulse-height on position of the ion pairs in electron collection chambers.[14] The dependence of pulse height on position was measured for these chambers by moving a probe with a polonium-alpha source on the end to various positions in the chamber and observing the pulses from the chamber's amplifier on a fast oscilloscope. No change in pulse height to within 5 percent was observed as a function of position.

Since the polonium alpha source was $2\frac{1}{4}$ mm outside the inner wall of the ionization chamber, the energy loss in the sensitive volume of the chamber must be calculated from range-energy data for alpha particles.[15] From the empirical range-energy relationship and the fact that the range of a polonium alpha particle in argon at 760 mm Hg pressure and 15°C is 41.4 mm, the energy lost in the ionization chamber by a polonium alpha particle from the source was found to be 5.0 Mev.

The basic amplifier noise level corresponded to about 0.15 Mev (Fig. 4). But due to the threshold characteristic of the pulse lengthener using subminiature tubes, the minimum measurable burst size was about 3.5 Mev (Fig. 6). This minimum could have been reduced but it was felt to be suitable for this application.

In argon, a minimum ionizing singly charged particle loses energy at the average rate of 1.49 Mev/(g cm^{-2}). For a diametrical traversal of one of these chambers, such a particle loses 0.06 Mev. For the traversal of the same thickness of matter, the energy lost by a minimum ionizing particle of charge Ze is Z^2 times that lost by a singly-charged minimum-ionizing particle. Note that the simultaneous diametrical traversal of 86 minimum-ionizing singly-charged particles is required to produce a burst of 5 Mev.

Further experimental and circuitry details are available in the doctoral dissertation (1954) of R. A. Ellis, Jr. on file at the State University of Iowa, and in reference 11.

TABLE I. General flight data.

Flight number	8	15	17	21	22
Position of release of balloon (geographical)	42°26′N 70°22′W	64°20′N 59°06′W	74°23′N 71°56′W	44°50′N 57°13′W	44°45′N 57°10′W
Date (1953)	July 18	Aug. 6	Aug. 9	Sept. 3	Sept. 3
Time of launching of rockoon (Greenwich standard time)	2227	1507	0554	0950	1151
Estimated geomagnetic latitude of rocket flight (centered dipole)	53°	76°	86°	56°	56°
Estimated altitude of firing of rocket (feet above sea level)	Did not fire	45 000	68 000	67 000	67 000
Estimated summit altitude (feet above sea level)	73 000	225 000	325 000	300 000	340 000
Duration of plateau (seconds)	...	160	200	163	220

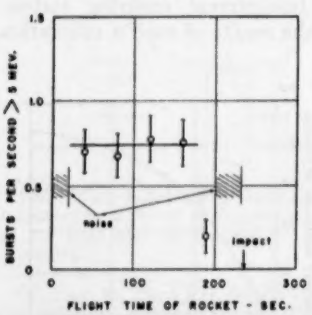

FIG. 8. Counting rate of bursts greater than 5 Mev during rocket phase of Flight 15.

III. RESULTS

Table I gives the date, time of launching, latitude, firing altitude, estimated peak altitude, and time duration of high-altitude plateau of each flight.

[14] B. Rossi, *High Energy Particles* (Prentice-Hall, Inc., New York, 1952).

[15] J. O. Hirschfelder and J. L. Magee, Phys. Rev. **73**, 207 (1948).

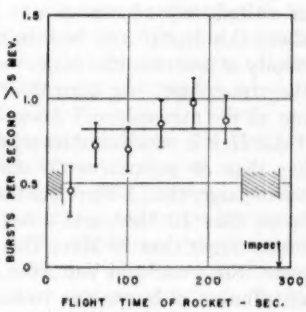

FIG. 9. Counting rate of bursts greater than 5 Mev during rocket phase of Flight 17.

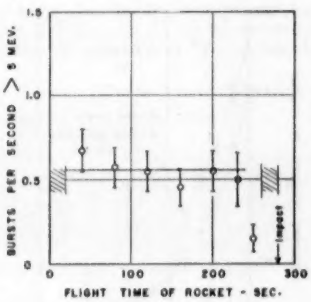

FIG. 11. Counting rate of bursts greater than 5 Mev during rocket phase of Flight 22.

The counting rate of cosmic-ray bursts larger than 5 Mev as a function of altitude for the balloon portion of all of the flights is shown in Fig. 7. For comparison, a curve of the form $\exp(-h/140)$ has been drawn among the observed points;[14] h is the atmospheric depth in g/cm².

An interesting check is that the observed counting rate of bursts larger than 5 Mev in these 6-inch diameter chambers was very closely equal to one-fourth the counting rate of bursts larger than 5.1 Mev observed by Coor[8] at 52° using spherical ionization chambers of 12-inch diameter—the ratio being independent of altitude up to 40 g/cm² (the highest balloon flight data of the present investigation).

The raw burst size distributions obtained below 30 000 feet (300 g/cm²) were almost entirely due to calibrating Po−α's. Hence for each flight, the corresponding distribution of bursts below 30 000 feet, normalized to the appropriate time interval, was subtracted from the total observed high-altitude data to obtain the net distribution of cosmic-ray bursts.

Ideally, the counting rate of bursts of all sizes as a function of time during the rocket portion of the flight may be expected to show an initial rapid increase; to level off at a constant value, which is referred to as the "plateau" counting rate; and finally to decrease rapidly as the ionization chamber is carried back down through the atmosphere. The duration of the constant-counting-rate period should be the time during which the sum of the atmospheric path and the apparatus wall thickness has a negligible effect on the primary radiation. The actual flight data show the expected plateaus but only an indication of the increase and decrease in the counting rate expected at the beginning and end, respectively, because of the loss of satisfactory signal due to microphonics. These microphonics, which could be produced in the laboratory by tapping the ionization chamber and/or the amplifier, are presumed to be excited by vibration of the rocket during the noisy burning period of the motor and by aerodynamic flutter of tail fins, etc., during passage through the denser atmosphere. They are commonly observed in rocket flights of high-gain amplifiers.

The flight periods above 40 km for which burst data are given appeared to be entirely free of microphonics. In one case only there were a few seconds of lost time due to weakening of the radio signal. This effect in the received signal is altogether different than that due to microphonics and is confirmed by readings of the input signal to the receiver.

Figures 8, 9, 10, and 11 show the observed counting rate curves for bursts larger than 5 Mev for the four successful rocket flights, from the time of firing to the time of impact.

The data from the plateaus of the rocket flights are presented in Fig. 12 as integral burst size distributions. The flight data are consolidated in Table II together with data obtained from Flight 8 for a twenty minute period during which the pressure-altitude data showed that the balloon and the suspended rocket remained at an altitude of 40 plus or minus 5 g/cm². Figure 13, which is a plot of the raw and corrected distributions from the plateau of Flight 21, shows clearly the manner in which the polonium alpha source contributed to the experimental distributions. The best flight evidence that

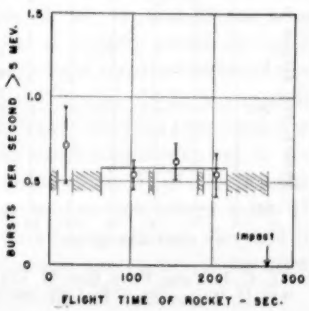

FIG. 10. Counting rate of bursts greater than 5 Mev during rocket phase of Flight 21.

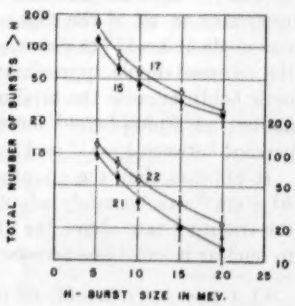

FIG. 12. Integral burst size distributions for high altitude plateau periods of Flights 15, 17, 21, and 22. Time duration of plateau period is different for each. Ordinate scale for Flights 15 and 17 on left, for Flights 21 and 22 on the right.

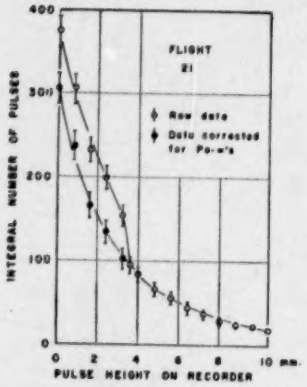

FIG. 13. Raw pulse-height distribution for high-altitude plateau period of Flight 21, and distribution after subtraction of pulses due to the calibrating Po$-\alpha$ source.

the different chambers could be considered identical in the interpretation of the data is found in the burst size distribution from Flights 21 and 22 which were made within three hours of each other at nearly the same location. The data from Flights 21 and 22 are plotted in Fig. 14. From Figs. 7 and 14 it is seen that the counting rates from these two chambers are in good agreement. In Table II the data from Flights 21 and 22 are combined.

IV. BASIS FOR INTERPRETATION

A. Causes of Bursts of Ionization

Coor[8] has pointed out that the only significant causes of bursts in an ionization chamber at high altitudes are: (a) traversals of single particles through the chamber without nuclear interactions in the chamber or its surroundings and (b) the passage through the chamber of the charged products of nuclear interactions (stars) produced in the chamber walls, the gas of the chamber, and the immediate surroundings.

B. Contributions of Stars to Plateau Data

An estimate of the contribution of nuclear interactions, due to all causes, in the walls and surroundings of the chambers while above the atmosphere can be based on the burst distribution obtained in Flight 8 at 73 000 ft (40 g cm^{-2}) (Table II), and the altitude dependence of stars in photographic emulsions reported by Lord.[16] Such an estimate is considered sufficiently applicable to all of the flights, even though Flight 8 was made at $\lambda = 53°$ (λ denotes geomagnetic latitude in the centered-dipole approximation to the earth's magnetic field), because the total omnidirectional intensity above the atmosphere[4,5] increases by only about 25 percent between $\lambda = 53°$ and $\lambda = 89°$.

It appears that the counting rate of all bursts at 40 g cm^{-2} can be safely adopted as an *upper limit* to the counting rate above the atmosphere of bursts due to nuclear interactions because the observed maximum in altitude-dependence of star production occurs at about this depth[16] and because the omnidirectional intensity of neutrons (the major producers of stars within the atmosphere) has been shown to fall off near the top of the atmosphere.[17] Accordingly, by reference to Table II, it is seen that stars represent a contribution of less than 36 percent to the observed rate of plateau bursts larger than 5 Mev, less than 18 percent to bursts larger than 10 Mev, and a negligible contribution to bursts larger than 20 Mev. This conclusion is in agreement with Coor[8] and Van Allen,[9] who showed that the distribution of bursts due to nuclear interactions had relatively more small bursts than the distribution due to traversals of heavy primaries. A fuller discussion of this matter is given by Whyte[18] and by Pomerantz and McClure.[10]

Ionization bursts larger than 5 Mev from nuclear interactions are visualized as being due almost entirely to "black prongs" emerging from the inner skin of the ionization chamber wall and to those originating in the filling gas. Since the coincident, diametrical traversal of some 86 minimum ionizing singly charged particles is required to dissipate 5 Mev in the chamber, no significant fraction of the observed bursts can be due to "gray" and "minimum" tracks. The range of most black prongs does not exceed 0.3 g cm^{-2}; hence it is probably not feasible to substantially reduce the contribution of stars by further reduction of the wall thickness of the chamber.

An estimate of the contributions of stars from first principles has been attempted. Such an estimate serves to check the general reasonableness of the above conclusions but is not of sufficient reliability to add significantly to the preceding discussion.

C. Unlikelihood of Contributions to Plateau Burst Data by Particles of $Z \leq 2$

(a) The geometrical factor of a spherical chamber of radius r is $2\pi^2 r^2$ cm^2 steradian in a hemispherical flux field. For the chambers used, $r = 7.5$ cm and the geometrical factor had the value 1110 cm^2 steradian. Thus,

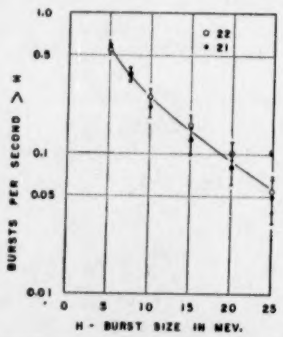

FIG. 14. Comparison of integral rate of bursts of size greater than H as a function of H for plateau period of Flights 21 and 22.

[16] J. J. Lord, Phys. Rev. **81**, 901 (1951).

[17] L. C. L. Yuan, Phys. Rev. **81**, 175 (1951).

[18] G. N. Whyte, Phys. Rev. **82**, 204 (1951).

above the atmosphere at the most northerly latitude, about 520 charged particles of all types pass through the chamber per second. The characteristics of the electron-collection chambers and the associated amplifier (Sec. II) were such that rate of "pileup" of accidentally coincident pulses to a detectable size was negligible by many orders of magnitude.

(b) The maximum expected energy which a proton can dissipate in the gas of the chamber by ionization is about 4 Mev if it makes a diametrical traversal and if it has precisely the optimum initial energy. Hence it is very unlikely that slow protons contribute to observed bursts of larger than 5 Mev. Likewise, single electrons cannot contribute.

(c) Slow α particles within a narrow energy range can, of course, contribute observable bursts of ionization, the maximum possible being about 14 Mev. The initial kinetic energy of an α particle upon its entrance into the chamber must lie between 5 Mev and 90 Mev in order that the expected ionization along a diametrical traversal exceed 5 Mev. The air range of a 90-Mev α particle is about 0.6 g cm^{-2} and its magnetic rigidity is 0.4×10^9 volts. Any such particles in the general nucleon cascade within the atmosphere are already included in the discussion of stars in Sec. IV-**B** above. *Primary* α particles of such a magnetic rigidity as would arrive at the apparatus above 50 km in the energy range 5–90 Mev are geomagnetically excluded south of $\lambda=65°$, and hence could not have contributed to the observations of Flights 21 and 22. And if, at the more northerly latitudes of Flights 15 and 17, there had been a sufficient intensity of such primary α particles, as a "slice" from a continuous spectrum, to contribute significantly to the observations, then there should have been a corresponding altitude dependence of the counting rate of bursts in the altitude range from 50 to 100 km. No such altitude dependence can be discerned in Figs. 8 and 9.

Hence, it is believed quite unlikely that primary α particles contribute to any observable extent to the observed rate of bursts of size greater than 5 Mev.

D. Interpretation of Observed Bursts as Due to Primary Particles of $Z>2$

Thus, by elimination, the interpretation of the plateau data in Flights 15, 17, 21, and 22 has been reduced to consideration of primary nuclei having Z greater than 2, and finally for *a posteriori* reasons to be mentioned later of nuclei having $Z\geq6$. No explicit subtraction of burst rate due to stars has been made due to uncertainty as to its exact magnitude; but in accordance with the discussion of Sec. IV-**B** it is thought that the star contribution does not exceed some 35 percent of the rate of bursts larger than 5 Mev and is probably lost in the statistical uncertainty of the rates of bursts larger than 10 and 20 Mev.

TABLE II. The observed burst size distributions. (From the high-altitude plateau portions of Flights 15, 17, 21, 22 and from a 20-minute period during which the apparatus of Flight 8 floated at 40 g cm^{-2}.)

Burst size, H (Mev)	Bursts/second greater than H (with statistical standard deviations)			
	Flight 8 (40 g/cm^2)	Flight 15	Flight 17	Flights 21 and 22
5	0.203 ±0.015	0.738 ±0.081	0.850 ±0.065	0.566 ±0.038
7.5	0.112 ±0.011	0.408 ±0.051	0.425 ±0.046	0.368 ±0.031
10	0.044 ±0.006	0.293 ±0.043	0.285 ±0.038	0.238 ±0.025
15	0.015 ±0.004	0.204 ±0.036	0.185 ±0.030	0.144 ±0.019
20	...	0.159 ±0.032	0.115 ±0.024	0.091 ±0.015

E. Attenuation of the Intensity of Heavy Nuclei Before They Reach the Chamber

A detailed calculation shows that an average primary traversed 1.2 g cm^{-2} of matter (mostly copper and aluminum) in the apparatus before reaching the sensitive volume of the ionization chamber. When the plateau data were obtained, the rockets were above 50 km during practically all of the time intervals. The effective path length traversed in the atmosphere by an average primary for the altitude range between 50 and 100 km, the maximum altitude reached, was taken to be 0.6 g cm^{-2} on the basis of the air mass *versus* zenith angle tables of Pressly.[19] The interaction mean free path for iron nuclei, $Z=26$ (the most unfavorable case), according to Bradt and Peters,[20] is about 35 g cm^{-2} in the materials around the chambers. This means that considerably less than one in ten primary iron nuclei and an even smaller fraction of primary nuclei of smaller Z made a disintegrating collision before reaching the chamber.

F. Geomagnetic Considerations

In the calculation of burst size distributions for comparison with the experimental distributions, explicit faith has been placed in the geomagnetic theory of Stoermer and of Lemaitre and Vallarta as worked out for the simplified representation of the earth's magnetic field as that of a centered magnetic dipole of moment 8.1×10^{25} gauss cm^3 with axis piercing the surface of the earth at 78.5° N and 69.0° W, and at 78.5° S and 111.0° E. The papers from which numerical data were taken were those of Alpher[21] for general data and those of Schremp[22] and Koenig[23] for shadow-cone data. The Koenig plots of percent solid angle accessible to particles of a given magnetic rigidity for various geomagnetic latitudes were particularly convenient for the present purpose.

G. Calculation of Expected Burst Size Distributions

The raw burst size distributions admit an immediate impression as to the general nature of the latitude de-

[19] E. C. Pressly, Phys. Rev. **89**, 654 (1953).
[20] H. L. Bradt and B. Peters, Phys. Rev. **77**, 54 (1950).
[21] R. A. Alpher, J. Geophys. Research **55**, 437 (1950).
[22] E. J. Schremp, Phys. Rev. **54**, 158 (1938).
[23] H. P. Koenig, Phys. Rev. **58**, 385 (1940).

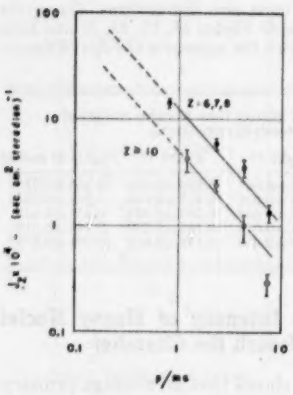

FIG. 15. Directional intensities of heavy nuclei from photographic emulsion work (references 7 and 24) as a function of minimum value of p/mc. See Sec. IV-G and Table III.

pendence of the intensity of heavy nuclei. But a much more refined interpretation is feasible and fruitful. The purpose of this section is to show how a calculated burst size distribution, for the chamber used, can be derived from fundamental data on the momentum spectra and absolute intensities of components of various Z. Comparison of the observed data with one or more families of calculated distributions can then be resorted to for the purpose of choosing the most nearly correct member of the family.

Spherical ionization chambers have the special virtue of presenting the same projected area to all directions. The burst size due to the traversal of a charged particle of a particular type depends on the path length in the gas of the chamber and on the average energy loss per unit distance due to ionization. Landau fluctuations and the dependence of the burst size on the position of formation of the ion pairs were neglected. The stopping power of the chamber gas was small enough so that the energy loss per unit distance could be considered constant over the path of a particle inside the chamber. Thus the burst size, due to the traversal of a particle which has a path length inside the chamber l and rate of ionization loss s per unit path length, is

$$H=kls. \tag{1}$$

A convenient set of dimensionless units is obtained by expressing l as the ratio of the actual path length to the diameter of the chamber and s as the ratio of the actual rate of ionization loss to the relativistic minimum rate. Then $k=1$ and H gives the burst size as the ratio of the actual burst size to that which would be produced when a minimum ionizing particle of the same type makes a diametrical traversal of the chamber. In these units, $H=ls$, and the calculated burst size applies to all types of particles, irrespective of Z.

The burst size distribution due to the traversal of particles through an ionization chamber can be calculated if the distributions of the particles with respect to s and l are known. For a sphere, the differential path length distribution $f(l)$ for a homogeneous flux of particles is independent of direction and is:

$$f(l)dl=2ldl, \quad 0\leq l\leq 1. \tag{2}$$

The distribution of particles with respect to s can be determined for any assumed distribution with respect to momentum p by using the Bethe-Bloch formula in the simplified form

$$s=1/\beta^2=1+(1/P^2), \tag{3}$$

wherein β is the ratio of particle velocity v to the velocity of light c; and P is the dimensionless ratio p/mc, with m as the rest mass of the particle. Relation (3) is of satisfactory accuracy in the range of present interest, namely $1\leq s\leq 60$.

In Fig. 15 are plotted the directional intensities of heavy nuclei derived from photographic emulsion data at various latitudes[7,24] as a function of the geomagnetic cut-off value of p/mc, P_c, in the vertical direction at the positions of the balloon flights in which they were obtained. (Numerically, $P\approx 0.52\times$ magnetic rigidity in units of 10^9 volts for all heavy nuclei.) The intensity of particles with $Z\geq 10$ at the most northerly latitude, is plotted at $p/mc=1.2$ (rather than at 0.8) because the residual atmosphere prevented particles of lesser value from reaching the emulsions. The data of Fig. 15 are well fitted, particularly for low values of p/mc, by an integral number spectrum of the form $KP^{-1.1}$, where K is a constant—a form identical to that proposed by Van Allen and Singer[1] for the total intensity spectrum over a similar range of P. Hence, in the range of P shown, the absolute directional intensity of particles with values of p/mc greater than P can be written

$$J(P)=KP^{-1.1}. \tag{4}$$

The corresponding differential number spectrum is

$$j(P)dP=(1.1KP^{-2.1})dP. \tag{5}$$

A differential distribution on s is obtained from Eqs. (3) and (5) as follows:

$$F(s)ds=j[P(s)]dP=j[P(s)](dP/ds)ds. \tag{6}$$

Thus,

$$F(s)=0.55K(s-1)^{-0.45}. \tag{7}$$

TABLE III. Adopted directional intensities.[a,b] (After Bradt, Peters, Kaplon *et al.*)

Nuclear charge Z	P	$J_Z(P)\times 10^4$ sec^{-1} cm^{-2} sterad^{-1}	K_Z in $J_Z(P)=K_ZP^{-1.1}$
6	0.8	5	3.9
7	0.8	5	3.9
8	0.8	5	3.9
13	1.2	2.7	3.3
19	1.2	1	1.2
26	1.2	0.5	0.6

[a] See reference 7.
[b] See reference 24.

[24] Lal, Pal, Kaplon, and Peters, Phys. Rev. 86, 569 (1952).

Over the domain of joint definition of $f(l)$ and $F(s)$, the rate that particles will traverse the chamber with s in ds and independently l in dl is proportional to

$$f(l)F(s)dlds. \tag{8}$$

Expression (8) is transformed to new variables $H=ls$ and s, with the result:

$$f(l)F(s)dlds=f(H/s)F(s)dHds\cdot\mathcal{J}\begin{pmatrix} l & s \\ H & s \end{pmatrix}, \tag{9}$$

wherein $\mathcal{J}(\ \ )$ is the Jacobian of the transformation. The right hand side of Eq. (9) is proportional to the rate of occurrence of bursts of height H in dH produced by a particle which has s in ds. The differential burst size distribution $g(H)$ is obtained by integrating the above expression over the entire range of s. If P_c is the lower limit of p/mc in a given calculation, then the limits for this integration are obtained by transforming the lines, $s=1$ and $s=1+1/P_c^2$, $l=0$, and $l=1$ into the (H,s) plane. The result is:

$$g(H,P_c)=1.1KH\int_1^{1+1/P_c^2}\frac{ds}{s^2(s-1)^{0.45}},\quad 0\leq H\leq 1,$$

and

$$g(H,P_c)=1.1KH\int_H^{1+1/P_c^2}\frac{ds}{s^2(s-1)^{0.45}},$$

$$1\leq H\leq(1+1/P_c^2). \tag{10}$$

Finally, the integral burst size distribution $G(H,P_c)$ is obtained by numerically integrating:

$$G(H,P_c)=\int_H^\infty g(H,P_c)dH. \tag{11}$$

An integral burst size distribution as so calculated is a universal one for all components of the primary beam which have integral number spectra of the form $KP^{-1.1}$ and which have the same value of P_c. To obtain a final burst size distribution—for comparison with experimental results—it is necessary to combine the distributions for the components of various Z (reverting to absolute units of H), using known or assumed absolute directional intensities for each component, the Koenig plots of fraction of the solid angle available for particles with different values P_c, and the geometrical factor of the chamber.

TABLE IV. Lowest possible values of P_c for penetration of apparatus plus residual atmosphere (1.8 g cm^{-2} for sum).

Z	P_c
6	0.40
7	0.42
8	0.44
13	0.51
19	0.57
26	0.62

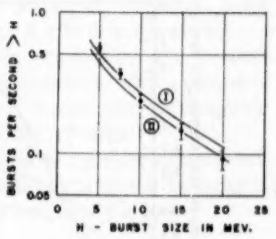

FIG. 16. Comparison of observed integral burst size distribution for Flights 21 and 22 (data combined) with the expected distribution (curve I). Observed rates are absolute; and curve I, likewise absolute, was independently calculated from emulsion data of other workers. See Sec. IV-G. Curve II is explained in Sec. V-A.

Table III, based on references 7 and 24 and Fig. 15, summarizes the basic data which were adopted as representing the known intensities and Z spectrum of heavy nuclei having P greater than the value shown. In accordance with previous discussion each component was taken to have an integral number spectrum of the form $J_Z(P)=K_ZP^{-1.1}$, where the subscript is specific to the Z of the component under consideration. It will be noted that within the C, N, O group and within the $Z\geq 10$ group a subdivision of component intensities has been made. This subdivision, though to some extent arbitrary, was based on study of the referenced Z distributions as well as others of a related nature.

In calculating families of expected burst size distributions at a given latitude, the cut-off value P_c is set by one or more of three considerations: (a) geomagnetic theory, (b) arbitrary assumption, and (c) the ionization range limit of the apparatus walls plus the residual atmosphere. In case (a) the value of P_c, in general, varies over the hemisphere of solid angle; but in any given direction its value is the same for all components with $Z\geq 2$, to within the approximation adopted herein that the ratio $Z/A=0.5$, irrespective of the atomic number Z and the atomic weight A.

The lowest possible values of P_c are determined by consideration (c) and are, of course, a function of Z. Their numerical values are listed in Table IV.

The calculations were performed in a piecewise manner appropriate to the case at hand.

V. INTERPRETATION

A. Discussion of Data from Flights 21 and 22 ($\lambda=56°$)

Flights 21 and 22 were made at $\lambda=56°$ which is about the same latitude as the most northerly point ($\lambda=55°$) at which the intensities of the heavy primaries have been measured by the photographic emulsion technique, as well as the northern limit for balloon methods because of the atmospheric depth limitation. Although emulsion observations yield only crude values of absolute intensities, they have well-established validity in the identification of tracks of heavy particles. Hence the comparison between observed ionization chamber data and those calculated from emulsion intensities provides an important measure of validation to the ionization chamber results.

In Fig. 16 is shown the observed burst size distribu-

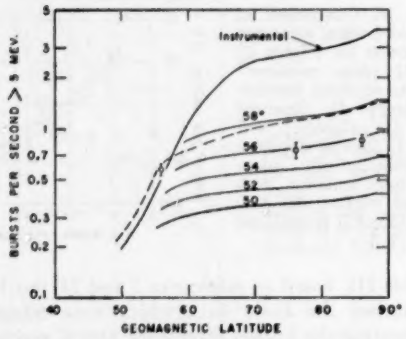

FIG. 17. Comparison of latitude dependence of observed rate of bursts greater than 5 Mev above the atmosphere with curves calculated on various assumptions. Solid curves calculated for spectra of Eqs. (12) of Sec. V-**B** of text with P_{min} assigned values equal to geomagnetic cutoff in vertical direction at geomagnetic latitudes 50°, 52°, 54°, 56°, and 58°, respectively, and finally the values given in Table IV for ionization range limit of apparatus plus residual atmosphere. The labels on curves specify the assumed spectral cutoff. Dashed curve calculated for spectra of Eqs. (16) of Sec. V-**B** of text assuming only instrumental cutoff.

tion data above the atmosphere obtained by combining the results of Flights 21 and 22. Curve I, likewise on an absolute scale, is the distribution calculated by the method of Sec. IV-**G** from the entirely independent emulsion data. The maximum difference between the calculated curve and the experimental points is for bursts greater in size than 20 Mev, and is 17 percent. The difference between the experimental and calculated values is less than twice the statistical standard deviation for each of the experimental points. Thus, there is very good agreement between the calculated and experimental distributions, especially if the uncertainties in the emulsion intensities are considered. To normalize the calculated curve to the experimental value for bursts larger than 15 Mev requires an over-all reduction of 14 percent in the K_Z's of Table III. The burst size distribution obtained by reducing all K_Z's by 14 percent is also plotted in Fig. 16 as Curve II. This curve is interesting in light of the discussion of the contribution of bursts due to stars (Sec. IV-**B**). In that discussion it was pointed out that the number of observed bursts in the size range 5 to 10 Mev was probably somewhat greater than the number due to traversals of heavy primaries, but that for bursts larger than 10 Mev, the observed bursts were produced almost entirely by heavy primaries. A comparison of the adjusted Curve II and the experimental points shows that there is complete agreement for bursts larger than 10 Mev and that the observed bursts in the size range 5 to 10 Mev are more numerous than those calculated on the assumption of a "zero wall thickness chamber." This is the result to be expected in view of the discussion of Sec. IV-**B**.

The intensity values of Table III will, however, be adhered to in spite of the indication that they are slightly too high.

Figure 16 and the associated discussion thus serve as an over-all validation of the ionization chamber technique for measuring the intensities of heavy nuclei above the atmosphere. See also reference 9. In addition, the previously expressed belief that nuclear stars are minor contributors to the burst size distribution is seen to be substantiated.

B. Interpretation of Data from Flights at Higher Latitudes

Interpretation of the observed burst size distributions of Flight 15 at $\lambda=76°$ and of Flight 17 at $\lambda=86°$ can now proceed with confidence.

For this purpose families of burst size distributions were calculated on the assumption that the integral number spectra of all heavy components of the primary radiation continued to have the form (4) down to some value P_{min} and that they were flat at lower values of P. That is, it was assumed that:

$$\begin{aligned} J_Z(P) &= K_Z P^{-1.1}, \quad P \geq P_{min}, \\ &= K_Z P_{min}{}^{-1.1}, \quad P \leq P_{min}, \end{aligned} \tag{12}$$

for all $Z \geq 6$, with values of K_Z given in Table III.

P_{min} was assigned values equal to the geomagnetic cutoffs in the vertical direction at geomagnetic latitudes 50°, 52°, 54°, 56°, and 58° and finally the values given in Table IV for the ionization range limit of the apparatus plus residual atmosphere.

Figures 17, 18, and 19 show the experimental points at latitudes 56°, 76°, and 86° for the counting rate of bursts larger than 5, 10, and 20 Mev, respectively. And they show families of smooth curves calculated for various values of P_{min} listed above. The uppermost curve in each of the figures is the one limited only by geomagnetic considerations and eventually at the more northerly latitudes by the ionization range of the apparatus. The continued rise of each of the curves north of the latitude equal to the labeled latitude of

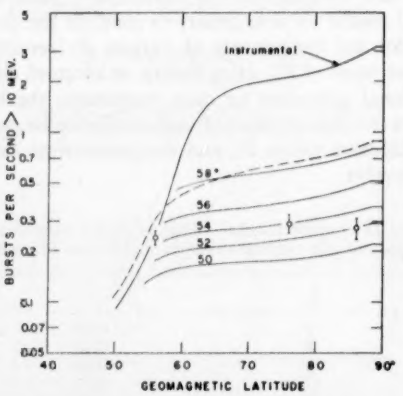

FIG. 18. Same as Fig. 17 except for rate of bursts greater than 10 Mev.

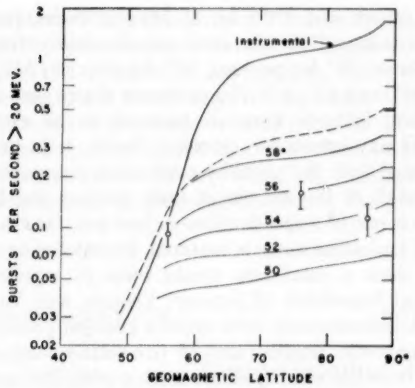

FIG. 19. Same as Fig. 17 except for rate of bursts greater than 20 Mev.

assumed cutoff ($P_{\min}$) is due to the progressive opening up of the earth's shadow cone as one goes to higher latitudes.[21–23] The values used for $P_{\min}$ in the vertical direction at various latitudes are listed in Table V. It is evident that the observed results are altogether inconsistent with the absence of a cutoff in the spectrum. Thus at 76° and at 86° the expected counting rates on the assumption of no cutoff (other than the instrumental one) are about four times as great as the observed ones for bursts larger than 5 Mev, about eight times as great as for bursts larger than 10 Mev, and about ten times as great as for bursts larger than 20 Mev.

The observed data are, however, clearly consistent with the spectral form (12) in which there is a *general spectral cutoff* at

$$P_{\min} \equiv (p/mc)_{\min} \approx 0.8. \tag{13}$$

The corresponding value of magnetic rigidity is

$$R_{\min} \approx 1.54 \times 10^9 \text{ volts}. \tag{14}$$

The spectral range between the value of $P_{\min}$ quoted in Eq. (13) and the instrumental limits listed in Table IV is rather small. It is therefore appropriate to note the reason for the large ratio between the apparatus cutoff curves in Figs. 17, 18, and 19 and those corresponding to a general cutoff at $P_{\min}=0.8$. Since the ionization chamber is already detecting particles of $Z \geq 10$ with rather high efficiency the contribution of such particles in the range ~ 0.8 to ~ 0.55 is not a major one. However, there is a great increase in efficiency in detection of C, N, O nuclei in the range ~ 0.8 to ~ 0.42. For example, the specific ionization corresponding to $P=0.68$ is 3.2 times minimum and only about 27 percent of C, N, O nuclei give bursts larger than 5 Mev and a negligible fraction give bursts larger than 10 Mev. But just above the instrumental cutoff, about 76 percent of C, N, O nuclei yield bursts greater than 5 Mev, about 57 percent greater than 10 Mev and about 47 percent greater than 20 Mev. Hence the comparisons exhibited in Figs. 17, 18, and 19 and discussed above refer most significantly to the C, N, O group. Their significance for nuclei having $Z \geq 10$ is not as strong.

The whole body of data appears to the present authors to be most naturally consistent with a complete absence of primary heavy nuclei having magnetic rigidities less than about 1.54×10^9 volts.

It is nonetheless of interest to consider other possibilities. The Rochester group[7] has proposed an integral number spectrum for heavy nuclei of the form:

$$J(\epsilon) = K/(1+\epsilon)^{1.35}, \tag{15}$$

where ϵ is the kinetic energy per nucleon.

Recently Ney[25] has reviewed all available emulsion intensity data from balloon flights and has proposed the integral number spectra:

$$J_{C,N,O}(\epsilon) = [0.0020/(1+\epsilon)^{1.35}] \text{ cm}^{-2} \text{ sec}^{-1} \text{ sterad}^{-1},$$

and (16)

$$J_{Z \geq 10}(\epsilon) = 0.0010/(1+\epsilon)^{1.5}.$$

The dashed curves in Figs. 17, 18, and 19 represent the expected counting rates in the chambers of the present investigation for the spectra (16). The calculated curves are clearly inconsistent with the experimental points at high latitudes.

VI. SIGNIFICANCE OF RESULTS

A. General Comments

(a) Throughout this paper explicit faith has been placed in the common belief that the "latitude effects" in cosmic-ray studies are to be attributed to a geomagnetic field conveniently described as that due to a point dipole of magnetic moment $M=8.1 \times 10^{25}$ gauss cm^3, located near the geometrical center of the solid earth. Some doubt in this belief has recently been expressed. But no significant modification has been offered; and it appears that the reasons for the doubt are much less convincing than the reasons for belief in a simple dipole field.

It is well known[26] that a full harmonic analysis of the observations of the surface magnetic field of the earth yields a more complex description of the geomagnetic field. The only feature of the more complex description

TABLE V. Geomagnetic cut-off values of P in the vertical direction at various latitudes.

λ	$P_{\min}$
50°	1.32
52°	1.10
54°	0.91
56°	0.75
58°	0.61

[25] E. P. Ney, Duke University, Cosmic Ray Conference of the National Science Foundation, November 30, December 1, 2, 1953 (unpublished).

[26] S. Chapman and J. Bartels, *Geomagnetism* (Oxford University Press, London, 1940), Vol. 2.

which appears to be significant in cosmic-ray effects is the slight displacement from the center of the earth of the "best dipole." This eccentric-dipole representation has been invoked by a number of writers in interpreting "longitude effects" and in making corrections to geomagnetic latitudes and to distances from the dipole to the point of observation. In the present work the centered-dipole representation has been employed, though it is realized that slight numerical corrections may eventually be worthwhile.

(b) Measurements above the atmosphere on the intensities of heavy nuclei are reasonably presumed to be free of albedo effects: i.e., of the effects of secondaries emerging from, and in some cases returning to, the atmosphere. In this sense their interpretation is notably simpler than the interpretation of total intensity measurements.[5] But due to the low intensity of the heavy nuclei it is more difficult to obtain precise results.

B. Conclusions

(a) The present paper apparently contains the only available information on the low-momentum end of the spectra of heavy primary cosmic rays. Although the accuracy of the data is not as high as would be desired, it appears that it will be difficult to substantially improve it.

(b) The data demonstrate a complete or nearly complete absence of primary heavy nuclei of $Z=6$, 7, and 8 having magnetic rigidities in the range 1.5×10^9 to 0.8×10^9 volts. As previously remarked, the observations are most naturally understood in terms of a complete absence. But the accuracy of the data is not such as to positively exclude an intensity in the above rigidity range of as much as 15 percent of the integral intensity for $R>1.5\times10^9$ volts.

(c) The present results are not as restrictive for nuclei having $Z\geq10$ but are again most naturally consistent with a complete spectral absence in the rigidity range 1.5×10^9 to about 1.1×10^9 volts. However, an increase of integral intensity of 30 percent between 1.5×10^9 and 1.1×10^9 is not positively excluded.

(d) The results are clearly inconsistent with the spectra of Eq. (16).

(e) Any contribution to the observed counting rates by primary Li, Be, or B nuclei must be by ones of magnetic rigidity considerably less than the general spectral cutoff at $R\sim1.5\times10^9$ volts. For this reason and for the further reason that the increase in counting rates with latitude is already completely accounted for by nuclei of $Z\geq6$ and of $R>1.5\times10^9$ volts, no further consideration has been given to Li, Be, and B.

(f) Special significance may be attributed to the fact that the cutoff in the spectra of the heavy nuclei occurs at very closely the same value of *magnetic rigidity* as the cutoff in the spectrum of primary protons,[1-5] and *not* at the same value of *velocity*. Thus, since $Z/A=1$ for a proton and ~0.5 for all heavier nuclei, pairs of "latitude knees" for the same cut-off velocity would be as follows: 58° for protons, 51° for heavies; 56°, 48°; 54°, 46°; and 52°, 43°. The existence of any such corresponding latitude knees is believed to be excluded beyond any reasonable question. Hence, it is strongly suggested that the physical mechanism responsible for the cutoff in the spectra of both protons and heavy nuclei is one of *magnetic character* and not, for example, one of ionization range in material, intersteilar or otherwise. Such a conclusion would seem to support the classical hypothesis of Janossy, Epstein, and Vallarta that a heliomagnetic field deflects charged particles of low magnetic rigidity and of non-solar-system-origin away from the vicinity of the earth's orbit. But such an hypothesis has recently fallen into disfavor for a number of reasons:[27]

(i) The model of the sun and the earth—each with its simple dipole magnetic moment, imbedded in a complete vacuum—is a significantly inadequate representation of present astrophysical knowledge.

(ii) The direct spectral observations of magnetic fields in the sun's atmosphere by Babcock, by Thiessen, and by von Kluber, though difficult and of limited accuracy, definitely exclude a general dipole moment as large as 0.6×10^{34} gauss cm^3—as would be needed to account for the cosmic ray cutoff.

(iii) The observed diurnal variation in total cosmic ray intensity at balloon altitudes is an order of magnitude smaller than that expected to be produced by such a solar magnetic dipole.[28]

(g) No promising alternative explanation of the cutoff in the spectra of primary cosmic rays is known to the present authors. But it now appears necessary that the explanation be of magnetic character.

VII. ACKNOWLEDGMENTS

The authors are particularly indebted to Lt. Malcolm S. Jones, Jr., U. S. N., formerly of the Nuclear Physics Branch of the Office of Naval Research, for able and enthusiastic support of all phases of this work, for personally leading the firing expedition, and for the resourceful development of a satisfactory rocket igniter under primitive shipboard conditions. Flights 8, 15, and 17 were launched from the U. S. Navy icebreaker—U. S. S. Staten Island—and Flights 21 and 22 from the U. S. Coast Guard icebreaker—U. S. C. G. C. Eastwind—with the cooperation and essential assistance of the officers and men of these vessels. The rocket propulsion units, known by the code name "Deacon," were manufactured by the Allegany Ballistics Laboratory of Cumberland, Maryland, and provided by the Navy Bureau of Aeronautics. The balloons were plastic ones

[27] The authors are particularly indebted to Professor Spitzer, Professor Schwarzschild, and Professor Gold for illuminating discussions of this matter.

[28] Firor, Jory, and Treiman, Phys. Rev. 93, 551 (1954).

of the General Mills Company of Minneapolis. Launching of the rockoons was supervised by engineers of the General Mills Aeronautical Laboratories. Firing circuits were made at the Naval Research Laboratory through a cooperative arrangement with Herman La Gow and Carl Medrow. The special nose shells were fabricated by Weber Brothers Metal Works of Chicago. The scientific apparatus, including telemeters, was designed and built at the State University of Iowa. Aerodynamic and mechanical design of the rocket fins and of the nose assemblies was also performed there and the components were built in the shops of the Department of Physics under the able supervision of J. G. Sentinella. Important experimental assistance was given by L. H. Meredith and Lee F. Blodgett of the Cosmic Ray Laboratory.

PHYSICAL REVIEW VOLUME 95, NUMBER 1 JULY 1, 1954

Cloud-Chamber Study of Charged *V* Particles*

CARL M. YORK, JR., R. B. LEIGHTON, AND E. K. BJØRNERUD
California Institute of Technology, Pasadena, California

(Received March 31, 1954)

An analysis of 103 charged *V*-particle decays is presented. These events have been observed with a double cloud chamber operated at 1750-m altitude. The events in the upper chamber appear to have markedly different properties from those in the lower. The particles in the upper chamber have measured properties which are in every respect consistent with those of the κ meson. Their lifetime is in the range 5×10^{-10} to 2×10^{-8} sec; their mass is $\sim1000\ m_e$; their transverse momentum distribution is consistent with a three-body decay scheme; the momentum in the center-of-mass system of their charged decay products is also consistent with three-body decay; and their frequency of production is greater than 0.4 percent of the total number of shower particles observed. On the other hand, the particles observed in the lower chamber have a lifetime in the range 10^{-11} to 3×10^{-10} sec; their transverse momentum distribution is consistent with a two-body decay scheme; their frequency of production is greater than 0.8 percent of the total number of shower particles; they are observed with approximately one-third of the frequency of Λ^0 particles; and they apparently can be produced in meson-nucleon collisions. The majority of the particles in the lower chamber are tentatively identified as charged hyperons with the aid of two cases which appear to have proton secondaries. The proposed decay scheme is $V_1^+\rightarrow p+\pi^0+Q$; and in order to fit all of the data, the alternate mode of decay, $V_1^+\rightarrow\pi^++n+Q$ must be introduced. The Q value is estimated to be $\lesssim125$ Mev.

I. INTRODUCTION

SINCE the original observation by Rochester and Butler[1] of the decay of a charged particle of mass greater than $900m_e$ into a light meson, extensive investigation of the decay of heavy charged particles has been carried out. The evidence has come from three distinct experimental sources, *viz.* cloud chambers in magnetic fields,[2–6] photographic emulsions,[7–10] and multiplate cloud chambers,[11] and has been interpreted in terms of a number of different particles:

(a) The majority of these observations can be explained in terms of a single particle (called a κ meson) of mass about $1000m_e$, which decays into a single, light, charged meson and two or more neutral particles. There is direct evidence that this charged meson is a μ meson from its characteristic decay into an electron.[7]

(b) There are also some data suggesting the existence of a different particle, the so-called χ meson,[8] of mass about $1000m_e$ which decays into a charged π meson and one neutral particle. The evidence relating to the χ meson is not very firm at present, but this decay scheme has been considered as a possibility in interpreting the present data.

(c) There is conclusive evidence for the existence of τ mesons ($m\approx965m_e$) which decay into three π mesons.[9]

(d) Recently, evidence has been presented which indicates that there may be a positively charged *V* particle of greater than nucleonic mass which decays into a nucleon and meson.[8–10,12]

(e) Finally, there are rather convincing indications of the existence of a "cascade" decay of a still heavier,

* Assisted in part by the joint program of the U. S. Office of Naval Research and the U. S. Atomic Energy Commission.

[1] G. D. Rochester and C. C. Butler, Nature **160**, 855 (1947).
[2] Seriff, Leighton, Hsiao, Cowan, and Anderson, Phys. Rev. **78**, 290 (1950).
[3] R. B. Leighton and S. D. Wanlass, Phys. Rev. **86**, 426 (1952).
[4] Armenteros, Barker, Butler, Cachon, and York, Phil. Mag. **43**, 597 (1952).
[5] Astbury, Chippindale, Millar, Newth, Page, Rytz, and Sahiar, Phil. Mag. **43**, 1283 (1952).
[6] Astbury, Chippindale, Millar, Newth, Page, Rytz, and Sahiar, Phil. Mag. **44**, 242 (1953).
[7] C. O'Ceallaigh, Phil. Mag. **42**, 1932 (1951).
[8] Report of the Bagneres Conference, 1953 (unpublished).
[9] Lal, Pal, and Peters, Phys. Rev. **92**, 438 (1953).
[10] Bonetti, Levi-Setti, Panetti, and Tomasini, Nuovo cimento **10**, 1729 (1953).
[11] Bridge, Courant, DeStaebler, and Rossi, Phys. Rev. **91**, 1024 (1953). (This reference contains a complete bibliography of the earlier work of this group.)
[12] York, Leighton, and Bjørnerud, Phys. Rev. **90**, 167 (1953).

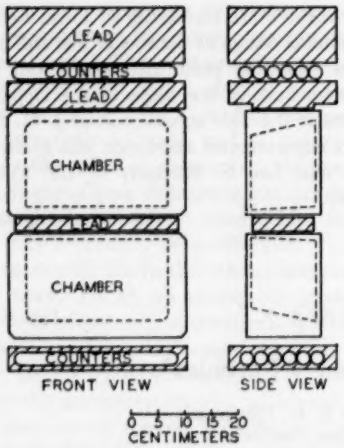

FIG. 1. The arrangement of counters and lead blocks around the cloud chambers. The dotted lines inside the chamber volume indicate the fiducial surfaces used in the lifetime study of Sec. IV. The magnet structure surrounding and supporting the apparatus is not shown.

negatively charged particle which gives rise to a V_1^0 particle and π meson.[4,13]

It is the object of this paper to present additional evidence regarding the nature of κ- and χ-meson decay and the existence of the heavy positive V particle. The cascade decay of heavy negative particles referred to above is not discussed nor is any analysis of τ-meson decays included.

II. APPARATUS AND MEASURING TECHNIQUES

The operation of the cloud chamber used in this experiment has been described in detail by Leighton, Wanlass, and Anderson.[14] However, several improvements and modifications have been made since their work was reported:

(1) A program for the measurement of no-field tracks in order to determine the maximum detectable momentum of the chamber has been carried out. A timing device was installed which turns off the magnet current for fifteen minutes every three hours. Tracks which penetrate the lead block between the two chambers without multiplication or appreciable scattering were selected from the pictures taken during these periods. The curvatures of these tracks were measured in exactly the same way as were the curved tracks obtained with the magnetic field and an histogram of the results was plotted. Two hundred and three tracks were included in the study, and from the width of the resulting distribution of measured no-field curvatures it has been concluded that the maximum detectable momentum for a track 15 cm long in the chamber is 3 Bev/c.

[13] Anderson, Cowan, Leighton, and van Lint, Phys. Rev. **92**, 1089 (1953).

[14] Leighton, Wanlass, and Anderson, Phys. Rev. **89**, 148 (1953).

(2) Several modifications were made in the thermostat system. Provision was made for recording the temperature variation of various parts of the chamber on the same film that was used to photograph the chamber. A study of these variations indicated that there was no observable change in the temperature conditions during the periods in which the magnetic field was turned off. This study also permitted a quantitative check on the gaseous distortions in the chamber. Considerable improvement in the temperature control was progressively attained, but because the events considered in this paper were selected from the total operation period of the apparatus, one can only say that the short-period temperature fluctuations of the cloud chambers were held to about ± 0.1°C during the course of the work.

The momentum and angle measurements were made from the stereoscopic photographs in the same way as were those of Leighton, Wanlass, and Anderson.[14] Ionization estimates were made by three independent observers and a range of possible ionization assigned in the same manner used by the above authors.

Various counter arrangements were used to trigger the apparatus. Of the 71 000 photographs taken of the cloud chamber, 14 000 were taken at 200-m elevation with a coincidence of one or more counters above the chamber and three or more below (this is called a 1–3 selection); 7000 were taken with the same counter selection at 1750 m; 22 000 were taken at 1750 m with 2–3 selection; and 28 000 were taken at 1750 m with 1–3 selection with lead shielding surrounding the lower counters. This shielding was accomplished by means of a cast lead block as shown in Fig. 1 and the counting rate with this arrangement was about 2.5 hr^{-1}.

III. A PRELIMINARY SURVEY OF THE DATA

Some of the especially interesting cases contained in the present data have already been reported.[3,12] The present analysis includes those cases and is based upon a total of 103 photographs of events which could be interpreted as charged V-particle decays, but not as π-μ decays or as scattering events. These events

TABLE I. Data on scattering events with observable "recoil blobs." (P_1 = momentum before collision, P_2 = momentum after collision, θ = angle of deflection, R_{calc} = calculated range of the recoil, R_{meas} = projected diameter of the recoil blob, p_T = transverse momentum of the scattered particle.)

Case	Type	P_1 (Mev/c)	P_2 (Mev/c)	θ	R_{calc} (mm)	R_{meas} (mm)	p_T (Mev/c)
1	p	—	420±70	84°	3.00	2.1±0.1	415±70
2	π^+	—	250±50	5°	0.04	1.0±0.2	20±5
3	π^-	30±7	18±5	33°	0.03	0.9±0.2	9±3
4	p	96±10	—	50°	0.20	1.0±0.2	73±8
5	π^+	—	102±10	15°	0.05	1.0±0.2	26±3
6	p	—	720±130	4°	0.12	1.0±0.3	50±10
7	π^+	490±100	—	20°	1.00	1.0±0.2	160±35
8	π^-	—	200±30	24°	0.30	1.2±0.2	80±12
9	π^-	214±25	—	30°	0.50	1.5±0.2	108±15
10	π^-	—	310±30	20°	0.50	1.5±0.2	108±15

were distinguished from the decay π mesons by the usual criteria derived from the dynamics of the π-μ decay. The cases which could be interpreted as π-μ decays are described in the Appendix. In the past[4] it has been considered reasonable to distinguish charged V-particle decays from scattering events by requiring that at least 75 Mev/c of transverse momentum p_T produce no visible recoil track at the point of deflection. However, since no very clear-cut basis for this particular criterion has yet been presented, it was decided to study the matter in some detail.

Ten events exhibiting a blob of ionization at the points of deflection of tracks in the chamber were selected from the last 20 000 pictures studied in this work. Table I summarizes the data for these events giving the nature of the particle (from ionization and momentum), the measured momenta before and after scattering, the angle of deflection, the measured diameter of the projected recoil blob, and the transverse momentum. In each case the recoil was assumed to be an argon nucleus and its range estimated from the curve of Blackett and Lees.[15] These ranges are entered in the column, R_{calc}. These data show that the size of the blob is greater in extent than the predicted range of the recoil for all values of $p_T \lesssim 160$ Mev/c. This is readily explained by the fact that the tracks observed in the present experiment are pre-expansion tracks, whereas Blackett and Lees used post-expansion tracks in the determination of their curve. During the expansion time of 16 milliseconds for the present chamber the ions diffuse approximately 1 mm. It is clear from these considerations that the critical factor in determining whether or not a recoil nucleus has been produced is not the range of that nucleus, but the *number of ions it forms* in the process of recoiling. In this connection it is worth while to consider the work of Crane and Halpern[16] who have studied the number of droplets formed by the 5-Mev/c recoil of A^{38} nuclei *in air*. From their work one can estimate that at least twenty droplets were produced by ions for a recoil momentum of 5 Mev/c. It is clear that the total number of ions formed must be proportional at least to the energy of the recoil and hence to the square of its momentum. Thus a 50-Mev/c recoil should produce approximately 2000 ions, which would appear as a very sizeable cluster of droplets. The number of droplets might of course be considerably smaller than the number of ions due to inefficiency of condensation, but an observable blob should certainly remain. It seems clear that the criterion used in this experiment for distinguishing decays from scattering events is sufficiently conservative to account completely for any differences in ion formation between the argon in the present chamber and air, as well as for inefficiency of condensation and statistical fluctuations. This criterion is that if an event for which $p_T \geq 50$ Mev/c gives rise to no observable cluster of droplets at the point of deflection, that event is almost surely not a scattering event.

TABLE II. Classification of charged V-particle decays according to their sign of charge and place of origin.

Origin	Charge Positive N^+	Charge Negative N^-	N^+/N^-
Above chamber	14	28	0.50±0.16
Plate between chambers	29	14	2.07±0.65
Total	43	42	1.02

[15] Rutherford, Chadwick, and Ellis, *Radiations from Radioactive Substances* (Macmillan Company, New York, 1930), p. 249.

[16] H. R. Crane and J. Halpern, Phys. Rev. **56**, 232 (1939). (The authors are indebted to Mr. V. A. J. van Lint for calling their attention to this work.)

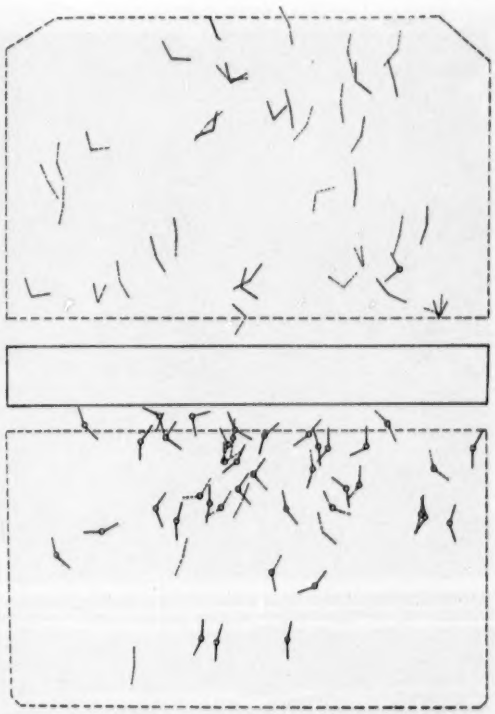

FIG. 2. The distribution of the charged V-particle decay points. A circle at the apex indicates production in the lead plate separating the two chambers. Solid lines indicate positive particles and dashed lines indicate negatives.

The first treatment of the data consisted of plotting the decay points of the charged V particles inside the cloud chambers as shown in Fig. 2. In carrying out this scheme two very marked features were noted. First, the decay points were distributed very differently in the two chambers, there being a striking number of very short decay lengths in the lower chamber,[17] and second, the charge ratio of the decaying particles was

[17] This feature was previously noted by Alford and Leighton (see reference 18).

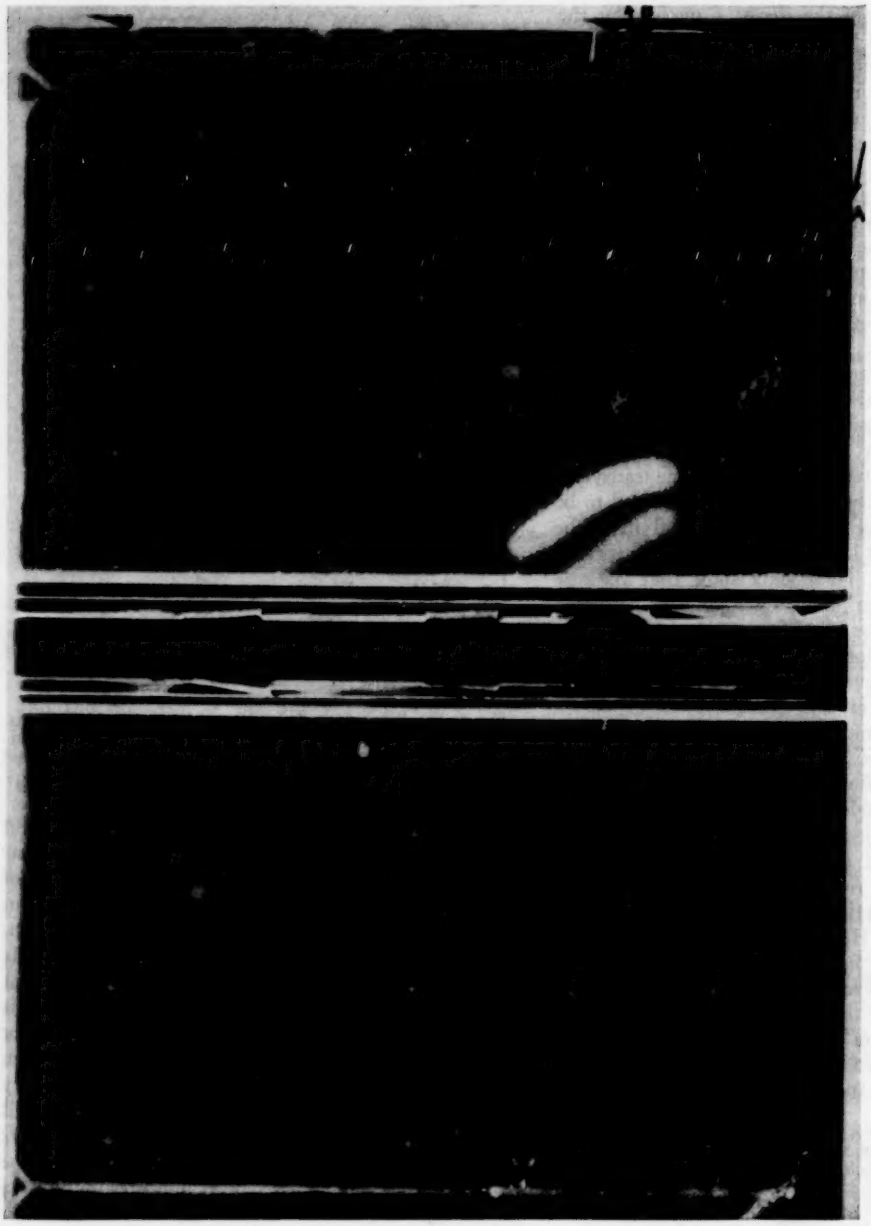

FIG. 3. Event No. 78113, which is listed in Table IV. The heavily ionizing charged V particle originates in the shower in the upper right-hand corner (A) and decays just above the lead plate separating the chambers. The secondary particle is ejected upward and to the left (B).

found to be quite different in the two chambers. A convenient way to indicate the asymmetry of charge is set forth in Table II where the number of positively and negatively charged V particles with origins above the apparatus or in the lead plate separating the two chambers is given. A table of this form has previously been published,[12] and the numbers have simply been brought up to date in the present version. The statistical probability that this (or any greater) charge asymmetry would be obtained as a fluctuation from a uniform charge distribution in the two chambers is about 0.002.

These marked asymmetries have already been tentatively interpreted in terms of a mixture of long- and short-lived charged V particles.[12] By considering the relative positions of the production layer and the cloud chamber, those charged V particles observed in the upper chamber were presumed to be predominantly long-lived particles with a negative excess of about

two to one at their point of production. (This need not imply that a single type of particle is observed, but only that the particles are predominantly long lived.) The charged V decays in the lower chamber are then supposedly a mixture of both long- and short-lived particles, and from the marked positive excess of this group of decays the short-lived particles should be predominantly if not entirely positively charged.

The next procedure consisted of determining the masses of the particles involved in the charged V decays from momentum measurements and ionization estimates. A photograph of such a decay event is shown in Fig. 3. A frequency distribution of the mass values has been plotted for all heavily ionizing primaries and secondaries in Fig. 4. It can be concluded that the masses of the measurable primary particles are in agreement with a mass of about $1000m_e$ and that the secondaries are all light mesons with two outstanding exceptions. These exceptions will be discussed in detail in Sec. VII.

A careful survey of the data was made for possible evidence of the existence of γ rays associated with the decay of the charged V particles.[11] One might expect to see electron cascades generated in the lead block between the chambers; however, in no case was such a cascade observed. It should be noted that this does not imply that there are no γ rays among the decay products of the charged V particles, because the thickness of the lead block (about six radiation lengths) makes it a very inefficient detector for low-energy cascade showers.

IV. LIFETIMES

The preliminary treatment of the data above suggested that two or more types of charged V particle with a marked difference in lifetime and sign of charge might exist. The evidence relating to the lifetimes will now be considered in detail.

The necessity for obtaining a sufficiently large, unbiased sample of V-particle decays of a single type, in order to determine their mean life with any precision, limits the use of cloud-chamber observations unless a definite classification of the particles can be made. The present data do not, in most cases, distinguish between the possible types of charged V particles. However, *limiting values* of the mean life τ of any given set of charged V decays can be made which do not involve a detailed knowledge of the nature of the particles observed. It is important to stress that the limiting lifetimes thus obtained may refer to an unknown mixture of two or more types of particles, but that even in such a case it may still be possible to obtain meaningful limits upon the lifetimes of the constituents of such a mixture.

The method used in the reduction of the data was essentially the same as that used by Alford and Leighton.[18] The minimum requirements of determination of the sign of charge and the existence of an approximate origin were satisfied for 84 charged V events at the time the analysis was carried out. Of these, 62 cases had their point of decay inside the fiducial surfaces. The rather large fraction, 26 percent, excluded by the fiducial limits can be compared to the 14 percent of the neutral V particles similarly excluded by Alford and Leighton. Most of the excluded charged V events are near the front glass or back piston of the chamber where neutral V's are difficult to identify.

The experimental quantities which were used in this analysis are as follows: x_i is the distance (in cm) between the point of entrance of the ith particle into the region of the chamber inside the fiducial limits and the point of decay. D_i is the corresponding distance (in cm) between the point of entrance and the point at which the particle would have left the fiducial region had it not decayed. D_i is usually called the gate length. t_i and T_i are the times taken to traverse the distances x_i and D_i, respectively, in the rest-system of the V particle. These proper times are related to the measured distances by the equation

$$t_i = (x_i/c)(M/P_ic) = (x_i/c)(1/\beta_i\gamma_i), \qquad (1)$$

where M is the mass of the particle in Mev and P_i is the measured momentum in Mev/c. A similar relation can be written for T_i. The quantities c, β, and γ have the usual significance.

In each case it is necessary to have an estimate of $\beta_i\gamma_i$, and if the particle has a known mass and measurable momentum, this product is easily obtained. However, since one rarely knows these two quantities, an alternate procedure must be employed. Upper and lower limits can be assigned to $\beta_i\gamma_i$ in each case and these quantities can, with the aid of Eq. (1), be used

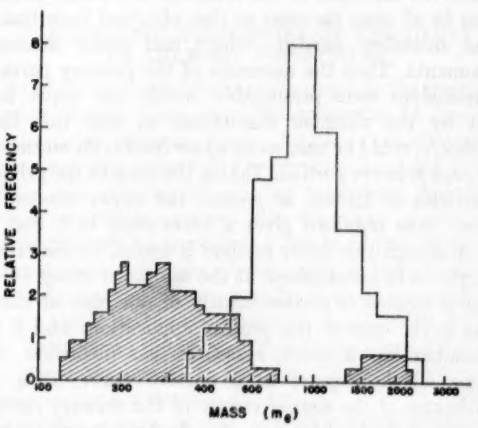

FIG. 4. Frequency distribution of the measured masses. The unshaded area gives the masses of the primary particles and the shaded area the masses of the secondaries. Ten positive and seven negative primaries are represented.

[18] W. L. Alford and R. B. Leighton, Phys. Rev. **90**, 622 (1953).

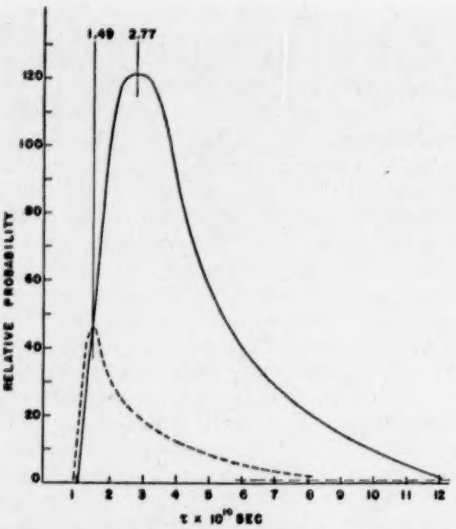

FIG. 5. Plots of the likelihood function for the two limiting lifetime estimates obtained from the data of the lower chamber. The solid curve is for the estimate of the upper limit and the dashed curve for the lower limit of the mean life.

to determine lower and upper limits, respectively, for the values of t_i and T_i.

In all but four of the 62 cases it was possible to assign an upper limit to the ionization of the primary particle. In 39 of the remaining cases the ionization was indistinguishable from minimum, and in these cases the upper limit was taken to be one and one half times minimum. These upper limits determined lower limits to $\beta_i\gamma_i$ in each case and, by Eq. (1), *upper limits to t_i and T_i.*

On the other hand, the sign of charge, as determined from the direction of curvature of the *parent* particle *was in all cases the same* as that obtained from that of the *secondary* particle, which had easily measured momenta. Thus the momenta of the primary particles themselves were presumably within the upper limit set by the chamber distortions, so that this limit, 3 Bev/c, could be used as an *upper limit to the momentum of each primary particle.* Taking the mass of the primary particles as $1000m_e$ *or greater*, the upper momentum limit thus obtained gives a lower limit to t_i and T_i.

Although this latter method is useful, its limitations ought to be emphasized. If the sample of decay events being treated is predominantly of one sign of charge (as is the case in the present application) and if the chamber has a small, *systematic* gas distortion of a type which appears as a smooth curve, then the estimates of the sign of charge of the primary particle might easily be biased to give better agreement with the true sign of charge than would have been obtained in the absence of the distortion. If such were the case, the maximum detectable momentum might no longer be a conservative estimate of the upper limit to the momentum of the V particle. It is clear that such a bias will be more important for short tracks near the edges of a chamber than for long tracks near the center. Thus the interpretation of any results obtained with this method must be made with due caution.

In order to treat the whole sample uniformly, only the two methods just described were used to establish limits to t_i and T_i, including 14 cases for which the momentum of the primary particle was measurable. This procedure has advantages in that it does not bias the sample by the selection of slow particles with long tracks for which the momentum is readily measurable, and it permits most of the observed cases to be included in the analysis. The data on the 58 cases finally included in the lifetime analysis thus consist of two sets of values of t_i and T_i, corresponding to an upper and a lower limit to each. Of the 30 cases in the lower chamber, four negative particles apparently had their origin in the lead above the upper chamber, but were treated in this analysis as if they originated in the plate between the chambers. In Table III the number of cases observed in each chamber, the average limiting values of t and T, the average value of x/D, and the ratio of the number of positive to the number of negative particles in each chamber are given. These data show the marked difference between the two chambers and the necessity for treating each chamber separately. It is seen that the limiting values of $\bar{T}$ for the two chambers are very nearly the same. This would be expected for identical chambers, provided no bias due to the selection of groups of particles with greatly different average velocities has been introduced.

(a) *Upper chamber:* For gate times which are small compared to the mean lifetime of the decaying particles, one expects the decay points to be uniformly distributed throughout the chamber, and hence the average value of x/D to be equal to one-half. It is immediately apparent from Table III that such is the case in the upper chamber, so that the "apparent" lifetime of the particles in the upper chamber is probably much greater than the average gate time, i.e.,

$$\tau(\text{upper chamber}) > 4.5\times10^{-10} \text{ sec.}$$

TABLE III. Comparison of the events used in the lifetime study. (r is the ratio of positive to negative particles, $\langle x/D\rangle_{Av}$ is the average value of the ratio of decay length to gate length, $\bar{t}$ is the average time of flight in the chamber before decay, and $\bar{T}$ is the average gate time.)

	No. of cases	$r=\frac{N_+}{N_-}$[a]	$\langle x/D\rangle_{Av}$[b]	$\bar{t}(10^{-10}$ sec) Upper limit	$\bar{t}(10^{-10}$ sec) Lower limit	$\bar{T}(10^{-10}$ sec) Upper limit	$\bar{T}(10^{-10}$ sec) Lower limit
Upper chamber	28	0.65±0.25	0.46±0.10	3.2	1.5	6.1	2.9
Lower chamber	30	2.00±0.77	0.31±0.09	1.7	0.8	5.4	2.4

[a] The errors quoted for r are probable errors.
[b] The errors quoted for $\langle x/D\rangle_{Av}$ are 95 percent confidence limits, *not* the usual probable errors.

That these events do not necessarily consist of a single type of particle is indicated by the fact that one negative case in this chamber could be identified as a cascade decay such as those recently reported.[13] A careful search was made for additional cases where a neutral V particle might have decayed in the plate, but none was found.

(b) *Lower chamber:* For the sample of 30 cases in the lower chamber the average ratio (x/D) is significantly different from 0.50, as can be shown by conventional statistical methods. A maximum-likelihood analysis[18] was therefore made to determine *limiting values* of τ. The likelihood function

$$L=\prod_{i=1}^{N}\frac{1}{\tau}\frac{\exp(-t_i/\tau)}{1-\exp(-T_i/\tau)}, \tag{2}$$

which is proportional to the probability of having obtained the particular set of experimental data, can be shown to have the property that if t_i and T_i are consistently overestimated, each by the same factors α_i, the best value of τ determined from this likelihood function is then correspondingly an overestimate of the lifetime of the sample, and similarly for underestimates.

The best value of the mean life (that value of τ for which L is a maximum) is given by

$$\tau=\frac{1}{N}\sum_{i=1}^{N}\left(t_i+\frac{T_i}{\exp(T_i/\tau)-1}\right). \tag{3}$$

By expanding the exponential functions in the parentheses, this can be written in a form more convenient for the calculation of τ:

$$\tau\simeq\frac{\sum T_i^2-(1/60)\tau^{-2}\sum T_i^4}{6\sum T_i-12\sum t_i}. \tag{4}$$

The calculation of τ for the two limiting sets of data gives

$$\tau(\text{upper limit})=2.77\times10^{-10}\text{ sec},$$
$$\tau(\text{lower limit})=1.49\times10^{-10}\text{ sec}.$$

The calculation of the likelihood function L was performed to determine the significance of these values, and the results are shown in Fig. 5. The ordinates of the curves were normalized to the value of L for $\tau\to\infty$, i.e.,

$$L=\prod_{i=1}^{N}\frac{1}{T_i},\quad\text{as}\quad\tau\to\infty.$$

In order to estimate the probable errors for these limiting values of the mean lifetime, the probability that $\tau\leq\tau_0$ must be calculated. This probability, $F(\tau_0)$ is given by the integral

$$F(\tau_0)=\int_0^{\tau_0}L(\tau)d\tau.$$

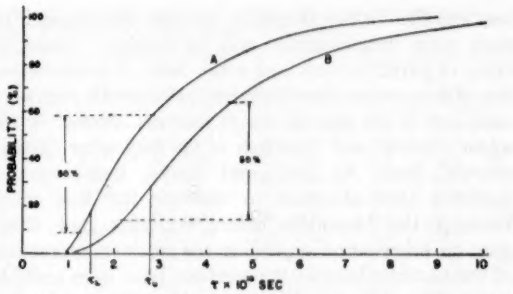

FIG. 6. The plot of $F(\tau_0)=\int_0^{\tau_0}L(\tau)d\tau$ *versus* τ, together with the assigned 50 percent confidence limits to each of the limiting estimates of the lifetime found in the lower chamber.

The integration can be performed graphically and the resulting curves are given in Fig. 6. As indicated in the figure, 50 percent confidence limits have been used to determine the probable errors on the two limiting values of the mean lifetime. The result is

$$\left[1.5\binom{+1.3}{-0.3}<\tau<2.8\binom{+2.0}{-0.6}\right]\times10^{-10}\text{ sec}.$$

These limits can be associated with the mean life of a specific particle only if the sample is composed entirely of particles of that type. If the sample is pure, then these limits indicate that the particle has a lifetime between them. If the sample is a mixture of particles, then the upper limit indicates that at least one type of particle with lifetime less than 2.8×10^{-10} sec is contained in the sample and the lower limit implies that another type of particle with lifetime greater than 1.5×10^{-10} sec is present. However, in view of the earlier remarks about possible bias in the determination of this lower limit, no very great significance will be attached to it.

V. ADDITIONAL PROPERTIES OF THE DECAY OF CHARGED V PARTICLES

In addition to the lifetimes discussed in the previous section several other measured properties of charged V particles deserve some detailed consideration. These are: the nature of the particles involved in the decay, the distribution of the transverse momenta of the secondary particles, and the value of the momentum p^* of the secondary particle in the center-of-mass system of the decay. Because the lifetime study showed a marked difference in the charged V's decaying in the upper and lower chambers, it seems reasonable to investigate the remaining decay properties by analyzing the events in the two chambers separately to bring out any further differences.

(a) The nature of the primary particles can be inferred in part from the direct measurement of their masses (see Fig. 4 above). However, it should be noted that the requirements of measurability demand that the particles travel a considerable distance at

low velocity before decaying, so that any sample of such mass measurements will be strongly biased in favor of particles with long mean lives. *It is interesting that of the seventeen heavily ionizing, measurable primaries contained in the data all except four are observed in the upper chamber and contribute to the long mean lifetime observed there.* As mentioned above, four negative particles were observed to traverse the lead plate between the chambers before decaying, but these give no information regarding the nuclear interaction of the particles because it would not have been possible to identify a star in the plate produced by a charged V particle.

In Fig. 4 it is seen that the masses of all except two of the secondary particles are consistent with either that of a π or μ meson. The two exceptions will be treated in detail in Sec. VII below. No secondary particle was observed to decay in flight, and only four traversed the lead plate separating the chambers. None of the secondary particles produced a nuclear interaction and therefore no conclusion can be drawn with regard to whether these were π or μ mesons.

(b) In considering the transverse momentum distribution of the secondary particles emitted in charged V-particle decay, the data from the upper and lower chambers have been treated separately. The resulting distributions are given in Figs. 7(a) and 7(b). Here the number of cases per 50-Mev/c interval is plotted against the transverse momentum. The shaded areas indicate the contribution of positive particles to the total distributions. In accord with the minimum-transverse-momentum criterion required to eliminate π-μ decays and scattering events, these distributions do not have any cases with p_T less than 50 Mev/c. The smooth curves represent the calculated distributions for two- and three-body decay with fifteen percent experimental errors folded in. The three-body decay curve has been calculated by assuming that a $1000m_e$ primary particle (κ meson) decays into a μ meson and two zero-rest-mass particles.[19] The two-body curve has been calculated for a momentum of the charged meson of 216 Mev/c in the center-of-mass system of the decay. This value of the momentum is that assumed for χ-meson decay and has been plotted for ease of comparison. The areas under the curves for $p_T > 50$ Mev/c have been normalized to be equal to the total areas contained in the frequency distributions of the experimental data.

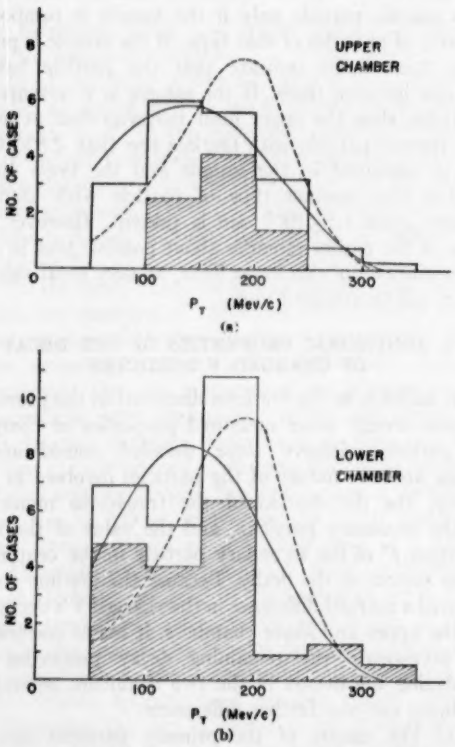

FIG. 7. Frequency distributions of the measured transverse momenta for the upper and lower chambers. The shaded areas indicate the contribution of positive particles to the total distribution. The solid curve is calculated for a three-body decay ($p^*=240$ Mev/c) and the dashed curve for a two-body decay ($p^*=216$ Mev/c).

By cutting off the distributions at 50 Mev/c, bias of the data is reduced due to contamination from scattering events as well as due to the difficulty of observing low transverse momentum cases. It is clear that such cases will in general involve small angles of deflection which might easily be overlooked in searching through the film for charged V events. Because the transverse momentum depends upon the measurability of the momentum of the secondary particle, the distributions of transverse momentum will be slightly biased to include more of the short-lived primary particles than of the longer-lived ones. However, a relatively inconsequential bias will result and the small amount of data does not warrant a correction for this effect.

Because there are relatively few cases involved in these distributions, it is not possible to make significant statistical tests of the "goodness of fit" of the theoretical curves and the experimental data. It is clear that many more cases would be needed to distinguish clearly between two- and three-body decay schemes. On the other hand, although the level of statistical significance is low, the transverse momentum distributions in the two chambers would appear to indicate some differences in the type of decay involved.

(c) In treating the determination of the momentum p^* of the secondary particle in the center-of-mass system, care has been taken not to introduce any bias into the data. All cases in which the primary particle was judged to be heavily ionizing and the transverse momentum of the secondary was measurable are listed in Table IV. The limits of ionization of the primary particle are used to obtain the limits on the

[19] C. M. York, Phil. Mag. 43, 985 (1952).

TABLE IV. Data on 9 cases with both momenta measurable and 5 cases with primary ionization >1.5×minimum and secondary momentum measurable. A signifies an origin above the chamber and P and origin in the plate.

Case	Origin and sign	p_1(Mev/c)	p_2(Mev/c)	$(I/I_0)_1$	$(I/I_0)_2$	θ	p_T(Mev/c)	p^*(Mev/c)	x(cm)	D(cm)
7029	$A(-)$	185±20	150±10	6−10	1.3−2.0	85°	150±10	160−155	11.5	13.2
17620	$A(-)$	1050±300	750±70	<1.5	<1.5	8°	109±10	179±20[a]	3.8	15.5
25343	$P(+)$	185±30	215±30	1.5−2.5	<1.5	51°	165±20	181−165	4.3	8.8
26622	$P(-)$	—	295±10	1.5−2.5	<1.5	33°	160±5	160−180	5.4	14.7
31589	$P(-)$	—	265±20	1.5−3.0	<1.5	40°	170±20	171−182	2.3	14.4
32530	$A(-)$	465±70	590±70	<1.5	<1.5	29°	285±40	320±80[a]	6.4	14.7
36726	$A(+)$	—	140±20	1.5−3.0	<1.5	108°	135±20	304−210	4.5	15.7
40840	$P(+)$	95±20	184±20	6−12	<1.5	87.5°	184±20	197−190	4.1	7.9
52999	$A(+)$	165±30	215±20	15−30	1.3−2.0	121°	185±20	250−234	2.5	6.2
54056	$P(-)$	—	325±75	1.5−3.0	<1.5	13°	73±15	112−177	0.8	13.7
55482	$P(-)$	—	182±20	1.5−2.5	2−4	53.5°	146±15	193−152	—	—
60452	$A(+)$	255±40	212±7	6−12	<1.5	99°	210±7	245−230	—	—
65550	$A(-)$	1500±600	120±30	<1.5	<1.5	41.5°	79±20	213±50[a]	11.9	13.9
78113	$A(+)$	107±4	251±8	10−15	<1.5	133°	182±6	310−296	—	—

[a] p^* calculated assuming a mass of $1000m_e$ for the primary particle.

velocity of the center-of-mass system of the decay. By applying a Lorentz transformation to the longitudinal component of momentum of the secondary particle, the corresponding limits to p^* are obtained. For completeness several cases in which the primary particle was essentially at minimum ionization but had a measurable momentum are included. These cases are indicated in the table and p^* has been calculated for them by assuming that the primary particle has a mass of $1000m_e$. As mentioned earlier, the table includes the values of the decay length x and the potential path length D for all of the cases.

The small number of cases and the errors inherent in the observations preclude any detailed interpretation of the values of p^*; however, the spread of values, especially in the upper chamber, seems to favor a non-unique value of p^*. This could result from either a mixture of several types of two-body decay, or from a single three-body decay scheme. In particular, the distribution is completely consistent with what might be expected for κ-meson decay.

VI. THE PRODUCTION OF CHARGED V PARTICLES

The most direct information with regard to the production of the charged V particles can be obtained from those events proceeding from an interaction in the lead plate separating the two cloud chambers. In Table V, 43 such cases have been classified according to the nature of the particle which initiated the nuclear event. It is seen that most of the events were caused by particles which were themselves secondaries of penetrating showers. A similar classification of data taken with the same apparatus and over the same period of time has been made for 118 *neutral* V particles and these results are included in the table. There is a striking similarity between the two sets of numbers. It seems reasonable to suggest that the charged V particles observed in the lower chamber are produced by a mechanism which is very similar to that of neutral V particles and that meson-nucleon collisions in lead can give rise to charged V particles. (A similar result has been obtained at the Brookhaven Laboratory[20] where artificially produced π mesons have bombarded hydrogen to produce charged V particles.) In each category the ratio of charged to neutral V particles has been taken and is seen to be the same for each within the limits of the statistics. This indicates that charged V particles in the lower chamber are observed with about one-third the frequency of neutral V particles independently of the character of the producing particle.

The frequency of production of charged V particles relative to the total number of shower particles has been calculated separately for the two chambers, using a method similar to that of Barker *et al.*[21] The geometry used in this experiment is shown in Fig. 1. In the lower chamber, only production in the lead block separating the two chambers has been considered. In calculating the curves shown in Fig. 7 it has been assumed (a) that particles of unique mass are observed to decay in each chamber, (b) that all of the shower particles have a differential momentum distribution of the form $P^{-3}dP$ for momenta in excess of 1 Bev/c, (c) that the penetrating showers are produced uniformly throughout the production layer, (d) that the cross section for penetrating shower production is insensitive

TABLE V. The number of penetrating showers occurring in the lead plate between the chambers giving rise to $V^{\pm}$ particles, classified according to the type of primary. Similar data for neutral V particles is included and the ratio R, calculated for each category.

Type of event	$V^{\pm}$	V^0	$R(V^{\pm}/V^0)$
Charged primary, accompanied by other shower particles	27	83	0.32±0.07
Charged primary, unaccompanied	11	21	0.52±0.19
Neutral primary, (acc. and unacc.)	5	14	0.36±0.18
Totals	43	118	0.36±0.05

[20] Fowler, Shutt, Thorndike, and Whittemore, Phys. Rev. **93**, 861 (1954).

[21] Barker, Butler, Sowerby, and York, Phil. Mag. **43**, 1201 (1952).

to the energy of the primary particles. For simplicity it is also assumed, (e), that all of the shower particles and decaying charged V particles travel vertically downward. If the detection efficiency as a function of the lifetime of the decaying particles is evaluated using the above assumptions, the frequency of production as a function of lifetime can then be obtained from the observed ratio of decaying V particles to total number of shower particles. From 1045 counted shower particles with momenta above 1 Bev/c, a weighted[22] total of 35 600 particles produced in the lead block above the upper chamber and 8400 produced in the lead between the chambers were estimated to have been seen during the course of the experiment. These are to be compared to 41 charged V's with momenta greater than 1 Bev/c observed in the upper chamber and 43 in the lower. The resulting curves of the frequency of production as a function of the mean lifetime are plotted in Fig. 8. For both curves a mass of $1000m_e$ for the decaying particles has been assumed, but the dotted line A' lying just above the curve for the lower chamber has been calculated assuming a mass of $2000m_e$ to show the small effect of this assumption. The vertical lines in the figure indicate the limits on the mean lifetimes estimated in Sec. IV and the attached arrows indicate the range in which the true mean lifetimes for the two groups of particles probably lie.

The particles in the lower chamber have a frequency of production which is insensitive to the lifetime for a fairly large range of values of the lifetime. An estimate of the lower limit to the lifetime of these particles can be obtained by assuming that their frequency at production is ten percent of all of the shower particles. This gives a lower limit of about 10^{-11} sec. If this same criterion of ten percent is applied to the upper chamber, one can estimate an upper limit to the lifetime of the particles decaying there of about 2×10^{-8} sec.

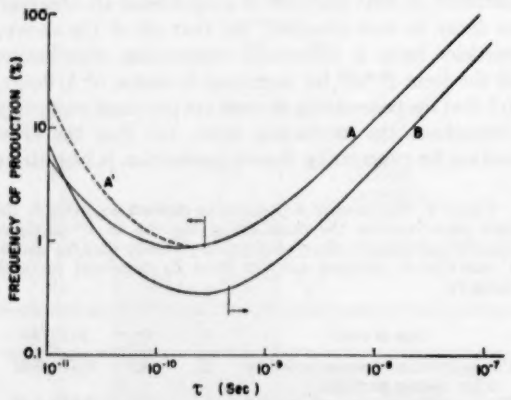

FIG. 8. The frequency of production *vs* lifetime curves for the upper chamber (curve B) and the lower chamber (curve A). The dashed curve, A', is calculated for the lower chamber assuming a mass of $2000m_e$. The lines with arrows attached, which intersect the curves, indicate the limiting lifetimes obtained in Sec. IV.

[22] It was necessary to weight the total according to the number of pictures taken with each counter arrangement.

VII. THE V_1^+ PARTICLE

In the previous sections several marked differences in the decay properties of the charged V particles in the upper and lower chambers have been noted. One of these differences which was briefly mentioned in the discussion of the masses of the secondary particles in Sec. V above, is that two charged V particles having secondary particles with masses greater than $1300m_e$ were found in the lower chamber. Both are positive and both have origins in the lead plate separating the two chambers. It should be emphasized that while these heavy secondaries are quite consistent in mass and charge with protons, the mass measurements do not exclude the possibility that they are somewhat lighter or heavier than protons. A tentative interpretation of these events as being examples of the decay of a charged counterpart of the familiar V_1^0 particle has already been made.[12] Table VI contains the data relevant to these two cases. In the preliminary discussion of these events the question of possible alternative interpretations was not treated for the sake of brevity. However, at least two other possible interpretations require some detailed consideration. The first is the possibility that these V_1^+ events are in fact $V_1^0(\Lambda^0)$ events in which the π-meson decay product is ejected backwards along the line of flight of the V_1^0 particle. The second is that a proton arising in a nuclear interaction in the lead might scatter in the argon gas of the chamber to produce the observed event.

Let us first consider the probability that the π meson of a V_1^0 decay would be ejected backwards along the line of flight of the parent V_1^0 particle. A careful, unprejudiced reprojection of the events was made to determine the accuracy with which the primary track could be lined up with the origin of the nuclear event in the lead block. In the first case this was ±2 mm at a distance from the decay point of 4.2 cm and in the secondary the uncertainty of alignment was ±2.5 mm at 2.9 cm. If random emission of the π meson in the *laboratory* system is assumed, one can calculate that the probability of occurrence for the first case is 1/1600 and 1/700 for the second. The *a priori* chance of observing two such independent events is thus very small indeed. It should be noted that the effect of considering the motion of the center-of-mass system is to decrease these probabilities. Furthermore, in these considerations we have ignored the requirement that the momenta of the π^- and p^+, transverse to the direction of flight of the V_1^0 particle, must balance. This requirement would not be fulfilled for either of these cases if the V_1^0 particle were produced in the nearby nuclear interaction. Thus it would be necessary either to postulate a multi-body decay for these particles or alternatively that they were produced elsewhere. Either of these possibilities would introduce

TABLE VI. Summary of the data pertaining to two cases of V_1^+ decay.

Case	P_{pri}(Mev/c)	I_{pri}(×min)	$M_{pri}(m_e)$	P_{sec}(Mev/c)	I_{sec}(×min)	$M_{sec}(m_e)$	θ	P_T(Mev/c)
1	—	3−7	—	360±60	3−7	1300−2300	20°	125±25
2	—	2−4	—	520±75	2−4	1300−2200	18°	160±40

an additional improbability into the interpretation of these events as V_1^0 decay.

In considering the possibility that the V_1^+ events are scattered protons, one ought first to inquire as to the probability of such an event. A careful survey of the total number of protons produced in nuclear interactions in the plate was carried out to determine the total path length of such proton tracks in the argon gas of the chamber. The criteria for selecting the tracks were that they originate in an interaction in the plate and that they have momenta and ionizations compatible with that of a proton. The protons were chosen from pictures taken with the various counter arrangements used, and from a total of 31.3 m of measured track, a weighted total of 570 m was estimated to have been observed throughout the course of the experiment. It is clear from the discussion of elastically scattered particles given in Sec. III above, that a recoil nucleus should be readily observable at these transverse momenta. However, it is possible that an inelastic scatter of the proton occurs with perhaps the ejection of one or more neutrons to balance the momentum. In estimating the cross section for such a process it is clear that not all angles of scattering will contribute to the type of event that is being considered here. For a given incident momentum and angle of deflection, transverse momentum balance requires a recoiling particle in the nucleus with a momentum at least equal to the transverse momentum of the deflected particle. When this momentum is sufficiently high, charged-particle emission will become probable and the event would not be considered a case of scattering. The momenta of the incident particles in the two events under discussion are unknown, but for the sake of discussion, assume that in both cases the incident particle has 350-Mev/c momentum, the lower of the two observed values of the momentum of the scattered particle. This is an extremely conservative value, especially if the cases represent inelastic scatters. If the transverse momentum at which charged particle emission becomes likely is taken to be 200 Mev/c, the maximum angle of deflection that needs to be considered is 35°. This value of the transverse momentum has been chosen so that a single nucleon inside the nucleus would be given a kinetic energy of 21 Mev. Since the change in the longitudinal component of momentum has been ignored, this value of the transverse momentum is considered to be conservative. In view of the elastic scattering criterion established above, no case of $p_T<50$ Mev/c would have been considered. Such a p_T corresponds in these events to an angle of deflection of 8°, so that the angular interval to be considered has been chosen to lie between 8° and 35°. The differential inelastic scattering cross section is assumed to be geometric and uniform for all angles of emission in the range of angles considered. Under the foregoing assumptions the mean free path for observing the above type of events in the argon gas of the cloud chamber is 6300 m and the probability of observing two events in the examined track length is then 0.0074. In view of the way in which the values were chosen in calculating this number, it may be considered an upper limit to the probability of observing the two events under discussion. Hence this alternative explanation of the V_1^+ events is not considered satisfactory.

As a result of these considerations the suggestion has been made[12] that the short-lived particles observed in the lower chamber are hyperons which decay according to the scheme,

$$V_1^+(\text{or } \Lambda^+)\rightarrow p+\pi^0+Q. \quad (5)$$

Because a large number of the short-lived particles give rise to secondary particles whose masses are consistent with that of light mesons, it is inferred that the charge-exchange counterpart of the above reaction is also observed, *viz.*,

$$V_1^+\rightarrow n+\pi^++Q. \quad (6)$$

Although there is no direct evidence in the present data, it is possible that some of the short-lived negative particles observed in the lower chamber represent the decay scheme,

$$V_1^-\rightarrow n+\pi^-+Q. \quad (7)$$

VIII. CONCLUSIONS

From the analysis of the data obtained in the two cloud chambers, it seems quite likely that the charged V particles observed in this experiment are composed of at least two types with quite different properties. The events in the upper chamber are predominantly due to a particle of mass about $1000m_e$ which decays into a light meson with a mean lifetime considerably greater than 5×10^{-10} sec and less than 2×10^{-8} sec. A study of the transverse momentum and momentum in the center-of-mass system of the secondary particle indicates that there is probably more than one additional neutral particle involved in the decay. From a consideration of the maximum value of the transverse momentum and the rest mass of the primary particle it seems likely that these neutral particles are of very small rest mass and presumably are neutrinos and/or photons. The frequency of production of these particles is greater than 0.4 percent of the total number of

shower particles. The properties of these V particles are in every respect consistent with those of the κ meson,[7] and similar in every way to the properties deduced from earlier cloud chamber work employing a similar geometric arrangement of the apparatus.[4,21]

The events in the lower chamber have a mean lifetime of less than 3×10^{-10} sec and greater than 10^{-11} sec. Although several of the events in this chamber are probably κ mesons, as indicated by mass measurements on the primaries, some other much shorter-lived particle must predominate to give such a low upper limit to the mean life of the sample. This particle apparently decays most of the time into a light meson and is predominantly positive. The transverse momentum distribution indicates that probably a two-body decay occurs with a momentum in the center-of-mass system of about 200 Mev/c or less for the secondary particles. The frequency of production of these events is equal to or greater than about 0.8 percent of the total number of shower particles. The two V_1^+ events discussed in detail in Sec. VII above have led to the suggestion that these short-lived particles in the lower chamber are hyperons with at least the two alternate modes of decay given by (5) and (6) above. However, if one accepts neither the interpretation of the V_1^+ cases nor the assumption that the charge exchange counterpart of the decay can occur, the evidence presented above still requires the introduction of a short-lived particle with a rather high rate of production. The observed frequency of occurrence, and the apparent long lifetime, of the much discussed χ meson[8] does *not* appear to satisfy the requirements imposed by the present data. However, the small number of observed cases of χ mesons, as well as of charged V particles in this experiment, make it impossible to exclude completely the possibility that the particles observed in the lower chamber are χ mesons.

On the other hand, with the acceptance of a charged hyperon as the short-lived particle in the lower chamber, several inferences can be drawn from the data. From the upper limit of the transverse momentum of about 200 Mev/c, the Q value of the decay scheme (6) can be estimated to be approximately 125 Mev, or less, in agreement with the values reported at the Bagnères Conference[8] for the hyperons observed in photographic emulsions. The striking similarity of production of these charged hyperons with the neutral hyperons (V_1^0 particles) as shown in Table VI indicates that they are produced by similar mechanisms. The fact that they are observed with one-third the frequency of the neutral V particles can in part be attributed to their shorter lifetime and perhaps to a higher energy threshold for production. The photographic emulsion work indicates that κ mesons are produced at least as frequently as the hyperons, so that from the curves in Fig. 8 an estimate of the lifetime of the κ meson of the order of about 3×10^{-9} sec can be obtained. As seen from the shape of the lower chamber curve, this conclusion is essentially independent of the lifetime and mass of the charged hyperon. Any predominance of κ mesons over hyperons at production will cause a corresponding increase in the estimate of the lifetime of the κ meson.

TABLE VII. Classification of π-μ decays according to place of origin and sign of charge.

Origin \ Sign	Positive	Negative	Total
Above plate	14	24	38
In plate	16	17	33
Total	30	41	

In the interpretation of Table II which gives the charge distributions observed in the two chambers, it ought to be emphasized that the asymmetries indicated by the table are statistically significant only if an explanation in terms of a single type of particle is attempted. If, however, there are several types of charged V particles, separated automatically according to lifetime by the geometry of the two chambers, then a further interpretation of the observed charge distributions as indicating a predominance of one sign of charge or the other at the point of production for each of these types of particles must be undertaken with caution.

APPENDIX

During the course of the experiment 65 events were observed which were consistent with the decay of a π meson into a μ meson. Fourteen of these cases were completely measurable and yielded an average Q value of 34 Mev, in excellent agreement with the known value. An histogram of the transverse momenta of all 65 cases was also plotted and showed good agreement with the expected distribution for π-μ decay. A careful study of the biases introduced by the difficulty of observing small angle deflections of a track was made, and was estimated to have had but a small effect on the 65 cases used in this histogram. The fact that very few cases were observed in the transverse momentum range, $p_T<10$ Mev/c and that all of these could have been π-μ decays, indicates that very few, if any, scattering events unaccompanied by recoil blobs were included in the histogram. Because this region of transverse momentum would be expected to contain more scattering events unaccompanied by recoil blobs than any higher momentum range, it can be concluded from this study that very few scattering events went undetected and that the transverse momentum criterion applied to the charged V events is conservative. Table VII gives the number of positively and negatively charged π-μ decays in the upper and lower chambers in the same way that Table II gives this information for the charged V events. The statistical probability that this or any greater asymmetry is due to a random fluctuation is 0.33.

The authors are indebted to Mr. J. D. Sorrels for performing some of the measurements on the π-μ decays.

Contributions of Bremsstrahlung Conversion in Trident Experiments

M. M. BLOCK* AND D. T. KING
Nucleonics Division, Naval Research Laboratory, Washington, D. C.
(Received March 16, 1954)

Determinations of the cross section for the direct creation of electron pairs by energetic charged particles in nuclear emulsions are dependent on the experimental criteria by which the observations are accepted, phenomenologically, as tridents. This paper discusses the extent to which materialization of a bremsstrahlung photon close to the path of the parent particle becomes experimentally indistinguishable from direct pair production. A study of 200 pairs arising from the conversion of bremsstrahlung photons from electrons with energies between 0.1 and 10 Bev leads to the conclusion that about 6 percent of the pairs materialize so close to their parent that they would be interpreted as tridents. An extension of the analysis to electrons of incident energy 100 Bev demonstrates that under typical experimental conditions about 70 percent of such secondary pairs would be accepted as tridents. Recently reported experiments which indicate a cross section for direct pair production by fast electrons much larger than that predicted by theory are discussed.

I. INTRODUCTION

EXPERIMENTS on tridents—the direct production of electron pairs by charged particles of great energy—have been reported in the literature.[1–5] These phenomena, found chiefly in photographic emulsions, consist of a primary track characteristic of a relativistic singly charged particle and three thin emergent tracks. The majority of tridents occur on electronic primaries. It has been pointed out[3] that a basic difficulty in the study of the direct production process arises from the inclusion of a fraction of those pairs—called B.S. pairs—which are due to the conversion of bremsstrahlung photons close to the track of the parent electron. For this fraction the point of materialization of the B.S. pair is superposed on the parent track within the spatial resolution possible under the experimental conditions. We refer to events of this type as "pseudo-tridents." Figure 1 is a photomicrograph which illustrates the track pattern of a typical B.S. pair. The orthogonal distance from the pair origin to the parent track is called r, and for Fig. 1 the projection of r in the emulsion plane is about 3 microns. The main limitation on spatial resolution of a close B.S. pair is determined by the dimensions (~0.4 micron) of the developed grains in nuclear emulsions. In our experience it is possible to distinguish a B.S. pair if the separation of the pair origin from the line of the parent track exceeds ~0.2 micron.

We develop a theory to show that the occurrence of pseudo-tridents is greater the higher the energy of the incident electron. The mean angles of both B.S. photon emission and the electron multiple scattering, which are the principal factors in the determination of the orthogonal distance r, are inversely proportional to the energy. At very great primary energies the major fraction of the B.S. photons are emitted in such a narrow forward cone that a substantial fraction materialize within the resolution distance of the parent track and are erroneously counted as tridents. In order to correct for the inclusion of these pseudo-tridents, we have undertaken a calculation of the distribution in r to be expected under various experimental conditions. In addition, the corresponding experimental distribution has been constructed from 200 events of the type shown in Fig. 1.

II. THEORETICAL TREATMENT

The calculation proceeds by computing the probability of the real and projected separations between the parent track and the origin of a B.S. pair. Figure 2 represents schematically the emission of a B.S. photon at $t=0$, which is assumed to be the point of entrance of the electron into the emulsion, and the subsequent conversion of the photon at distance t measured in the forward direction of the emitting electron. At $t=T$, the parent electron leaves the emulsion. The three-dimensional distance between parent and pair origin is r, while the projection of r in the plane of the emulsion is x. The major contribution to r is due to the multiple scattering of the electron in traversing the distance t; the contribution arising from the angles of radiative emission is small for most values of t employed and has been neglected.[6] All distances will be expressed in radiation lengths (~3.0 cm for nuclear plates).

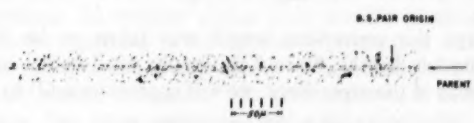

FIG. 1. A photomicrograph of a typical B.S. pair found in a G5 emulsion. The projected distance between the pair origin and the track of the parent electron has been measured for 200 observations of this type and is here about three microns.

* On military leave of absence from Duke University, Durham, North Carolina.

[1] C. F. Powell, Nuovo cimento Suppl. **6**, 379 (1949).

[2] Bradt, Kaplon, and Peters, Helv. Phys. Acta **23**, 24 (1950).

[3] Hooper, King, and Morrish, Phil. Mag. **42**, 304 (1951).

[4] S. J. Goldsack and M. L. T. Kannangara, Phil. Mag. **44**, 811 (1953).

[5] J. E. Naugle and P. S. Freier, Phys. Rev. **92**, 1086 (1953); Report Duke University Cosmic Ray Conference, 1953 (unpublished).

[6] B. Rossi and K. Greisen, Revs. Modern Phys. **13**, 240 (1941).

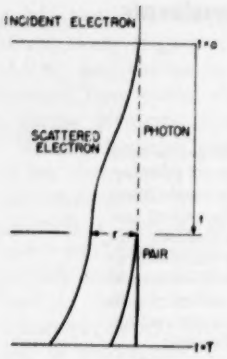

FIG. 2. A schematic diagram to represent the formation of a B.S. pair. The parent electron enters the emulsion at $t=0$, at which point the B.S. photon is assumed to originate. The effect of the angles of emission in the radiative collision has been neglected. At t the photon forms a pair and the parent electron has been scattered away a distance r, leaving the emulsion at $t=T$.

For our purpose it is necessary to calculate the probability that an electron has been scattered a distance x away from the path of the photon at the point of pair conversion. Let $H(t,x)dx$ be the probability that an electron traversing a distance t is scattered a projected distance between x and $x+dx$. Multiple scattering theory[6] indicates that $H(t,x)$ is Gaussian, and thus we can put

$$H(t,x)=\frac{1}{(2\pi)^{\frac{1}{2}}\alpha t^{3/2}}\exp\left(-\frac{x^2}{2\alpha^2 t^3}\right). \tag{1}$$

In order to evaluate the parameter α, we note from (1) that

$$\langle x^2\rangle_{Av}=\int_{-\infty}^{\infty}x^2H(t,x)dx=\alpha^2t^3.$$

It can be shown[6] that $\langle x^2\rangle_{Av}=t^2\langle\theta_p^2\rangle_{Av}/3$, where $\langle\theta_p^2\rangle_{Av}$ is the mean square of the projected angle of multiple scattering. $\langle\theta_p^2\rangle_{Av}$ may be expressed by the experimentally determined[7] relation for G5 emulsion, $\langle\theta_p^2\rangle_{Av}^{\frac{1}{2}}=25t^{\frac{1}{2}}/E$, where E is the electron energy in Mev, t is in units of 100 microns, and θ_p is in degrees. Expressed in more convenient units, θ_p in radians, t in radiation lengths (cm), and E in Mev, we obtain $\langle\theta_p^2\rangle_{Av}^{\frac{1}{2}}=7.57t^{\frac{1}{2}}/E$. Thus $\alpha=4.35/E$.

Further, let $Q(t)dt$ be the probability that a photon traversing a distance t materializes between t and $t+dt$. Since we find only those B.S. photons which form pairs in T, we normalize so that $\int_0^T Q(t)dt$ is unity. Then

$$Q(t)=\frac{7/9\exp(-7t/9)}{1-\exp(-7T/9)},\quad 0\leqslant t\leqslant T, \tag{2}$$

where the conversion length was taken to be 9/7 radiation lengths. Since T is usually small in the conditions of the experiment, we will approximate (2) by

$$Q(t)dt=dt/T,\quad t\leqslant T\ll 1. \tag{3}$$

We are now able to evaluate $N(x')$, the fraction of the B.S. pairs for which $-x'\leqslant x\leqslant x'$. Since (1) and (3) are independent, the simultaneous probability is given by their product. Thus

$$N(x')=\int_{-x'}^{x'}\int_0^T H(t,x)Q(t)dxdt.$$

After transformation to the dimensionless variables

$$\eta=x'/\alpha t^{3/2},\quad \eta_{x'}=x'/\alpha T^{3/2},$$

$$N(x')=(4/3)\eta_{x'}{}^{2/3}I(\eta_{x'}) \tag{4}$$

where

$$I(\eta_{x'})=\int_{\eta_{x'}}^{\infty}E(\eta)\eta^{-5/3}d\eta,$$

and

$$E(\eta)=\int_0^{\eta}\frac{\exp(-z^2/2)}{(2\pi)^{\frac{1}{2}}}dz.$$

In addition, we consider the quantity $N(r')$, the fraction of the B.S. pairs within a true distance r' from the parent. Expressed in radial distance, (1) is replaced by

$$G(t,r)=\frac{r}{\alpha^2t^3}\exp(-r^2/2\alpha^2t^3), \tag{1a}$$

where $G(t,r)dr$ is the probability that an electron travelling through t scatters between r and $r+dr$. From (1a) and (3), proceeding as before but now employing the dimensionless variables

$$\eta=r'/\alpha t^{3/2}\quad\text{and}\quad \eta_{r'}=r'/\alpha T^{3/2},$$

we find

$$N(r')=\tfrac{2}{3}\eta_{r'}J(\eta_{r'}), \tag{4a}$$

where

$$J(\eta_{r'})=\int_{\eta_{r'}}^{\infty}\frac{1-\exp(-\eta^2/2)}{\eta^{5/3}}d\eta.$$

Functions (4) and (4a) were numerically evaluated and are plotted in terms of the quantities $\eta_{x'}$ and $\eta_{r'}$ in Fig. 3.

The distribution $P(x)dx$, the probability for B.S. pairs to lie in the projected interval between $|x|$ and $|x+dx|$, is immediately obtainable by differentiation of the integral distribution $N(x')$ of Fig. 3, and is

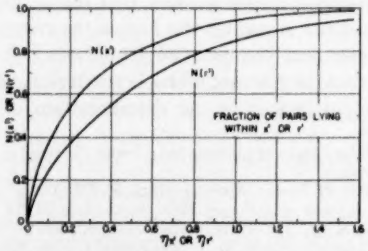

FIG. 3. The fraction of B.S. pairs formed within a projected distance x' or radial distance r' from the track of the parent electron as a function of the dimensionless variables $\eta_{x'}$, $\eta_{r'}$, respectively.

[7] Gottstein, Menon, Mulvey, O'Ceallaigh, and Rochat, Phil. Mag. 42, 708 (1951).

given by

$$P(x)=\left[\frac{dN(x')}{dx'}\right]_{x'=x}=\left[\frac{dN(x')}{d\eta_{x'}}\cdot\frac{d\eta_{x'}}{dx'}\right]_{x'=x}$$
$$=\frac{1}{\alpha T^{3/2}}\left[\frac{dN(x')}{d\eta_{x'}}\right]_{x'=x}. \quad (5)$$

In the application of the theory to experiment three effects have not been considered. Firstly, it has been assumed that the photon is emitted at the point of entry of the electron into the emulsion. A more exact theory would take into account the distance traversed by the electron before photon emission. In practice this distance can be shown to be small; if it is neglected in relation to T, an underestimate of $N(x')$ or $N(r')$ results. Secondly, if two or more B.S. pairs are formed alongside the same parent the above effect is more pronounced. This, however, is relatively rare in comparison with single photon conversion. Thirdly, if the path length $T\gtrsim 1$, so that (3) is no longer valid, the calculated $N(x')$, $N(r')$ are too small since materialization is more probable at smaller distances. These effects are generally rather small and their neglect leads to a considerable simplification of the analysis. As a result, our calculation of the number of unresolved B.S. pairs is a minimum estimate.

In order to examine the general character of these distributions as functions of track length and energy, it is instructive to consider $\langle r^2\rangle_{Av}$, the mean square radial separation, which is given from (1a) and (2) by

$$\langle r^2\rangle_{Av}=\int_0^\infty\int_0^T\frac{r^3}{\alpha^2t^\beta}\exp\left(-\frac{r^2}{2\alpha^2t^\beta}\right)\frac{7/9\exp(-7t/9)}{1-\exp(-7T/9)}dtdr.$$

Within the conditions of present experiments where $T\ll 1$, $\langle r^2\rangle_{Av}^{\frac{1}{2}}=\alpha T^{3/2}/\sqrt{2}$, a result which corresponds to the distribution developed from (4a). As experimental techniques improve, it will be possible to examine electromagnetic cascades of great path length, $T\to\infty$. It is noteworthy that under such circumstances $\langle r^2\rangle_{Av}^{\frac{1}{2}}\to 5.05\alpha$, and the distribution width becomes independent of path length. For small T, a more exact expansion of $\langle r^2\rangle_{Av}$ in T leads to

$$\langle r^2\rangle_{Av}^{\frac{1}{2}}=(\alpha T^{3/2}/\sqrt{2})(1-3T/20).$$

In our experimental comparison the largest value of T employed is 0.5 and for this figure we see that the error introduced by neglect of the expansion in T is an overestimate in $\langle r^2\rangle_{Av}^{\frac{1}{2}}$ of only $\sim$7 percent.

III. EXPERIMENTAL COMPARISON

We have compared an experimental study of 200 B.S. pairs with the preceding analysis. The measurements were made in Ilford G5 emulsions 400 microns thick, 4×7 cm, which had been exposed to the cosmic radiation at altitudes exceeding 95 000 ft, at geomagnetic latitude 55°N, for about six hours. Data were collected from 26 plates which had been exposed under different amounts of absorbers. The search was confined to thin tracks inclined to the emulsion plane at angles less than 5°. Two hundred pairs were found which were associated with a thin and approximately parallel track; we have assumed all events of this nature to be B.S. pairs, since the occurrence of other processes of this phenomenological appearance is negligible. The projected distance between pair origin and the nearest thin parallel track was measured in each case; the fractional number of B.S. pairs per micron interval in x are given as a histogram in Fig. 4.

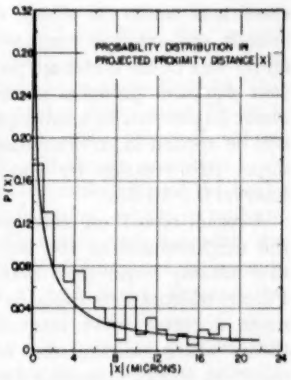

FIG. 4. Comparison of the experimental normalized histogram with the theoretical curve of the probability for a B.S. pair to form within the projected interval between $|x|$ and $|x+dx|$ from the parent track. The energies of the parent particles fall between 0.1 and 10 Bev, and experimental values of $|x|$ exceeding 20 microns have not been included.

The distribution in the emulsion path lengths of the parent tracks was obtained, and we have assumed a differential energy distribution of the form $E^{-1.6}dE$, deduced from the π^0-meson energy spectrum.[8] The probability distribution for the parameter $\alpha T^{3/2}$, which is required for the analysis, was obtained by numerical means from the above distributions in length and energy. The appropriate terms in (5) were weighted in accordance with the experimental variations in length and energy, and an averaged value of $P(x)$ obtained. This is compared with the experiment in Fig. 4. The agreement appears to be satisfactory, particularly in view of the fact that B.S. pairs originating at distances exceeding about 50 microns tend to escape observation. This leads to an error in normalization which causes a small distortion of the histogram.

IV. CONCLUSIONS

An important application of this analysis is the estimation of the fraction of B.S. pairs which are pseudotridents. In nuclear plates it is usually possible to resolve distances of 0.2 micron in projection and 0.4 micron in depth. For purposes of calculation, an elliptical resolution function with these dimensions as semiaxes has been assumed. For our experiment, the appropriately weighted values of $N(r')$ were obtained and integrated over the above elliptical resolution characteristic. We deduce that 6 percent of the total number of B.S. pairs produced under our experimental

[8] Carlson, Hooper, and King, Phil. Mag. 41, 701 (1950).

conditions would lie within our minimum resolution criteria and are thus pseudo-tridents. A factor of two either way in the minimum projected and depth resolution distances produces a variation in this result of about 30 percent. In a subsequent paper this correction will be applied in an evaluation of the cross section for direct pair creation by fast electrons in the energy interval 0.1–10 Bev.

A recent report[9] on tridents with primary energies in the neighborhood of 100 Bev indicates a production rate notably larger than that indicated by theory.[9,10] Fifteen tridents were found in 37 cm of track. We have made a conservative estimate from electromagnetic theory which indicates that about 80 B.S. photons of quantum energy exceeding 100 Mev would be emitted and that, of these, about 14 percent would materialize as B.S. pairs under the conditions of the experiment. Thus an average of about 11 B.S. pairs would be expected. Cascading effects, which would tend to increase this number, have been neglected. An application of our analysis to the experiment has been made. If we assume a mean primary energy of 100 Bev and a mean path length of 0.47 radiation length, we find a value of 1.4×10^{-6} radiation length (cm) for the parameter $\alpha T^{3/2}$. If we employ the same elliptical resolution variation as before, the expected proportion of B.S. pairs which are pseudo-tridents is 67 percent. Therefore, it is reasonable to suppose that approximately 7 of the 15 tridents reported are not, in fact, attributable to the direct pair creation process. It has been pointed out previously that this may be regarded as a minimum estimate. Consideration of this large correction factor leads to a trident cross section more nearly in agreement with theory. It can be shown that even if the minimum resolution distances are halved, our conclusions remain substantially the same; a similar remark can be made with regard to halving the primary energy. We therefore consider the contributions of bremsstrahlung conversion to constitute a major source of error in trident experiments at great energies.

[9] H. J. Bhabha, Proc. Roy. Soc. (London) **A152**, 559 (1935).
[10] G. Racah, Nuovo cimento **14**, 93 (1937).

ACKNOWLEDGMENTS

We are indebted to Dr. M. M. Shapiro for his continued support and to Dr. W. W. Wada and Mr. P. H. Fowler for many helpful discussions. The nuclear emulsions were processed by Mr. B. Stiller and Mr. F. O'Dell and the measurements were made by Mrs. N. T. Redfearn.

PHYSICAL REVIEW VOLUME 95, NUMBER 1 JULY 1, 1954

Decay Scheme of the τ Meson

N. BAKER AND O. BERGMANN
Department of Mathematical Physics, University of Adelaide, Adelaide, South Australia
(Received March 2, 1954)

A statistical examination of the data at present available on τ-meson decay shows that it is consistent with a two-body decay scheme: $\tau\rightarrow\pi+X^0\rightarrow\pi+\pi^++\pi^-$. The mass of the intermediate particle X^0 would have to be about $595m_e$ and the Q value for its decay about 22 Mev.

As is well known, the τ meson exhibits the characteristic decay scheme $\tau^\pm\rightarrow\pi^\pm+\pi^++\pi^-$ with a Q value of about 76 Mev. This is usually regarded as a spontaneous 3-body decay, and various theories have been worked out on this basis,[1] but no definite conclusions as to the validity of these theories have been reached, because of the scarcity of the observations.

We have considered whether the data now available are consistent with the decay scheme, $\tau^\pm\rightarrow\pi^\pm+X^0$, where X^0 denotes a hypothetical neutral particle which after a very short lifetime decays into $\pi^++\pi^-$. We were led to this supposition by the fact that several authors[2] have proposed the existence of neutral particles which decay into two π mesons, although their proposals have not been widely accepted.

For the analysis of this process, mechanics alone suffices. In the rest frame of the τ meson, we expect an energy-distribution function consisting of a sharp line at an energy E for the first π meson and for each of the remaining π mesons a uniform distribution between the limits

$$E_{\max,\min}=\tfrac{1}{2}(M-2m-E)\pm\tfrac{1}{2}(E^2-m^2)^{\frac{1}{2}}\cdot\{(M^2-2ME-3m^2)/(M^2-2ME+m^2)\}^{\frac{1}{2}},\quad(1)$$

where M, m are the masses of the τ and π mesons, respectively. The mass of the X^0 particle is given by

$$x=(M^2-2ME+m^2)^{\frac{1}{2}}.\quad(2)$$

In order to test the predictions of our hypothesis, we have made a statistical analysis of fourteen events, eleven of which are summarized in a paper by Amaldi *et al.*[3] and three more by Lal *et al.*[4] In most of the cases we have used standard deviations derived directly from the experimenters' estimates of errors; for the

[1] R. H. Dalitz, Phil. Mag. **44**, 1068 (1953); Proc. Phys. Soc. (London) **66**, 710 (1953).
[2] E.g., the ξ^0 meson proposed by Danysz, Lock, and Yekutieli, Nature **169**, 364 (1952).
[3] Amaldi, Baroni, Castagnoli, Cortini, and Manfredini, Nuovo cimento **10**, 937 (1953).
[4] Lal, Pal, and Peters, Phys. Rev. **92**, 438 (1953); Proc. Indian Acad. Sci. **38**, 398 (1953).

particles of reference 4 the errors in the Q values only were given and the standard deviations for the three secondary particles were estimated by assuming them equal. We got the best Q value $\bar{Q}=76.07$ Mev by weighting the experimental values inversely with the squares of their standard deviations.

In the calculations we have used as the mass of the π meson the value $276.44m_e$ (which corresponds, according to Amaldi *et al.*[3] to the weighted mean of π^+ and π^- meson masses), which combines with the above Q value to give a mass $978.10m_e$ for τ.

With the aid of the statistic χ^2 we make a test of the constancy of the Q value, i.e., of the hypothesis that the τ meson has decayed from rest in the cases analyzed. Supposing the Q_i to be normally distributed with the respective estimated standard deviations σ_i about a fixed mean, then

$$\sum_{i=1}^{14}(Q_i-\bar{Q})^2/\sigma_i^2=\chi^2, \tag{3}$$

with 13 degrees of freedom. We found $\chi^2=7.33$, so that $P>0.50$, which is satisfactory.

The next step was to examine the existence and position of the sharp energy value. Both upper and lower bounds for it can be found by examining the particle of lowest energy, *viz.*, in the event $B1$ of reference 2, and comparing the observed value 1.04 Mev with $E_{\min}$ calculated from Eq. (1). The range indicated for the kinetic energy is about 32–43 Mev. Incidentally it follows from energy and momentum conservation that the kinetic energy of no secondary particle can exceed $Q(M+m)/2M$, or approximately 50 Mev.[1]

The main problem in testing the sharp value is to choose the appropriate secondary particle to which we may ascribe this value. In overcoming this difficulty, we suppose the sharp value of the kinetic energy of one of the secondary particles to be T Mev; and, letting T_i be the kinetic energy (with standard deviation σ_i) of any arbitrary secondary chosen from the ith τ decay, we consider the expression

$$\sum_{i=1}^{14}(T_i-T)^2/\sigma_i^2=K^2. \tag{4}$$

As a rough estimate of the possible range of the sharp value, we choose the secondary particle in each event so as to minimize K^2 which will be distributed like χ^2 with 14 degrees of freedom if each T_i is an estimate of the sharp value T, supposing that this exists. Taking a significance level of $P=0.05$, T is limited to the range 35–38 Mev.

Although, strictly speaking, one should consider all the 3^{14} ways in which it is possible to choose the set of T_i, weighting each in accordance with the probability that each T_i of the set estimates T, this procedure is impracticable. Instead we proceed thus: We consider only secondary particles with energies less than twice their standard deviation away from T. Subject to this restriction we choose the "worst admissible" set T_i so as to maximize K^2, and find with what probability $K^2<\chi^2$ with 14 degrees of freedom. If $T=36$ Mev, the "worst" set gives $P>0.01$; the "best" set defined by making K^2 a minimum, as explained above, gives $P\simeq 0.15$. This is a reasonable indication that a sharp value $T=36$ is consistent with the data. A small range of values, narrower than 35–38 Mev, will also be consistent.

Finally we have to test the uniformity of the background of the energy distribution, which is uniform between the limits (1). To avoid confusion with the sharp value, we examine the distribution of the secondaries with lowest energy in each event. Because the sharp value, which we fix as 36 Mev, is greater than the corresponding $\frac{1}{2}(E_{\min}+E_{\max})-m$, the required distribution for the kinetic energy is uniform between $E_{\min}-m$ and $\frac{1}{2}(E_{\min}+E_{\max})-m$. We divide the range into 3 equal parts so that the expected number of particles in each is not much less than 5, in accordance with statistical practice, and apply a χ^2 test. We get $P>0.10$ which is not a "significant" contradiction of our hypothesis.

The above statistical analysis, although not rigorous, seems adequate for the few observations available at present.

We have shown that the data available at present are consistent with a sharp value in the neighborhood of 36 Mev, but the smallness of the number of observed τ decays and the large size of the standard deviations, particularly for the particle of highest energy, makes it impossible to decide between the decay schemes so far proposed. Moreover, it must be borne in mind that the spontaneous 3-body decay might well occur besides that we have proposed, each with a certain probability, which would introduce further unknown parameters.

According to (2) and the value of 36 Mev which we have accepted for the kinetic energy of the distinguished particle, the intermediate particle has a mass $x=595m_e$; the Q value for its decay would then be 22 Mev. This is much higher than the proposed Q value for the ζ^0 meson.[2]

In all the above considerations we have disregarded the distinction of the π mesons by their charges, because in the events we have discussed, the experimenters have not been able to determine them. Assuming that the charges of all the secondary particles are known, our statistical considerations (in particular the test of the sharp value) would only be correct if we admit the possibility of doubly charged intermediate particles, which is hardly convincing. Rejecting this possibility, the particle with the sharp energy value would have to have the same sign as the τ meson, and this restricts the choice of the set T_i in (4).

Note added in proof.—We are indebted to Dr. R. H. Dalitz for details of recently observed particles. The individual energies of the π mesons in one of these events, found by the Bristol group, are 16.0, 16.9, and 41.3 Mev, of which the first two have positive charges. The standard deviation for each was about 0.9 Mev. These results together with data already available are not consistent with the scheme proposed, for any choice of the sharp value.

Radiochemical Evidence for the $Cu^{65}(p,p\pi^+)Ni^{65}$ Reaction*

SI-CHANG FUNG† AND ANTHONY TURKEVICH
Institute for Nuclear Studies, University of Chicago, Chicago, Illinois
(Received March 29, 1954)

A study of the formation of the radioactive nickel isotopes in the irradiation of copper foil with high-energy protons has shown the presence of 2.56-hr Ni^{65}. The energy dependence of the cross section for the formation of this species, and its recoil properties, indicate that it is formed by the $Cu^{65}(p,p\pi^+)Ni^{65}$ reaction.

INTRODUCTION

THERE have been several attempts to demonstrate radiochemically the production of mesons in the irradiation of complex nuclei with high-energy particles.[1] These have usually involved examination for products with charges sufficiently higher than the target nucleus to require the accompanying formation of negative mesons. The results to date have been negative, due either to the low intensities available, or to the masking effect of secondary reactions produced in the target by alpha particles (or particles with higher charge) made in a primary interaction of the high-energy particle with the target. It is, therefore, of some interest to report radiochemical evidence for, and some characteristics of, a nuclear reaction unambiguously involving mesons.

The reaction studied was the production of 2.56-hr Ni^{65} in the irradiation of copper with protons.[2] Since the heaviest stable isotope of copper is Cu^{65}, the reduction in charge without reduction in mass number can only be accomplished with protons by the emission of one nucleon and two positive charges. The simplest interpretation is to assume that the reaction involved is $Cu^{65}(p,p\pi^+)Ni^{65}$. Quite obviously the production of Ni^{65} from impurities in the copper or via other particles than protons had to be excluded. Likewise the energy dependence of this reaction and the recoil properties of the product had to be consistent with the stated interpretation. In the following we give evidence on these points.

EXPERIMENTAL PROCEDURES

All the irradiations were made with the internal beam of the University of Chicago 170-inch synchrocyclotron. The radial position of the probe target was used to select the particle energy. A clamp arrangement held a thin pure copper foil (less than 10^{-2} percent zinc) sandwiched between 0.25-mil aluminum foils. The edges of all the foils were flush with each other so that all were exposed to the same beam intensity.

The target was arranged so that the proton beam first hit an aluminum foil *A*, then the copper foil, then four aluminum foils in the order *B*, *C*, *D*, and *E*. The Na^{24} or Na^{22} activity in foil *D* was used as a monitor of the beam intensity. The cross section for the production of these sodium isotopes from aluminum as a function of energy was taken from Stevenson and Folger,[3] Marquez,[4] and Fung.[5] After an irradiation, nickel was separated radiochemically from the copper foil and from the aluminum foils *A*, *B*, *C*, and *E*.

The chemistry consisted of repeated precipitations of nickel dimethyl glyoxime, with and without holdback carriers, together with numerous acid scavenging steps using copper, palladium, and antimony sulfides, and ammoniacal scavengings with iron and chromium. On several occasions the adequacy of the chemistry was tested by recycling.

The radioactivity was measured with end-window atmospheric pressure methane proportional counters. 2.6-hr and 36-hr half-lives were the main periods observed in the radiochemically purified nickel, and it was assumed that they were Ni^{65} and Ni^{57}, respectively.

The Ni^{57} and Ni^{65} radioactivities were found predominantly in the copper, and measured the production of these nuclides in proton reactions with copper. The amount of these nuclides in the aluminum foils *C* and *E* was very small (a few percent of the amount in foil *B*), presumably resulting from the activation of impurities in the aluminum. The amount of Ni^{57} and Ni^{65} in the aluminum foils *A* and *B* (after correcting for the amounts in *C* and *E*) measured the loss backward and forward from the copper due to recoil effects.

RESULTS

Table I gives the cross sections observed for the production of Ni^{57} (column 2) and Ni^{65} (column 3) from copper as a function of proton energy between 100 Mev and 440 Mev (column 1). It is seen that the cross section for producing Ni^{57} stays relatively constant (~1.5 mb) in this energy range. The value of 1.4 mb at 350 Mev is in satisfactory agreement with the value of 1.8 mb obtained by Batzel, Seaborg, and Miller with 340-Mev protons.[2] On the other hand, the

* This work was supported in part by a grant from the U. S. Atomic Energy Commission.

† Present address: Department of Chemistry and Laboratory for Nuclear Science, and Department of Physics, Massachusetts Institute of Technology, Cambridge, Massachusetts.

[1] See, e.g., Bonner, Friedlander, Pepkowitz, and Perlman, Phys. Rev. **71**, 511 (1947).

[2] Batzel, Miller, and Seaborg, Phys. Rev. **84**, 671 (1951) studied the spallation of copper with 340-Mev protons and found both Ni^{57} and Ni^{65} among the products. They ascribed the formation of the latter to secondary neutrons causing (n,p) reactions (see text).

[3] P. C. Stevenson and R. L. Folger (private communication).

[4] L. Marquez (private communication).

[5] Si-Chang Fung (to be published).

TABLE I. Cross section for producing Ni^{65} and Ni^{57} and their recoil properties in the proton bombardment of copper.

Energy of proton Mev	Cross section for forming Ni^{57} (millibarns)	Cross section for forming Ni^{65} (millibarns)	Cross section for the reaction $Cu^{65}(p,p\pi^+)Ni^{65}$ [a] (millibarns)	Percent of Ni^{57} caught on Al foil[b] For.	Back.	Percent of Ni^{65} caught on Al foil[b] For.	Back.
100	1.3	0.006	0	1.14			
200	1.9			1.11			
200	1.8	0.009	0.003	1.06			
250	1.4	0.021	0.015				
250	1.5			1.07			
300	1.5			1.01			
300	1.3	0.032	0.026	1.05		1.47	
350	1.4	0.056	0.050				
400	1.4	0.078	0.072	0.93		1.11	
400	1.4			1.00			
430	1.4	0.087	0.081	0.91	0.095	1.10	0.06
430	1.3			0.93			
440	1.1	0.084	0.078	0.84		1.12	
440	1.2	0.092	0.086	0.77		1.12	
440	1.3	0.093	0.087	0.82		1.11	
440	1.3	0.088	0.082	0.96		1.17	

[a] The values in this column were obtained from those in the preceding one by subtracting 0.006 mb ascribable to secondary neutrons (see text).
[b] The main copper foil had a thickness of 23.9 mg/cm².

cross section for making Ni^{65} rises from 0.006 mb at 100 Mev to around 0.09 mb at 440 Mev, with a sharp rise occurring above 200 Mev.

Table I also indicates the recoil properties of Ni^{57} and Ni^{65} from 23.9 mg/cm² copper. It is seen that Ni^{65} recoils forward an amount comparable to, but always a little more than, Ni^{57}. The backward recoil was determined only at 430 Mev. It is very small for both nuclides, but the asymmetry seems definitely larger for Ni^{65}.

Because of the low cross section for producing the Ni^{65}, assorted extraneous mechanisms for making it had to be considered. In the first place, spallation or a fission-type reaction on impurities with charge higher than copper could give rise to Ni^{65}. To test this, the production of Ni^{66} (by milking its Cu^{66} daughter) was investigated. It was found that the ratio Ni^{66}/Ni^{65} was $\sim$0.005 in our experiments, whereas spallation and fission reactions form this pair in ratios much closer to unity. For example, this ratio varies between 0.5 and 1 in the 450-Mev proton spallation of elements between holmium and thorium[6] and is 0.2 in the spallation of arsenic by 190-Mev deuterons.[7]

A second possible extraneous source of Ni^{65} are (n,p) reactions in the copper induced either by neutrons formed in the target or by stray neutrons in the cyclotron. The contribution of these was investigated by studying the production of Ni^{65} relative to Ni^{57} under different experimental conditions. Ni^{57} is made from copper in high yield by the primary proton beam and should be made in low yield, if at all, with lower-energy neutrons. Important contributions from neutrons born in the target can be excluded on the basis of an experiment involving a target made up of five copper foils of standard thickness and somewhat wider. These gave a Ni^{65}/Ni^{57} ratio of 0.0272 in each foil under certain conditions of irradiation, counting, and decay, compared to a ratio of 0.0247 obtained in single-foil irradiations. The average path length of secondary neutrons is considerably larger in this thick-foil experiment than in the thin-foil experiment. The small increase in the Ni^{65}/Ni^{57} ratio observed indicates a possible seven percent contribution form secondary neutrons to the cross section of formation of Ni^{65} at 440 Mev.

A second argument for excluding large contributions from secondary neutrons is the asymmetry of the recoils. Bernardini *et al.*[8] have shown that the ratio of forward to backward black prongs (energy less than 30 Mev) in all stars in photographic plates induced by 375-Mev protons and 300-Mev neutrons is approximately two to one. This same asymmetry would then be expected for the secondary neutrons and for the recoil products from their (n,p) reactions. On the other hand, in the experiments reported here, the Ni^{65} recoil activity found in the forward aluminum foil was about seventeen times as great as in the backward one. We conclude, then, that secondary neutrons born in the target are not the main cause of Ni^{65}.

The general neutron background at the cyclotron is excluded both by the recoil behavior described above and by an experiment in which two parts of a copper

[6] Paul Kruger, Ph.D. thesis, University of Chicago, January, 1954 (unpublished).
[7] H. H. Hopkins, Phys. Rev. **77**, 717 (1950).
[8] Bernardini, Booth, and Lindenbaum, Phys. Rev. **85**, 826 (1952).

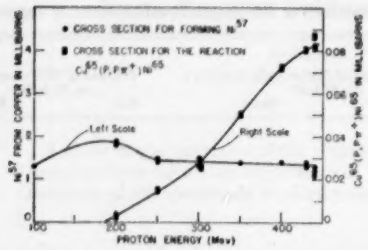

FIG. 1. The cross section for producing Ni^{57} and Ni^{65} in the proton bombardment of copper.

target were analyzed for Ni^{57} and Ni^{65} production. The first part was the leading edge of the target that received the main part of the proton beam. The other was a strip 1.4 cm further out radially. This was irradiated with only one-third the number of protons. The Ni^{65}/Ni^{57} ratio was 0.0247 in the leading edge and 0.0250 in the outer piece. Since it is not likely that any general neutron background is confined to the beam region, the constancy of this ratio precludes any important contribution to the formation of Ni^{65} by this mechanism.

The possibility that the Ni^{65} is caused by secondary particles other than neutrons is made unreasonable by the large cross section that would have to be assigned to reactions of usual character, e.g., $(d,2p)$, $(He^4,3pn)$, etc., and by the directional properties and the effect of thickness discussed above.

From the activation of thick and thin targets at 440 Mev (see above), about 7 percent of the Ni^{65} produced is ascribed to secondary neutrons. This is a 0.006-mb apparent cross section, close to that found at 100 Mev. We ascribe the Ni^{65} made at the low energy to this origin. The cross section at intermediate energies is corrected for the neutron effect by assuming 0.006 mb for this mode of production at all energies. The corrected values of the cross section for the reaction $Cu^{65}(p,p\pi^+)$-Ni^{65} are given in column 4 of Table I. These should be good to about $\pm 5\times 10^{-3}$ mb. These corrected values for forming Ni^{65} and the cross sections for forming Ni^{57} are plotted in Fig. 1.

DISCUSSION

The most reasonable interpretation of the curve in Fig. 1 giving the cross section for forming Ni^{65} is that it represents the reaction $Cu^{65}(p,p\pi^+)Ni^{65}$. The observed apparent threshold at around 200 Mev is consistent with this picture. For example, the production of π^+ at 90° in the proton bombardment of carbon has a very similar energy dependence (see Fig. 2). The recoil behavior of the Ni^{65} formed is likewise consistent in that it is similar to that of Ni^{57} which also requires the absorption of energy of the order of 100 Mev to extract the required particles from Cu^{63}.

The absolute value of the cross section appears to be reasonable by the following argument: The $Cu^{65}(p,p\pi^+)$-Ni^{65} process can be thought of as due to the reaction

$$p+p\rightarrow p+n+\pi^+$$

occurring inside the nucleus. If the final nucleus is to be Ni^{65}, the requirement exists that the resulting neutron acquire less than about 10-Mev kinetic energy and thus remain in the nucleus, and that the proton and meson get out without further interaction. This "meson-production scattering" inside the nucleus might then be compared to "elastic scattering" inside the nucleus. An example of this is the $Ni^{64}(p,n)Cu^{64}$ reaction being studied radiochemically by Koch and Turkevich.[9] This can be regarded as arising from the scattering process

$$p+n\rightarrow p+n$$

occurring inside the nucleus, with again a restriction on the final energy of the proton left in the nucleus. This reaction has a cross section of ~1 mb at 440 Mev.[9]

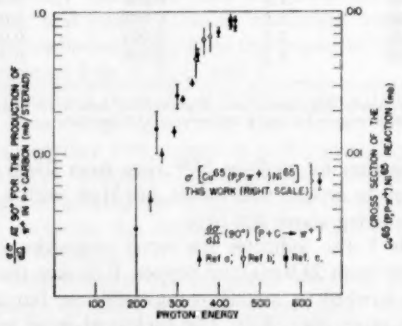

FIG. 2. Comparison of the energy dependence of the cross section of the $Cu^{65}(p,p\pi^+)Ni^{65}$ reaction with the energy dependence of the production of positive mesons in the proton bombardment of carbon at 90°. The references in the figures are as follows: (a) D. A. Hamlin, University of California Radiation Laboratory Report UCRL 2414, November 20, 1953 (unpublished); (b) Passman, Block, and Havens, Phys. Rev. **88**, 1247 (1952); (c) A. Rosenfeld, University of Chicago (private communication). (The numbers on the right-hand side of the diagram should read 0.10 and 0.01.)

The total production of π^+ in the 440-Mev proton bombardment of protons (leading to an unbound neutron and proton) is 1 to 2 mb.[10] The total (n,p) cross section at these energies is 34 mb.[11] Thus the ratio of the cross section of the $p(p,p\pi^+)n$ reaction to the (p,n) scattering cross section is about the ratio of the cross section for the $Cu^{65}(p,p\pi^+)Ni^{65}$ reaction to that of the $Ni^{64}(p,n)Cu^{64}$ process. We conclude that the absolute cross section observed is a reasonable one for the interpretation made.

ACKNOWLEDGMENT

The cooperation in this work of the directing and operating staff of the 170-inch synchrocyclotron is appreciatively acknowledged.

[9] R. C. Koch and A. Turkevich, University of Chicago (private communication).
[10] A. Rosenfeld, University of Chicago (private communication).
[11] V. A. Nedzel, Phys. Rev. **90**, 169 (1953).

Photoproduction of Charged Pi Mesons from Hydrogen and Deuterium*

T. L. JENKINS, D. LUCKEY,† T. R. PALFREY,‡ AND R. R. WILSON
Cornell University, Ithaca, New York

(Received March 12, 1954)

Photoproduction cross sections of charged pi mesons from hydrogen and deuterium have been measured as a function of meson angle at gamma-ray energies of 200, 235, and 265 Mev. The angular range extends from 30° to 180° in the laboratory system. Absolute cross sections have been determined. A least-squares fit of the measured cross sections has been made to the expression $A+B\cos\theta+C\sin^2\theta$, which assumes only S and P wave scattering. The coefficients so determined are qualitatively consistent with electric and magnetic dipole absorption together with the assumption of a resonant state of angular momentum $\frac{3}{2}$ and of energy close to 300 Mev. Comparison with neutral meson production indicates some direct charged meson production in the P state.

I. INTRODUCTION

IT is of interest to study the system consisting of a single meson and a single nucleon interacting with each other. Much emphasis has been given to the scattering of mesons by protons, but the problem can also be studied from another point of view, namely, production of mesons by gamma rays incident on protons. The first photoproduction experiment from hydrogen was that of Steinberger and Bishop.[1] Other experiments are in progress or have been completed at other laboratories.[2,3]

We have measured the photoproduction cross sections of charged pi mesons from hydrogen as a function of meson angle at gamma-ray energies of 200, 235, and 265 Mev. A magnetic deflection method was used to detect the mesons and determine their energy. This obviates some of the difficulties inherent in the early measurements. In the expectation of obtaining reliable absolute cross sections, the intensity of the synchrotron beam has been carefully calibrated.

(a) Identification of the Mesons

Figure 1 shows the general arrangement of the apparatus. The gamma-ray beam of the Cornell synchroton passed through a lead collimator onto the meson producing target. A double-focusing magnet bent mesons produced at an angle θ to the gamma-ray beam through 90° to a counter telescope. The front slits of the magnet determined the angular acceptance; the rear slits and the strength of the magnetic field determined the energy of mesons counted in the telescope. An ion chamber placed behind the target monitored the gamma-ray beam. The production of mesons from hydrogen and deuterium was studied by carbon-polyethane and light-heavy water subtractions.

Mesons were identified by (1) having momenta and charge such that the magnetic field would deflect them into the counter telescope, and (2) having a sufficient range to penetrate the absorbers in the counter telescope. Protons and heavier particles of the same momentum as the mesons studied could not penetrate the absorbers. Electrons and positrons of high energy (100 to 200 Mev) would cause counts; however, they were important only at forward angles.

Some of the confirming experimental evidence that the counts were due to mesons are the following:

(1) Experimental work at Cornell using a two-magnet system and a cloud chamber showed that momentum separation at 135° gives a pure meson beam.[4]

(2) Range curves taken by placing absorbers in the counter telescope were in agreement with that expected for a meson beam with the predicted energy spread.

(3) The mesons were stopped in a carbon absorber after traversing the counter telescope. Trays of Geiger counters were located at the top and bottom of the

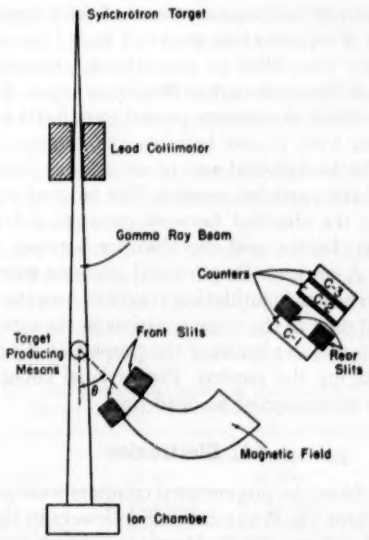

FIG. 1. Experimental layout (not to scale).

* Supported by joint program of U. S. Office of Naval Research and the U. S. Atomic Energy Commission.
† General Electric Fellow 1953.
‡ Now at Purdue University, Lafayette, Indiana.
[1] J. Steinberger and A. S. Bishop, Phys. Rev. **86**, 171 (1952).
[2] White, Jacobson, and Schulz, Phys. Rev. **88**, 836 (1952).
[3] Jarmie, Repp, and White, Phys. Rev. **91**, 1023 (1953).
[4] Camac, Corson, Littauer, Shapiro, Silverman, Wilson, and Woodward, Phys. Rev. **82**, 745 (1951).

carbon absorber, and were in delayed coincidence with the counter telescope. The stopped particles had a mean life of about 2 microseconds, in agreement with the known lifetime of the mu mesons.

(4) An excitation curve for the production of 54-Mev mesons from beryllium at 90° was made by varying the maximum energy of the synchrotron.[5] Below the threshold for meson production no counts within the statistics were observed. However, electrons and positrons with sufficient energy to traverse the system could still have been produced by the gamma-ray beam.

(b) The Magnet System

The magnet, which weighed five tons, was double-focusing with horizontal and vertical focal lengths equal ($n=\frac{1}{2}$). Mesons with energy up to 85 Mev could be bent through 90° with about a 25-cm radius of curvature. The meson-producing target was placed at the focus of the magnet so that mesons of a given momentum emerged in parallel bundles. Different momenta were bent through different angles. A lead slit about 8 cm wide and located 40 cm from the exit of the magnet selected the momenta counted by the telescope. The front slits (uranium) determined the angular acceptance and limited the meson trajectories to the usable part of the field. All the slits, the counter telescope, and the target holder were mounted rigidly to the magnet yoke so that the complete system remained identical when the magnet was moved from angle to angle.

(c) The Counter Telescope

The counter telescope consisted of three proportional counters of square cross section 2 in.×2 in. and 6 in. long; they were filled at atmospheric pressure with a mixture of 5 percent carbon dioxide in argon. The walls through which the mesons passed were 0.003-in. brass. Absorbers were placed between the counter walls to reduce the background and to set a lower limit on the range of the particles counted. For most of the measurements the absorber between counters C-1 and C-2 was $\frac{1}{16}$-in. Lucite, and the absorber between C-2 and C-3 was $\frac{1}{16}$-in. lead. Proportional counters were chosen in preference to scintillation counters because of their lower response to the stray neutrons in the synchrotron room. No use was made of the proportional properties in identifying the mesons. Proportional counters also have the advantage of no dead time.

(d) Electronics

Pulses from the proportional counters were preamplified and sent via White cathode followers to the detection room where 204-B Atomic amplifiers were used. Shaped pulses were fed into a Rossi coincidence circuit which had a resolving time of about 0.5 microsecond. Those input pulses which caused coincidences were watched by a pulse-height analyzer; the gain of the amplifiers were adjusted so that the pulses causing the coincidences were well above the discrimination level.

(e) Targets

The targets used were cylinders 1 inch in diameter with their axes perpendicular to the plane of the pole pieces and the gamma-ray beam. If the beam were uniform over the target, then the target geometry would be independent of the angle of the magnet system with respect to the gamma-ray beam. Various special targets were constructed for certain aspects of the experiment. These included a carbon target designed to produce as many electrons as the polyethane target (used at forward angles), a carbon target having the same average stopping power as the polyethane target (used at low meson energies), and a small polyethane target $\frac{1}{2}$ in. high and $\frac{1}{2}$ in. in diameter (used to check the calibration of the solid angle).

(f) The Gamma-Ray Beam

The gamma-ray beam used in this experiment was the bremsstrahlung from 304–309 Mev electrons striking a 0.040-inch tungsten target in the Cornell synchrotron. The resulting spectrum of gamma rays has been measured at Cornell by J. W. DeWire and in the energy region of this experiment was not significantly different from the Bethe-Heitler spectrum. The calculations were made assuming a Bethe-Heitler spectrum. The gamma-ray beam was spread in time by turning off the rf slowly, so that the period of expulsion was 1.5 milliseconds centered about the peak of the magnetic cycle. Electrons striking the target lay in the energy range from 304 to 309 Mev, with an average energy of 307 Mev. The gamma-ray beam was collimated by a $\frac{1}{2}$ in.×$\frac{1}{2}$ in. square slit of lead located at a distance of 1.5 meters from the target. For some of the angles, additional collimation was used behind this collimator. The measurements at 180° were made using a $\frac{3}{8}$ in. ×$\frac{1}{2}$ in. collimator in order that the beam would not hit the poles of the magnet. The beam was monitored by a thick-walled (copper) air-filled ionization chamber (standard at Cornell) located behind the meson producing target. The chamber was calibrated with the pair spectrometer and by use of shower curves in aluminum.

II. CALCULATION OF THE CROSS SECTION

(a) Expression for the Cross Section

Because we were studying a two-body process, the measurement of the energy and angle of the meson uniquely specified the reaction including the gamma-ray energy. The computation of a cross section from the observed counting rate required a knowledge of (1) the

[5] D. Luckey, Phys. Rev. **90**, 711 (1953).

gamma-ray beam, (2) the magnet system, (3) the losses due to decay in flight of pi mesons, (4) the kinematics of the reaction, and (5) the structure of the target. The properties of the gamma-ray beam which had to be known were the spatial distribution of the intensity across the beam, the energy spectrum of the gamma rays and the intensity. The intensity was measured by the monitoring ionization chamber. The magnet system can be described by the meson energy which is a function of the magnet current and the solid angle which is a function of meson energy at a fixed magnet current. The structure of the target had to be known both physically and chemically. From the definition of differential cross section we have that the number of mesons, N_π, produced is given by

$$N_\pi = Nt' \int_\nu \left(\frac{d\sigma}{d\Omega}\right) \Omega(\nu) N(\nu) d\nu,$$

where N is the number of target nuclei, t' is the effective target thickness, $d\sigma/d\Omega$ is the differential cross section, $\Omega(\nu)$ is the solid angle, and $N(\nu)d\nu$ is the energy spectrum of the gamma rays.

In practice the integration is done over meson energy T rather than ν. Ω is then a property of the magnet system which was measured. The number of gamma rays was obtained from the bremsstrahlung spectrum and the charge collected on the ion chamber. The effective thickness of the target was calculated from the spatial distribution of the beam and the geometry of the target and experimentally measured by changing the target size. The effective thickness differs by about 10 percent from that one would calculate geometrically. N_π is obtained by correcting the counting rate for the various losses. The differential cross section was then obtained and, via the known kinematics, transformed to the center-of-mass system.

(b) Corrections to the Counting Rates

The following corrections were applied to the observed counting rates to get N_π:

(1) π-μ decay in flight;
(2) scattering out of the meson beam in the various absorbers and air;
(3) nuclear absorption of the pi mesons in various materials;
(4) penetration of the rear slit;
(5) high-energy electrons at forward angles;
(6) absorbers in front of the magnet;
(7) distortion of the low-energy spectrum of mesons due to scattering of higher-energy mesons in the front slits;
(8) misalignment of the gamma-ray beam with respect to the target.

The distance from the meson-producing target to the counter telescope was 100 cm. Thus ten to twenty

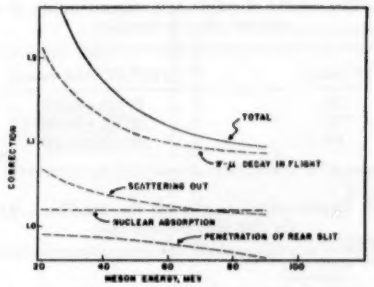

FIG. 2. Corrections to counting rate as a function of meson kinetic energy in the magnet.

percent, depending on the energy, of the mesons would decay in flight. Most of the residual μ mesons could not traverse the telescope because of the good vertical geometry. The actual correction as a function of meson energy is shown in Fig. 2 (this includes the small number of μ mesons which could still penetrate the counter).

Nuclear absorption is a small correction because of the thinness of the absorber placed in the meson beam. The absorption cross section was taken as that corresponding to a radius of $1.4\times10^{-13}A^{\frac{1}{3}}$ cm. The correction was two percent, of which about half was due to absorption in the meson-producing target and half due to lead absorber between C-2 and C-3.

Multiple scattering by the various materials in the meson path could cause counting losses because of the good vertical geometry of the telescope. A correction of between two and five percent was determined by calculation. The calculation was checked by placing a scatterer directly in front of the counter telescope and then observing the decrease of the coincidence counting rate. Figure 2 shows the variation of this small correction with meson energy.

The correction for penetration of the slit edges by the mesons amounted to about three percent at most, and is shown in Fig. 2.

Table I summarizes the corrections which depend upon the energy of the meson and shows the estimated errors in these corrections.

At forward angles it was necessary to make a correction for scattered electrons. At 30° a correction of 13 percent to the 200-Mev photon and 5 percent to the 235-Mev point was determined experimentally. This was done by performing the following auxiliary experi-

TABLE I. The magnitudes and errors of those corrections which depend upon the meson kinetic energy.

Correction factor	Meson kinetic energy 30 Mev	50 Mev	80 Mev
Decay	1.16±0.02	1.11±0.01	1.09±0.01
Nuclear absorption	1.02±0.01	1.02±0.01	1.02±0.01
Multiple scattering	1.05±0.02	1.03±0.01	1.02±0.01
Slit penetration	0.99±0.01	0.98±0.02	0.97±0.02
Total	1.23±0.03	1.14±0.03	1.10±0.03

TABLE II. The results of solid-angle measurements at different magnetic field intensities.

T (Mev)	$\int\Omega(T)dT$ (Mev-sterad)
31	0.103±0.007
54	0.151±0.008
84	0.189±0.009

TABLE III. Experimental results for the reaction $\gamma+p\rightarrow\pi^{+}+n$ for 200-Mev gamma rays.

θ_{cm}	Corrected center-of-mass cross section (μb/sterad)	Statistical error (%)	Corr. for loss	Special corrections
39	7.0±1.1	13.5	1.13	1.13[a]
59	10.5±1.2	7.7	1.15	1.02[a]
75	9.5±1.3	10.6	1.17	
107	9.6±1.3	10.2	1.22	
135	11.9±1.9	13.7	1.28	

[a] Electrons.

ments: (1) A search for negative particles being produced from hydrogen was made; this was also done at 90° and no negative mesons were found. Hence, the negative rate from hydrogen at 30° could be expected to estimate the number of scattered electrons. (2) By placing a fourth counter behind the counter telescope with sufficient absorber in front of it to stop the meson beam, electrons could be detected in this counter either directly or through the production of a small shower. The efficiency of the electron counter, about 30 percent, was calibrated using a high-Z target which essentially produces only electrons. (3) By varying the thickness of the target and looking for a nonlinearity in the counting rate, the number of electrons can be estimated since the electron rate will vary as the square of the target thickness. An attempt was made to move to 15° in the laboratory, but the electron rate was too large for the subtraction technique.

For the highest photon energy studied and at forward angles, the meson energy was greater than could be detected by the magnet-counter system. Aluminum absorbers were placed in front of the magnet so that the energy spectrum of the incident mesons would be shifted downward into the range of the magnet. A total correction of between seventeen and sixty percent was necessary due to (a) the nonlinearity of the range-energy curve, (b) nuclear absorption, and (c) conversion of gamma rays produced by neutral mesons into electrons which could then be counted. In order to test the absorber method, the same mean energy of mesons was studied at two different magnet current settings, with and without an absorber. When the above corrections were applied, the results agreed within the statistics.

(c) Solid Angle Measurements and Resolution

The solid angle and resolution of the magnet system were studied and calibrated by means of the current carrying wire technique. A small mirror was mounted on the wire near the target holder. The mirror reflected a beam of light to a screen; hence measuring the relative angle between the mirror and the light beam. With the current and tension adjusted to correspond to a given meson energy T, the wire was positioned so that it just grazed one of the defining apertures, and the position of the light beam recorded. The wire was then moved so that it grazed some other part of the aperture. In this manner a projection of the aperture corresponding to the given energy was traced out on the screen. The solid angle $\Omega(T)$ can then be calculated from a knowledge of the geometry of the screen and light source. With a given magnetic field the apertures were traced out for many different energies which could pass through the system. The integral $\int\Omega(T)dT$ could then be computed.

To reach high meson energies, it was necessary to saturate the iron of the magnet. The main effect of the saturation is a loss of vertical focusing. At high current, the integrated energy solid angle falls below that predicted for an ideal magnet. Solid angle measurements were made at magnet currents corresponding to mean meson energies of 31, 54, and 84 Mev. The results of these measurements and their estimated accuracy are shown in Table II. The integrated solid angles at other meson energies were determined by interpolation based on a knowledge of the point of saturation and the behavior of an ideal magnet.

The band of gamma-ray energies accepted by the magnet system is relatively independent of the experimental angle. The full widths at half-maximum were

TABLE IV. Experimental results for the reaction $\gamma+p\rightarrow\pi^{+}+n$ for 235-Mev gamma rays.

θ_{cm}	Corrected center-of-mass cross section (μb/sterad)	Statistical error (%)	Corr. for loss	Special corrections
39	9.7±1.1	7.6	1.10	1.05[a]
59	11.6±1.0	4.3	1.10	
75	13.3±1.2	4.8	1.11	
107	14.6±1.3	3.3	1.13	
135	14.8±1.4	5.0	1.18	
161	15.8±1.7	7.0	1.21	
180	11.3±1.2	7.2	1.22	

[a] Electron contamination.

TABLE V. Experimental results for the reaction $\gamma+p\rightarrow\pi^{+}+n$ for 265-Mev gamma rays.

θ_{cm}	Corrected center-of-mass cross section (μb/sterad)	Statistical error (%)	Corr. for loss in magnet	Absorber correc.
39	8.0±1.0	8.0	1.10	1.61
59	11.6±1.1	5.6	1.10	1.30
75	18.2±1.7	4.7	1.10	1.17
107	19.9±1.7	3.4	1.11	
135	19.9±1.8	5.2	1.13	
161	17.0±2.4	11.7	1.15	
180	14.8±1.5	5.8	1.17	

estimated to be 15 Mev at 200 Mev, 22 Mev at 235 Mev, and 30 Mev at 265 Mev. The extreme limits which can contribute were estimated to be 200±10, 235±15, and 265±20 Mev. In arriving at the above estimates, the broading of the intrinsic magnetic resolution by the finite size of the target and the energy loss therein has been included.

III. EXPERIMENTAL RESULTS

(a) Photoproduction from Hydrogen

Tables III, IV, and V give our results for the cross sections for the reaction $\gamma+p\rightarrow\pi^+ +n$ at gamma-ray energies of 200, 235, and 265 Mev. The tables also show the statistical error in the counting rate and the magnitudes of the various corrections applied. The errors given on the cross sections include the statistical counting rate error plus estimates of the errors in the corrections and in the determination of the solid angle.

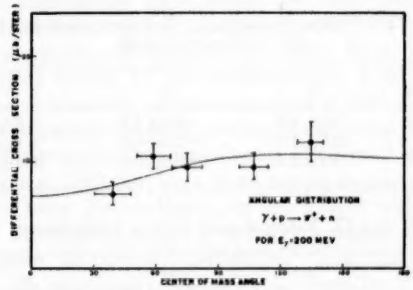

FIG. 3. Angular distribution at $E_\gamma=200$ Mev.

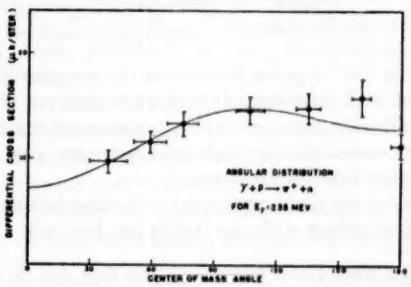

FIG. 4. Angular distribution at $E_\gamma=235$ Mev.

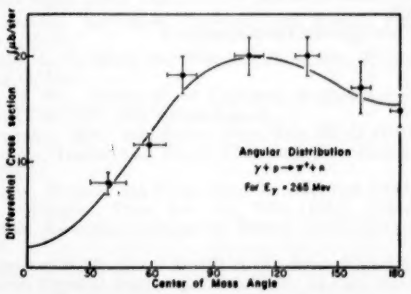

FIG. 5. Angular distribution at $E_\gamma=265$ Mev.

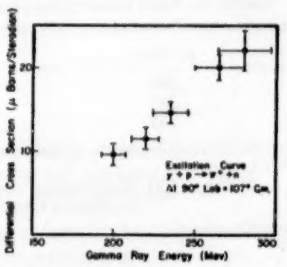

FIG. 6. Excitation curve for $\gamma+p\rightarrow\pi^+ +n$ at 90° lab $=107°$ c.m.

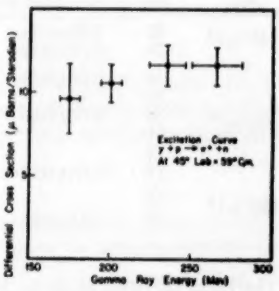

FIG. 7. Excitation curve for $\gamma+p\rightarrow\pi^+ +n$ at 45° lab $=59°$ c.m.

In addition, the absolute scale of the cross section may be in error because of uncertainties in the calibration of the gamma-ray beam and other systematic errors.

The angular distributions are shown in Figs. 3, 4, and 5. Excitation functions at 45° and 90° are shown in Figs. 6 and 7.

Table VI shows the total cross sections for the reaction at the various energies.

(b) Photoproduction from Deuterium

Table VII shows the experimental ratios of charged pi-meson production from deuterium to the production from hydrogen.

(c) Search for Negative Mesons from Hydrogen

A special search was made for negative mesons produced from hydrogen with a bremsstrahlung spectrum of maximum energy 310 Mev. The experiment was performed at 90° in the laboratory system with the magnet set to accept 34-Mev mesons. Special large targets were constructed to increase the counting rates. To check that the targets contained the same amount of carbon the negative rate was also measured for 78-Mev mesons. In both cases no negative particles were detected from hydrogen within the counting statistics. The positive rate from hydrogen was also measured from the same target. The negative rate was 1 percent±4 percent of the positive rate for 34-Mev mesons at 90°.

IV. DISCUSSION

Arbitrarily assuming that only S and P waves contribute to the cross section in this energy region, one can write

$$\sigma'=A+B\cos\theta+C\sin^2\theta.$$

TABLE VI. Total cross sections for the reaction $\gamma+p\rightarrow\pi^{+}+n$.

E (Mev)	$\sigma_{\text{total}}(10^{-28}$ cm$^2)$
200	1.22±0.09
235	1.64±0.06
265	1.96±0.08

TABLE VII. Experimental results for charged meson production from deuterium.

θ_{lab}	Mev	π^+ from deuterium / π^+ from hydrogen	π^- from deuterium / π^+ from hydrogen	(π^-/π^+) from deuterium
45°±7°	48	1.07±0.14	0.57±0.09	0.54±0.11
	78	0.77±0.13	0.76±0.06	0.98±0.19
90°±7°	34	0.73±0.14	0.77±0.16	1.06±0.32
	46		0.81±0.17	
	54	0.72±0.09	1.07±0.15	1.49±0.25
	64		0.74±0.09	
	72		0.69±0.06	
	84	0.58±0.13	0.76±0.09	1.31±0.34
180°±7°	34		0.98±0.27	
	46	0.92±0.18	0.87±0.19	0.85±0.26

The cross sections given in Table III, IV, and V were least squares fitted to the above expression. The values of the coefficients so obtained are given together with their standard deviations in Table VIII. The errors in the coefficients are correlated. That the data are well fitted can be seen in Figs. 3, 4, and 5.

Following Brueckner and Watson[6] and Feld,[7] one can write the following relationships between the above coefficients and the amplitudes a and b (respectively for electric dipole and magnetic dipole absorption), assuming that the p-wave contribution to the process goes through a definite state of total angular momentum $\frac{3}{2}$:

$$A=a^2+b^2, \quad B=2ab\cos\phi, \quad C=\tfrac{3}{2}b^2.$$

ϕ is the phase angle between the S and P waves. Table IX gives the values of a^2, b^2, and ϕ, together with their standard deviations.

The dependence of a^2 with increasing energy is reminiscent of other S-wave dipole transitions such as the magnetic dipole photodisintegration of the deuteron. The amplitude of the P wave increases very rapidly with energy and invites comparison with the neutral photomeson production data. If one assumes that both neutral and charged photoproduction in the P state go through the same state of total angular momentum, then one must allow another internal degree of freedom to determine the branching ratio. Brueckner and Watson and Feld have assigned an isotopic spin of $\frac{3}{2}$ to the state, in which case it follows that the neutral production should be twice the charged production in the P-wave state. It appears that the P-wave part of neutral production is equal or less than the charged production.[8–10] This indicates that the above assumptions are wrong. Perhaps this implies that electric quadrupole absorption is also important in the process. Chew[11] has indicated, that there can be a direct interaction in the P state in the case of charged production which may not occur in neutral production. This might account for the discrepancy in the branching ratio. The behavior of ϕ with energy is just that expected if there were a resonant state at about 300 Mev. Thus, ϕ should change by 180° in going from below the resonant energy to above it, if the phase of the S wave does not change too rapidly. It thus appears that our data are consistent with the existence of a single resonant state of angular momentum $\frac{3}{2}$ and isotopic spin $\frac{3}{2}$.

We are in excellent agreement with other laboratories where comparison with our results can be made.

TABLE VIII. Values of coefficients in least-squares fit of form $\sigma'=A+B\cos\theta+C\sin^2\theta$.

E (Mev)	A	B	C
200	8.5±2.2	−1.9±1.3	1.8±2.9
235	10.0±1.0	−2.8±0.8	4.5±1.6
265	8.7±1.1	−6.9±0.9	10.4±2.0

TABLE IX. Values of coefficients in Feld's theory.

E (Mev)	a^2	b^2	ϕ
200	7.4±4.2	1.2±1.9	109°±20°
235	7.0±2.1	3.0±1.1	108°± 5°
265	1.7±2.4	6.9±1.3	175°±25°

[6] K. A. Brueckner and K. M. Watson, Phys. Rev. **86**, 923 (1952).
[7] B. T. Feld, Phys. Rev. **89**, 330 (1953).
[8] Jenkins, Luckey, and Wilson, Bull. Am. Phys. Soc. **29**, No. 1, 18 (1954).
[9] A. Silverman and M. Stearns, Phys. Rev. **88**, 1225 (1952).
[10] Goldschmidt-Clermont, Osborne, and Scott, Phys. Rev. **89**, 329 (1953).
[11] G. Chew (private communication).

400-Mev Neutron-Proton Scattering*

A. J. HARTZLER AND R. T. SIEGEL
Carnegie Institute of Technology, Pittsburgh, Pennsylvania
(Received March 5, 1954)

The angular distribution of neutron-proton scattering has been measured at a neutron energy of 400 Mev, with energy resolution of 7 percent. The counter telescope used to detect recoil protons was calibrated in an auxiliary experiment which also gave information about proton-proton scattering at several energies in the 400-Mev region.

The n-p cross section has the same general characteristics observed at lower energies, with a minimum at about 100° (c.m. neutron scattering angle) and a large exchange peak at 180°. The p-p results indicate an isotropic cross section below 400 Mev, and a rise at small angles at 428 Mev.

I. INTRODUCTION

WITH the availability of large synchrocyclotrons it has been possible to extend neutron-proton scattering experiments far beyond the "classical" region of <10 Mev to energies as high as 300 Mev.[1-8] Although these high-energy experiments are not completely understood theoretically, certain experimental features of the angular distributions are clear. First, a deep minimum occurs in the center-of-mass (c.m.) cross section at about 90°, with a large peak at 180° (neutron scattering angle) caused by exchange scattering. Second, recent cloud-chamber experiments by Powell[9] and coworkers at Berkeley have given strong support to the Serber force (half-ordinary, half-exchange) with a 90-Mev distribution which is symmetric about the 90° minimum. In contrast, DePangher[8] finds that at 300 Mev the small-angle scattering is lower by a factor of two or three than the 180° exchange scattering. Further, high-energy measurements show that the ratio $4(d\sigma/d\Omega)_{n-p}{}^{90°}/(d\sigma/d\Omega)_{p-p}{}^{90°}$ is approaching unity, the lower limit permitted by the charge-independence hypothesis.

It is naturally of interest to study the n-p interaction at even higher energies. In the experiment reported here, the neutron beam of the 440-Mev Carnegie cyclotron was used to measure the angular distribution of n-p scattering at a mean incident energy of 400 Mev. As in all such experiments to date, the recoil protons have been detected and the angular distribution of scattered neutrons deduced from the kinematic relations summarized below. The symbols are mostly those used by Hadley *et al.*[1]

$m_n=m_p=1$;
E_n = incident neutron lab KE $=\gamma-1$, $\gamma=1/(1-\beta^2)^{\frac{1}{2}}$;
E_p = recoil proton lab KE;
Φ, φ = recoil proton lab and c.m. angle, respectively;
Θ, θ = scattered neutron lab and c.m. angle, respectively;

$$\tan\Phi=[2/(\gamma+1)]^{\frac{1}{2}}\cot(\theta/2);$$

$$E_p=\tfrac{1}{2}E_n(1+\cos\varphi)=\tfrac{1}{2}E_n(1-\cos\theta);$$

$$J=\frac{d(\cos\Phi)}{d(\cos\theta)}=\frac{1}{8\cos\Phi}[(\gamma+1)-(\gamma-1)\cos^2\Phi]\frac{1}{\gamma+1}.$$

Primarily we are interested in the *variation* of recoil proton counting rate with laboratory angle, which yields *relative* differential cross sections. When these have been obtained for all angles, *absolute* cross sections can be calculated by normalization of the integrated relative cross section to the total n-p cross section as measured by a transmission experiment.[10]

II. GENERAL DESCRIPTION OF THE EXPERIMENT

The experimental arrangement is shown schematically in Fig. 1. The neutron beam emerged from the

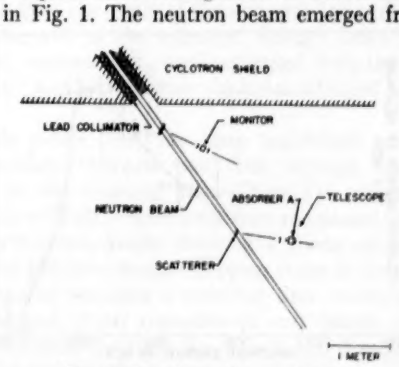

FIG. 1. Experimental arrangement.

* Work supported in part by the U. S. Atomic Energy Commission.

[1] Hadley, Kelly, Leith, Segrè, Wiegand, and York, Phys. Rev. **75**, 351 (1949).

[2] Brueckner, Hartsough, Hayward, and Powell, Phys. Rev. **75**, 555 (1949).

[3] Kelly, Leith, Segrè, and Wiegand, Phys. Rev. **79**, 96 (1950); **83**, 923 (1951).

[4] R. H. Fox, University of California Radiation Laboratory Report UCRL-867, 1950 (unpublished).

[5] Guernsey, Mott, and Nelson, Phys. Rev. **88**, 15 (1952).

[6] Randle, Taylor, and Wood, Proc. Roy. Soc. (London) **213**, 392 (1952).

[7] Selove, Strauch, and Titus, Phys. Rev. **92**, 724 (1953).

[8] J. DePangher, Phys. Rev. **92**, 1084 (1953), University of California Radiation Laboratory Report UCRL-2153 (unpublished).

[9] Reported by Professor Powell at the Annual Meeting of the American Physical Society in New York, January 26-28, 1954 [Bull. Am. Phys. Soc. **29**, No. 1, 49 (1954)].

[10] V. A. Nedzel, Phys. Rev. **91**, 440 (1953) reports a total n-p cross section of $(33.6\pm1)\times10^{-27}$ cm² at 400 Mev.

shielding wall through a three-inch diameter hole and was monitored by a scintillation telescope counting recoil particles from a one-inch thick polyethylene plate. This monitor telescope was fixed at approximately 30° to the beam, and a copper absorber between its two counters insured that only the neutrons above 350 Mev were monitored.

The beam then impinged upon the scattering apparatus, in which recoil particles from polyethylene, carbon, and with no scatterer in place were counted as a function of angle by a three-crystal scintillation telescope. A copper absorber (A) between the last two counters was adjusted in thickness at each angle to make the apparatus insensitive to protons produced in n-p collisions of incident energy less than 365 Mev. A wide range of absorber thicknesses (0.03 in. to 4.45 in.) was necessary for this purpose in the angular region studied. As a result of variations in the loss of protons by nuclear absorption and scattering, there was a large change in telescope efficiency with angle. In order to avoid uncertain calculations of these effects, the efficiency was measured experimentally, as described in Sec. VI.

To obtain the n-p angular distribution, the number of coincidence counts per unit monitor ($=10\,000$ counts) at each angle was measured for each type of scatterer, and the net hydrogen effect was calculated. The CH_2 and carbon scatterers were of approximately equal stopping power; their weights were such that the hydrogen effect was given by

$$R_H=(R_{CH_2}-R_{B1})-0.73(R_C-R_{B1})$$
$$=R_{CH_2}-0.73R_C-0.27R_{B1},$$

where R_{B1} is the "no scatterer" rate.

The n-p data gathered during ten cyclotron runs were normalized to the results of run No. 5 (September 17, 1953), which included the most comprehensive set of measurements. The normalization procedure was as follows: let R_C^1 and R_C^2 be the counting rates obtained from carbon (with background subtracted) at a certain angle on days 1 and 2, respectively. The ratio R_C^1/R_C^2 indicates the change in experimental (i.e., monitoring) conditions between the two days and is therefore the normalizing factor to be used in reducing the data to a single scale. The ratio $R_{CH_2}^1/R_{CH_2}^2$ should be equal to this factor, as should all similar ratios calculated for the angles common to the two runs. By combining all the available data from each pair of runs it was possible to obtain the normalization factors to an accuracy much greater than that of any individual hydrogen effect measurement. The accuracy of each normalizing factor was then calculated both from statistical considerations and from the spread in individual values obtained as above, the two methods yielding the same results.

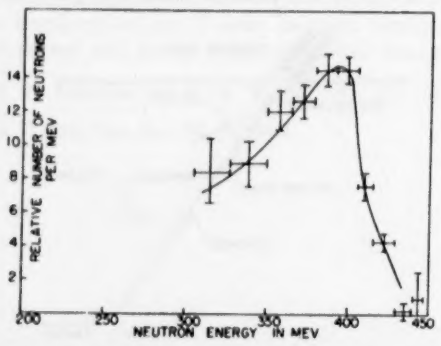

FIG. 2. Differential range curve of recoil protons at 23.0° to the neutron beam. The abscissae have been altered from inches of copper to Mev to facilitate comparison with Fig. 3.

III. THE NEUTRON BEAM

The neutrons were produced by bombardment of a 1-in. thick beryllium target in the cyclotron at a radius corresponding to 427-Mev proton energy. Neutrons emitted in the forward direction were collimated by seven feet of lead spaced at various depths in a total thickness of thirteen feet of magnetite concrete. The defining aperture for this beam was a 2-in. diameter hole at 27 feet from the internal target.

The spectrum of the neutrons was deduced from a differential range curve (Fig. 2) of protons ejected at 23° to the beam from an effective hydrogen target. Since the efficiency of the telescope varies with absorber thickness, this range curve does not give the true neutron spectrum directly. The telescope was therefore calibrated (with the same technique described in Sec. VI) at the fixed 23° angle for changes in efficiency introduced by the absorbers, and this effect unfolded from the range curve to give the spectrum of Fig. 3. The errors shown in this figure were obtained by considering the extreme spectra compatible with the errors in Fig. 2. Although the uncertainties in the spectrum of Fig. 3 are not small, their effect on the accuracy of the entire experiment is unimportant. (See Sec. VI.)

Exposures of x-ray film were made at frequent intervals during the experiment for alignment purposes, as well as to study the uniformity of the beam. The radiographs at the position of the scatterer showed a circular spot about three inches in diameter, the top and bottom being somewhat diffuse because the source of neutrons is a vertical line. Because the scatterers were smaller than the beam, it was desirable for the neutron intensity to be uniform over a large part of the beam area. Many x-ray photographs indicated that this was in fact the case. As another test for uniformity, one entire cyclotron run was made with scatterers and table shifted $\frac{1}{4}$ in. sideways relative to the beam center. Results consistent with the other runs were obtained. Finally, the counter telescope was fixed at 18° to the beam and the thinnest carbon scatterer rotated until it was parallel to the beam direction. No effect on the

counting rate (within ~1 percent) was observed. On the basis of these tests it was concluded that the beam was sufficiently uniform for our purposes.

Before the experiment was begun the beam was investigated for charged particle contamination. As a test a magnetic sweeping field was used to remove any such impurities; the observed change in rate in a single scintillation counter placed in the beam corresponded to less than 0.1 percent charged particles. Nuclear plates were also exposed in and near the beam, the number of tracks counted again indicating about 0.1 percent contamination.

Under normal cyclotron conditions the intensity of neutrons above 365 Mev was about 2×10^5 cm^{-2} sec^{-1}.

IV. GEOMETRY AND SCATTERERS

The angular aperture of the recoil telescope was defined by the second counter, a stilbene crystal 3 cm wide ×6 cm high. This was located 80 cm from the scatterer when angles greater than 9° were being investigated, and was moved out to twice that distance for the smaller angles. (See Table I.) At 2.3° it was necessary to move it to 210 cm in order to keep the first counter well away from the direct neutron beam, but at zero degrees a distance of 80 cm was again chosen as a compromise between large scattered flux and good angular resolution. At the 80-cm distance the resolution curve for nonzero angles should be trapezoidal with a full width at half-maximum of 3.2°. Hence measurements at five degree intervals effectively do not overlap.

TABLE I. Geometry and scatterers.

Geometry	Distance of counter No. 2 from scatterer center (cm)	Solid angle subtended by counter No. 2 (sterad)
α	80	2.81×10^{-3}
β	160	7.03×10^{-4}
γ	210	4.08×10^{-4}
Scatterer set	**Weight of CH_2 scatterer (g)**	**Weight of C scatterer (g)**
I	11.43	13.44
II	22.92	26.88
III	42.50	49.83

The scatterers were accurately machined and weighed plates of polyethylene and carbon 4.45 cm square. Three different sets of matched scatterers with surface densities in the ratios 1.00:2.00:3.72 were used (see Table I), the thinnest set being employed primarily at angles above 57.6° where the energy of the recoil protons is lowest.

Several tests confirmed that the geometrical properties of the apparatus were as expected. It was observed that the counting rates from either carbon or polyethylene scatterers (after subtraction of background) were unchanged on displacement of the first counter along the telescope axis, and also that these rates varied inversely as the square of the "defining" distance to counter No. 2. In addition, different sets of scatterers were used at 57.6°, 9.1°, and 4.6° to verify that at each of these angles a proportionality existed between surface density and scattered flux.

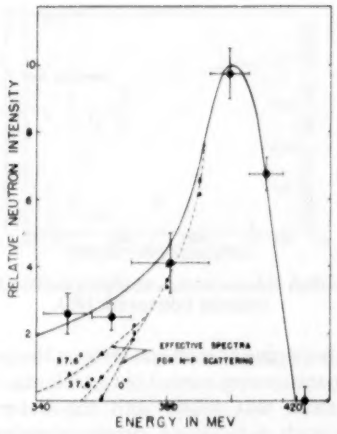

FIG. 3. Corrected neutron spectrum from 427-Mev protons on Be. The dotted curves show the effect of absorber A at the scattering angles indicated.

V. APPARATUS AND PERFORMANCE

The three scintillation counters each consisted of a stilbene crystal mounted on a Lucite light-pipe and viewed by an RCA 5819 photomultiplier. The first two crystals, $4\times6\times\frac{1}{2}$ cm and $3\times6\times\frac{1}{2}$ cm, respectively, were viewed from the sides and covered with 0.001-in. aluminum foil to shield them from external light. The third crystal, $5\times10\times\frac{1}{2}$ cm, was viewed normal to its large surface, and was always positioned 15.0 cm behind the second counter. Absorber A (Fig. 1) was 7.5 cm wide×12.5 cm high. At each angle its thickness was equal to the range of a proton ejected by a 365-Mev neutron from the center of the scatterer and proceeding along the axis of the telescope. Energy losses in the crystals, scatterer, etc., were computed from the tables of Aron,[11] and the absorber thickness adjusted accordingly.

Anode pulses from the three multipliers were fed into cathode followers and then through fifty-foot cables to the counting area. There the pulses were amplified with distributed amplifiers and passed through inverter-limiters, finally entering a diode coincidence circuit of standard design. Clipping stubs at the coincidence chassis provided a resolving time of about 10^{-8} second. Both triple coincidences and double coincidences between counters No. 1 and No. 2 were then amplified and scaled.

[11] W. A. Aron, University of California Radiation Laboratory Report UCRL-1325, 1951 (unpublished).

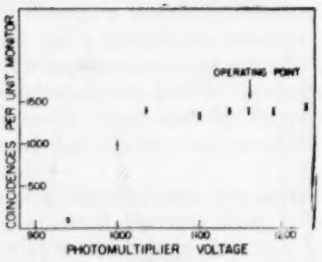

FIG. 4. High voltage plateau of triple coincidence circuit taken on October 14, 1953.

At the beginning of each run tests on the performance of the apparatus were carried out as follows. A discriminator plateau was taken with the linear amplifier following each coincidence circuit, showing plateaus about thirty volts wide. The master high-voltage control on all three multipliers was then varied to measure a plateau as shown in Fig. 4. Such plateaus were about 150 volts wide, while an electrostatic voltmeter on each supply indicated drifts of less than twenty volts during the course of any run.

Delay curves were found to be flat-topped in the neighborhood of coincidence and also near 5×10^{-8} sec (corresponding to one cyclotron radio-frequency cycle). The number of accidental coincidences was measured by delaying each of the counters in turn by one rf cycle; as expected, most accidentals were caused by a true double coincidence between counters No. 1 and No. 2 occurring simultaneously with a random single count in No. 3. Except during the measurement of proton recoils at 0°, these accidental coincidences were always less than $\frac{1}{2}$ percent of the counts observed from any scatterer.

Detection of scattered protons at 0° to the beam involves special difficulties, because the counter telescope must be placed in the direct neutron flux. At full beam strength this causes overloading of the multipliers as well as impossibly high accidental rates, so a cyclotron level about 5 percent of normal was used during the 0° measurements. With this intensity accidental rates averaged about 20 percent of the counting rates. In order to avoid errors in the measurement of accidentals during these 0° runs, only data taken with constant monitor rate (±4 percent) were accepted.

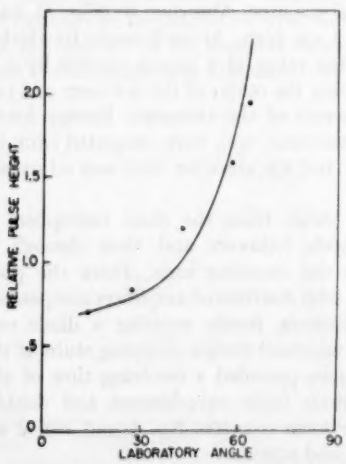

FIG. 5. Pulse height in counter No. 1 *vs* telescope angle. Experimental points are normalized at 13.8° to curve (calculated for 400-Mev *n-p* recoil protons).

For the calibration experiment, the external proton beam from the cyclotron was scattered with the same apparatus used with neutrons. The greater intensity of protons made possible more detailed checks of the equipment than were possible with the neutron beam. The accidental coincidences at small angles to the proton beam were often several percent of the total counting rates, and a much sharper peaking of the accidental rates about one rf cycle of delay was observed. With the proton beam, delay curves were followed out to four rf cycles with no loss of accidental rates, indicating that attenuation in the delay cables introduced no error.

The counting rate per unit monitor count was measured with the proton beam over a wide range of beam intensities in order to detect possible dead-time losses in the counting system. Such losses were observed at high beam strengths, and corrections to the data were made accordingly. With the neutron beam losses were never a problem.

One test remains to be described. If the recoil particles detected by our telescope are really protons from 400-Mev *n-p* collisions, their energies and thus dE/dx in the stilbene crystals are easily calculated. In order to leave no doubt about the nature of the particles giving triple coincidences, a study was made of the pulse amplitudes from the first counter of the telescope as a function of angle. The pulses were analyzed by a twenty-four-channel pulse-height selector[12] which was triggered by the triple coincidences, and the data obtained for each scatterer processed in the usual way to find the location of the average pulse height from an effective hydrogen scatterer. These average amplitudes, normalized at 13.8° to the curve calculated for recoil protons from *n-p* collisions, are shown in Fig. 5. Considering the 10-percent resolution of the crystal, there is excellent agreement between the points and the curve.

The pulse-height distributions from carbon are somewhat broader than those from hydrogen, but have similar average amplitudes. Both characteristics indicate a quasi *n-p* scattering as the source of most particles observed from carbon.

VI. CALIBRATION OF THE APPARATUS

As pointed out in Sec. II, the efficiency of the counter telescope may be expected to vary considerably with

[12] This pulse-height analyzer was lent to us by DeBenedetti, Stearns, and Stearns of this laboratory.

angle. One way to measure this efficiency is to place the counters directly in a proton beam of variable energy and observe the ratio of triple coincidences to double coincidences between the first two counters. This gives the transmission of absorber A, i.e., the efficiency of the telescope. However, the scattered protons detected in the n-p experiment do not strike the telescope as a parallel, monoenergetic beam, but as a spreading flux from a small source (the scatterer), with energy varying over the aperture of the counters.

The high-intensity ($\sim 4\times 10^6$ cm^{-2} sec^{-1}) external proton beam of the Carnegie cyclotron provided a way of calibrating the counter telescope which automatically compensated for these effects. By scattering this beam (enlarged so that it was 2.5 in.$\times$2.5 in. square) from hydrogen in the same geometry used with the neutron beam, a scattered flux which had the same

TABLE II. Net counter telescope efficiency *vs* angle. Errors average ±3 percent of the values given.

Φ	Absorber A (inches of Cu)	Net efficiency
0	4.45	0.35
2.3	4.43	0.35
4.6	4.39	0.36
6.8	4.33	0.36
9.1	4.23	0.37
13.8	4.00	0.38
18.5	3.65	0.40
23.0	3.23	0.41
27.8	2.77	0.44
32.6	2.28	0.48
37.4	1.80	0.50
42.4	1.34	0.53
47.2	0.93	0.56
52.4	0.58	0.60
57.6	0.33	0.56
60.7	0.24	0.58
63.2	0.14	0.55
65.5	0.07	0.60
68.2	0.03	0.41

energy-angle distribution as the recoil protons from n-p collisions was obtained. The ratio triples/doubles then gave the telescope efficiency under the proper experimental conditions.

After passing through the monitor scatterer, the protons had an energy of 428 Mev as measured by a Bragg curve. They were degraded with polyethylene absorbers to 410, 395, 380, 365, 357 Mev successively, thus spanning the useful energy region of the neutron spectrum. At each proton energy (including 428 Mev), double and triple coincidences were measured as a function of angle from 68.2° to 18.5°, background usually being prohibitive at smaller angles. However, at 0° the efficiency could be measured by direct transmission, and values between 18.5° and 0° obtained by interpolation.

Figure 6 is a sample plot of efficiency *vs* energy at a fixed angle. Such data correspond to a transmission *vs* energy measurement in a particular geometry, so a

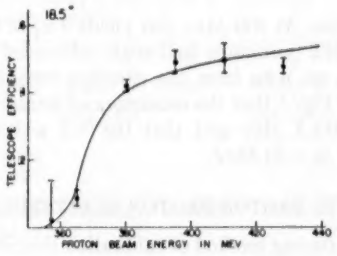

FIG. 6. Telescope efficiency at 18.5° as a function of incident proton energy.

smooth curve may be drawn through the points. Ordinates taken from this and similar graphs at other angles were folded into the neutron spectrum to obtain net efficiencies shown in Fig. 7 and Table II. The average error of about 3 percent quoted for these efficiencies was derived from (1) random errors assigned to the efficiencies on the basis of fluctuation of the experimental points about a smooth curve, and (2) variation in the net efficiencies introduced by using extreme shapes of the neutron spectrum allowed by the data of Fig. 3. The former errors are closely related to actual counting statistics, but are often smaller because of the regular and predictable variation with energy of the efficiency at any one angle. The latter type of error is much less important because of the sharp peak in the spectrum.

Complete proton range curves were also taken at various incident energies. Since the telescope is a "poor" geometry device for this purpose, the initial slopes of these curves should give nuclear cross sections for protons in copper. However, fragments from nuclear collisions made by the protons will penetrate a small thickness of Cu and lower the apparent cross section deduced from the beginning of the range curve. These fragments also cause a hump in the Bragg curves for 428-Mev protons at small copper thicknesses. Therefore, the slope of the range curves between 0.5 in. and 1.5 in. was chosen as a measure of the nuclear absorption

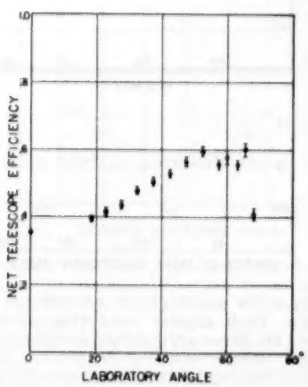

FIG. 7. Net telescope efficiency *vs* angle.

cross section. At 400 Mev this yields a σ_a of 0.50 barn ± 10 percent (minimum half-angle subtended $= 18°$).

Finally, we note from the effective neutron spectra plotted in Fig. 3 that the maximum of intensity always lies at 400 ± 5 Mev and that the full width at half-maximum is ~ 30 Mev.

VII. PROTON-PROTON SCATTERING

The scattering method of calibration described above requires correction for charged particles which are produced in p-p collisions and detected along with elastically scattered protons. The principal contaminants are mesons from $p+p \rightarrow \pi^+ + d$. a process which has been investigated in this energy region.[13] The evidence indicates a c.m. angular distribution for the π mesons of the form $(0.2+\cos^2\theta)$, and a total cross section rising linearly from 0.6 mb at 365 Mev to 1.3 mb at 430 Mev. Corrections for these mesons have been applied to both the double and triple coincidences, taking into account the attenuation in absorber A. These changes are generally less than 3 percent, so systematic errors resulting from uncertainty in the meson production cross section are probably less than 1 percent.

When the meson corrections have been made to the observed double coincidence rates, they should be proportional to the differential p-p scattering cross sections. After transformation to the center-of-mass system these data are summarized in Table III and Fig. 8. Since only one of the scattered protons is detected, cross sections are given for angles greater than 90°. The symmetry of the distributions about that point demonstrates that there is no systematic error introduced by large meson production at small angles, and also that there is no loss of protons in the scatterer or first crystal of the telescope at large angles.

Below 400 Mev these p-p data indicate no deviation from isotropy from 30°–90° within a few percent. At 410 Mev data are sparse, but at 428 a rise of about 10 percent at 40° (and 140°) is visible. This is in excellent agreement with the results of Mott, Sutton, *et al.* at 437 Mev and in disagreement with the results of Marshall *et al.* at 429 Mev.[14] It is worthy of note that in the experiments reported here n-p and p-p scattering have both been measured with the same apparatus and in identical geometries.

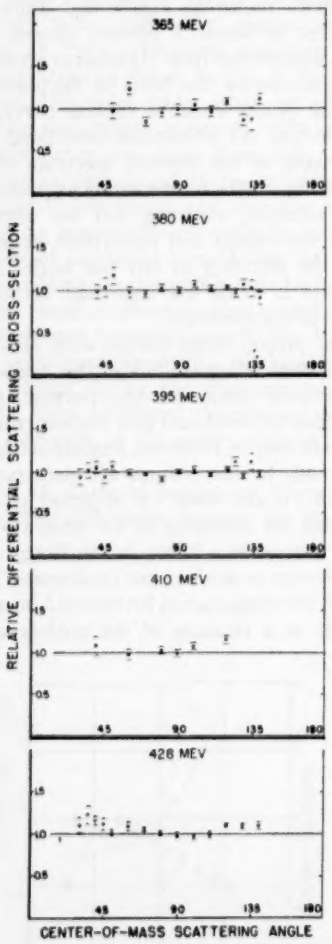

FIG. 8. Barycentric proton-proton scattering at five incident proton energies. Each angular distribution is normalized to $(d\sigma/d\Omega)_{p-p}^{90°} = 1.00$. Errors are standard deviations from counting statistics only.

TABLE III. Barycentric proton-proton scattering cross sections, relative to $(d\sigma/d\Omega)_{p-p}^{90°} = 1.00$, at five incident energies. Errors are statistical standard deviations from counting only.

C.m. scattering angle	Incident proton energy in Mev 365	380	395	410	428
30			0.94 ±0.09		1.11 ±0.09
35			1.02 ±0.09		1.24 ±0.10
40		0.99 ±0.08	1.05 ±0.07	1.08 ±0.11	1.16 ±0.05
45		1.04 ±0.11	0.95 ±0.08		1.12 ±0.07
50	0.98 ±0.08	1.18 ±0.10	1.07 ±0.05		1.02 ±0.04
60	1.14 ±0.07	0.98 ±0.06	0.99 ±0.03	0.98 ±0.06	1.09 ±0.05
70	0.85 ±0.05	0.96 ±0.04	0.98 ±0.02		1.05 ±0.02
80	0.96 ±0.05	1.03 ±0.04	0.91 ±0.03	1.03 ±0.04	1.01 ±0.02
90	1.00 ±0.06	1.00 ±0.03	1.00 ±0.02	1.00 ±0.04	1.00 ±0.02
100	1.05 ±0.06	1.07 ±0.04	1.02 ±0.04	1.08 ±0.04	0.97 ±0.02
110	0.97 ±0.06	1.02 ±0.03	0.97 ±0.02		0.99 ±0.04
120	1.09 ±0.03	1.04 ±0.02	1.03 ±0.02	1.16 ±0.05	1.10 ±0.02
125		0.97 ±0.05	1.12 ±0.05		
130	0.87 ±0.07	1.07 ±0.06	0.95 ±0.03		1.09 ±0.03
135	0.88 ±0.13	1.03 ±0.09	1.12 ±0.10		
140	1.12 ±0.06	0.91 ±0.07	0.97 ±0.04		1.10 ±0.04

[13] Fields, Fox, Kane, Stallwood, and Sutton, Bull. Am. Phys. Soc. **29**, No. 4, 50 (1954).

[14] Mott, Sutton, Fox, and Kane, Phys. Rev. **90**, 712 (1953); Marshall, Marshall, and Nedzel, Phys. Rev. **92**, 834 (1953). Some uncertainty remains in our p-p data because of the process $p+p \rightarrow \pi^+ + n + p$, which is negligible at lower energies but perhaps not at 428 Mev. A further correction equal to 40 percent of that already made for the two-body production would reduce the rise observed in the p-p cross section at 428 Mev to about 8 percent at 40°, barycentric angle. Results at and below 410 Mev would be unaffected within the experimental error.

TABLE IV. Laboratory n-p counts normalized to geometry α and scatterers II (see Table I). Errors are statistical standard deviations from counting only.

Φ \ No.	1 May 31	2 June 3	3 June 5	4 June 7	5 Sept. 17	6 Sept. 19	7 Sept. 30	8 October 2	9 October 14	10 October 16	Weighted average
0								3642±304		3092±435	3757±250
2.3					2538±327	2682±90					2672±76
4.6			2213±128		2224±78	2226±61	2155±84				2208±40
6.8			1685±81			1582±48	1682±61				1632±35
9.1	1528±63	1680±75	1491±58		1488±26	1427±35					1486±19
13.8					1166±26	1200±28	1166±42	1119±32	1202±26	1191±33	1177±13
18.5	878±33	971±46		949±34	902±20	924±22	885±25				911±11
23.0				701±25	763±33						707±16
27.8	555±25	664±30			567±21					503±23	543±14
32.6				432±16	406±28						425±16
37.4	386±16	434±20		412±33	357±27	396±28					386±12
42.4		397±15			392±19					402±16	397±10
47.2	455±20	473±26			451±20						453±14
52.4	474±22				534±25						500±17
57.6	439±20				464±23	410±36	465±22		429±27	424±19	445±9
60.7									432±35		432±35
63.2		493±33		394±48	496±32	532±27	453±42		484±33		489±14
65.5					524±42		429±36		498±34		480±22
68.2		203±33			338±30		323±36		314±29		289±14

VIII. n-p RESULTS AND ERRORS

In Table IV the n-p counts per unit monitor observed during each run are assembled along with their statistical counting errors, with weighted mean values given in the last column. The corresponding barycentric cross sections, normalized to unity at $\theta=90°$, are displayed in Table V and Fig. 9. The errors quoted for both the p-p and n-p cross sections (Tables III and V) are standard deviations computed for the following sources of uncertainty: (1) counting statistics in the n-p experiment; (2) random errors arising from counting statistics of the calibration (p-p) experiment; (3) uncertainties in the neutron spectrum; (4) uncertainties in measurement of dead-time losses, accidentals, etc. Not included are errors which may originate in plateau interpretation, mechanical alignment, scatterer impurities,[15] beam nonuniformity, and in the meson corrections to the p-p data. These may contribute an additional 3 percent error to be superimposed on the results given in Tables III and V.

We have not made the usual correction at small angles to compensate for change in slope of the cross section across the telescope aperture. Because of the resolution employed, these corrections are negligible except at 2.3° and 0°. With the data as presented in Table V, this correction would raise the cross section at 2.3° by

TABLE V. Barycentric neutron-proton scattering cross sections at 400 Mev relative to $(d\sigma/d\Omega)_{n-p}^{90°}=1.00$. Errors are combined statistical standard deviations from n-p counting, spectrum errors, and calibration errors.

Lab angle Φ	$J_{np}=\frac{d\cos\Phi}{d\cos\theta}$	c.m. angle θ	Relative $(d\sigma/d\Omega)_{n-p}$
0	0.207	180	8.74 ±0.59
2.3	0.207	175	6.20 ±0.22
4.6	0.208	170	5.14 ±0.18
6.8	0.209	165	3.77 ±0.14
9.1	0.211	160	3.40 ±0.09
13.8	0.218	150	2.70 ±0.07
18.5	0.227	140	2.08 ±0.06
23.0	0.239	130	1.62 ±0.06
27.8	0.255	120	1.26 ±0.05
32.6	0.276	110	0.972±0.044
37.4	0.302	100	0.923±0.036
42.4	0.336	90	1.00 ±0.04
47.2	0.377	80	1.20 ±0.04
52.4	0.433	70	1.44 ±0.06
57.6	0.508	60	1.61 ±0.05
60.2	0.558	55	1.66 ±0.15
63.2	0.623	50	2.19 ±0.08
65.5	0.686	45	2.17 ±0.13
68.2	0.773	40	2.16 ±0.13

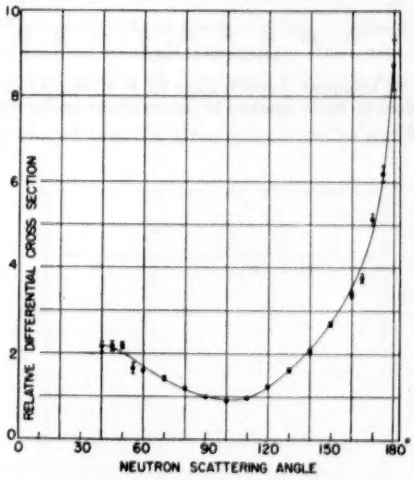

FIG. 9. Barycentric neutron-proton angular distribution at 400 Mev, normalized to $(d\sigma/d\Omega)_{n-p}^{90°}=1.00$. Errors are those given in Table V (see also Sec. VIII). (Near 90° the black dots are larger than the errors.)

[15] Chemical analysis of the polyethylene showed that its formula was $CH_{2.00}$ within about 0.5 percent error. The carbon contained less than 0.1 percent impurity.

2 percent, which is less than the experimental error at that point. At 0° a difficulty arises which is connected with the observed counts *vs* angle from carbon (Fig. 10). (Also shown in this figure are the counting rates, uncorrected for efficiency, from hydrogen and at small angles from an aluminum scatterer.) One sees that the cross sections for the production of high-energy protons by neutrons on carbon or aluminum are almost independent of angle between 5° and 30°. At higher angles interpretation is difficult because the telescope efficiency is known only for protons of selected energy, and not for recoils from quasi *n-p* collisions within nuclei. The tremendous peak in the carbon and aluminum counting rates below 5° is, we believe, a result of Rutherford scattering of the charged contaminants in the neutron beam. The sizes of the peaks and their relative magnitudes for aluminum and carbon are consistent with this hypothesis, but their persistence at 0° is not. It is difficult to imagine a nuclear effect which would produce as sharp a rise, and consequently the 0° measurement is open to suspicion. This is why no curvature corrections have been made at this angle.

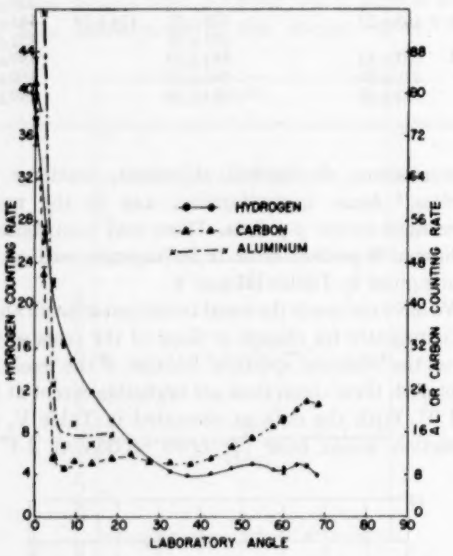

FIG. 10. Observed counts *vs* angle for H, C, and Al scatterers, normalized to equal numbers of scattering centers for the three elements.

IX. SUMMARY

The *n-p* angular distribution (Fig. 9) shows certain interesting features in contrast to lower energy results. The minimum in the curve has shifted to about 100°, and there is clearly a lack of symmetry about 90°. At small angles the cross section seems to be leveling off at a relative value of ~2.5. Extrapolation to this magnitude at 0° and integration to a total cross section of 34 mb[16] gives $(d\sigma/d\Omega)_{n-p}^{90°}=1.5$ mb. This is large enough so that the condition imposed by charge independence (see Sec. I) is easily satisfied, since $(d\sigma/d\Omega)_{p-p}^{90°}=3.5$ mb at 400 Mev. In fact, extrapolation of the *n-p* cross section to any reasonable value at 0° does not change this conclusion.

Further experiments at small neutron scattering angles would be of interest to ascertain whether the symmetry about 90° displayed by the scattering at lower energies is really destroyed at 300 Mev and above, as is suggested by these data and those of DePangher.[8] If so, the Serber potential cannot describe the *n-p* interaction at these energies.

The authors wish to thank Mr. Eugene Maier for help with the calculations and many members of the laboratory for helpful discussions.

[16] See reference 10. The meson production contributions to this total cross section arise mostly from $n+p\rightarrow\pi^0+d$, which according to charge independence has one-half the cross section for $p+p\rightarrow\pi^+ +d$. This gives only about 0.5 mb at 400 Mev. See R. H. Hildebrand, Phys. Rev. **89**, 1090 (1953).

Meson Showers and High-Energy Interactions in Light and Heavy Nuclei

R. W. PARSONS, FRANÇOISE A. BRISBOUT, AND V. D. HOPPER
Physics Department, University of Melbourne, Melbourne, Australia
(Received October 27, 1953; revised manuscript received March 4, 1954)

A study has been made of nuclear disintegrations produced in electron-sensitive emulsions exposed to cosmic radiation at 80 000 ft. Of 93 stars containing more than three shower particles, 29 were interpreted as being induced in the light nuclei C, N, O, and 64 in the heavy nuclei Ag and Br. The low-energy tracks appear to be emitted isotropically from a slowly moving nucleus and the forward collimation of the remaining tracks is discussed. The average numbers of shower particles from the heavy and light nuclei are 7.7 and 6.4_5, respectively, and it is shown that these figures are consistent with multiple processes of meson production. The difference between the angular distributions of shower particles from heavy and light nuclei is discussed on the assumption that it is mainly due to scattering.

INTRODUCTION

A STUDY has been made of stars containing meson showers in 400μ Ilford G5 nuclear emulsions exposed at altitudes between 80 000 and 90 000 feet.[1] In order to be certain of the primary direction, stars with three or more shower particles were selected and a few of these, which were close to the air or glass surface or whose primary directions were steeply inclined to the emulsion surface, were omitted. Using this method of selection, 93 stars, 12 produced by neutral primaries and 81 by singly charged particles, were analyzed. In addition, several stars giving meson showers produced by alpha particles and heavier nuclei were studied. The primary directions of large showers produced by neutral particles were estimated as the mean of the shower particle directions. In no case was it assumed that a collimation of nonshower particles was related to the primary direction.

MEASUREMENTS OF TRACKS AND IDENTIFICATION OF TARGET NUCLEI

By measuring the azimuth and dip angles of the tracks, the latter angles being corrected for the shrinkage factor which varied from plate to plate, the angle θ of each track relative to the primary direction in the original undeveloped emulsion was calculated. As the grain density of the tracks also varied with development, the minimum grain density of each plate was measured and grain densities in grains per 50μ were standardized to a minimum of 12. Tracks with grain densities up to 25 percent above minimum were classed as shower particles. The grain density of a completely black track parallel to the emulsion surface was taken as 120, a proton track of range 100μ therefore having a grain density of about 115, corresponding to 5 gaps per 50μ, and an α track of range 100μ having a grain density of 117, corresponding to 3 gaps per 50μ. Checks were made to insure that different observers obtained the same value of grain density for a given track, and graphs were drawn relating these estimated grain densities to the ranges and energies of charged particles.

From the lengths of tracks which ended in the emulsion and from their grain or gap densities, the particles which produced the tracks could often be identified. Where possible, scattering measurements and delta-ray counts were made on long tracks which did not end in the emulsion and these combined with grain density measurements gave a means of identification. Where identification was not possible it was assumed that tracks of range greater than 100μ, excluding shower particles, were protons, those with ranges between 100μ and 30μ were alpha particles, between 30μ and 10μ, lithium nuclei, and recoils less than 10μ were assumed to have a charge 4.

From the above measurements, the total charge Z of the nonshower tracks was estimated. Figure 1B shows the number of stars with a given Z plotted against Z for stars without recoils, and Fig. 1A shows the number of stars with recoils. It is seen from this latter figure that there are no stars with recoils with $Z<13$. The assumption of 4 units of charge for the recoils is probably an underestimate but it is seen that even so no stars were obtained with Z between 8 and 12, and there is a separation between stars having $Z\leqslant 8$ and $Z\geqslant 12$. It is concluded that the stars with $Z\leqslant 8$ are due to the

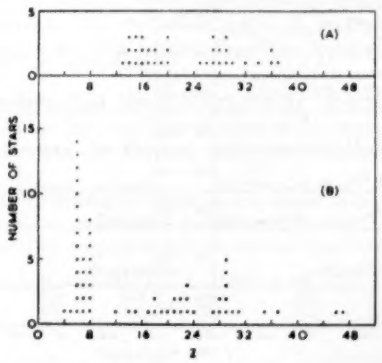

FIG. 1. The number of stars with a given Z is plotted against Z for stars with recoils (A), and without recoils (B), showing the separation of the stars into those produced in light and heavy nuclei.

[1] Darby, Hopper, Laby, and Wilson, Australian J. Phys. 6, 471 (1953).

disintegrations of C, N, and O nuclei in the emulsion, and those with $Z \geq 12$ are due to Ag and Br.

Of 29 light nuclei events, 25 of which had charged primaries, only two stars have $Z<6$. From this, it is inferred that practically all the charge of a light nucleus goes into the nonshower tracks since scattering measurements show that these are very seldom due to mesons, and hence the shower tracks must be mainly mesons. (Camerini, Fowler, Lock, and Muirhead[2] have shown that the small admixture of protons amongst the shower tracks is approximately compensated by the number of π mesons of energy less than 150 Mev among the nonshower class.) If this is also true of showers from heavy nuclei, there must in general be for these a residual nucleus, which in some cases may be the observed recoil, while in others would be of too short range to be detected.

ANGULAR DISTRIBUTION OF TRACKS

In Fig. 2, the number of tracks per 0.1 interval of $\cos\theta$ is plotted against $\cos\theta$ for seven intervals of grain density, the results for the shower tracks being discussed later. From this it is seen that a considerable fraction of the high-energy protons is emitted from heavy nuclei in the backward hemisphere, and this supports the contention that the primary direction should not be deduced from any collimation of a group of nonshower particles.

The tracks would be expected to fall into three main categories: (1) The shower tracks created in nucleon-nucleon collisions which should be strongly collimated in the forward direction; (2) knock-on tracks, mainly due to protons that have not suffered many collisions before escaping from the nucleus and should therefore be collimated but to a lesser extent; and (3) lower-energy tracks due to particles which have evaporated from the remaining excited nucleus, and which, but for the slight forward movement of this nucleus, should be isotropically emitted in the laboratory system. A critical test for isotropy is found in the excess forward fraction of tracks $(F-B)/T$, where F and B are the numbers of forward and backward tracks in a given energy range and $T=F+B$. Values are listed in Table I.

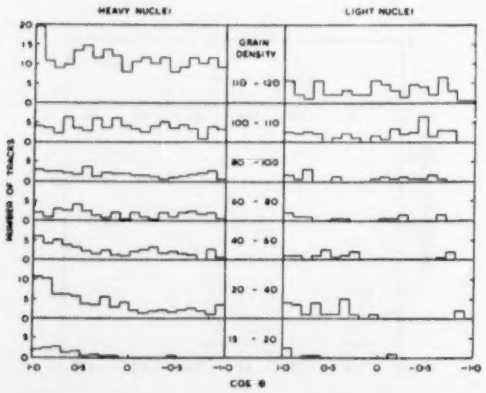

FIG. 2. The number of tracks per 0.1 interval of $\cos\theta$ is plotted against $\cos\theta$ for seven intervals of grain density.

[2] Camerini, Fowler, Lock, and Muirhead, Phil. Mag. 41, 413 (1950).

Tracks with Grain Density Greater than 60

It is seen from Table I that there is very little departure from isotropy for proton energies up to 50 Mev, the values of $(F-B)/T$ for all tracks up to this energy being 0.11 ± 0.04 and $-0.0_4\pm0.1$ for heavy and light nuclei, respectively. These figures are reasonably consistent with isotropic emission from a moving nucleus. If a very high-energy particle passes through a nucleus which as a result is excited to an energy E, the forward momentum of the excited nucleus will be E/c. If E is taken as the total energy of all the particles, including neutrons, emitted with energies less than 50 Mev, it is estimated from the data given in Table I to be 500 Mev and 130 Mev for the average heavy and light star, respectively. The mean proton energy in this region is 10 Mev and using this value the calculated ratio $(F-B)/T$ is 0.04 and 0.06 for heavy and light stars, respectively.

From Fig. 2, it is seen that even above 50 Mev there is a considerable number of nonshower tracks emitted almost isotropically in the backward hemisphere from heavy nuclei, and a few tracks emitted backwards from light nuclei. If E also includes these tracks, plus an equal number emitted in the forward hemisphere, the values of E for the average heavy and light nucleus are 1270 Mev and 220 Mev and the corresponding values of $(F-B)/T$ are 0.10 and 0.11, respectively. Some of these tracks may therefore be due to evaporation particles, but there is still an appreciable forward component which cannot be explained on this hypothesis and which must be associated with knock-on particles.

Tracks of Grain Density Between 15 and 60

Scattering measurements indicate that these tracks are almost always heavier than mesons. The measured forward excess $(F-B)$/star is 2.1 and 1.0, while the total number of these tracks per star is 4.5 and 1.3 for heavy and light nuclei, respectively. The numbers of tracks per star for increasing numbers of shower particles are given in Table II.

It is observed that the number of tracks of grain density 15–60 per star is nearly independent of the mean number $\bar{n}_s$ of shower particles for values of $\bar{n}_s$ from about 4 to 8 for both heavy and light nuclei. There is however a slight increase for large showers ($\bar{n}_s=13.5$) for heavy nuclei. Only two events were observed for light nuclei with $n_s>9$. The results for the heavy nuclei are in good agreement with those plotted by Camerini *et al.*[3] in their Fig. 7 which show

[3] Camerini, Lock, and Perkins, *Progress in Cosmic Ray Physics*, edited by J. G. Wilson (North-Holland Publishing Company, Amsterdam, 1952), first edition.

TABLE I. Excess forward fraction of tracks for different energy regions for light and heavy nuclei.

Grain density	120–110	110–100	100–80	80–60	60–40	40–20	20–15	<15
Proton energy (Mev)	0–8	8–15	15–30	30–50	50–85	85–300	300–800	>800
$(F-B)/T$								
Heavy	0.09 ±0.05	0.17 ±0.10	0.24 ±0.10	0.14 ±0.10	0.26 ±0.10	0.50 ±0.10	0.93 ±0.2	0.90 ±0.05
Light	0.0 ±0.1	−0.2 ±0.2	0.1 ±0.3	0.1 ±0.3	0.6 ±0.3	0.8 ±0.2	0.5 ±0.5	0.94 ±0.07
Tracks/star								
Heavy	7.8	2.7	1.2	1.2	1.6	2.7	0.4	7.7
Light	2.1	1.3	0.4	0.3	0.4	0.8	0.1	6.4_5

an almost constant number of protons of energy 25–800 Mev for $\bar{n}_s$ from 3 to 6 with a rise of about 2 for $\bar{n}_s=14$, although Camerini *et al.*[4] show a slight rise also for $\bar{n}_s=6$ in the equivalent Fig. 5 of that reference. The inference drawn from Table II is that only a very small fraction of the tracks in this grain density range can be due to meson-nucleon collisions.

If some of these tracks in the grain density region 15–60 are the result of knock-on particles, it might be expected that their number would depend on the number of collisions suffered by the primary nucleon. If the primary particle produces mesons in several successive collisions in the nucleus, the number of knock-on tracks would depend on the number of shower particles n_s. The results thus suggest that in either light or heavy nuclei the primary particle has about the same number of meson producing collisions for $\bar{n}_s=4$ and $\bar{n}_s=8$ with a slight increase for $\bar{n}_s=13.5$ for heavy nuclei. In other words a pluro multiple rather than a plural mechanism is favored for the production of mesons, large showers differing from small ones in the number of mesons produced per collision rather than in the number of collisions of the primary nucleon.

Although the number of tracks in this region of grain density 15–60 might be expected to be proportional to the number of collisions suffered by the primary particle, the constant of proportionality is not likely to be the same for heavy as for light nuclei. Fast nucleons resulting from meson producing collisions of the primary would knock out more fast particles from heavy than from light nuclei because the average distance traveled before escaping from the former is greater. It follows that the ratio of the average number of collisions of the primary nucleon in heavy and light nuclei would be less than 4.5/1.3 and this is confirmed by the analysis in the next section where the average numbers of primary collisions in heavy and light nuclei are estimated as 1.64 and 1.3, respectively. That fast nucleons have more collisions in escaping from heavy than from light nuclei is also suggested by the greater degree of forward collimation of the tracks in the grain density region 15–60 for light nuclei.

[4] Camerini, Davies, Fowler, Franzinetti, Muirhead, Lock, Perkins, and Yekutieli, Phil. Mag. **42**, 1241 (1951).

Also evidence given by Camerini *et al.*[3] suggests that even for stars where only one meson is produced, the number of tracks of grain density 15–60 will be about 2.5 for heavy nuclei. If the number of tracks is proportional to the number of meson producing collisions in the nucleus, 1.8 collisions would be sufficient to produce the observed number 4.5 tracks of grain density 15–60 for heavy nuclei as stated above.

Tracks of Grain Density <15 (Shower Particles)

For the stars studied, the value of n_s ranged from 3 to 19 for the heavy nuclei, the mean being 7.7/star, and from 3 to 14 for the light, the mean being 6.4_5/star. Assuming as a first approximation, that the showers consist entirely of mesons, the ratio of the values of n_s for the average heavy and light stars, *viz.*, 1.19±0.10, can be explained by two quite different models. In the first, the incident particle may have meson producing collisions so frequently on passing through the first half of a heavy nucleus (corresponding in distance to the diameter of a light nucleus) that it has insufficient energy to produce many more mesons in traversing the remainder of the nucleus. This would correspond to a mainly plural interaction. In the second model, corresponding to a mainly multiple interaction, the incident particle has a small cross section for meson producing collisions in nuclear matter and produces several mesons per collision, the number of collisions in heavy nuclei being only slightly greater than the number in light nuclei.

Assuming that the average energy of the primary particles for light and heavy stars is the same, the two solutions can be derived from the following crude

TABLE II. Number of tracks per star related to shower size for heavy and light nuclei.

	Heavy nuclei			Light nuclei		
n_s	3–5	6–9	10–19	3–5	6–9	10–14
$\bar{n}_s$	3.8	7.5	13.5	4.0	7.9	13.5[a]
Grain density	Tracks/star			Tracks/star		
15–60	4.6±0.4	4.1±0.4	5.5±0.9	1.5±0.3	1.1±0.3	1.0
>60	12.5±0.7	11.8±0.8	14.5±1.0	4.2±0.5	4.3±0.5	3.0

[a] Mean of two stars $n_s=13$ and $n_s=14$ having the same numbers of tracks in the two grain density ranges.

model. The nucleus is assumed to consist of nucleons randomly distributed throughout a sphere of radius $1.4A^{\frac{1}{3}}\times10^{-13}$ cm and the primary particle is supposed to interact with any nucleons in a cylinder of cross section σ which traverses the nucleus. In its first collision with a nucleon in the nucleus it is assumed that m mesons are created, qm in the second, q^2m in the third, and so on; the chance of a given number of collisions depending on the probability of that number of nucleons being present in the cylinder. It is assumed that no mesons are produced in meson nucleon collisions inside the nucleus. (Camerini *et al.*[4] give evidence from which they infer that only a very small fraction of the mesons can interact with nucleons before escaping.) With this model for the average heavy and light star, values of $q=0.75$ and $m=5.1$ will give the required ratio of 1.19. The average numbers of collisions for heavy and light nuclei are 1.64 and 1.3, the corresponding cross section σ being 16 millibarns. For the same value of q, another solution is obtained corresponding to a mainly plural process but this gives the extremely high value of $\sigma=170$ millibarns, and an incident particle would have, on the average, six collisions traversing a light nucleus and twelve collisions traversing a heavy nucleus, the number of mesons created in the last six collisions for a heavy nucleus contributing only $(0.75)^6\times$ the number of mesons created in the first six collisions. The ratio 1.19 can be satisfied for any value of q between 0.5 and 1.0, and for any value of q in this region there are two values of m, the higher corresponding to mainly multiple meson production and the lower to mainly plural production.

FIG. 3. Star produced from disintegration of a light nucleus giving fourteen shower particles. (Z is estimated as 6 from the nonshower particles.)

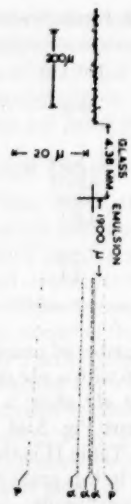

FIG. 4. An oxygen nucleus with energy ~60 Bev/nucleon interacts with a nucleus in the glass backing of the emulsion and does not produce a meson shower.

No solutions for the latter case were acceptable since σ and hence the number of collisions would be too large to explain the apparent independence of the number of nonshower tracks on the number of shower particles as is seen in Table II. Lock and Yekutieli[5] estimate that for stars produced by protons of energy up to 800 Mev, the mean value of the scattering cross section is 30 millibarns. For protons of energy several Bev, which produce stars with meson showers, the higher value of σ which corresponds to plural production thus seems unlikely. It is concluded that meson production is mainly a multiple process and for the stars considered the average multiplicity is 4 to 5 charged mesons per collision.

The hypothesis of multiple meson production is also supported by consideration of some individual stars. Figure 3 shows a star from a light nucleus with an estimated value of Z for the nonshower particles of 6, and 14 shower particles. The evaporation prongs were most probably two alpha particles and a proton, and there was in addition one fast proton of energy 250 Mev. If the nucleus was correctly identified as a light one, a maximum of six nucleons can take part in the meson producing collisions, and several mesons must therefore be produced at single collisions.

The fact that very high-energy particles can interact without meson production also contradicts the assumption that σ is high and that a nucleon suffers many collisions in passing through a nucleus. An example of an event which illustrates this is shown in Fig. 4, where a primary particle with charge 8 and an energy of about 60 Bev/nucleon interacts with a nucleus in the glass backing of the emulsion and produces no meson shower.

[5] W. O. Lock and G. Yekutieli, Phil. Mag. 43, 231 (1952).

Scattering of the Shower Particles

Although the average numbers of shower particles from heavy and light stars are almost the same, there is a considerable difference in the angular distribution of their tracks. The half-angle, *viz.*, that angle containing half the shower particles, for the average showers of multiplicity n_s is given for heavy and light nuclei in Table III. It should be pointed out that for any given value of n_s for a light atom or for a heavy atom there are considerable fluctuations about the mean half-angle and on the mainly multiple hypothesis these can be explained by different degrees of inelasticity at the nucleon-nucleon encounter.[6]

It is seen that the half-angles are consistently larger for heavy than for light nuclei. In order to study the effect in more detail, P, the fraction of tracks per unit interval of $\cos\theta$ emitted at an angle θ to the primary direction, is plotted against $\cos\theta$ for heavy and light nuclei in Fig. 5, and this confirms the wider distribution of shower particles from heavy nuclei. If we make the assumptions that the difference is solely due to scattering, and that there is twice as much scattering in a heavy nucleus as in a light one since the former has twice the diameter of the latter, then the average distribution of mesons from nucleon-nucleon interactions will be as shown in the figure. This curve is obtained by adding to the light curve the difference between the curves for light and heavy nuclei.

If this explanation is correct and mesons are in fact scattered before escaping from the nucleus in which they are produced, it will be of interest to speculate how such scattering occurs. If the scattering takes place with nucleons, an increase of the number of tracks in the grain density interval 15–60 with increasing n_s would be expected, and this is not in accord with the results of Table II. An alternative suggestion might be that the mesons are scattered by alpha groups or larger combinations of nucleons. This interpretation, requiring the temporary existence of nuclear aggregates inside the nucleus, is similar to that suggested by Camerini *et al.*[3] to explain the emission of high-energy fragments from nuclei. In this case the energy per nucleon imparted to the scattering center may not be sufficient for it to escape and would then be added to the thermal excitation energy.

TABLE III. Dependence of mean half-angles on number of shower particles.

n_s		3, 4	5, 6	7, 8	9–12	13–19
Half-angles	Heavy	25°	35°	27°	27°	17°
	Light	23°	17°	13°	13°	15°

[6] W. Heisenberg, Z. Physik **126**, 569 (1949).

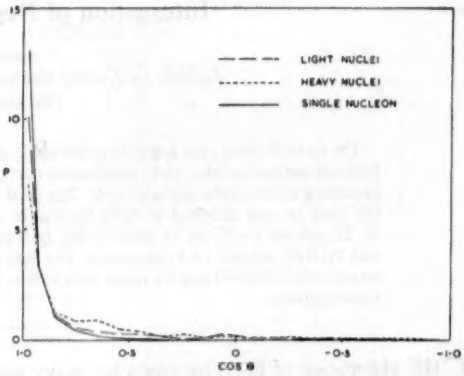

FIG. 5. P, the fraction of tracks per unit interval of $\cos\theta$ emitted at an angle θ to the primary direction, plotted against $\cos\theta$ for the shower tracks from light and heavy nuclei. The estimated angular distribution of shower tracks from the average nucleon-nucleon collision is also plotted.

CONCLUSION

For high-energy interactions such that at least three shower particles are produced, stars induced in light nuclei C, N, O can be separated from those induced in heavy nuclei Ag, Br. In both cases, the low-energy tracks can be explained on the assumption of evaporation from a moving nucleus, but there is a forward collimation of tracks in the grain density interval of 15 to 60 grains/50μ which cannot be explained in this way. This forward component must be related to the primary event and the apparent independence of the number of tracks in this interval on the number of shower particles show that they are not due to meson nucleon interactions and also suggests that the number of primary collisions does not depend to any marked extent on the number of shower particles. This, coupled with the observations of the average number of shower particles from heavy and light nuclei, favors a multiple rather than a purely plural mechanism for meson production. To explain the independence of the number of tracks in the nonshower group on the number of shower particles, it is suggested that the meson scattering inside the nucleus is from nuclear aggregates.

ACKNOWLEDGMENTS

The authors wish to acknowledge the assistance given by the members of the Melbourne cosmic-ray balloon team, Mr. G. R. Trefry of the Commonwealth Meteorological Branch, and the Supply Department. Miss Jean Laby and other members of the group also assisted with some of the measurements. We wish to thank Professor L. H. Martin for his continued interest and support.

Interaction of Negative Pions with Iodine*

LESTER WINSBERG†
Institute for Nuclear Studies, University of Chicago, Chicago, Illinois
(Received March 29, 1954)

The interaction of slow negative pions with iodine was studied radiochemically. From the yields of twenty-five radioactive nuclides, yield distribution curves were obtained for the isotopes of each of the seven elements preceding iodine in the periodic table. The total yields of each element and the displacement in mass units of the peak of each distribution from the line of maximum stability were found to be: Te 58 percent (−3), Sb 22 percent (−2), Sn 11 percent (0), In 3 percent (+1), Cd 0.7 percent (+1), Ag 0.12 percent (+2), and Pd 0.03 percent (+3 estimated). The sum of these yields accounts satisfactorily for essentially all the interactions of slow negative pions with iodine. The results reported here are compared with those of other investigations.

THE absorption of negative pions by heavy nuclei has been studied with photographic plates and counters.[1,2] With few exceptions these methods of detection suffer from the same weakness: the products of the reaction are not determined with certainty except for a few of the lighter particles such as protons, neutrons, and alphas. The radiochemical method of analysis, on the other hand, enables one to determine definitely if a given nuclide is formed in the reaction providing it is radioactive and can be detected and identified unambiguously by its decay characteristics. The other methods of studying meson reactions supply direct information about the neutrons and charged particles which are emitted. Thus the radiochemical and other approaches supplement each other.

Because of low meson intensities, radiochemical investigations were not feasible before the University of Chicago synchrocyclotron came into operation. With this machine, collimated beams of both π^- and μ^- mesons of various energies can be obtained.[3,4] At this laboratory, the interaction of negative pions with nitrogen and oxygen,[5] bromine,[6] zinc,[7] arsenic,[8] and mercury[9] has been investigated as well as the interaction of μ^- mesons with zinc[7] and iodine.[10]

Iodine is a favorable element for this type of study since it is monoisotopic, a large number of the expected products are radioactive and have convenient half-lives, it is suitable for rapid chemical manipulations with kilogram quantities, and it is readily available in elementary form.

The interaction of negative pions with iodine is reported here. The corresponding muon reaction is reported in the following paper.[10]

THE YIELD OF 6-DAY Te^{118} AND 2.8-DAY Sb^{122}

The irradiations were carried out at the University of Chicago synchrocyclotron. The meson beam of maximum intensity contains approximately one to three million negative pions per minute with an energy of about 122 Mev. This intensity has proved to be sufficient for radiochemical work. The mesons are produced when the beam of 450-Mev protons strikes a beryllium target, Fig. 1. The mesons are bent by the fringing field of the magnet into a direction depending on the energy and pass through an appropriate hole in a 12-ft iron shield. The beam is then bent away from the hole by a deflecting magnet. The range of these pions is approximately 56 g per cm² copper.[4]

Among the many radioactive products formed in the interaction of negative pions with iodine are 6-day Te^{118} and 2.8-day Sb^{122}. In order to determine their yields, compartmented samples of iodine were irradiated by monitored beams of negative pions, Fig. 2. Various arrangements of absorber (to slow down the pions), collimator, and sample were employed.

The pions passed through the copper absorber and a collimator with a 1-in. diameter hole before striking the sample. In the case of the first two experiments shown in Fig. 2 the beam was monitored by placing 4 in.×6 in.×½ in. scintillation counters[11] on either side of the absorber-collimator combination at the beginning and end of the irradiation. During the irradiation, variations in the beam intensity were determined by measuring the wattage on the beryllium target by means of a thermocouple. In the third experiment the beam was continuously monitored with the scintillation counters, as shown in Fig. 2.

The iodine sample was divided into four 1-kilogram sections marked 1–4. In the first experiment, section 1 was contained in a 400-ml tall-form beaker, section 2 was a ring of iodine around this inner beaker confined

* This work assisted in part by the U. S. Office of Naval Research and the U. S. Atomic Energy Commission.
† Now at the Weizmann Institute of Science, Rehovot, Israel.
[1] R. Marshak, *Meson Physics* (McGraw-Hill Book Company, Inc., New York, 1952); A. Turkevich, Ann. Rev. Phys. Chem. **4**, 119 (1953). The latter article reviews the literature up to 1953.
[2] W. John and W. F. Fry, Phys. Rev. **91**, 1234 (1953).
[3] Anderson, Marshall, Kornblith, Miller, and Schwarcz, Rev. Sci. Instr. **23**, 707 (1952).
[4] L. Winsberg, Rev. Sci. Instr. (to be published).
[5] A. Turkevich and J. B. Niday, Phys. Rev. **84**, 1253 (1951).
[6] T. T. Sugihara and W. F. Libby, Phys. Rev. **88**, 587 (1952).
[7] A. Turkevich and S. Fung, Phys. Rev. **92**, 521 (1953).
[8] A. Turkevich and J. B. Niday, Phys. Rev. **90**, 342 (1953).
[9] N. Sugarman and A. Haber, Phys. Rev. **92**, 730 (1953).
[10] L. Winsberg, Phys. Rev. **95**, 205 (1954).
[11] Anderson, Fermi, Martin, and Nagle, Phys. Rev. **91**, 155 (1953).

by a 1-liter beaker and sections 3 and 4 were in 6-in. crystallizing dishes. In the second and third experiments, sections 1 and 2 were placed as shown in a sawed-off 1-liter beaker (Fig. 2). Sections 3 and 4 were placed around the 1-liter beaker as in the first experiment.

The intensity of the pions impinging on the sample was obtained by correcting the counting rate of the two scintillation counters for the presence of muons and a penetrating component, presumed to be high energy electrons.[4,12] The correction was 15 percent in the first and second experiments and 70 percent in the third experiment. The pion intensities thus determined were 40 000 counts per minute in the first experiment, 250 000 in the second, and 10 000 in the third. The great variation in intensity was due to the amount of copper absorber used to slow down the pions, the position of the absorber relative to the sample, the length of the collimator, and the intensity of the proton beam striking the beryllium target. A few percent correction was made in the first and second experiments for the absorption of pions in the counters. A correction was made in the third experiment for pions which stopped in the second scintillator thus causing a coincidence event but not interacting with the sample. This was due to the energy spread of the beam.

In the second experiment, in which the thinnest absorber (34 g Cu/cm²) was used, the average range of the pions entering the sample was 22 g/cm² corresponding to an energy of approximately 70 Mev. The range-energy relationships were calculated from values given for protons.[13] Because of the fairly large spread in energy, approximately 27 g/cm² Cu equivalent was required to stop the entire pion beam. The total iodine target was 31 g/cm² in thickness in the direction of the beam. This is equivalent to 28 g/cm² Cu. As a result, no appreciable fraction of the pions should have leaked out the back end of the target in any of the experiments.

Sections 2 and 3 in the first experiment and section 3 in the other two experiments were analyzed separately to indicate if any appreciable fraction of the pions could have leaked out the sides of the sample. The fraction scattering out the side of the sample the beam enters was assumed to be negligible.

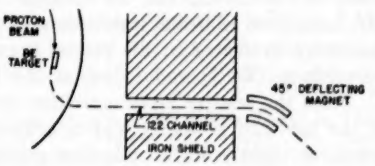

FIG. 1. Meson beam from the 122-Mev π^- channel.

[12] R. L. Martin, Phys. Rev. 87, 1052 (1952).
[13] W. A. Aron, University of California Radiation Laboratory Report UCRL-1325, May, 1951 (unpublished).

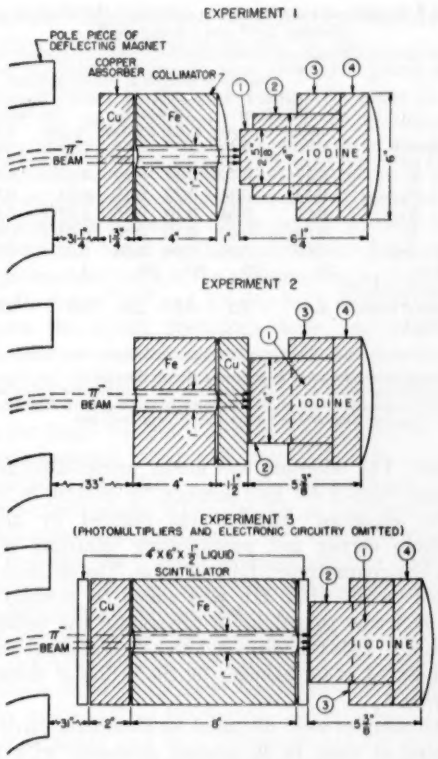

FIG. 2. Top view of experimental arrangements for determining the yield of 6-day Te^{118} and 2.8-day Sb^{122}.

At the end of the irradiation each of the sections was dissolved in 3 liters of ethyl ether, 35 ml 5–6*N* HBr and carrier solutions containing 30 mg tellurium and antimony in the form of the tellurite and antimonous ions. The mixture, which appeared to be a homogeneous solution, was shaken mechanically for 2 to 12 hours in order to insure radiochemical exchange between the radioactive isotopes and the carriers.

A solution of 120 ml 1*N* HBr was then added. The mixture was shaken for 1 or more hours in order to extract the carriers from the ether layer and then was transferred to a 6-liter separatory funnel. One-half liter more of ethyl either was added to decrease the density of the ether solution and thus cause the water layer to settle to the bottom where it could be readily removed. The ether layer was washed with 50 ml 1*N* HBr. The combined water layers were heated to drive off the small amount of ether and iodine present and H_2S was then passed in to precipitate the sulfides of tellurium and antimony. Antimony sulfide was leached out with concentrated HCl and separated from the tellurium fraction.

The tellurium precipitate was digested with a perchloric acid-sulfuric acid mixture to destroy organic impurities and separate out any silica that might be

TABLE I. Results of experiments to determine the absolute yields of 6-day Te^{118} and 2.8-day Sb^{122}.

Section	Fraction of activity in various sections					
	Exper. 1 (55 Mev[a])		Exper. 2 (70 Mev[a])		Exper. 3 (35 Mev[a])	
	6-day Te^{118}	2.8-day Sb^{122}	6-day Te^{118}	2.8-day Sb^{122}	6-day Te^{118}	2.8-day Sb^{122}
1	0.77	0.79	0.54	0.59	0.07(?)	0.07
2	0.14	0.11	0.22	0.17	0.81	0.80
3	0.04	0.04	0.10	0.10	0.07(?)	0.07
4	0.02(?)	0.02	0.10	0.10	0.03(?)	0.04(?)
Glass (est.)	0.03	0.04	0.04	0.04	0.02	0.02
Total A (counts/min)[b]	10	20	40	80	3	7
Measured yield, percent	3.6	2.9	3.1	2.8	2.9	2.8

[a] Approximate energy of π^- mesons entering sample.
[b] Approximate total activity of sample at end of irradiation for a chemical yield of 50 percent and a counting geometry of 50 percent (the latter includes backscattering and self-scattering of beta particles).

present. The tellurium was finally precipitated as the element from a $3N$ HCl solution by passing in SO_2.[14]

The antimony fraction was purified by adding tellurium carrier and precipitating tellurium sulfide from the concentrated HCl solution. The solution was diluted to $3N$ HCl, HF was added to complex tin, and H_2S was passed in to precipitate the sulfide of antimony. This was dissolved and the antimony finally precipitated as the element by the action of chromous chloride.[15]

The samples were mounted on aluminum cards and counted at close to 50 percent geometry with thin-window methane-flow proportional counters designed by N. Sugarman.[9] The calculation of the disintegration rate from the activity followed the procedure of Reed and Turkevich.[16]

In Table I are given the results of these experiments to determine the absolute yields of 6-day Te^{118} and 2.8-day Sb^{122} from the stopping and absorption in iodine of negative pions of various energies. The fraction of the total activity found in each section is presented. The values followed by a question mark were due to activities too small relative to the background of the counters to have much significance. The approximate total activity of each sample and the measured yield are given at the bottom of the table.

The results of Table I suggest that essentially no pions could have leaked out the back end of the sample and at most only a small fraction out the sides.

The values of the yield, Table I, were obtained by dividing the total disintegration rate at saturation by the corrected pion intensity. The average values of the yields, 3.2 percent for 6-day Te^{118} and 2.8 percent for 2.8-day Sb^{122}, have an uncertainty of approximately 20 percent. This is a statistical average of the estimated probable error of 15 percent for the determination of the number of pions which were captured by the sample and 10 percent each for the uncertainty of the total activity of the sample and the calculation of the disintegration rate from the activity.

A WIDE-CHANNEL SCINTILLATION SPECTROMETER

The absorption of a negative pion by iodine results in the formation of many nuclides, some of which decay by beta particle emission and some by K electron capture or isomeric transition. The beta activities were measured as before with a proportional counter. The x-ray and gamma activities were measured with a scintillation spectrometer constructed in this laboratory.

A canned thallium-activated sodium-iodide crystal, one-half in. thick and one and one-half in. in diameter was attached to an RCA 5819 photomultiplier by means of a quarter-in. thick Lucite disk. The photomultiplier was surrounded by a mu-metal shield and finally an aluminum can.[17] The ensemble was sealed light-tight with black rubber cement and mounted on Lucite shelving identical to that designed by Sugarman for the proportional counter.[9] The distance from detector to top shelf was made to be as nearly equal as possible to that of the proportional counter.

The cathode of the photomultiplier was supplied with 900 volts. The signal went through a preamp to a conventional linear amplifier with a maximum gain of about 1000 and capable of supplying an output pulse of 100 volts. Pulse-height selection was performed by a single-channel differential analyzer with base level adjustable up to 100 volts and window to 50 volts. The low counting rates encountered in this work permitted the analyzer to operate at the relatively long resolving time of 10 microseconds. The output signal from the analyzer went to a conventional scaler. A Streeter-Amet traffic counter, such as was used in conjunction with the proportional counters, recorded the readings every twenty minutes.

The top-shelf geometry of the scintillation counter was determined by comparison with the geometry of a low shelf. The latter was calculated from the dimensions of the crystal and its distance from the low shelf. Long-lived tellurium standards were prepared from antimony irradiated in the proton beam of the synchrocyclotron (Te I) and iodine at the betatron (Te II). From the relative x-ray activities on the two shelves, the top-shelf geometry was determined to be 27 percent. A slightly higher effective geometry, 28 percent, was obtained by counting a 200-kilovolt gamma-ray activity.

[14] L. E. Glendenin, in *Radiochemical Studies: The Fission Products* (McGraw-Hill Book Company, Inc., New York, 1951), Paper No. 274, National Nuclear Energy Series, Plutonium Project Record, Vol. 9, p. 1613.
[15] W. F. Boldridge and D. N. Hume, in *Radiochemical Studies: The Fission Products* (McGraw-Hill Book Company, Inc., New York, 1951), Paper No. 272, National Nuclear Energy Series, Plutonium Project Record, Vol. 9, p. 1595.
[16] G. W. Reed and A. Turkevich, Phys. Rev. **92**, 1473 (1953); G. W. Reed, doctoral dissertation, University of Chicago, 1952 (unpublished).
[17] R. K. Swank and J. S. Moenich, Rev. Sci. Instr. **23**, 502–504 (1952).

The energy scale was calibrated with the aid of the tellurium standards and with cadmium, indium, tin, and antimony standards prepared by activation at the betatron. With the possibility of selecting either full or one-tenth gain on the amplifier, the counting range extended from 10 to 1000 kev.

The Te I standard, which had been prepared long before the scintillation counter came into operation, consisted mostly of 150-day Te^{121m} in equilibrium with its 17-day Te^{121} daughter with a lesser amount of 104-day Te^{123m} also present. The counter was calibrated with this standard from time to time.

The analyzer was set in such a way as to achieve the best compromise between a high counting efficiency and low background. Thus in the case of the x-ray of tellurium, 10 to 15 percent of the low-energy part of the x-ray peak was cut off in order to reduce the background from several hundred to about 25 counts per minute. The fraction of the peak being counted was determined from the spectrum of one of the fairly active standards. Depending on the radiation being measured, the window width used for determining the activity of samples from the pion reaction was from 10 to 20 volts.

In this work the scintillation counter was used primarily to count x-ray activity. The measured activities were corrected for geometry, absorption in the sample itself and in the aluminum covering the crystal,[18] K fluorescence yield,[19] fraction of peak being counted, the contribution of the Compton continuum from any gamma radiation also present, and the branching ratio (if different from 1). If the x-ray resulted from conversion of a gamma ray, additional corrections were made for percent conversion and the ratio of conversion in the K shell to the total conversion. Information about the decay schemes was obtained from the compilation of Hollander, Perlman, and Seaborg.[20] A few nuclides were detected by their gamma radiation and the appropriate corrections were made.[18,21]

OTHER YIELDS

In order to get the maximum activation of radioactive nuclides other than 6-day Te^{118} and 2.8-day Sb^{122}, 1 to 2 kilogram quantities of iodine were exposed to the full pion beam for periods of time ranging from 1 to 64 hours. The sample was placed as in Fig. 3 behind a copper absorber $1\frac{1}{2}$ to 2 in. thick. In a few cases a solution of one kilogram of iodine in 2.5 liter of ethyl ether saturated with $2N$ HBr was irradiated in order to reduce the time required for the chemical operations. This was necessary for the detection of activities with half-lives of an hour or less.

The absorber served to slow down the pions sufficiently for most of the pion endings to occur in the sample. By using different thicknesses of absorber it was possible to vary the average energy of the pions entering the sample from approximately 45 to 70 Mev.

The samples were analyzed for two or more of the seven elements preceding iodine in the periodic table by procedures based on those previously developed.[22] The preliminary steps in the analysis were as described above for 6-day Te^{118} and 2.8-day Sb^{122}. In most of the analyses the initial operations were performed by hand with a six-liter separatory funnel instead of mechanical shakers and required approximately an hour or two. This time was as little as twenty minutes when the target was in the form of a solution. When the analysis included silver and palladium, the carriers were added to $7N$ HBr. In more dilute solution these elements precipitate. When the size of the target was two kilograms, twice as much ether and acid solution were required. As a result of more efficient chemical operations, the isolated activities were usually greater from the one kilogram samples.

Tin proved to be the most troublesome element since it precipitates as the oxide under a variety of conditions. In order to insure radiochemical exchange the tin was added as the fluoride complex in most of the experiments and in a few cases as the oxalate. With a few exceptions the chemical yields were either very small or the tin fraction was lost entirely. Fortunately, enough analyses were successful to enable the determination of the tin yields. The indium yields were also low in the first few experiments. The loss of indium seemed to result from prolonged boiling of the extracted water layer.

The purified carriers were mounted as elementary tellurium and antimony, tin oxide, indium oxide, cadmium ammonium phosphate, silver chloride, and palladium iodide.

The yield of a prominent radioisotope of each element, 27-hour Sn^{121}, 49-day In^{114m}, 54-hr Cd^{115}, 7.5-day Ag^{111}, and 13.4-hr Pd^{109}, was determined relative to the value for 6-day Te^{118} and 2.8-day Sb^{122} since the latter activities were a measure of the number of pions captured by the sample. The yields of the

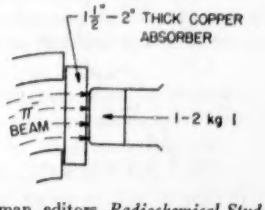

FIG. 3. Position of sample for maximum activation by negative pions.

[18] A. H. Compton and S. K. Allison, *X-rays in Theory and Experiment* (D. Van Nostrand and Company, Inc., New York, 1935); C. M. Davidson and R. D. Evans, Revs. Modern Phys. **24**, 79 (1952).

[19] Broyles, Thomas, and Haynes, Phys. Rev. **89**, 715 (1953).

[20] Hollander, Perlman, and Seaborg, Revs. Modern Phys. **25**, 469 (1953).

[21] T. B. Novey, Phys. Rev. **89**, 672 (1953); J. R. Arnold, Phys. Rev. **93**, 743 (1954).

[22] C. D. Coryell and N. Sugarman, editors, *Radiochemical Studies: The Fission Products* (McGraw-Hill Book Company, Inc., New York, 1951), Part VI, National Nuclear Energy Series, Plutonium Project Record, Vol. 9, Div. IV.

other radioisotopes of the given element were then determined relative to the secondary standard. The half-lives of the secondary standards are sufficiently long to permit precautions for insuring radiochemical exchange.

The activities ranged from a few to 2000 counts per minute. In cases where it was desirable to accentuate a given beta activity, the sample was counted through an 11 or 22 mg/cm^2 aluminum absorber.

In the case of 150-day Te^{121m} and 104-day Te^{123m} the yields were determined by counting gamma radiation in the 200- and 600-kev regions. The relative counting efficiencies of the 214-kev and 506-, 575-kev gammas of Te^{121m} were determined from the Te I standard. Although the sum of the two yields was probably determined quite well, the assignment of the individual values as based on gamma counting was not consistent with the measured x-ray activity. As a result the possibility of the yield of Te^{123m} being greater than that of Te^{121m} cannot be excluded. Because of the long half-lives, it was not possible to resolve the components by following the decay of the activities nor was it possible to determine the yield of 58-day Te^{125m}.

In order to test the interference from general room background and scattering of the direct beam, a 4-hr irradiation was performed with the deflecting magnet off. The correction from this effect was less than 1 percent for most of the radioactive nuclides and was, therefore, neglected. The effect in the case of 9.3-hr Te^{127} which can be formed by $I^{127}(n,p)Te^{127}$ was found to be about 7 percent. The yields of both 9.3-hr Te^{127} and 110-day Te^{127m} were corrected for this effect.

The results of these yield determinations are shown in Table II. In the first column is listed the number of nucleons which must have been emitted for the nuclide to have been formed. The values of the yields are given in the last column. The mean deviation of the results ranged from as small as a few percent of the value for 60-day Sb^{124} to as high as one-fourth of the value in the case of 9.3-hr Te^{127}. Each value was based on 2 or more determinations. Altogether 25 experiments were performed in addition to the three absolute yield determinations of 6-day Te^{118} and 2.8-day Sb^{122}.

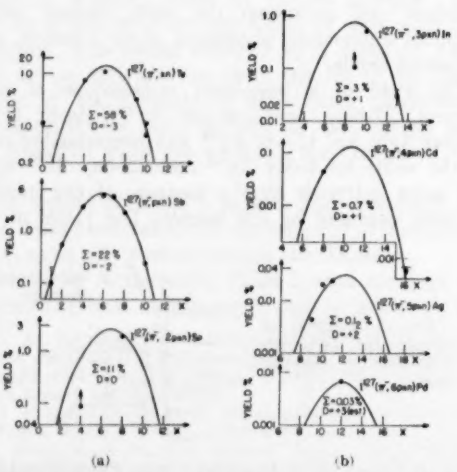

FIG. 4. Isotopic yields from the interaction of negative pions with iodine. D=displacement of peak from line of maximum stability.

DISCUSSION

The yields given in Table II are plotted in Fig. 4 for each element as a function of the number of neutrons which must have been emitted, free or bound in a heavier particle, to form the isotope.

The yield distribution curve was best defined for antimony. The measured yields of 7 antimony isotopes could be readily fitted with a smooth curve having a definite peak at 6 neutrons and a width at half-maximum height of 4 mass units. In the corresponding (π^-,pxn) reaction on As^{75}, Turkevich and Niday[8] found the peak to be at 5.5 neutrons and the width at half-height to be 3.

For none of the other elements was there enough data to enable one to draw a complete curve. The antimony curve was, therefore, fitted to the points for each of the other elements and drawn in as shown in Fig. 4. Except for Te^{127} discussed below, in every case where the entire isotopic yield was determined, the experimental value agreed with the fitted curve within the experimental error.

Several values of the yield fell far below the fitted curve in Fig. 4. In every case these were due to an isomeric state of low spin. The corresponding high-spin state could not be measured either because it was stable or the half-life was outside the range of detection. In the cases where both isomeric states or only the state with high spin could be detected, the yields fell on or close to the curve (again with the exception of Te^{127}). Where only the yield of the high-spin isomer could be determined, the curve (Fig. 4) was drawn through a point about 10 percent higher than the experimental value to account for the yield of the other isomer. This is roughly the fractional yield of 4.5-hr In^{115m} compared to the total value read off the curve. The tellurium curve was drawn so that the sum of the yields of masses 121 and 123 is 10 percent greater than the measured sum for the isomeric states.

The ratio of the yields of the low-spin to the high-spin Cd^{115} isomers, 0.39, agrees well with the values obtained from other high energy reactions.[23,24]

On the basis of the above analysis of the yield data, the distribution curve of the tellurium isotopes appears to have a peak at 6 neutrons, Fig. 4. The corresponding

[23] M. Lindner and I. Perlman, Phys. Rev. **78**, 499 (1950).
[24] P. Kruger, doctoral dissertation, University of Chicago, 1954 (unpublished); P. Kruger and N. Sugarman (to be published).

$Zn(\pi^-,xn)Cu$ reaction was found to have a maximum probability for the emission of 2–3 neutrons.[7]

The sums of the yields for each element as obtained from the smooth curves of Fig. 4 are for tellurium, 58 percent; antimony, 22 percent; tin, 11 percent; indium, 3 percent; cadmium, 0.7 percent; silver, 0.12 percent; and palladium 0.03 percent. Because of uncertainty about radiochemical exchange and how to draw in the smooth curve, the values for tin, silver, and palladium are somewhat in doubt. The total of all the smooth-curve yields is 95 percent, which agrees with the expected 100 percent within the experimental error. It thus appears that we have accounted for essentially all of the interactions of slow π^- mesons with iodine.

TABLE II. Yields from the interaction of π^- mesons with iodine.

Nucleons emitted (n = neutron, p = proton)	Nuclide	Yield, percent
0	9.3-hr Te^{127}	0.55
0	110-day Te^{127m}	0.58
$4n$	104-day Te^{123m}	7.3
$6n$	150-day Te^{121m}	10.9
$9n$	6-day Te^{118}	3.2
$10n$	2.2-hr Te^{117}	0.77
pn	2.7-yr Sb^{125}	~0.1
$p2n$	60-day Sb^{124}	0.55
$p4n$	2.8-day Sb^{122}	2.8
$p6n$	16-min Sb^{120}	1.8
$p6n$	6-day Sb^{120}	2.7
$p7n$	39-hr Sb^{119}	4.5
$p8n$	5.1-hr Sb^{118}	2.2
$p10n$	60-min Sb^{116}	0.24
$2p4n$	27-hr Sn^{121}	0.09
$2p8n$	14-day Sn^{117m}	1.9
$3p7n$ and $3p8n$	1-hr $In^{116 \text{ and } 117}$	0.5
$3p9n$	4.5-hr In^{115m}	0.10
$3p10n$	49-day In^{114m}	0.55
$3p13n$	2.8-day In^{111}	0.03
$4p6n$	2.9-hr Cd^{117}	0.0048
$4p8n$	54-hr Cd^{115}	0.012
$4p8n$	43-day Cd^{115m}	0.031
$4p16n$	6.7-hr Cd^{107}	<0.0007
$5p9n$	5.2-hr Ag^{113}	0.0044
$5p10n$	3.2-hr Ag^{112}	0.020
$5p11n$	7.5-day Ag^{111}	0.024
$5p12n$	270-day Ag^{110}	<0.026
$6p12n$	13.4-hr Pd^{109}	0.0066

A comparison of these results can be made with a similar study of the negative pion activation of bromine[6] and with the prong distribution observed in photographic plates,[1,25,26] Table III. The comparison with the photographic plate results is strictly valid only for 0-prong events. In the other cases a prong consisting of an alpha particle instead of a proton corresponds in the radiochemical studies to the emission of two protons. This, however, will not change the general conclusions very much.

TABLE III. Yields of negative pion interactions with iodine, bromine, and photographic plates.

Number of protons out, or prong number	Yield, percent I^{127}	Yield, percent $Br^{79,81}$	Yield, percent Photographic emulsion
0	58	34	28
1	22	31	23
2	11	21	23
3	3	7	16
4	0.7		7.6
5	0.12		1.4
6	0.03		0.1
Reference	This work	6	1 (based on results of references 25 and 26)

Two features are noticeable from the comparison of the data as given in Table III. The 0-prong (no proton out) events are about twice as numerous in the case of iodine as in the other 2 cases; the events in which 2 or more protons are emitted are about one-half or one-third as numerous for iodine. This result probably reflects the larger Coulombic barrier of the more highly charged iodine nucleus.

A second characteristic to notice in the iodine results as shown in Fig. 4 is the position of the peak of the yield distributions. These occur at the following isotopes, the number in parentheses being the difference in mass units between that of the isotope and that of the line of maximum stability:[27] $Te^{121}(-3)$, $Sb^{120}(-2)$, $Sn^{118}(0)$, $In^{115}(+1)$, $Cd^{112}(+1)$, $Ag^{110}(+2)$, $Pd^{109}(+3$ estimated). There is a definite shift from the neutron deficient to the neutron excess side of stability with increasing charge emission. A similar shift was observed in the interaction of deuterons of energy 100 Mev or less with antimony.[23] This shift appears to depend on the amount of energy imparted to the target nucleus. Such a shift was not observed in higher-energy reactions.[23] In the latter case, neutron-deficient isotopes are the predominant products.

The isotope with the largest mass number difference from I^{127} that we have detected is 13.4-hr Pd^{109}. Its formation requires the emission of 6 protons and 12 neutrons. The 140-Mev rest mass of the pion is insufficient to form this nuclide by the emission of unbound nucleons alone. Therefore, this nuclide must have been formed either with a pion in flight or by the emission of heavier particles.

The multiplicity, or the average number of neutrons emitted per pion capture, can be calculated from the yield distribution curves on the assumption that all the emitted neutrons are unbound. This value, 6.2, agrees very well with the value of 6.4 obtained for

[25] Menon, Muirhead, and Rochat, Phil. Mag. **41**, 583 (1950).
[26] F. L. Adelman, Phys. Rev. **85**, 249 (1952).
[27] *General Electric Chart of the Nuclides*, Knolls Atomic Power Laboratory, November, 1952 (unpublished).

neutrons of energy less than 15 Mev from interpolation of the results of Tongiorgi and Edwards.[28] This agreement indicates that nearly all the neutrons are emitted unbound and with an energy of less than 15 Mev. Similarly, most of the charged particles observed in photographic emulsions are of relatively low energy and most are singly charged, presumably being protons.[25,26,29]

In order to account for the experimental observations on the interaction of negative pions with complex nuclei, it has been proposed that the primary nuclear interaction occurs between the negative pion and a few nucleons.[1] The simplest of these reactions are

$$\pi^-+(p+n)\rightarrow n+n+140 \text{ Mev}, \quad (1)$$

$$\pi^-+(p+p)\rightarrow n+p+140 \text{ Mev}. \quad (2)$$

The nucleons from the reaction may escape from the nucleus without further interaction[30] or suffer collisions with other nucleons. These in turn may escape or transfer energy to still more nucleons. Thus one would expect the entire range of nuclear excitation up to the rest mass of the pion. The great variety of nuclides which result from the absorption of negative pions, Fig. 4, support such a viewpoint.

On the basis of the above equations, one would also expect to find the products of reactions in which only two neutrons or one neutron and one proton are emitted. The product in the former case would be Te^{125}, which we could not detect. The product in the latter case, corresponding to reaction (2), is 2.7-yr Sb^{125} the yield of which is at most about 0.1 percent. The yield could not be determined precisely because there was not sufficient activity nor could the decay be followed because of the long half-life.

The consequences of the two-nucleon model, based on Eqs. (1) and (2), has been compared by Tamor[31] to a model in which the negative pion interacts with an alpha particle (multi-nucleon model). Marshak[1] has brought these calculations up to date and finds the results of the multi-nucleon model in good agreement with data obtained from photographic plates. In such a model the reaction by which 2.7-yr Sb^{125} is formed has no special significance.

The most difficult yields to explain are those of 110-day Te^{127m} and 9.3-hr Te^{127}, because these are products of pion absorption with no emission of nucleons. Moreover, the isotopic yield is far greater than one would expect by extrapolating the tellurium curve of Fig. 4. This, in addition to the nearly equal yields of the two isomers, as opposed to those observed for all the other isomeric states which were measured, indicates that some special reaction was involved in the production of Te^{127}. Four possibilities can be considered, $I^{127}(\pi^-,\pi^0)Te^{127}$, $I^{127}(\pi^-$, gamma radiation$)Te^{127}$, $I^{127}(\mu^-,\nu)Te^{127}$, and $I^{127}(n,p)Te^{127}$, the latter being a secondary reaction of neutrons born in the sample.

The third reaction does not appear to be of major importance because of the relatively weak intensity of the muons in the beam and because the range of the muons was greater than the sample size.

In order to investigate the other three possibilities, the effect of size of sample (50 grams to 2 kilograms to vary the probability of escape of neutrons), various size copper absorbers (to vary the energy of the beam), and variation of distance of sample from absorber (to determine the effect of neutrons born in the absorber), were studied. Although the yields measured for 9.3-hr Te^{127} varied greatly, it was not possible to distinguish between the first two and the last possibilities. Furthermore, the errors of the yield determination were large because of the difficulty of resolving the decay curve. In fact, a 40 percent difference was also observed in the yield of 2.2-hr Te^{117} from samples irradiated as a solution as compared to that from the 1-kilogram solid samples. This too may have been due to an error in resolving the decay curve.

Even with the thinnest samples (50 g) there was some 9.3-hr component. Much more work is necessary in order to determine the origin of Te^{127}.

ACKNOWLEDGMENTS

I am deeply grateful for the cordiality extended me while at the Institute for Nuclear Studies. I wish to thank Professor H. L. Anderson, Mr. L. Kornblith, Jr., Mr. C. Bordeaux, and members of the operating crew for irradiations at the synchrocyclotron; Mr. B. C. Cook and his group for irradiations at the betatron; Professor Anderson, Dr. R. L. Martin, Dr. M. Glicksman, and Mr. G. Yodh for the use of their counting equipment; Dr. D. Engelkemeir and Mr. R. K. Swank of the Argonne National Laboratory and Professor J. R. Arnold for valuable advice on assembling the scintillation counter; Mr. C. Benford and Mr. J. Sherman for building the electronic equipment; Mr. E. Blume for aid in assembling the scintillation counter; and Dr. M. Anbar and Dr. A. Samuels for assistance in preparing the x-ray and gamma standards. Above all, I wish to express my deep gratitude to Professor N. Sugarman and Professor A. Turkevich for the hospitality they extended me and for their invaluable advice on many aspects of this work.

[28] V. C. Tongiorgi and D. A. Edwards, Phys. Rev. **88**, 145 (1952).
[29] W. B. Cheston and L. J. B. Goldfarb, Phys. Rev. **78**, 683 (1950).
[30] R. Serber, Phys. Rev. **72**, 1114 (1947).
[31] S. Tamor, Phys. Rev. **77**, 412 (1950).

Interaction of Negative Muons with Iodine*

LESTER WINSBERG†
Institute for Nuclear Studies, University of Chicago, Chicago, Illinois
(Received March 29, 1954)

The interaction of negative muons with iodine was studied radiochemically. The yield of the $I^{127}(\mu^-,\nu)Te^{127}$ reaction was determined to be 8.2±1.6 percent. The sum of the yields of all antimony isotopes is approximately 1 percent. From the yield of 58-day Te^{125m} and upper limits to the yields of 104-day Te^{123m} and 6-day Te^{118}, yield distribution curves were drawn to fit the extremes of the experimental errors. The multiplicity was thus determined to be 1.7±0.4 neutrons per muon captured. A yield distribution curve which best fits the data is presented.

THE nuclear interaction of negative muons has been shown to be relatively weak compared to pion interactions.[1,2] To account for this, the primary interaction has been postulated to be

$$\mu^- + p = n + \nu + 106 \text{ Mev}, \quad (1)$$

with the neutrino carrying off most of the energy. The state of the interacting proton determines the energy of the resulting neutron. The probability of escape of this neutron and other nucleons in turn depends on its energy. In principle, it should, therefore, be possible to gain insight into these fundamental phenomena by determining the identity of the product nucleus and its energy of recoil and the distribution in number and energy of the emerging nucleons and neutrino(s).

At present it is practically impossible to detect the neutrino directly. The recoil of the product nucleus is barely detectable in photographic plates and cloud chambers for interactions involving light nuclei. However, with the aid of photographic plates, information has been obtained on the charged particles which are emitted.[3] In addition, the multiplicity, or average number of neutrons emitted per muon captured, has been determined for several elements.[4] Some information has also been obtained on the energy of the neutrons produced from muon interactions with iron.[5] Identification of the product nuclei resulting from the interaction of muons with zinc has been recently reported.[6]

A more quantitative determination of the yields of the radioactive product nuclei has been hindered by the preponderance of pions in the meson beams available until now from high-energy accelerators. Recently, a method has been developed for obtaining a pion-free muon beam by absorbing the pions in a graphite filter and magnetically deflecting the emerging muons from the main beam.[7] This now makes possible quantitative radiochemical investigations from which the distribution in number of the escaping neutrons can be determined.

The element iodine was chosen for this study for the reasons given in the preceding paper.[8]

THE YIELD OF 9.3-HR Te^{127}

Of the various radioactive products formed in the interaction of muons with I^{127} the nuclide isolated with the highest counting rate was 9.3-hr Te^{127}. In order to determine its yield a compartmented sample of 4 kg of iodine was irradiated by a monitored beam of negative muons from the University of Chicago synchrocyclotron,[7] Fig. 1.

The muons which initially had an energy of approximately 50 Mev passed through the two scintillation counters, an iron collimator with a 2-in. hole, and a copper absorber and were captured by the target of iodine which was divided into four 1-kg sections, marked 1–4. Sections 1 and 2 were in a sawed-off 1-liter beaker. Sections 3 and 4 were rings of iodine around the beaker, confined by a 6-in. crystallizing dish with its height made up to 4 in. by a ring sawed off another crystallizing dish.

The intensity of the muon beam impinging on the sample was determined from the coincidence rate of the two scintillation counters to be approximately 10 000/min. A 15 percent contribution to the counting

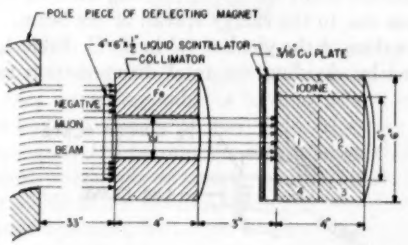

FIG. 1. Top view of setup for determining the yield of 9.3-hr Te^{127}. Photomultipliers and electronic circuitry are omitted.

* This research assisted in part by the U. S. Office of Naval Research and the U. S. Atomic Energy Commission.
† Now at the Weizmann Institute of Science, Rehovot, Israel.
[1] R. D. Sard and M. F. Crouch, *Progress in Cosmic Ray Physics* (Interscience Publishers, Inc., 1954), Vol. 2, p. 3.
[2] A. Turkevich, Ann. Rev. Phys. Chem. **4**, 132 (1953).
[3] H. Morinaga and W. F. Fry, Nuovo cimento **10**, 308 (1953).
[4] M. Widgoff, Phys. Rev. **90**, 891 (1953).
[5] V. L. Niklas and K. H. Lauterjung, Z. Naturforsch. **8A**, 214 (1953).
[6] A. Turkevich and S. C. Fung, Phys. Rev. **92**, 521 (1953).
[7] L. Winsberg, Rev. Sci. Instr. (to be published).
[8] L. Winsberg, preceding paper [Phys. Rev. **95**, 198 (1954)].

rate from a penetrating component presumed to be high-energy electrons was subtracted. The irradiations were from 3 to 7 hours under average synchrocyclotron operating conditions.[7] At the end of the irradiation each of the sections was dissolved in ether, tellurium carrier and dilute HBr solution were added, and the mixture was shaken mechanically for several hours to insure radiochemical exchange between the radioactive tellurium isotopes and the added carrier. The carrier was purified, mounted, and counted by the procedure described in the preceding paper.[8]

The scintillators and the copper plate together have a total equivalent copper thickness of 8 g/cm² and slow the muons down to an average energy of approximately 35 Mev and range of 9 gCu/cm². The range-energy relationships were calculated from values given for protons.[9] Because of the fairly large spread in energy, 22 g/cm² Cu equivalent is required to stop more than 99 percent of the beam as determined by a range curve.[7] The total iodine target is 25 g/cm² in thickness, which is equivalent to 22 gCu/cm². As a result no appreciable fraction of the muons should have leaked out the back end of the target. In two experiments the copper plate was left out and a small correction for leakage (2 percent) was made. In order to check whether any muons could have leaked out the sides of the sample, Secs. 3 and 4 were analyzed separately.

In Table I is given the fraction of the total activity found in each section and in the last column the approximate activities which were obtained. As can be seen from Table I, only approximately 5 percent of the total activity was found in the outer sections. Since the path necessary for a muon to scatter into the outer sections is approximately the range of the muons, it appears that only a negligible number could have leaked out the sides of Secs. 3 and 4. The fraction of muons scattering backward into the scintillator was probably negligible also. The fraction of muons absorbed in the walls of the inner beaker was estimated by interpolating the activities found in Secs. 1 and 4, 2 and 3. A 1 percent correction was made for muons which stopped in the second scintillator thus causing a coincidence event but not interacting with the sample. This was due to the energy spread of the beam.

The values of the yield of 9.3-hr Te^{127}, Table I, were obtained by dividing the total disintegration rate at saturation by the corrected muon intensity. Since the tellurium sample from Sec. 1 in experiment 2 was lost, its activity had to be estimated from the activities in Sec. 1 of experiments 1 and 3. The value of the yield from experiment 2 was, therefore, not included in the average value of the yield.

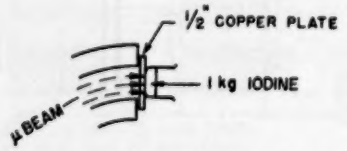

FIG. 2. Position of sample for maximum activation by negative muons.

TABLE I. Distribution of activity of 9.3-hr Te^{127} in iodine samples.

Section	Fraction of activity in various sections Exp. 1	Exp. 2[a]	Exp. 3[a]	A[b] counts/min
1	0.58	(0.57)	0.54	20
2	0.33	0.38	0.38	12
3	0.04	0.01	0.02	1
4	0.03	0.03	0.04	1
Glass (est.)	0.02	0.01	0.02	
Measured yield, percent	5.4	(4.7)	5.1	

[a] No copper plate in front of sample.
[b] Approximate activity of sample at end of irradiation for chemical yield of 50 percent and counting geometry of 50 percent (the latter includes back-scattering and self-scattering of beta particles).

The final value 5.2 percent has an uncertainty of approximately 20 percent, which is a statistical average of the estimated probable error of approximately 10 percent each in the determination of the muon intensity, the total activity of 9.3-hr Te^{127}, and the calculation of the disintegration rate from the activity.

Another possible source of error is the formation of 9.3-hr Te^{127} by way of the $I^{127}(n,p)$ reaction from the neutrons born in the sample. An upper limit to this effect can be estimated from the yield of 9.3-hr Te^{127} in the interaction of π^- mesons with iodine. In the preceding paper the value for the yield of this nuclide was found to be approximately 0.6 percent.[8] If this is assumed to be due entirely to secondary neutrons, then the corresponding yield in the muon reaction would be this value times the ratio of the multiplicities (1.6/6) or 0.16 percent, which is well within the experimental error.

OTHER YIELDS

In order to get sufficient activation of other radioactive nuclides, 1-kg quantities of iodine were exposed to the full muon beam for periods of time ranging from 1 to 140 hr. The sample was placed as in Fig. 2 behind a ½-in. copper plate or 20 in. farther from the magnet behind a ⅛-in. to ½-in. copper plate. The copper plate served to slow down the muons sufficiently for the maximum number of muon endings to occur in the sample. The thickness of the copper plate was determined by the energy of the beam, which in turn depended on the position of the beryllium target.[7] Tellurium, antimony, and in a few experiments tin carriers were added and radiochemical operations performed as in the pion study.[8] The beta, x-ray, and gamma activity of the tellurium samples and the beta activity of the antimony and tin samples were measured as in the preceding paper.[8]

The yields of the various nuclides detected were calculated relative to the value of 5.2 percent for

[9] W. A. Aron, University of California Radiation Laboratory Report UCRL-1325, May, 1951 (unpublished).

9.3-hr Te^{127}, since this activity was a measure of the number of muons captured by the sample. The results are shown in Table II. In the first column is listed the number of nucleons which must have been emitted after muon capture for the nuclide to have been formed. The indicated uncertainties in the values of the yields as given in the last column are a rough estimate of the counting errors.

The initial activity of 9.3-hr Te^{127} was 100 to 900 counts/min at top-shelf geometry (~50 percent). The activities of the others ranged from less than 1 count/min for 60-day Sb^{124} to as much as 25 counts/min for the combined conversion-electron and beta activity of the long-lived tellurium isotopes.

The interference from general room background and the scattering of particles or photons emerging from the 102 channel was negligible. This was shown by a 56-hr irradiation under typical operating conditions but with the deflecting magnet off. No tellurium or antimony activities could be detected from this irradiation.

The yield of 110-day Te^{127m}, the upper state of Te^{127}, was determined by counting through a 22-mg/cm² aluminum absorber. This amount of absorber was sufficient to cut out all the conversion electrons and still permit the betas from the 9.3-hr daughter to be counted. The yield of the reaction $I^{127}(\mu^-,\nu)Te^{127}$ was, therefore, the sum of the yields of the two isomeric states of Te^{127}, 8.2 percent. The uncertainty of this yield is approximately 20 percent of the value.

The yield of 58-day Te^{125m} was obtained by counting the x-rays with a scintillation spectrometer.[8] The contribution to the total x-ray activity from 110-day Te^{127m} was calculated from its beta activity and subtracted. In order to estimate the total yield of Te^{125}, i.e., of the isomeric states plus the stable ground state, it was assumed that the fraction of the yield going to the upper state of both Te^{125} and Te^{127} was the same. This seems plausible since the spins and parities of the upper and the next lower states are identical for both isotopes.[10] Actually the relative yield of high-spin states appears to be greater for higher energy of nuclear excitation.[8] It might, therefore, be expected that the above assumption would give too large a total yield for Te^{125} since a reaction involving the emission of two neutrons should leave the final nucleus with a relatively larger number of high-spin states than for the case where no neutrons were emitted. An effect which perhaps acts in the opposite direction is the presence of a lowermost $\frac{1}{2}+$ state in Te^{125} which does not occur in Te^{127}. If these perturbations are disregarded, the yield of Te^{125} comes to (34 ± 10) percent. The large uncertainty is due to the instability of the scintillation spectrometer during the first few months of its operation and to the above assumption regarding the fraction of the Te^{125} yield appearing as 58-day Te^{125m}.

[10] Hollander, Perlman, and Seaborg, Revs. Modern Phys. **25**, 469 (1953).

TABLE II. Yields from interaction of μ^- mesons with iodine.

Nucleons emitted (n = neutron, p = proton)	Nuclide	Yield, percent
0	9.3-hr Te^{127}	5.2 (standard)
0	110-day Te^{127m}	3.0±0.2
$2n$	58-day Te^{125m}	12.6±2.5
$4n$	104-day Te^{123m}	<5
$9n$	6-day Te^{118}	<0.03
$p2n$	60-day Sb^{124}	0.23±0.07
$p4n$	2.8-day Sb^{122}	0.16±0.02
$2pxn$	Sn	none found

The upper limit to the yield of 104-day Te^{123m} was obtained by looking for the unconverted 159-kev gamma ray. A possible activity of 1 or 2 counts/min above the background of approximately 110 counts/min was found. However, the counting error was so great that no more than an upper limit to the yield could be determined. The total yield for mass 123 is less than 10 percent on the assumption that the emission of 4 neutrons leaves the Te^{123} nucleus with an equal distribution of high-spin and low-spin states.

The upper limit 0.03 percent to the yield of 6-day Te^{118} was calculated from the smallest amount of this activity (~½ counts/min) which could have been detected in one of the long irradiations. To this extent no 6-day Te^{118} was found.

Of all the radioactive antimony isotopes only 2.8-day Sb^{122} was unambiguously identified. Only a small fraction of this activity could possibly be due to pion contamination in the muon beam since its yield from pions is almost the same as for 6-day Te^{118}.[8] The upper limit to the yield of the latter is far less than the value of 0.16 percent found for the yield of 2.8-day Sb^{122} from muons.

After the decay of the 2.8-day isotope a small amount of activity remained which was attributed to 60-day Sb^{124}. The most active long-lived sample which was obtained initially had an activity of ~1.6 counts/min and decayed with a half-life of 40 to 70 days.

DISCUSSION

The yields of most of the tellurium isotopes with masses near that of I^{127} cannot be determined directly since they are either stable or have long-lived isomeric states and are formed in low yield. However, if we subtract from 100 percent the measured yield of Te^{127}, the yield which was estimated for Te^{125}, and the sum of the yields of the antimony isotopes, shown below to be about 1 percent, we obtain 57 percent for the yields of the other tellurium isotopes. Possible tin yields are assumed to be negligible as is the production of iodine isotopes by the direct emission of an electron.[1] In order to get a reasonable looking yield distribution curve for tellurium, most of this 57 percent must be attributed to

stable Te^{128}. We have taken its yield to be 45±15 percent.

Yield curves which fit the extremes of the data are shown in Fig. 3. All of them comply with the restrictions that the sum of all the yields equals 100 percent, with the upper limits of the yields of Te^{122} and Te^{118} (Table II), and with the values of the known yields.

The value of the neutron multiplicity calculated from these curves is 1.7±0.4. This compares favorably with the value of 1.6 obtained by interpolating Widgoff's results.[4] In Fig. 4 is drawn the distribution curve which best fits the experimental results and gives a multiplicity of 1.6. Its width at half of the maximum value is two neutrons.

The antimony yields are plotted in Fig. 5 as a function of the number of neutrons (free or bound in a deuteron or triton) that must have been emitted for the isotope to have been formed. Drawn through the two experimental points are several hypothetical yield curves. In no case was it possible to draw a reasonable looking curve which results in a value of less than 1 percent for the sum of the yields of all the antimony isotopes. The maximum the sum of the yields can be is several percent. The solid line in Fig. 5 is the tellurium curve of Fig. 4 fitted to the antimony data.

This result for the sum of the antimony yields agrees with the work of Morinaga and Fry[3] who found that 2.4 percent of the negative muons stopped in photographic emulsions are accompanied by the emission of charged particles. Of these, more than one-half involved the emission of one proton and no other charged particle. In the case of iodine, a reaction of the latter type results in the formation of antimony isotopes.

Because of the occurrence of many stable and long-lived tin isotopes, it is difficult to set a limit on the total tin yields. The absence of tin radioisotopes to the extent that they could have been detected suggests that the sum of all the tin yields is less than one percent.

In Table III are given the values of the yields as read off Figs. 4 and 5. As can be seen, roughly 80 percent of the reactions result in the emission of one or

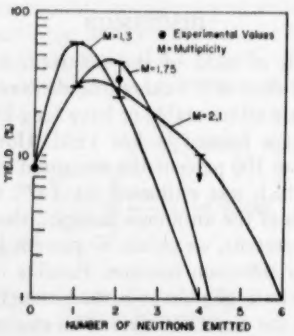

FIG. 3. Possible yield curves of tellurium isotopes from reaction of μ^- mesons with iodine.

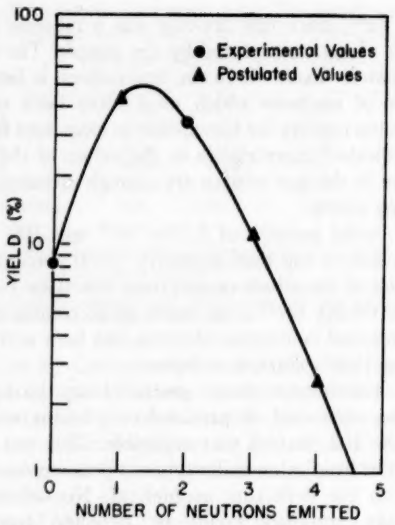

FIG. 4. Yields of tellurium isotopes assuming multiplicity = 1.6.

two neutrons. The most probable interaction involves the emission of one neutron. A similar result was found in the interaction of negative muons with zinc.[6]

If the primary interaction Eq. (1) occurs with a free proton at rest, the neutron which is formed recoils with an energy of about 5.5 Mev. This is less than the binding energy of the neutron in heavy nuclei and hence only Te^{127} would be expected to be formed from I^{127} by μ^- mesons. The combined yield 8.2 percent of the isomers of Te^{127} indicates that the probability of such a simple unperturbed reaction to occur is small. Godfrey found a similar result in the interaction of negative muons with the mass-12 isotope of carbon.[11]

The high yield (92 percent) of reactions in which one or more nucleons are emitted is consistent with the point of view presently in vogue that the primary interaction is represented by Eq. (1) but is strongly perturbed by the interplay of nuclear forces.[12]

The formation of 2.8-day Sb^{122} with a yield of 0.16 percent requires the emission of a proton and 4 neutrons. For this process to occur, the parent Te^{127} nucleus must have had at least 50 Mev of excitation even if a deuteron or triton were emitted. Morinaga and Fry[3] found muon interactions involving carbon nuclei in photographic emulsions in which the energy imparted to the nucleus was as high as 45 Mev. Likewise, Niklas and Lauterjung[5] found neutrons with energies up to approximately 45 Mev from the capture of negative muons in iron.

It is seen that in a small percentage of the interactions a relatively large fraction of the 107-Mev rest mass of muons can be transferred to the nucleus. This is in

[11] T. N. K. Godfrey, Phys. Rev. **92**, 512 (1953).
[12] J. Tiomno and J. A. Wheeler, Revs. Modern Phys. **21**, 153 (1949).

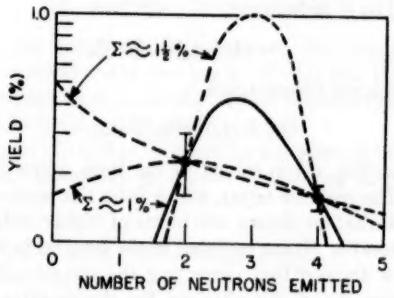

FIG. 5. Possible yield curves of antimony isotopes from reaction of μ^- mesons with iodine.

contradiction to calculations based on the Fermi-gas model which predict that the greatest possible excitation energy is 40 Mev.[1]

The 3.0 percent yield of 110-day Te^{127m} (spin 11/2)[10] relative to 5.2 percent for 9.3-hr Te^{127} (spin 3/2) is plausible when compared to slow-neutron capture by Te^{126} to form these isomers. In the latter case the spin of the target nucleus is 0 and the formation of low-spin states is thus favored. A ratio of 10 to 1 for the cross section of 9.3-hr Te^{127} relative to that of 110-day Te^{127m} is actually found.[13] On the other hand, the target nucleus in the muon reaction is I^{127} with a spin of 5/2 and, furthermore, the neutrino can escape with orbital angular momentum. Hence, it seems reasonable that the yields of the Te^{127} isomers should be more nearly equal.

[13] Seren, Friedlander, and Turkel, Phys. Rev. **72**, 888 (1947).

TABLE III. Yields of μ^- reactions from iodine as read off Figs. 4 and 5.

Number of neutrons (n) and protons (p) emitted	Yield, percent
0	8.2
$1n$	43
$2n$	34
$3n$	11
$4n$	2–3
$1p2n$	0.23
$1p3n$	0.4
$1p4n$	0.16
Rest	<1

ACKNOWLEDGMENTS

I am indebted to Professor H. L. Anderson, Mr. L. Kornblith, Jr., Mr. C. Bordeaux, and members of the operating crew for the irradiations at the synchrocyclotron; to Professor Anderson, Dr. R. L. Martin, Dr. M. Glicksman, and Mr. G. Yodh for the use of their counting equipment; and to Professor A. Turkevich and Professor N. Sugarman for their advice and hospitality during the course of this work.

PHYSICAL REVIEW VOLUME 95, NUMBER 1 JULY 1, 1954

Elastic Scattering of Pions by Nucleons and Pion Production in Nucleon-Nucleon Collisions*

JOHN L. GAMMEL
Los Alamos Scientific Laboratory, University of California, Los Alamos, New Mexico
(Received March 3, 1954)

If the ideas about the pion-nucleon interaction discussed by Chew are taken seriously, it is important to know the accuracy of his calculation of the phase shifts for pion-nucleon scattering resulting from the second-order Tamm-Dancoff approximation. In this paper, exact solutions (found by numerical methods) of the integral equations for the scattering amplitudes resulting from the second-order Tamm-Dancoff approximation are compared with his approximate results.

Aitken, Mahmoud, and Watson have shown that a similar integral equation occurs in a theory (based on the same ideas as those discussed by Chew) of pion production in nucleon collisions. The accuracy of their approximate solution of this integral equation is discussed.

I. INTRODUCTION

As Chew[1] has stated, a theory of the pion-nucleon interaction in which the region of interaction is spread out (or in which a cutoff is introduced in momentum space) makes possible an evaluation of higher-order effects in the scattering. Even when the coupling is weak, the second-order perturbation results may be seriously in error because reactive effects in the scattering may be important.

The scattering amplitudes $(k'|K|k_0)$ satisfy an integral equation of the form[2]

$$(k'|K|k_0)=(k'|V|k_0)+\int\frac{1}{\omega_k-\omega_0}(k'|V|k)(k|K|k_0)k^2dk, \quad (1)$$

* This work was supported by the U. S. Atomic Energy Commission.

[1] Geoffrey F. Chew, Phys. Rev. **89**, 591 (1953).

[2] Throughout this paper, all masses are expressed in units of μ, all momenta in units of μc, and all energies in units of μc^2. μ is the mass of the pion (about 280 electron masses).

where k_0 is the initial momentum of the meson in the center-of-mass system and $\omega_0=(k_0^2+1)^{\frac{1}{2}}$ its initial energy. The phase shifts for pion nucleon scattering are related to $(k'|K|k_0)$ as follows:

$$\frac{1}{\pi\omega_0 k_0}\tan\delta=(k_0|K|k_0). \tag{2}$$

The construction of the potential $(k'|V|k_0)$ from quantum field theory has been discussed by Brueckner and Watson.[3] For pseudoscalar symmetric coupling, the terms in $(k'|V|k)$ proportional to f^2 are[4]

$$(k'|V|k)=\frac{1}{3\pi}f^2\lambda\frac{k'k}{(\omega_k\omega_k)^{\frac{1}{2}}}\frac{1}{\omega_{k'}+\omega_k-\omega_0}, \tag{3}$$

where $\lambda=4$, -2, and -2 for the spin and isotopic spin states $(\frac{3}{2},\frac{3}{2})$, $(\frac{3}{2},\frac{1}{2})$, and $(\frac{1}{2},\frac{3}{2})$, respectively.[5] Also, f^2 is related to g^2 as follows:

$$f^2=(1/4\pi)g^2(\mu/2M)^2. \tag{4}$$

Perturbation theory takes

$$(k_0|K|k_0)=(k_0|V|k_0). \tag{5}$$

That is, Eq. (1) is solved in the Born approximation only. The reactive terms, which from the point of view of perturbation theory are terms of higher order than the second in f^2, are included in the integral in Eq. (1).

Chew showed that correcting the second-order perturbation theory by allowing for the reactive effects removes the most serious discrepancy between perturbation theory and what is supposed about the phase shifts from experimental evidence. That is, the reactive effects make the $(\frac{3}{2},\frac{3}{2})$ phase shift much larger in magnitude than the others occurring in the pion-nucleon scattering.

However, his treatment of Eq. (1) is approximate, and if his suggestions are to be taken seriously, it is important to know the accuracy of his results.

It ought not be claimed that the need for other than moderately accurate solutions (as Chew's are) is really very great, since Eq. (1) with the potential Eq. (3) diverges, so that it is necessary to cut off the integral in Eq. (1) at its upper limit or to use a source function in the integrand (we use a cutoff). Therefore Eq. (1) with Eq. (3) could not represent a final theory of the pion-nucleon scattering even if it were known that terms arising from the fourth- and higher-order Tamm-Dancoff approximations were negligible. However, because Chew's suggestions do seem to lead to results in reasonable agreement with experimental evidence, and because equations like Eq. (1) have not been studied without approximation to see what sort of approximations do give accurate results, it was decided to carry out these calculations.

Aitken, Mahmoud, and Watson[6] found that an integral equation very similar to Eq. (1) occurs in a theory of pion production in nucleon-nucleon collisions based on the same ideas as those discussed by Chew.[1] This equation has also been solved numerically in order to test the accuracy of their approximate solutions.

II. RANGE OF PARAMETERS

Four values of the upper limit for the integral in Eq. (1) are studied. This cutoff should be something like the ratio of the nucleon mass to the pion mass ($1836/280=6.557$), and this is one of the values used. Chew suggested that lower values might be better, and in fact in his original paper,[1] he used very low values. Other values used here are $K=3.5$, $K=4.25$, and $K=5.0$.

Values of k_0 ranging from 0.5375 to 2.0 are used (pion energy in the laboratory system from 25.48 to 272.5 (Mev). Values of f^2 from 0 to 0.6 are used.

[3] K. Brueckner and K. Watson, Phys. Rev. **90**, 699 (1953). The existence of an integral equation like Eq. (1) depends on the possibility of constructing this potential. Equation (24) of reference 3 is

$$(k|\Omega|k_0)=\frac{1}{k_0^2}\delta(k-k_0)+\frac{1}{\omega_k-\omega_{k_0}}\int(k|V|k'')(k''|\Omega|k_0)k''^2dk''.$$

Since

$$(k'|K|k_0)=\int(k'|V|k)(k|\Omega|k_0)k''^2dk'',$$

we need only multiply Eq. (24), reference 3, by $k^2(k'|V|k)$ and integrate over k to get our Eq. (1).

[4] K. Brueckner and K. Watson, Phys. Rev. **92**, 1023 (1953). Using an expansion of the potential $(k'|V|k)$ in powers of f^2 in Eq. (1) falls into the general category known as the Tamm-Dancoff approximation. Thus in this paper we are dealing with the second order Tamm-Dancoff approximation.

[5] For the $(\frac{1}{2},\frac{1}{2})$ state, the potential has to be renormalized. See G. F. Chew, this issue [Phys. Rev. **95**, 285 (1953)]. This state is not considered in this paper. In working our Eq. (3), only the term

$$H'=(g/2M)\boldsymbol{\sigma}\cdot\nabla\boldsymbol{\tau}\cdot\boldsymbol{\phi}$$

in the nonrelativistic limit (for the nucleon) of the pseudoscalar symmetric coupling is retained. As is well known, it leads only to P-state interactions. The term

$$H'=(g^2/2M)\boldsymbol{\phi}\cdot\boldsymbol{\phi}$$

leads to an S-wave interaction, for which the potential $(k'|V|k)$ is

$$(k'|V|k)=\lambda\frac{1}{(\omega_k\omega_{k'})^{\frac{1}{2}}}.$$

With this expression for $(k'|V|k)$, which separates into a product of two functions, one a function of k' only and the other a function of k only, Eq. (1) may be solved exactly as follows: Let

$$\Lambda(k_0)=\int\frac{k'^2dk'}{\sqrt{\omega_{k'}}}\frac{1}{\omega_{k'}-\omega_0}(k'|K|k_0).$$

This is an as yet undetermined function of k_0. Equation (1) is

$$(k|K|k_0)=\frac{\lambda}{\sqrt{\omega_k\omega_0}}+\frac{\lambda}{\sqrt{\omega_k}}\Lambda.$$

Substituting this into the previous equation gives

$$\Lambda=\frac{\lambda}{\sqrt{\omega_0}}\int\frac{k^2dk}{\omega_k(\omega_k-\omega_0)}+\lambda\Lambda\int\frac{k^2dk}{\omega_k(\omega_k-\omega_0)}.$$

If

$$-M=\int\frac{k^2dk}{\omega_k(\omega_k-\omega_0)},$$

the previous equation is

$$\Lambda=-(\lambda/\sqrt{\omega_0})M-\lambda M\Lambda,$$

which is easily solved for Λ. Substituting this into the expression for $(k|K|k_0)$ above gives

$$(k_0|K|k_0)=\frac{\lambda}{\omega_0}\frac{1}{1+\lambda M}.$$

[6] Aitken, Mahmoud, and Watson, Phys. Rev. **93**, 1349 (1954).

III. METHOD OF SOLUTION

First, the range of integration in the integral in Eq. (1) is broken into two parts: $(0,2k_0)$ and $(2k_0,K)$. This required $2k_0 \leqslant K$, so that at the high energies the low cutoffs could not be used.

Equation (1) is then replaced by a system of twenty-five linear equations as follows [replacing $(k'|K|k_0)$ by $K(k')$]:

$$K(k_i)=(k_i|V|k_0)+\sum_{j=0}^{n} w_j G(k_i,k_j)K(k_j)\tfrac{1}{3}\Delta_1 + \sum_{j=n}^{24} w_j G(k_i,k_j)K(k_j)\tfrac{1}{3}\Delta_2. \quad (6)$$

In this equation,

$$\Delta_1=2k_0/n, \quad \Delta_2=(K-2k_0)/(24-n); \quad (7)$$

n is chosen to make Δ_1 and Δ_2 as nearly equal as possible. Also

$$\begin{aligned} k_i &= i\Delta_1, && i\leqslant n; \\ k_i &= 2k_0+(i-n)\Delta_2, && n\leqslant i\leqslant 24. \end{aligned} \quad (8)$$

The w_j are weight factors corresponding to the method of numerical integration (we use Simpson's rule: $w_0=1$, $w_1=4$, $w_2=2$, $\cdots$, $w_n=1$, $w_{n+1}=4$, $\cdots$, $w_{24}=1$). The kernel $G(k_i,k_j)$ is

$$G(k_i,k_j)=\frac{1}{\omega(k_j)-\omega(k_0)}(k_i|V|k_j). \quad (9)$$

It would be a straightforward matter to solve Eq. (6) (it takes only one minute to solve a system of twenty-five linear equation on the Los Alamos MANIAC), but a singularity occurs in the kernel Eq. (9) for $j=\frac{1}{2}n$.

The following method was used to avoid this singularity. $K(k_0)$ through $K(k_n)$ are replaced by new unknowns:

$$Z(k_j)=K(k_j)+K(k_{n-j}),$$

$$Y(k_j)=\frac{1}{k_j-k(\frac{1}{2}n)}[K(k_j)-K(k_{n-j})], \quad j\leqslant \tfrac{1}{2}n. \quad (10)$$

This requires n to be an even integer.

The first sum in Eq. (6) is replaced by

$$\sum_{j=0}^{n} w_j G(k_i,k_j)K(k_j) = \tfrac{1}{2}\sum_{j=0}^{n/2} w_j[G(k_i,k_j)+G(k_i,k_{n-i})]Z(k_j)\tfrac{1}{3}\Delta_1 + \tfrac{1}{2}\sum_{j=0}^{n/2} w_j[G(k_i,k_j)-G(k_i,k_{n-i})] \times[k_j-k(\tfrac{1}{2}n)]Y(k_j)\tfrac{1}{3}\Delta_1. \quad (11)$$

If new kernels are defined as

$$\begin{aligned} G^+(k_i,k_j)&=\tfrac{1}{2}[G(k_i,k_j)+G(k_i,k_{n-i})], \\ G^-(k_i,k_j)&=\tfrac{1}{2}[k_j-k(n/2)][G(k_i,k_j)-G(k_i,k_{n-i})], \end{aligned} \quad (12)$$

Eq. (6) becomes

$$\begin{aligned} &\tfrac{1}{2}Z(k_i)+\tfrac{1}{2}[k_i-k(\tfrac{1}{2}n)]Y(k_i) \\ &=(k_i|V|k_0)+\sum_{j=0}^{n/2} w_j G^+(k_i,k_j)Z(k_j)\tfrac{1}{3}\Delta_1 \\ &\quad+\sum_{j=0}^{n/2} w_j G^-(k_i,k_j)Y(k_j)\tfrac{1}{3}\Delta_1 \\ &\quad+\tfrac{1}{2}G[k_i,k(\tfrac{1}{2}n)]\{Z[k(\tfrac{1}{2}n)] \\ &\quad+k(\tfrac{1}{2}n)Y[k(\tfrac{1}{2}n)]\}\tfrac{1}{3}\Delta_2 \\ &\quad+\sum_{j=n+1}^{24} G(k_i,k_j)K(k_j)\tfrac{1}{3}\Delta_2, \quad i\leqslant n; \end{aligned} \quad (13)$$

$$K(k_i)=\text{same thing}, \qquad i>n.$$

Since K is a regular function, so are Z and Y. It can be seen that G^+ and G^- are regular, so that the system Eq. (6) with the singular kernel Eq. (9) has been replaced by the system Eq. (13) in which everything is finite.

However, we have replaced the $n+1$ unknowns $K(k_i)$ by $n+2$ unknowns $Z(k_i)$ and $Y(k_i)$. Therefore we need an additional requirement. For this we have chosen to require that $Y(k_i)$ be continuous. We actually required that

$$Y(\tfrac{1}{2}n)=Y[\tfrac{1}{2}n-1]. \quad (14)$$

IV. RESULTS OF THE PHASE-SHIFT CALCULATION

According to Eq. (3), the result of the calculation depends on the product $f^2\lambda$, and the result also depends on the cutoff K.

Table I presents the phase shifts as a function of $f^2\lambda$, the cutoff K, and the energy E_{lab} in the laboratory system.

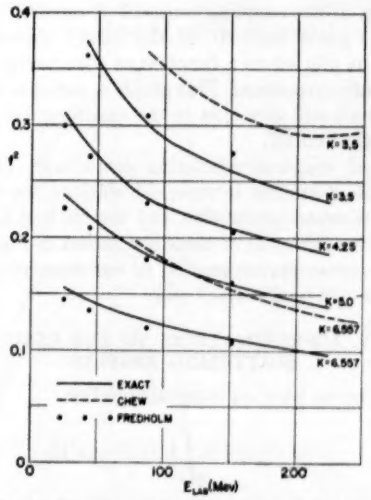

FIG. 1. The value of f^2 for which $\delta_{33}=90°$ at the energy shown on the abscissa.

TABLE I. Phase shifts in degrees as a function of the coupling constant $f^2\lambda$, the cutoff K, and the energy E_{lab}.

f^2 \ K	3.5	4.25	5.0	6.577
		$E_{lab}=25.48$ Mev		
−0.6	3.316	3.191	3.104	3.066
−0.45	2.760	2.640	2.558	2.504
−0.3	2.089	1.996	1.930	1.870
−0.225	1.695	1.624	1.564	1.509
−0.15	1.236	1.187	1.154	1.105
−0.075	0.6837	0.6673	0.6509	0.6290
+0.075	−0.9079	−0.9517	−1.006	−1.181
+0.15	−2.225	−2.580	−3.256	−32.87
+0.225	−4.416	−6.643	−26.14	+1.466
+0.3	−9.112	−52.60	6.319	0.08861
+0.45	37.88	5.562	1.433	−1.356
+0.6	9.218	2.482	−0.03172	−2.645
		$E_{lab}=43.96$ Mev		
−0.6	6.678	6.413	6.288	6.102
−0.45	5.615	5.365	5.224	5.114
−0.3	4.314	4.117	3.991	3.858
−0.225	3.535	3.370	3.268	3.141
−0.15	2.606	2.503	2.424	2.330
−0.075	1.469	1.430	1.398	1.343
+0.075	−2.046	−2.163	−2.306	−2.763
+0.15	−5.232	−6.272	−8.316	43.29
+0.225	−11.23	−19.51	71.03	6.280
+0.3	−27.16	51.48	10.32	0.3145
+0.45	33.06	9.473	2.937	−2.598
+0.6	14.68	4.832	0.1999	−5.294
		$E_{lab}=88.26$ Mev		
−0.6	16.23	15.44	15.08	14.89
−0.45	13.86	13.17	12.72	12.45
−0.3	10.94	10.36	9.933	9.590
−0.225	9.122	8.626	8.266	7.920
−0.15	6.878	6.543	6.292	5.985
−0.075	3.993	3.866	3.740	3.585
+0.075	−6.124	−6.613	−7.253	−9.412
+0.15	−17.14	−22.39	−35.58	27.05
+0.225	−40.97	−80.93	38.54	
+0.3	−88.02	40.48	17.39	14.98
+0.45	38.72	17.91	7.100	−4.962
+0.6	25.46	10.96	1.893	−11.07

f^2 \ K	3.5	4.25	5.0	6.577
		$E_{lab}=25.48$ Mev		
		$E_{lab}=151.7$ Mev		
−0.6	28.54	26.96	26.43	26.25
−0.45	24.79	23.19	22.53	21.95
−0.3	19.96	18.54	17.81	17.18
−0.225	16.85	15.67	14.98	14.27
−0.15	12.94	12.12	11.59	10.96
−0.075	7.689	7.358	7.093	6.740
+0.075	−12.68	−14.19	−16.00	−23.10
+0.15	−35.75	−50.76	−79.12	28.72
+0.225	−72.28	70.51	39.94	10.62
+0.3	75.67	43.44	24.23	3.828
+0.45	47.31	25.70	12.42	−5.587
+0.6	36.19	17.93	5.521	−13.93
		$E_{lab}=223.5$ Mev		
−0.6	43.10	41.3	39.97	39.78
−0.45	37.57	35.66	34.12	33.20
−0.3	30.60	28.79	26.67	25.96
−0.225	26.22	24.56	22.35	21.72
−0.15	20.49	19.27	18.03	16.83
−0.075	12.46	11.93	11.30	10.57
+0.075	−24.67	−23.63	−28.38	−45.46
+0.15	−54.59	−68.75	79.41	31.56
+0.225	−86.94	72.37	40.16	14.92
+0.3	+72.98	53.69	26.96	7.101
+0.45		37.36	14.79	−3.810
+0.6		28.86	7.393	−13.00
		$E_{lab}=272.5$ Mev		
−0.6			49.73	49.39
−0.45			41.97	41.06
−0.3			33.44	31.96
−0.225			28.44	26.77
−0.15			22.44	20.81
−0.075			14.23	13.20
+0.075			−36.67	−59.49
+0.15			76.52	34.11
+0.225			47.25	17.84
+0.3			35.01	9.570
+0.45			22.58	−1.927
+0.6			14.68	−11.21

In Fig. 1, the coupling constant f^2 required to make the $(\frac{3}{2},\frac{3}{2})$ phase shift 90° at the energy shown on the abscissa is plotted as a function of that energy for the four cutoffs considered. This graph is useful in choosing an f^2 which will give a fit to the experimental data for a prescribed cutoff.

The off diagonal scattering amplitudes $(k|K|k_0)$, $k\neq k_0$, are of interest in some calculations, for example, the photomeson production and the nucleon Compton effect. Two examples of these are shown in Fig. 2.[7]

An accurate approximation to our scattering results exists, as will be discussed now.

V. APPROXIMATIONS TO THE EXACT SCATTERING RESULTS

Suppose we have an integral equation

$$y(x)=f(x)+\lambda\int K(x,x')y(x')dx'. \tag{15}$$

The integral Eq. (1) is of this form. For Eq. (1) there exists a value of λ for which $y=\infty$. [More precisely, for a given cutoff K there exists a value of $f^2\lambda$ for which $(k|K|k_0)=\infty$, or for which the phase shift is 90°. We may find this value of $f^2\lambda$ from Fig. 1 if we remember that $\lambda=4$ for the $(\frac{3}{2},\frac{3}{2})$ state.] Let us call this value of λ, λ_∞.

The iteration solution of Eq. (15),

$$y(x)=f(x)+\lambda\int K(x,x')f(x')dx$$

$$+\lambda^2\int K(x,x')K(x',x'')f(x'')dx''+\lambda^3\cdots, \tag{16}$$

could not converge for $\lambda>\lambda_\infty$.

There is another (perhaps well-known) expression for $y(x)$ which is related to the Fredholm theory of integral

[7] The author will be glad to supply tables of these to workers interested in special values of the cutoff and coupling constants.

equations; namely,

$$y(x)=\frac{f(x)+\lambda\int K(x,x')f(x')dx-\lambda f(x)\int K(x',x')dx'+\cdots}{1-\lambda\int K(x,x)dx+\cdots}, \tag{17}$$

which is formally identical with Eq. (16) provided $\lambda<\lambda_\infty$. However, Eq. (17) can still represent $y(x)$ for $\lambda>\lambda_\infty$, and probably represents it for all $\lambda<\infty$.

The point we want to make is that retaining terms to the first order in λ in the numerator and denominator in Eq. (17) provides an accurate approximation to the solutions of Eq. (1) which we have found by numerical integration.

We may write Eq. (17) as follows:

$$y(x)=\frac{f(x)\left[1+\frac{1}{f(x)}\lambda\int K(x,x')f(x')dx'-\lambda\int K(x',x')dx'\right]}{1-\lambda\int K(x',x)dx'}=\frac{f(x)(1+\lambda\Delta_I(x)-\lambda\Delta_F)}{1-\lambda\Delta_F}. \tag{18}$$

$\Delta_I(x)$ is so labeled because it results from iterating the solution in the numerator, and Δ_F is so labeled because Eq. (17) is related to the Fredholm theory of integral equations.

The value of y at only one value of $x=x_0$ [or the value of $(k|K|k_0)$ at only $k=k_0$, according to Eq. (2)] is needed to find the phase shifts. Chew's approximation for the phase shift, Eq. (1′) of reference 1, results if one takes

$$y(x_0)=f(x_0)/[1-\lambda\Delta_I(x_0)]. \tag{19}$$

He has not given an expression for the off diagonal elements.

Table II presents Δ_F and $\Delta_I(x_0)$, for which we have the following expressions:

$$\frac{2}{\lambda}\frac{1}{f^2}\Delta_I(x_0)=\frac{2}{3\pi}\omega_0\int_1^{\omega_k}d\omega\frac{k^3}{\omega_k^2(\omega_k-\omega_0)}, \tag{20}$$

and

$$\frac{2}{\lambda}\frac{1}{f^2}\Delta_F=\frac{2}{3\pi}\int_1^{\omega_k}d\omega\frac{k^3}{(2\omega_k-\omega_0)(\omega_k-\omega_0)}. \tag{21}$$

The zeros of the denominators of Eqs. (18) and (19) should reproduce Fig. 1. It is seen that Eq. (18) is very accurate in this respect, while Eq. (19) fails badly, especially for larger cutoffs.

Figure 3 compares the extent to which the two approximations reproduce the exact results for the $(\frac{3}{2},\frac{3}{2})$ phase shift as a function of energy for various coupling constants and cutoffs.

To calculate the off-diagonal scattering amplitudes, it is necessary to know $\Delta_I(k)$ for $k\neq k_0$. This quantity is tabulated in Table III for the same cutoffs and energies used in the exact calculations.

Approximate values of $(k|K|k_0)$ calculated from Eq. (18) are compared to our exact results for several

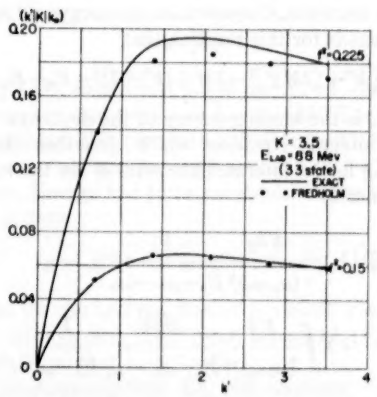

FIG. 2. $(k'|K|k_0)$ as a function of k' according to the approximations described in the text.

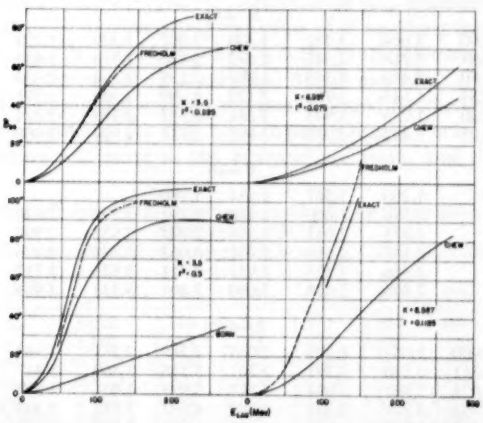

FIG. 3. δ_{33} as a function of energy for several cutoffs and coupling constants according to the approximations described in the text.

TABLE II. $2\Delta_I(k_0)/f^2\lambda$ and $2\Delta_F/f^2\lambda$ [see Eqs. (20) and (21)] as a function of the energy E_{lab} and the cutoff K.

	$K=3.5$		$K=4.25$		$K=5.0$		$K=6.557$	
E_{lab} (Mev)	$2\Delta_F/f^2\lambda$	$2\Delta_I/f^2\lambda$	$2\Delta_F/f^2\lambda$	$2\Delta_I/f^2\lambda$	$2\Delta_F/f^2\lambda$	$2\Delta_I/f^2\lambda$	$2\Delta_F/f^2\lambda$	$2\Delta_I/f^2\lambda$
25.48		0.9134	1.698	1.135	2.212	1.351	3.464	1.789
43.96	1.373	1.058	1.850	1.306	2.383	1.547	3.623	2.031
88.26	1.630	1.359	2.171	1.683	2.760	1.991	4.151	2.600
151.7	1.807	1.600	2.442	2.033	3.109	2.435	4.637	3.209
223.5		1.704		2.292		2.817		3.799
272.5		1.666		2.379		2.996		4.127

cutoffs and coupling constants in Fig. 3. Of course Eq. (18) fails quite badly near the values of f^2 and K for which either the exact or approximate K is infinite. Even in this case, the approximation Eq. (18) may be looked upon as accurate in the sense that it reproduces the exact results for a very slightly different value of f^2.

VI. PION PRODUCTION IN NUCLEON-NUCLEON COLLISIONS

Aitken, Mahmoud, and Watson[6] have discussed the three reactions

$$\begin{aligned} &p+p\rightarrow\pi^++d,\\ &p+p\rightarrow\pi^++n+p,\\ &n+p\rightarrow\pi^++n+n. \end{aligned} \tag{22}$$

In the initial state for these processes, one of the nucleons has a momentum $\mathbf{p}$ and the other a momentum $-\mathbf{p}$ (center-of-mass system). The connection between the total energy available in the center-of-mass system and p is

$$E_a=2[(p^2+M^2)^{\frac{1}{2}}-M]. \tag{23}$$

The threshold for pion production occurs at $E_a=1$, or 294 Mev in the laboratory system. The threshold for production of two pions occurs at $E_a=2$, or at 613 Mev in the laboratory system. In this calculation we cover the range of energies for which only a single meson may be produced.

In the intermediate state, the nucleon of momentum $\mathbf{p}$ emits a pion of momentum $\mathbf{k}_0$. Now the reactions may proceed in two ways, which are coherent with each other, so that the final expression for the cross sections should contain the sum of two terms squared. In the first way, the nucleons scatter to their final state momenta. In the second way, the pion emitted by the first nucleon is scattered by the second nucleon, and its momentum in the final state is $\mathbf{k}'$. Since we are going to assume that a pion and nucleon interact only in a $(\frac{3}{2},\frac{3}{2})$ state, the second way cannot occur for the third reaction, since the total charge ($T_z=\frac{1}{2}$) is not sufficient to lead to a $T=\frac{3}{2}$ state (the neutron cannot emit a π^+ particle, and the proton cannot emit a π^- particle). This means that the first two reactions should have larger cross sections than the third (this is essentially the point of the paper of Aitken, Mahmoud, and Watson).

For either way, for the first reaction, a final state interaction[6] between the nucleons leads to the formation of a deuteron. Conservation of energy and momentum demands for this reaction that

$$[k'^2+(2M)^2]^{\frac{1}{2}}-2M+(k'^2+1)^{\frac{1}{2}}=E_a-E_d, \tag{24}$$

where E_d is the binding energy of the deuteron.

This integral equation which describes the pion scattering in the intermediate state is (in the notation of reference 6)

$$\begin{aligned} (k'|t_1(\tfrac{3}{2},\tfrac{3}{2})|k_0)=&\frac{k'k_0}{(\omega_{k'}\omega_0)^{\frac{1}{2}}}\frac{1}{E_a-\omega_{k'}-\omega_0}\\ &+\lambda\int\frac{k'k}{(\omega_k\omega_k)^{\frac{1}{2}}}\frac{k^2dk}{E_a-\omega_{k'}-\omega_k}\frac{1}{E_a-\omega_k}\\ &\times(k|t_1(\tfrac{3}{2},\tfrac{3}{2})|k_0), \end{aligned} \tag{25}$$

TABLE III. $2\Delta_I(k)/f^2\lambda$ as a function of the momentum k, the energy E_{lab}, and the cutoff K.

k \ E_{lab} (Mev)	25.48	43.96	88.26	151.7	223.5	272.5
			$K=3.5$			
0.0	0.8622	0.9671	1.150	1.202	0.9397	0.4454
0.7	0.9433	1.055	1.261	1.357	1.233	0.9617
1.4	1.083	1.205	1.442	1.592	1.568	1.428
2.1	1.202	1.331	1.588	1.769	1.794	1.697
2.8	1.293	1.426	1.696	1.895	1.945	1.870
3.5	1.363	1.499	1.777	1.987	2.052	1.988
			$K=4.25$			
0.00	1.064	1.181	1.400	1.507	1.335	1.198
0.85	1.218	1.347	1.602	1.776	1.776	1.636
1.70	1.456	1.599	1.897	2.139	2.254	2.233
2.55	1.645	1.796	2.120	2.399	2.568	2.591
3.40	1.786	1.943	2.281	2.582	2.780	2.824
4.25	1.892	2.053	2.401	2.715	2.929	2.986
			$K=5.0$			
0	1.260	1.387	1.634	1.780		
1	1.516	1.660	1.958	2.195	2.292	2.240
2	1.875	2.037	2.388	2.708	2.932	2.996
3	2.147	2.319	2.701	3.063	3.346	3.456
4	2.346	2.525	2.925	3.311	3.624	3.757
5	2.496	2.679	3.090	3.491	3.823	3.969
			$K=6.557$			
0.000	1.655	1.797	2.085	2.289	2.261	1.563
1.311	2.220	2.391	2.767	3.116	3.369	3.447
2.623	2.897	3.094	3.544	3.999	4.401	4.599
3.934	3.379	3.591	4.080	4.587	5.057	5.303
5.245	3.726	3.947	4.458	4.995	5.501	5.773
6.557	3.987	4.213	4.738	5.293	5.821	6.108

[6] K. M. Watson, Phys. Rev. **88**, 1163 (1952).

TABLE IV. Δ [see Eq. (29)] calculated by various methods as a function of the coupling constant f^2 and the energy E_{lab} for $K=6.557$.

f^2	$E_{lab}=320$ Mev Δ_{exact}	Δ_{Fred}	$E_{lab}=350$ Mev Δ_{exact}	Δ_{Fred}	$E_{lab}=370$ Mev Δ_{exact}	Δ_{Fred}	Δ_{AMW}
0.0375	1.10	1.10	1.05	1.07	1.03	1.06	1.37
0.075	1.55	1.58	1.55	1.63	1.57	1.66	2.15
0.1125	2.71	3.05	3.05	3.68	3.40	4.28	5.04
0.15	13.8	−299	−216	−10.0	−16.1	−6.145	−14.5
0.1875	−4.16	−2.71	−2.84	−1.99	−2.31	−1.691	−2.98
0.225	−1.87	−1.30	−1.39	−1.06	−1.22	−0.95	−1.66
	$E_{lab}=410$ Mev		$E_{lab}=500$ Mev		$E_{lab}=600$ Mev		
0.0375	0.99	1.04	0.93	1.00	0.89	0.96	1.37
0.075	1.63	1.75	1.82	1.99	2.27	2.33	2.15
0.1125	5.17	7.25	36.6	−58.3	−4.28	−5.06	5.04
0.15	−5.34	−3.46	−2.00	−1.79	−1.09	−1.18	−14.5
0.1875	−1.66	−1.31	−0.96	−0.89	−0.87	−0.67	−2.98
0.225	−0.97	−0.78	−0.63	−0.58	−9.43	−0.46	−1.66

where $\lambda=4f^2/3\pi$. This is Eq. (33) of reference 6. The only difference between it and our Eq. (1) is that the sign of K and t are opposite, and the connection between E_a and k_0 is different. For pion-nucleon scattering, $E_a=\omega_0$, whereas for pion production in nucleon-nucleon collisions there is no strict connection between the two.

Aitken, Mahmoud, and Watson wrote the solution of Eq. (25) in the form

$$(k'|t_1(\tfrac{3}{2},\tfrac{3}{2})|k_0)=\frac{\lambda k'k_0}{(\omega_{k'}\omega_0)^{\frac{1}{2}}}\frac{1}{E_a-\omega_{k'}-\omega_0}\Delta. \quad (26)$$

That is, they took the inhomogeneous term (or Born's approximation) and multiplied it by a numerical factor Δ which is supposed to allow for the reactive effects. Then they made further approximations based on the following observations about the magnitudes of the quantities k' and k_0 which are especially appropriate near threshold ($E_a=1$).

Since both nucleons are brought nearly to rest in these reactions, the first nucleon must emit a pion of momentum nearly equal to $\mathbf{p}$, coming nearly to rest in so doing. Thus,

$$k_0\approx p. \quad (27)$$

From Eq. (23), we see that $p\approx M^{\frac{1}{2}}$ for $E_a\approx 1$. Assuming $M\gg 1$, we have then $p\approx\omega_p$, or $k_0\approx\omega_0\approx M^{\frac{1}{2}}$. The second nucleon scatters this pion into a final momentum state $\mathbf{k}'$, the second nucleon having a momentum $-\mathbf{k}'$ in the final state. Energy has to be conserved in the over-all process, so that

$$(k'^2+M^2)^{\frac{1}{2}}-M+(k'^2+1)^{\frac{1}{2}}=E_a. \quad (28)$$

Of course, for the first reaction, k' is strictly connected with E_a through Eq. (24). Near threshold $(E_a=1)k'$ will be small, so that $\omega_{k'}\approx 1\approx E_a$.

With these assumptions, Eq. (26) becomes

$$(k'|t_1(\tfrac{3}{2},\tfrac{3}{2})|k_0=-\lambda k'M^{-\frac{1}{2}}\Delta. \quad (29)$$

Aitken, Mahmoud, and Watson then found the following approximate value of Δ, namely:

$$\Delta=(1-4f^2M^{\frac{1}{2}}K_c/3\pi)^{-1}, \quad (30)$$

where K_c is the momentum-space cutoff used in the calculation. With Eqs. (29) and (30) they evaluated the cross sections for the three reactions Eq. (22). The results are given in their Eqs. (46), which we reproduce for convenience,

$$\sigma[p+p\to\pi^++d]=\sigma_0\left[\frac{\nu/M}{1-\nu r_0}\right]q_{deut}^3[1+(4/9)M^{-\frac{1}{2}}\Delta]^2,$$

$$\sigma[p+p\to\pi^++n+p]=\frac{3\sqrt{2}}{8}\sigma_0T_0^2M^{-\frac{1}{2}}[1+(4/9)M^{-\frac{1}{2}}\Delta]^2, \quad (31)$$

$$\sigma[n+p\to\pi^++n+n]=\frac{3\sqrt{2}}{16}\sigma_0T_0^2M^{-\frac{1}{2}},$$

where $\sigma_0=2\pi[4f^2]^2[M^{5/2}]$. The value of q_{deut} appearing in the first of these being the value of k' resulting from our Eq. (24). $\nu=(ME_d)^{\frac{1}{2}}$ and r_0 is the ^3S effective range for low-energy $n-p$ scattering. As we expected, Eqs. (31) contain the sum of two terms squared for the first two reactions, the first term representing a nucleon-nucleon scattering in the intermediate state, and the

TABLE V. Quantities useful in calculating R [see the equation following Eq. (32)].

E_{lab} (Mev)	320	350	370	410	500	600
E_a	1.082	1.179	1.244	1.372	1.656	1.966
p	2.718	2.843	2.923	3.077	3.398	3.722
q	0.3835	0.5764	0.6793	0.8561	1.184	1.494
q_{deut}	0.3558	0.5701	0.6818	0.8724	1.227	1.565
Δ_F	3.344	3.565	3.705	3.970	4.493	4.961
$\Delta_f(q)$	2.822	3.085	3.254	3.575	4.228	4.780
T_0	0.07621	0.1658	0.2249	0.3416	0.5972	0.8973

second (which contains Δ) representing a pion-nucleon scattering in the intermediate state. As we further expected, the possibility of a pion-nucleon scattering is absent for the third reaction (there is no term containing Δ). Their work leading to Eq. (31) involved integration over the momentum k', since they allowed for the fact that Eq. (28) does not really hold for the second reactions, but a spectrum of values of k' is possible, the upper limit of the spectrum of pion kinetic energies being given by

$$T_0+1+2\{[\tfrac{1}{4}(T_0^2+2T_0)+M^2]^{\frac{1}{2}}-M\}=E_a. \quad (32)$$

In a sense our calculation provides a value of their Δ. Our exact solutions of Eq. (25) will not be of the form of Eq. (29) with Eq. (30). However, in order to avoid repeating the work of Aitken, Mahmoud, and Watson, we have evaluated Δ using Eq. (29) and our exact solutions for k' given by Eq. (28) and k_0 given by Eq. (27).

The values of Δ found in this way are shown in Table IV, and compared with the values found in a similar way from the Fredholm approximation and the values found from the approximation of Aitken, Mahmoud, and Watson. A table of quantities useful in calculating the Fredholm approximation and the cross sections is given in Table V.

With these values of Δ, we may calculate

$$R=\frac{\sigma[p+p\rightarrow\pi^+ +d]+\sigma[p+p\rightarrow\pi^+ +n+p]}{[n+p\rightarrow\pi^+ +n+n]}$$

as a function of energy. As mentioned before, it was the point of the work of Aitken, Mahmoud, and Watson that this should be much greater than one. The results of this calculation are shown in Fig. 4 for $f^2=0.1125$.

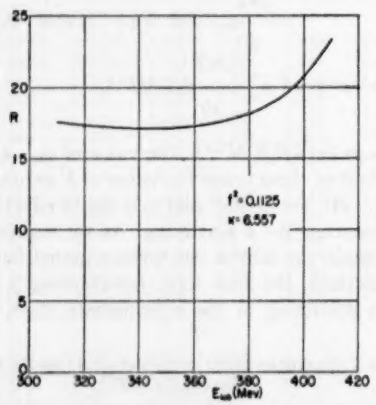

FIG. 4. The ratio R as a function of energy.

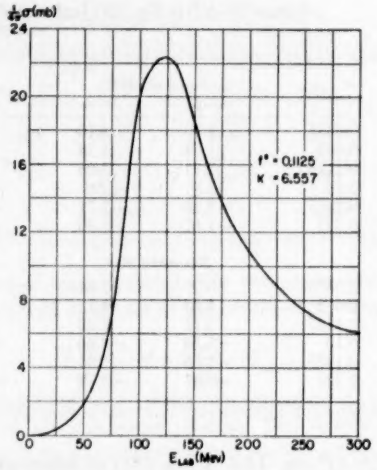

FIG. 5. The π^+-p total cross section as a function of energy.

VII. CONCLUDING REMARKS

Whether or not Chew's ideas correspond in any way to reality cannot be decided until the fourth-order Tamm-Dancoff corrections have been calculated. It will be necessary also to calculate the effects of nucleon recoil and the effects of other terms in the nonrelativistic limit of the pseudoscalar symmetric coupling.

However, this calculation has several encouraging features. The first is that according to Fig. 1, less coupling constant is required than would have been supposed from Chew's approximate calculation to make the $(\frac{3}{2},\frac{3}{2})$ phase shift 90° at a given energy. Secondly, with Chew's approximation, it is difficult to make the π^+-p total cross section decrease sufficiently rapidly beyond its peak to fit the experiments.

In Fig. 5, a graph of the π^+-p total cross section is shown which indicates this difficulty may not be present with the exact solutions.

VIII. ACKNOWLEDGMENTS

The author is deeply indebted to Professor Kenneth Watson for valuable advice about the calculation and his encouragement while it was being carried out and to Mr. Robert Bivins for coding the calculations of the exact solutions for the Los Alamos MANIAC.

Two-Body Forces and Nuclear Saturation. I. Central Forces*†

K. A. Brueckner, C. A. Levinson, and H. M. Mahmoud
Indiana University, Bloomington, Indiana

(Received March 1, 1954)

The problem of nuclear saturation for the rapidly varying and nonmonotonic potentials of pseudoscalar meson theory has been investigated. In these potentials, variational methods using independent-particle trial functions are grossly inadequate. Although the problem can be approached using more general variational functions with interparticle correlation, the evaluation of the resulting expressions is very difficult since indirect correlations involving many more than two particles become important at high densities. An alternative procedure has been developed which allows a rather straightforward evaluation of the many-body energy even when the potentials are of great complexity. This method depends on a treatment of the coherent particle motion which is exact in the limit of very many scatterers, and treats the incoherent motion as a perturbation. In this case the many-body potential energy can be simply expressed in terms of the low-energy scattering amplitudes. This method has been applied to the two-body potentials given by pseudoscalar meson theory when the effects of nucleon pair formation are assumed to be small. In this approximation the many-body forces of the theory are negligible. These potentials give an excellent fit to the low-energy scattering parameters of the two-nucleon system and also an approximately correct description of scattering up to 90 Mev. They are characterized by repulsive cores of radii 0.3–$0.4\hbar/\mu c$ and quite weak interactions in odd states. The many-body energy has been evaluated neglecting the tensor contributions which average to zero in first approximation. The result shows saturation at an energy per particle (neglecting Coulomb energy) of 12 Mev at a nuclear radius of $1.15\times10^{-13}\ A^{\frac{1}{3}}$ cm. The method has also been applied to potentials of the Lévy type in which the odd-state potentials are rather strong and attractive. To give saturation with these near normal density, a 3-body force of the type given by the pair terms in the pseudoscalar coupling with a coupling constant $g^2/4\pi\sim3$ is required. Finally, the method can easily be extended to the determination of the elastic interaction of a slow neutron with a nucleus. The resulting "Weisskopf" potential has a depth of 35 Mev.

I. INTRODUCTION

THE saturation of nuclear forces, which is one of the most characteristic features of the structure of the nucleus, can be understood most easily from two simple viewpoints.[1] If the two-body forces are everywhere attractive, and if many-body forces are neglected, then the nuclear density tends to increase to the point where all of the nucleon pairs are sufficiently close to take advantage of the attractive interactions, and a collapsed state of the nuclear matter results. It follows immediately that such collapse can be most simply prevented either by the action of repulsive two-body forces or by the presence of repulsive many-body forces. The former possibility has been thoroughly discussed in the literature under the limitation of consideration of monotonic potentials with exchange forces; as is well known, the resulting requirement on the two-body forces is that the exchange character of the potential be such that the repulsion in states of odd orbital angular momentum cancels the known attraction in even states. This simple explanation of the nuclear saturation appears unfortunately to be ruled out by the experimentally determined characteristics of the scattering which seem to show considerably less than the requisite amount of exchange.

An alternative explanation arising from the effects of repulsive many-body forces has recently been discussed in detail by Drell and Huang,[2] who have shown that the partially phenomenological introduction of the many-body forces given by the pseudoscalar meson theory leads to an adequate explanation of the observed saturation. Their result, as they emphasize, is only qualitative since the parameters which were used to relate the potential strengths to the constants of meson field theory are given only very roughly by the theory. The possible inadequacy of this treatment is apparent if the 6th- and 8th-order contributions to the two-body forces, as well as to the many-body forces, are considered. As Klein[3] has shown, the expansion of the pair contributions to the two-body forces in power of g^2 (for $g^2/4\pi\approx15$) diverges very badly even at the range of the forces, so that the inclusion of the very large (attractive) 8th-order two-body force would very much alter the characteristics of the potentials considered by Drell and Huang.

It is the purpose of this paper to consider a further possible origin of saturation arising from the singular and nonmonotonic character of the two-nucleon potentials of field theory. The motivation for these considerations will be discussed in the next section and the results summarized; the approximation method used in this paper will be discussed in detail in Sec. III; a comment on the applicability of this method to potentials of the Lévy type will be made in Sec. IV; the method will be used in Sec. V to obtain the Weisskopf[4] potential for slow neutron scattering; some corrections to the approximation will be evaluated in Sec. VI; and finally, some concluding remarks will be made in Sec. VII. Some of the difficulties which arise in other approximation methods are discussed in Appendix A.

* Supported in part by a grant from the National Science Foundation and by the joint program of the U. S. Office of Naval Research and the U. S. Atomic Energy Commission.

† The contents of this paper were first presented at The Fourth Rochester Conference on High Energy Physics.

[1] See, for example, G. Breit and E. P. Wigner, Phys. Rev. **53**, 998 (1938).

[2] S. D. Drell and K. Huang, Phys. Rev. **91**, 1527 (1953).

[3] A. Klein, Phys. Rev. **89**, 1158 (1953).

[4] Feshbach, Porter, and Weisskopf, Phys. Rev. **90**, 166 (1953).

II. DISCUSSION OF METHOD AND SUMMARY OF RESULTS

One of us (K.A.B.) and K. M. Watson[5] have recently discussed the two-body potentials of pseudoscalar meson theory (this paper will be referred to as I) and in particular the role of the meson pair term which arises in nonrelativistic approximation to the pseudoscalar coupling. This term gives rise to the well-known central force in the Lévy potential[6] and further accounts for the many-body forces considered by Drell and Huang.[2] Their results, however, are obtained by the use of perturbation theory, and the applicability of this method to the very strongly coupled pair field is doubtful. The reasons for reducing the effects of the pair terms are summarized in I; it is further shown in I that the nuclear forces which arise when the effects of pair formation are neglected give a quite satisfactory description of the two-body forces. These potentials are given in Figs. 1 and 2. The theory in this approximation is quite simple in that the coupling is now not so strong and a perturbation treatment is no longer grossly misleading. In fact, for the nuclear force problem, the effects neglected in a perturbation treatment, which includes 2nd- and 4th-order contributions, can be approximately evaluated and do not seem to change quantitatively the results of the theory. Following the success of this model in the two-body problem, the many-body problem has been considered with the hope of establishing the extent to which many-body forces are needed to account for saturation. These considerations are simplified by the absence of many-body forces in the theory, insofar as the effects of the pair term can be neglected. A characteristic of the gradient coupling terms in the theory is that the contributions to the many-body forces are almost negligibly small; the three-body force is given in Appendix B where its small effect is demonstrated. One can therefore regard the many-body forces as arising entirely from the nonlinear coupling of the theory, i.e., the pair coupling.

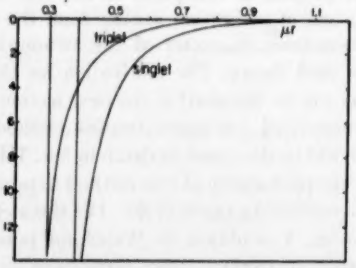

FIG. 1. Even-state central potentials. The core radii indicated here are $0.300\hbar/\mu c$ and $0.384\hbar/\mu c$ for the triplet and singlet states, respectively. These were given incorrectly as 0.300×10^{-13} cm and 0.384×10^{-13} cm in I (reference 5). The vertical scale is in units of the meson rest energy of 140 Mev.

[5] K. A. Brueckner and K. M. Watson, Phys. Rev. **92**, 1023 (1953).

[6] M. M. Lévy, Phys. Rev. **88**, 725 (1952).

Consideration of these questions naturally requires first a careful examination of the saturation problem with two-body forces alone considered. The problem of estimating the interaction and kinetic energies in nuclear matter is of course an extremely complex one; it has conventionally been approached for simple monotonic potentials through the application of a variational method. If we write for the Hamiltonian of the system, considering only two-body forces,

$$H=\sum_{1}^{A} T_i+\tfrac{1}{2}\sum_{i\neq j=1}^{A} V_{ij}, \tag{1}$$

then the expression

$$E=\int \Psi^*(\mathbf{r}_1,\cdots,\mathbf{r}_A)H\Psi(\mathbf{r}_1,\cdots\mathbf{r}_A)d\mathbf{r}_1\cdots d\mathbf{r}_A \tag{2}$$

for the energy takes a minimum if Ψ is the correct ground-state eigenfunction. One therefore gets an upper bound on the energy through the use of an arbitrary function for Ψ. A simple approximation uses a properly symmetrized product of plane waves to describe the particles in the nucleus, which is evidently equivalent to the use of Born approximation in the evaluation of the energy. This method can give perhaps qualitatively correct results if the potentials are not too strong, i.e., if Born approximation holds in the treatment of scattering, for example. It, however, is grossly inadequate if, for example, the potentials are singular and everywhere attractive, in which case the magnitude of the potential energy is badly underestimated, or if the potentials are nonmonotonic with, for example, a repulsive core. If in the region of repulsion the potential is of great strength (or possibly infinite) the Born approximation gives a very large (or infinite) overestimate of the contributions from this region and consequently a very inadequate upper bound on the total energy. This difficulty is particularly apparent in the case of the potentials of pseudoscalar meson theory which are nonmonotonic with a rather large region of repulsion (usually assumed to be of infinite strength). This inadequacy of the Born approximation method can be rectified if more suitable trial functions are used.

A simple modification, as suggested by Jastrow[7] and used by Drell and Huang,[2] is to change the simple independent-particle trial function by the introduction of a multiplicative function of the interparticle separations which goes to zero when the interparticle separation is less than the repulsive core radius. A difficulty immediately encountered here, however, arises from the loss of orthogonality in the original single-particle function. This leads to a very considerable modification in the procedures which must be used in evaluating the variational integrals, particularly if the density is sufficiently high so that the interparticle spacing is of the order of magnitude of the radii of the repulsive cores, at

[7] R. Jastrow (private communication).

which density the effect of the repulsive cores on the kinetic energy completely dominates the problem. Some of the difficulties of this method are discussed in Appendix A. Because of the complexity encountered in a quantitative evaluation using this technique, we have not at present been able to obtain satisfactory results with such methods.

A new approximation method has been developed, however, which is quite simple and which appears to give in a direct way a much better approximation to the true situation in the nucleus. It is the primary purpose of this paper to discuss this approximation method and to present the results which it gives. The essentials of this method are: first, a separation of the motion of nucleons in nuclear matter into a coherent (or single-particle) and incoherent (or correlated) part; and second, an exact treatment of the former component with neglect of the latter. The incoherent effects can then be treated as a perturbation to test the validity of the approximation made. The motivation for this approximation arises primarily from two sources; first, it is well known from the success of the shell model that particles in the nucleus to a very good approximation move independently so that correlation effects are small. Second, this method is very simple and is an excellent starting point for a perturbation treatment of the neglected effects. The simplicity arises from the fact that the coherent motion of a particle through a scattering medium is a plane wave motion (in a refracting medium), and that the potential determining the properties of the medium can be simply expressed in terms of the scattering amplitudes for the two-body encounters. This is conventionally expressed by the statement that the coherent motion of a particle in a scattering medium can be expressed in terms of an "optical" potential.

The details of this method are given in Sec. III; the results may be summarized as follows: with the approximation of neglecting incoherent components in the motion, the evaluation of the energy can be carried out with the use of a wave function which is a product of single particle plane waves. These plane waves are, however, not simply related to the plane waves of a Born approximation treatment. They are rather the result of the collective effect of many nucleons, the scattered wavelet from each nucleon combining coherently to give an advancing wave front which is effectively a plane wave modified by the refracting properties of the medium.

The plane waves of this function describe a degenerate Fermi gas with allowable wavelengths determined by the boundary conditions at the nuclear surface, and with energies

$$E_k = k^2/2M + V_k, \tag{3}$$

where $k^{-1} = \lambda$ is the wavelength and V_k is the interaction appropriate to the wavelength (since the refracting properties of the medium depend on the wavelength).

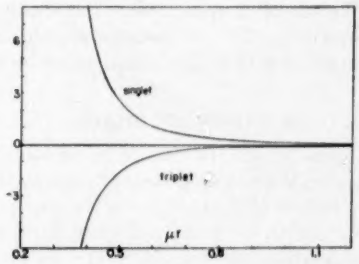

FIG. 2. Odd-state central potentials. The vertical scale is in units of the meson rest energy of 140 Mev.

The total kinetic energy of the system is then simply the Fermi energy; the potential energy (see Sec. III) is expressed in terms of the scattering amplitudes calculated in terms of the particle kinetic energies in the medium. The result is that for parameters of the two-body potential which satisfy the low-energy properties of the two-body system, the total energy of the nucleus (potential plus kinetic) has a minimum of about 12 Mev per particle at a nuclear radius of

$$R = 1.15 \times 10^{-13} A^{\frac{1}{3}} \text{ cm}, \tag{4}$$

and therefore that saturation near normal density results without the inclusion of many-body forces. This value of the radius is somewhat less than that usually given for the nucleus; it is, however, in good agreement with the mean radius determined by electromagnetic effects. These probably give a better measure of the mean density in the nucleus than do the measurements by specifically nuclear methods.

The success of this result for saturation can be attributed to the following properties of the two-body potential used:

1. Effect of repulsive core on S phase shifts at high energy. This is particularly important in preventing collapse to high densities, where the large negative S phase shifts have the effect of introducing a very strong repulsive term into the energy.
2. Weak repulsion in odd states (much less, however, than the Wigner condition on exchange strength).
3. Weakening of triplet even potential resulting from averaging out of tensor force in uncorrelated nuclear medium.

The method used for this determination of the saturation properties of the nucleus can be immediately extended to a determination of the interaction energy of an externally incident particle, such as a low-energy neutron. Such experiments have recently been carried out by Barschall *et al.*[8] and have been the subject of an extremely interesting analysis by Weisskopf *et al.*[4] The evaluation of this potential is carried out in Sec. V. The result cannot be compared directly with the empirical

[8] Miller, Adair, Bockelman, and Darden, Phys. Rev. **88**, 83 (1952); and H. H. Barschall, Phys. Rev. **86**, 431 (1952).

result of Weisskopf; however, since the nuclear radius given by our method is considerably smaller than that which he used. This result is discussed in more detail in Sec. V.

III. COHERENT MODEL

Let us consider the motion of a nucleon through nuclear matter. We will suppose that the wave function describing the rest of the particles in the ground state is known; its precise form will not enter explicitly into these considerations at this stage. The nucleon under consideration in its motion through the nucleus undergoes constant collision with its neighbors. These can lead to momentum and energy transfers and excitation of the nucleus; this excitation may be lost in subsequent inelastic scatterings of the nucleon. Thus the motion of a particle through the nucleus may be perturbed by the possibility of such repeated inelastic transitions. The nucleon can also undergo collisions with zero momentum transfer, in which case the phase of its motion may change, but otherwise the nuclear structure and its own motion are unaffected. These collisions we call coherent; the encounters which lead to excitation are incoherent since the scattered nucleon after transferring energy to the nucleus proceeds incoherently relative to its initial motion. We would like to argue now that the incoherent contributions to the motion may be small and that the motion is largely a coherent one.

Collisions involving momentum transfer (excluding exchange scattering for the present) are forbidden for particles moving in a Fermi gas of infinite extent in coordinate and momentum space since the scattering would necessarily be into previously occupied states.[9] The situation in the nucleus is, of course, not as extreme as this; the exclusion principle may still be expected to act strongly to inhibit momentum transfers for particles moving deep in the Fermi gas. However, collisions will occur which are able to bring both of the pair of colliding particles out of their states in the Fermi gas to unoccupied states, in which energy conservation is violated to an extent depending both on the degree of excitation and on the original depth in the Fermi gas of the scattered particles. Further effects, therefore, cannot come from the whole nuclear volume but only from a restricted region, the scattered excited wave being damped exponentially. Subsequent scatterings of these two nucleons on other nucleons in the nucleus can finally return the two originally excited nucleons to their original states. Simple consideration shows that at least three collisions are necessary to bring about this excitation and return of the system to its original ground state. Such events can, of course, affect the motion of the nucleon, but they can be expected to be not too important (except for nucleons near the surface of the Fermi gas) since they involve not only three scatterings (compared to one for the coherent motion) but also nonconservation of energy between incoherent scatterings which further serves to depress the contributions from such processes. We shall therefore for the present neglect such perturbations on the coherent nucleon motion but shall return to this point later in making an estimate of the corrections from incoherent collisions.

Let us next formalize these qualitative observations.[10] Consider the Schrödinger equation for the nucleons in the nucleus,

$$(E-H_0)\psi(1,\cdots A)=\sum_\alpha V_\alpha\psi(1,\cdots A), \tag{5}$$

where α is summed over all pairs of nucleon coordinates. H_0 is the sum of the kinetic energy operators. If we introduce the scattering matrix t_α related to v_α by the integral equation,

$$t_\alpha=v_\alpha+v_\alpha(E-H_0)^{-1}t_\alpha, \tag{6}$$

which can be written formally as

$$v_\alpha=t_\alpha[1+(E-H_0)^{-1}t_\alpha]^{-1}, \tag{7}$$

then we can write Eq. (5) in the equivalent form,

$$(E-H_0)\psi=\sum_\alpha t_\alpha\psi_\alpha. \tag{8}$$

As defined by Eqs. (5) and (7), ψ_α is

$$\psi_\alpha=[1+(E-H_0)^{-1}t_\alpha]^{-1}\psi, \tag{9}$$

and therefore satisfies the equation

$$\begin{aligned}(E-H_0)\psi_\alpha&=(E-H_0)\psi-t_\alpha\psi_\alpha\\&=\sum_{\beta\neq\alpha}t_\beta\psi_\beta.\end{aligned} \tag{10}$$

Let us next separate t_α into a coherent part and an incoherent part, where the coherent part gives forward and backward (exchange) scattering only, i.e., we write

$$t_\alpha=t_{c\alpha}+I_\alpha. \tag{11}$$

Equation (8) for ψ then becomes

$$(E-H_0)\psi=\sum_\alpha t_{c\alpha}\psi_\alpha+\sum_\alpha I_\alpha\psi_\alpha. \tag{12}$$

The arguments of Watson[10] now show that this equation is equivalent, in the limit of an infinite number of scatterers (or neglecting corrections of order $1/A$), to

$$\psi=F\psi_c, \tag{13}$$

where ψ_c satisfies the equation

$$(E-H_0)\psi_c=\sum_\alpha t_{c\alpha}'\psi_c\equiv V_c\psi_c, \tag{14}$$

and F is an operator which gives the effects of incoherent scatterings. The scattering matrix t_α' which appears in the defining Eq. (14) for ψ_c differs from t_α in that t_α' is evaluated for the kinetic energies in the nuclear medium. This is equivalent to using in evaluating t_α', instead of

[9] Considerations of this sort are discussed in a general way by V. Weisskopf, Helv. Phys. Acta **23**, 187 (1950).

[10] For a much more detailed discussion of the following points, see for example K. M. Watson, Phys. Rev. **89**, 575 (1953); and N. C. Francis and K. M. Watson, Phys. Rev. **92**, 291 (1953).

Eq. (6), the modified equation,

$$t_\alpha' = v_\alpha + v_\alpha(\mathcal{E}-H_0)^{-1}t_\alpha', \tag{15}$$

where $\mathcal{E}$ is now not the total energy E but rather the kinetic energy in the nuclear medium. Physically this has the reasonable meaning that the scattering of the particles moving in the uniform "optical" potential V_c is determined by the momenta in the medium.

We shall approximate Eq. (13) at present by neglecting the effects of F and setting it equal to unity; the error introduced by this approximation will be discussed in Sec. VI. We then have the approximate equation for the nuclear wave function,

$$(E-H_0)\psi = \sum_\alpha t_{c\alpha}'\psi. \tag{16}$$

The reduction of Eq. (5) to this form is often called the "optical model" approximation.

The solution of Eq. (16) is simple; the $t_{c\alpha}'$, since they give only forward or backward (exchange) scattering, can give only plane wave motion. Hence a solution is a product of plane waves or, more generally to include the possibility of exchange, an antisymmetrized product of such waves. The boundary conditions on the problem, i.e., the vanishing of the wave function on the nuclear surface, restricts the allowable plane wave states to a discrete set of standing waves. Thus the wave function which is a solution to Eq. (16) describes a degenerate Fermi gas. We shall therefore use such a trial function in our variational expression [Eq. (2)] for the total energy.

We now notice some simple features of this result. First, the singularities of the potential are only indirectly present in the t_c. For example, the "optical" well energy for low momenta in the nuclear ground state depends only on the low-energy scattering characteristics of the potentials (i.e., the scattering parameters) and not on the details of the potential, as is reasonable. The effects of a repulsive core in the potential make themselves felt only at quite high energies where the S phase shifts change sign. We further note that if Born approximation were valid, the t_c's would reduce to the v_c's and an estimate of the energy would reduce to the (now valid) Born approximation estimate. This result is, of course, more general in that even if the Born approximation is not valid, the above equation [Eq. (10)] still is, in the limit of many scatterers ($1/A \to 0$). It is further important to note that the considerations by Watson,[10] Lax,[11] and Foldy[12] of the many-body problem show that the solutions are expressed far more naturally through the scattering matrices than the potentials. The reduction of the multiple scattering equations, which characteristically result in the above form of Eq. (16), may be a fairly good approximation even when the detailed arguments justifying it are not. This is, of course, true only when many scatterers are being considered, as is the case in the nuclear structure.

[11] M. Lax, Revs. Modern Phys. **23**, 287 (1951).
[12] L. Foldy, Phys. Rev. **67**, 107 (1945).

Let us now see how the variational expression of Eq. (2) for the energy can be modified to take advantage of this result. We see that the motion of any given nucleon is specified by the coherent scattering amplitude and the kinetic energy. We can therefore replace in the variational integral the v_{ij} by the t_{cij}', i.e.,

$$E \cong \int \Psi_c^*\Big(\sum_1^A T_i + \tfrac{1}{2}\sum_{i\neq j=1}^{A} t_{cij}'\Big)\Psi_c d\mathbf{r}_1\cdots d\mathbf{r}_A. \tag{17}$$

At this stage we shall also make an approximation which is not strictly valid in this treatment, that is, to set the tensor force contribution equal to zero. This follows in the usual treatment from the fact that in an uncorrelated medium, the tensor potential averages to zero. Since we are instead dealing with the scattering amplitudes, this is no longer strictly true. We shall, however, in the interest of simplicity neglect the tensor contribution, thus introducing some error into our result. The correct evaluation of the tensor force effects can, of course, easily be done if the scattering has been evaluated with the tensor force properly taken into account.

We note that in the approximation of Eqs. (16) and (17), we actually can get the true lowest eigenvalue since as we have shown, the solution to this modified problem is a degenerate Fermi gas of particles interacting through an "optical" potential. Thus the wave function ψ is a Slater determinant of plane waves, each wave moving in a uniform potential determined by its wavelength.

We note that the allowable plane wave states, being still fixed by the boundary conditions, form the same discrete set as for the usual Fermi gas of noninteracting particles. The expectation value of the kinetic energy is therefore still the usual Fermi energy,

$$\langle \textstyle\sum_i T_i\rangle = AT_F = \tfrac{3}{5}A(k_F^2/2M), \tag{18}$$

where k_F is the maximum momentum in the Fermi gas.

The expectation value of the scattering amplitude is also easily determined. We have

$$\langle t_{cij}'\rangle = \int \varphi_i^*(x_i)\varphi_j^*(x_j)(x_i,x_j|t|x_i,x_j) \times[\varphi_i(x_i)\varphi_j(\alpha_j)-\varphi_i(\alpha_j)\varphi_j(x_i)]d\mathbf{r}_i d\mathbf{r}_j, \tag{19}$$

including the exchange term. The states $\varphi_i(x_i)$ are plane wave states with spin and isotopic spin functions, normalized in the nuclear volume,

$$\varphi_i(\mathbf{x}_i) = \frac{e^{i\mathbf{k}_i\cdot\mathbf{r}_i}}{v^{\frac{1}{2}}}\chi_i^{k_i}\lambda_i^{s_i}. \tag{20}$$

The above expectation value thus gives

$$\langle t_{cij}'\rangle = (\mathbf{k}_i,\mathbf{k}_j|t_{\text{ord}}'|\mathbf{k}_i,\mathbf{k}_j) - (\mathbf{k}_j,\mathbf{k}_i|t_{\text{exch}}'|\mathbf{k}_i,\mathbf{k}_j), \tag{21}$$

where the matrix elements with respect to spin and isotopic spin still must be evaluated. The ordinary term

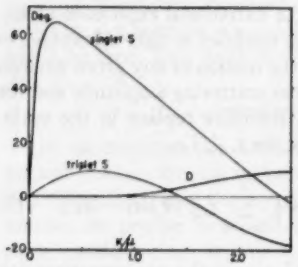

FIG. 3. Scattering phase shifts in even states for the potentials of I.[5] The S waves were computed by numerical integration; the sum of the D waves which is given was obtained by Born approximation.

corresponds to coherent scattering in the forward direction; the exchange term corresponds to a scattering in which the nucleons interchange place (i.e., backward scattering), leaving the nucleus unexcited, thus corresponding to a coherent contribution. We next write

$$\begin{aligned}(\mathbf{k}_i,\mathbf{k}_j|\,t_{\rm ord}'\,|\mathbf{k}_i,\mathbf{k}_j)&=-a_{\mathbf{k}_{ij}}(0)_{\rm ord}4\pi v/M,\\(\mathbf{k}_j,\mathbf{k}_i|\,t_{\rm exch}'\,|\mathbf{k}_i,\mathbf{k}_j)&=-a_{\mathbf{k}_{ij}}(\pi)_{\rm exch}4\pi v/M,\end{aligned}\tag{22}$$

where $a_{\mathbf{k}_{ij}}(0)$ (or π) is the scattering amplitude for the relative momentum $\mathbf{k}_{ij}=\frac{1}{2}(\mathbf{k}_i-\mathbf{k}_j)$ in the forward (or backward) direction. The nuclear volume v comes from the Kronecker delta function over total momentum. If we now go from the discrete sum over momentum states to an integral, and make use of the relation

$$\frac{4v}{(2\pi)^3}\int^{k_F}d\mathbf{k}=A,\tag{23}$$

(the factor of 4 coming from the four available spin and isotopic spin states per momentum state), we find

$$\langle V\rangle=\tfrac{1}{2}\sum_{ij}\langle t_{ij}\rangle=-\tfrac{1}{2}\frac{A^2}{v}\frac{1}{16}\frac{4\pi}{M}\sum_{\rm spins}\times\frac{\int d\mathbf{k}_i d\mathbf{k}_j\left[a_{\mathbf{k}_{ij}}(0)_{\rm ord}-a_{\mathbf{k}_{ij}}(\pi)_{\rm exch}\right]}{\int d\mathbf{k}_i d\mathbf{k}_j}.\tag{24}$$

To carry out the spin sum, we resolve the scattering amplitudes into the substates of spin and isotopic spin by use of spin and isotopic spin projection operators (t referring to triplet state, s to singlet)

$$\begin{aligned}a=a_{ss}&\tfrac{1}{4}(1-\boldsymbol{\tau}_1\cdot\boldsymbol{\tau}_2)\tfrac{1}{4}(1-\boldsymbol{\sigma}_1\cdot\boldsymbol{\sigma}_2)\\&+a_{st}\tfrac{1}{4}(1-\boldsymbol{\tau}_1\cdot\boldsymbol{\tau}_2)\tfrac{1}{4}(3+\boldsymbol{\sigma}_1\cdot\boldsymbol{\sigma}_2)\\&+a_{ts}\tfrac{1}{4}(3+\boldsymbol{\tau}_1\cdot\boldsymbol{\tau}_2)\tfrac{1}{4}(1-\boldsymbol{\sigma}_1\cdot\boldsymbol{\sigma}_2)\\&+a_{tt}\tfrac{1}{4}(3+\boldsymbol{\tau}_1\cdot\boldsymbol{\tau}_2)\tfrac{1}{4}(3+\boldsymbol{\sigma}_1\cdot\boldsymbol{\sigma}_2).\end{aligned}\tag{25}$$

The spin and isotopic spin matrix elements are then easily evaluated in terms of these substates.

We also make use of the fact that this classification of the substates of spin and isotopic spin corresponds to a separation into even and odd spatial states, and that

$$a_{\mathbf{k}_{ij}}(\pi)=\pm a_{\mathbf{k}_{ij}}(0)\tag{26}$$

for even and odd spatial states, respectively. Thus, making the transformation in the integral to relative and total momentum coordinates

$$\mathbf{k}_i-\mathbf{k}_j=2\mathbf{k},\quad \mathbf{k}_i+\mathbf{k}_j=\mathbf{p},\tag{27}$$

we find

$$\langle V\rangle=-\frac{4A}{\pi M}\int_0^{k_F}[a_{ss}(0)+3a_{st}(0)+3a_{ts}(0)+9a_{tt}(0)]P(k)dk,\tag{28}$$

where

$$P(k)=k^2\left(1-\tfrac{3}{2}\frac{k}{k_F}+\tfrac{1}{2}\frac{k^3}{k_F{}^3}\right)\tag{29}$$

is the probability of finding the relative momentum k in the Fermi gas. The evaluation of the potential energy is thus simply expressed in terms of the scattering amplitudes averaged over the relative momentum distribution in the nucleus. For this stationary state problem, the scattering amplitudes are of the form

$$a_k(0)=\lambda\sum_l(2l+1)\tan\delta_l.\tag{30}$$

The tangent of the phase shift occurring in this formula corresponds to the use of a standing wave boundary condition.

We finally introduce convenient dimensionless units following the notation of Drell and Huang,[2] i.e., for the total nuclear volume we write

$$v=A\cdot(4/3)\pi\eta^3/\mu^3,\tag{31}$$

where $\mu^{-1}=1.40\times10^{-13}$ cm is approximately the mean interparticle spacing at normal density, and η is then a parameter which determines the density of the nucleus relative to the normal. In terms of this parameter, we have

$$k_F=(9\pi/8)^{\frac{1}{3}}\mu/\eta=1.52\mu/\eta,\tag{32}$$

and

$$T_F=\tfrac{3}{5}(k_F{}^2/2M)=14.7\ \text{Mev}/\eta^2.\tag{33}$$

We have determined the phase shifts, for the pseudoscalar meson theory potential considered in I, by numerical integration for the S and P states and by Born approximation for the D states. These results are given in Figs. 3 and 4. The small contributions from the P states are very sensitive to the repulsive core radius

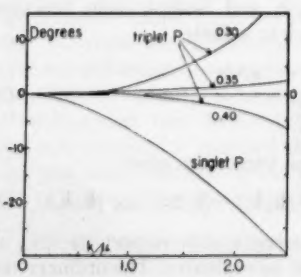

FIG. 4. Scattering phase shifts in odd states from the potentials of I.[5] The triplet scattering is given for repulsive core radii of 0.30, 0.35, and $0.40\hbar/\mu c$.

used; they are given for several values of the core. The small contribution from the triplet S state is due to the absence of the tensor force which accounts for a large part of the triplet even binding in the deuteron. The negative values of the S triplet and singlet phase shifts at high energy reflects the strong influence of the repulsive core at high energy.

To exhibit more explicitly the regions of relative momentum from which the contributions to the potential energy come, we have plotted in Fig. 5 the integrand of Eq. (28) for several values of the density. It is apparent from these that almost all of the binding comes from quite low-momentum values and hence that the low-energy behavior of the central force scattering is of decisive importance in determining the magnitude of the binding. The behavior of the phase shifts at higher energy has the principal effect of determining the curvature and shape of the total energy curve near normal density and hence the density at which the energy is a minimum. The total energy is shown in Fig. 6 where the minimum in the energy for the P-state core radii equal to $0.4\hbar/\mu c$ occurs at a density corresponding to the spacing parameter $\eta=0.82$, and hence a

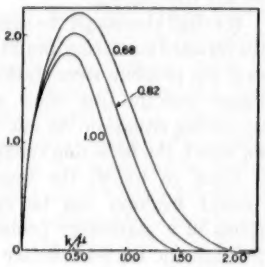

FIG. 5. Contributions to the potential energy as a function of relative momentum k. This is a plot of the integrand of Eq. (28) showing the predominance of low-momentum contributions in the integral. The three curves are for various values of the density parameter η of Eq. (31). The vertical scale is in arbitrary units.

nuclear radius

$$R=(0.82/\mu)A^{\frac{1}{3}}$$
$$=1.15\times10^{-13}A^{\frac{1}{3}}\text{ cm}. \quad (34)$$

The average binding energy per particle at this density is about 12 Mev.

This result, depending as it does only on the general characteristics of the low-energy scattering, should not depend in any detailed way on the potential used. To verify this, we have made a similar calculation using for the even states square well potentials with repulsive core radii of $0.3\hbar/\mu c$ and $0.4\hbar/\mu c$ for the triplet and singlet states, respectively. The singlet well depth and range were adjusted to fit the low-energy scattering parameters. The treatment of the even triplet states is more ambiguous since the tensor force, which contributes a sizeable fraction of the interaction in the two-body problem, is absent in the saturation calculation. To approximate this effect, we have somewhat arbitrarily used a well range which would be correct for the two-body problem if the tensor force were absent, but assumed a central well depth less than that required to give

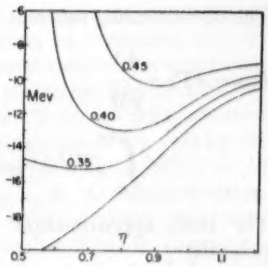

FIG. 6. Total energy per nucleon as a function of the density parameter η as calculated from the phase shifts of Figs. 3 and 4. The energies are given for several values of the radius of the triplet odd repulsive core and also with the effects of the odd states completely omitted (lowest curve).

two-body binding. The modified well depth could then be taken to be a parameter of the problem, to be adjusted (over a reasonable range) to give the correct magnitude of the energy at saturation. The P-state potentials were taken to be repulsive cores with adjustable radii. The calculations based on this model are, of course, straightforward, so that we present the results only. It was found that the effective triplet well depth should be about one-half the triplet depth which would alone be correct for the two-body problem in the absence of tensor forces. To give sufficient repulsion in odd states, the core radii were about $0.4\hbar/\mu c$. For this choice of the parameters, the binding energy was about 18 Mev and the nuclear radius $1.2\times10^{-13}A^{\frac{1}{3}}$ (see Fig. 7). The close similarity of these results to those based on the much more complicated meson potential illustrates the insensitivity of the saturation calculation to details of the model. The saturation can, as is the case of the meson potential, be attributed to the combined effects of repulsive core, weak exchange character, and reduction of the triplet contributions due to the loss of the tensor force binding.

To show in more detail the relation of this model to the usual Born approximation calculation, we have considered the scattering from a simple spin independent square well with no exchange, both by Born approximation and by the use of the above method. In the former case, the simple evaluation of the energy gives, for a short-range potential of range R and depth V_0,

$$E_{\text{Born}}=AT_F-(A^2/2v)\pi R^3V_0. \quad (35)$$

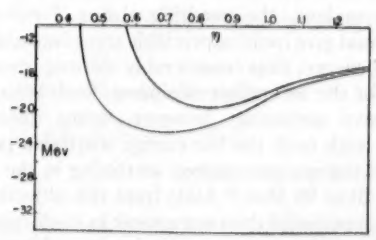

FIG. 7. Total energy per nucleon as a function of the density parameter η, calculated for square wells with repulsive cores of $0.3\hbar/\mu c$ and $0.4\hbar/\mu c$ in the triplet and singlet even states, respectively. The upper curve is for the repulsive cores in singlet and triplet odd states equal to $0.4\hbar/\mu c$, the lower curve is for the triplet odd core reduced to $0.3\hbar/\mu c$.

The corresponding coherent calculation gives

$$E_{\rm coh}=AT_P-\frac{4A}{\pi M}\times\int_0^{k_F}P(k)[6a_{\rm even}(k)+10a_{\rm odd}(k)]dk. \quad (36)$$

The Born approximation gives for a short-ranged potential

$$a_{\rm even}=M\lambda^2\int_0^\infty\cdot\sin^2(kr)V(r)dr \cong\tfrac{1}{3}MV_0R^3. \quad (37)$$

The integral over k is then easily done, neglecting the odd waves as is valid for a short-range potential, and using $(4/3)\pi k_F^3v(2\pi)^{-3}=\frac{1}{4}A$, we get

$$E_{\rm coh}=AT_P-\frac{24A}{\pi M}\frac{k_F^3}{24}\frac{MV_0R^3}{3} =AT_P-\frac{A^2}{2v}\pi R^3V_0, \quad (38)$$

so that as soon as the Born approximation is valid in treating the scattering, the two results of Eqs. (35) and (37) are identical, as expected. The coherent result gives a larger binding at low densities where the momenta are low and Born approximation is not valid, but otherwise the two results are closely the same. One can thus expect that the results of Wigner showing collapse in this case will be reproduced by the coherent method. This actually follows directly, of course, from Eq. (35) since the kinetic energy depends on the density parameter as η^{-2} while the potential energy at high densities varies as η^{-3}. Thus, the attractive potential energy eventually dominates over the repulsive kinetic energy, and the minimum in the energy occurs as η goes to zero.

IV. POTENTIALS OF THE LÉVY TYPE; EFFECTS OF MANY-BODY FORCES

For a potential of the Lévy type,[6] in which the dominant term in the central forces is spin- and isotopic spin-independent, the resulting strong P-wave scattering would give quite appreciable contributions to the potential energy, thus considerably shifting inward the position of the saturation minimum. Such behavior of the P-wave scattering, however, seems difficult to reconcile with both the low-energy scattering parameters[13] and the nucleon-nucleon scattering in the energy range of 20 to 90 Mev.[14] Aside from this objection, the Lévy-type potential does not appear in itself capable of giving saturation near normal density, although the large repulsive core ($r_c=0.38\hbar/\mu c$) of such a potential would prevent collapse from occurring past perhaps $\eta=0.5$ to 0.6. A very small contribution from the repulsive 3-body forces considered by Drell and Huang,[2] therefore, would be sufficient to move the minimum in the total energy curve to normal density. This is clear from their work since they showed that the contribution of the three-body forces, in a perturbation treatment using a pseudoscalar coupling constant of about 12, is about 150 Mev at a density of $\eta=0.8$. Since only a few Mev of repulsion, increasing rapidly with increasing density (as is characteristic of the 3-body forces) is required to offset the attractive P-wave contributions, a few percent of the three-body term of Drell and Huang would be sufficient to give approximately the correct position and magnitude of minimum energy.

[13] J. Blatt and M. Kalos, Phys. Rev. **91**, 444 (1953).
[14] R. Jastrow (private communication).

V. OTHER APPLICATIONS: THE REAL PART OF THE WEISSKOPF POTENTIAL FOR NEUTRON SCATTERING

Having obtained a reasonable model for the nuclear ground state, we can next easily determine the interaction energy of a low-energy neutron being coherently (i.e., elastically) scattered by the nucleus. In this case, the interaction is computed exactly as before except that we do not sum over the momentum of the particle we are considering.

We shall also adopt the same convention of calculating the forward scattering amplitudes in the nuclear medium as if the problem were stationary. This is, of course, no longer strictly true since we are considering a true scattering situation. At low incident energies, however, for which the reflection coefficient at the nuclear surface is close to unity, the quasi-stationary state in the nuclear medium can be approximately described in terms of a stationary problem perturbed by flux loss through the nuclear surface. This approach, of course, does not allow us to determine the absorption coefficient which can be evaluated only by more detailed considerations of the sort to be discussed in Sec. VI.

In our approximation the "optical potential" then is, for a particle of momentum k (for simplicity averaging over the spin and isotopic spin of the incident particle), following the procedures used in obtaining Eq. (28),

$$V_k=-\frac{1}{\pi Mk}\int_{\frac{1}{2}(k-k_F)}^{\frac{1}{2}(k+k_F)}[3a_{st}+3a_{ts}+a_{ss}+9a_{tt}] \times[\tfrac{1}{4}k_F^2-(k/2-l)^2]ldl, \quad (39)$$

where the scattering amplitudes are as before evaluated in the forward direction.

Using the density and Fermi energy corresponding to the minimum in the saturation curve of Fig. 4, this integral can be evaluated for any value of K to give an interaction energy. To find the potential felt by an incoming particle of energy E, we then must evaluate the equation

$$E=(k^2/2M)+V_k, \quad (40)$$

which relates the total energy to the wavelength. The result is that for an external energy of 3 Mev, the

potential energy in the nuclear medium is 35 Mev. The calculation also shows that the potential strength is nearly independent of the total energy over a several Mev energy range at this energy.

The large value of the interaction energy which we have found results principally from the small nuclear radius given by our methods. It is not at present clear that this is in serious disagreement with the empirical result of Weisskopf[4] adjusted to compensate for a higher nuclear density.

VI. CORRECTIONS TO THE MODEL

Let us return to Eq. (13). The function F, which gives the effect of incoherent scatterings, corrects Eq. (16) to give the modified equation,[10]

$$\begin{aligned}(E-H_0-V_c)\psi&=[\sum_\alpha I_\alpha+\sum_{\alpha\neq\beta} I_\alpha(E-H_0-V_c)^{-1}I_\beta\\&+\sum_{\alpha\neq\beta\neq\gamma} I_\alpha(E-H_0-V_c)^{-1}\\&\times I_\beta(E-H_0-V_c)^{-1}I_\gamma+\cdots]\psi_c. \quad (41)\end{aligned}$$

If we now regard the correction terms in I_α as perturbing terms in the Hamiltonian, with the unperturbed Hamiltonian H_0+V_c, then we can obtain the first-order shift in the energy by evaluating the diagonal terms in the perturbing energy.‡ It is apparent that the first correction must be of third order in I_α, since the incoherent scattering operator acts on a pair of nucleons, and cannot act successively on the same two nucleons. Thus one incoherent scattering which excites 2 nucleons from the ground state must be followed by 2 incoherent scatterings to return each of the 2 excited nucleons to the ground state. We therefore are led to consider such typical processes as

$$\begin{aligned}&\mathbf{k}_1+\mathbf{k}_2\rightarrow\mathbf{k}_1'+\mathbf{k}_l',\\&\mathbf{k}_1'+\mathbf{k}_3\rightarrow\mathbf{k}_\alpha+\mathbf{k}_3',\\&\mathbf{k}_2'+\mathbf{k}_3'\rightarrow\mathbf{k}_\beta+\mathbf{k}_\gamma,\end{aligned} \quad (42)$$

where α,β,γ must be equal to 1, 2, or 3 in any order (to give a diagonal contribution). There are in addition 5 other similar processes which differ only in the order in which the intermediate scatterings take place. The contribution to the shift in the energy for this particular process is

$$\begin{aligned}\Delta E=\sum_{\alpha\neq\beta\neq\gamma=1}^{3}&(\mathbf{k}_\beta,\mathbf{k}_\gamma|I|\mathbf{k}_2',\mathbf{k}_3')\\&\times(\mathcal{E}_2+\mathcal{E}_3+\mathcal{E}_1-\mathcal{E}_\alpha-\mathcal{E}_2'-\mathcal{E}_3')^{-1}\\&\times(\mathbf{k}_\alpha,\mathbf{k}_3'|I|\mathbf{k}_1',\mathbf{k}_3)(\mathcal{E}_1+\mathcal{E}_2-\mathcal{E}_1'-\mathcal{E}_2')^{-1}\\&\times(\mathbf{k}_1',\mathbf{k}_2'|I|\mathbf{k}_1,\mathbf{k}_2), \quad (43)\end{aligned}$$

‡ We neglect the first-order change in the wave function which gives rise to effects similar to those calculated here. These together with other formal features of the model will be discussed in a future paper.

to be summed over $\mathbf{k}_1'$, $\mathbf{k}_2'$, $\mathbf{k}_3'$ with the restriction of total momentum conservation. In evaluating this expression, we shall content ourselves with an upper limit since, as we shall show, the correction is quite small. To obtain the average value of the energy shift, we must multiply the particular contribution of Eq. (43) by the number of triad combinations $A(A-1)(A-2)/3!$ in the nucleus and average over $\mathbf{k}_1$, $\mathbf{k}_2$, $\mathbf{k}_3$. As remarked above, there are six typical direct matrix elements; this factor of six cancels the 3! in the number of triads. To approximate the integral we shall replace $\mathcal{E}_1$, $\mathcal{E}_2$, $\mathcal{E}_3$ by their average values T_F, and set the intermediate energies in the energy denominators all equal to $\mathcal{E}_1'$. This tends to increase rather markedly the value of the integral since the energy denominators are given too small values in this approximation for small k_1'. We make a related approximation in relaxing the restrictions on k_1' near its minimum value k_F (lower values being excluded by the exclusion principle) which arise from momentum conservation. Again, this tends to increase the value of the integral. Our approximations tend, therefore, to give us a considerable overestimate of the effect. For the incoherent scattering operators I_α, we shall for simplicity use the Born approximation scattering from a spin-independent Yukawa potential adjusted to give approximately the same central scattering as we have considered in Sec. III, i.e.,

$$V(r)=V_0(0.4+0.6P_x)e^{-\mu r}/\mu r, \quad (44)$$

where P_x is the space exchange operator. The exchange mixture corresponds to our weakly repulsive p-state scattering; we take a well depth $V_0=0.18\mu$ which is about 70 percent of the strength required to give binding in the deuteron. The corresponding incoherent scattering amplitude is

$$\begin{aligned}(\mathbf{k}'|I|\mathbf{k})&=\frac{4\pi V_0}{v\mu}\left[\frac{0.4}{\mu^2+(\mathbf{k}-\mathbf{k}')^2}+\frac{0.6}{\mu^2+(\mathbf{k}+\mathbf{k}')^2}\right]\\&=f(\mathbf{k}-\mathbf{k}')+g(\mathbf{k}+\mathbf{k}'). \quad (45)\end{aligned}$$

Inserting this into Eq. (43) with the approximations to the energies discussed above, we find

$$\begin{aligned}\Delta E_{hi}=\frac{A^3vM^2}{(2\pi)^3}\sum_{\alpha\neq\beta\neq\gamma=1}^{3}&\int d\mathbf{k}(3/5k_F^2-k^2)^{-2}\\&\times[f(\mathbf{k}_1+\mathbf{k}_2-\mathbf{k}_\beta-\mathbf{k})+g(\mathbf{k}_1+\mathbf{k}_2-\mathbf{k}_\gamma-\mathbf{k})]\\&\times[f(\mathbf{k}-\mathbf{k}_\alpha)+g(\mathbf{k}_\alpha-\mathbf{k}_3)]\\&\times[f(\mathbf{k}_1-\mathbf{k})+g(\mathbf{k}-\mathbf{k}_2)]. \quad (46)\end{aligned}$$

This integral can be further simplified; we note that since the functions f and g are rapidly decreasing functions of their arguments (the momenta being quite large), the largest contribution comes from the product of the three direct terms which all depend on the same argument. In this approximation, taking proper account

of the spin and isotopic spin matrix elements, Eq. (46) reduces to

$$\Delta E_{hh}=\frac{A^3vM^2}{(2\pi)^3}\int d\mathbf{k}(3/5k_F^2-k^2)^{-2}[f^3(\mathbf{k}-\mathbf{k}_1)$$
$$-\tfrac{1}{4}f^2(\mathbf{k}-\mathbf{k}_1)g(\mathbf{k}-\mathbf{k}_1)-\tfrac{1}{4}f^2(\mathbf{k}-\mathbf{k}_1)g(0)$$
$$+\tfrac{1}{16}f(\mathbf{k}-\mathbf{k}_1)g^2(\mathbf{k}-\mathbf{k}_1)+\tfrac{1}{16}f(\mathbf{k}-\mathbf{k}_1)g(\mathbf{k}-\mathbf{k}_1)$$
$$\times g(0)-\tfrac{1}{4}g^2(\mathbf{k}-\mathbf{k}_1)g(0)].$$

The terms in $g(0)$ result from backward scattering and must be dropped, since the definition of I excludes such contributions. Using Eq. (45), we finally find for the change in energy per particle:

$$\Delta E_{hh}/A=\frac{A^2}{v^2}\frac{8}{\pi}M^2/\mu^3(0.025)V_0^3$$
$$\times\int_{k>k_F}d\mathbf{k}(\tfrac{3}{5}k_F^2-k^2)^{-2}[\mu^2+(\mathbf{k}-\mathbf{k}_1)^2]^{-3}$$
$$=0.15\text{ Mev},$$

using the values of Sec. III for the density and Fermi momentum. This shift in the energy is positive and therefore tends to decrease the binding energy. The effect, however, is quite small and because of the approximations made in evaluating the correction, the correct result is probably rather smaller.

This calculation shows how the corrections to the "coherent" model typically appear; the smallness of the correction shows that there is at least no serious error in our neglect in first order of the incoherent contributions to the motion.

VII. CONCLUSIONS

The approximation method we have developed has allowed a relatively straightforward evaluation of the mean kinetic and potential energies of nucleons moving in a nuclear medium. This method is much more general than the usual (essentially Born approximation) methods used for potentials of a restricted simple type in that it can be applied to potentials of arbitrary complexity for which the Born approximation is inapplicable. If the scattering amplitudes are known or can be evaluated, then as we have shown, the determination of the energy follows very simply. This method also shows in a very graphic way the intimate (and very natural) connection of the saturation problem with the low-energy scattering characteristics of the potentials.

The application of these techniques to a specific problem of considerable interest, namely the two-body potentials of pseudoscalar meson theory[5] (adjusted to fit the low-energy scattering parameters) shows that these potentials also have the necessary characteristics to give an approximately correct description of nuclear saturation. As discussed in more detail in Sec. III, the necessary requirement on the two-body interaction is that the potentials be short-range (to depress D-wave scattering), repulsive at small distances (to depress s-phase shifts at high energy), have a weakly repulsive effect on P-wave scattering (to give the correct position of the saturation minimum) and contain a rather strong admixture of tensor force in the even triplet states (to reduce central triplet even force contributions in the nuclear medium). It would appear from our results that any potential of these general characteristics (which do not appear to be incompatible with the scattering at low and medium energies) would give an approximately equivalent result.

We have further shown in Sec. VI that a typical type of term correcting the method used in this paper is quite small and does not appreciably affect the results. It is not felt, however, that this constitutes a definitive proof of the validity of the procedures which we have used. It is also to be noted that since the properties of the scattering amplitudes at low energy are of decisive importance in the description of saturation, it remains to be shown that the potentials we have used are compatible with the nucleon-nucleon scattering over the range of relative momenta which enter in an important manner into our results. In this connection it will also be necessary to correct for the effects of the tensor force in the weakly correlated nuclear medium.

Finally, a point of particular interest is the relation of our result to the shell model. A modification of the methods used here is, of course, necessary in dealing not with nuclear matter of essentially infinite extent but with finite nuclear volume and the resulting important surface effects. Our method deals naturally with weakly correlated nuclear matter, as is required in the shell model; we have not shown, however, that effects of correlation are everywhere small. It is particularly difficult at this stage to understand the apparently coherent motion of the surface nucleons of the shell model, since it is for these that the qualitative arguments we have given and approximate calculations we have made are least applicable. We hope to consider not only this question but also further questions related to the methods we have used in later papers.

The authors would like to acknowledge a number of discussions of the content of this paper with Dr. N. C. Francis.

APPENDIX A. DIFFICULTIES WHICH ARISE FROM THE USE OF NON-ORTHOGONAL FUNCTIONS

The method used by Drell and Huang[2] employs as a trial function in the variational expression, Eq. (2):

$$\Psi(\mathbf{r}_1,\cdots\mathbf{r}_A)=S(\varphi_1(\mathbf{x}_1),\cdots\varphi_A(\mathbf{x}_A))\prod_{i<j}f(\mathbf{r}_{ij}),\quad\text{(A1)}$$

where $S(\varphi_1(\mathbf{x}_1)\cdots\varphi_A(\mathbf{x}_A))$ is a Slater determinant of orthonormal plane waves $\varphi_i(\mathbf{x}_i)$ ($\mathbf{x}_i$ the space and spin coordinate). $f(\mathbf{r})$ is a correlation function which vanishes for $r<r_c$ (r_c the repulsive core radius) and for $r>r_c$ has a form which is to be determined by a variational pro-

cedure. To exhibit the difficulties which arise from the introduction of the correlation functions, let us consider a typical term involving the potential energy

$$\langle V\rangle=\tfrac{1}{2}A^2N\int\varphi_1^*(\mathbf{x}_1)\cdots\varphi_A^*(\mathbf{x}_A)\prod_{i<j}f^2(\mathbf{r}_{ij})V(\mathbf{r}_{12})\times S(\varphi_1(\mathbf{x}_1)\cdots\varphi_A(\mathbf{x}_A))d\mathbf{r}_1\cdots d\mathbf{r}_A, \quad (A2)$$

where N is a normalizing factor. If we for simplicity neglect exchange terms in the evaluation of this integral (the method is easily extensible to the more general case) then we have approximately, with $\varphi_1^*(\mathbf{x}_1)\varphi_1(\mathbf{x}_1)=1$,

$$\langle V\rangle=\tfrac{1}{2}A^2N\int V(\mathbf{r}_{12})\prod_{i<j}f^2(\mathbf{r}_{ij})d\mathbf{r}_1\cdots d\mathbf{r}_A. \quad (A3)$$

Let us now consider an approximate evaluation of the integral over $\mathbf{r}_3,\cdots\mathbf{r}_A$. We write

$$\prod_{i<j}f^2(\mathbf{r}_{ij})=f^2(\mathbf{r}_{12})\prod_k f^2(\mathbf{r}_{1k})f^2(\mathbf{r}_{2k})\prod_{i<j}{}' f^2(\mathbf{r}_{ij}), \quad (A4)$$

where the product $\prod_{i<j}'$ is over the correlation functions not explicitly included elsewhere. We next note that

$$I(\mathbf{r}_{12})=\int d\mathbf{r}_k f^2(\mathbf{r}_{1k})f^2(\mathbf{r}_{2k})\prod_{i<j}{}' f^2(\mathbf{r}_{ij})\equiv\int d\mathbf{r}_{1k}f^2(\mathbf{r}_{1k})f^2(\mathbf{r}_{12}+\mathbf{r}_{1k})\prod_{i<j}{}' f^2(\mathbf{r}_{ij}) \quad (A5)$$

can be written as a term independent (roughly) of $\mathbf{r}_{12}$ and a smaller term depending on $\mathbf{r}_{12}$, i.e.,

$$I(\mathbf{r}_{12})=\int d\mathbf{r}_{1k}\prod_{i<j}{}' f^2(\mathbf{r}_{ij})+\int d\mathbf{r}_{1k}[f^2(\mathbf{r}_{1k})f^2(\mathbf{r}_{12}+\mathbf{r}_{1k})-1]\times\prod_{i<j}{}' f^2(\mathbf{r}_{ij}). \quad (A6)$$

The first integral is roughly over the whole nuclear volume minus the volume excluded from the range of the integration by the correlation function, i.e. (for large A),

$$\int d\mathbf{r}_{1k}\prod_{i<j}{}' f^2(\mathbf{r}_{ij})\approx v-Av_1, \quad (A7)$$

where v_1 is in order of magnitude

$$v_1\approx\int[1-f^2(\mathbf{x})]d\mathbf{x}. \quad (A8)$$

The second integral, however, is only over a volume characterized by the range of the correlation functions; we approximate it by

$$\int d\mathbf{r}_{1k}[f^2(\mathbf{r}_{1k})f^2(\mathbf{r}_{12}+\mathbf{r}_{1k})-1]=\Delta(r_{12}). \quad (A9)$$

Thus, we get roughly

$$I(r_{12})=\prod_{k=3}^{A}[v-Av_1+\Delta(r_{12})]. \quad (A10)$$

If we write $v=Av_0$, where v_0 is the volume per particle, then for large A,

$$I(r_{12})=[A(v_0-v_1)]^A\left[1+\frac{\Delta(r_{12})}{A(v_0-v_1)}\right]^A=\text{constant}\times\exp[\Delta(r_{12})/(v_0-v_1)], \quad (A11)$$

and

$$\langle V\rangle=\tfrac{1}{2}A^2N\int d\mathbf{r}_{12}V(\mathbf{r}_{12})\exp[\Delta(r_{12})/(v_0-v_1)]. \quad (A12)$$

We can write this in somewhat simpler form if we replace

$$\Delta(r)=\int[f^2(\mathbf{x})f^2(\mathbf{x}+\mathbf{r})-1]d\mathbf{x}$$

by

$$\Delta(r)=\int[1-f^2(\mathbf{x})][1-f^2(\mathbf{x}+\mathbf{r})]d\mathbf{x}+\int[f^2(\mathbf{x})+f^2(\mathbf{x}+\mathbf{r})]d\mathbf{x}\equiv g(r)+\Delta_c. \quad (A13)$$

The first term $g(r)$ vanishes if r is greater than the range of the correlation function; the second term integrates to a constant and only affects the normalization. Thus,

$$\langle V\rangle\cong\tfrac{1}{2}A^2\int d\mathbf{r}V(\mathbf{r})\exp[g(r)/(v_0-v_1)]\Big/\int d\mathbf{r}\exp[g(r)/(v_0-v_1)], \quad (A14)$$

is now properly normalized.

The effects of this correcting exponential factor are not at all small, particularly at high density where the volume per particle v_0 becomes comparable to the volume v_1 excluded by the correlation functions. At high densities this approximate expression also breaks down and a more careful evaluation is necessary. Another case for which the effects are very large results if the correlation functions are assumed to be long-ranged, for example, to fall off only as r. In this case, the integral for the function $g(r)$ diverges linearly (except for the limitation imposed by the finite nuclear size) so that the corrections introduced through the correlation functions become of order $A^{\frac{1}{3}}$. Thus the effect is infinite for an infinite nuclear medium.

The complexity of this result for a variational calculation is apparent since the variational parameters appear

in a complicated way in the exponential function. A preliminary examination of the variational problem using the two-body potential discussed in Sec. III and using one and two parameter variational functions was not found to yield reasonable binding. The extremely singular potentials of the meson theory render a simple variational calculation rather inadequate. It is further felt that the procedures of the Sec. III are simpler and more accurate.

APPENDIX B. THREE-BODY FORCES

The three-body potential can be obtained by evaluating the matrix elements of the operator[5]

$$V=h^-(E-H_0)^{-1}h^-(E-H_0)^{-1}h^+(E-H_0)^{-1}h^+, \quad \text{(A15)}$$

where the operators h^+, h^- act to create or annihilate mesons respectively. The interaction term h we take to be (neglecting the pair terms of the pseudoscalar theory)

$$h=\sum_{i=1}^{3}\frac{f}{\mu}\boldsymbol{\sigma}_i\cdot\boldsymbol{\nabla}\boldsymbol{\tau}_i\cdot\boldsymbol{\varphi}(\mathbf{r}_i). \quad \text{(A16)}$$

The evaluation of the expression for V is simple and gives

$$V=-\left(\frac{f}{\mu}\right)^4(2\pi)^{-6}\int\frac{d\mathbf{k}d\mathbf{k}'(\omega+\omega')}{\omega^3\omega'^3}\boldsymbol{\sigma}_2\cdot\mathbf{k}\boldsymbol{\sigma}_3\cdot\mathbf{k}'$$
$$\times[\mathbf{k}\cdot\mathbf{k}'\boldsymbol{\tau}_2\cdot\boldsymbol{\tau}_3-\boldsymbol{\sigma}_1\cdot\mathbf{k}\times\mathbf{k}'\boldsymbol{\tau}_1\cdot\boldsymbol{\tau}_2\times\boldsymbol{\tau}_3]e^{i(\mathbf{k}\cdot\mathbf{r}_{23}+\mathbf{k}'\cdot\mathbf{r}_{13})}$$
$$+(2\text{ cyclic permutations on }1,2,3). \quad \text{(A17)}$$

In taking the expectation value of the potential in an uncorrelated medium, we need consider only the contributions which arise from averaging over the angles of $\mathbf{r}_{13}$, $\mathbf{r}_{23}$, and $\mathbf{r}_{12}$. This gives

$$V=-\left(\frac{f^2}{4\pi}\right)^2\frac{1}{9}\frac{2}{\mu\pi}(\boldsymbol{\sigma}_2\cdot\boldsymbol{\sigma}_3\boldsymbol{\tau}_2\cdot\boldsymbol{\tau}_3-\boldsymbol{\sigma}_1\cdot\boldsymbol{\sigma}_2\times\boldsymbol{\sigma}_3\boldsymbol{\tau}_1\cdot\boldsymbol{\tau}_2\times\boldsymbol{\tau}_3)$$
$$\times\frac{e^{-x}}{x}\left[k_0(x')-\frac{k_1(x')}{x'}\right]\approx$$
$$+(\text{all permutations of }1,2,3), \quad \text{(A18)}$$

where $x=\mu r_{13}$, $x'=\mu r_{23}$.

The expectation value of this three-body potential has been evaluated using the approximate methods of Drell and Huang[2] and found to give only about $\frac{1}{10}$ Mev of repulsion. The effect hence is negligible.

PHYSICAL REVIEW VOLUME 95, NUMBER 1 JULY 1, 1954

Some General Relations between the Photoproduction and Scattering of π Mesons

KENNETH M. WATSON
Department of Physics, University of Wisconsin, Madison, Wisconsin
(Received February 19, 1954)

With a partial wave analysis of the photomeson cross sections are combined the principle of charge independence, the hypothesis of time reversibility, and the unitarity of the scattering matrix. This leads to a natural starting point for the study of the photo cross sections. It also leads to some close relations between the photoproduction and scattering of pions in that the complex phases of the matrix elements for photoproduction are explicitly given in terms of the scattering phase shifts. One consequence of this is that there must be an S-wave contribution to the π^0 photoproduction on whose amplitude a lower limit can be given in terms of the S-wave pion-nucleon scattering. A second, independent lower limit on the S-wave term for the π^0 cross sections can be expressed in terms of the π^-/π^+ ratio. Several other nontrivial conditions are imposed on the cross sections.

I. INTRODUCTION

THE purpose of the present note is to discuss certain general relations between photomeson production and meson-nucleon scattering. These follow from the restrictions imposed by the principle of charge independence and by the usual symmetry conditions on the scattering matrix [for example, its unitarity and detailed reversibility].

These arguments (the results of which are given in Sec. II) are purely formal. They do, however, lead to a number of specific relations to be satisfied by the photo cross sections, including two independent lower limits on the S-wave term for neutral photomeson production. One of these is a function of the S-wave meson-nucleon scattering phase shifts. The S- and P-wave interference terms for the photomeson cross sections are also obtained as explicit functions of the scattering phase shifts.

Some of the formal restrictions given here have recently been obtained also by Ross.[1] His analysis was based on a rather specific model, however, whereas we emphasize their very general nature. The present results have also been obtained independently by Fermi[2]

[1] M. Ross, Phys. Rev. **94**, 454 (1954). I am indebted to Dr. Ross for sending me his results prior to publication.
[2] E. Fermi (unpublished). I am indebted to Professor Fermi for informing me of his work.

and by Aizu.[3] We observe finally that our arguments could be more simply made following the S-matrix approach of Nakano and Nishijima.[4] We have chosen a different means of discussion [given in the Appendix] for the sake of physical clarity. Briefly stated, we argue that the multipole matrix elements for photoproduction are essentially *real* quantities (in an appropriate representation). Because of the meson-nucleon interaction in the final state, the phases of the various meson partial waves are shifted relative to each other by the amount of the *scattering* phase shifts. The interference of these waves in the photo cross section is thus dependent on the scattering phase shifts.

Since the photoproduction of π^- mesons from free neutrons cannot be easily done, this reaction would seem to be most easily studied using deuterium. For this reason it is necessary to say something about the role played by the deuteron binding on the cross sections. In Sec. IV we shall show that on the basis of some rather general assumptions the observed π^-/π^+ ratio from deuterium should be the same as from free neutrons and protons as long as the cross sections are being studied near the energetic threshold.

II. THE FORMAL REQUIREMENTS ON THE CROSS SECTIONS

We shall suppose the γ-ray energy to be low enough that only final S and P waves for the meson with respect to the nucleon need be considered.[5,6] We denote the momentum vectors of the photon and meson by $\boldsymbol{\kappa}$ and $\mathbf{q}$, respectively. By $\hat{e}$ we denote the polarization vector of the photon. Then, following the notation of reference 5 we may write the scattering matrix for photoproduction as

$$T=A\boldsymbol{\sigma}\cdot\hat{e}-B[-i\boldsymbol{\sigma}\cdot(\boldsymbol{\kappa}\times\hat{e})\times\mathbf{q}+(\boldsymbol{\kappa}\times\hat{e})\cdot\mathbf{q}]\kappa^{-1}q^{-1} -C[i\boldsymbol{\sigma}\cdot(\boldsymbol{\kappa}\times\hat{e})\times\mathbf{q}+2(\boldsymbol{\kappa}\times\hat{e})\cdot\mathbf{q}]\kappa^{-1}q^{-1} +\tfrac{1}{2}E[\boldsymbol{\sigma}\cdot\boldsymbol{\kappa}\hat{e}\cdot\mathbf{q}+\boldsymbol{\sigma}\cdot\hat{e}\boldsymbol{\kappa}\cdot\mathbf{q}]\kappa^{-1}q^{-1}, \quad (1)$$

where $\boldsymbol{\sigma}$ is the nucleon spin operator. The coefficients A, B, C, and E are complex numbers which are functions of q and represent the strength of the various multipole moments for the interaction of the γ ray. The electric dipole absorption strength to produce an S-state meson is given by A. The B and C terms describe magnetic dipole absorption of the γ ray with emission of the meson into a P state, the total angular momentum being $j=\frac{1}{2}$ and $j=\frac{3}{2}$, respectively. The electric quadrupole absorption to produce a P-state meson in the $j=\frac{3}{2}$ state is represented by the E term. There is some theoretical reason[5] for feeling that the electric quadrupole term can be neglected.

[3] K. Aizu (unpublished). I am indebted to Professor C. N. Yang for informing me of Aizu's analysis, which was presented at the Japanese Conference on High Energy Physics in the Fall of 1953 (unpublished).

[4] T. Nakano and K. Nishijima, Progr. Theoret. Phys. (Japan) **8**, 53 (1952).

[5] K. Brueckner and K. Watson, Phys. Rev. **86**, 923 (1952).

[6] B. T. Feld, Phys. Rev. **89**, 330 (1953).

The four basic photomeson reactions are:

$$\begin{aligned}&\gamma+p\rightarrow\pi^++n,\\&\gamma+n\rightarrow\pi^-+p,\\&\gamma+p\rightarrow\pi^0+p,\\&\gamma+n\rightarrow\pi^0+n.\end{aligned} \quad (2)$$

We shall use the superscripts "+," "−," or "0" to indicate the first three processes, respectively. The fourth will be designated by $(n\rightarrow\pi^0)$.

For each of these four processes we may expect a different matrix T of the form of Eq. (1). If we make use of the charge independence hypothesis, these T's are not independent, but satisfy the relationships[7]

$$\begin{aligned}T^+&=[\sqrt{2}t_3+(1/\sqrt{2})t_1]-\sqrt{2}S\\T^-&=[\sqrt{2}t_3+(1/\sqrt{2})t_1]+\sqrt{2}S\\T^0&=[2t_3-\tfrac{1}{2}t_1]+S\\T(n\rightarrow\pi^0)&=[2t_3-\tfrac{1}{2}t_1]-S.\end{aligned} \quad (3)$$

Thus the four scattering matrices T depend upon the three quantities t_3, t_1, and S, which themselves are undetermined by the symmetry principle alone. The term S arises from nucleon recoil and leads to final meson-nucleon states of isotopic spin $I=\frac{1}{2}$, only. t_3 and t_1 describe the pure isotopic spin states $I=\frac{3}{2}$ and $I=\frac{1}{2}$, respectively, for the final state containing the meson and nucleon.

Evidently, if we combine Eqs. (1) and (3), the latter equations will represent conditions on the coefficients A, B, C, and E of Eq. (1) on introducing the appropriate notation for the t's and S. Thus let

$$t_1(j,l,\phi), \quad S(j,l,\phi)$$

describe the amplitude for producing a final $I=\frac{1}{2}$ state with angular momentum j and orbital angular momentum l. Similarly, $t_3(j,l,\phi)$ is the amplitude for a final $I=\frac{3}{2}$ state with the same total (and orbital) angular momentum. In these expressions ϕ represents the γ-ray multipole transition and for Eq. (1) may be:

$$\begin{aligned}\phi&=e_1-\text{electric dipole},\\&=m_1-\text{magnetic dipole},\\&=e_2-\text{electric quadrupole}.\end{aligned}$$

With this notation, Eqs. (3) imply that the A of Eq. (1) may be written as

$$\begin{aligned}A^+&=[\sqrt{2}t_3(\tfrac{1}{2},0,e_1)+(1/\sqrt{2})t_1(\tfrac{1}{2},0,e_1)]-\sqrt{2}S(\tfrac{1}{2},0,e_1),\\A^0&=[2t_3(\tfrac{1}{2},0,e_1)-\tfrac{1}{2}t_1(\tfrac{1}{2},0,e_1)]+S(\tfrac{1}{2},0,e_1);\end{aligned} \quad (4)$$

A^- is obtained from A^+ and $A(n\rightarrow\pi^0)$ from A^0 by changing the sign of S [see Eqs. (3)]. B, C, and E have the same structure but involve $(j=\frac{1}{2},\ l=1,\ \phi=m_1)$, $(j=\frac{3}{2},\ l=1,\ \phi=m_1)$, and $(j=\frac{3}{2},\ l=1,\ \phi=e_2)$, respectively.

[7] K. M. Watson, Phys. Rev. **85**, 852 (1952).

The t's and S's represent twelve complex functions of q which are completely undetermined by the symmetry principles used thus far. The importance of introducing these quantities is, however, that their complex phases can be calculated explicitly in terms of the phase shift for meson-nucleon scattering in the appropriate final state. This is done in the Appendix and depends upon the assumed unitarity of the scattering matrix $[S=1+2\pi iT]$ and the principle of time reversibility for dynamical systems.

From the results in the Appendix each t and S in Eqs. (4) can be written as

$$e^{i\gamma}N,$$

where γ and N are real and γ is determined by the phase shifts for meson-nucleon scattering. (Of course, all the t's and S's are undetermined to within a common, irrelevant phase factor.) Thus

$$\begin{aligned} t_3(\tfrac{1}{2},0,e_1)&=ie^{i\alpha_3}d_3,\\ t_1(\tfrac{1}{2},0,e_1)&=ie^{i\alpha_1}d_1,\\ S(\tfrac{1}{2},0,e_1)&=ie^{i\alpha_1}\delta D, \end{aligned} \tag{5}$$

where α_3 and α_1 are the phase shifts used by Anderson, Fermi, Martin, and Nagle[8] to describe the S-wave pion scattering in the $I=\frac{3}{2}$ and $I=\frac{1}{2}$ states, respectively. The d_1, d_3, and δD are *real* functions of q, and near the energetic threshold they are constant. These refer to electric dipole absorption of the γ ray. The phase shifts α_1 and α_3 are to be evaluated at the energy of the meson and nucleon (referred to the center-of-mass system) in the final state.

The remaining t's and S's, as obtained in the Appendix, are

$$\begin{aligned} &t_3(\tfrac{3}{2},1,m_1)=e^{i\alpha_{33}}M_3^{\frac{1}{2}}, \quad t_3(\tfrac{1}{2},1,m_1)=e^{i\alpha_{31}}M_3^{\frac{1}{2}}\\ &t_1(\tfrac{3}{2},1,m_1)=e^{i\alpha_{13}}M_1^{\frac{1}{2}}, \quad t_1(\tfrac{1}{2},1,m_1)=e^{i\alpha_{11}}M_1^{\frac{1}{2}}\\ &S(\tfrac{3}{2},1,m_1)=e^{i\alpha_{13}}\delta M_1^{\frac{1}{2}}, \quad S(\tfrac{1}{2},1,m_1)=e^{i\alpha_{11}}\delta M_1^{\frac{1}{2}}\\ &t_3(\tfrac{3}{2},1,e_2)=ie^{i\alpha_{33}}E_3^{\frac{1}{2}}, \quad t_1(\tfrac{3}{2},1,e_2)=ie^{i\alpha_{13}}E_1^{\frac{1}{2}},\\ &S(\tfrac{3}{2},1,e_2)=ie^{i\alpha_{13}}\delta E_1^{\frac{1}{2}}. \end{aligned} \tag{6}$$

These α's are the P-wave phase shifts used by Fermi *et al.*[8] (The first subscript is twice the isotopic spin, the second is twice the total angular momentum.) These terms correspond to magnetic dipole absorption of the γ ray. The M's δM's, E's, and $\delta E_1^{\frac{1}{2}}$ are *real* functions of q, which vary linearly with q near the energetic threshold but are otherwise undetermined (as are d_3, d_1, and δD) by our symmetry arguments (presumably a dynamical theory is required to determine these).

We may now use Eqs. (3), (5), and (6) to write out in detail the coefficients A, B, C, and E of Eq. (1):

$$\begin{aligned} A^+&=i\left\{\sqrt{2}e^{i\alpha_{33}}d_3+e^{i\alpha_1}\left[\frac{d_1}{\sqrt{2}}-\sqrt{2}\delta D\right]\right\},\\ B^+&=\sqrt{2}e^{i\alpha_{31}}M_3^{\frac{1}{2}}+e^{i\alpha_{11}}\left[\frac{1}{\sqrt{2}}M_1^{\frac{1}{2}}-\sqrt{2}\delta M_1^{\frac{1}{2}}\right],\\ C^+&=\sqrt{2}e^{i\alpha_{33}}M_3^{\frac{1}{2}}+e^{i\alpha_{13}}\left[\frac{1}{\sqrt{2}}M_1^{\frac{1}{2}}-\sqrt{2}\delta M_1^{\frac{1}{2}}\right],\\ E^+&=i\left\{\sqrt{2}e^{i\alpha_{33}}E_3^{\frac{1}{2}}+e^{i\alpha_{13}}\left[\frac{1}{\sqrt{2}}E_1^{\frac{1}{2}}-\sqrt{2}\delta E_1^{\frac{1}{2}}\right]\right\}, \end{aligned} \tag{7}$$

and

$$\begin{aligned} A^0&=i\{2e^{i\alpha_3}d_3-e^{i\alpha_1}(\tfrac{1}{2}d_1-\delta D)\},\\ B^0&=2e^{i\alpha_{31}}M_3^{\frac{1}{2}}-e^{i\alpha_{11}}(\tfrac{1}{2}M_1^{\frac{1}{2}}-\delta M_1^{\frac{1}{2}}),\\ C^0&=2e^{i\alpha_{33}}M_3^{\frac{1}{2}}-e^{i\alpha_{13}}(\tfrac{1}{2}M_1^{\frac{1}{2}}-\delta M_1^{\frac{1}{2}}),\\ E^0&=i\{2e^{i\alpha_{33}}E_3^{\frac{1}{2}}-e^{i\alpha_{13}}(\tfrac{1}{2}E_1^{\frac{1}{2}}-\delta E_1^{\frac{1}{2}})\}. \end{aligned} \tag{8}$$

The matrix elements A^-, B^-, C^-, and E^- for the $n\to\pi^-$ reaction are obtained from those of Eqs. (7) by changing the signs of δD, $\delta M_1^{\frac{1}{2}}$, $\delta M_1^{\frac{1}{2}}$, and $\delta E_1^{\frac{1}{2}}$. To obtain $A(n\to\pi^0)$, $B(n\to\pi^0)$, $C(n\to\pi^0)$, and $E(n\to\pi^0)$ we again change the sign of δD, $\delta M_1^{\frac{1}{2}}$, $\delta M_1^{\frac{1}{2}}$, and $\delta E_1^{\frac{1}{2}}$ in Eqs. (8).

The differential cross section, as obtained from Eq. (1) is (θ is the angle between $\mathbf{q}$ and $\boldsymbol{\kappa}$)

$$\begin{aligned} \sigma(\theta)=(q/\mu c)\sigma_0\{&|A|^2+|B|^2+\tfrac{1}{2}|C|^2(5-3\cos^2\theta)\\ &+2\,\mathrm{Im}[A^*(C-B)]\cos\theta-\mathrm{Re}[B^*C](3\cos^2\theta-1)\\ &+\mathrm{Re}[A^*E]\cos\theta-\tfrac{1}{2}\,\mathrm{Im}[E^*(B-C)](3\cos^2\theta-1)\\ &+\tfrac{1}{8}|E|^2(1+\cos^2\theta)\}. \end{aligned} \tag{9}$$

Here "Im" means "imaginary part of" and "Re" means "real part of." The factor before the bracket is chosen to make A, B, C, and E dimensionless and of order unity. For this purpose we arbitrarily take

$$\sigma_0=1.1(10)^{-2},\ \mathrm{cm}^2/\mathrm{sterad}. \tag{10}$$

An alternate form for Eq. (9) is

$$\sigma(\theta)=(q/\mu c)\sigma_0\{e_0+e_2'+e_2\cos^2\theta+e_1\cos\theta\}, \tag{11}$$

where e_0 is defined to be $|A|^2$ and thus represents the S-state term, which is constant near the energetic threshold. e_2' and e_2 vary as $(q/\mu c)^2$ and e_1 as $(q/\mu c)$ near threshold.

For energies not near threshold it may be desirable to include in σ_0 the kinematical "recoil correction,"

$$\sigma_0\simeq\frac{1}{(1+\kappa/M)^2}, \tag{12}$$

to the usual density of states factor.

Making use of the energy dependence, four e's in Eq. (11) can in principle be determined for each of the four basic photo cross sections. This gives a total of 16 coefficients which are expressed in terms of the 12 d's, M's, C's, δD, $\delta E_1^{\frac{1}{2}}$, and δM's.

[8] Anderson, Fermi, Martin, and Nagle, Phys. Rev. **91**, 155 (1953).

As in Eq. (9) we shall continue to denote differential cross sections by $\sigma(\theta)$. Total cross sections will be indicated by σ. We shall use $+$, $-$, 0, and $n\to\pi^0$ to designate the four reactions of expressions (2).

In Sec. IV we shall give some discussion of the photoproduction of mesons from deuterons, which may give some information concerning these reactions.

III. DISCUSSION OF THE CROSS SECTIONS

Among the implications of the analysis just given two of the most interesting have to do with the S-wave contribution to the π^0 cross sections. It is known that this is much smaller,[9,10] near threshold than is the S-wave term for the π^+ cross sections.[11] Nevertheless, we shall be able to establish two, independent lower limits on the S-wave amplitudes for producing π^0 mesons. One results from the π^-/π^+ ratio,

$$\Re(\theta)=\sigma^-(\theta)/\sigma^+(\theta) \quad \text{or} \quad \Re=\sigma^-/\sigma^+, \tag{13}$$

near threshold, and the other depends upon the S-wave pion-nucleon scattering amplitudes. The first depends upon the fact that $R(\theta)$ can differ from unity only if one or more of the "nucleon recoil" terms δD, $\delta M_1^{\frac{1}{2}}$, or $\delta M_1^{\frac{3}{2}}$ is different from zero. These quantities are also present, however, in the π^0 amplitudes of Eqs. (8). The second lower limit depends upon the observation that it is *impossible* to make a choice of the "parameters" d_3, d_1, and δD in such a manner that [see Eqs. (7) and (8)]

$$A^+\neq 0 \quad \text{and} \quad A^0=0$$

(unless $\alpha_1=\alpha_3$, which is certainly not the case,[8,12] except at some specific energies).

Returning to Eq. (13) we note that if

$$\delta D=0,$$

then R can differ from unity only when P-wave contributions are important and we must have

$$\Re=1+(q/\mu c)^2 \text{ times a constant}$$

near threshold. Such a striking energy dependence should not be difficult to detect. It seems more reasonable, however, to assume that $\delta D\neq 0$, so we suppose

$$\Re=1+\epsilon, \tag{14}$$

where ϵ is a constant (near threshold). Let us now define [see Eqs. (7) and (8)]

$$\begin{aligned} D&\equiv\sqrt{2}d_3+(1/\sqrt{2})d_1,\\ D_0&=2d_3-\tfrac{1}{2}d_1. \end{aligned} \tag{15}$$

These are real quantities which are constant near threshold. The smallness of the S-wave term in σ^0 implies that

$$D_0\ll D, \tag{16}$$

(close to threshold) so to a first approximation

$$\begin{aligned} d_1&=4d_3,\\ \text{and}\qquad d_3&=(1/3\sqrt{2})D. \end{aligned} \tag{17}$$

Then, in the energy range for which α_1 and α_3 are small

$$\begin{aligned} A^+&=ie^{i\alpha_1}\{D-\sqrt{2}\delta D+\tfrac{1}{3}D[-i(\alpha_1-\alpha_3\\ &\qquad -\tfrac{1}{2}(\alpha_1-\alpha_3)^2]\},\\ A^0&=ie^{i\alpha_1}\{D_0+\delta D+(\sqrt{2}/3)D[-i(\alpha_1-\alpha_3)\\ &\qquad -\tfrac{1}{2}(\alpha_1-\alpha_3)^2]\}. \end{aligned} \tag{18}$$

The matrix elements of A^- and $A(n\to\pi^0)$ are obtained by changing the sign of δD. From this we obtain the cross sections very near threshold:

$$\begin{aligned} \sigma^+(\theta)&=(q/\mu c)\sigma_0[D-\sqrt{2}\delta D]^2,\\ \sigma^-(\theta)&=(q/\mu c)\sigma_0[D+\sqrt{2}\delta D]^2,\\ \sigma^0(\theta)&=(q/\mu c)\sigma_0[D_0+\delta D]^2,\\ \sigma(\theta)(n\to\pi^0)&=(q/\mu c)\sigma_0[D_0-\delta D]^2, \end{aligned} \tag{19}$$

which are independent of θ.

Comparison with Eq. (14) shows that

$$\delta D\simeq(\epsilon/4\sqrt{2})D. \tag{20}$$

Since ϵ is probably appreciably less than unity,[11] Eq. (20) leads us to expect that $\delta D\ll D$, and that perhaps δD and D_0 are of about the same magnitude. Knowledge of δD would also permit us to put a lower limit on the average of the π^0 cross sections [see Eqs. (19)]:

$$\tfrac{1}{2}[\sigma^0+\sigma(n\to\pi^0)]\geq(q/\mu c)\sigma_0\delta D^2\simeq\sigma^+(\epsilon^2/32)(1+\tfrac{1}{2}\epsilon). \tag{21}$$

(A more specific discussion is given as "Model I" below.)

Returning to the general equations (7) and (8), it is instructive to put a lower limit on $|A^0|^2$ by treating d_1, d_3, and δD as adjustable parameters. We minimize subject to the condition that $|A^+|^2$ is held *constant*. This leads to the *minimum* value,[13]

$$\begin{aligned} |A^0|^2/|A^+|^2\geq\tfrac{1}{2}-3\cos^2(\alpha_1-\alpha_3)\{[1+8\cos^2(\alpha_1-\alpha_3)]^{\frac{1}{2}}\\ +1+2\cos^2(\alpha_1-\alpha_3)\}^{-1}. \end{aligned} \tag{22}$$

Expression (22) increases from a zero lower limit at $\alpha_1-\alpha_3=0$ to

$$|A^0|^2/|A^+|^2\geq\tfrac{1}{2},$$

at $|\alpha_1-\alpha_3|=\pi/2$. The right-hand side of (22) is plotted in Fig. 1. Remembering that (22) represents only a lower limit, we must be prepared to expect that $|A^0|^2$ will not be at all negligible for a considerable range of γ-ray energies. Indeed, when $(\alpha_1-\alpha_3)$ is not small, Eq. (22) implies that $|A^0|^2$ and $|A^+|^2$ are of

[9] A. Silverman and M. Stearns, Phys. Rev. **88**, 1225 (1952).
[10] Goldschmidt-Clermont, Osborne, and Scott, Phys. Rev. **89**, 329 (1953).
[11] G. Bernardini, Phys. Rev. **93**, 930 (1954).
[12] Bodansky, Sachs, and Steinberger, Phys. Rev. **93**, 1367 (1954); J. Tinlot and A. Roberts, Phys. Rev. **90**, 951 (1953).

[13] Equation (22) also represents a lower limit on $\{|A^0|^2+|A(n\to\pi^0)|^2\}/\{|A^+|^2+|A^-|^2\}$, subject to the condition that the denominator is held constant.

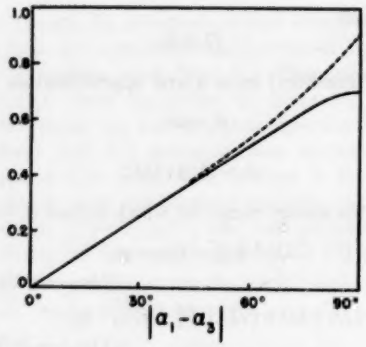

FIG. 1. The solid curve represents the square root of the expression (22). This is a lower limit on the ratio of the π^0 to the π^+ S-wave amplitudes for photoproduction. The dotted curve is the square root of the same ratio obtained from Eq. (23). These curves permit an indication of the S-wave–P-wave interference.

about the same size. This has a simple physical origin—when charge-exchange scattering (which depends upon $\alpha_1-\alpha_3$) is important, a meson which originally was produced with a charge may lose this via charge-exchange scattering before being emitted. Thus, even if there were no mechanism for directly producing π^0 mesons, they would still be emitted as a result of charge-exchange interactions.

Another estimate of $|A^0|$ can be obtained by taking D constant and $D_0=\delta D=0$ for all energies [see Eq. (15)]. This neglects any contribution from expression (21) to the S wave in σ^0, so it also may very well underestimate $|A^0|$. We now obtain

$$|A^+|^2+|A^0|^2=D^2,$$

and

$$|A^0|^2=(4/9)D^2[1-\cos(\alpha_1-\alpha_3)]. \tag{23}$$

Using these equations we again calculate $|A^0|/|A^+|$. This result is also plotted in Fig. 1. We note that for $|\alpha_1-\alpha_3|<60°$ this does not differ very much from that value obtained from the inequality (22).

An upper bound may also easily be obtained for $|A^0|/|A^+|$. This is just the reciprocal of the expression (22). Thus both upper and lower limits for this ratio are determined by the phase shifts α_1 and α_3. Not only does this hold for the electric dipole amplitudes, but all the other multipole transition terms are likewise restricted by the expression (22) and its reciprocal if we replace α_1 and α_3 by the appropriate scattering phase shifts.

As mentioned above it is reasonable to expect D_0 and δD to have comparable magnitudes. Since it is sometimes helpful to try definite models, we shall introduce[14] (to avoid confusion we shall explicitly mention it when using a model hereafter):

$$\text{Model I: } D_0=\delta D. \tag{24}$$

[14] This model was suggested to the author by G. Bernardini.

The justification for this model is that one might expect a much smaller electric dipole moment for the $(n\to\pi^0)$ process than for the $(p\to\pi^0)$ process. As we expect D_0 and δD to be comparable in magnitude we may hope that Eq. (24) is in any case qualitatively correct.

Using Eq. (24) and Eqs. (19) and (20) we would conclude that

$$\sigma^0=\sigma^+(\epsilon^2/8)(1+\tfrac{1}{2}\epsilon), \tag{25}$$

as long as only S waves need be considered and $(\alpha_1-\alpha_3)\simeq 0$. Thus the value of σ^0 could be obtained from (σ^-/σ^+) and σ^+.

The S wave for π^0 production will probably be most easily detected through its interference with the P-wave term. The interference term may be readily calculated from Eqs. (7), (8), and (9). These expressions are particularly simple if we were to assume:

Model II: The predominant P-wave term is[6] M_3^1. Then

$$\begin{aligned}\mathrm{Im}[A^{+*}(C^+-B^+)]&=-\sqrt{2}\{\cos(\alpha_3-\alpha_{33})\sqrt{2}d_3\\&\quad+\cos(\alpha_1-\alpha_{33})[(d_1/\sqrt{2})-\sqrt{2}\delta D]\}M_3^1,\\ \mathrm{Im}[A^{0*}(C^0-B^0)]&=-2\{\cos(\alpha_3-\alpha_{33})2d_3\\&\quad-\cos(\alpha_1-\alpha_{33})(\tfrac{1}{2}d_1-\delta D)\}M_3^1.\end{aligned} \tag{26}$$

[For the corresponding case with electric quadrupole radiation, M_3^1 should be replaced by $(M_3^1-\frac{1}{2}E_3^1)$—Eqs. (7), (8), and (9).] If the phase shift α_{33} goes through 90°, we may expect a change in the sign of these interference terms. Since the experimental $\sigma^+(\theta)$ shows constructive interference in the backward direction near threshold, we conclude that $\mathrm{Im}[A^{+*}(C^+-B^+)]$ is negative in this energy range. If Model I is valid, $\mathrm{Im}[A^{0*}(C^0-B^0)]$ is also negative. Indeed, if we combine Models I and II, we can give an explicit expression for the $p\to\pi^0$ cross section:

$$\begin{aligned}\sigma^0(\theta)=(q/\mu c)\sigma_0\{&e_0+\tfrac{1}{2}(q/\mu c)^2\\&\times[0.14][5-3\cos^2\theta]+e_1\cos\theta\},\end{aligned} \tag{27}$$

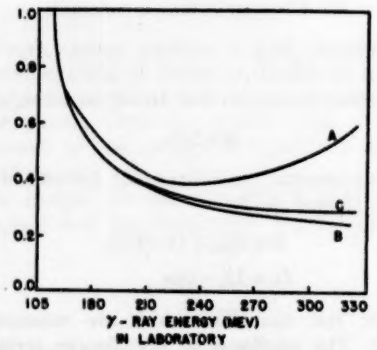

FIG. 2. The square root of the ratio of S- to P-wave contributions to the total π^0 cross section. The expression (28) is that plotted. Curves (A), (B), and (C) refer, respectively, to the value of expression (28) for the Fermi-Metropolis, the Glicksman, and the Martin scattering phase shifts, respectively, (see reference 15). These curves are essentially the ratio of S- to P-wave amplitudes.

where

$$e_0 \simeq \tfrac{1}{8}\epsilon^2(1+\tfrac{1}{2}\epsilon)+[4/9-\tfrac{1}{3}\epsilon][1-\cos(\alpha_1-\alpha_3)],$$
$$e_1 \simeq -(q/\mu c)[0.37]\{(\epsilon/\sqrt{2})\cos(\alpha_3-\alpha_{33}) - \tfrac{2}{3}\sqrt{2}[\cos(\alpha_1-\alpha_{33})-\cos(\alpha_3-\alpha_{33})]\}.$$

Equation (27) represents a combination of our two lower limits on $|A^0|$. That is, the approximate equality of expressions (22) and (23) (see Fig. 1) suggests that we may reasonably take D, D_0, and δD constant, since the dependence on $|\alpha_1-\alpha_3|$ seems to be so important. These three parameters are then fixed by σ^+ and the π^-/π^+ ratio, $R=1+\epsilon$, at threshold if we use Model I [which is not unlikely to be at least qualitatively correct]. When $|\alpha_1-\alpha_3|$ is not small, expression (22) determines the value of e_0 [actually, Eq. (23), to which e_0 essentially reduces when the ϵ terms are negligible] and is not dependent on our use of Model I. We shall discuss below the sensitivity of Eq. (27) to our use of Model II.

The numerical coefficients in Eq. (27) were obtained using Eq. (25) and the experimental[11] value of σ^+ for the S-wave amplitude and the σ^0 cross sections[9,10] at somewhat higher energies for the P-wave amplitude.

For an indication of the order of magnitude of the various terms in Eq. (27), we have plotted in Fig. 2 the quantity

$$[e_0\{0.28(q/\mu c)^2\}^{-1}]^{\frac{1}{2}}, \tag{28}$$

which is the ratio of S- to P-wave amplitudes, for the Fermi-Metropolis, Glicksman, and Martin[15] scattering phase shifts. The S-wave term is evidently not negligible.

In Fig. 3 we have plotted the angular asymmetry ratio (i.e., the ratio of the number of mesons produced in the forward hemisphere to those in the backward hemisphere), as deduced from Eq. (27) for the above three sets of scattering phase shifts.

We should now like to argue that, with the possible exception of the $[5-3\cos^2\theta]$ angular dependence, Eq. (27) may very well give us a reasonable description of the cross section $\sigma^0(\theta)$. The value of e_0 is independent of our assumption that only $M_3^{\frac{1}{2}}$ leads to P-wave production and so are Eq. (28) and the resulting curves of Fig. (2) [to the extent that the total cross section σ^0 is known experimentally].

On the other hand, the value of e_1 is dependent on our assumption that only $M_3^{\frac{1}{2}}$ is of importance—however, not as much so as might appear. Had we included the other possible multipole terms, e_1 would be replaced by a sum of terms of the form given in Eq. (27), one for each multipole and meson partial wave state. Each of these terms would be obtained by replacing α_{33} in Eq. (27) by the appropriate phase shift and modifying the coefficient [0.37] to correspond to the actual multipole strength.

At low energies, for which the phase shifts are small, these terms will add together to give an expression of the form

$$e_1 = -(q/\mu c)[0.37](\epsilon/\sqrt{2}),$$

except for an uncertainty in the actual value of the coefficient [0.37]. e_1 will deviate from this value only when some of the phase shifts become large. To the extent that α_{33} is the important P-wave phase shift we can expect the $M_3^{\frac{1}{2}}$ term to determine then the behavior of e_1, at least qualitatively [the coefficient (0.37) may of course be modified somewhat]. The degree to which this argument is valid depends, naturally, on the actual values of the phase shifts.

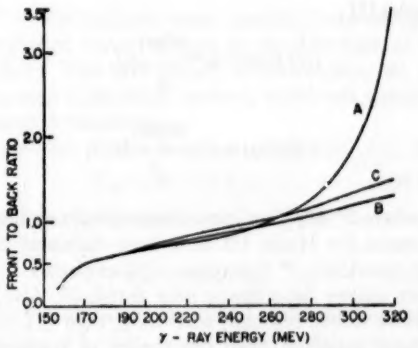

FIG. 3. The ratio of the number of π^0 mesons produced in the forward hemisphere to that in the backward hemisphere (in the center-of-mass system) is given as a function of the γ-ray energy in the laboratory system. The curves (A), (B), and (C) refer to the same sets of phase shifts as the corresponding curves of Fig. 2. This ratio was obtained from Eq. (27).

We may now summarize our arguments by stating that we feel Eq. (27) to be a reasonable estimate for the actual π^0 cross section as long as higher partial waves are not important. It seems likely that the term $|A^0|$ is not much greater than its lower limit since it has not shown up experimentally. Figures 1 and 2 indicate that $|A^0|$ is large enough to be detected rather easily via its interference with the P wave. Figure 3 implies that this interference is smaller between 220 and 280 Mev than might have been thought from Fig. 2. This results from the special form of e_1 in Eq. (27). The absence of any reported asymmetry about 90° in the experimental cross sections obtained to date is probably not inconsistent with Eq. (27), but may very well prove to be incompatible with some of the suggested sets of phase shifts (see Fig. 3).

The π^+ cross sections can evidently be analyzed in the same manner. Since this has been done by Ross,[1] we shall not repeat the arguments. We do emphasize again, however, that the photo cross sections are sensitive as to the choice of scattering phase shifts and may help in making a choice between alternate sets of these.

A third model may prove useful in the analysis of the cross sections. This model would imply that we replace Eqs. (5) and (6) by [at least for positive phase shifts]:

[15] E. Fermi and N. Metropolis (unpublished). R. L. Martin, Phys. Rev. **94**, 765 (1954). M. Glickmsan, reported by H. Bethe at the 1954 Rochester Conference on High Energy Physics (to be included in the proceedings of the conference).

Model III:

$$t_1(\tfrac{1}{2},0,\phi)=ie^{i\alpha_1}\frac{\sin\alpha_1}{q}d_1',$$
$$t_3(\tfrac{3}{2},1,\phi)=e^{i\alpha_{33}}\frac{\sin\alpha_{33}}{q^2}M_3'^{\dagger}, \tag{29}$$

etc., where d_1', $M_3'^{\dagger}$, etc., are constant, real numbers. The arguments for Model III have been discussed in some detail previously.[16] Equations (29) evidently give the correct energy dependence near threshold. Also, if α_{33} describes simple resonant scattering, then $t_3(\frac{3}{2},1,\phi)$ has the form expected from the theory of resonance reactions.[16] It is not easy to justify Model III on general grounds over an extended energy range. However, it may provide a useful hypothesis for studying the cross sections in certain energy ranges.[17]

We may obviously apply our general framework for analyzing the cross sections to other models. For instance, one might try using one of the approximations to meson theory to deduce certain additional relations among our parameters.

IV. THE PRODUCTION OF CHARGED MESONS FROM DEUTERONS

It seems that the study of the (π^-/π^+) ratio, $\mathfrak{R}(\theta)$ can be most easily done with a deuterium target. To interpret such results it is necessary to study the effect of the deuteron binding on $\mathfrak{R}$. We shall conclude that near threshold the observed $\mathfrak{R}(\theta)$ from deuterium should be the same as that from free protons and neutrons if certain general conditions are met. These conditions are subject to an experimental test.

We shall assume: (1) The electromagnetic interaction which produces a meson is the same for a nucleon bound in a deuteron as for a free nucleon. This is essentially the "impulse approximation."[18] Once produced, the meson may undergo a complicated interaction with the two nucleons, however.

(2) The energy range studied can be taken low enough that only mesons produced into S states [with respect to the nucleon from which they were produced] need be considered. We further assume that direct π^0 production with exchange scattering to produce a charged meson is negligible [partly because of the smallness of the S-wave term in π^0 production and partly because of the estimated smallness of such an exchange process at low energies]. We finally assume that the S-wave matrix element is essentially constant for the energy range involved.

(3) Coulomb forces are neglected, which means that the meson energy must be at least a few Mev.

We then write the transition matrix for producing a meson from a free nucleon [either nucleon "1" or nucleon "2"] as

$$T^{\pm}=D^{\pm}f(q)\{\tau^{(1)\pm}\boldsymbol{\sigma}_1\cdot\hat{\epsilon}\exp[i(\boldsymbol{\kappa}-\mathbf{q})\cdot\mathbf{z}_1]+\tau^{(2)\pm}\boldsymbol{\sigma}_2\cdot\hat{\epsilon}\exp[i(\boldsymbol{\kappa}-\mathbf{q})\cdot\mathbf{z}_2]\}. \tag{30}$$

The superscripts "+" or "−" refer, as usual, to the charge of the meson produced, the τ's are the appropriate isotopic spin operators, and $\mathbf{z}_1$ and $\mathbf{z}_2$ are the coordinates of the two nucleons. We have used assumption (2) above to express the dependence of T on charge by the real, dimensionless constants D^+ and D^-, which are of order unity.

Thus the ratio $\mathfrak{R}$ of Eq. (13) is in this notation

$$\mathfrak{R}(\theta)=\mathfrak{R}=(D^-/D^+)^2. \tag{31}$$

We now define a modified operator, T_0, by

$$T_0=T^{\pm}/D^{\pm}. \tag{32}$$

With an appropriate choice of phases, we can write

$$T_0=f(q)\{\tau_x^{(1)}\boldsymbol{\sigma}_1\cdot\hat{\epsilon}\exp[i(\boldsymbol{\kappa}-\mathbf{q})\cdot\mathbf{z}_1]+\tau_x^{(2)}\boldsymbol{\sigma}_2\cdot\hat{\epsilon}\exp[i(\boldsymbol{\kappa}-\mathbf{q})\cdot\mathbf{z}_2]\}, \tag{33}$$

which describes the production of mesons of either charge. We shall now consider the production of pions from deuterons using T_0 as the basis mechanism for their production. We suppose that all other interactions involved are charge independent [actually, we need require only charge symmetry].

Let $T_0(d)$ be the resulting transition matrix for producing charged mesons in deuterium. $T_0(d)$ is [see Eq. (33)] invariant with respect to the charge-symmetry operator R_x which represents a rotation through an angle of 180° about the x axis in charge space:

$$T_0(d)=R_x^{-1}T_0(d)R_x.$$

But R_x interchanges neutrons and protons and positive and negative mesons.[7,19] Thus,

$$T_0^+(d)=T_0^-(d), \tag{34}$$

to within a phase factor.

Since the electromagnetic interaction is weak, $T_0(d)$ is linear in T_0. Therefore, the actual matrix elements in deuterium, $T(d)$, can be obtained from $T_0(d)$ by multiplying by the appropriate constants $D^{\pm}$ [see Eq. (32)][20]:

$$T^+(d)=D^+T_0^+(d),\qquad T^-(d)=D^-T_0^-(d). \tag{35}$$

This, in turn, implies that the observed π^-/π^+ ratio

[16] K. Watson, Phys. Rev. 88, 1163 (1952).
[17] G. Bernardini (private communication), has suggested that on the basis of this model the π^-/π^+ ratio should reflect any marked energy dependence in the phase shift α_1.
[18] G. Chew and M. Goldberger, Phys. Rev. 87, 778 (1952).
[19] N. M. Kroll and L. L. Foldy, Phys. Rev. 88, 1177 (1952).
[20] There is an approximation involved at this point. That is, it is assumed that double charge exchange scattering is negligible. This would permit a π^- meson to become a π^+ meson after two charge exchanges, for instance. Estimates indicate that this type of process gives only about a 1 percent contribution near threshold.

from deuterium should be

$$\frac{\sigma_{\gamma+d\to\pi^-}(\theta)}{\sigma_{\gamma+d\to\pi^+}(\theta)}=\left(\frac{D^-}{D^+}\right)^2=\Re, \tag{36}$$

which is what we set out to demonstrate.

The model implied by assumptions (1) and (2) permits detailed calculations of the cross sections $\sigma_{\gamma+d\to\pi^-}(\theta)$ and $\sigma_{\gamma+d\to\pi^+}(\theta)$ The formal method has been developed previously.[21] This involves a calculation of the multiple scattering of the meson before it "leaves" the nucleons. Estimates of the importance of this multiple scattering indicate that it may give corrections of only about 10 percent to the calculation of Chew and Lewis[22] and Lax and Feshbach,[23] who neglected it. It is thus reasonable to use the calculation of these authors to check the validity of the model. A simple consequence of this model is that $\sigma_{\gamma+d\to\pi^-}(\theta)/\sigma_{\gamma+d\to\pi^+}(\theta)$ should be *independent* of angle near threshold, as is implied by Eq. (36).

The author is indebted to Professor G. Bernardini for several discussions of his experimental program, which provided much of the stimulus for this investigation. He is indebted to Professor R. G. Sachs for several stimulating discussions of the problems treated. He is also indebted to Professor M. Gell-Mann for pointing out a different derivation than that given here as well as some additional consequences of the arguments.†

APPENDIX. DISCUSSION OF THE PHASES

To derive Eqs. (5), (6), and (12), we shall suppose that photomeson production can be developed within the general framework of quantum mechanics. We suppose the system to be described by a Hamiltonian $H+V$, where V represents the interaction of the electromagnetic field with the pertinent particles and H represents the remainder of the Hamiltonian. Evidently, photomeson production may be described as a transition between two eigenstates of H, say "a" and "b," which represent, respectively, the physical states containing a nucleon and a γ ray and a nucleon and a meson. Let the respective eigenvectors be Ψ_a and Ψ_b, which are expected to be extremely complex at small distances (possibly containing virtual heavy mesons, V particles, etc.), but upon which physical requirements impose known asymptotic forms at large distances.

We then have for the transition matrix for radiative absorption,

$$T_{ab}=(\Psi_a,V\Psi_b), \tag{A-1}$$

since V is a (weak) electromagnetic interaction. No approximation is implied concerning the states Ψ_a and Ψ_b. Since Ψ_a can be factored into a "nucleon wave function" and a "photon wave function," we can absorb the photon wave function in the definition of V in Eq. (A-1). This will permit us to consider Ψ_a as describing only a (physical) nucleon, which will simplify our subsequent discussion.

The transition matrix for photoproduction, T_{ba}, is[24]

$$T_{ba}=(\Psi_b^{(-)},V\Psi_a), \tag{A-2}$$

where $\Psi_b^{(-)}$ is related to Ψ_b by the Wigner[25] time reversal operator K:

$$i^{-2M}\Psi_b^{(-)}=K\Psi_{(-b)}. \tag{A-3}$$

Here M is the azimuthal component of the nucleon spin wave function $\mathcal{S}^M$ when referred to the direction $\mathbf{q}$ of the meson as the axis of quantization. The state "$(-b)$" is obtained from "b" by reversing the direction of all momenta and angular momenta. The choice (A-3) of phases is particularly convenient, since it implies that when Ψ_b is a plane wave,

$$\Psi_b=e^{i\mathbf{q}\cdot\mathbf{x}}\mathcal{S}^M,$$

we have

$$\Psi_b^{(-)}=\Psi_b$$

(using the customary representation for K).

We shall calculate T_{ba} [Eq. (A-2)] by breaking the state Ψ_b into partial wave eigenstates of the angular momentum l and the total angular momentum j of the meson-nucleon system. Equations (A-1) and (A-2) evidently remain valid whether Ψ_b (and $\Psi_b^{(-)}$) refer to incident plane waves or to separate eigenstates of j and l. As a matter of fact, for pure eigenstates of (j,l) which have no accidental degeneracies (which seems forbidden by physical requirements) the state Ψ_b is *unique*. This means that $\Psi_b^{(-)}$, which is also a solution of the Schrödinger equation with the same eigenvalues can differ from Ψ_b only by a constant phase factor, which can evidently be calculated from just the asymptotic form of Ψ_b. (That we can calculate this phase from just the asymptotic form of Ψ_b is perhaps the most crucial point in our analysis.)

To calculate these phases, we suppose Ψ_b to represent a pure isotopic spin state and write its explicit form for an incident plane wave (when the meson and nucleon are far apart)

$$\Psi_b(r\to\infty)=f_0^{\frac{1}{2}}(qr)\mathcal{S}^M+3f_1^{\frac{1}{2}}(qr)\Lambda_{\frac{1}{2}}^M+3f_1^{\frac{1}{2}}(qr)\Lambda_{\frac{1}{2}}^M+\cdots. \tag{A-4}$$

Here $\mathbf{r}$ is the relative coordinate of the meson and nucleon and $f_l^j(qr)$ is the radial wave function for scattering in the state (j,l). The Λ_j^M's are eigenstates of j and may be written

$$\begin{aligned}\Lambda_{\frac{1}{2}}^M&=\tfrac{1}{3}(\boldsymbol{\sigma}\cdot\mathbf{r}/r)(\boldsymbol{\sigma}\cdot\mathbf{q}/q)\mathcal{S}^M,\\ \Lambda_{\frac{1}{2}}^M&=(\mathbf{q}/q)\cdot[\mathbf{r}/r-\tfrac{1}{3}(\boldsymbol{\sigma}\cdot\mathbf{r}/r)\boldsymbol{\sigma}]\mathcal{S}^M.\end{aligned} \tag{A-5}$$

[21] K. Watson, Phys. Rev. **89**, 575 (1953).
[22] G. Chew and H. Lewis, Phys. Rev. **84**, 779 (1951).
[23] M. Lax and H. Feshbach, Phys. Rev. **88**, 509 (1952).
† In particular, I should like to thank Professor Gell-Mann for noting a numerical error in one of the coefficients of Eq. (9) in the original manuscript [which was also in reference 5].

[24] The state $\Psi_b^{(-)}$ contains *incoming* scattered waves for the meson, whereas Ψ_b has outgoing scattered waves. The necessity for the use of $\Psi_b^{(-)}$ in Eq. (A-2) was demonstrated in reference 16 and also by Gell-Mann and Goldberger, Phys. Rev. **91**, 398 (1953).
[25] E. P. Wigner, Göttinger Nachr. **31**, 546 (1953).

We are neglecting states with $l>1$. The $f_l{}^j$'s in Eq. (A-4) are

$$f_l{}^j = i^l \exp(i\delta_{jl}) \frac{\sin[qr - \frac{1}{2}\pi l + \delta_{jl}]}{qr}, \tag{A-6}$$

where δ_{jl} is the appropriate scattering phase shift.

Quite evidently, we have [see Eq. (A-3)]

$$Kf_l{}^j = (-1)^l \exp(-2i\delta_{jl}) f_l{}^j, \tag{A-7}$$

which along with Eqs. (A-4) and (A-5) permits us to write down $\Psi_b{}^{(-)}$ in terms of Ψ_b for a pure (j,l) state.

Let us first consider only S waves, from which we can derive Eqs. (5). Then $\Psi_b = f_0{}^{\frac{1}{2}}(qr)\mathcal{S}^M$ and

$$\Psi_b{}^{(-)} = \exp(-2i\delta_{\frac{1}{2}0})\Psi_b. \tag{A-8}$$

Thus Eq. (A-2) becomes

$$\begin{aligned} T_{ba} &= \exp(2i\delta_{\frac{1}{2}0})(\Psi_b, V\Psi_a) \\ &= \exp(2i\delta_{\frac{1}{2}0})(\Psi_a, V\Psi_b)^* \\ &= \exp(2i\delta_{\frac{1}{2}0})(T_{ab})^*, \end{aligned} \tag{A-9}$$

since V is Hermitean.

Now, still restricting ourselves to S waves, let us write T in operator form as in Eq. (1):

$$T = \mathfrak{D}\boldsymbol{\sigma}\cdot\hat{e}. \tag{A-10}$$

Here $\mathfrak{D}$ is essentially the A of Eq. (1) except that it has a creation (or absorption) operator for one meson as a factor and it now refers to a pure isotopic spin state for the meson-nucleon system.

The postulated time-reversal invariance for our system implies[16] that

$$KTK^{-1} = T^\dagger. \tag{A-11}$$

Applied to Eq. (A-10) this gives

$$\begin{aligned} &K\mathfrak{D}K^{-1} = \mathfrak{D}^\dagger, \\ \text{or} \\ &\mathfrak{D} = K^{-1}\mathfrak{D}^\dagger K \end{aligned} \tag{A-12}$$

(since $K\boldsymbol{\sigma}K^{-1} = -\boldsymbol{\sigma}$ and $K\hat{e}K^{-1} = -\hat{e}$).

We designate the eigenvectors of the occupation number operators by ω_0 and ω_1 where ω_0 describes the "existence of one nucleon" and ω_1 describes the existence of one nucleon and one meson. If we choose

$$\omega_0 = K\omega_0,$$

it follows that (if ω results from applying the creation operator to ω_0)

$$K\omega_1 = -\omega_1 \tag{A-13}$$

because of the pseudoscalar nature of the pion field.[26]

Referring to Eq. (A-10), we have

$$\begin{aligned} T_{ba} &= (\omega_1, \mathfrak{D}\omega_0)(\mathcal{S}^M, \boldsymbol{\sigma}\cdot\hat{e}\mathcal{S}^{M_a}), \\ T_{ab} &= (\omega_0, \mathfrak{D}\omega_1)(\mathcal{S}^{M_a}, \boldsymbol{\sigma}\cdot\hat{e}\mathcal{S}^M), \end{aligned} \tag{A-14}$$

where the M and M_a are nucleon spin components. The quantity $(\omega_1, \mathfrak{D}\omega_0)$ is a complex number which determines the amplitude of the transition—it is one of the quantities $I_1(\frac{1}{2},0,e_1)$, $I_3(\frac{1}{2},0,e_1)$ or $S(\frac{1}{2},0,e_1)$.

Combining Eqs. (A-9) and (A-14), we have

$$(\omega_1, \mathfrak{D}\omega_0) = \exp(2i\delta_{\frac{1}{2}0})(\omega_0, \mathfrak{D}\omega_1)^*. \tag{A-15}$$

Making use of Eqs. (A-12) and (A-13), we have

$$\begin{aligned} (\omega_1, \mathfrak{D}\omega_0) &= (\omega_1, K^{-1}\mathfrak{D}^\dagger K\omega_0) \\ &= (K\omega_1, \mathfrak{D}^\dagger K\omega_0)^* \\ &= -(\omega_1, \mathfrak{D}^\dagger\omega_0)^* \\ &= -(\omega_0, \mathfrak{D}\omega_1). \end{aligned} \tag{A-16}$$

Comparison with Eq. (A-15) shows that

$$(\omega_0, \mathfrak{D}\omega_1) = -\exp(2i\delta_{\frac{1}{2}0})(\omega_0, \mathfrak{D}\omega_1)^*,$$

or

$$\begin{aligned} -(\omega_1, \mathfrak{D}\omega_0) = (\omega_0, \mathfrak{D}\omega_1) &= i\exp(i\delta_{\frac{1}{2}0}) \\ &\text{times a real number.} \end{aligned} \tag{A-17}$$

Since this holds for either of the pure isotopic spin states for the meson nucleon system, Eqs. (5) follow immediately on identifying $\delta_{\frac{1}{2}0}$ with the appropriate α.

Only a slight modification is required to obtain the relations (6) and (12). Referring to Eq. (A-8), let us take, for instance,

$$\Psi_b = f_1{}^{\frac{1}{2}}\Lambda_{\frac{1}{2}}{}^M; \tag{A-18}$$

then

$$\Psi_b{}^{(-)} = \exp(-2i\delta_{\frac{1}{2}1})\Psi_b.$$

This relation is formally the same as (A-8), so (A-9) holds also for the $j=\frac{1}{2}$, $l=1$ state. Equation (A-10) is modified in that $\boldsymbol{\sigma}\cdot\hat{e}$ is replaced by the appropriate operator from Eq. (1):

$$\begin{aligned} T = \mathfrak{D}_a[&i\boldsymbol{\sigma}\cdot(\boldsymbol{\kappa}\times\hat{e})\times\mathbf{q}/q + (\boldsymbol{\kappa}\times\hat{e})\cdot\mathbf{q}/q]\kappa^{-1} \\ &+ \mathfrak{D}_p[-i\boldsymbol{\sigma}\cdot(\boldsymbol{\kappa}\times\hat{e})\times\mathbf{q}/q + (\boldsymbol{\kappa}\times\hat{e})\cdot\mathbf{q}/q]\kappa^{-1}. \end{aligned} \tag{A-19}$$

Here $\mathfrak{D}_a$ absorbs and $\mathfrak{D}_p$ produces the meson. Since the coefficients of $\mathfrak{D}_a$ and $\mathfrak{D}_p$ above change sign under time reversal, Eqs. (A-12) are modified to read

$$\begin{aligned} \mathfrak{D}_a &= -K^{-1}\mathfrak{D}_p{}^\dagger K, \\ \mathfrak{D}_p &= -K^{-1}\mathfrak{D}_a{}^\dagger K. \end{aligned} \tag{A-20}$$

The minus sign in these equations changes the sign of Eq. (A-16) so we now have

$$(\omega_1, \mathfrak{D}_p\omega_0) = (\omega_0, \mathfrak{D}_a\omega_1).$$

This modifies Eq. (A-17) in that the factor of i does not appear and Eqs. (6) follow immediately. Equations (12) are obtained in just the same manner as was Eq. (A-17).

We mention again, that all the terms in T are undetermined, of course, to within a *common* irrelevant phase factor. This has not appeared above because we have always made a specific choice of phases.

[26] For instance, if $\boldsymbol{\sigma}\cdot\nabla\phi$ is to remain invariant then $K\phi K^{-1} = -\phi$ since $K\boldsymbol{\sigma}K^{-1} = -\boldsymbol{\sigma}$. R. G. Sachs, Phys. Rev. **87**, 1100 (1952) has explicitly constructed K for this case.

Canonical Transformation for an Electron-Positron Field Coupled to a Time-Independent Electromagnetic Field. II*

H. E. Moses
Department of Mathematics, New York University, Washington Square, New York, New York
(Received February 3, 1954)

A prescription for constructing well-defined field operators from a single particle operator is given in a form in which electrons and positrons appear in a symmetric way. Such a prescription removes certain trivial infinities arising from the conventional "hole" theory approach. The canonical transformation derived in a previous paper is used to calculate the vacuum expectation values of various operators to the second order in electron charge. It is shown that, despite the fact that the scattering operator does not exist when the electromagnetic field is constant in time, one obtains the usual results for current and charge densities. In addition, the striking result is proved that for certain purely electrostatic fields the expectation values of the number operator are finite but that when a magnetostatic field is also present the expectation values are infinite.

1. INTRODUCTION

In a previous paper[1] we obtained an integro-difference equation for the canonical transformation for an electron-positron field, coupled to a time-independent electromagnetic field in terms of single-particle transformations or eigenfunctions. The canonical transformation for the field was solved to the second order in the electron charge by means of a perturbation procedure. The usual treatment of field problems is weighted with implicit assumptions on the character of the operators involved. It was the objective to present more explicitly than is usually done the various assumptions made on the spectra of the operators involved. That is, the canonical transformation was found under the assumption that the spectrum of the single-particle Hamiltonian interacting with the electromagnetic field was the same as that for the field-free Hamiltonian, and that the electron-positron field interacting with the electromagnetic field could be described with the aid of annihilation and creation operators of the same character as those of the free electron-positron field.

This paper is to be regarded as a direct extension of reference 1. We shall calculate the vacuum expectation values of various operators to the second order. It will be shown that, despite the fact that the scattering operator does not exist, the expectation value of the charge and current operators is the same as that obtained from a scattering operator formalism, for example, that of Schwinger.[2] In addition, we shall prove the surprising result, mentioned in reference 1, that for electromagnetic fields which consists of suitable electrostatic fields only, the vacuum expectation of the number operator is finite and the canonical transformation exists rigorously. It will be shown, however, that when a magnetic field is also present the vacuum expectation of the number operator is infinite. A form of this proof is also given by Friedrichs[3] who treats the same problem from a different point of view.

2. FIELD OPERATORS

We shall now obtain expressions for field operators in terms of the annihilation and creation operators $A^{\pm}(s)$ and $B^{\pm}(v)$. The field operators which we want can be obtained from operators which occur in the single-particle theory.

Let us introduce matrices $L^{\epsilon}(s;s')$ for single-particle operators L as given in the $H^{(0)}$ representation, i.e.,

$$L^{\epsilon}(s;s')=\sum_{\mu}\int \bar{\chi}^{(0)}(X,\mu;s)L^{X,\mu}\chi^{(0)}(X,\mu;s')dX, \quad (1)$$

where $L^{X,\mu}$ is the single particle operator L in the X-representation.

In the case of a simple fermion field a well-defined field operator $[L]_A$ can be constructed from single particle operators L by means of the formula,

$$[L]_A=\int\int L^{\epsilon}(s;s')A^{+}(s)A^{-}(s')dsds'; \quad (2)$$

(see, e.g., Friedrichs[4]).

It is essential that the creation and annihilation operators appear in the order shown in (2) for operators such as $[L]_A$ to be defined. This fact motivates the following definition for field operators which was suggested by Friedrichs[5] for the case of the electron-positron field.

$$[L]_A=\int\int L^{\epsilon}(s;s')\epsilon'[A^{\epsilon}(s)A^{-\epsilon'}(s')]_{\epsilon'}dsds', \quad (3)$$

where

$$[A^{\epsilon}(s)A^{-\epsilon'}(s')]_{\epsilon'}=A^{\epsilon}(s)A^{-\epsilon'}(s') \quad \text{for} \quad \epsilon'>0$$
$$=A^{-\epsilon'}(s')A^{\epsilon}(s) \quad \text{for} \quad \epsilon'<0. \quad (4)$$

* This paper is based, in part, on the report IMM-NYU No. 179, Institute for Mathematics and Mechanics, New York University, March, 1952 (unpublished).

[1] H. E. Moses, Phys. Rev. **89**, 115 (1953).

[2] J. Schwinger, Phys. Rev. **75**, 651 (1949).

[3] K. O. Friedrichs, *Mathematical Aspects of the Quantum Theory of Fields* (Interscience Publishers, Inc., New York, 1953), Part V, Sec. 28.

[4] K. O. Friedrichs, reference 3, Part II.

[5] K. O. Friedrichs (private communication).

The symmetric way in which electrons and positrons were introduced and this prescription for obtaining field operators makes it unnecessary to consider a positron as being a "hole" in a "sea" of electrons. Furthermore, field operators obtained in this way have the desirable property that the expectation value in a vacuum of any such field operator $[L]_A$ is given by

$$(\Psi_0,[L]_A\Psi_0)=0,$$

where Ψ_0 is the vacuum state with respect to the operator N, i.e., $N\Psi_0=0$. It should be mentioned that Snyder[6] has a similar prescription for obtaining well-defined field operators, and Belinfante[7] has a similar procedure for avoiding the "hole" theory of the positron.

One can also construct field operators using the annihilation and creation operators $B^{\pm(v)}$. The field operator $[L]_B$ is defined by

$$[L]_B=\int\int L^v(v;v')_{\iota'}[B^{\iota}(v)B^{-\iota'}(v')]_{\iota'}dvdv', \quad (5)$$

where $L^v(v;v')$ is the matrix element of the single-particle operator L in the H representation, i.e.,

$$L^v(v;v')=\sum_\mu\int\bar\chi(X,\mu;v)L^{X,\mu}\chi(X,\mu;v')dx. \quad (6)$$

We shall now give expressions for several field operators, though we shall not use all of them. (See earlier report by the author[8] for details of the derivations.)

1. The unperturbed Hamiltonian $\mathfrak{IC}^{(0)}$ of the electron-positron field is obtained by using Eq. (3), where L is taken to be the unperturbed single-particle Hamiltonian $H^{(0)}$. That is,

$$\mathfrak{IC}^{(0)}=[H^{(0)}]_A=\int|E(s)|A^+(s)A^-(s)ds, \quad (7)$$

where $E(s)$ is the eigenvalue of $H^{(0)}$ corresponding to the case where the complete set of variables introduced in reference 1 have the values collectively denoted by s. It is useful to note that for any state $\Phi\underset{N}{\leftrightarrow}\{\Psi_n(s)_n\}$, we have

$$\mathfrak{IC}^{(0)}\Phi\underset{N}{\leftrightarrow}\{\sum_{i=1}^n|E(s_i)|\Psi_n(s)_n\},$$

as is required in the more conventional treatment of the problem.

2. The number operator N is obtained from Eq. (3) by taking L to be EI, where I is the identity operator and E is the operator $H^{(0)}/|H^{(0)}|$, whose eigenvalue is ϵ. Thus,

$$N=[EI]_A=\int A^+(s)A^-(s)ds, \quad (8)$$

as required.

3. The charge operator Q is obtained from Eq. (3) by taking L to be the single-particle operator eI, where e is the electron charge. Then,

$$\begin{aligned}Q=[eI]_A&=\int A^+(s)A^-(s)\delta_{\epsilon,+}ds\\&\quad-\int A^+(s)A^-(s)\delta_{\epsilon,-}ds\\&=e[N_+-N_-],\end{aligned} \quad (9)$$

as required.

4. The current operator J_i is obtained from Eq. (3) where L is taken as $L=e\alpha_i$:

$$\begin{aligned}J_i=[e\alpha_i]_A&=e\int\int\alpha_i{}^s(s;s')A^{\epsilon}(s)A^-(s')\delta_{\epsilon',+}dsds'\\&\quad-e\int\int\alpha_i{}^s(s;s')A^+(s')A^{\epsilon}(s)\delta_{\epsilon',-}dsds',\end{aligned} \quad (10)$$

where

$$\alpha_i{}^s(s;s')=\sum_\mu\int\bar\chi^{(0)}(X,\mu;s)\alpha_i{}^\mu\chi^{(0)}(X,\mu;s')dX. \quad (11)$$

In Eq. (11), $\alpha_i{}^\mu$ is the Dirac operator as expressed in the familiar matrix form.

5. The field charge density operator $\rho(X_0)$ for the charge density at X_0 is obtained by using for L the single-particle charge density at X_0, namely, $L^{X,\mu}=e\delta(X-X_0)$. That $L^{X,\mu}=e\delta(X-X_0)$ is the single-particle charge density is clear from the fact that if we have the single-particle state $\Psi(X,\mu)$, the expectation value of L is

$$\sum_\mu\int\bar\Psi(X,\mu)L^{X,\mu}\Psi(X,\mu)dX=e\sum_\mu\bar\Psi(X_0,\mu)\Psi(X_0,\mu),$$

which is just the charge density at X_0 usually assumed in the single-particle theory.

From Eq. (3), and Eqs. (15) and (15a) of reference 1, we have

$$\begin{aligned}\rho(X_0)&=e[\delta(X_{op}-X_0)]_A\\&=e\sum_\mu\int\int\bar\chi^{(0)}(X_0,\mu;s)\chi^{(0)}(X_0,\mu;s')\\&\qquad\times\epsilon'[A^{\epsilon}(s)A^{-\epsilon'}(s')]_{\epsilon'}dsds'\\&=\tfrac{1}{2}e\sum_\mu[\Xi^+(X_0,\mu)\Xi^-(X_0,\mu)-\Xi^-(X_0,\mu)\Xi^+(X_0,\mu)]\\&\quad+\tfrac{1}{2}e\Big[\sum_\mu\int\bar\chi^{(0)}(X_0,\mu;s)\chi^{(0)}(X_0,\mu;s)\delta_{\epsilon,+}ds\\&\quad-\sum_\mu\int\bar\chi^{(0)}(X_0,\mu;s)\chi^{(0)}(X_0,\mu;s)\delta_{\epsilon,-}ds\Big].\end{aligned} \quad (12)$$

[6] H. S. Snyder, Phys. Rev. **78**, 98 (1950).

[7] F. J. Belinfante, preprint "A Positon Theory Without Holes" (1953). The author is grateful to Professor Belinfante for making this preprint available to him. See also Phys. Rev. **93**, 935 (1954).

[8] H. E. Moses, Report No. IMM-NYU No. 179, Institute of Mathematical Sciences, New York University, New York, 1952 (unpublished).

The first expression for $\rho(X)$ can be used to show

$$\int \rho(X)dX = Q,$$

as required. The second expression shows that the charge density is substantially the Heisenberg charge density, except that here the usually troublesome constant term has been eliminated.

6. The field current density operator at X_0 which we denote by $j_i(X_0)$ is similarly obtained by choosing L as $L^{X,\mu} = e\alpha_i{}^{\mu}\delta(X-X_0)$. An expression analogous to that for $\rho(X)$ is obtained.

7. The total energy $\mathfrak{H}$ is defined using expression (5) with L equal to the single-particle Hamiltonian H. One obtains

$$\mathfrak{H} = [H]_B = \int |E(v)|\, B^+(v)B^-(v)dv. \tag{13}$$

We have

$$\mathfrak{H} \underset{M}{\leftrightarrow} \{\sum_{i=1}^{n} |E(v_i)|\, \zeta_n(v)_n\},$$

where

$$\Phi \underset{M}{\leftrightarrow} \{\zeta_n(v)_n\}.$$

THE SCATTERING OPERATOR

In the scattering problems the total Hamiltonian is split up into the sum of two parts one of which is the unperturbed Hamiltonian and the other is the perturbation. In terms of the field Hamiltonians this splitting up is written

$$\mathfrak{H} = \mathfrak{H}^{(0)} + \mathcal{V}. \tag{14}$$

If there exists a class of solutions $\Phi(t)$ of the Schrödinger equation

$$i\frac{\partial}{\partial t}\Phi(t) = \mathfrak{H}\Phi(t) \tag{15}$$

such that the limits $\Phi_{\pm}$ exist where

$$\Phi_{\pm} = \lim_{t\to\pm\infty} \exp(it\mathfrak{H}^{(0)})\Phi(t), \tag{16}$$

then the scattering operator S is defined by

$$\Phi_+ = S\Phi_-. \tag{17}$$

When the scattering operator exists one usually formulates an initial value problem by prescribing Φ_-, the state of the system in the infinite past, in the N representation and by finding Φ_+, the state in the infinite future, also usually in the N representation.

We shall show, however, that in our problem the limits $\Phi_{\pm}$ do not exist and, therefore, that the scattering operator cannot be defined. We proceed as follows: The solution of Eq. (15) is

$$\Phi(t) = \exp(-it\mathfrak{H})\Phi(0), \tag{18}$$

or in terms of the M representation of the field,

$$\zeta_n(v)_n(t) = \exp[-it\sum_{i=1}^{n} |E(v_i)|]\zeta_n(v)_n, \tag{18a}$$

where

$$\Phi(0) \underset{M}{\leftrightarrow} \zeta_n(v)_n.$$

From Eq. (35) of reference 1, together with the orthogonality relations (36), we can find $\Phi(t)$ in the N representation, namely,

$$\Psi_n(s)_n(t) = \sum_{n'} \int \bar{T}_{n':n}(v)_{n'}:(s)_n \zeta_{n'}(v)_{n'}(t)(dv)_{n'}. \tag{19}$$

Hence, $\exp(it\mathfrak{H}^{(0)})\Phi(t)$ as given in the N representation is, on using Eq. (18a),

$$\exp(it\mathfrak{H}^{(0)})\Phi(t) \underset{N}{\leftrightarrow} \exp[it\sum_{i=1}^{n} |E(s_i)|]\Psi_n(s)_n(t)$$

$$= \sum_{n'} \int \bar{T}_{n':n}(v)_{n'}:(s)_n \exp[it(\sum_{i=1}^{n} |E(s_i)| - \sum_{i=1}^{n'} |E(v_i)|)] \times \zeta_{n'}(v)_{n'}(dv)_{n'}. \tag{20}$$

If we let $t \to \pm\infty$ in expression (20), the exponential factor under the integral sign merely oscillates for terms of the sum in which n' does not equal n. Such terms arise because particles are being created or destroyed. Hence the limits of $\exp(it\mathfrak{H}^{(0)})\Phi(t)$ as $t \to \pm\infty$ do not exist, and thus the scattering does not exist in a true sense. Generally speaking, scattering operators will not exist in field-theoretical problems where the perturbation is independent of the time. In order to have scattering operators, the perturbation must be functions of time which die out sufficiently rapidly as $t \to \pm\infty$. This is the reason adiabatic switching on and off of the perturbations is usually assumed.

Since the scattering operator does not exist in a rigorous sense, we must resort to formulations of the initial value problem other than that used when the scattering operator exists. The most obvious formulation is to prescribe $\Phi(0)$ is the N representation and to obtain $\Phi(t)$ also in the N representation. For this purpose we can use the canonical transformation of reference 1. If, then, we have

$$\Phi(0) \underset{N}{\leftrightarrow} \{\Psi_n(s)_n\},$$

where the functions $\Psi_n(s)_n$ are prescribed, we have from Eq. (35) of reference 1 and Eqs. (18a) and (19) of the present paper:

$$\Psi_n(s)_n(t) = \sum_{n''} \int \Psi_{n''}(s'')_{n''}(ds'')_{n''} \times \sum_{n'} \int \bar{T}_{n':n}(v')_{n'}:(s)_n T_{n':n''}(v')_{n'}:(s'')_{n''} \times \exp\{-it\sum_{i=1}^{n'} |E(v_i')|\}(dv')_{n'}. \tag{21}$$

A second type of initial value problem is based on the assumption of the validity of the adiabatic theorem for quantized fields. If the theorem were valid, it would state that if we prescribe an arbitrary state Φ in the infinite past as being given in the N representation by

$$\Phi \underset{N}{\leftrightarrow} \{\Psi_n(s)_n\},$$

then at any finite time, i.e., after the electromagnetic field has been switched on infinitely slowly, the solution of the Schrödinger equation $\Phi(t)$ is given in the M representation by

$$\Phi(t) \underset{M}{\leftrightarrow} \{\exp[-it\sum_{i=1}^{n}|E(v_i)|]\Psi_n(v)_n\},$$

where the functions $\Psi_n(v)_n$ are the same as those used to describe Φ in the N representation.

The validity of the adiabatic theorem for fields has not been discussed very much, though its validity is often implicitly assumed. Friedrichs[9] has proved the validity of the theorem for the case of a neutral meson field coupled to a source.

If we assume the validity of the adiabatic theorem, then we prescribe the state in the infinite past as given above. Then, at any finite time, $\Phi(t)$ is given in the N representation by

$$\Psi_n(s)_n(t)=\sum_{n'}\int T_{n':n}(v)_{n'}:(s)_n\Psi_{n'}(v)_{n'} \times\exp[-it\sum_{i=1}^{m'}|E(v_i)|](dv)_{n'}. \quad (22)$$

The solutions of the Schrödinger equation given by (21) or (22) will be described as belonging to the first and second initial conditions respectively. That is, the first and second initial conditions correspond to the prescription of the state at $t=0$ and $t=-\infty$, respectively.

4. VACUUM EXPECTATION OF VALUES OF OPERATORS

We shall restrict ourselves to the case in which we have a vacuum initially. That is, in (21) or (22) (corresponding to the first or second initial conditions) we shall set

$$\Psi_0=1, \qquad \Psi_n(s)_n=0 \quad \text{for} \quad n\neq 0. \quad (23)$$

We shall then indicate the results for the expectation values for various operators to the second order in electron charge e when $t\to\infty$. Such a calculation simulates the results one would obtain if a scattering operator existed. At finite time t, we have for the expectation value of N using the first initial condition

$$\langle N\rangle_t=-4e^2\int\int|u_{-+}^{(1)}(s;s')|^2 \times[\cos t(|E(s)|+|E(s')|)-1]dsds'. \quad (24)$$

If the interaction potentials are sufficiently smooth, the oscillatory term will vanish by the Riemann-Lebesgue theorem as $t\to\infty$. Hence, for $t=\infty$ the expectation value is given by

$$\langle N\rangle_\infty=4e^2\int\int|u_{-+}^{(1)}(s;s')|^2dsds'. \quad (25)$$

Using the second boundary condition, we have for any time t,

$$\langle N\rangle_t=2e^2\int\int|u_{-+}^{(1)}(s;s')|^2dsds'. \quad (26)$$

Since this expression is independent of the time, it will also hold when $t=\infty$. It is to be noted that the expectation value obtained using the second initial condition is just one-half that obtained using the first initial condition. Such factors also occur in a similar calculation of Friedrichs in his treatment of the neutral meson field.[9] This factor of one-half presumably occurs in many problems in field theory.

It is to be further noted that the expressions for $\langle N\rangle_\infty$ is within a factor just that for $T_{0:0}^{(2)}$, which to the second order is the only matrix element of the transformation that might not be finite. Hence if $\langle N\rangle_\infty$ is finite, the canonical transformation will exist to the second order.

For the unperturbed Hamiltonian $\mathfrak{H}^{(0)}$ corresponding to the kinetic energy of the electron-positron field one obtains, using the first initial condition, the result

$$\langle\mathfrak{H}^{(0)}\rangle_\infty=2e^2\int\int|u_{-+}^{(1)}(s;s')|^2 \times[|E(s)|+|E(s')|]dsds'. \quad (27)$$

Using the second initial condition, one obtains just one-half of the above result.

The expectation value of the charge density operator, using *either* initial condition is given by

$$\langle\rho(X)\rangle_\infty=2e^2R\sum_\mu\int\int u_{-+}^{(1)}(s;s')\chi^{(0)}(X,\mu;s) \times\bar{\chi}^{(0)}(X,\mu;s')dsds', \quad (28)$$

where R stands for the real part of what follows.

For the current density one obtains

$$\langle j_i(X)\rangle_\infty=2e^2R\sum_\mu\int u_{-+}^{(1)}(s;s') \times\chi^{(0)}(X,\mu;s)\bar{\alpha}^i\bar{\chi}^{(0)}(X,\mu;s')dsds'. \quad (29)$$

[9] K. O. Friedrichs, reference 3, Part III.

5. EXPRESSIONS FOR THE EXPECTATION VALUES

We shall use the expressions for $u^{(1)}$ and $\chi^{(0)}$ to obtain the expectation values as ordinary integrals instead of the symbolic integrals used above.

From Eqs. (32), (31), and (30) of reference 1 we find

$$u_{-+}^{(1)}(s;s')=-[|E(s)|+|E(s')|]^{-1}\times\sum_{\mu}\int\bar{\chi}^{(0)}(X,\mu;s)[\sum_{i}\alpha_i{}^{\mu}A_i(X)+\phi(X)]\chi^{(0)}(X,\mu;s')dX\cdot\delta_{\epsilon,-}\delta_{\epsilon',+}. \quad (30)$$

We shall first calculate $\langle\rho(X)\rangle_{\infty}$. Since it can be shown that the vector potential contributes nothing, let us assume $A_i(X)=0$. Substituting into (28) we have

$$\langle\rho(X)\rangle_{\infty}=-2e^2R\int dX'\phi(X')\sum_{\mu}\sum_{\mu'}\times\iint\frac{dsds'}{[|E(s)|+|E(s')|]}\bar{\chi}^{(0)}(X',\mu';s)\times\chi^{(0)}(X',\mu';s')\chi^{(0)}(X,\mu;s)\times\bar{\chi}^{(0)}(X,\mu;s')\delta_{\epsilon,-}\delta_{\epsilon',+}. \quad (31)$$

To simplify this expression we shall use some properties of the single-particle eigenfunctions $\chi^{(0)}$. First of all, we now explicitly use the fact that the variable s consists of the triple set of eigenvalues consisting of the momentum vector P, the sign of the energy ϵ, and spin component in the direction of the momentum τ. Integrals over s are to be replaced by summations and integrations as follows:

$$\int ds=\sum_{\tau}\sum_{\epsilon}\int dP,$$

where dP is integration over the vector space P. Furthermore, we note

$$E(s)=\epsilon(m^2+P^2)^{\frac{1}{2}}=\epsilon\omega(P), \quad (32)$$

where

$$\omega(P)=(m^2+P^2)^{\frac{1}{2}}. \quad (32a)$$

We use

$$|E(s)|=(m^2+P^2)^{\frac{1}{2}}=\omega(P). \quad (32b)$$

Hence, $|E(s)|$ depends only on the vector P.

The eigenfunctions $\chi^{(0)}(X,\mu;s)$ can be written

$$\chi^{(0)}(X,\mu;s)\equiv\chi^{(0)}(X,\mu;P,\tau,\epsilon)=\chi^{(0)}(\mu;P,\tau,\epsilon)e^{iP\cdot X}/(2\pi)^{\frac{1}{2}}, \quad (33)$$

where $P\cdot X$ is the inner product of the vectors P and X. The coefficients $\chi^{(0)}(\mu;P,\tau,\epsilon)$ are independent of X. These are the usual "spinor coefficients" of the plane wave.

Equation (31) becomes

$$\langle\rho(X)\rangle_0=-\frac{2e^2R}{(2\pi)^6}\int dX'\phi(X')\times\iint\frac{dPdP'}{[\omega(P)+\omega(P')]}e^{i(P-P')\cdot(X-X')}\times\sum_{\tau}\sum_{\tau'}\sum_{\mu}\sum_{\mu'}[\bar{\chi}^{(0)}(\mu';P,\tau,-)\chi^{(0)}(\mu;P,\tau,-)\times\chi^{(0)}(\mu';P',\tau',+)\bar{\chi}^{(0)}(\mu;P',\tau',+)]. \quad (34)$$

It can be shown that spinor coefficients satisfy the following identity

$$\sum_{\tau}\bar{\chi}^{(0)}(\mu;P,\tau,\epsilon)\chi^{(0)}(\mu',P,\tau,\epsilon)=\frac{1}{2\epsilon\omega(P)}[\epsilon\omega(P)\delta(\mu',\mu)-\sum_{j=1}^{3}P_j\alpha_j{}^{\mu}(\mu',\mu)-m\beta^{\mu}(\mu',\mu)]. \quad (35)$$

In Eq. (35), $P_j(j=1,2,3)$ are the Cartesian components of the momentum P. The quantities $\alpha_i{}^{\mu}(\mu,\mu')$ and $\beta^{\mu}(\mu,\mu')$ are the elements of the usual Dirac matrices.

After substituting Eq. (35) into (34), we get traces of products of the matrices $\alpha_i{}^{\mu}$ and β^{μ}. Using the well-known values of the traces of products of the Dirac operators such as $\mathrm{tr}\alpha_i=0$, $\mathrm{tr}\alpha_i{}^2=4$, etc., we obtain the result.

$$\langle\rho(X)\rangle_0=\frac{2e^4R}{(2\pi)^{9/2}}\iint dPdP'\times\frac{[-\omega(P)\omega(P')+P\cdot P'+m^2]}{\omega(P)\omega(P')[\omega(P)+\omega(P')]}\times e^{-i(P'-P)\cdot X}\phi^F(P'-P), \quad (36)$$

where $\phi^F(P)$ is the Fourier transform of $\phi(X)$, the electrostatic potential.

$$\phi^F(P)=\frac{1}{(2\pi)^{\frac{1}{2}}}\int e^{iP\cdot X}\phi(X)dX. \quad (37)$$

It should be noted that the integrand is almost an invariant in four-dimensional space. It is convenient to introduce new variables in the integrand, namely the vector $P_1=P'-P$ and the vector P.

Then we have

$$\langle\rho(X)\rangle_{\infty}=\frac{2eR}{(2\pi)^{9/2}}\iint dP_1dP\times\frac{[-\omega(P)\omega(P+P_1)+\omega^2(P)+P_1\cdot P]}{\omega(P)\omega(P+P_1)[\omega(P)+\omega(P+P_1)]}\times e^{-iP_1\cdot X}\phi^F(P_1). \quad (36a)$$

The result (36a) can be shown to be the same as the usual one, for if one expands $[-\omega(P)\omega(P+P_1)+\omega(P)+P_1\cdot P]/\{\omega(P+P_1)[\omega(P)+\omega(P+P_1)]\}$ in a series about $P_1=0$, one can evaluate the integral as a series, each nonvanishing term of which, (aside from the first nonvanishing term) corresponds to a term of the series obtained by Schwinger [Eq. (2.47), reference 2] for the time independent external charge. The first term of the series obtained from (36a) is the usual logarithmically-divergent charge renormalization. Hence, $\langle\rho(X)\rangle_\infty$ as obtained above is the usual result for polarization of the vacuum.

If the vector potential $A_i(X)$ is not identically zero, one similarly obtains the usual result for $\langle j_i(X)\rangle_\infty$.

For the expectation value of $\langle N\rangle_\infty$ using, say, the first initial condition (the second initial condition differs only by a factor one-half) one finds in a manner similar to that for $\langle\rho(X)\rangle_\infty$, when the vector potential $A_i\equiv 0$, the following result:

$$\langle N\rangle_\infty=-4e^2\int\int dPdP_1 \times\frac{|\phi(P_1)|^2[-\omega(P)\omega(P+P_1)+\omega^2(P)+P_1\cdot P]}{\omega(P)\omega(P+P_1)[\omega(P+P_1)+\omega(P)]^2}. \quad (38)$$

As in the case of the integral for $\langle\rho(X)\rangle_\infty$, one may evaluate the integral by expanding $[-\omega(P)\omega(P+P_1)+\omega^2(P)+P\cdot P_1]/\{\omega(P+P_1)[\omega(P)+\omega(P+P_1)]^2\}$ as a power series in P_1. In contrast to the case of the integral for $\langle\rho(X)\rangle_\infty$, the first, as well as all other, nonvanishing terms arising after the integrations are finite for suitable electrostatic potentials $\phi(X)$. Hence $\langle N\rangle_\infty$ is finite to the second order. From this result Friedrichs (reference 3) concludes $\langle N\rangle_\infty$ is finite and the canonical transformation exists to all orders. This result is true despite the fact that $\langle\mathcal{H}\rangle_\infty$ is infinite.

If the vector potential $A_i(X)$ is not identically zero, one obtains for $\langle N\rangle_\infty$ in addition to the term on the right-hand side of (38) the terms

$$4e^2\sum_{j=1}^{3}\int\int \times\frac{dPdP_1|A_j^F(P_1)|^2[+\omega(P)\omega(P+P_1)+\omega^2(P)+P_1\cdot P]}{\omega(P)\omega(P+P_1)[\omega(P)+\omega(P+P_1)]^2},$$

where $A_j^F(P_1)$ is the Fourier transform of $A_j(X)$. In obtaining these terms we have used Lorentz condition $\mathrm{div}A_i(X)=0$. Otherwise the derivation is similar to that used to obtain Eq. (38). On expanding $[+\omega(P)\omega(P+P_1)+\omega^2(P)+P_1\cdot P]/\{\omega(P+P_1)[\omega(P)+\omega(P+P_1)]^2\}$ in a power series in P_1 and integrating with respect to P, one obtains a divergent term for any nonzero functions $A_i(P_1)$. Hence, when the vector potential is not zero, $\langle N\rangle_\infty$ is infinite unless one uses a renormalization procedure.

Since the number operator N is invariant under a Lorentz transformation, we can generalize our result and say that for a class of time-dependent potentials $\phi(X,t)$, $A_i(X,t)$ which can be transformed by a Lorentz transformation to a suitable electrostatic potential, the expectation value $\langle N\rangle$ is finite, even though the expectation values of other operators may be infinite.

The Equations of Motion of Charged Test Particles in General Relativity

D. M. CHASE*
Princeton University, Princeton, New Jersey, and Naval Research Laboratory, Washington, D. C.
(Received November 27, 1953)

The Lorentz equations of motion without radiation damping are derived for charged test particles from the field equations, $R_{\mu\nu}-\frac{1}{2}g_{\mu\nu}R=T_{\mu\nu}$, of ordinary general relativity. No restriction is placed on the strength of the background gravitational and electromagnetic fields.

1. INTRODUCTION

THE recent attempts of Einstein to formulate a satisfactory unified field theory appear to have been thus far unsuccessful in that the equations of motion for charged particles as derived from his new unified field equations by the quasistatic approximation procedure[1] are incompatible with the Lorentz equations of motion and, in fact, up to the Newtonian gravitational approximation are independent of the electromagnetic field.[2] The particle moves as if uncharged, however much charge is loaded on it. This apparent failure of the current unified field theory in respect of the equations of motion regenerates some interest in the problem of the derivation of equations of motion in the standard theory, in which the electromagnetic field is introduced *a posteriori* by means of an energy-momentum tensor. Moreover, it is quite reasonable to expect that even a unified theory will contain equations which, to a suitable approximation, can be written in the form $\bar{G}_{\mu\nu}\equiv\bar{R}_{\mu\nu}-\frac{1}{2}\bar{g}_{\mu\nu}\bar{R}=\bar{T}_{\mu\nu}$, where $\bar{R}_{\mu\nu}$ is a curvature tensor formed in the usual way from the part $\bar{g}_{\mu\nu}$ of the metric field which characterizes the gravitational field alone and $\bar{T}_{\mu\nu}$ is the ordinary energy tensor of the electromagnetic field formed from field quantities which satisfy Maxwell's equations.[3] In such a theory the derivation of equations of motion would proceed precisely as in the standard theory and, in the given approximation, would lead to the same result

The problem of the derivation of the equations of motion of charged particles from the field equations of the standard theory has been previously investigated chiefly by Weyl,[4] Einstein,[5] and Infeld and Wallace.[6] The latter authors, using an adaptation of the new approximation method and neglecting nonlinear gravitational terms in $R_{\mu\nu}$ and gravitational-electromagnetic interaction terms in $T_{\mu\nu}$, were able to derive the Lorentz equations of motion with or without radiation damping terms according as the retarded or the symmetric solution was taken for the electromagnetic field. It would be desirable to derive the equations of motion *without any restriction upon the strength of the gravitational field.*[7] Such a derivation is to be given here by extending to charged test particles a method used by Infeld and Schild[8] to derive the geodesic motion of uncharged test particles.

2. CONCEPTUAL STRUCTURE

A charged particle is represented by a world line along which the metric field $g_{\mu\nu}$ is singular. We consider a sequence of particles with masses and charges tending to zero and the corresponding sequence of gravitational and electromagnetic fields. More precisely, following IS, we envisage a sequence of Riemannian 4-spaces $R_{(N)}$ $(N=1, 2, \cdots \infty)$ with coordinates x^ρ, with a world line $L_{(N)}$ in each given by

$$x^\rho=\xi^\rho(u), \tag{2.1}$$

and with a metric tensor $g_{\mu\nu}(x^\rho,e_N,m_N)$ which depends on two parameters, e_N and m_N, which in turn are to be specified functions of N and represent, respectively, the electric charge and the mass of the particle whose world line is $L_{(N)}$. Along $L_{(N)}$, $g_{\mu\nu}(x^\rho,e_N,m_N)$ has a singularity of the type representing a charged particle. In addition, in each $R_{(N)}$ is defined an electromagnetic field tensor $F^\mu{}_\nu(x^\rho,e_N)$ which along $L_{(N)}$ has a singularity of the type representing an electric monopole. For a test particle we must take $\lim_{N\to\infty}e_N=0$, $\lim_{N\to\infty}m_N=0$; then the background gravitational and external electromagnetic fields are

$$\lim_{N\to\infty} g_{\mu\nu}(x^\rho,e_N,m_N)=g_{\mu\nu}(x^\rho,0,0)\equiv g_{(0)\mu\nu}(x^\rho),$$

$$\lim_{N\to\infty} F^\mu{}_\nu(x^\rho,e_N)=F^\mu{}_\nu(x^\rho,0)\equiv F_{(e)}{}^\mu{}_\nu(x^\rho),$$

respectively. The world line of the test particle, which we wish to determine in terms of these *background* fields, is given by $\lim_{N\to\infty}L_{(N)}\equiv L_{(0)}$.

It is necessary to make some assumption concerning

* National Science Foundation Predoctoral Fellow.

[1] Einstein, Infeld, and Hoffmann, Ann. Math. **39**, 65 (1938); A. Einstein and L. Infeld, Ann. Math. **41**, 797 (1940); A. Einstein and L. Infeld, Can. J. Math. **1**, 209 (1949).

[2] L. Infeld, Acta Phys. Polon. **10**, 284 (1950); J. Callaway, Phys. Rev. **92**, 1567 (1953).

[3] A. Papapetrou, Proc. Roy. Irish Acad. **A52**, 69 (1948); B. Kursunoğlu, Phys. Rev. **88**, 1369 (1952) and **89**, 522 (1953).

[4] H. Weyl, *Raum, Zeit, Materie* (Julius Springer, Berlin, 1923), Sec. 38.

[5] A. Einstein, Sitzber. preuss. Akad. Wiss., Physik-math. Kl. 235 (1927).

[6] L. Infeld and P. R. Wallace, Phys. Rev. **57**, 797 (1940).

[7] In the case of application to a unified theory as described in the foregoing, however, such a derivation offers no special advantage, since reduction of the field equations to the form $\bar{G}_{\mu\nu}=\bar{T}_{\mu\nu}$ presumably would already require a restriction to weak gravitational fields.

[8] L. Infeld and A. Schild, Revs. Modern Phys. **21**, 408 (1949); hereafter referred to as IS.

the manner in which e and m tend to zero. Apart from electromagnetic radiation damping terms, e and m appear in the Lorentz equations of motion only through their ratio e/m. Consequently, it is clear that the only physically reasonable assumption is to take e_N/m_N equal to a nonvanishing constant, independent of N:[9]

$$e_N/m_N=k. \tag{2.2}$$

We may then take $m_N=1/N$ and proceed.

3. THE FIELD EQUATIONS

With the aid of (2.2) the metric field can be expanded in the form

$$g_{\mu\nu}(x^\rho,m)=g_{(0)\mu\nu}(x^\rho)+mb_{\mu\nu}(x^\rho)+m^2c_{\mu\nu}(x^\rho)+\cdots, \tag{3.1}$$

exactly as in the case of an uncharged particle.[8] The same considerations obtain with regard to the orders of $b_{\mu\nu}$, $c_{\mu\nu}$, etc. We note that the Schwarzschild metric modified for a charged particle contains e and m only in the quantity $1-(2m/r)+(e^2/r^2)$ and, since $e=km$, is therefore developable in powers of m/r, thus satisfying the conditions necessary for the application of our method.[10]

We now choose a coordinate system[11] such that, at all points of L,

$$g_{(0)\mu\nu}=\eta_{\mu\nu};\quad g_{(0)\mu\nu,\rho}=0, \tag{3.2}$$

where a comma denotes partial differentiation and

$$\eta_{00}=-\eta_{11}=-\eta_{22}=-\eta_{33}=1,\quad \eta_{\mu\nu}=0\quad(\mu\neq\nu). \tag{3.3}$$

Taking $x^0=t$ as the parameter along L, we may write (2.1) as

$$x^r=\xi^r(t). \tag{3.4}$$

Latin suffixes range over 1, 2, 3, and Greek suffixes over 0, 1, 2, 3. By means of a Lorentz transformation we can, for any assigned point Q of L, make

$$(\xi^{r\prime})_Q=0, \tag{3.5}$$

where the prime denotes differentiation with respect to t. Setting

$$z^r=x^r-\xi^r,\quad r=(z^rz^r)^{\frac{1}{2}}, \tag{3.6}$$

we say that a function $f(z^r)$ is at least of order n if $r^{-n}f(z^r)$ is bounded as $z^r\to 0$. From (3.2) it then follows that

$$g_{(0)\mu\nu}=\eta_{\mu\nu}+a_{\mu\nu}, \tag{3.7}$$

where $a_{\mu\nu}$ is of order 2.

[9] Actually, it suffices to assume that e is representable as

$$e_N=\sum_{p=1}^{\infty}a_pm_N^p,$$

$a_1\neq 0$, so that $\lim_{N\to\infty}(e_N/m_N)=\lim_{m_N\to 0}(e_N/m_N)=a_1\equiv k$.

[10] See reference 6, Sec. 2.

[11] E. Fermi, Rend. accad. nazl. Lincei **21**, 21 and 51 (1922); T. Levi-Civita, Math. Ann. **97**, 291 (1927).

The Einstein-Maxwell field equations are

$$G_{\mu\nu}\equiv R_{\mu\nu}-\tfrac{1}{2}g_{\mu\nu}R=T_{\mu\nu}, \tag{3.8}$$

$$F_{\lambda\mu,\nu}+F_{\mu\nu,\lambda}+F_{\nu\lambda,\mu}=0, \tag{3.9}$$

$$F_{\mu}{}^{\nu}{}_{;\nu}=0, \tag{3.10}$$

where

$$T_{\mu\alpha}=F_{\mu\alpha}F_{\nu}{}^{\alpha}-\tfrac{1}{4}g_{\mu\nu}F_{\alpha\beta}F^{\alpha\beta}, \tag{3.11}$$

and the semicolon denotes covariant differentiation.[12] Substituting

$$g_{\mu\nu}=\eta_{\mu\nu}+a_{\mu\nu}+mb_{\mu\nu}+m^2c_{\mu\nu}+\cdots \tag{3.12}$$

into $G_{\mu\nu}$, we find

$$G_{\mu\nu}=A_{\mu\nu}+mB_{\mu\nu}+m^2C_{\mu\nu}+\cdots, \tag{3.13}$$

where $A_{\mu\nu}$ is the Einstein tensor of the background field $\eta_{\mu\nu}+a_{\mu\nu}$, $B_{\mu\nu}$ is linear in $b_{\mu\nu}$, etc. We express $T_{\mu\nu}$ in terms of the mixed components $F^{\alpha}{}_{\beta}$ only by writing

$$T_{\mu\nu}=g_{\mu\beta}F^{\beta}{}_{\alpha}F_{\nu}{}^{\alpha}-\tfrac{1}{4}g_{\mu\nu}g_{\alpha\gamma}g^{\beta\delta}F^{\gamma}{}_{\delta}F^{\alpha}{}_{\beta}. \tag{3.14}$$

Substituting into (3.14) from (3.1) and separating the different powers of m, we obtain

$$T_{\mu\nu}=T_{(0)\mu\nu}+mT_{(1)\mu\nu}+m^2T_{(2)\mu\nu}+\cdots, \tag{3.15}$$

where

$$T_{(0)\mu\nu}=g_{(0)\mu\beta}F^{\beta}{}_{\alpha}F_{\nu}{}^{\alpha}-\tfrac{1}{4}g_{(0)\mu\nu}g_{(0)\alpha\gamma}g_{(0)}{}^{\beta\delta}F^{\gamma}{}_{\delta}F^{\alpha}{}_{\beta}, \tag{3.16}$$

and $T_{(1)\mu\nu}$ is linear in the $b_{\mu\nu}$ and quadratic in the $F^{\mu}{}_{\nu}$ with coefficients formed of the $g_{(0)\mu\nu}$. The electromagnetic field tensor $F^{\alpha}{}_{\beta}$ can be written as

$$F^{\alpha}{}_{\beta}=F_{(p)}{}^{\alpha}{}_{\beta}+F_{(e)}{}^{\alpha}{}_{\beta}, \tag{3.17}$$

where $F_{(p)}{}^{\alpha}{}_{\beta}$, the field due to the particle, is proportional to the charge e, and $F_{(e)}{}^{\alpha}{}_{\beta}$, the external field, is independent of e. Accordingly, each of the coefficients $T_{(n)\mu\nu}$ in (3.15), being quadratic in $F^{\alpha}{}_{\beta}$, can be written as

$$T_{(n)\mu\nu}=T_{(n)}{}^{(0)}{}_{\mu\nu}+eT_{(n)}{}^{(1)}{}_{\mu\nu}+e^2T_{(n)}{}^{(2)}{}_{\mu\nu}, \tag{3.18}$$

where the three terms contain products of the form $F_{(e)}F_{(e)}$, $F_{(e)}F_{(p)}$, and $F_{(p)}F_{(p)}$, respectively, and the $T_{(n)}{}^{(i)}{}_{\mu\nu}$ $(i=0,\ 1,\ 2)$ are independent of e and m.

We assume that the background fields satisfy the field equations; then

$$A_{\mu\nu}=T_{(0)}{}^{(0)}{}_{\mu\nu}. \tag{3.19}$$

In virtue of (3.15), (3.18), (3.19), and (2.3), Eqs. (3.8) become

$$mB_{\mu\nu}+m^2C_{\mu\nu}+\cdots-m(T_{(1)}{}^{(0)}{}_{\mu\nu}+kT_{(0)}{}^{(1)}{}_{\mu\nu})$$
$$-m^2(T_{(2)}{}^{(0)}{}_{\mu\nu}+kT_{(1)}{}^{(1)}{}_{\mu\nu}+k^2T_{(0)}{}^{(2)}{}_{\mu\nu})-\cdots=0. \tag{3.20}$$

Since we are concerned with conditions in the limit as $m\to 0$, we ignore all powers of m higher than the first. The field equations then reduce to

$$B_{\mu\nu}=T_{(1)}{}^{(0)}{}_{\mu\nu}+kT_{(0)}{}^{(1)}{}_{\mu\nu}. \tag{3.21}$$

[12] We employ for electromagnetic quantities Gaussian units, and for mass and length such units that G, the Newtonian gravitational constant, $=1/2$ and $c=1$. The $T_{\mu\nu}$ defined here is 4π times the usual one.

Following IS, we introduce $\beta_{\mu\nu}$ and $\bar{\beta}_{\mu\nu}$ by the relations

$$b_{\mu\nu}=\beta_{\mu\nu}-\tfrac{1}{2}\eta_{\mu\nu}\eta^{\rho\sigma}\beta_{\rho\sigma},$$
$$\beta_{\mu\nu}=\bar{\beta}_{\mu\nu}+b_{\mu,\nu}+b_{\nu,\mu}-\eta_{\mu\nu}\eta^{\rho\sigma}b_{\rho,\sigma},$$

with b_μ a solution of

$$\eta^{\rho\sigma}b_{\mu,\rho\sigma}=\eta^{\rho\sigma}\beta_{\mu\rho,\sigma}.$$

From the observations at the beginning of this section and from Sec. 2 of IS it follows that the $b_{\mu\nu}$ and hence the $\bar{\beta}_{\mu\nu}$ are of order -1 in r. By introducing the above substitutions into the explicit expression for $B_{\mu\nu}$, it can be shown[8] that to terms of order -3 and -2 (but no higher) in r,

$$B_{\mu\nu}=\tfrac{1}{2}\eta^{\rho\sigma}\bar{\beta}_{\mu\nu,\rho\sigma}, \tag{3.22}$$

provided that $\bar{\beta}_{\mu\nu}$ is a solution of

$$\eta^{\rho\sigma}\bar{\beta}_{\mu\rho,\sigma}=0. \tag{3.23}$$

By (3.21), the field equations become

$$\eta^{\rho\sigma}\bar{\beta}_{\mu\nu,\rho\sigma}=-2\Lambda_{\mu\nu} \tag{3.24}$$

together with (3.23), where we have put

$$\Lambda_{\mu\nu}=-T_{(1)}{}^{(0)}{}_{\mu\nu}-kT_{(0)}{}^{(1)}{}_{\mu\nu}. \tag{3.25}$$

Hereafter, we omit the bar from $\bar{\beta}_{\mu\nu}$.

Denoting with a prime partial differentiation with respect to t at constant z^r, we have

$$f_{,r}=\frac{\partial f}{\partial x^r}=\frac{\partial f}{\partial z^r},\quad f_{,0}=f'-f_{,r}\xi^{r\prime}.$$

In consequence, (3.24) can be written

$$\beta_{\mu\nu,mm}+\beta_{\mu\nu,r}\xi^{r\prime\prime}-\beta_{\mu\nu}{}''+2\beta_{\mu\nu,r}{}'\xi^{r\prime}$$
$$-\beta_{\mu\nu,rs}\xi^{r\prime}\xi^{s\prime}=2\Lambda_{\mu\nu}. \tag{3.26}$$

We put

$$\beta_{\mu\nu}=\beta_{-1\mu\nu}+\beta_{0\mu\nu}+\beta_{1\mu\nu}+\cdots, \tag{3.27}$$

where $\beta_{-n\mu\nu}$ is the part of $\beta_{\mu\nu}$ which varies as r^{-n}. This convention will be used for other quantities as well. Note that every differentiation with respect to a z^r lowers the order by one; thus $\beta_{-1\mu\nu,\,r-1}$ and $\beta_{0\mu\nu,mm-2}$ are of order -2. Substituting (3.27) into (3.26) and equating to zero expressions of order -3 in r and those of order -2 in r, as in IS, we obtain, on choosing any particular point Q on the world line L and introducing a coordinate system such that $(\xi^{r\prime})_Q=0$,

$$\beta_{-1\mu\nu,mm-2}=2\Lambda_{-3\mu\nu}, \tag{3.28}$$

$$\beta_{0\mu\nu,mm-2}+\beta_{-1\mu\nu,r-1}\xi^{r\prime\prime}=2\Lambda_{-2\mu\nu}, \tag{3.29}$$

in the spatial section $t=t_Q$. Proceeding similarly with (3.23) and its time derivative at constant z^r, we obtain

$$\beta_{-1\mu m,m-1}=0, \tag{3.30}$$

$$\beta_{0\mu m,m-1}-\beta_{-1\mu 0}{}'=0, \tag{3.31}$$

$$\beta_{-1\mu m,m-1}{}'+\beta_{-1\mu 0,r-1}\xi^{r\prime\prime}=0. \tag{3.32}$$

Since $b_{\mu\nu}$ is of order -1 in r and $F_{(s)}{}^{\alpha}{}_{\beta}$ of order 0, in view of the statement following (3.16) $T_{(1)}{}^{(0)}{}_{\mu\nu}$ is of order -1; hence, from (3.25),

$$\Lambda_{-n\mu\nu}=-kT_{(0)}{}^{(1)}{}_{-n\mu\nu}\quad\text{for } n\geq 2, \tag{3.33}$$

and $T_{(1)}{}^{(0)}{}_{\mu\nu}$ does not enter the field equations (3.28) and (3.29). Furthermore, since $F_{(p)}{}^{\alpha}{}_{\beta}$ will be found to contain no terms of lower order than -2, we see from (3.7) and (3.16) that terms in $T_{(0)}{}^{(1)}{}_{\mu\nu}$ which contain $a_{\mu\nu}$ are at least of order 0 so that the relevant part of $T_{(0)\mu\nu}$ is given by

$$T_{(0)mn}=F^m{}_sF^s{}_n+F^m{}_0F^0{}_n-\tfrac{1}{2}\delta_{mn}F^s{}_0F^s{}_0+\tfrac{1}{4}\delta_{mn}F^s{}_rF^s{}_r,$$
$$T_{(0)0n}=-F^s{}_0F^s{}_n, \tag{3.34}$$
$$T_{(0)00}=-\tfrac{1}{2}(F^s{}_0F^s{}_0+\tfrac{1}{2}F^r{}_sF^r{}_s).$$

We now show that it is sufficient to take for the electromagnetic field of the particle the monopolar solution of Maxwell's equations in flat space. The covariant equations are

$$F_{\mu}{}^{\nu}{}_{,\nu}=g^{\nu\beta}(F_{\mu\beta,\nu}-\Gamma^{\alpha}{}_{\beta\nu}F_{\mu\alpha}-\Gamma^{\alpha}{}_{\mu\nu}F_{\alpha\beta})=0. \tag{3.35}$$

Inserting (3.12), we can write these schematically as

$$\eta^{\nu\beta}F_{\mu\beta,\nu}+a,F+a,F+O(-p+2)+O(m)=0, \tag{3.36}$$

where aF, denotes terms bilinear in $a_{\mu\nu}$ and partial derivatives of $F_{\mu\nu}$, a,F denotes terms bilinear in $F_{\mu\nu}$ and partial derivatives of $a_{\mu\nu}$, $O(-p+2)$ denotes terms of order $-p+2$ in r, where p is the order of $F_{\mu\nu}$, and $O(m)$ denotes terms which are products of $F_{\mu\nu}$ or its derivatives with positive powers of m and which may be neglected since $F_{\mu\nu}$ of the particle is itself proportional to e and hence to m. The first three sets of terms in (3.36) are, respectively, of orders $-p-1$, $-p+1$, $-p+1$. Therefore, to the lowest two orders in r, (3.36) are Maxwell's equations in a flat space:

$$\eta^{\nu\beta}F_{\mu\beta,\nu}=0. \tag{3.37}$$

It follows that the solutions for flat space are correct to the two lowest orders in r, i.e., to orders -2 and -1 for the monopolar solution. Accordingly, since we need the particle field, $F_{(p)\alpha\beta}=\gamma_{\alpha,\beta}-\gamma_{\beta,\alpha}$, correct only to order -2 in r, we may take

$$\gamma^0=e\sum_{l=1}^{\infty}\frac{1}{(2l-2)!}\frac{d^{2l-2}}{dt^{2l-2}}(r^{2l-3})$$
$$-e\sum_{l=1}^{\infty}\frac{1}{(2l-1)!}\frac{d^{2l-1}}{dt^{2l-1}}(r^{2l-2}),$$
$$\gamma^m=-e\sum_{l=1}^{\infty}\frac{1}{(2l-2)!}\frac{d^{2l-2}}{dt^{2l-2}}(r^{2l-3}\xi^{m\prime}) \tag{3.38}$$
$$+e\sum_{l=1}^{\infty}\frac{1}{(2l-1)!}\frac{d^{2l-1}}{dt^{2l-1}}(r^{2l-2}\xi^{m\prime}),$$

which satisfy (3.37).[8,12] The only term of (3.38) yielding a nonvanishing contribution to $F_{(p)}{}_{-2}{}^{\alpha}{}_{\beta}$ is

$$\gamma_{-1}{}^{0}=e/r. \tag{3.39}$$

From (3.18), (3.24), and (3.39) we obtain

$$T_{(0)}{}^{(1)}{}_{-3\mu\nu}=0, \tag{3.40}$$

$$\left.\begin{aligned} T_{(0)}{}^{(1)}{}_{-2mn}&=-(z^m/r^3)F_{(e)}{}^{n}{}_{0}-(z^n/r^3)F_{(e)}{}^{m}{}_{0}\\ &\quad+\delta_{mn}(z^s/r^3)F_{(e)}{}^{s}{}_{0},\\ T_{(0)}{}^{(1)}{}_{-20n}&=(z^s/r^3)F_{(e)}{}^{s}{}_{n},\\ T_{(0)}{}^{(1)}{}_{-200}&=(z^s/r^3)F_{(e)}{}^{s}{}_{0}. \end{aligned}\right\} \tag{3.41}$$

4. THE EQUATIONS OF MOTION

From (3.28), (3.33), and (3.40) we deduce

$$\beta_{-1\mu\nu}=p_{\mu\nu}/r, \tag{4.1}$$

where the $p_{\mu\nu}$ are constants. Now, from (3.30),

$$p_{\mu m}=0, \quad \beta_{-1\mu m}=0. \tag{4.2}$$

Hence, from (3.29) and (3.33),

$$\beta_{0\mu m,nn_{-2}}=-2kT_{(0)}{}^{(1)}{}_{-2\mu m}. \tag{4.3}$$

Setting $\mu=0$ in (3.32) and using (3.31) and (4.1), we find

$$\beta_{0mn,mn_{-2}}-(p_{00}/r^3)z^s\xi^{s\prime\prime}=0. \tag{4.4}$$

We proceed to evaluate $\beta_{0mn,mn_{-2}}$. From (3.41) and (4.3),

$$\begin{aligned}\beta_{0mn,ss_{-2}}=-2k[&(1/r)_{,m}F^{n}{}_{0}+(1/r)_{,n}F^{m}{}_{0}\\ &-\delta_{mn}(1/r)_{,s}F^{s}{}_{0}],\end{aligned} \tag{4.5}$$

where we omit the label (e) from $F_{(e)}{}^{\alpha}{}_{\beta}$. Equations (4.5) are correct to order -2 in r. Therefore, if we expand $F^{n}{}_{0}(x^r)$ in a power series,

$$F^{n}{}_{0}(x^r)=F^{n}{}_{0}(\xi^r)+z^s\left[\frac{\partial}{\partial x^s}F^{n}{}_{0}(x^r)\right]_{x^r=\xi^r}+\cdots,$$

we need retain only the first term for insertion into (4.5). We then obtain for the most general solution of (4.5)

$$\begin{aligned}\beta_{0mn}(x^r)=-k[&r_{,m}F^{n}{}_{0}(\xi^r)+r_{,n}F^{m}{}_{0}(\xi^r)\\ &-\delta_{mn}r_{,s}F^{s}{}_{0}(\xi^r)+\psi_{mn}(x^r)],\end{aligned} \tag{4.6}$$

where $\psi_{mn,ss}=0$. From (4.6) we find

$$\beta_{0mn,mn_{-2}}=k[2(z^s/r^3)F^{s}{}_{0}(\xi^r)-\psi_{mn,mn}]. \tag{4.7}$$

By hypothesis on β_{0mn}, ψ_{mn} varies as r^0 and, being a harmonic function, is therefore a constant. Hence,

$$\psi_{mn,mn}=0. \tag{4.8}$$

From (4.4), (4.7), and (4.8), we now have

$$2k(z^s/r^3)F^{s}{}_{0}(\xi^r)-p_{00}(z^s/r^3)\xi^{s\prime\prime}=0,$$

or, since $p_{00}=-2$ by calculation[8,12] and $k=e/m$,

$$(z^s/r^3)[eF^{s}{}_{0}(\xi^r)+m\xi^{s\prime\prime}]=0.$$

But this equation implies

$$m\xi^{s\prime\prime}=-eF^{s}{}_{0}, \tag{4.9}$$

in which $-F^{s}{}_{0}$ is the external field evaluated at the particle. In the particular coordinate system employed, (4.9) are the Lorentz equations of motion without radiation damping. Generalized to an arbitrary coordinate system, (4.9) become

$$mc\left(\frac{d^2\xi^{\alpha}}{ds^2}+\left\{\begin{matrix}\alpha\\ \mu\nu\end{matrix}\right\}\frac{d\xi^{\mu}}{ds}\frac{d\xi^{\nu}}{ds}\right)=-\frac{e}{c}F^{\alpha}{}_{\nu}\frac{d\xi^{\nu}}{ds}, \tag{4.10}$$

where the proper cotime s and Christoffel symbols $\left\{\begin{matrix}\alpha\\ \mu\nu\end{matrix}\right\}$ refer to the background field.

5. CONCLUSION

The present treatment appears to provide a particularly simple derivation of the equations of motion of a charged test particle from the field equations of general relativity. Moreover, an approximation based on the smallness of an intrinsic property of the particle, the mass, seems rather more satisfying than an approximation based on the smallness of the fields to which it is subjected. For an ideal test particle, i.e., one of vanishingly small charge and mass, the present method involves no approximation. Concerning the anatomies of the two approaches, one may say that both linearize the gravitational field in the left-hand side of (3.8) and uncouple the two fields in the right-hand side, but the present treatment does so by assuming a weak test-particle field, the other by assuming a weak external field

The failure of the present method to yield radiation damping could be foreseen from the start, for it is inherent in the mode of calculation, or rather in the problem itself, if the latter concerns an ideal test particle: the radiation damping terms are proportional to $e^2(=k^2m^2)$, whereas by neglecting terms of higher degree in m than the first we obtain only those terms in the equations of motion which are linear in e and m. There appears nothing to prevent our carrying the calculations to the next higher order of approximation, so as to determine the radiation damping.

6. ACKNOWLEDGMENTS

I wish to thank Professor J. A. Wheeler, who suggested this problem, and, for enlightening comment, Dr. A. W. Sáenz, Mr. Joseph Callaway, and Mr. J. R. H. Dempster.

[12] The second summation in each of Eqs. (3.38) represents the difference between the retarded and the symmetric solutions. Its contribution vanishes (see Sec. 5).

Compton Scattering*

W. B. CHESTON
Department of Physics, University of Minnesota, Minneapolis, Minnesota
(Received March 5, 1954)

The canonical transformation of Bloch and Nordsieck is used to examine the infrared divergences present in double Compton scattering and radiative corrections to single Compton scattering.

INTRODUCTION

SCHAFROTH[1] and subsequent authors[2,3] have demonstrated that the infrared catastrophes which exist in double Compton scattering and in the radiative correction to single Compton scattering (to order e^6) cancel each other identically. The divergence in the former case results from real photons and that in the latter from virtual photons. A quasi-philosophical argument based on the inability of a photon detector of finite resolution to distinguish between real and virtual photons of extremely low energy has been suggested.[2] It is the purpose of this note to point out that it is possible to find a canonical transformation which will remove those terms in the interaction Hamiltonian (nonrelativistic) between charged particles and the photon field which cause the individual divergences. The canonical transformation employed is a generalization of that discussed by Block and Nordsieck;[4] this transformation has been used successfully in dipole approximation to discuss such diversified phenomena as, for example, radiative corrections in electron scattering[5] and radiative effects in π-μ decay.[6] It seems reasonable to discuss such low-energy divergences using nonrelativistic theory; the high-energy divergences which result in such a treatment are both expected and unavoidable.

REMOVAL OF THE INFRARED CATASTROPHES

It is well-known that the Bloch-Nordsieck transformation when applied to the nonrelativistic Hamiltonian of nonbound charged particles interacting with a photon field removes all terms linear in *both* (p/m_0c) and e; it produces, as a by-product, a nonrelativistic analog of mass-renormalization of the charged particle.[7] (We adopt the notation, m_0= observable mass of the charged particle.) The proof of the above contention is straightforward and is discussed elsewhere[7] in some detail; it is only sketched below.

The Hamiltonian for the system is chosen to be:

$$H=\frac{p^2}{2m_0}\left(1+\frac{\delta m}{m_0}\right)-\frac{(4\pi e^2)^{\frac{1}{2}}}{m_0c}\left(1+\frac{\delta m}{m_0}\right)\mathbf{p}\cdot\mathbf{A}+\frac{4\pi e^2}{2m_0c^2}\left(1+\frac{\delta m}{m_0}\right)A^2+H_{\rm rad}, \quad (1)$$

where

$$\mathbf{A}=\sum_k \mathbf{A}_k=\sum_k \hat{e}_k\left(\frac{hc}{k\Omega}\right)^{\frac{1}{2}}\{\Pi_k\cos\mathbf{k}\cdot\mathbf{x}+Q_k\sin\mathbf{k}\cdot\mathbf{x}\},$$

$$H_{\rm rad}=\tfrac{1}{2}hc\sum_k k\{\Pi_k^2+Q_k^2\},$$

$$\Pi_k=(2)^{-\frac{1}{2}}(a_k^*+a_k), \quad Q_k=(-2)^{-\frac{1}{2}}(a_k^*-a_k).$$

The quantity $\delta m/m_0$ is the mass renormalization parameter which is proportional, in first approximation, to e^2. [The remaining symbols in Eq. (1) have their conventional meaning.] A canonical transformation is now performed on the Hamiltonian of Eq. (1) in the following manner:

$$H'=\exp(-i\eta)H\exp(i\eta)=H+\exp(-i\eta)[H,\exp(i\eta)] \quad (2)$$

where

$$\eta=\sum_k\left(\frac{4\pi e^2}{hck^3\Omega}\right)^{\frac{1}{2}}\left(\hat{e}_k\cdot\frac{\mathbf{p}}{m_0c}\right)\times\{Q_k\cos\mathbf{k}\cdot\mathbf{x}-\Pi_k\sin\mathbf{k}\cdot\mathbf{x}\}=\sum_k\eta_k. \quad (3)$$

The transformation when applied to $H_{\rm rad}$ of Eq. (1) yields:

$$\exp(-i\eta)H_{\rm rad}\exp(i\eta)=H_{\rm rad}+\frac{4}{3\pi}\left(\frac{e^2}{m_0c^2}\right)\frac{p^2}{2m_0}\int_0^{k^{\max}}dk+\frac{(4\pi e^2)^{\frac{1}{2}}}{m_0c}\mathbf{p}\cdot\mathbf{A}. \quad (4)$$

Equation (4) is exact. The following commutation relationships are used in the derivation of Eq. (4) and

* This work was begun during the author's stay at Washington University, St. Louis, Missouri. During that time, this work was supported, in part, by the joint program of the U. S. Office of Naval Research and the U. S. Atomic Energy Commission.

[1] M. Schafroth, Helv. Phys. Acta **22**, 501 (1949); **23**, 542 (1950).
[2] L. Brown and R. Feynman, Phys. Rev. **85**, 231 (1952).
[3] A. Mitra, Nature **169**, 1009 (1952).
[4] F. Bloch and A. Nordsieck, Phys. Rev. **52**, 54 (1937).
[5] A. Nordsieck, Phys. Rev. **52**, 59 (1937).
[6] H. Primakoff, Phys. Rev. **84**, 1255 (1951).
[7] See, for example, G. Morpurgo, Nuovo cimento, Suppl. Vol. **8**, 109 (1951).

subsequent expressions:

$$[\Pi_k, \exp(i\eta)] = \left(\frac{4\pi e^2}{\hbar c k^3 \Omega}\right)^{\frac{1}{2}} \left(\hat{e}_k \cdot \frac{\mathbf{p}}{m_0 c}\right) \times \cos \mathbf{k}\cdot\mathbf{x} \exp(i\eta), \quad (5a)$$

$$[Q_k, \exp(i\eta)] = \left(\frac{4\pi e^2}{\hbar c k^3 \Omega}\right)^{\frac{1}{2}} \left(\hat{e}_k \cdot \frac{\mathbf{p}}{m_0 c}\right) \times \sin \mathbf{k}\cdot\mathbf{x} \exp(i\eta). \quad (5b)$$

In addition:

$$\exp(-i\eta)\left[-\frac{(4\pi e^2)^{\frac{1}{2}}}{m_0 c}\mathbf{p}\cdot\mathbf{A}\right]\exp(i\eta) = -\frac{(4\pi e^2)^{\frac{1}{2}}}{m_0 c}\mathbf{p}\cdot\mathbf{A} - \frac{8}{3\pi}\left(\frac{e^2}{m_0 c^2}\right)\frac{p^2}{2m_0}\int_0^{k^{\max}} dk + i\frac{(4\pi e^2)^{\frac{1}{2}}}{m_0 c}\sum_{k\neq k'}\{\eta_k \mathbf{p}\cdot\mathbf{A}_{k'} - \mathbf{p}\cdot\mathbf{A}_{k'}\eta_k\} + O(e^3). \quad (6)$$

It is not possible to calculate the transformed term in $(\mathbf{p}\cdot\mathbf{A})$ exactly since the commutator

$$[\mathbf{p}, \exp(i\eta)]$$

cannot be expressed in any convenient closed form. A power series expansion in $(e^2/\hbar c)$ is required and results in Eq. (6). Finally, we evaluate

$$\exp(-i\eta)\left[\frac{4\pi e^2}{2m_0 c^2}A^2\right]\exp(i\eta) = \frac{4\pi e^2}{2m_0 c^2}A^2 + \frac{4\pi e^2}{2m_0 c^2}\frac{(4\pi e^2)^{\frac{1}{2}}}{m_0 c\Omega}\left\{\mathbf{A}\cdot\mathbf{J} + \mathbf{J}\cdot\mathbf{A} + \frac{(4\pi e^2)^{\frac{1}{2}}}{m_0 c\Omega}J^2\right\}, \quad (7)$$

where

$$\mathbf{J} = \sum_k \frac{1}{k^2}\hat{e}_k(\hat{e}_k\cdot\mathbf{p}).$$

The first three terms in Eq. (7) lead to

$$\frac{4\pi e^2}{2m_0 c^2}A^2 + \frac{4}{3\pi}\left(\frac{e^2}{m_0 c^2}\right)\int_0^{k^{\max}} dk \cdot \frac{(4\pi e^2)^{\frac{1}{2}}}{m_0 c}\mathbf{p}\cdot\mathbf{A}. \quad (7a)$$

The last term in Eq. (7) is evaluated in a straight forward manner and yields

$$B(k^{\max})(e^2/\hbar c)^2(p^2/2m_0), \quad (7b)$$

the value of the constant B depending on the cut-off value, $k^{\max}$. We see that this term is interpretable as a mass renormalization proportional to e^4 and will be neglected. If we now set

$$\frac{\delta m}{m_0} = \frac{4}{3\pi}\left(\frac{e^2}{m_0 c^2}\right)\int_0^{k^{\max}} dk, \quad (8)$$

and combine the results of Eqs. (2)–(8), we discover

$$H' = \frac{p^2}{2m_0} + \frac{4\pi e^2}{2m_0 c^2}A^2 + i\frac{(4\pi e^2)^{\frac{1}{2}}}{m_0 c} \times \sum_{k\neq k'}\{\eta_k \mathbf{p}\cdot\mathbf{A}_{k'} - \mathbf{p}\cdot\mathbf{A}_{k'}\eta_k\} + H_{\text{rad}} + \text{terms higher order in } e \text{ and/or } (p/m_0 c). \quad (9)$$

The Hamiltonian of Eq. (9) contains no terms which will lead to the long wavelength divergences in Compton scattering mentioned above.

To demonstrate the appearance of the separate long-wavelength divergences in the Compton processes in the more usual perturbation treatment, it is necessary to return to Eq. (7) and expand $\exp(\pm i\eta)$ in a power series in η.

$$\exp(-i\eta)\left[\frac{4\pi e^2}{2m_0 c^2}A^2\right]\exp(i\eta) = \frac{4\pi e^2}{2m_0 c^2}\left\{A^2 + i[\eta, A^2] + \frac{i^2}{2}[\eta,[\eta, A^2]] + \cdots\right\}. \quad (7c)$$

The first-order (in a perturbation sense) matrix element of the second term in Eq. (7c) yields a nonvanishing result in the double Compton process. The cross section calculated for the double process from this matrix element contains a term which is logarithmically divergent at long wavelengths:

$$d\sigma = -\frac{2}{3\pi}\left(\frac{e^2}{m_0 c^2}\right)^2\left(\frac{e^2}{\hbar c}\right)\left(\frac{\hbar k_0}{m_0 c}\right)^2 \ln\left(\frac{\hbar k^{\min}}{m_0 c}\right) \cdot (1-\cos\theta)(1+\cos^2\theta)d\Omega, \quad (10)$$

where k_0 = wave number of incident photon, θ = angle of scattering, and $k^{\min}\to 0$. The first-order matrix element of the third term in Eq. (7c) yields a nonvanishing result in the radiative correction to the single Compton process; this matrix element is of fourth order in e and when combined with the first-order matrix element of the first term in Eq. (7c) yields the cross section of Eq. (10) with opposite sign.[1–3]

The author wishes to acknowledge many informative discussions with Dr. H. Primakoff on the applicability of the Bloch-Nordsieck transformation to a variety of physical processes.

Correlations in Space and Time and Born Approximation Scattering in Systems of Interacting Particles

LÉON VAN HOVE
Institute for Advanced Study, Princeton, New Jersey
(Received March 16, 1954)

A natural time-dependent generalization is given for the well-known pair distribution function $g(\mathbf{r})$ of systems of interacting particles. The pair distribution in space and time thus defined, denoted by $G(\mathbf{r},t)$, gives rise to a very simple and entirely general expression for the angular and energy distribution of Born approximation scattering by the system. This expression is the natural extension of the familiar Zernike-Prins formula to scattering in which the energy transfers are not negligible compared to the energy of the scattered particle. It is therefore of particular interest for scattering of slow neutrons by general systems of interacting particles: G is then the proper function in terms of which to analyze the scattering data.

After defining the G function and expressing the Born approximation scattering formula in terms of it, the paper studies its general properties and indicates its role for neutron scattering. The qualitative behavior of G for liquids and dense gases is then described and the long-range part exhibited by the function near the critical point is calculated. The explicit expression of G for crystals and for ideal quantum gases is briefly derived and discussed.

I. INTRODUCTION

IN two special cases, the first Born approximation for the scattering of x-rays or particles by a system S of interacting particles is known to express the differential cross section in terms of simple density distribution functions for the particles of S.

(i) If S is in a pure quantum state and if this state does not change in the scattering process, the latter is elastic and the differential cross section is expressible in terms of the density distribution $\rho(\mathbf{r})$ for one particle of the system (supposed for simplicity to be composed of identical particles). This applies for example to the elastic scattering of x-rays or electrons by the electrons of an atom.[1,2]

(ii) If the energy transfers occurring in the scattering process are negligible compared to the energy of the scattered photon or particle, the momentum transfer is essentially unique for each scattering angle and the differential cross section per unit angle is expressible in terms of the pair distribution function $g(\mathbf{r})$ of S, which describes the average density distribution as seen from a particle of the system. This is the so-called static approximation which applies, for example, to the sum of elastic and inelastic scattering of x-rays and electrons by the electrons of an atom,[3,4] as well as to that part of the scattering of x-rays by solids, liquids, and gases which leaves the atomic quantum states unchanged.[5,6]

The purpose of the present paper is to show that in Born approximation the scattering cross section is always expressible in terms of a suitably generalized pair distribution function $G(\mathbf{r},t)$ depending on a space vector $\mathbf{r}$ and a time interval t, and to study this function in some detail for a number of systems. For scattering theory this would be of rather academic interest in connection with x-ray scattering, for which the conditions of case (ii) above are usually well fulfilled. The same holds for electrons, for which, however, the Born approximation is of much more limited applicability than for x-rays. For slow neutrons, on the contrary, (wavelength $\gtrsim 1$A) now used in a rapidly growing variety of scattering experiments,[7] the energy transfers are usually comparable to or larger than the incident energy, whereas the first Born approximation holds quite well provided the neutron-nucleus interaction is described by means of the Fermi pseudopotential. The need has thus arisen for an improvement of the static approximation for scattering by general systems, and correction terms valid at relatively high neutron energies have been calculated by Placzek and by Wick.[8] We present here a general solution to this problem, applicable at all neutron energies, by describing the Born approximation scattering in terms of the time-dependent pair-distribution function G.

Furthermore, the fact that G has often, even for complicated systems, a number of qualitative properties which are easy to visualize, makes it in many cases a practical tool for the discussion of scattering experiments. Its use for the analysis and interpretation of experimental data has been illustrated elsewhere on the case of slow neutron scattering by ferromagnetic crystals.[9]

The generalized pair-distribution function $G(\mathbf{r},t)$, to which neutron scattering gives direct experimental access, turns out to be a very natural extension of the conventional $g(\mathbf{r})$ function. Independently of its use in scattering theory, it is of genuine interest from the general standpoint of statistical mechanics. Its physical

[1] I. Waller, Z. Physik **51**, 213 (1928).
[2] N. F. Mott, Proc. Roy. Soc. (London) **A127**, 658 (1930).
[3] I. Waller and D. R. Hartree, Proc. Roy. Soc. (London) **A124**, 119 (1929).
[4] P. M. Morse, Physik. Z. **33**, 443 (1932).
[5] I. Waller, dissertation, Uppsala, 1925 (unpublished).
[6] F. Zernike and J. Prins, Z. Physik **41**, 184 (1927); P. Debye and H. Memke, Ergeb. Tech. Röntgenk. **II** (1931).
[7] See, e.g., D. J. Hughes, *Pile Neutron Research* (Addison-Wesley Publishing Company, Cambridge, 1953).
[8] G. Placzek, Phys. Rev. **86**, 377 (1952); G. C. Wick, Phys. Rev. **94**, 1228 (1954).
[9] L. Van Hove, Phys. Rev. **93**, 268 (1954).

meaning is particularly simple in the absence of quantum effects: $G(\mathbf{r},t)$ is then, for the system under consideration, the average density distribution at a time $t'+t$ as seen from a point where a particle passed at time t'. This definition has to be slightly modified for a quantum system, in view of the noncommutativity of the operators representing particle positions at different times. In all cases $G(\mathbf{r},t)$ describes the correlation between the presence of a particle in position $\mathbf{r}'+\mathbf{r}$ at time $t'+t$ and the presence of a particle in position $\mathbf{r}'$ at time t', averaged over $\mathbf{r}'$. It essentially reduces to $g(\mathbf{r})$ for $t=0$.

The concept of time-dependent correlations has already been used in connection with neutron scattering by crystals in unpublished work by Glauber.[10]

The choice of a proper definition of the pair distribution $G(\mathbf{r},t)$ for general quantum-mechanical systems requires some care since it deals with correlations between noncommuting quantities. We will be led to it conveniently by starting from the Born scattering formula and following a natural extension of the well-known procedure to introduce the $g(\mathbf{r})$ function in the static approximation. This is done in the next section, where a number of general properties of $G(\mathbf{r},t)$ are also derived.

The use of the pair distribution G to describe neutron scattering data is indicated in Sec. III. This distribution is the proper function in terms of which to analyze the angular and energy distribution of neutrons scattered by general systems of nuclei, in exactly the same way as the $g(\mathbf{r})$ function is the proper function with which to analyze angular distributions in x-ray scattering. In full analogy with the x-ray case, it is expected to be useful mainly for systems too complicated to allow an explicit calculation of either the scattering or the pair distribution. Liquids and dense gases are clearly the principal examples of such systems.

The advantage of using pair distribution functions for the analysis of scattering data is their simple and intuitively clear physical meaning, which makes their qualitative behavior rather easy to visualize. It is therefore of importance to form as complete a picture of this behavior as possible, and, in absence of sufficient experimental data, it is indicated to discuss systems for which the pair distribution function can be entirely or partly calculated. In the present paper we treat mainly liquids and dense gases, for which the general shape of G is easy to guess and its long-range part near the critical point can be calculated (Sec. IV). We also consider more briefly crystals (Sec. V) and the ideal quantum gases (Sec. VI).

With the experimental data available so far, the best example of the usefulness of pair distributions in space and time for the analysis of scattering data is provided by the case of magnetic scattering of neutrons by ferromagnetic crystals.[11] A short account of the analysis has already been published.[9] The full discussion will appear as a separate paper.

[10] R. J. Glauber (private communication); Phys. Rev. **87**, 189 (1952); Phys. Rev. **94**, 751 (1954), and forthcoming paper.

II. THE PAIR DISTRIBUTION IN SPACE AND TIME

A. Definition

The correct definition of $G(\mathbf{r},t)$ for a general quantum-mechanical system is best inferred from the Born approximation scattering formula. The nature of the scattered particle and the details of the scattering law are, of course, largely irrelevant for this purpose. We will assume that the scattered particle is nonrelativistic and interacts with the particles of the system S through a potential $V(r)$ depending on distance only. For simplicity S is supposed to be composed of one single type of particle. The differential scattering cross section per unit solid angle and unit interval of outgoing energy ϵ of the scattered particle is given in the first Born approximation by

$$\frac{d^2\sigma}{d\Omega d\epsilon}=\frac{m^3}{2\pi^2\hbar^6}\frac{k}{k_0}W(\kappa)\sum_{n_0}p_{n_0}\sum_n\left|\left[\sum_{j=1}^N\exp(i\boldsymbol{\kappa}\cdot\mathbf{r}_j)\right]_{n_0}^n\right|^2 \cdot\delta\left\{k^2-k_0^2+\frac{2m}{\hbar^2}(E_n-E_{n_0})\right\}, \quad (1)$$

where m, $\mathbf{k}_0$, and $\mathbf{k}=\mathbf{k}_0-\boldsymbol{\kappa}$ are the mass and the initial and final wave vectors of the scattered particle. The operators $\mathbf{r}_j$ represent the position vectors of the N particles of the scattering system S, whose initial and final quantum states are labeled by n_0, n and have energies E_{n_0}, E_n, respectively. The bracket $[\cdots]_{n_0}^n$ denotes a matrix element and p_{n_0} is the statistical weight of the initial state n_0 (usually the Boltmann factor divided by the sum of states). The function $W(\kappa)$ is defined by

$$W(\kappa)=\left\{\int\exp(i\boldsymbol{\kappa}\cdot\mathbf{r})V(r)d\mathbf{r}\right\}^2.$$

If, besides the momentum transfer $\hbar\boldsymbol{\kappa}$, we introduce the energy transfer

$$\hbar\omega=\hbar^2(k_0^2-k^2)/2m,$$

Eq. (1) can be written

$$\frac{d^2\sigma}{d\Omega d\epsilon}=A\,S(\boldsymbol{\kappa},\omega), \quad (2)$$

$$A=\frac{m^2}{4\pi^2\hbar^5}\frac{k}{k_0}W(\kappa), \quad (3)$$

$$S(\boldsymbol{\kappa},\omega)=\sum_{n_0}p_{n_0}\sum_n\left|\left[\sum_{j=1}^N\exp(i\boldsymbol{\kappa}\cdot\mathbf{r}_j)\right]_{n_0}^n\right|^2 \cdot\delta\left\{\omega+\frac{E_{n_0}-E_n}{\hbar}\right\}, \quad (4)$$

[11] H. Palevsky and D. J. Hughes, Phys. Rev. **92**, 202 (1953); G. L. Squires (to be published). We are indebted to these authors for communication of their results before publication.

where, for given momentum and energy transfers, $\mathcal{S}(\kappa,\omega)$ is independent of the mass and energy of the scattered particle as well as of the interaction potential, whereas A depends only on the properties of the individual particles of S. This separation of two factors in the differential cross section is quite general; it is an immediate consequence of the use of momentum and energy transfers as independent variables.

It is now an easy matter to express in terms of a pair distribution the function $\mathcal{S}(\kappa,\omega)$ which, in the first Born approximation, contains the scattering properties of the system S. If it is remembered that in the static approximation [case (ii) of the introduction] the differential cross section per unit solid angle,

$$\frac{d\sigma}{d\Omega}=\int\frac{d^2\sigma}{d\Omega d\epsilon}d\epsilon, \tag{5}$$

is essentially, as a function of κ, the Fourier transform over $\mathbf{r}$ of the $g(\mathbf{r})$ function, it is natural to expect $\mathcal{S}(\kappa,\omega)$ to be essentially the Fourier transform over $\mathbf{r}$ and t of the pair distribution in space and time $G(\mathbf{r},t)$. We therefore define the latter through the equivalent equations:

$$\mathcal{S}(\kappa,\omega)=(2\pi)^{-1}N\int\exp[i(\kappa\cdot\mathbf{r}-\omega t)]\cdot G(\mathbf{r},t)d\mathbf{r}dt, \tag{6}$$

or

$$G(\mathbf{r},t)=(2\pi)^{-3}N^{-1}\int\exp[i(\omega t-\kappa\cdot\mathbf{r})]\cdot\mathcal{S}(\kappa,\omega)d\kappa d\omega. \tag{7}$$

The coefficient $(2\pi)^{-1}N$ in (6) is introduced for convenience. It makes $G(\mathbf{r},t)$ independent of N and asymptotically equal to the number density for the large systems of statistical mechanics, in which the limit $N\to\infty$ is to be taken. From Eqs. (4) and (7) one gets, successively,

$$\begin{aligned}G(\mathbf{r},t)=(2\pi)^{-3}N^{-1}\sum_{n_0}p_{n_0}\sum_n\sum_{l,j=1}^{N}\int d\kappa\exp(-i\kappa\cdot\mathbf{r})\\ \cdot[\exp(-i\kappa\cdot\mathbf{r}_l)]_n{}^{n_0}\cdot\exp(iE_nt/\hbar)\\ \cdot[\exp(i\kappa\cdot\mathbf{r}_j)]_{n_0}{}^n\cdot\exp(-iE_{n_0}t/\hbar),\end{aligned} \tag{8}$$

$$\begin{aligned}G(\mathbf{r},t)=(2\pi)^{-3}N^{-1}\sum_{l,j=1}^{N}\int d\kappa\exp(-i\kappa\cdot\mathbf{r})\\ \cdot\langle\exp\{-i\kappa\cdot\mathbf{r}_l(0)\}\cdot\exp\{i\kappa\cdot\mathbf{r}_j(t)\}\rangle.\end{aligned}$$

The last formula contains the Heisenberg operator $\mathbf{r}_j(t)$, defined for all j and t by

$$\mathbf{r}_j(t)=\exp(itH/\hbar)\mathbf{r}_j\exp(-itH/\hbar),$$

where H is the Hamiltonian of the system.[12] The bracket $\langle\cdots\rangle$ stands for the average of the expectation value of the enclosed operator:

$$\langle\cdots\rangle=\sum_{n_0}p_{n_0}[\cdots]_{n_0}{}^{n_0}. \tag{9}$$

With the help of the convolution formula for the Fourier transform of an (ordered) product, we obtain finally the expression

$$G(\mathbf{r},t)=N^{-1}\left\langle\sum_{l,j=1}^{N}\int d\mathbf{r}'\cdot\delta(\mathbf{r}+\mathbf{r}_l(0)-\mathbf{r}')\delta(\mathbf{r}'-\mathbf{r}_j(t))\right\rangle, \tag{10}$$

which defines $G(\mathbf{r},t)$ entirely in terms of space and time variables, with the proper ordering of the operators belonging to different times.

For $t=0$, all operators commute and the integration can be carried out, leading to

$$G(\mathbf{r},0)=N^{-1}\langle\sum_{l,j=1}^{N}\delta(\mathbf{r}+\mathbf{r}_l(0)-\mathbf{r}_j(0))\rangle,$$

or

$$G(\mathbf{r},0)=\delta(\mathbf{r})+N^{-1}\sum_{l\neq j}\langle\delta(\mathbf{r}+\mathbf{r}_l-\mathbf{r}_j)\rangle=\delta(\mathbf{r})+g(\mathbf{r}), \tag{11}$$

according to the familiar definition of the conventional pair distribution $g(\mathbf{r})$. Similarly, in the scattering formula, if the incident energy is sufficiently large compared to the energy transfers, the momentum transfer for a given scattering angle is independent of the outgoing energy, and the differential cross section per unit solid angle becomes

$$\begin{aligned}\frac{d\sigma}{d\Omega}&=\int\frac{d^2\sigma}{d\Omega d\epsilon}d\epsilon=\hbar A\int\mathcal{S}(\kappa,\omega)d\omega\\ &=\hbar AN\int\exp(i\kappa\cdot\mathbf{r})\delta(t)G(\mathbf{r},t)d\mathbf{r}dt\\ &=[m/(2\pi\hbar^2)]^2NW(\kappa)\left\{1+\int\exp(i\kappa\cdot\mathbf{r})g(\mathbf{r})d\mathbf{r}\right\},\end{aligned}$$

the familiar formula in the static approximation. Just as measurement of $d\sigma/d\Omega$ provides an experimental determination of $g(\mathbf{r})$ in the latter approximation, the pair distribution in space and time $G(\mathbf{r},t)$ is experimentally accessible through measurements of $d^2\sigma/d\Omega d\epsilon$.

B. General Properties

We will now discuss a few immediate properties of the pair distribution in space and time. $G(\mathbf{r},t)$, which is in general complex, has the Hermitian symmetry,

$$G(-\mathbf{r},-t)=\{G(\mathbf{r},t)\}^*, \tag{12}$$

[12] The introduction of a time variable to eliminate the δ function in Eq. (1) and the subsequent consideration of time-dependent operators have become familiar in scattering theory. See, e.g., A. Akhiezer and I. Pomeranchuk, J. Phys. (U.S.S.R.) **11**, 167 (1947); G. C. Wick, reference 8.

easily derived as follows: from (10),

$$\{G(\mathbf{r},t)\}^*=N^{-1}\Big\langle\sum_{l,j}\int d\mathbf{r}'\delta(\mathbf{r}'-\mathbf{r}_j(t))\delta(\mathbf{r}+\mathbf{r}_l(0)-\mathbf{r}')\Big\rangle$$

$$=N^{-1}\Big\langle\sum_{l,j}\int d\mathbf{r}''\delta(\mathbf{r}-\mathbf{r}_j(t)+\mathbf{r}'')\delta(\mathbf{r}_l(0)-\mathbf{r}'')\Big\rangle$$

$$=N^{-1}\Big\langle\sum_{l,j}\int d\mathbf{r}''\delta(\mathbf{r}-\mathbf{r}_j(0)+\mathbf{r}'')\times\delta(\mathbf{r}_l(-t)-\mathbf{r}'')\Big\rangle$$

$$=G(-\mathbf{r},-t).$$

In the second step the integration variable is $\mathbf{r}''=\mathbf{r}'-\mathbf{r}$; the third step uses the invariance of the expectation value under the unitary transformation $\exp(itH/\hbar)$, whereas the last is based on the even character of the δ function. Property equation (12) is equivalent with the fact that $S(\kappa,\omega)$ is a real-valued function.

Complex values of $G(\mathbf{r},t)$ reflect quantum properties of the system. Indeed, under classical conditions, the operators in (10) reduce to commuting c numbers and G takes the real, positive value:

$$G(\mathbf{r},t)=N^{-1}\langle\sum_{l,j}\delta(\mathbf{r}+\mathbf{r}_l(0)-\mathbf{r}_j(t))\rangle.$$

As announced in the introduction, it is seen to describe the average density distribution at time $t'+t$ as seen from a point which was occupied by a particle at time t'; this distribution is independent of t', here given the value 0.

When quantum effects are present,—they are for any actual system in certain ranges of r and t values—, G is complex and the simple physical interpretation given above cannot hold in view of the noncommutativity of particle positions at different times. How this noncommutativity enters into the expression of G can best be seen by introducing suitable density operators. Let us consider in space a volume element ΔV centered at point $\mathbf{r}$ and define the Heisenberg operator $\Delta P(\mathbf{r},t)$ satisfying $\Delta P(\mathbf{r},t)\psi=\psi$ for all states ψ of the system for which, with probability one, at least one particle is in ΔV at time t, and $\Delta P(\mathbf{r},t)\psi=0$ for all states such that, with probability one, no particle is in ΔV at time t. One has, in the limit of infinitesimal ΔV,

$$\Delta P(\mathbf{r},t)/\Delta V=\sum_j\delta(\mathbf{r}-\mathbf{r}_j(t)),$$

and thus, taking identical volume elements around each point,

$$G(\mathbf{r},t)=N^{-1}\Delta V^{-2}\int d\mathbf{r}''\langle\Delta P(\mathbf{r}'',0)\cdot\Delta P(\mathbf{r}''+\mathbf{r},t)\rangle. \quad (13)$$

For a system homogeneous in space (like a gas or a liquid), enclosed in a volume $V=N/\rho$, we get the very simple formula:

$$G(\mathbf{r},t)=\rho^{-1}\Delta V^{-2}\langle\Delta P(\mathbf{r}'',0)\cdot\Delta P(\mathbf{r}''+\mathbf{r},t)\rangle, \quad (14)$$

where $\mathbf{r}''$ is an arbitrary point in V. From Eq. (13) or (14) follows immediately that the real part of G is related to the average value of the symmetrized product,

$$\tfrac{1}{2}\{\Delta P(\mathbf{r}'',0)\cdot\Delta P(\mathbf{r}''+\mathbf{r},t)+\Delta P(\mathbf{r}''+\mathbf{r},t)\cdot\Delta P(\mathbf{r}'',0)\},$$

and is therefore the natural extension to quantum systems of the classical, real-valued, pair distribution function in space and time, whereas the imaginary part reduces essentially to the average value of the commutator of $\Delta P(\mathbf{r}'',0)$ and $\Delta P(\mathbf{r}''+\mathbf{r},t)$.

In the case of systems for which the symmetric or antisymmetric character of the wave function is of little importance, and which can thus be regarded as composed of distinguishable particles (Boltzmann statistics), the G function splits naturally into a part G_s describing the correlation between positions of one and the same particle at different times, and a part G_d referring to pairs of distinct particles (the subscripts stand for "self" and "distinct," respectively). They are defined as follows:

$$G_s(\mathbf{r},t)=N^{-1}\Big\langle\sum_{j=1}^{N}\int d\mathbf{r}'\cdot\delta(\mathbf{r}+\mathbf{r}_j(0)-\mathbf{r}')\times\delta(\mathbf{r}'-\mathbf{r}_j(t))\Big\rangle, \quad (15)$$

$$G_d(\mathbf{r},t)=N^{-1}\Big\langle\sum_{j\neq l=1}^{N}\int d\mathbf{r}'\cdot\delta(\mathbf{r}+\mathbf{r}_l(0)-\mathbf{r}')\times\delta(\mathbf{r}'-\mathbf{r}_j(t))\Big\rangle. \quad (16)$$

They verify separately the symmetry condition (12) and equations of type Eq. (13) with density operators $\Delta P_j/\Delta V$ defined for individual particles. For $t=0$, they reduce to

$$G_s(\mathbf{r},0)=\delta(\mathbf{r}),\quad G_d(\mathbf{r},0)=g(\mathbf{r}). \quad (17)$$

For the systems of large numbers of particles studied in statistical mechanics, solids, liquids, or gases, the pair distribution $G(\mathbf{r},t)$, in the definition [Eqs. (9) and (10)] of which the statistical weights p_{n_0} must be given the Boltmann value

$$p_{n_0}=Z^{-1}\exp(-\beta E_{n_0}),\quad Z=\sum_{n_0}\exp(-\beta E_{n_0}) \quad (18)$$

(β^{-1} = temperature T multiplied by Boltzmann constant k_B), has especially simple asymptotic expressions for large r or $|t|$. For such systems, the particles in regions widely separated in space are statistically independent, and so are the properties of the system at two widely distant times. For sufficiently large r or large $|t|$, we can thus write asymptotically

$$\langle\sum_{l,j=1}^{N}\delta(\mathbf{r}+\mathbf{r}(0)-\mathbf{r}')\delta(\mathbf{r}'-\mathbf{r}_j(t))\rangle\simeq\rho(\mathbf{r}'-\mathbf{r})\rho(\mathbf{r}'),$$

where

$$\rho(\mathbf{r}')=\langle\sum_{j=1}^{N}\delta(\mathbf{r}'-\mathbf{r}_j(t))\rangle \tag{19}$$

is the average density at point $\mathbf{r}'$, independent of the time t. Hence, from Eq. (10), we can write the asymptotic formula

$$G(\mathbf{r},t)\simeq N^{-1}\int d\mathbf{r}'\cdot\rho(\mathbf{r}'-\mathbf{r})\rho(\mathbf{r}'), \tag{20}$$

the right-hand side of which is the often considered autocorrelated density.[13] In particular, for an homogeneous system, $\rho(\mathbf{r}')$ is a constant, the number density $\rho=N/V$ (V volume of the system), and Eq. (20) reduces to

$$G(\mathbf{r},t)\simeq\rho. \tag{21}$$

It is the difference between G and its asymptotic value (20) which represents the correlation between pairs of particles. The instantaneous part of this correlation is contained in $G(\mathbf{r},0)=\delta(\mathbf{r})+g(\mathbf{r})$ and is well known from the study of the familiar $g(\mathbf{r})$ function. The interest of G for $t\neq 0$ is to describe in addition its time dependence: if we consider a given, fixed point of space through which a particle passes at time 0, the density distribution of the system is disturbed around this point not only at time 0, but before and afterwards. The average time variation of this disturbance is represented by the G function. As formally expressed by Eq. (20), the disturbance is negligible far from the fixed point at all times, and everywhere in the system long before and long after time 0. Except in the case of long-range order or under critical conditions, to be discussed later on, the size and duration of the disturbance are characterized by a length R_0 and a time T_0 of microscopic dimensions such that Eq. (20) holds for all t if $r\gg R_0$ and for all r if $|t|\gg T_0$. R_0 is the *range* of the pair correlation, T_0 its *relaxation time*. To establish from first principles the existence of R_0 and T_0, and, *a fortiori*, to calculate G in terms of intermolecular forces, are difficult problems of statistical mechanics, unsolved except in very special cases. The relaxation time T_0 in particular is obviously related to the irreversible return of a locally perturbed system to equilibrium, and thus depends on the ergodic properties of the system. Such problems will not be touched upon here. We hope to have shown, however, that quite apart from its interest for scattering theory, the pair distribution in space and time is an important extension of the conventional $g(\mathbf{r})$ function from the standpoint of general statistical mechanics.

The separation of G into its asymptotic value and a correlation term G',

$$G'(\mathbf{r},t)=G(\mathbf{r},t)-N^{-1}\int d\mathbf{r}'\cdot\rho(\mathbf{r}'-\mathbf{r})\rho(\mathbf{r}'), \tag{22}$$

has also a simple significance for scattering. Insertion in (6) gives

$$S(\boldsymbol{\kappa},\omega)=\delta(\omega)\cdot\left|\int\exp(i\boldsymbol{\kappa}\cdot\mathbf{r})\cdot\rho(\mathbf{r})d\mathbf{r}\right|^2$$

$$+(2\pi)^{-1}N\int\exp[i(\boldsymbol{\kappa}\cdot\mathbf{r}-\omega t)]\cdot G'(\mathbf{r},t)d\mathbf{r}dt. \tag{23}$$

The first term of the right-hand side represents elastic scattering ($\omega=0$); for an homogeneous system of large dimensions it reduces to $N\rho\delta(\omega)\delta(\boldsymbol{\kappa})$, i.e., to forward elastic scattering, which in the first Born approximation is indistinguishable from the unscattered beam. The second term represents inelastic scattering: since G' tends to zero for r and $|t|\to\infty$, the energy distribution has no peak of form $\delta(\omega)$ in any scattering direction, nor has its angular distribution any peak of form $\delta(\boldsymbol{\kappa})$ in the forward direction. In some cases, however, the convergence of G' to zero may be slow. This will then produce, through the Fourier transform in the last term of (23), singularities of weaker type in the angular and energy distribution of inelastically scattered particles. A simple example of this situation is provided by slow neutron scattering in crystals and will be discussed in Sec. V.

The range R_0 and relaxation time T_0 determine the orders of magnitude $\hbar/R_0$, $\hbar/T_0$ of average momentum and energy transfers in those scattering processes which are appreciably affected by the collective properties of the system S. Let us consider incident particles with momentum of order $\hbar/R_0$, and let us determine under which condition the values of G for $|t|\sim T_0$ make an important contribution to the scattering. The condition is that the angle of scattering depends appreciably on both momentum and energy transfers [if it depends essentially on momentum transfer alone, the static approximation applies and the scattering depends on $G(\mathbf{r},0)$ only]. It requires that the spread $\hbar\Delta k$ in the length $\hbar k$ of the final momentum, due to energy transfers of order $\hbar/T_0$, is at least comparable to the momentum transfers $\hbar/R_0$. Since $\Delta k\sim(vR_0)^{-1}$, where v is the velocity of the incident particle, the condition is $v\lesssim R_0/T_0$ or $T_1\gtrsim T_0$, where T_1 is the time R_0/v in which the incident particle travels over a correlation range. In the latter form, the physical meaning of the condition is obvious: the time variation of G affects the total scattering and angular distribution only for a particle spending at least a time of order T_0 over a correlation length R_0. If on the contrary $T_1\ll T_0$, the scattering is not affected by the values of G for $|t|\sim T_0$. Apart from the distribution of outgoing energies, it is then entirely determined by the value of G for $|t|\ll T_0$, and the static approximation gives a good description of the

[13] For large $|t|$, Eq. (20) is valid also for systems with a small number of particles if the initial state is a pure quantum state, nondegenerate in energy. The asymptotic convergence for $|t|\to\infty$ may then, however, hold only in the mean, as is the case for a harmonic oscillator.

effect of collective properties of S on the scattering, in the sense that $d\sigma/d\Omega$ can be calculated by replacing $G(\mathbf{r},t)$ by $G_{id}(\mathbf{r},t)+G(\mathbf{r},0)-G_{id}(\mathbf{r},0)$, where G_{id} is the pair distribution function for an ideal gas of same density and temperature as S.

For incident particles of wavelength $\sim R_0$, the ratio T_1/T_0 is essentially equal to the ratio of average energy transfer to incident energy. A very crude estimate of R_0 and T_0 for actual substances, solids or liquids at average temperatures, gives $R_0\sim10^{-8}$ cm, $T_0\sim10^{-13}$ sec, and thus $T_1/T_0\sim10^5/v$ if the incident velocity v is measured in cm sec^{-1}. This gives $T_1/T_0\sim10^{-6}$ for photons of arbitrary wavelength, and $T_1/T_0\sim1$ for neutrons of wavelength around 1 A or somewhat larger, i.e., exactly of the right order R_0 for which collective effects on scattering are most conveniently observed. For electrons of wavelength around 1 A, one finds $T_1/T_0\sim10^{-4}$.

Before closing this section, we mention an extension of the $G(\mathbf{r},t)$ function to systems of identical particles with spin, to be used later in connection with spin-dependent scattering. If a_j is an operator depending on the spin of the jth particle, the same for each particle, a spin-dependent pair correlation is defined by

$$\Gamma(\mathbf{r},t)=N^{-1}\Big\langle\sum_{l,j=1}^{N}\int d\mathbf{r}'\cdot a_l(0)\delta(\mathbf{r}+\mathbf{r}_l(0)-\mathbf{r}') \times a_j(t)\delta(\mathbf{r}'-\mathbf{r}_j(t))\Big\rangle, \quad (24)$$

in terms of the Heisenberg operators,

$$a_j(t)=\exp(itH/\hbar)a_j\exp(-itH/\hbar).$$

For a system of Boltzmann particles with spin-independent Hamiltonian H and for the thermal distribution (18), there is no correlation between spins nor between spins and positions. Using the definitions (15) and (16) we then find

$$\Gamma(\mathbf{r},t)=\langle a^2\rangle_{\mathrm{Av}}G_s(\mathbf{r},t)+\langle a\rangle_{\mathrm{Av}}^2G_d(\mathbf{r},t), \quad (25)$$

where a is any of the a_j's and $\langle\cdots\rangle_{\mathrm{Av}}$ denotes an average over the spin states of the corresponding particle. Correlations involving the spins can be produced either by the symmetry requirements of the wave functions (Bose-Einstein and Fermi-Dirac particles) or by spin interactions. The first case is illustrated in Sec. VI. The second case occurs in ferromagnetic substances and will be discussed in a separate paper.

The extension of the foregoing considerations to systems composed of different types of particles is straightforward and will not be given here.

III. NUCLEAR SCATTERING OF SLOW NEUTRONS

As mentioned before, it is for the scattering of slow neutrons that use of the pair distributions in space and time is of most practical interest. We consider in the present section scattering due to the nuclear interaction between neutrons and the nuclei of the scattering system S. If the true interaction is replaced by the corresponding Fermi pseudopotential,

$$V(r)=(2\pi a\hbar^2/m)\delta(r),$$

where m is the neutron mass and a the scattering length of the nuclei assumed all identical, the Born approximation formula can be applied.[14] Equations (2), (3), and (6) give then, for the cross section of S,

$$\frac{d^2\sigma}{d\Omega d\epsilon}=\frac{a^2N}{2\pi\hbar}\frac{k}{k_0}\int\exp[i(\boldsymbol{\kappa}\cdot\mathbf{r}-\omega t)]\cdot G(\mathbf{r},t)d\mathbf{r}dt. \quad (26)$$

If the nuclei of S have a nonvanishing spin, this equation assumes a to be spin independent. For nuclei with a spin-dependent scattering length, or for nuclei belonging to different isotopes (the mass differences being neglected), Eq. (26) is simply replaced by

$$\frac{d^2\sigma}{d\Omega d\epsilon}=\frac{N}{2\pi\hbar}\frac{k}{k_0}\int\exp[i(\boldsymbol{\kappa}\cdot\mathbf{r}-\omega t)]\cdot\Gamma(\mathbf{r},t)d\mathbf{r}dt,$$

with the spin- or isotope-dependent scattering lengths a_j to be used in the definition (24) of Γ.[14] In most cases the nuclei can be treated as Boltzmann particles and the spin or isotope disorder can be considered perfect, so that Eq. (25) applies, and, remembering $G=G_s+G_d$, we obtain

$$\frac{d^2\sigma}{d\Omega d\epsilon}=\frac{d^2\sigma_{\mathrm{coh}}}{d\Omega d\epsilon}+\frac{d^2\sigma_{\mathrm{inc}}}{d\Omega d\epsilon}, \quad (27)$$

$$\frac{d^2\sigma_{\mathrm{coh}}}{d\Omega d\epsilon}=\frac{\langle a\rangle_{\mathrm{Av}}^2N}{2\pi\hbar}\frac{k}{k_0}\int\exp[i(\boldsymbol{\kappa}\cdot\mathbf{r}-\omega t)]\cdot G(\mathbf{r},t)d\mathbf{r}dt, \quad (28)$$

$$\frac{d^2\sigma_{\mathrm{inc}}}{d\Omega d\epsilon}=\frac{\{\langle a^2\rangle_{\mathrm{Av}}-\langle a\rangle_{\mathrm{Av}}^2\}N}{2\pi\hbar}\frac{k}{k_0}\int\exp[i(\boldsymbol{\kappa}\cdot\mathbf{r}-\omega t)] \cdot G_s(\mathbf{r},t)d\mathbf{r}dt. \quad (29)$$

Equations (28) and (29) are the so-called coherent and incoherent scattering cross sections.

The separation Eq. (23) of elastic and inelastic scattering applies to Eq. (28). A similar separation can be performed for Eq. (29) by considering the limit of G_s for $|t|\to\infty$. In the static approximation we get, as in Sec. II,

$$d\sigma_{\mathrm{coh}}/d\Omega=\langle a\rangle_{\mathrm{Av}}^2N\Big\{1+\int\exp(i\boldsymbol{\kappa}\cdot\mathbf{r})g(\mathbf{r})d\mathbf{r}\Big\}, \quad (30)$$

$$d\sigma_{\mathrm{inc}}/d\Omega=\{\langle a^2\rangle_{\mathrm{Av}}-\langle a\rangle_{\mathrm{Av}}^2\}N. \quad (31)$$

The incoherent cross section no longer depends on the structure of S. Equation (30), identical to the Zernike-

[14] The relevant information on slow neutron scattering will be found, for example, in J. M. Cassels, Progr. Nuclear Phys. **1**, 185 (1950).

Prins formula for x-ray scattering, has often been used before in connection with slow neutrons.[15–19]

The physical interest of Eqs. (28) and (29) is entirely similar to that of the familiar Eq. (30). It mainly concerns systems for which a complete calculation of pair distributions in terms of elementary forces cannot be carried out. Indeed, whenever an explicit calculation is possible, it leads to the differential cross sections as directly as to the pair distributions. For more complicated systems, however, like liquids or dense gases, the pair distributions, dealing with two-particle configurations in space and time, are much easier to visualize than the cross sections, and a qualitative prediction of their behavior is almost always possible, thus providing great help in understanding the main features of the scattering. For such systems, on the other hand, the pair distribution is the proper quantity in terms of which to interpret the scattering data, and since it contains very important information on the local structure of the system, its experimental determination is desirable. Equations (28), (29) provide the basis for such a determination.

Complete measurements of $d^2\sigma/d\Omega d\epsilon$, i.e., of the angular and energy distribution of scattered neutrons, will provide a direct determination of G or G_s by inversion of a 4-dimensional Fourier integral (2-dimensional for isotropic systems). At present, for intensity reasons, energy distributions of scattered neutrons are still difficult to observe, even when they spread over wide ranges. Progress will, however, undoubtedly be made in this direction[20] and it is to be hoped that complete sets of experimental values for $d^2\sigma/d\Omega d\epsilon$ will eventually become available.

A simpler but much less direct and less satisfactory approach to the experimental study of G or G_s can be made by measuring transmissions (i.e., total cross sections) or angular distributions in their dependence on the incident wavelength λ_0. For angular distributions, the contribution to the scattering of values of G or G_s with $t \neq 0$ will manifest itself through the fact that the differential cross section

$$\int (d^2\sigma/d\Omega d\epsilon) f(\epsilon) d\epsilon, \tag{32}$$

where $f(\epsilon)$ is determined by the detector used, does no longer depend on λ_0 and on the scattering angle θ through the single combination $\lambda_0^{-1} \sin(\theta/2)$, as it does in the static approximation with $f(\epsilon)$ constant. Since a quantity like Eq. (32) has a complicated functional expression in G or G_s, the analysis of its experimental values is bound to be much more difficult than it would be for $d^2\sigma/d\Omega d\epsilon$, and the choice of a detailed procedure would require careful consideration.

The next sections deal with the properties of G and G_s for special systems. Their aim is to form a more accurate picture of the behavior to be expected for these functions and to illustrate the correspondence between some of their properties and simple features of the angular and energy distributions obtained in scattering.

IV. LIQUIDS AND DENSE GASES

The discussion of pair distributions in space and time for liquids and dense gases presents the same difficulties as the corresponding discussion for the instantaneous pair distribution $g(\mathbf{r})$. Although the general behavior of the distribution functions can easily and safely be guessed, no reliable method has yet been found to calculate them in terms of the intermolecular forces.[21] We will therefore limit ourselves to a description of their most immediate properties.

Except for the case of substances of light atomic mass taken at very low temperatures, like liquid helium for example, the particles in a liquid or a dense gas have a mean de Broglie wavelength $\lambda_B = \hbar(2Mk_BT)^{-\frac{1}{2}}$ small compared to the distance between particles or, what amounts to the same, to the range of interatomic forces. M is the mass of the particles in the system. Under these conditions, the distinction between $G_s(r,t)$ and $G_d(r,t) = G - G_s$ is possible and these functions, which are independent of the direction of $\mathbf{r}$, verify, as already mentioned,

$$G_s(r,0) = \delta(\mathbf{r}), \quad G_d(r,0) = g(r), \tag{33}$$

$$\lim_{r' \to \infty} G_s(r',t) = \lim_{|t'| \to \infty} G_s(r,t') = 0, \tag{34}$$

$$\lim_{r' \to \infty} G_d(r',t) = \lim_{|t'| \to \infty} G_d(r,t') = \rho, \tag{35}$$

where ρ is the number density. Except in the neighborhood of the critical point, the convergence in Eqs. (34) and (35) takes place over a length R_0 of the order of intermolecular distances and a time T_0 of the order of the time needed by an average particle of the system to travel over a distance R_0. T_0 is essentially identical with the Debye relaxation time.

Under the same condition of a mean de Broglie wavelength small compared to interatomic distances ($\lambda_B \ll R_0$), no quantum effects will manifest themselves in G_d, which deals with pairs of particles separated by distances of order R_0, and $G_d(r,t)$ is thus a real-valued, positive function, even in t. The situation is slightly dif-

[15] O. Chamberlain, Phys. Rev. **77**, 305 (1950).
[16] Placzek, Nijboer, and Van Hove, Phys. Rev. **82**, 392 (1951).
[17] L. Goldstein, Phys. Rev. **84**, 466 (1951).
[18] P. C. Sharrah and G. P. Smith, J. Chem. Phys. **21**, 288 (1953).
[19] Henshaw, Hurst, and Pope, Phys. Rev. **92**, 1229 (1953).
[20] Crude information on energy distributions of neutrons scattered by solids has been obtained by P. Egelstaff, Nature **168**, 290 (1951); B. N. Brockhouse and D. G. Hurst, Phys. Rev. **88**, 542 (1952); R. D. Lowde, Proc. Roy. Soc. (London) **A221**, 206 (1954).

[21] The determination of pair distribution functions based on the superposition approximation of Kirkwood, J. Chem. Phys. **3**, 300 (1935), cannot be considered reliable for dense systems. It has been discussed for a gas of hard spheres by B. R. A. Nijboer and L. Van Hove, Phys. Rev. **85**, 777 (1952), and by B. R. A. Nijboer and R. Fieschi, Physica **19**, 545 (1953).

ferent for $G_s(r,t)$, which for very small times

$$|t| \sim h/k_B T \sim (\lambda_B/R_0)T_0,$$

is entirely concentrated in the region $r \sim \lambda_B$ where quantum effects are appreciable. For small displacements of this order, however, the potential acting on a particle is practically constant, so that the ideal gas value can be adopted for G_s:

$$G_s(r,t) \simeq \{2\pi t(k_B T t - ih)/M\}^{-3/2} \times \exp\{-Mr^2/[2t(k_B T t - ih)]\}.$$

This holds for $|t| \ll T_0$. For larger times, the form of G_s is affected by the interatomic forces, but quantum effects become negligible, and G_s thus also becomes real-valued positive and even in t. Characteristic shapes of G_s and G_d are given in Fig. 1 for three ranges of t values: $|t| \ll T_0$ (the curve for G_s is to be understood as representing the real part of the function if $|t| \lesssim h/k_B T$), $|t| \sim T_0$, and $|t| \gg T_0$.

For quantum liquids like liquid helium at low temperature the situation is, of course, entirely different. The distribution function G has complex values for all nonvanishing times. We will not try to make a guess at its theoretical shape but want to stress the interest of its experimental determination.

After these general considerations, let us return to the case of the so-called classical liquids ($\lambda_B \ll R_0$) which will now be studied in the neighborhood of the critical point. When critical conditions are approached, the qualitative behavior of G_s is not expected to be greatly modified. G_d, however, is known to exhibit long-range correlations resulting from the occurrence in the system of spontaneous density fluctuations of macroscopic size. In contrast with the short-range part of the pair distribution, these long-range phenomena can be explicitly studied, at least for temperatures T slightly above the critical temperature T_c, by the methods of macroscopic fluctuation theory. The applicability of such methods is actually not restricted to the neighborhood of the critical point. They make a general study possible for the scattering from macroscopic density fluctuations, by permitting the calculation of the value and the time dependence of the Fourier components of G_d:

$$\int \{G_d(r,t) - \rho\} \exp(i\kappa \cdot \mathbf{r}) d\mathbf{r},$$

for macroscopic κ^{-1}. This question, studied by Landau and Placzek for light scattering,[22] will not be treated in full generality in the present paper, where we limit ourselves to the more special case of critical fluctuations.

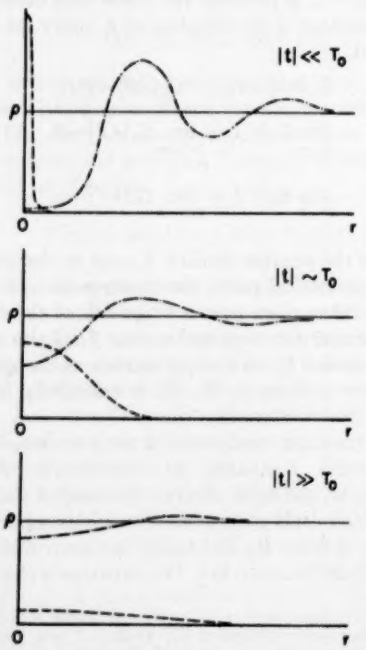

FIG. 1. The dependence of $G_s(r,t)$, (– – – –) and $G_d(r,t)$, (–·–·–) on r for three values of t. The solid line corresponds to the average density of the system.

The behavior of $g(r) = G_d(r,0)$ near the critical point, for $T > T_c$ and for r large compared to the intermolecular distance, has been determined by Ornstein and Zernike.[23] It is given by

$$G_d(r,0) \simeq \rho + (4\pi r_0^2 r)^{-1} e^{-\kappa_0 r}, \quad r \gg r_0, \tag{36}$$

where r_0 is a length slowly varying with temperature and density, of the order of the range of the forces, with value 1 at the critical point, and κ_0 is the reciprocal length

$$\kappa_0 = r_0^{-1}(\rho k_B T \chi_T)^{-\frac{1}{2}}, \tag{37}$$

defined in terms of the isothermal compressibility $\chi_T = \rho^{-1}(\partial\rho/\partial p)_T$. Equation (36) holds for $r \gg r_0$, in the temperature and density region where $r_0\kappa_0 \ll 1$. Its derivation assumes the system monophasic. Through its dependence on χ_T, the range κ_0^{-1} of the pair correlation becomes infinite at the critical point, where Eq. (36) reduces to

$$G_d(r,0) \simeq \rho + (4\pi r_0^2 r)^{-1}, \quad r \gg r_0. \tag{38}$$

We have now to determine the time variation of G_d for $r \gg r_0$. The long-range part of the pair distribution $G_d(r,t)$ can be identified with the average shape at time t of the spontaneous macroscopic density fluctuations in the system, as seen from a point through which a particle passed at time 0. Following Onsager,[24] it is

[22] L. Landau and G. Placzek, Physik. Z. Sowjetunion **5**, 172 (1934). For a more detailed exposition, see J. Frenkel, *Kinetic Theory of Liquids* (Clarendon Press, Oxford, 1946), pp. 244 ff. The author is indebted to G. Placzek for illuminating discussions and communication of unpublished work on this subject.

[23] L. S. Ornstein and F. Zernike, Proc. Acad. Sci. Amsterdam **17**, 793 (1914); Physik. Z. **19**, 134 (1918). The length r_0 in our Eq. (36) is related by $6r_0^2 = \epsilon^2$ to the length ϵ defined in the latter paper.

[24] L. Onsager, Phys. Rev. **37**, 405 (1931); **38**, 2265 (1931).

natural to assume that macroscopic variables which have taken nonequilibrium values as a consequence of spontaneous fluctuations have on the average in their return to equilibrium the same time variation as if their initial nonequilibrium values had been produced by suddenly released artificial constraints. This time variation is given by the well-known phenomenological laws of irreversible processes, in our case the Navier-Stokes equations for viscous flow supplemented by the continuity equation, and the equation for energy transport involving heat conduction.

Since we deal with fluctuations of small amplitude, all equations can be linearized and treated by Fourier analysis. We then find three independent plane-wave fluctuations of wave vector $\mathbf{k}$: two corresponding to damped waves propagating with sound velocity in the directions of $\mathbf{k}$ and $-\mathbf{k}$, and one of nonpropagating nature, with a time dependence given by the factor

$$\exp(-\tfrac{1}{4}\Lambda_0 k^2 t), \tag{39}$$

with

$$\Lambda_0 = 4\varkappa(\rho c_p)^{-1} = 4\varkappa(\rho c_v)^{-1}(\chi_S/\chi_T). \tag{40}$$

$\varkappa$ is the coefficient of heat conduction, c_p and c_v are the specific heats per particle, at constant pressure and volume, respectively, and χ_S is the adiabatic compressibility

$$\chi_S = \rho^{-1}(\partial\rho/\partial p)_S$$

(S: entropy). As expected, the fluctuations of the two first modes are found to be adiabatic and the third mode is a fluctuation at constant pressure.[25]

When the critical point is approached, whereas fluctuations of the two first modes remain normal, the magnitude of the spontaneous fluctuations at constant pressure increases indefinitely. They alone thus contribute to the long-range part of the pair correlation, and the time dependence of G_d for $r \gg r_0$ and $t>0$ can be obtained by multiplying each Fourier component of Eq. (36) by the corresponding factor (39), i.e., by calculating the convolution of Eq. (36) with the Fourier transform,

$$\frac{1}{(2\pi)^3}\int \exp(-\tfrac{1}{4}\Lambda_0 k^2 t)\exp(i\mathbf{k}\cdot\mathbf{r})d\mathbf{k} = (\pi\Lambda_0 t)^{-3/2}\exp\left(-\frac{|\mathbf{r}-\mathbf{r}'|^2}{\Lambda_0 t}\right),$$

of (39). One has thus, remembering that G_d is even in t,

$$G_d(r,t) \simeq \rho + (4\pi r_0^2 r)^{-1}(\pi\Lambda_0|t|)^{-3/2} \times \int \exp\left\{-\frac{|\mathbf{r}-\mathbf{r}'|^2}{\Lambda_0|t|} - \kappa_0 r'\right\}\frac{d\mathbf{r}'}{r'}. \tag{41}$$

[25] The foregoing analysis of spontaneous fluctuations has been carried out by L. Landau and G. Placzek (reference 22) to account for the occurrence of a triplet line in the fluctuation scattering of light by liquids, and to calculate the line widths.

Integration over the angles then gives

$$G_d(r,t) \simeq \rho + (4\pi r_0^2 r)^{-1}\Psi[\kappa_0(\Lambda_0|t|)^{\frac{1}{2}}, r(\Lambda_0|t|)^{-\frac{1}{2}}], \tag{42}$$

where the function Ψ of two dimensionless arguments is defined by

$$\Psi(v,w) = 2\pi^{-\frac{1}{2}}\exp(-w^2) \times \int_0^\infty \exp(-x^2 - vx)\sinh(2wx)dx. \tag{43}$$

It is easily expressed in terms of the error integral:

$$\Psi(v,w) = \exp(\tfrac{1}{4}v^2 - vw)\cdot\psi(\tfrac{1}{2}v - w) - \exp(\tfrac{1}{4}v^2 + vw)\cdot\psi(\tfrac{1}{2}v + w),$$

$$\psi(x) = \frac{1}{\pi^{\frac{1}{2}}}\int_x^\infty \exp(-y^2)dy.$$

The behavior of G_d for large r and for large and small $|t|$ is immediately obtained from

$$\Psi(v,w) \simeq \exp(-vw), \qquad \text{for } w \gg 1,\ w \gg v; \tag{44}$$

$$\Psi(v,w) \simeq 4\pi^{-1/2}v^{-2}w\exp(-w^2), \quad \text{for } v \gg 1,\ v \gg w. \tag{45}$$

Equation (44) shows that the expression Eq. (42) reduces to Eq. (36) in the limit of $t \to 0$. Its strict validity is, however, restricted to values of $|t|$ large compared to the microscopic relaxation time T_0 considered before, since the phenomenological equations used in our derivation apply only to quantities averaged over a time interval large compared to the duration of microscopic fluctuations. This limitation accounts for the occurrence of a spurious discontinuity at $t=0$ in the derivative of the right-hand side of (42) with respect to t; this derivative, if calculated correctly for t of microscopic order of magnitude, would be found continuous and equal to zero at $t=0$. Apart from the condition $|t| \gg T_0$, the derivation of Eq. (42) requires of course $r_0\kappa_0 \ll 1$ and $r \gg r_0$ as for Eq. (36). It is, however, interesting that the latter condition can be abandoned for all times for which the expression (42) differs appreciably from its value (36) at $t=0$. Indeed, it follows from (41) that whenever $|t| \gg \Lambda_0^{-1}r_0^2$ the value of $G_d(r,t)$ for all r, even of order r_0, is overwhelmingly determined by the values of $G_d(r,0)$ for $r \gg r_0$. If now $|t|$ is not large enough to satisfy this condition

$$|t| \lesssim \Lambda_0^{-1}r_0^2,$$

we get

$$v \lesssim \kappa_0 r_0 \ll 1, \quad w \gtrsim r/r_0.$$

Hence, for $r \gg r_0$, the asymptotic form (44) of Ψ can be used, and $G_d(r,t) \simeq G_d(r,0)$ for $r \gg r_0$. To present this conclusion differently, we can say that as $|t|$ increases, the time dependence of the long-range part of G_d sets in only for times[26]

$$|t| \gg \Lambda_0^{-1}r_0^2 \sim (\chi_T/\chi_S)T_0 \sim (\kappa_0 r_0)^{-2}T_0 \gg T_0,$$

[26] The following estimate is made by using values of $\varkappa$, c_v, and χ_S calculated for rarefied gases, with the help of kinetic theory for $\varkappa$.

at which the short-range part of the pair distribution has completely reduced to the instantaneous value of the local macroscopic density, the variation of which is correctly described by Eq. (42) for all r. It is finally to be remarked that Λ_0^{-1} increases indefinitely when the critical point is approached, corresponding to an increasingly slower time variation of the macroscopic part of the pair correlation.

The above discussion is valid for monophasic systems near the critical point, i.e., for gases at densities near the critical density ρ_c and temperatures slightly above the critical temperature T_c. The relevant condition for its applicability is that the dimensionless quantity,

$$\kappa_0 r_0 = (\rho k_B T \chi_T)^{-\frac{1}{2}},$$

be small compared to one, let's say of order 0.1 or smaller. A more concrete idea about the corresponding density and temperature ranges is obtained by using the approximate expression for χ_T given by the van der Waals equation of state. One finds that at the critical density or a density differing from it by less than some 5 percent, one must have $T-T_c \lesssim 0.005 T_c$.[25]

For temperatures approaching T_c from below, the system is no longer monophasic at densities near ρ_c and the previous treatment is then not strictly applicable. It seems, however, likely that the long-range part of the pair distribution and its time variation will not be radically different from what we have found them to be for T above T_c.

Let us now indicate a few consequences of the above discussion for the scattering of neutrons by liquids and dense gases, for neutron wavelengths of the order of the separation between particles or larger. Away from critical conditions and apart from the forward elastic peak, which is entirely coherent, the differential cross section $d^2\sigma/d\Omega d\epsilon$ is a smooth function of outgoing energy and angle of scattering, corresponding to average momentum and energy transfers or order $\hbar R_0^{-1}$ and $\hbar T_0^{-1}$, respectively. This applies to coherent and incoherent scattering alike, although the collective properties of the liquid will evidently affect the scattering to a greater extent in the coherent case. Qualitative shapes to be expected for the angular and energy distribution could easily be obtained from Fig. 1 by Fourier transformation.

When critical conditions are approached, whereas no rapid change is expected to occur for incoherent scattering, the occurrence of a tail of increasing range in the pair distribution G_d reflects itself in an increasing amount of coherent scattering characterized by small momentum and energy transfers. Using for the latter our customary notations $\hbar\kappa$, $\hbar\omega$, we obtain by Fourier transformation of Eq. (41) over space and time [the Fourier transform over space gives the product of Eq. (39) by the Fourier transform of Eq. (36); one has then to make a Fourier transformation over time] the following expression,

$$\left(\frac{d^2\sigma_{\text{coh}}}{d\Omega d\epsilon}\right)_{\text{crit}} = \frac{4\langle a\rangle_{\text{Av}}^2 N}{\pi\hbar}\cdot\frac{k}{k_0}\cdot\frac{1}{r_0^2(\kappa^2+\kappa_0^2)}\cdot\frac{\Lambda_0\kappa^2}{\Lambda_0^2\kappa^4+16\omega^2}, \tag{46}$$

for the part of the differential cross section originating from long-range correlations. Near the critical point ($\kappa_0 r_0 \lesssim 0.1$), it is the main part of the cross section in the region $\kappa \ll r_0^{-1}$. From Eq. (46) this critical scattering is seen to have momentum and energy transfers of order $\kappa \sim \kappa_0$, $\omega \sim \Lambda_0\kappa_0^2/4$, respectively. Their relative magnitude compared to average momentum and energy transfers in noncritical scattering is easily estimated to be, very crudely,[26]

$$R_0\kappa_0 \sim (\rho k_B T \chi_T)^{-\frac{1}{2}},$$
$$\tfrac{1}{4} T_0 \Lambda_0 \kappa_0^2 \sim (R_0\kappa_0)^4 \sim (\rho k_B T \chi_T)^{-2}.$$

The most important feature revealed by this estimate is that in critical scattering, the energy transfers decrease very much faster than the momentum transfers when the critical point is approached, thus restoring the validity of the static approximation and causing the scattering to be not only more abundant than under normal conditions but also completely different in all its properties. The total cross section, for example, which under normal conditions is proportional to the incident neutron wavelength $2\pi/k_0$ as soon as the incident energy is small compared to $\hbar/T_0$,[27] has a completely different wavelength dependence in the immediate neighborhood of the critical point. Its main contribution comes then from the critical scattering represented by Eq. (46), which has to be integrated over outgoing energies and angles, with the result:

$$\sigma_{\text{coh}} \simeq \frac{\pi\langle a\rangle_{\text{Av}}^2 N}{(r_0 k_0)^2} \log\left(\frac{4k_0^2}{\kappa_0^2}+1\right). \tag{47}$$

Application of Eq. (46) at the critical point itself, where κ_0 and Λ_0 vanish, would lead to an infinite value for the total cross section (47). As was shown by Placzek for the case of light scattering,[28] the occurrence of this spurious conclusion is due to the fact that our entire treatment of scattering assumes the range of the pair correlations to be small compared to the dimensions of the vessel containing the system. We indeed have always assumed the system large enough to make surface effects negligible. Application of Eqs. (46) and (47) therefore requires κ_0^{-1} to be small compared to the dimensions of the vessel. Practically this condition is violated only in a temperature interval of $\sim 10^{-12}$ degree around T_c, in which the scattering would depend on the size and shape of the vessel.

We will not in the present paper consider the case of rarefied gases. The natural way of treating it is by an

[27] This dependence on incident wavelength follows directly from the presence of the denominator k_0 in Eq. (28).

[28] G. Placzek, Physik. Z. **31**, 1052 (1930).

expansion of G_s and G_d in powers of the density, entirely similar to the familiar expansion of the $g(r)$ function. The ideal Bose-Einstein and Fermi-Dirac gases will be considered in Sec. VI.

V. CRYSTALS

For crystals, the harmonic nature of the forces permits explicit calculations of the scattering cross sections and pair distributions. Such calculations have often been made for scattering.[29] We will here briefly derive the expressions for the $G(\mathbf{r},t)$ function, describing the correlations in position between any two particles of the crystal, and the $G_s(\mathbf{r},t)$ function, describing the correlation of a particle with itself. The calculation is most easily done by starting from Eq. (8), a fact generally valid for systems which have plane waves as independent modes of motion.

We restrict ourselves to a single crystal of infinite extension, with Bravais lattice (one atom per cell). The lattice vectors are denoted by $\mathbf{R}$, and the position vector of the particle with equilibrium position at $\mathbf{R}$ is written $\mathbf{R}+\mathbf{u}_R$.[30] Defining for each $\mathbf{R}$, including the origin $\mathbf{R}=0$ of the lattice, the pair distribution G_R for particles of equilibrium positions 0 and $\mathbf{R}$, we have

$$G=\sum_R G_R, \quad G_s=G_0. \tag{48}$$

From Eq. (8),

$$G_R(\mathbf{r},t)=(2\pi)^{-3}\int d\boldsymbol{\kappa}\cdot\exp\{-i\boldsymbol{\kappa}\cdot(\mathbf{r}-\mathbf{R})\}$$
$$\cdot\langle\exp\{-i\boldsymbol{\kappa}\cdot u_0(0)\}\cdot\exp\{i\boldsymbol{\kappa}\cdot\mathbf{u}_R(t)\}\rangle_T. \tag{49}$$

The Heisenberg operators are defined as usual. The subscript T indicates that the thermal distribution must be used in the definition (9) of the average.

We have first, since the commutator is a c number,

$$\langle\exp\{-i\boldsymbol{\kappa}\cdot\mathbf{u}_0(0)\}\cdot\exp\{i\boldsymbol{\kappa}\cdot\mathbf{u}_R(t)\}\rangle_T$$
$$=\langle\exp\{i\boldsymbol{\kappa}\cdot[\mathbf{u}_R(t)-\mathbf{u}_0(0)]\}\rangle_T\cdot$$
$$\cdot\exp\{\tfrac{1}{2}[\boldsymbol{\kappa}\cdot\mathbf{u}_0(0),\,\boldsymbol{\kappa}\cdot\mathbf{u}_R(t)]\}. \tag{50}$$

Next, in view of the fact that

$$\boldsymbol{\kappa}\cdot\{\mathbf{u}_R(t)-\mathbf{u}_0(0)\}$$

is a linear combination of coordinates of independent harmonic oscillators and has thus a Gaussian probability distribution,[31] the first factor in the right-hand side of Eq. (50) has the value

$$\exp\{-\tfrac{1}{2}\langle[\boldsymbol{\kappa}\cdot(\mathbf{u}_R(t)-\mathbf{u}_0(0))]^2\rangle_T\}.$$

Replacing the commutator in the second factor by its average, we get

$$\langle\exp\{-i\boldsymbol{\kappa}\cdot\mathbf{u}_0(0)\}\cdot\exp\{i\boldsymbol{\kappa}\cdot\mathbf{u}_R(t)\}\rangle_T$$
$$=\exp\{-\sum_{\beta,\gamma}[M_{\beta\gamma}(0,0)-M_{\beta\gamma}(\mathbf{R},t)]\kappa_\beta\kappa_\gamma\}, \tag{51}$$

where $\beta,\gamma=x,\,y,\,z$ and

$$M_{\beta\gamma}(\mathbf{R},t)=M_{\gamma\beta}(\mathbf{R},t)=\langle u_0{}^\beta(0)u_R{}^\gamma(t)\rangle_T. \tag{52}$$

Inserting into (49), we get

$$G_R(\mathbf{r},t)=\{N(\mathbf{R},t)/8\pi^3\}^{\frac{1}{2}}$$
$$\times\exp\{-\tfrac{1}{2}\sum_{\beta,\gamma}N_{\beta\gamma}(\mathbf{R},t)(r_\beta-R_\beta)(r_\gamma-R_\gamma)\}, \tag{53}$$

with the 3×3 matrix $N_{\beta\gamma}(\mathbf{R},t)$ defined as the inverse of

$$2\{M_{\beta\gamma}(0,0)-M_{\beta\gamma}(\mathbf{R},t)\},$$

and with

$$N(\mathbf{R},t)=\det\{N_{\beta\gamma}(\mathbf{R},t)\}.$$

Equation (53) is a Gaussian distribution around the equilibrium position $\mathbf{R}$. For $t\neq0$ it has complex coefficients, the imaginary parts of which are of quantum origin.[32]

The correlation equation (52) between displacements is easily calculated using the functions $\omega_j(\mathbf{q})$, $\mathbf{e}_j(\mathbf{q})$ which express the frequency and unit vector of polarization of a plane-wave vibration (phonon) in terms of the wave vector $\mathbf{q}$ and the polarization index $j=1,\,2,\,3$. One finds

$$M_{\beta\gamma}(\mathbf{R},t)=\{\hbar v_0/(16\pi^3M)\}$$
$$\times\sum_j\int d\mathbf{q}\{e_j{}^\beta(\mathbf{q})e_j{}^\gamma(\mathbf{q})/\omega_j(\mathbf{q})\}\cdot\{1-\exp(-\hbar\beta\omega_j(\mathbf{q})\}^{-1}$$
$$\cdot\{\exp[-i(\mathbf{R}\cdot\mathbf{q}-t\omega_j(\mathbf{q}))]+\exp[-\hbar\beta\omega_j(\mathbf{q})]$$
$$\times\exp[i(\mathbf{R}\cdot\mathbf{q}-t\omega_j(\mathbf{q}))]\}, \tag{54}$$

where M is the atomic mass of the crystal, v_0 the volume of the cell, β^{-1} the quantity k_BT and where the integration is extended over a cell of the reciprocal lattice.[33] As functions of $\mathbf{q}$, ω_j, and $\mathbf{e}_j$ have the periodicity of the reciprocal lattice.

Equation (54) shows that $M_{\beta\gamma}(\mathbf{R},t)$ approaches zero when R or $|t|$ increase indefinitely. $N_{\beta\gamma}(\mathbf{R},t)$ approaches then the inverse $N_{\beta\gamma}{}^{(\infty)}$ of the real matrix $2M_{\beta\gamma}(0,0)$. Hence, asymptotically, for large $|t|$ or for large R but finite $|\mathbf{r}-\mathbf{R}|$,

$$G_R(\mathbf{r},t)\simeq G_R{}^{(\infty)}(\mathbf{r})=\{N^{(\infty)}/8\pi^3\}^{\frac{1}{2}}$$
$$\times\exp\{-\tfrac{1}{2}\sum_{\beta,\gamma}N_{\beta\gamma}{}^{(\infty)}(r_\beta-R_\beta)(r_\gamma-R_\gamma)\}.$$

[29] A. fairly complete list of references is given in G. Placzek and L. Van Hove, Phys. Rev. **93**, 1207 (1954). The unpublished work of R. J. Glauber (reference 10), which makes use of the correlations (52) below, must also be mentioned.

[30] When in subscript, R stands for the vector $\mathbf{R}$.

[31] This theorem is due to F. Bloch, Z. Physik **74**, 295 (1932), especially footnote on p. 309.

[32] The above method for the calculation of scattering cross sections or pair distributions is applicable quite generally to systems with harmonic forces. Its main advantage is the very brief derivation of Eq. (51) based on Bloch's theorem. Alternative methods found in the literature are less general or more laborious: they have to rederive Bloch's theorem in disguised form.

[33] We define here the reciprocal lattice vectors as the vectors whose inner products with the vectors $\mathbf{R}$ of the crystal lattice are integral multiples of 2π.

This equation expresses the asymptotic vanishing of correlations between particles with widely separated equilibrium positions, and between neighboring particles considered at widely separated times.

For $t=\pm\infty$, the limiting values of the pair distributions Eq. (48) are thus

$$G(\mathbf{r},\infty)=\sum_R G_R^{(\infty)}(\mathbf{r}), \tag{55}$$

$$G_s(\mathbf{r},\infty)=G_0^{(\infty)}(\mathbf{r}). \tag{56}$$

The elastic part of coherent and incoherent neutron scattering follows immediately by insertion into Eqs. (28) and (29):

$$\left(\frac{d^2\sigma_{\text{coh}}}{d\Omega d\epsilon}\right)_{\text{el}}=\left[\langle a\rangle_{\text{Av}}^2\frac{(2\pi)^3N}{\hbar v_0}\right]\times\exp\{-\sum_{\beta,\gamma}M_{\beta\gamma}(0,0)\kappa_\beta\kappa_\gamma\}\delta(\omega)\sum_{\boldsymbol{\alpha}}\delta(\boldsymbol{\kappa}-\boldsymbol{\alpha}),$$

$$\left(\frac{d^2\sigma_{\text{incoh}}}{d\Omega d\epsilon}\right)_{\text{el}}=\left[(\langle a^2\rangle_{\text{Av}}-\langle a\rangle_{\text{Av}}^2)\frac{N}{\hbar}\right]\times\exp\{-\sum_{\beta,\gamma}M_{\beta\gamma}(0,0)\kappa_\beta\kappa_\gamma\}\delta(\omega).$$

It contains the familiar Debye-Waller factor and, in the coherent case, the interference condition $\boldsymbol{\kappa}=\boldsymbol{\alpha}$, where $\boldsymbol{\alpha}$ denotes the vectors of the reciprocal lattice.[33] The cross sections for inelastic scattering can be derived from the difference between G, G_s and their asymptotic values (55), (56); one obtains then immediately expressions previously derived by Glauber.[10]

It is of some interest to study the nature of the convergence of G and G_s toward their asymptotic limits. G is found to approach (55) both for $|t|\to\infty$, r fixed and for $r\to\infty$, t fixed, the convergence being in $|t|^{-3/2}$ in the former case, in r^{-1} in the latter. G_s approaches (56) for $|t|\to\infty$, with a convergence in $|t|^{-3/2}$. The convergence is very slow in all cases. As seen from Eqs. (28) and (29), this fact is closely related to the occurrence of singularities in the angular and energy distribution of neutrons scattered inelastically by a single crystal; these singularities have been studied in detail elsewhere.[34] The convergence of the pair distributions for large $|t|$ has also another important physical significance: it implies that the crystal, despite its over-all lack of ergodicity, exhibits locally a type of ergodic behavior, the return toward local equilibrium being in $|t|^{-3/2}$.[35]

We will here restrict ourselves to establishing the law of asymptotic convergence of pair distributions for $|t|\to\infty$. This law is entirely determined by certain special crystal vibrations, already met before in connection with the frequency distribution function of the crystal.[36] Applying the result thus obtained to G_s, we will then establish in an indirect way the existence, asserted before without proof,[34] of singularities in the energy distribution of incoherently scattered neutrons.

The convergence of G_R to $G_R^{(\infty)}$ is determined by the convergence of $M_{\beta\gamma}(\mathbf{R},t)$ to 0 for $|t|\to\infty$, which according to Eq. (54) is to be discussed by the method of stationary phases. For large $|t|$, the main contribution to the integral in (54) comes from the neighborhood of the points $\mathbf{q}_c$ where for some $j=j_c$,

$$\text{grad}\,\omega_j(\mathbf{q})=0. \tag{57}$$

It has been shown that such points always exist for general values of the force constants of the crystal.[36] Their existence is implied by the periodicity of $\omega_j(\mathbf{q})$ in $\mathbf{q}$. In suitable local coordinates preserving the volume element $d\mathbf{q}$, the expansion of $\omega_{j_c}(\mathbf{q})$ near $\mathbf{q}_c$ can be written

$$\omega_{j_c}(\mathbf{q})=\omega_c+a_c\sum_{\beta=1,2,3}\epsilon_\beta^c\xi_\beta^2+\cdots,\quad \xi=\mathbf{q}-\mathbf{q}_c,$$

with $\omega_c=\omega_{j_c}(\mathbf{q}_c)$, $\epsilon_\beta^c=\pm1$, $a_c>0$. Inserting in (54) and carrying out the integration over ξ, one gets for $M_{\beta\gamma}(\mathbf{R},t)$ the asymptotic form:

$$M_{\beta\gamma}(\mathbf{R},t)\simeq\{\hbar v_0/(16\pi^3M|t|^3)\}\sum_c\{e_{j_c}^\beta(\mathbf{q}_c)e_{j_c}^\gamma(\mathbf{q}_c)/(a_c^3\omega_c)\}\{1-\exp(-\hbar\beta\omega_c)\}^{-1}\{\exp(-i\mathbf{R}\cdot\mathbf{q}_c)\mathcal{E}_c(t)+\exp(-\hbar\beta\omega_c+i\mathbf{R}\cdot\mathbf{q}_c)\mathcal{E}_c^*(t)\}, \tag{58}$$

with

$$\mathcal{E}_c(t)=\exp[it\omega_c+i(\pi/4)(t/|t|)\textstyle\sum_\beta\epsilon_\beta^c].$$

$\mathcal{E}_c^*$ is the complex conjugate of $\mathcal{E}_c$. The sum $\sum_c$ extends over all solutions of Eq. (57). The decrease of $M_{\beta\gamma}$ for large $|t|$ is seen to be in $|t|^{-3/2}$. From (58) it is now an elementary matter to find the following asymptotic formula for G_R:

$$G_R(\mathbf{r},t)-G_R^{(\infty)}(\mathbf{r})\simeq G_R^{(\infty)}(\mathbf{r})\,|t|^{-3/2}\times\sum_c\{P_c(\mathbf{r})\mathcal{E}_c(t)+P_c'(\mathbf{r})\mathcal{E}_c^*(t)\}. \tag{59}$$

P_c and P_c' denote polynomials of second degree in the components of $\mathbf{r}$. Their explicit expression is not needed for our purpose. The asymptotic convergence of G_R, and thus of G and G_s, is again in $|t|^{-3/2}$.

Through the Fourier transform over t in Eq. (29), each term of the expression (59), taken for $\mathbf{R}=0$, contributes a singularity to the energy distribution of incoherently scattered neutrons. The analytic nature of the singularity is best obtained by Fourier transformation of simple functions of t with asymptotic behavior $|t|^{-3/2}\mathcal{E}_c(t)$ or $|t|^{-3/2}\mathcal{E}_c^*(t)$ for large $|t|$. We take for example the function,

$$f_c(t)=|t|^{-3/2}\mathcal{E}_c(t)(1\pm i\alpha/t)^{-3/2},$$

where $\alpha>0$ and the upper (lower) sign is taken when $\epsilon_c=\sum_\beta\epsilon_\beta^c=3$ or -1 (-3 or 1). It has the following

[34] See G. Placzek and L. Van Hove, reference 29.

[35] Properties of local ergodicity have been studied for a one-dimensional system of particles with harmonic interaction between nearest neighbors by G. Klein and I. Prigogine, Physica **19**, 1053 (1953).

[36] L. Van Hove, Phys. Rev. **89**, 1189 (1953).

Fourier transform:[37]

$$\tilde{f}_c(\omega)=\int_{-\infty}^{\infty} e^{-i\omega t} f_c(t)\,dt=\begin{cases}\tilde{f}(\omega-\omega_c) \text{ for } \epsilon_c=3\\ -\tilde{f}(\omega_c-\omega) \text{ for } \epsilon_c=1\\ -\tilde{f}(\omega-\omega_c) \text{ for } \epsilon_c=-1\\ \tilde{f}(\omega_c-\omega) \text{ for } \epsilon_c=-3\end{cases},$$

with

$$\tilde{f}(\omega)=\begin{cases}0 \text{ for } \omega<0\\ 4(\pi\alpha)^{\frac{1}{2}}\exp(-\alpha\omega) \text{ for } \omega>0.\end{cases}$$

Hence, in the energy distribution of neutrons scattered in an arbitrary direction, the term in $\mathcal{E}_c(t)$ of (59) produces a singularity at $\omega=\omega_c$: near $\omega=\omega_c$, the energy distribution has the form $A\tilde{f}_c(\omega)+F(\omega)$, where A is a constant and $F(\omega)$ a continuous function, the first derivative of which has at most a finite discontinuity at $\omega=\omega_c$. Both A and F depend on the scattering direction. One can easily show that the scattering processes responsible for this singularity involve excitation by the neutron of one phonon of wave vector $\mathbf{q}_c$ and polarization j_c.[38] Similarly, the term in $\mathcal{E}_c^*(t)$ produces a singularity at $\omega=-\omega_c$, with an energy distribution of form $A'\tilde{f}_c(-\omega)+F'(\omega)$, where A' and F' have meanings similar to A and F. This singularity is due to annihilation by the neutron of one phonon again characterized by $\mathbf{q}_c$ and j_c.

VI. IDEAL QUANTUM GASES

To illustrate the effect of Bose-Einstein and Fermi-Dirac statistics on pair correlations we treat very briefly the case of ideal quantum gases. It is instructive to consider particles with nonvanishing spin and to study simultaneously the correlations imposed by the statistics on particle positions and on spin orientations. This is done by calculating the spin-dependent pair distribution function Γ defined in Eq. (24); a_j is an arbitrary function of the jth particle spin, the same function for each particle.

The expressions of Γ for the Fermi gas and for the Bose gas without condensed phase are very similar and their derivation, to be based on the analog of Eq. (8) for Γ, is quite straightforward. Only the final result will be given here:

$$\Gamma(\mathbf{r},t)=\rho\langle a^2\rangle_N\{f(\mathbf{r},t)\pm(2s_0+1)^{-1}n_\mp(\mathbf{r},t)\}\cdot\{n_\mp(\mathbf{r},t)\}^*+\rho\langle a\rangle_N^2. \quad (60)$$

The upper and lower signs refer to Bose and Fermi particles, respectively. The averages $\langle a^2\rangle_N$ and $\langle a\rangle_N^2$ have the same meaning as in Eq. (25). s_0 is the spin of the particles in units of $\hbar$. The functions f and $n_\pm$ are defined by

$$f(\mathbf{r},t)=(2\pi)^{-3}\rho^{-1}\int\exp\{-i(\mathbf{k}\cdot\mathbf{r}-\omega_k t)\}\,d\mathbf{k}$$

$$=-\frac{2}{\rho}\left(1-i\frac{|t|}{t}\right)\left(\frac{M}{4\pi\hbar|t|}\right)^{\frac{3}{2}}\exp\left(-\frac{iMr^2}{2\hbar t}\right),$$

$$n_\mp(\mathbf{r},t)=(2\pi)^{-3}\rho^{-1}\int\exp\{-i(\mathbf{k}\cdot\mathbf{r}-\omega_k t)\}\cdot\{B\exp(\hbar\beta\omega_k)\mp1\}^{-1}d\mathbf{k}. \quad (61)$$

M is the mass of the particles, β is $(k_BT)^{-1}$, and ω_k stands for $\hbar k^2/2M$. The constant $B\geqslant\frac{1}{2}(1\pm1)$ is determined by $n_\mp(0,0)=1$.

According to Eq. (60), the range of the pair correlations in space and time is determined by the convergence of $n_\mp$ to zero for r or $t\to\infty$. This convergence can be discussed in all cases from Eq. (61). We consider here only the case $B>1$, for which expansion in powers of B^{-1} gives

$$n_\mp(r,t)\simeq\rho^{-1}\left(\frac{M}{2\pi\hbar}\right)^{\frac{3}{2}}\sum_{l=1}^{\infty}\frac{(\pm1)^{l-1}}{B^l(l t_T-it)^{\frac{3}{2}}}\times\exp\left\{-\frac{Mr^2}{2\hbar(l t_T-it)}\right\}, \quad (62)$$

where $t_T=\hbar\beta=\hbar/(k_BT)$ is a measure of the relevant relaxation time. For B not too close to one, an estimate of the spatial range of the pair correlations is obtained from the first term of the series. It gives

$$r\sim(h/M)^{\frac{1}{2}}(t_T^2+t^2)^{\frac{1}{4}},$$

and for $t\lesssim t_T$, reduces essentially to the mean de Broglie wavelength $(h^2\beta/2M)^{\frac{1}{2}}=\lambda_B$. The expansion Eq. (62) becomes impractical when B is close to one, in particular for the Bose gas. For the latter and for $0<B-1\ll1$ a more convenient expression has been obtained by Placzek[39] for $n_-(r,0)$; it can be used for $n_-(r,t)$ by introducing it into the identity,

$$n_\mp(r,t)=\rho\int n_\mp(r',0)f(|\mathbf{r}-\mathbf{r}'|,t)\,d\mathbf{r}',$$

and shows that the correlation range becomes of order $(B-1)^{-1/2}\lambda_B$, thus increasing indefinitely as condensation is approached.

From Eq. (60) the difference between Γ and its asymptotic value $\rho\langle a\rangle_N^2$ is seen to depend on the spin through $\langle a^2\rangle_N$ only. This fact is obviously due to the absence of spatial correlation between particles in different spin states. Applied to neutron scattering by

[37] The various cases correspond to the possible signatures of the stationary point of $\omega_{j_c}(\mathbf{q})$ at $\mathbf{q}_c$: minimum, saddle point of one of two types, maximum, respectively.

[38] This is shown for cubic crystals in reference 34.

[39] G. Placzek, Proceedings of the Second Berkeley Symposium on Mathematical Statistics and Probability (University of California Press, Berkeley, 1951), pp. 581–588, especially Eq. (36).

nuclei with spin-dependent scattering length a, it illustrates how little sense is made by the conventional terminology of calling coherent (or incoherent) the part of the scattering containing $\langle a\rangle_{\rm Av}^2$ (or $\langle a^2\rangle_{\rm Av}-\langle a\rangle_{\rm Av}^2$), as soon as some correlation exists between spins, resulting either from symmetry requirements of the wave function or from spin interactions. It is only for systems of Boltzmann particles with free nuclear spins that this terminology is physically reasonable.[40]

For a Bose gas in the condensation region, the pair distribution Γ has the following expression:

$$\Gamma(\mathbf{r},t)=\rho\langle a^2\rangle_{\rm Av}[\{f(\mathbf{r},t)+(2s_0+1)^{-1}(n(\mathbf{r},t)+n_0)\}\cdot(n(\mathbf{r},t)+n_0)^*-(2s_0+1)^{-1}n_0^2]+\rho(\langle a^2\rangle_{\rm Av}-\langle a\rangle_{\rm Av}^2)\times(2s_0+2)^{-1}n_0^2+\rho\langle a\rangle_{\rm Av}^2. \quad (63)$$

The function f is the same as above; n and n_0 are defined by

$$n(\mathbf{r},t)=(2\pi)^{-3}\rho^{-1}\int \exp\{-i(\mathbf{k}\cdot\mathbf{r}-\omega_k t)\}\cdot\{\exp(\hbar\beta\omega_k)-1\}^{-1}d\mathbf{k},$$

$$n_0=1-n(0,0)=1-(\rho_c/\rho),$$

where ρ_c is the condensation density at temperature T. The quantity $\rho-\rho_c=n_0\rho$, supposed to be positive, is the density of the condensed phase. The asymptotic behavior of n is easily shown to be in λ_T/r for $r\to\infty$ and in $(t_T/|t|)^{\frac{3}{2}}$ for $t\to\infty$.

In the derivation of Eq. (63), the only point which is not quite elementary is the calculation of the thermal average $\langle N_\alpha N_\beta\rangle$, where N_α, N_β denote the number of particles of momentum zero in spin states α, β ($\alpha,\beta=1,\cdots 2s_0+1$). With the help of generating functions for the distribution of values of the N_α's, one easily shows that

$$\langle N_\alpha N_\beta\rangle=\frac{2s_0+1}{2s_0+2}\langle N_\alpha\rangle^2-\frac{1}{2s_0+1}\langle N_\alpha\rangle, \quad (\alpha\neq\beta)$$

$$\langle N_\alpha^2\rangle=2\frac{2s_0+1}{2s_0+2}\langle N_\alpha\rangle^2+\frac{2s_0}{2s_0+2}\langle N_\alpha\rangle.$$

In the right-hand sides, the second terms can be neglected in comparison with the first ones in the limit of an infinite number of particles.

In the special case $t=0$, $a_j=1$, Eqs. (60) and (63) reduce to the instantaneous pair distributions derived for ideal quantum gases by London.[41]

VII. CONCLUDING REMARKS

Our aims have been to introduce the time-dependent generalization of the familiar pair distribution function, to indicate its interest from the standpoint of statistical mechanics, and to establish its role in scattering theory, showing at the same time how slow neutron scattering makes it experimentally accessible.

The use of scattering experiments for the study of the pair distribution in space and time seems to us to be of real interest for systems of nontrivial and poorly known dynamical properties, mainly liquids and dense gases. It is our hope that increasingly complete and accurate data on such systems will become available. The case of liquid helium, with its marked quantum properties and its complex-valued pair distribution, undoubtedly deserves special attention.[42]

From the theoretical standpoint, the determination of the $g(\mathbf{r})$ function in terms of the intermolecular forces is well known to be a difficult and challenging problem for liquids and dense gases. Both the difficulty and the theoretical interest of a determination of the time-dependent pair distribution are likely to be greater, in view of the fact that the relaxation properties of the system are involved. On a more modest scale, approximate discussions of the time dependence of G, based on suitable models, would probably be instructive and might provide considerable help in the analysis of scattering experiments, since for some time to come, complete angular and energy distributions will not be readily measurable.

The author wishes to express his gratitude to Dr. G. Placzek for many stimulating discussions and suggestions on the various aspects of the present work.

[40] This remark holds of course also for isotope disorder. Other terminologies, introduced by G. C. Wick, Physik. Z. **38**, 689 (1937), and J. M. Cassels, Progr. Nuclear Phys. **1**, 185 (1950), have the same limitation.

[41] F. London, J. Chem. Phys. **11**, 203 (1943).

[42] Theoretical discussions of neutron scattering for various models of liquid helium have been given by A. Akhiezer and I. Pomeranchuk, J. Phys. (U.S.S.R.) **9**, 461 (1945); Goldstein, Sweeney, and Goldstein, Phys. Rev. **77**, 319 (1950); L. Goldstein and D. W. Sweeney, Phys. Rev. **80**, 141 (1950).

Theory of Unstable Heavy Particles*

HIROSHI ENATSU,† *Department of Physics, Columbia University, New York, New York*

AND

HIROICHI HASEGAWA AND PONG YUL PAC, *Department of Physics, Kyoto University, Kyoto, Japan*

(Received May 1, 1953; revised manuscript received November 24, 1953)

In order to explain the nature of unstable heavy particles which are found in the penetrating components of cosmic rays, a possible model is presented. A mass relation for elementary particles is derived from the conditions for the elimination of divergences of the nucleon and heavy-nucleon self-energies. By choosing a suitable set of interactions, the lifetimes of these particles are calculated. Their production is evaluated, and their contribution to the magnetic moments of nucleons is also discussed. It is found that the predictions of the present theory are not qualitatively at variance with experimental results.

INTRODUCTION

THE results of several experiments[1] on the nature of particles in the penetrating component of cosmic rays indicate the presence of unstable heavy particles which have long lifetimes and which seem to be produced with comparatively large cross section. That is, they have lifetimes $\sim 10^{-9}-10^{-10}$ sec, and their abundance in nature is about 1/100 that of π mesons.

Attempts to account for these results in terms of current field theory have been made by many authors.[2,3] In particular, in his paper on the so-called V particles, Pais[3] put forward a theory in a general and purely deductive manner without referring to any particular set of interactions. Since the results obtained are promising, there appears to be general acceptance of the ideas involved. However, it was felt that because there was no satisfactory indication of the masses of the new particles, further investigations should be pursued in connection with the problem of the mass spectrum.

With regard to the last point, one of the present authors[4] has suggested a new theory of cohesive mesons which are responsible for the elimination of the nucleon self-energy divergences by π mesons, and which lead to a mass relation for some of the unstable heavy particles. Indeed, it appears that this theory would lead to values of the masses which are in qualitative agreement with those of V particles, notwithstanding the uncertainty attached to the present field theory and to the method of approximation. Since the possibility of identifying V particles with the particles anticipated by this theory is still open, it is necessary to investigate more closely their lifetimes for disintegration into lighter particles, their production rates, and other properties.

The purpose of the present paper is to find a model which leads to results in comparison with the majority of the experimental facts concerning the nature of V particles. Our survey differs slightly from those of other authors in that the coupling scheme is specified as far as possible. We shall show that by a suitable choice and by consideration of previous results, at least the neutral V particle problem may be well treated by means of a simple but definite model.

MASS RELATION

Several experiments in a number of different laboratories have shown evidence of the existence of various new particles. These facts seem to be of decisive importance for the development of quantum field theory. Up to now, however, no attempt has been made to solve the problem of mass quantization. In this connection, it was first suggested by Nambu[5] that, together with nucleons, π mesons, and μ mesons, the mass values of new particles correlate in an interesting fashion to Sommerfeld's fine structure constant α. That is, if all mass values are multiplied by α, the results will approximately be equal to the integers or half-integers which are shown in Table I. An interesting correspondence exists between these mass numbers and the statistics of elementary particles mentioned above: the boson possesses an integral value and the fermion has

TABLE I. Masses of elementary particles and magic numbers.

Particle	e	μ	π	ζ	ν	τ	χ	N	V
Mass	1	210	276	~550	~800	977	~1470	1836	~2200
Mass/137 (nearest integer or half-integer)	0.008	1.5	2.0	4.0	6.0	7.0	{10.5 {11.0	13.5	{16.0 {16.5

* A preliminary presentation of this work was made by H. Enatsu, Phys. Rev. **85**, 483 (1952).

† Now at Kyoto University, Kyoto, Japan.

[1] Report on Copenhagen Conference, June, 1952 (unpublished). Proceedings of the Third Annual Rochester Conference on High Energy Physics, 1952 (Interscience Publishers, Inc., New York, 1953).

[2] Nambu, Nishijima, and Yamaguchi, Progr. Theoret. Phys. Japan **6**, 615, 619 (1951); K. Aidzu and T. Kinoshita, Progr. Theoret. Phys. Japan **6**, 630 (1951); H. Miyazawa, Progr. Theoret. Phys. Japan **6**, 630 (1951); S. Oneda, Progr. Theoret. Phys. Japan **6**, 633, 1015 (1951); R. Sachs, Phys. Rev. **84**, 305 (1951); D. C. Peaslee, Phys. Rev. **86**, 127 (1951); H. P. Noyes, Phys. Rev. **87**, 344 (1952); R. J. Finkelstein, Phys. Rev. **88**, 555 (1952).

[3] A. Pais, Phys. Rev. **86**, 663 (1952).

[4] H. Enatsu, Progr. Theoret. Phys. Japan **6**, 643 (1951); Phys. Rev. **85**, 483 (1952); **89**, 1304 (1953). These papers will be referred to as I, II, and III, respectively.

[5] Y. Nambu, Progr. Theoret. Phys. Japan **7**, 595 (1952); and T. Inoue (private communication).

a half-integral value, while this rule is not applicable to the electron itself. We desire to make a modification of the above description as follows: "This scheme of mass magic numbers for elementary particles is provided when they are measured in Heisenberg's natural units ($\hbar=c=r_0=1$) where $r_0=2.8\times10^{-13}$ cm is the classical electron radius." This can easily be seen by the fact that the mass of the electron is 1/137 in Heisenberg's units. One must recognize at this point that, as stressed by Heisenberg, the classical electron radius r_0 has a universal significance. An interpretation of these magic mass numbers as fundamental numbers of field theory has not yet been found.

It thus appears that, so far as the mass spectrum is concerned, the situation is in some respects analogous to the case of the optical spectrum in the pre-Bohr epoch, and the mass spectrum suggests a profound relation between elementary particles, which is entirely lacking in the current quantum theory of fields.

As previously noted, one of the present authors (H.E.)[4] pointed out an intimate relation between masses of elementary particles by setting up conditions to compensate divergences in the self-energies of nucleons. Since the argument presented there is incomplete, we will supplement it here with a fuller account and some minor modifications. The method of mixed fields for the nucleon, in terms of which the compensation of the diverging parts of the self-energy would be achieved, was worked out in detail by Pais.[6] At that time it seemed to be of academic interest only. In several instances, however, recent observations have confirmed the existence of numerous unstable particles. Under these circumstances, the introduction of the so-called realistic viewpoint for the self-energy problem[7] is again required. Indeed, the experimental evidence reveals that the V particles are created and annihilated as the result of a nuclear interaction in which the electromagnetic field is of minor importance. This suggests that it would be useful to try to carry out a compensation program for the self-energy of nucleons due to π mesons, although the realistic viewpoint is unfavorable for the solution of the problem involving vacuum polarization. Furthermore, the particular stability of the proton makes it attractive. Thus, applying the recent covariant formalism, an attempt along this direction was made by one of us[4] as a representative case of mixed fields.

In the first place, we tentatively assume that π mesons are of the symmetrical pseudoscalar type with pseudovector coupling (for simplicity here we take a neutral form)

$$L_1=-i\left(\frac{g}{\kappa_0}\right)\bar{\psi}_N\gamma_5\gamma_\nu\psi_N\frac{\partial\phi_\pi}{\partial x_\nu}+\text{h.c.},\quad \kappa_0=\kappa c/\hbar. \tag{1}$$

Of course, we have some doubts about the type and coupling of π mesons, especially of the neutral π meson; but as for the theoretical situation, it may be stated at the present stage that conclusions derived from the assumption that the π meson is of pseudoscalar type are not inconsistent with the experimental results. The justification for such a postulate of a symmetrical nature for π mesons will depend on further development of theory and experiment. Here we shall invoke the principle of simplicity. The calculations of nucleon self-energies have been performed by the Feynman-Dyson techniques with inclusion of the so-called translation effects, which were described fully in paper I. Unfortunately, the present field theory contains some ambiguities. Thus, the method adopted there is not completely satisfactory. A practical advantage of the present field-theoretical method is that it leads us to results which are in agreement with observation when used for the calculation of physical processes in quantum electrodynamics such as the Lamb shift and the additional spin magnetic moment of electron. One may say, therefore, that this attempt to find a mass relation of elementary particles is of heuristic character.

Next, we consider the case of cohesive mesons (c mesons, for short) for π mesons. Generally, as was shown in I, the self-energy of a nucleon arising from a coupling with the matrix γ_5 has opposite sign to that from the corresponding coupling without it. This is true exactly for the spin-zero meson field with an interaction of ordinary type. Thus, cohesive scalar mesons with vector coupling should be chosen to cancel out divergences caused by π mesons which include quadratic and logarithmic parts.

By using the following interaction, the compensation problem was solved in I,

$$L_2'=-i\left(\frac{G}{\mu_0}\right)\bar{\psi}_N\gamma_\nu\psi_N\frac{\partial\phi_c}{\partial x_\nu}+\text{h.c.},\quad \mu_0=\frac{\mu c}{\hbar}. \tag{2}$$

The convergence relations have been expressed in a simple way, namely,

$$G^2=3\left(\frac{\mu}{\kappa}\right)^2g^2, \tag{3}$$

and

$$8m^2+75\kappa^2-15\mu^2=0,\quad (m=1836m_e). \tag{4}$$

It was found that the theory in its original form gave us an interesting mass for the c meson, i.e., $\mu=1474m_e$, which seemed to be within the limit of error of recent experimental determinations of the masses of new particles. One might try to take the point of view that, since the mass obtained does not differ too much from the observed mass and the V particle is not involved in our model, a modification in the right direction might be made by changing slightly one of the nucleon masses in the intermediate states. In an attempt to see how this may be done, we observed that, in the c meson case, its mass could be reduced by assuming still heavier masses of intermediate-state nucleons. As to the interaction (1) itself, no change will be necessary.

[6] A. Pais, Verhandel. Koninkl. Akad. Wetenschap. Amsterdam Afdeel Natuurk. **19**, 1 (1947).
[7] W. Pauli and F. Villars, Revs. Modern Phys. **21**, 434 (1949).

In this way, it seems plausible to require that the interaction scheme (2) should be replaced by the following modified expression:

$$L_2=-i\left(\frac{G}{\mu_0}\right)\bar{\psi}_V\gamma_\nu\psi_N\frac{\partial\phi_c}{\partial x_\nu}+\text{h.c.}, \tag{5}$$

of which the prototype was originally assumed by Nambu *et al.* and Oneda.[2] Here ψ_V is the wave function of the V particle. The diverging parts of the self-energy of a nucleon arising from the interactions (1) and (5) become

$$\delta m_\pi=m\left(\frac{g^2}{4\pi\hbar c}\right)\left(\frac{m}{\kappa}\right)^2\left\{\left(\frac{-3}{8\pi}\right)\frac{KK_0}{M^2}+\left(\frac{1}{120\pi}\right)\left(75\frac{\kappa^2}{m^2}+65\right)\log(K+K_0)M^{-1}\right\}, \tag{6}$$

and

$$\delta m_c=m\left(\frac{G^2}{4\pi\hbar c}\right)\left(\frac{m}{\mu}\right)^2\left\{\left(\frac{1}{8\pi}\right)(2\beta-1)\frac{KK_0'}{M^2}+\left(\frac{1}{120\pi}\right)\left(-20\beta^3+25\beta^2-22\beta-2+35\frac{\mu^2}{m^2}-40\beta\frac{\mu^2}{m^2}\right)\times\log(K+K_0')M_1^{-1}\right\}, \tag{7}$$

where

$$M=\frac{mc}{\hbar},\quad M_1=\frac{m_1c}{\hbar},\quad \beta=\frac{m_1}{m},$$
$$K_0=(K^2+M^2)^{\frac{1}{2}},\quad K_0'=(K^2+M_1^2)^{\frac{1}{2}},\quad K\to\infty, \tag{8}$$
$$m_1=\text{mass of the } V \text{ particle}.$$

As was shown in II, the convergence relations are

$$G^2=N\left(\frac{3}{2\beta-1}\right)\left(\frac{\mu}{\kappa}\right)^2g^2, \tag{9}$$

and

$$\frac{\mu^2}{m^2}=\frac{1}{120\beta-105}\left\{(2\beta-1)\left(75\frac{\kappa^2}{m^2}+65\right)-(60\beta^3-75\beta^2+66\beta+6)\right\}. \tag{10}$$

The factor N has a numerical value 1 or 3 according to whether the c meson obeys the symmetrical theory or the neutral theory, because in the symmetrical theory we assume that $g^2=g_{\text{ch}}{}^2=2g_{\text{neut}}{}^2$. Although at present there is a remarkable lack of symmetry regarding the charge properties of observed particles, it seems also plausible that the limited evidence available could be reconciled with the assumption of charge symmetry. Whichever we may choose, it is evident that our theory gives the same mass relation for each of them. Taking the V masses as $2200m_e-2400m_e$, it is found that the corresponding c meson masses are $1040m_e-800m_e$.

The interaction (5) gives us a divergent self-energy of the V particle. However, as was shown in III, if we assume the coupling

$$L_3=-i\left(\frac{L}{\kappa_0}\right)\bar{\psi}_V\gamma_5\gamma_\nu\psi_V\frac{\partial\phi_\pi}{\partial x_\nu}+\text{h.c.}, \tag{11}$$

we can eliminate this difficulty. In this case, the convergence conditions are given by the following substitutions in (9) and (10), because we assume a complete symmetry between nucleon and heavy nucleon in the expressions (1), (5), and (11):

$$g\to L,\quad m\to m_1,\quad m_1\to m.$$

The numerical values for the masses of these particles were given more fully in III.

Having thus obtained some of the mass relations, we shall here discuss some problems connected with them. The first question which arises is the extent to which the ordinary perturbation method furnishes reliable answers apart from the ambiguities mentioned above. That perturbation theory is not applicable to meson theory is well known. Although the results are uncertain because of the largness of the coupling constants and most likely all of the present field-theoretical computations for events involving new particles are quantitatively unsatisfactory, many attempts are needed to find a model which leads to qualitative agreement with experiment to the second order in the coupling constant. Once we have found a suitable model, we have to ask to what extent higher-order corrections may be expected to modify the results. Considering the relatively large coupling constant, the present argument should be extended as far as possible by a fourth-order calculation, but we do not intend to do so in this paper. Therefore, higher-order corrections may seriously modify the conclusions obtained.

Apart from the higher-order problem, we shall consider some other methods of treatment that do not involve the rather problematic perturbation method. In the case of strong coupling the perturbation theory will give erroneous results which are too large by some numerical factors (>1). This fact was pointed out by Tomonaga[8] for the case of the nucleon self-energy. It is thus expected that, as far as the main term to the second order for the self-energy is concerned, we may infer the expression for it in the strong and intermediate coupling theories from our results by multiplying them by some numerical factors. Such a modification may alter the relation (9); however, the effect for the mass relation (10) may be smaller. One must bear in mind that the above qualitative reasoning might be theoretically incomplete. The main point of the foregoing

[8] S. Tomonaga, Progr. Theoret. Phys. Japan **1**, 83 (1946); also see K. M. Watson and E. W. Hart, Phys. Rev. **79**, 918 (1950).

remarks is to indicate that in our case the mass relation can be determined by the logarithmic divergences without referring directly to the coupling constants.

Next, we can make some further remarks concerning the numerical values of the various masses. According to recent experiments, there seem to be several heavy mesons, i.e., χ, υ, and ζ, which decay into two π mesons or τ and π mesons. Accepting this result for the moment, this means that they are of the scalar or vector type. At the present stage we are not sure about the exact relationship between these heavy mesons and the c meson. As pointed out in III, it may be necessary for us to assume more c mesons. One further point may be noted. In the formula (10), the masses of V particles and c mesons depend on those of nucleons and π mesons. Since we cannot know their mechanical masses accurately, we are still at liberty to select values for the masses for the V particle and the c meson.

We also note that some other particles could play a part in the self-energy of nucleons. For instance, the τ meson might conceivably be related to the self-energy of nucleons. According to the detailed discussion of the τ meson given by Fukuda *et al.*,[9] its coupling constant is taken to be $\sim 1/1000$; thus it is inferred that the effect of the τ meson on the self-energy of a nucleon would be negligible in comparison with those of the π meson and the c meson. Furthermore, the existence of other particles (κ mesons, etc.) must be taken into account. In this respect our model will still not be free from serious modification as a result of future experimental developments.

Finally, in the present situation it is impossible to exclude ambiguities involved in the mass determinations. Nevertheless, even in the mass values and Q values for the V particles the experimental information seems to indicate an appreciable fine structure. If this is so, it would be necessary to devise some additional mechanism in order to explain it. In this connection we shall employ an alternative treatment of the proton self-energy caused by the electromagnetic field without employing the original c-meson theory developed in the previous paper.[10] As was shown already, the divergent mass correction caused by the electromagnetic field for the proton is

$$\delta m_{el.} = m\left(\frac{e^2}{4\pi\hbar c}\right)\left(\frac{3}{2\pi}\right)\log(K+K_0)M^{-1}. \quad (12)$$

TABLE II. Masses of V particles and c mesons for the proton in units of m_e. (It is assumed that $m=1836m_e$, $\kappa=276m_e$, and $g^2=10e^2$.)

V mass	1900	2000	2100	2200	2300	2400	2500
c mass	1406	1288	1175	1065	947	813	650

Accordingly, in the proton case the condition (10) is modified as follows:

$$\frac{\mu^2}{m^2}=\frac{1}{120\beta-105}\left\{(2\beta-1)\left(75\frac{\kappa^2}{m^2}+65\right)\right.$$
$$\left.+180(2\beta-1)\left(\frac{e\kappa}{gm}\right)^2-(60\beta^3-75\beta^2+66\beta+6)\right\}. \quad (10')$$

At the present stage nothing can be said about the relation between the coupling constants e^2 and g^2. Here the numerical values of the c-meson mass are given in Table II, with the convention that the constant g^2 is ten times as large as e^2. Comparing them with the result in II, we see that the shift of the mass values of V particle is found to be about $\sim 30m_e$ in the mass or ~ 15 Mev in the Q value. The foregoing discussion is somewhat premature in the sense that such fundamental problems as the proton-neutron mass difference and the charge independence of nuclear forces remain untouched.

We have thus far considered the mass relation of elementary particles from the point of view of the compensation to which strong fermion-boson interactions are correlated. We can, in principle, extend this method to all other types of couplings. To carry out such a program would be a profitable subject for the mass spectrum theory, but we shall not discuss here the detailed analysis of other cases.

DECAY OF HEAVY PARTICLES

We now proceed to investigate the decay of the heavy particles into lighter ones. Our treatment will not go beyond that previously obtained by many authors. First we shall be concerned with the determination of a scheme of interactions which is necessary to allow the unstable particles to disintegrate with lifetimes of the order of $\sim 10^{-9}-10^{-10}$ sec.

Regarding the interpretation of the decay processes

$$\text{(i)}\quad V^{\pm}\rightarrow V^0+\pi^{\pm},\quad V^0\rightarrow N+\pi, \quad (13)$$

and

$$\text{(ii)}\quad v^{\pm}\rightarrow v^0+\pi^{\pm},\quad v^0\rightarrow 2\pi. \quad (14)$$

Nambu *et al.* and Oneda[2] have pointed out that among many possible couplings the following ones would be allowed or should at least be taken into account:

$$\left.\begin{array}{l} G_1(VN\pi),\quad G_2(VNv),\quad G_3(VV\pi),\\ \qquad\qquad G_4(VVv),\quad g_1(NN\pi),\quad g_2(NNv)\\ G_1^2\sim 10^{-11}-10^{-13},\quad G_2^2\sim 10^{-2}-10^{-3},\\ \qquad\qquad g_2^2\sim 10^{-7}-10^{-9},\\ G_3^2\gtrsim g_1^2,\quad G_4^2\leq g_2^2,\quad g_1^2\sim 1-10^{-1} \end{array}\right\}, \quad (15)$$

where $G(VNv)$ denotes an interaction which relates the V particle, nucleon, and v meson and which has a coupling constant given symbolically by G; the estimation of coupling constants might be accompanied by

[9] Fukuda, Hayakawa, and Miyamoto, Progr. Theoret. Phys. Japan **5**, 283, 352 (1950); Ozaki, Oneda, and Sasaki, Progr. Theoret. Phys. Japan **5**, 25, 165 (1950).

[10] H. Enatsu and P. Y. Pac, Progr. Theoret. Phys. Japan **6**, 665 (1951).

uncertainties of the order of 100 owing to the method of calculations.

Let us inspect the interactions from the standpoint of the self-energy. Calling our attention to the order of magnitude of coupling constants, we find that G_1, G_3, and g_2 are extremely small compared with the others, so that we discard them entirely. Thus, we are left with

$$G_2(VN\upsilon), \quad G_3(VV\pi), \quad \text{and} \quad g_1(NN\pi). \tag{16}$$

In other words, if one analyzes the processes (13) and (14) in which the typical decay modes

$$V\rightarrow N+\pi \tag{17}$$

and

$$\upsilon\rightarrow\pi+\pi \tag{18}$$

are involved, one sees that the only couplings which may have a possibility of contributing seriously to the self-energy of nucleons and V particles are those given in (16). This result is very similar to that drawn from our reasoning in the preceding section. The agreement is seen not only for the type of coupling, but also for the order of the coupling constant. Our analysis is in substance identical with that given by Pais.[3]

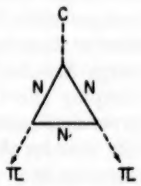

FIG. 1. Decay of a neutral c meson into two charged π mesons.

So far we have restricted our considerations to an analysis of the work of preceding authors. For later calculation the results may be summarized as follows.

(1) To compensate for the self-energy of nucleons and V particles caused by π mesons whose couplings are given by (1) and (11), it is necessary to introduce c mesons having the coupling (5).

(2) The c mesons, which may be identified with the χ, υ, and ζ particles obey the symmetrical (or neutral) theory.

(3) For the order of magnitude of the coupling constants one estimates

$$\frac{g^2}{4\pi\hbar c}\sim\frac{L^2}{4\pi\hbar c}\sim 1-10^{-1}, \quad \frac{G^2}{4\pi\hbar c}\sim 10-1. \tag{19}$$

(4) In order to allow V particles and c mesons to decay with lifetimes $\sim 10^{-9}-10^{-10}$ sec, one needs only assume the following interactions:

$$f(nnc), \quad \frac{f^2}{4\pi\hbar c}\sim 10^{-7}-10^{-9}, \quad (n=N, V). \tag{20}$$

In order to find the exact form for the coupling (20), we shall first confine ourselves to the c-meson decay (Fig. 1), in which a selection rule will be effective.

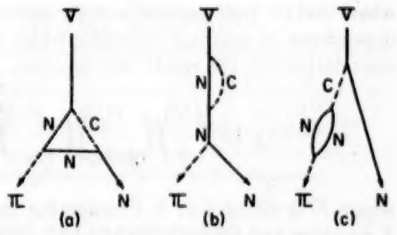

FIG. 2. Decay of a V particle into a proton and a π meson.

Then, from the work of Fukuda *et al.* and others,[9] it is readily seen that there remains only one possible case, that is, the neutral scalar type with scalar coupling

$$L_4=-f\bar{\psi}_n\psi_n\phi_c+\text{h.c.} \tag{21}$$

The evaluation is carried out by the standard Feynman-Dyson method using regulators. For simplicity, we discard the so-called translation effect,[11] and the couplings (11) and (21) for $n=V$ in the present and following sections. With $m=1836m_e$ and $\mu=800m_e$, we find

$$\tau_1^{-1}\approx 1.2\times 10^{24}\left(\frac{f^2}{4\pi\hbar c}\right)\left(\frac{g^2}{4\pi\hbar c}\right)^2 \text{ sec}^{-1}, \tag{22}$$

for the 2π decay of the c meson. The competing processes are

$$c\rightarrow\pi+\gamma \tag{23}$$

and

$$c\rightarrow\gamma+\gamma. \tag{24}$$

We have ascertained that the former is forbidden and the latter is a relatively rare event compared with the 2π decay.

We now consider the case of V-particle decay with the emission of a proton and a π meson. As was already suggested by Oneda,[2] because of the mass relation,

$$m_1<m+\mu, \tag{25}$$

the decay of the V particle would take place according to the scheme shown in Fig. 2. It should be noted that in our case these schemes are completely determined by the couplings mentioned above. Taking the masses of the V particle and the c meson to be $2200m_e$ and $1000m_e$, presumably, and performing the momentum integral numerically, one obtains

$$\tau_2^{-1}\approx 0.4\left(\frac{1}{2\pi}\right)^4\left(\frac{G^2}{4\pi}\right)\left(\frac{g^2}{4\pi}\right)\left(\frac{f^2}{4\pi}\right)\times\frac{mX^3}{\left(-\frac{1}{2}X^2+X-\frac{\kappa^2}{m_1^2}\right)}, \tag{26}$$

[11] According to Fukuda *et al.*[9] it often happens that the matrix element for the 2π decay of neutral heavy mesons tends to zero when the equality $\kappa^+=\kappa^-$ holds for the masses of the π mesons which are created. We have confirmed that this fact would not be changed by taking account of the translation effect. Therefore we discarded the possibility of taking a symmetrical scalar field with vector coupling for the interaction Lagrangian density L_4.

where $X=1-1/\beta^2$, and $\hbar=c=1$. In view of the internal dependence of coupling constants which is revealed in the relation (9), the result (26) becomes

$$\tau_2^{-1}\approx 2.5\times 10^{21}\left(\frac{N}{2}\right)\left(\frac{f^2}{4\pi\hbar c}\right)\left(\frac{g^2}{4\pi\hbar c}\right)^2 \text{ sec}^{-1}, \quad (27)$$

where N is either 1 or 3. Considering the lifetimes of V particles and taking $g^2/4\pi\hbar c\sim 10^{-1}$, one can estimate the order of magnitude of the coupling constant to be

$$\frac{f^2}{4\pi\hbar c}\sim 10^{-9}-10^{-12}, \quad (28)$$

which is of the order anticipated by several authors.[2,3]

It might be remarked that this estimate can hardly be trusted because of the neglect of translation effects and the adoption of the regulator method. However, so long as we limit ourselves to the neutral heavy particles, this result seems to show that the present model is reasonable. As for the decay of charged unstable particles, at the present time we know too little in the way of experimental facts; hence, we shall content ourselves with referring to the detailed discussion made by Pais.[3]

PRODUCTION OF HEAVY PARTICLES

Heavy particles are observed[1] in a cloud chamber which is operated by the passage of the penetrating particles produced in the condensed materials above the chamber, and it is confirmed that the heavy particles are generated in the nuclear reaction which gives rise to bundles of these penetrating showers. The number of heavy particles in the penetrating showers is about one hundredth that of penetrating particles. In view of the experimental information, we see that the heavy particles are produced mainly in nucleon-nucleon collisions. We shall now check to what extent the production of heavy particles may be explained by means of the set of interactions which we have introduced in former sections. The lowest-order Feynman diagrams for this production are shown in Fig. 3. In our model the production is mainly due to the processes (a) and (b) in Fig. 3. The process (c) can be disregarded because of the smallness of f^2. In the center-of-mass system the threshold energies for V production are about $(11/8)mc^2$ for process (a) and $(5/4)mc^2$ for process (b). Total cross sections of the processes are calculated numerically for incident nucleon energies of $E_0=2mc^2$ and $E_0=5mc^2$ in the cm system. The former is sufficient to produce a penetrating shower in lead. Averaging over the charges of the incident nucleons, we obtain

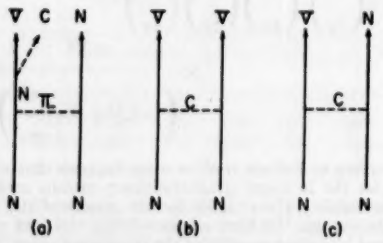

FIG. 3. Production of V particles and c mesons by nucleon-nucleon collisions.

$$\sigma_a=\left(\frac{g^2}{4\pi\hbar c}\right)^2\left(\frac{G^2}{4\pi\hbar c}\right)\left(\frac{M^4}{\mu_0^2\kappa_0^4}\right)(\alpha_1A_1+\alpha_2A_2), \quad (29)$$

and

$$\sigma_b=\frac{\pi}{4}\left(\frac{G^2}{4\pi\hbar c}\right)^2\left(\frac{M_1-M}{\mu_0}\right)^4\left(\frac{1}{M^2}\right)(\alpha_1'A_1'+\alpha_2'A_2'), \quad (30)$$

where α_1, α_2, α_1', and α_2' are constants given in Table III, and A_1, A_2, A_1', and A_2' are calculated by numerical integration and given in Table IV. The terms α_2A_2 and $\alpha_2'A_2'$ come from the exchange effect, being much smaller than the ordinary terms α_1A_1 and $\alpha_1'A_1'$.

For the process (a), the cross section for $E_0=5mc^2$ is much larger than that for $E_0=2mc^2$. This suggests that our calculation is incomplete for this energy, and the effect of damping must be considered. However, for the energy $E_0=2mc^2$, which is just above the threshold, the damping effect seems to be small; hence at this energy we shall compare the cross section for the process (a) with that for the process (b). Now the ratio of the cross sections is

$$\frac{\sigma_a}{\sigma_b}\approx\left(\frac{4}{\pi}\right)\left(\frac{2\beta-1}{3N(\beta-1)^4}\right)\left(\frac{M}{\kappa_0}\right)^2\left(\frac{\alpha_1A_1}{\alpha_1'A_1'}\right). \quad (31)$$

Since $M^2/\kappa_0^2(\beta-1)^4$ is over 2×10^4, the above ratio is about 2×10^4. Thus, the heavy particles are created through the process (a) even in this energy region. By taking into account the relation (9), the total cross section for the heavy particle production becomes

$$\sigma_a\approx\left(\frac{g^2}{4\pi\hbar c}\right)^3\left(\frac{18}{2\beta-1}\right)\left(\frac{A_1}{\kappa_0^2}\right)\left(\frac{104}{5}\right)\left\{\begin{matrix}3\\2\end{matrix}\right\},$$

$$\left\{\begin{matrix}\text{symmetrical}\\ \text{neutral}\end{matrix}\right\}. \quad (32)$$

TABLE III. Numerical values for the parameters α_1, α_2, α_1', and α_2' of Eqs. (29) and 30. Case (A): total cross section. Case (B): neutral V production only.

Type of c meson	Symmetrical theory				Neutral theory			
α	α_1	α_2	α_1'	α_2'	α_1	α_2	α_1'	α_2'
(A)	18	9/2	7/2	1/2	6	3/2	1	−1/2
(B)	9	9/4	3	3/4	3	3/4	1/2	−1/4

Alternatively this can also be written as

$$\sigma_a \approx \left(\frac{g^2}{4\pi\hbar c}\right)^3 \left(\frac{A_1}{\kappa_0^2}\right) \left\{\begin{matrix}3\\2\end{matrix}\right\} 2.4\times 10^4. \qquad (33)$$

If we assume that the value $g^2/4\pi\hbar c \sim 10^{-1}$, this is nearly of the order of the nucleon geometrical cross section.

At first sight, this result may be interpreted to mean that the heavy particles are produced with a cross section fairly large compared with that of the penetrating particles.[12] Consequently, we are tempted to conclude that the model is inconsistent with the experimental data. However, for comparison with experiment there are two points to be noted. The first is that the penetrating particles, which mainly consist of π mesons, are generated in multiple and their number is much larger than the number of π mesons which would be obtained by assuming single production. Accordingly, granting that the cross section for single production of π mesons is of the same order as that of the heavy particle corresponding to process (a) in Fig. 3, the number of observed π mesons would be much larger than that of the heavy particles. Second, it must be taken into account that, because of their short lifetimes, some of the heavy particles produced may decay before they enter the region of illumination of the cloud chamber, while the π meson would be able to survive for a longer time.

From these considerations we may be allowed to conclude that the predictions of the present theory regarding the production of heavy particles accompanied by penetrating showers are not unreasonable.

MAGNETIC MOMENTS OF NUCLEONS

In this section we will briefly survey the possible contribution of the c mesons to the magnetic moments of nucleons, by a method more or less similar to that of Case.[13]

As is well known, the effective interaction due to the additional magnetic moments of nucleons which are to be ascribed to the presence of mesons has a form

$$H_{eff} = K\left(\frac{F^2}{4\pi\hbar c}\right)\left(\frac{e\hbar}{2mc}\right)(-\bar{\psi}\sigma_{\mu\nu}F_{\mu\nu}\psi), \qquad (34)$$

where K is a numerical constant.

Turning to our model, we have first to estimate the relative order of magnitude of the coupling constant F^2 in (34). Since we assume that π mesons and c mesons are of the types $PS(pv)$ and $S(v)$, respectively, this is done by applying the Dyson theorem concerning derivative couplings. In this way, we find

$$F_\pi^2 = \left(\frac{2m}{\kappa}\right)^2 g^2 \text{ for } \pi \text{ mesons}, \qquad (35)$$

and

$$F_c^2 = [(m_1-m)/\mu]^2 G^2, \text{ for } c \text{ mesons}. \qquad (36)$$

The latter expression will be modified by means of the relation (9) as follows:

$$F_c^2 = N\left(\frac{3}{4}\right)\left(\frac{2m}{\kappa}\right)^2 g^2 \frac{(\beta-1)^2}{(2\beta-1)}. \qquad (37)$$

Hence, with $\beta=1.2$ (i.e., $m_1=2200m_e$), one obtains

$$\frac{F_\pi^2}{F_c^2} = \frac{4(2\beta-1)}{3N(\beta-1)^2} = \frac{46.6}{N} \gg 1. \qquad (38)$$

Consequently, if the constant K for the c meson were of the same order of magnitude as that for the π meson, the contribution given by the former would be negligible in comparison with that given by the latter. To see how this can be determined, we have carried out the calculation for the case of the c meson. The result can be written in the following form. The constant K may be split into a sum of two terms which correspond to the nucleon and meson currents, respectively,

$$K_1 = K_1^N + K_1^M \text{ for the proton}, \qquad (39)$$

and

$$K_2 = K_2^N + K_2^M \text{ for the neutron}, \qquad (40)$$

where

$$K_1^N = -(I_1-I_3)/4\pi, \qquad (41)$$

$$K_1^M = (I_2-I_4)/2\pi, \qquad (42)$$

$$K_2^N = -(I_1-I_3)/2\pi, \qquad (43)$$

$$K_2^M = -(I_2-I_4)/2\pi. \qquad (44)$$

The explicit forms for the I's are

$$I_1 = 2\delta+1+(\delta^2-\lambda)P+2\delta(\delta^2-3\lambda)Q, \qquad (45)$$

$$I_2 = -2\delta+1+(-\delta^2+\delta+\lambda)P + 2(-\delta^3+\delta^2+3\lambda\delta-2\lambda)Q, \qquad (46)$$

$$I_3 = (\beta+1)[2+\delta P+2(\delta^2-2\lambda)Q], \qquad (47)$$

$$I_4 = (\beta+1)[-2+(-\delta+1)P+2(-\delta^2+\delta+2\lambda)Q], \qquad (48)$$

TABLE IV. Numerical values for the parameters A_1, A_2, A_1', and A_2' of Eqs. (29) and (30).

E_0[a]	A_1	A_2	A_1'	A_2'
$2\,mc^2$	1.11	0.07	2.57	0.90
$5\,mc^2$	35.50	−2.90	12.1×10^{-12}	-0.1×10^{-2}

[a] Energy of the incident nucleon in the center-of-mass system.

[12] In the same approximation, we have estimated roughly the cross section for π meson production by nucleon-nucleon collisions

$$\sigma_\pi \approx \left(\frac{g^2}{4\pi\hbar c}\right)^3 \left(\frac{B}{\kappa_0^2}\right) \times 0.2\times 10^4, \text{ for } E_0 = 2mc^2,$$

where B is a numerical constant of the order of 1. This may be compared with σ_a.

[13] K. M. Case, Phys. Rev. **76**, 1 (1949).

TABLE V. Numerical values for I_1–I_3 and I_2–I_4.

β [a]	1.09	1.14	1.20	1.25	1.31
λ [b]	0.47	0.39	0.32	0.25	0.18
I_1–I_3	−5.49	−2.45	−1.23	+0.19	+1.09
I_2–I_4	−2.86	−4.48	−6.20	−8.25	−10.62

[a] $\beta = m_1/m$.
[b] $\lambda = (\mu/m)^2$.

where

$$P = \log\left(\frac{\beta^2}{\lambda}\right), \tag{49}$$

$$Q = \frac{1}{(4\lambda-\delta^2)^{\frac{1}{2}}} \cos^{-1}\left(\frac{2\lambda-\delta}{2\beta\lambda^{\frac{1}{2}}}\right), \tag{50}$$

$$\delta = \lambda - \beta^2 + 1, \tag{51}$$

and

$$\lambda = \left(\frac{\mu}{m}\right)^2. \tag{52}$$

Numerical values of these quantities are given in Table V.

Comparing these results with those of Case, one sees that any difference in the constant K between the π meson and the c meson is not so large as to compensate for the weight owing to the relation (38). Therefore, we can conclude that in our model the effect of the c meson on the magnetic moments of the nucleon is slight. This conclusion would probably not be altered seriously in the higher order approximation because of the condition (38).

CONCLUDING REMARKS

The principal aim of this investigation has been to present an additional model which throws light on the nature of unstable heavy particles from the point of view of the self-energy. In spite of the qualitative agreement with experimental results, the model proposed here may require revision in the future, because one can not say anything about particles which may still be undiscovered. Such a possibility is likely enough in view of recent experiments. Moreover, it is uncertain at present whether or not divergences are eliminated in the higher order approximation. In other words, while it may be admitted that as a first approximation the predictions of our theory are qualitatively in conformity with experimental results, it is still a moot question whether the higher order effects may require serious modifications.

Further, even if the elimination of divergences for the self-energy could be achieved, the difficulties would not all be solved. In fact, the divergences which appear in the decay processes make the compensation problem still more serious. In this respect, the present treatment is certainly inconsistent. Noyes[2] has suggested an interesting method to avoid this difficulty. In our case the introduction of a new interaction which is the same type as that of Noyes may be considered in the case of the meson self-energy.

In conclusion, although the method shares the well-known defects of current field theory and the results obtained are preliminary, the theory seems to furnish a reasonable field-theoretical approach to the problem of explaining, by a simple model, a wide range of experimental facts (at least for the neutral heavy particles).

We should like to express our sincerest thanks to Professor H. Yukawa (Columbia University) and Professor T. Inoue (Kyoto University) for their kind interest in this work. One of us (H.E.) wishes to express his thanks to the Fulbright Foundation in Japan for a grant under the Fulbright Act and to the Department of Physics at Columbia University (where the last part of this research was carried out) for its hospitality. It is also a pleasure for one of us (P.Y.P.) to thank the Yukawa Yomiuri Fellowship for financial aid.

Nuclear Scattering of High-Energy Electrons*

J. H. SMITH
Knolls Atomic Power Laboratory,† Schenectady, New York
(Received February 11, 1954)

The Born approximation is used to calculate matrix elements for the elastic and inelastic scattering of high-energy electrons by nuclei. Curves and simple numerical relations are given to describe the manner in which scattered amplitudes depend upon nuclear characteristics.

INTRODUCTION

THE highly energetic beams of electrons now available from accelerators offer promise in the examination of nuclear structure. Indeed, Hofstadter, Fechter, and McIntyre[1] have investigated the scattering of electrons of about 100 Mev by various nuclei and have obtained not only a very accurate value for the nuclear radius but also more detailed information about the charge distribution in the nucleus, especially near its surface. This is to be expected since λ of these electrons is about 2×10^{-13}, just about the right order for the exploration of nuclear structure.

For an adequate analysis of these experiments, extensive numerical calculations including exact solution of the Dirac equation are necessary. Such calculations have been made by Yennie, Ravenhall, and Wilson[2] with very interesting results. However, these calculations require much time and expensive high-speed computing machines, and it will be difficult to explore in this manner the influence on the scattering of all parameters in the charge distribution.

It was therefore felt that a thorough investigation by means of the Born approximation would still have value. We fully realize that the results of this paper can be expected to be directly valid only for very light nuclei. There is some hope however that for heavy nuclei the Born approximation might give at least a *part* of the scattered amplitude: Baranger[3] has shown that to a certain approximation, the scattered amplitude may be represented as the Born approximation amplitude plus a correction depending primarily on $Ze^2/\hbar c$. Some aspects of the Born approximation have been discussed by Schiff[4] after this thesis was written but before its publication.

It is shown that analysis of the cross section for elastic scattering can provide information on nuclear radii and charge distribution. The latter is described herein by two parameters, one directly related to possible changes in proton population from nuclear center to "edge," and the second related to the sharpness of definition of a nuclear boundary.

The differential cross section for inelastic scattering summed over nuclear energy levels, is found to depend on the relative location of pairs of particles. Information on possible regularities in the internal "construction" of nuclei might be obtained from this quantity. Models chosen for the calculation of the inelastic effects include several kinds of crystal lattice patterns for proton pair distributions and a box in which nucleons are correlated due only to the action of the Pauli principle.

ELASTIC SCATTERING

In the Born approximation, the differential cross section for the elastic scattering of an unpolarized beam of electrons of energy E and charge e by a nucleus of charge Ze into the solid angle $d\Omega(=\sin\theta d\theta d\phi)$ is

$$d\sigma=\left(\frac{e^2\cos\tfrac{1}{2}\theta}{2E\sin^2\tfrac{1}{2}\theta}\right)^2 \times\left|\int\Phi_0^*\Phi_0\sum_{j=1}^{Z}\exp(i\mathbf{q}\cdot\mathbf{R}_j)d\mathbf{R}_1\cdots d\mathbf{R}_Z\right|^2 d\Omega, \quad (1)$$

where $|\mathbf{q}|=(2E/\hbar c)\sin\tfrac{1}{2}\theta$, $\mathbf{R}_j$ is the jth spatial coordinate in the nuclear system, and Φ_0 is the ground state wave function for the target nucleus. The electron-nucleus interaction has been taken to be Coulomb in form:

$$V=-\sum_{j=1}^{Z}\frac{e^2}{|\mathbf{R}_j-\mathbf{r}_e|}, \quad (2)$$

where $\mathbf{r}_e$ is the electronic coordinate.

The first factor in $d\sigma$ describes the Rutherford scattering by a single proton; its value is 10^{-30} cm^2 per unit solid angle for $E=100$ Mev and $\theta=90°$. The second factor gives interference effects amongst wavelets scattered by various protons. Were the probability distribution known for the nucleus, it would be possible to predict exactly the angular distribution of scattered particles. In lieu of this, there are hypothesized spatial nucleon configurations from which are calculated the corresponding scattered amplitudes.

$|\Phi_0|^2$ in the integral for $d\sigma$ contains all proton configuration coordinates symmetrically, so that the square

* Based on Ph.D. thesis submitted to Cornell University, February, 1951.
† Operated by the General Electric Company for the U. S. Atomic Energy Commission.
[1] Hofstadter, Fechter, and McIntyre, Phys. Rev. **91**, 422, (1953); **92**, 978 (1953).
[2] Yennie, Wilson, and Ravenhall, Phys. Rev. **92**, 1325 (1953); Phys. Rev. (to be published).
[3] E. U. Baranger, Cornell University thesis (1954). Part of her results were published in Phys. Rev. **93**, 1127 (1954).
[4] L. I. Schiff, Phys. Rev. **92**, 988 (1953).

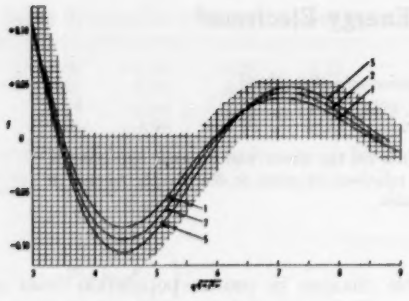

FIG. 1. Nuclear form factor for elastic scattering: models 1, 2, and 5.

of the matrix element is

$$Z^2\left|\int \phi_0^*\phi_0 \exp(i\mathbf{q}\cdot\mathbf{r})d\tau\right|^2, \tag{3}$$

where

$$\phi_0^*\phi_0 = \int \Phi_0^*\Phi_0 \prod_{j=1}^{Z}{}' d\mathbf{R}_j,$$

i.e., $|\phi_0|^2 d\tau$ is the probability that there is one proton in $d\tau$, with the positions of all other protons arbitrary. It is convenient to compare the scattering by an extended nucleus with Z protons to that by a point charge of strength Ze. The relevant ratio is just

$$\left|\int \phi_0^*\phi_0 \exp(i\mathbf{q}\cdot\mathbf{r})d\tau\right|^2, \tag{4}$$

the first power of which may quite naturally be referred to as a "nuclear form-factor" F.

Possible variation in charge density in the nucleus is allowed through use of the model described by

$$|\phi_0|^2 = N^{-1}\begin{cases}1+f(r^2/a^2), & r\leq a,\\ (1+f)\exp[-(r-a)/da], & r>a,\end{cases} \tag{5}$$

where the normalization constant is

$$N = 4\pi a^3\{\tfrac{1}{3}(1+\tfrac{3}{5}f)+d(1+f)(1+2d+2d^2)\}.$$

Of the parameters in $|\phi_0|^2$, f and d obviously determine the shape of the proton density, -- the average internal charge behavior, and the sharpness of a boundary. Even though adoption of a picture with spherical symmetry renders impossible any analysis of quadrupole moments, there nevertheless is ample opportunity for study of the two features mentioned.

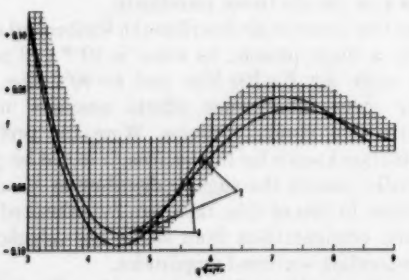

FIG. 2. Nuclear form factor for elastic scattering: models 2 and 4.

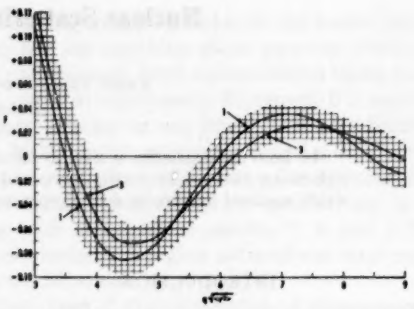

FIG. 3. Nuclear form factor for elastic scattering: models 1 and 3.

The nuclear form factor, F, is examined against the dimensionless quantity $q\bar{r}\equiv q\sqrt{\langle r^2\rangle}$. $q\bar{r}$ is taken as more appropriate than qa since the latter places undue emphasis on a single aspect of the models used for the density.

The variations employed in "internal" and "external" charge distributions are given in Table I. The numbers in the left-hand column are model numbers to which reference will be made in later discussions, and f and d have already been mentioned. Two models calculated, 6 and 9, are written explicitly since no choice for f and d describes them.

For nearly all models employed, a characteristic diffraction pattern is found in the scattered beam, maxima and minima occurring in the product of the Rutherford scattering and the square of the form factor. With model 9, the exponential density which lies closest to the shape adopted by Stanford workers,[1,2,4] the calculated form factor displays no diffraction effects. F is plotted *versus* $q\bar{r}$ for a representative selection of these models in Figs. 1, 2, 3, and 4. Careful numerical analysis of F^2 *versus* $q\bar{r}$ shows that d, $\bar{r}$, and f affect the scattering in ways which are independent of one another

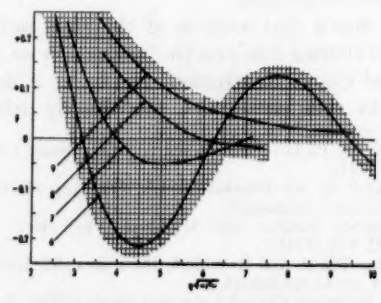

FIG. 4. Nuclear form factor for elastic scattering: models 6, 7, 8, and 9.

or coupled in a calculable way. These features of the scattering will now be discussed.

First, the ratio of the two values of F^2 taken at its first and second maxima depends significantly on d, but hardly at all on f. This is illustrated in Table II. The constraint that $dF/d(q\bar{r})=0$ serves to express F^2 at maxima as a function of d and f alone, so the variation of the above ratio with $q\bar{r}$ need not be considered. It is clear that a fuzzy boundary tends to decrease the second maximum relative to the first.

Secondly, the values of $q\bar{r}$ at which the first maximum in F^2 occurs may be found once an assignment of d is made. As mentioned, the condition $dF^2/d(q\bar{r})=0$ expresses $q\bar{r}$ (first maximum) as a function of f and d. However, it is seen from Table III that the variation of $q\bar{r}$ (first maximum) with f is of no importance.

Finally, there is the evaluation of the internal parameter f. For this, one can refer to the absolute value of F^2 at first maximum. A large value of f, implying a sharp peak in charge density near the nuclear surface, has the effect of increasing the form factor. (See the form factor in Fig. 4 for model 6, a simple shell of charge.) Empirical formulae which have been found to fit the characteristics of F^2 at extrema as just discussed are:

TABLE I. Nuclear density models and their characteristic parameters.

Model number	f	d
1	0.0	0.0
2	0.4	0.0
3	0.0	0.1
4	0.4	0.1
5	1.0	0.0
6	$\lvert\phi_0\rvert^2=\delta(r-a)/4\pi a^2$	
7	0.0	0.2
8	0.0	0.5
9	$\lvert\phi_0\rvert^2=(b^3/8\pi)\exp(-br)$	
10	0.4	0.2
11	1.0	0.1
12	1.0	0.2

$$F^2(\text{first maximum})/F^2(\text{second maximum})=5.86+(18.6d)^{1.43}, \quad (6)$$

$$q\bar{r}(\text{first maximum})=4.48+(3.9d)^{2.6}, \quad (7)$$

$$F^2(\text{first maximum})=F_{00}^2\frac{\{1+[(1+d)^5+0.56]f\}^4}{1+(6.65d)^{2.12}}, \quad (8)$$

where

$$F_{00}^2=(0.0862)^2.$$

Equations (6), (7), and (8) fit a large set of detailed calculational results to less than 2 percent in most cases. It may be of interest to give examples of the theoretical accuracy with which they indicate d, F, and f can be measured, and to point out experimental difficulties which would be met. Of course, for any information to be obtained from experiment, it is necessary to measure $d\sigma/d\Omega$ as a function of angle of scattering, and calculate

$$(d\sigma/d\Omega)_{\text{exp}}(2e^2EZ\cos^2\tfrac{1}{2}\theta)^{-2}(\hbar cq)^4=(F^2)_{\text{exp}}. \quad (9)$$

TABLE II. Ratios of maxima in F^2 and characteristics of corresponding nuclear density.

$\frac{F^2(\text{first maximum})}{F^2(\text{second maximum})}$	d	f
5.86	0	0.
5.90	0	0.4
6.06	0	1.0
8.28	0.1	0
8.41	0.1	0.4
12.3	0.2	0
12.9	0.2	0.4

If the ratio of F^2 at its first two maxima were known to 10 percent, d could be fixed to within ± 0.025. Since d is a rather fine detail of nuclear structure, this accuracy appears satisfactory. Even for a heavy nucleus, $d\sigma/d\Omega$ for elastic scattering is only about 10^{-30} cm^2. Thus, there is the problem of a measurement only barely within current accurate experiments—coupled with the possibility that inelastic effects and background may mask the elastically scattered beam.

Should d be found to be 0.1 to about 10 percent, $q\bar{r}$ would be calculable from (7) to 0.5 percent. But since $\bar{r}$ is known only in terms of $q[=(2E/\hbar c)\sin\frac{1}{2}\theta]$, it is likely that the experimental determination of the scattering angle at the peak of a rather broad maximum will limit the accuracy of $\bar{r}$.

For intermediate values of both f and d, a value of F^2 accurate to 10 percent would fix f to about ± 0.1.

Although the situation suggested by the preceding discussion is an agreeable one, it cannot be inferred that the measurements mentioned would necessarily establish numbers for the parameters. Other features of the elastic scattering, such as absolute values of maxima beyond the first, location of minima, etc., should be given accurately. Indeed, it may be impossible to satisfy all requirements with a three-parameter density function. Possible reasons for such failure would be lack of spherical symmetry in the charge distribution, an

TABLE III. $q\bar{r}$ at first maximum in F^2 for various values of f and d.

$q\bar{r}$ (first maximum)	f	d
4.46	0	0
4.46	0.4	0
4.50	1	0
4.58	0	0.1
4.57	0.4	0.1
4.56	1	0.1
5.05	0	0.2
5.01	0.4	0.2
4.98	1	0.2

internal structure of the nucleons which would modify the Coulomb interaction at very small distances, significantly large magnetic effects, and of course, breakdown of the Born approximation.

INELASTIC SCATTERING

The cross section for inelastic scattering in which the nucleus is left in an excited state characterized by Φ_α and the electron has a final energy E_β, is given by

$$\frac{d\sigma}{dq_\beta}=\frac{4}{\pi}\left(\frac{e^2}{\hbar c}\right)^2\frac{E_\beta\cos^2\frac{1}{2}\theta}{E}\frac{}{q_\beta^3}$$

$$\times\left|\int\Phi_\alpha^*\Phi_0\sum_{j=1}^{Z}\exp(i\mathbf{q}_\beta\cdot\mathbf{R}_j)d\mathbf{R}_1\cdots d\mathbf{R}_Z\right|^2, \quad (10)$$

where

$$(\hbar cq_\beta)^2=E^2+E_\beta^2-2EE_\beta\cos\tfrac{1}{2}\theta. \quad (11)$$

It is possible to measure transitions to a definite excited state α of the nucleus by measuring the energy of the scattered electron. However, we shall find that more information on nuclear structure is revealed if we sum over all possible final states α. Theoretically, this is most easily done by keeping q_β fixed; experimentally, of course, it would be easiest to measure at constant angle θ.

The two types of summation are not identical as can be seen from (11); however, if E is several hundred Mev, the difference is not large. The transition probabilities (10), for given q_β, are closely related to those for the photoelectric effect; therefore, experimentally[5] the most important excitation energies will be of the order of 15–30 Mev. It can easily be shown from (11) that under these conditions, and with q_β held fixed, θ will not vary much with excitation energy within the range for which the cross section (10) is large. Therefore, although the sum is performed for q fixed, this is closely equivalent to keeping θ constant. Indeed, when the important energy changes in the scattering are small compared to the energy of the incident electron, q and θ are related by

$$|q|=(2E/\hbar c)\sin\tfrac{1}{2}\theta, \quad (12)$$

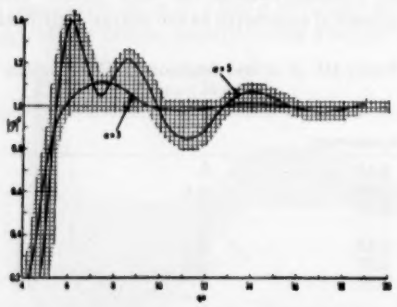

FIG. 5. Square of nuclear form factor for inelastic scattering (simple cubic structure model).

[5] K. Strauch, Ann. Rev. Nuclear Sci. **2**, 105 (1953).

independent of the final energy of the electron. Moreover, for the purpose of actual summation of (11), both E_β and $\cos^2\frac{1}{2}\theta$ may be regarded as constant.

The sum rule applied to (10) gives then for the total inelastic scattering into $d\Omega$:

$$\sum_{\alpha\neq0}d\sigma_\alpha=\left(\frac{e^2\cos\frac{1}{2}\theta}{2E\sin^2\frac{1}{2}\theta}\right)^2\left\{\int\Phi_0^*\Phi_0\zeta^*\zeta d\mathbf{R}-\left|\int\Phi_0^*\Phi_0\zeta d\mathbf{R}\right|^2\right\}d\Omega, \quad (13)$$

where

$$\zeta=\sum_{j=1}^{Z}\exp(i\mathbf{q}\cdot\mathbf{R}_j). \quad (14)$$

The second term in the curly bracket in (13) gives the elastic scattering, while the first term is the total scattering. From (14),

$$\zeta^*\zeta=Z+\sum_{j,k}{}'\exp[i\mathbf{q}\cdot(\mathbf{R}_k-R_j)].$$

$|\Phi_0|^2$ integrated over all coordinates save one (or two) can be expected to have the same form regardless of which coordinate (or pair of coordinates) remains, so for the purpose of integration, one may write

$$\zeta=Z\exp(i\mathbf{q}\cdot\mathbf{R}_1),$$

and

$$\zeta^*\zeta=Z+Z(Z-1)\cos[\mathbf{q}\cdot(\mathbf{R}_1-\mathbf{R}_2)].$$

In combination with $\zeta^*\zeta$, $|\Phi_0|^2$ is integrated over all coordinates save two to give a "two-particle density" which characterizes the correlation in location of pairs of protons: this density is hereafter called $\Pi(\mathbf{R}_1,\mathbf{R}_2)$. Combined with ζ, $|\Phi_0|^2$ is integrated over all but one coordinate and, thus, gives the "single particle density," $\rho(\mathbf{R}_1)$, such as was used in the discussion of elastic scattering. Corresponding to the form factor F, there now exists a factor,

$$|\mathfrak{F}|^2=\int\int\{1+(Z-1)\cos\mathbf{q}\cdot(\mathbf{R}_1-\mathbf{R}_2)\}\times\Pi(\mathbf{R}_1,\mathbf{R}_2)d\mathbf{R}_1d\mathbf{R}_2-\left|\int\rho(R_1)\exp(i\mathbf{q}\cdot\mathbf{R}_1)d\mathbf{R}_1\right|^2, \quad (15)$$

which describes the effect of nucleon spatial distribution on the inelastic scattering.

CRYSTAL MODELS

As the first model for illustration of possible effects of nuclear structure on inelastic scattering, consider the following normalized two-particle density,

$$\Pi(\mathbf{R}_1,\mathbf{R}_2)=[(Z-1)V_1b^3\pi^{\frac{1}{2}}]^{-1}\times\sum_{\mathbf{n}\neq0}\exp[-(\mathbf{R}_{12}-a\mathbf{n})^2/b^2]. \quad (16)$$

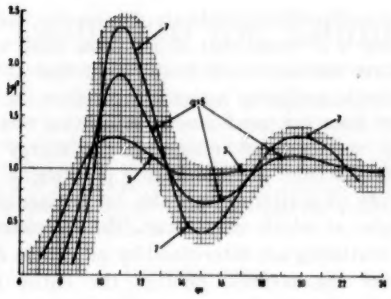

FIG. 6. Square of nuclear form factor for inelastic scattering (face-centered cubic structure model).

This is based on the assumption that the particles are arranged as in a regular crystal lattice, smeared out to some extent in a manner similar to thermal motion. In (16), V_1 = total nuclear volume; extends over $(Z-1)$ occupation points; $\mathbf{R}_{12}=\mathbf{R}_1-\mathbf{R}_2$; $\mathbf{n}$ = a numerical vector locating occupation points in a lattice, e.g., in a simple cubic structure, $\mathbf{n}$ is a triplet of integers; a = edge of basic cubic cell in lattice, and b = parameter determining certainty with which a proton can be found at or near an occupation point.

Apart from the assumption of a crystalline structure, this model may also be seriously in error due to the fact that it effectively fails to recognize the edge effects which arise for a finite nucleus. The parameter b is taken as proportional to a:

$$b=a|\mathbf{n}|/\alpha. \tag{17}$$

Introduction of $\mathbf{n}$ in (17) means that the sharpness of correlation between nucleons decreases as their distance $|\mathbf{n}|$ increases, thus making the assumed structure more similar to a liquid than to a solid. The additional parameter α permits adjustment of this sharpness independent of $|\mathbf{n}|=n$.

The scattered intensity in this case is found quite readily to vary as

$$|\mathfrak{F}|^2=1+\sum_{\mathbf{n}\neq 0}\frac{\sin nqa}{nqa}\exp\left[-\frac{(nqa)^2}{2\alpha}\right]$$
$$-9Z\left[\frac{\sin qR_0-qR_0\cos qR_0}{(qR_0)^3}\right]^2, \tag{18}$$

where

$$R_0=a(3Z/4\pi\rho)^{\frac{1}{3}}, \tag{19}$$

and ρ is the average number of protons assigned to each unit cell in the lattice.

$|\mathfrak{F}|^2$ for Pb is plotted *versus* qa in Figs. 5 and 6. Figure 5 presents the data for a simple cubic lattice structure, while Fig. 6 corresponds to the assumption of a face-centered cubic structure. The curves are not given for small qa, since it is in this range that the calculation is least realistic in regard to edge effects. As is to be expected, large values of the parameter α consistently give the sharpest interference patterns. While separate peaks in $|\mathfrak{F}|^2$ for the simple cubic structure can be identified as constructive interference in scattering from specific pairs of lattice points, the same is not true for the face-centered lattice model. For this latter case, none of the "resolution factors" α was sufficiently large to prevent the smearing of adjacent peaks into each other.

Since the Born approximation is really not valid for such a heavy nucleus as Pb, it is not appropriate to discuss any quantitative details of $\mathfrak{F}$. The curves given are of value in demonstrating the kind of inelastic scattering which might be expected and in providing a form factor which can perhaps be corrected to give accurate results.

"FERMI PARTICLE" MODEL

The last model to be considered is one in which the Z protons are constrained to be within a cubic box of edge L and to be correlated only through the Pauli exclusion principle. For such a model, it can be shown[6] that the square of the inelastic form factor is

$$|\mathfrak{F}|^2=1-Q\int_0^X\frac{\sin\nu x}{\nu x}\left(\frac{\sin x-x\cos x}{x^2}\right)^2dx, \tag{20}$$

where

$$Q^{-1}=\int_0^X\left(\frac{\sin x-x\cos x}{x^2}\right)^2dx,$$

$$x=2\pi N r_{12}/L,$$

$$\nu=qL/2\pi N,$$

$$N=Z^{\frac{1}{3}}/2,$$

$$X=2\pi N R_{12}/L,$$

where R_{12} is the upper limit for inter-particle distances in the nucleus. In Figs. 7 and 8, $|\mathfrak{F}|^2$ is plotted *versus* qr_0, where r_0 is the radius of a spherical volume con-

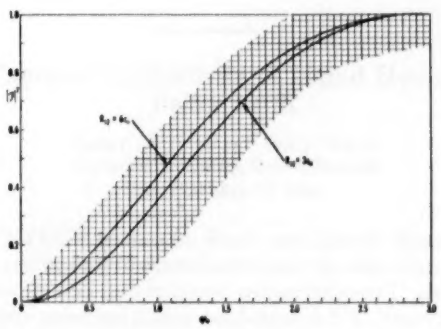

FIG. 7. Square of nuclear form factor for inelastic scattering (Fermi particle model).

[6] J. H. Smith, Ph.D. thesis, Cornell University, 1951 (unpublished).

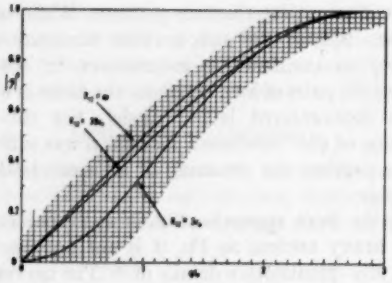

FIG. 8. Square of nuclear form factor for inelastic scattering (Fermi particle model).

taining one nucleon. Thus,

$$L^3=\tfrac{1}{3}4\pi A r_0^3.$$

For comparison with the crystalline model results, it may be said that a for the simple cubic structure is only slightly greater than $2r_0$.

The principal dependence of $|\mathfrak{F}|^2$ is on qr_0. In addition, there is a somewhat less important dependence on R_{12}/r_0. One possible choice is $R_{12}=A^{\frac{1}{3}}r_0$, and indeed, $4\pi R_{12}^3/3$ describes the nuclear volume correctly. The choice $R_{12}=2A^{\frac{1}{3}}r_0$ probably would overestimate the nuclear size. More generally, one can use $R_{12}=gr_0$, in which case a given value of g would mean that some nucleus with A between g^3 and $g^3/8$ was described. The values $g=3$, 6, and 12 were calculated, corresponding to either Pb with $g=6$ or 12, or to Al with $g=3$ or 6. The cases $X\to\infty$ for an infinite nucleus and $g=20$ to bridge the gap to finite dimensions are also included.

COMPARISON OF ELASTIC AND INELASTIC SCATTERING

In the limit of large q, the inelastic scattering is Z times the scattering from a single proton, as if the protons scattered independently. For small q, the elastic scattering is Z^2 times that of a proton. Both of these results are well known. It is also clear that at large q the inelastic scattering is much larger than the elastic.

Apart from the possibility of separating elastic and inelastic scattering by measuring the energy of the scattered electron, the interference phenomena for the two types of scattering can also be distinguished by the angles at which they occur. The interferences in elastic scattering are determined by qR, where R is the radius of the nucleus, because the entire nucleus participates in the phenomenon. The inelastic scattering, on the other hand, depends primarily on the correlation of neighboring protons, and hence on qr_0. The interference phenomena in elastic scattering, therefore, occur at smaller angles (smaller q) than those for inelastic. Taking Pb as an example—in spite of the inapplicability of the Born approximation—we have $R=6r_0$. Hence, the first maximum of elastic scattering occurs at $qr_0\approx 0.75$. At this value of q, the Fermi model gives an inelastic scattering of less than 40 percent of the asymptotic value, and only at much higher qr_0 is the asymptotic value approached. For the crystal model, even higher qr_0 are significant: the first maximum occurs at $qr_0>3$. There will thus be no confusion between elastic and inelastic maxima.

In conclusion, we should like to repeat our warning that the results of this paper must not be used for heavy nuclei because the Born approximation is not valid for these

ACKNOWLEDGMENTS

The author wishes to express his gratitude to Professor H. A. Bethe for valuable suggestions and guidance in this work and to Professor R. P. Feynman for helpful discussions.

Letters to the Editor

PUBLICATION of brief reports of important discoveries in physics may be secured by addressing them to this department. The closing date for this department is five weeks prior to the date of issue. No proof will be sent to the authors. The Board of Editors does not hold itself responsible for the opinions expressed by the correspondents. Communications should not exceed 600 words in length and should be submitted in duplicate.

Temperature Dependence of Organic Scintillation Materials

J. B. BIRKS
Physics Department, Rhodes University, Grahamstown, South Africa
(Received May 6, 1954)

THE author[1] has developed a quantitative photon cascade theory of the scintillation process in organic materials. This theory has been shown to give a value for the scintillation efficiency of anthracene in excellent agreement with the experimental results.[2] It also integrates a wide range of other scintillation phenomena.[1]

According to the theory, the scintillation process consists of a series of m photon emissions, each of quantum efficiency q_0 and decay time t_0, occurring in cascade. About half of the emissions are in the vacuum ultraviolet region, near the ionization energy, and correspond to the new primary fluorescence band, predicted by the theory. The remainder are in the normal visible fluorescence band. Intermediate emissions occurring in the strong absorption bands, between 2000 and 3000 A, are rapid ($\sim 10^{-11}-10^{-12}$ sec) and of 100 percent quantum efficiency.

The over-all quantum efficiency q of the scintillation process is thus given by

$$q=(q_0)^m. \tag{1}$$

If the internal quenching is small, so that q_0 approximates to unity, the scintillation decay time t_I is given by

$$t_I=mt_0. \tag{2}$$

If we measure the scintillation pulse height S in arbitrary units, so that

$$S=Aq, \tag{3}$$

we obtain from (1) and (2) that

$$\log S=\log A+Bt_I, \tag{4}$$

where

$$B=\log q_0/t_0. \tag{5}$$

For q_0 in the range from 0.9 to 1.0, $\log q_0$ is proportional to q_0, and hence since

$$q_0/t_0=1/t_{00}, \tag{6}$$

where t_{00} is the molecular decay time in the absence of internal quenching, we find that B is a constant within this range.

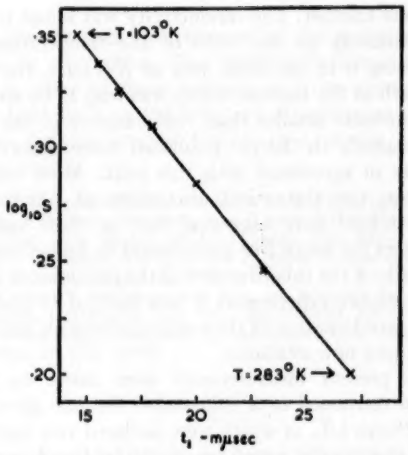

FIG. 1. Plot of logarithm of scintillation pulse height S *versus* scintillation decay time t_I.

Liebson[3] has studied the temperature variation of S and t_I for anthracene from 103°K to 283°K. Within this temperature range q_0 lies between 0.9 and 1.0. His results have been analyzed in terms of (4), and $\log_{10}S$ is plotted as a function of t_I in Fig. 1. A linear relationship is found, in accordance with the theory.

The molecular quantum efficiency q_0 of anthracene at room temperature is 0.9. Substituting q_0 and the experimental value of B (obtained from the slope of the graph) into (5), we obtain a value of $t_0=3.8$ mμsec for the molecular decay time of anthracene at room temperature. This is in excellent agreement with the experimental value of $t_0=3.5\pm1.0$ mμsec obtained by Birks and Little.[4]

[1] J. B. Birks, *Scintillation Counters* (Pergamon Press, London; McGraw-Hill Book Company, Inc., New York, 1953).
[2] J. B. Birks and M. E. Szendrei, Phys. Rev. **91**, 197 (1953).
[3] S. H. Liebson, Nucleonics **10**, No. 7, 41 (1952).
[4] J. B. Birks and W. A. Little, Proc. Phys. Soc. (London) **A66**, 921 (1953).

Thermal Conductivity of Liquid Helium Below 1.0°K

HENRY A. FAIRBANK* AND J. WILKS
Clarendon Laboratory, Oxford, England
(Received May 12, 1954)

SIXTEEN years ago, Kurti and Simon[1] showed in preliminary measurements that the very high heat transport observed in liquid helium between 1° and the lambda point had disappeared below 0.5°K. Two vessels containing paramagnetic salt and liquid helium were connected by a capillary tube full of the liquid, and the thermal conductivity was deduced from the rate at which the two capsules came into thermal equilibrium

with one another. The conductivity was found to vary approximately as the cube of the temperature; by expressing it in the usual way as $K=\frac{1}{3}\lambda Cv$, the mean free path of the thermal waves was seen to be an order of magnitude smaller than the diameter of the tube. Subsequently de Klerk[2] published some observations roughly in agreement with this work. More recently, however, the theoretical discussions of Landau and Khalatnikov[3] have suggested that at these low temperatures the mean free path should be limited only by the walls of the tube. In view of the preliminary nature of the earlier experiments it was decided to make another determination of the conductivity with the better techniques now available.

The present measurements were made on liquid helium contained in a thin-walled German silver tube of 0.29-mm i.d., to which were soldered two thermometers. Our results, which are shown in Fig. 1, were obtained by the conventional method of supplying heat to one end and observing the temperatures at two points along the capillary.[4] At all temperatures below about 0.6°K the heat flow was accurately proportional to the temperature gradient. Although the magnitudes of the temperature gradients observed varied as much as a factor 10, all the experimental points lie on a smooth curve. We also note that, as a sealed capsule technique[5] was employed, the specimen took several hours to warm up and it was possible to obtain good equilibrium conditions for each measurement.

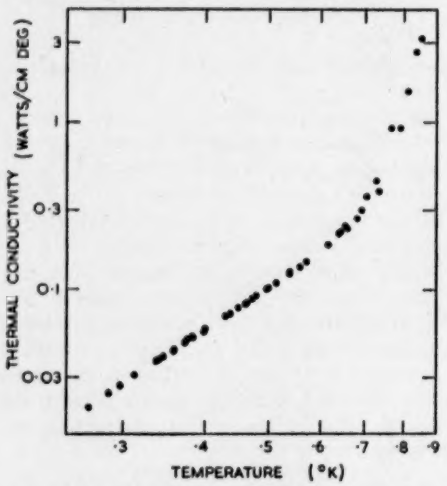

FIG. 1. Thermal conductivity of liquid helium as a function of temperature.

There is a pronounced break in the curve between 0.6° and 0.7° corresponding to the similar break in the specific heat curve.[6] At higher temperatures the heat flows rise very quickly with the temperature and tend towards the values given by Keesom, Saris, and Meyer[7]; we have not examined this region in detail since we may expect a complicated dependence of heat flow on temperature, as observed by the above-mentioned authors at somewhat higher temperatures. Below 0.6°, however, the heat flow is proportional to the temperature gradient and it is clear that the underlying mechanism is quite different. On calculating the mean free path of the phonons, using the values of Kramers, Wasscher, and Gorter[6] for the specific heat and extrapolating the values given by Atkins and Chase[8] for the velocity of sound, we obtain values which are about equal to the diameter of the tube at 0.6° and increase slowly as the temperature falls, being about 30 percent greater at 0.26°. This is quite consistent with the liquid behaving as a continuum whose thermal conductivity is limited by boundary scattering, the increase in mean free path with falling temperature being possibly associated with an increase in the amount of specular reflection at the walls.[9]

Further experiments using a tube of larger diameter are now in progress and a full account of all this work will be published later.

We wish to thank Mr. E. L. Simmons for his assistance with the measurements, and the John Simon Guggenheim Memorial Foundation for a grant to one of us (H.A.F.)

* On leave from Yale University.

[1] N. Kurti and F. Simon, Nature **142**, 207 (1938).
[2] D. de Klerk, Physica **12**, 513 (1946).
[3] L. D. Landau and I. M. Khalatnikov, J. Exptl. Theoret. Phys. (U.S.S.R.) **19**, 637, 709 (1949).
[4] J. L. Olsen and C. A. Renton, Phil. Mag. **43**, 946 (1952).
[5] Kurti, Rollin, and Simon, Physica **2**, 266 (1936); Hull, Wilkinson, and Wilks, Proc. Phys. Soc. (London) **A64**, 379 (1951).
[6] Kramers, Wasscher, and Gorter, Physica **18**, 329 (1952).
[7] Keesom, Saris, and Meyer, Physica **7**, 817 (1940).
[8] K. R. Atkins and C. E. Chase, Proc. Phys. Soc. (London) **A64**, 826 (1951).
[9] Berman, Simon, and Ziman, Proc. Roy. Soc. (London) **A220**, 171 (1953).

Melting Curves of Deuterium and Hydrogen

P. F. CHESTER* AND J. S. DUGDALE
Division of Physics, National Research Council, Ottawa, Canada
(Received May 6, 1954)

THERE has recently been considerable theoretical interest in the general behavior of the melting curve of simple substances.[1] Earlier experimental work[2] on the melting curves of hydrogen and deuterium had shown that up to one hundred kg/cm² (the highest pressure to which the measurements on deuterium had then been carried) the melting curves of these isotopes were very accurately parallel, i.e., a displacement of the deuterium melting curve in the direction of the positive pressure axis by about 171 kg/cm² would superpose it on that of hydrogen. It appeared, therefore, of importance to establish whether this phenomenon persisted over a wide pressure range.

For this purpose the melting curve of deuterium was determined up to a pressure of about 2800 kg/cm² and

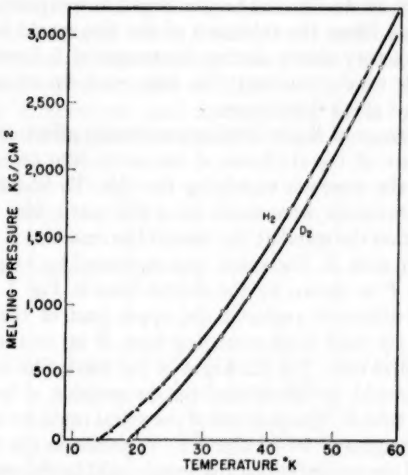

FIG. 1. The melting curves of hydrogen and deuterium. ○ Present measurements. ▲ Previous low-pressure measurements. (See reference 2.)

that of hydrogen was redetermined (in order to obtain a more accurate comparison) over the same pressure range. The method used was that of the blocked capillary.[3] The pressure was determined by means of Bourdon gauges calibrated before and after the experiments against a free piston gauge and the temperature by means of a platinum resistance thermometer. The limits of experimental error were, for the pressure measurements ± 7 kg/cm² and for the temperature ± 0.01°K. The results are shown in Fig. 1 while Table I gives the pressure separation of the two curves for various temperatures.

It is seen that within the experimental error the two curves remain parallel over a pressure range some 27 times greater than that covered in the earlier experiments on deuterium. The striking behavior of the melting curve of these isotopes may be expected to throw light both on the influence of zero-point energy on the melting process and on the nature of this process itself.

TABLE I. The pressure separation of the melting curves of hydrogen and deuterium.

Temperature °K	Pressure separation kg/cm²
Present experiments	
25.05	176
28.78	178
32.91	179
37.10	170
40.31	169
43.16	176
46.25	171
49.21	166
51.74	161
54.23	160
56.98	168
Mean pressure separation = 170 kg/cm²	
rms deviation = 6 kg/cm²	
Earlier experiments*	
19.00	169.7
20.00	171.1
21.00	172.3

* See reference 2.

* National Research Laboratories Post-doctorate Fellow.

[1] E. g., J. de Boer, Proc. Roy. Soc. (London) **215**, 4 (1952); C. Domb, Phil. Mag. **42**, 131 (1951); L. Salter, Phil. Mag. **45**, 369 (1954); F. E. Simon, *The L. Farkas Memorial Volume* (Research Council of Israel, Jerusalem, 1952), p. 37.

[2] For complete references and data see Woolley, Scott, and Brickwedde, J. Research, Natl. Bur. Standards **41**, 379 (1948).

[3] H. Kamerlingh Onnes and W. van Gulik, Proc. Acad. Sci. Amsterdam **28**, 1184 (1926).

Experimental Evidence for Structure in the Helium II Film*

W. C. KNUDSEN AND J. R. DILLINGER
Department of Physics, University of Wisconsin, Madison, Wisconsin

(Received May 10, 1954)

FURTHER work on the measurement of the linear velocity of the He II film[1,2] has revealed effects which suggest the existence of structure in the film. The apparatus used is shown schematically in Fig. 1. *BCD*

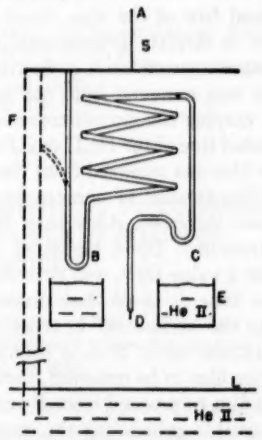

FIG. 1. Schematic diagram of experimental arrangement.

represents a copper wire bent into the shape of a spiral. As shown by the solid lines, this wire extends up from *B* and is fastened to a thin horizontal disk supported by an advance wire *S*. *E* is a small annular reservoir of He II which can be raised or lowered by a mechanism not shown. *L* represents the level of He II in a strip silvered Dewar. Provisions for enclosing the entire structure of Fig. 1 in an isothermal region are not shown.

If the He II in *E* is brought into contact with *B* but not *C*, the film will proceed along the spiral from *B* to *D* and form drops at *D*, since *D* is lower than the level of the liquid in *E*. The time between contact at *B* and the

falling of the first drop from D will be called t_l. It will equal the time for a film of full thickness to be established on the structure from B to D plus the time for sufficient helium to flow to form the first drop. If the He II in E is brought into contact with C, a film of full thickness will be established on the structure from C to D and He will flow to form a drop at D. The time between contact at C and the falling of the first drop from D will be called t_s. t_l-t_s is the time required for a film of full thickness to be established on the structure from B to C and will depend on the amount of film present on the spiral at the instant flow over the spiral is initiated. If the spiral is dry at the instant flow is initiated from B and again dry when initiated from C, the film presumably proceeds over the spiral with a rather well-defined front profile at a velocity limited by the critical velocity at which frictional forces come into play. This velocity, which we have called the linear velocity, is the length of the path B to C divided by t_l-t_s.

The amount of film present on the spiral at the time contact was made between B and the He II in E could be controlled in the following way. With film flowing from B to D and forming drops, contact of B with the He II in E was broken at the instant a drop fell from D. This left the spiral covered with a film of full thickness which could be removed by flow up from B along S to A. Point A was attached to a structure which was maintained free of the film. Since the volume rate of film flow is directly proportional to the periphery of the surface over which it is flowing, the rate at which the film was removed from the spiral could be controlled by varying the circumference of S. The spiral was suspended free of the He II in E for a time t_d during which the film was removed from the spiral by film flow along S. The amount of film on the spiral would decrease as t_d was increased. After each time t_d a value for t_l was determined. Upon repeating this film removal procedure a value for t_s was determined for each value of t_d. The time t_l-t_s is that during which film must flow onto the surface BC in order to establish a film of full thickness on it. If t_d is sufficiently long to permit all of the film to be removed, then t_l-t_s is the time for the full film to proceed from B to C and is that which is to be used in calculating the linear velocity.

In studying the dependence of t_l-t_s on the amount of film initially present on the spiral it has been found that certain thicknesses of the film are more stable than others. For large values of the periphery of the support S, t_l-t_s rises to a maximum constant value as t_d is increased. When the periphery is sufficiently small, there are five ranges of t_d during which t_l-t_s remains essentially constant. Between these constant values t_l-t_s rises rather abruptly. The largest constant value of t_l-t_s corresponds to the maximum value obtained with the larger peripheries. The first two constant values of t_l-t_s are precisely those reported earlier. The second constant values does not correspond to the condition in which all the film has been removed as was previously assumed. Since the thickness of the film would be decreasing very slowly during the ranges of t_d for which t_l-t_s is nearly constant, the film must be especially stable at these thicknesses.

Existence of stable thicknesses should affect the dependence of the thickness of the static film on height above the reservoir supplying the film. To investigate this, provisions were made for a full static film to be present on the spiral at the instant the reservoir E made contact with B. The spiral was supported by means of a tube F as shown by the dotted lines in Fig. 1. This dotted structure replaced the upper part of the wire shown by solid lines extending from B up to the thin horizontal disk. The thickness of the static film on the spiral would be determined by the position of level L on the tube F. The position of the spiral could be varied up to heights of 20 cm above L. Variation in the thickness of the static film on the spiral could be determined by the corresponding variation in t_l-t_s. t_l-t_s, and thus the thickness, changed slowly with height in the regions above and below 14 cm. In the vicinity of 14 cm the thickness changed considerably faster with height.

Details of this work will be submitted soon for publication.

* Work supported by the Wisconsin Alumni Research Foundation and the U. S. Atomic Energy Commission.

[1] W. C. Knudsen and J. R. Dillinger, Phys. Rev. **91**, 489 (1953).

[2] W. C. Knudsen and J. R. Dillinger, Abstracts of the Third International Conference on Low Temperature Physics and Chemistry, The Rice Institute, December 17–22, 1953 (unpublished).

Search for Antiferromagnetism in the Silicides V_3Si, Cr_3Si, and Mo_3Si

W. C. Koehler and E. O. Wollan
Oak Ridge National Laboratory, Oak Ridge, Tennessee

(Received May 10, 1954)

THE structure type $A15$[1] is characteristic of β wolfram and of the silicides V_3Si, Cr_3Si, and Mo_3Si[2] and as far as is known has no other representatives. In this structure silicon (or one quarter of the wolfram atoms) occupies body-centered cubic positions and the remaining transition metal atoms are found in closely packed linear rows. It has recently been suggested that the spins of the transition metal atoms in the silicides alternate in sign along the closely packed rows, and that the electronic configurations of the atoms in the solid are not essentially different from those of the corresponding isolated atoms.[3] If the free atom configurations of the transition group atoms are characteristic of these atoms in the silicides, then one may expect to find appreciable localized atomic magnetic moments in the lattice and such moments will lead to pronounced coherent scattering effects in a neutron diffraction pattern if there is some degree of correlation

in orientation of neighboring moments or to pronounced diffuse scattering effects if there is not such correlation.

Neutron diffraction data have been obtained for polycrystalline samples of V_3Si, Cr_3Si, and Mo_3Si at room temperature and also at 20.4°K, in order to study the magnetic structures of these materials.

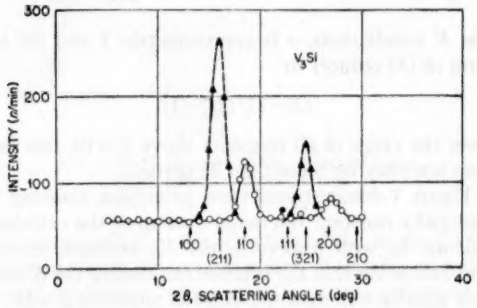

FIG. 1. Room temperature diffraction pattern of V_3Si. The dashed curves are antiferromagnetic intensities to be expected on Zener's model.

The neutron diffraction patterns at room temperature of the three silicides exhibit marked differences in relative line intensities because of the relative values of the scattering amplitudes of the several nuclei involved, but in each case the positions and intensities of the diffraction lines correspond to those to be expected from nuclear scattering alone. At 20.4°K the patterns are not essentially different from those at room temperature except for small changes due to different Debye factors at the two temperatures. A portion of the room temperature pattern of V_3Si is illustrated in Fig. 1. Since V

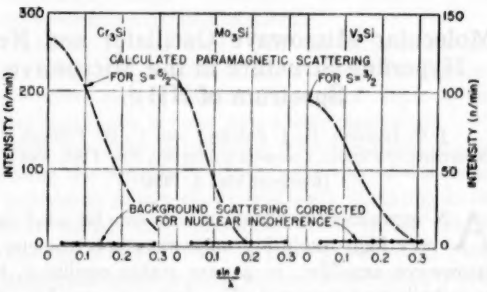

FIG. 2. Comparison of observed and expected diffuse scattering. The observed scattering has been corrected for nuclear incoherent effects.

has a very small coherent scattering cross section, the coherent scattering is due almost entirely to the silicon lattice. Also illustrated in Fig. 1 are magnetic coherent reflections which are to be expected on Zener's model.[3] This model requires a unit cell whose edges are twice those of the chemical unit cell, and the indices which refer to the doubled cell are enclosed by parentheses. It is clear that any aligned moments present in V_3Si are much smaller than those calculated from free atom configurations; an upper limit of $0.2\mu_B$ has been estimated for these moments from the sensitivity of the measurements. Similar results have been obtained from Cr_3Si and Mo_3Si.

It is also of interest to examine the diffuse scattering data. If moments of the order of several Bohr magnetons are indeed present but are uncorrelated in orientation, a pronounced angularly dependent paramagnetic scattering should be observed. Figure 2 shows the calculated paramagnetic scattering from the several silicides. To compare this with experiment, the observed diffuse scattering has been corrected for isotopic and spin disorder effects, and the residue is plotted as a function of $\sin\theta/\lambda$ for each compound. The angular dependence of the residual background scattering is in every case nearly isotropic and its magnitude is such as to be accounted for by multiple scattering alone. The maximum uncorrelated moment consistent with these data is about $0.2\mu_B$ in each case.

In the course of this work we have redetermined the silicon coherent scattering cross section from elemental silicon to be 2.16 ± 0.06b which is to be compared with Weiss' value of 2.0 ± 0.2b from small-angle scattering measurements.[4]

We are indebted to Mr. D. E. LaValle for chemical preparations, and to Dr. H. Yakel and Mr. R. M. Steele for x-ray analyses of the samples.

[1] *Strukturbericht* (Akademische Verlagsgesellschaft, Leipzig, 1937 and 1943), Vol. 3, p. 628, and Vol. 7, p. 3.
[2] D. H. Templeton and C. H. Dauben, Acta Cryst. **3**, 261 (1950).
[3] C. Zener, Phys. Rev. **81**, 440 (1951).
[4] R. J. Weiss, Phys. Rev. **83**, 379 (1951).

Moseley's Law Applied to Proportional Counter Resolution of Adjacent Elements

C. H. HENDEE AND S. FINE
Philips Laboratories, Irvington-on-Hudson, New York
(Received March 12, 1954; revised manuscript received May 10, 1954)

THE proportional counter, by virtue of its ability to furnish information concerning intensity (counts/sec) and energy (pulse amplitude) of incident radiation, can be used in certain applications as an x-ray spectrometer in a nondispersive system.[1] A knowledge of the energy resolution and its variation with energy is important for the maximum utilization of the proportional counter in this manner.

The energy resolution of a proportional counter is determined by the magnitude of the statistical fluctuation in the initial absorption ionization and subsequent gas multiplication. The "half-width" of a peak in the pulse-height distribution (PHD) is an abbreviated term for the amplitude difference between those pulses comprising the PHD that occur at half the maximum rate.

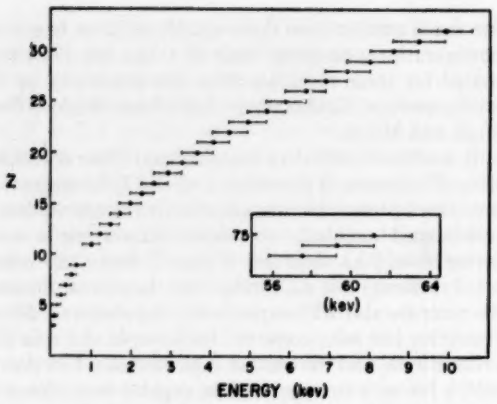

FIG. 1. $K\alpha$ energies and calculated PHD half-widths as a function of atomic number, based on 15 percent half-width for $_{29}$Cu. Insert shows the half-widths for the $K\alpha$ of $_{73}$Ta, $_{74}$W, and $_{75}$Re.

A more generally used quantity is the "percent half-width" which is the ratio of the half-width to the pulse amplitude at maximum rate ($\times 100$).

From an extension of some work by Frisch[2] and Fano[3] on the statistical fluctuations in multiplicative processes, it was found for the peaks in the PHD of a proportional counter, that

$$(\text{half-width}) \propto (\text{energy})^{\frac{1}{2}}. \quad (1)$$

This has been experimentally verified[4] in this Laboratory using rare-gas filled proportional counters to detect x-radiations ranging in energy from 5 to 50 kev. Although radiations below 5 kev have not been directly checked, the escape pulses from the counter offered a means of extending this range into the soft x-ray region to 1 kev.

It is interesting to note that Moseley's Law, giving the relation between energy of characteristic lines and atomic number,

$$(Z-\sigma) \propto (\text{energy})^{\frac{1}{2}}, \quad (2)$$

has a similar form. Two consequences follow: (a) The half-width of the PHD produced by the characteristic radiation of an element is approximately proportional to the atomic number of the element. The percent half-width, therefore, is a means of identifying elements, provided the half-width for a known energy has been determined. (b) The ability of a proportional counter to resolve characteristic x-radiations of adjacent elements is approximately constant over all the elements. That is,

$$B(Z)/[E(Z+1)-E(Z)] \cong \text{const}, \quad (3)$$

where $B(Z)$ is the half-width of the PHD given by x-rays from an emitter of atomic number Z, and $E(Z)$ is the energy of the x-rays.

In order to determine the degree of approximation and the validity of (b), Eqs. (1) and (2) are combined:

$$B(Z) \propto [E(Z)]^{\frac{1}{2}} \propto (Z-\sigma). \quad (4)$$

Then,

$$\frac{B(Z)}{E(Z+1)-E(Z)} \propto \frac{Z-\sigma}{(Z+1-\sigma)^2-(Z-\sigma)^2} = \frac{Z-\sigma}{2(Z-\sigma)+1}. \quad (5)$$

For K x-radiations, σ is approximately 1 and the last term of (5) reduces to

$$(Z-1)/(2Z-1).$$

Over the range of all elements above $Z=10$, this ratio does not vary by more than $2\frac{1}{2}$ percent.

Figure 1 demonstrates these principles, showing the nominally constant fractional overlap of the calculated half-widths with respect to the $K\alpha$ emission energies and indicating that the counter can resolve the K emission equally well over the range of elements $Z>10$.

It has been shown that the resolution of x-rays of adjacent elements is a constant intrinsic property of the proportional counter over all the elements. Beyond that limitation, its use as a spectrometric device for the identification of elements is contingent on the absorption properties of the gas-filling and window and the x-ray intensity available from the source.

[1] Curran, Angus, and Cockroft, Phil. Mag. **40**, 36 (1949); J. H. Kahn, Oak Ridge National Laboratory Report ORNL-1089, USAEC, Nov. 8, 1951 (unpublished); D. West, in *Progress in Nuclear Physics* (Academic Press, Inc., New York, 1953), Vol. 3.
[2] O. R. Frisch, (unpublished).
[3] U. Fano, Phys. Rev. **72**, 26 (1947).
[4] (To be published).

Molecular Microwave Oscillator and New Hyperfine Structure in the Microwave Spectrum of NH_3†

J. P. GORDON, H. J. ZEIGER,* AND C. H. TOWNES
Department of Physics, Columbia University, New York, New York
(Received May 5, 1954)

AN experimental device, which can be used as a very high resolution microwave spectrometer, a microwave amplifier, or a very stable oscillator, has been built and operated. The device, as used on the ammonia inversion spectrum, depends on the emission of energy inside a high-Q cavity by a beam of ammonia molecules. Lines whose total width at half-maximum is six to eight kilocycles have been observed with the device operated as a spectrometer. As an oscillator, the apparatus promises to be a rather simple source of a very stable frequency.

A block diagram of the apparatus is shown in Fig. 1. A beam of ammonia molecules emerges from the source and enters a system of focusing electrodes. These electrodes establish a quadrupolar cylindrical electrostatic

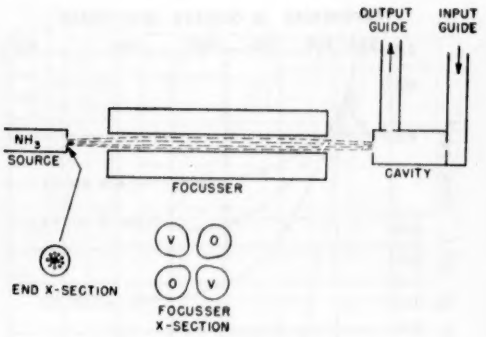

FIG. 1. Block diagram of the molecular beam spectrometer and oscillator.

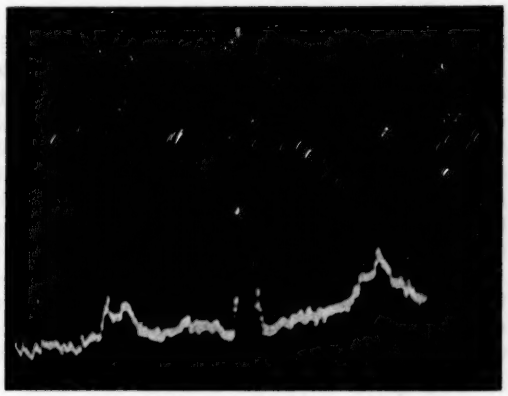

FIG. 2. A typical oscilloscope photograph of the NH_3, $J=K=3$ inversion line at 23 870 Mc/sec, showing the resolved magnetic satellites. Frequency increases to the left.

field whose axis is in the direction of the beam. Of the inversion levels, the upper states experience a radial inward (focusing) force, while the lower states see a radial outward force. The molecules arriving at the cavity are then virtually all in the upper states. Transitions are induced in the cavity, resulting in a change in the cavity power level when the beam of molecules is present. Power of varying frequency is transmitted through the cavity, and an emission line is seen when the klystron frequency goes through the molecular transition frequency.

If the power emitted from the beam is enough to maintain the field strength in the cavity at a sufficiently high level to induce transitions in the following beam, then self-sustained oscillations will result. Such oscillations have been produced. Although the power level has not yet been directly measured, it is estimated at about 10^{-8} watt. The frequency stability of the oscillation promises to compare favorably with that of other possible varieties of "atomic clocks."

Under conditions such that oscillations are not maintained, the device acts like an amplifier of microwave power near a molecular resonance. Such an amplifier may have a noise figure very near unity.

High resolution is obtained with the apparatus by utilizing the directivity of the molecules in the beam. A cylindrical copper cavity was used, operating in the $TE011$ mode. The molecules, which travel parallel to the axis of the cylinder, then see a field which varies in amplitude as $\sin(\pi x/L)$, where x varies from 0 to L. In particular, a molecule traveling with a velocity v sees a field varying with time as $\sin(\pi vt/L)\sin(\Omega t)$, where Ω is the frequency of the rf field in the cavity. A Fourier analysis of this field, which the molecule sees from $t=0$ to $t=L/v$, gives a frequency distribution whose amplitude drops to 0.707 of its maximum at points separated by a $\Delta\nu$ of $1.2v/L$. The cavity used was twelve centimeters long, and the most probable velocity of ammonia molecules in a beam at room temperature is 4×10^4 cm/sec. Since the transition probability is proportional to the square of the field amplitude, the resulting line should have a total width at half-maximum given by the above expression, which in the present case is 4 kc/sec. The observed line width of 6–8 kc/sec is close to this value.

The hyperfine structure of the ammonia inversion transitions for $J=K=2$ and $J=K=3$ has been examined, and previously unresolved structure due to the reorientation of the hydrogen spins has been observed. Figure 2 is a typical scope photograph of these new magnetic satellites on the 3,3 line. The observed spectra for the 3,3 line is shown in Fig. 3, which contains all the observed hyperfine structure components, including the quadrupole reorientation transitions of the nitrogen nucleus, which have been previously observed as single lines.

Within the resolution of the apparatus, the hyperfine structures of the upper and lower inversion levels are

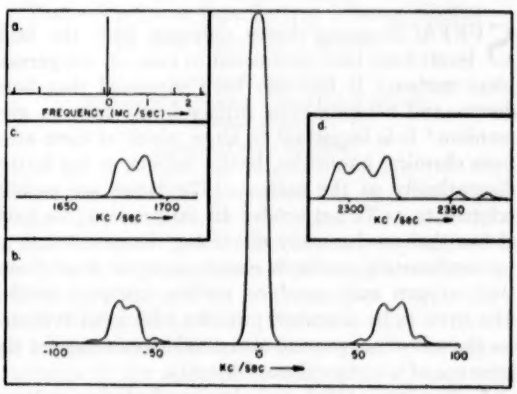

FIG. 3. The observed hyperfine spectrum of the 3,3 inversion line. (a) Complete spectrum, showing the spacings of the quadrupole satellites. (b) Main line with magnetic satellites. (c) Structure of the inner quadrupole satellites. (d) Structure of the outer quadrupole satellites. The quadrupole satellites on the low-frequency side of the main line are the mirror images of those shown, which are the ones on the high-frequency side.

identical, as evidenced by the fact that the main line is not split. Symmetry considerations require that the hydrogen spins be in a symmetric state under 120-degree rotations about the molecular axis. Thus for the 3,3 state, $I_H=3/2$, and one expects each of the quadrupole levels to be further split into four components by the interaction of the hydrogen magnetic moments with the various magnetic fields of the molecule. At the present writing, the finer details of the expected magnetic splittings have not been worked out.

This type of apparatus has considerable potentialities as a more general spectrometer. Since the effective dipole moments of molecules depend on their rotational state, some selection of rotational states could be effected by such a focuser. Similarly, a focuser using magnetic fields would allow spectroscopy of atoms. Sizable dipole moments are required for a strong focusing action, but within this limitation, the device may prove to have a fairly general applicability for the detection of transitions in the microwave region.

The authors would like to acknowledge the expert help of Mr. T. C. Wang during the latter stages of this experiment.

† Work supported jointly by the Signal Corps, the U. S. Office of Naval Research, and the Air Force.

* Carbide and Carbon post-doctoral Fellow in Physics, now at Project Lincoln, Massachusetts Institute of Technology, Cambridge, Massachusetts.

Oxygen and the Surface Energy-Level Structure on Germanium

EDWARD N. CLARKE
Physics Laboratories, Sylvania Electric Products, Bayside, New York

(Received April 28, 1954)

SURFACE energy levels different from the bulk levels have been postulated to exist on the germanium surface.[1] It has also been suggested that both donor- and acceptor-type surface levels exist on germanium.[2] It is important to know which of these arise from chemical impurities, lattice defects, or the lattice discontinuity at the surface. (The latter are usually referred to as Tamm levels.) In earlier work, we have shown that mechanically disturbing the germanium as by sandblasting produces surface acceptor levels,[3] and that oxygen may produce surface acceptor levels.[4] The work to be described provides additional evidence for the role of oxygen and also provides evidence for the presence of a surface donor impurity.

A very thin (10^{-2} cm), low-conductivity n type, etched single crystal of germanium is heated in a vacuum of 10^{-7} mm Hg. Heating is achieved by passing a large ac current through the crystal. The crystal is then quenched rapidly by shutting off the current, and the conductivity measured. In Fig. 1 the solid lines represent the resulting conductivity, measured at 195°K, as a function of heat treatment temperature. Similar curves are obtained for conductivity at room temperature. The times 2, 4, and 9 hours refer to the total heating time at temperatures higher than 700°C before reaching the corresponding level of conductivity. It is expected that the heat treatment will change the conductivity for two reasons: (1) introduction of Frenkel defects[5] as shown by the dashed line in Fig. 1, and (2) changes in impurities on the surface. The large excess conductivity actually observed is ascribed to changes in impurities on the surface. Further investigations to be described later show that the excess conductivity, i.e., all of that above the dashed curve, is n-type conductivity. The conductivity data thus show that we have either introduced donors or removed acceptors, or both.

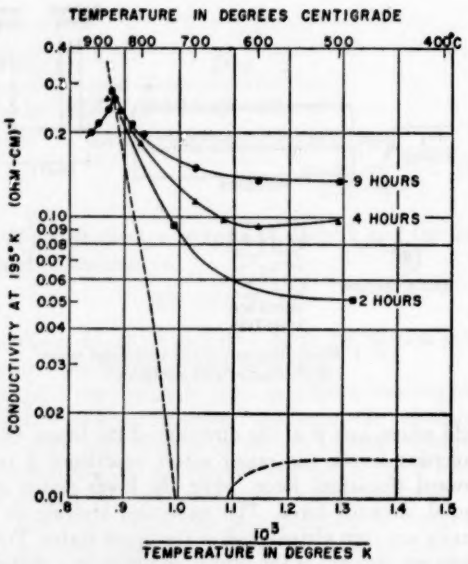

FIG. 1. Conductivity of a thin single crystal of germanium after heating and quenching from various high temperatures in vacuum (vacuum interrupted on several occasions during the experiment to produce the results in Fig. 2). Conductivity of starting material is 0.0137 (ohm-cm)$^{-1}$ at 195°K. Dashed curve represents the effect of Frenkel defects quenched in at the various temperatures.

That we have removed acceptor levels by heating in vacuum, and that these acceptors result from the presence of oxygen is shown by having the vacuum heated germanium react with oxygen. Figure 2(a) shows conductivity measured at 195°K as a function of heating time in oxygen. The oxygen is present at a pressure of about 0.5 mm Hg. The conductivity decreases markedly with heating in oxygen. We have been able to produce surfaces that react rapidly with oxygen even at room temperature and below. If the germanium is heated once again in vacuum, the conductivity is increased as shown in Fig. 2(b) and can be returned to its initial value by heating at a higher tem-

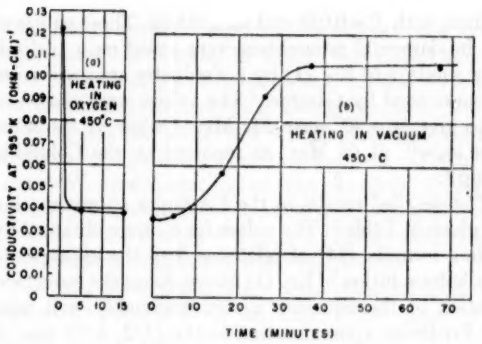

FIG. 2. (a) Conductivity after heating in oxygen; (b) conductivity after heating in vacuum.

perature. The reduction in conductivity with reaction between germanium and oxygen suggests that oxygen produces electron traps on the germanium surface, and if we assume bulk mobilities[6] the observed reductions in conductivity correspond to a trapping of about 5×10^{11} electrons/cm^2 of surface.

The above suggests that if oxygen is allowed to react with germanium having a fairly wide *p*-type or near-intrinsic surface region, the conductivity will increase rather than decrease, with the electrons entering the oxygen levels from the valence band leaving mobile holes behind; we have observed this in earlier work.[4]

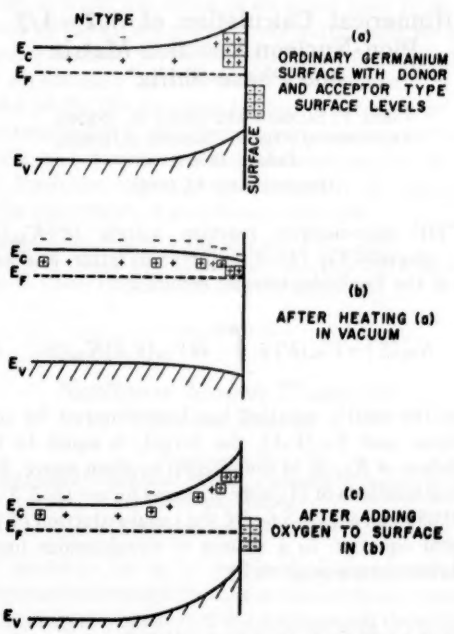

FIG. 3. Proposed model of the etched germanium surface after heating in vacuum and after admitting oxygen to the surface. E_C is the bottom of the conduction band, E_V the top of the valence band, and E_F the Fermi level.

It is found that the excess conductivity results from impurities, some of which have diffused deeply into the germanium. With removal of the germanium from the vacuum system, the conductivity decreases corresponding to oxygen reacting with the germanium. However, there is still much excess conductivity remaining. Rectification measurements show that this is *n* type. Slow etching of the surface in conjunction with conductivity measurements show that about 70 percent of the excess conductivity is limited to a surface region several microns in thickness. With further etching, the conductivity levels off at a value much larger than that of the original crystal indicating that some of the donors have diffused deeply into the germanium.

Figure 3 shows a model of the etched germanium surface as it is affected by heating in vacuum, and by reaction with oxygen.

The nature of the donor centers is as yet unknown. However, there exists the interesting possibility that oxygen might also be responsible for the donor levels. In this case, the oxygen might be that which has entered the germanium lattice rather than sitting on the surface where it produces electron traps.

Whether or not oxygen can account for most of the surface levels on the etched germanium surface remains to be seen. Our work, thus far, suggests that oxygen can account for at least 10^{12} to 10^{13} surface levels per cm^2.

[1] J. Bardeen, Phys. Rev. **71**, 717 (1947).
[2] W. H. Brattain and J. Bardeen, Bell System Tech. J. **32**, 1 (1953).
[3] E. N. Clarke and R. L. Hopkins, Phys. Rev. **91**, 1566 (1953).
[4] E. N. Clarke, Phys. Rev. **91**, 756 (1953).
[5] S. Mayburg (to be published).
[6] M. Prince, Phys. Rev. **92**, 681 (1953).

Improved Calculation of the *P*-Wave Pion-Nucleon Scattering Phase Shifts in the Cut-Off Theory*

GEOFFREY F. CHEW
Department of Physics, University of Illinois, Urbana, Illinois
(Received May 10, 1954)

IN earlier papers[1,2] the author has proposed a perturbation method for evaluating the cut-off form of the Yukawa theory. This method was applied in lowest order to the problem of pion-nucleon scattering and results presented[3] for a renormalized $f^2=0.2$ and a cut-off energy, $\omega_{max}=3.2\mu$. However, these values of the fundamental parameters do not lead to an actual resonance in the state of isotopic spin 3/2 and total angular momentum 3/2, a resonance which is now strongly indicated experimentally.[4,5] A larger cut-off energy is required to give genuine resonance and with such a larger cutoff the variational approximation used in reference 3 is not quantitatively reliable.[6] Also, higher-order effects, neglected previously, become more

important. The purpose of this note is to report a calculation of the P-wave phase shifts which is improved with respect to these earlier deficiencies.

Fourth-order corrections to the scattering, in the sense of reference 2, have been analyzed and the only important ones found to be those resulting from nucleon propagation function modification. Thus Eq. (8) of reference 2 for the reaction matrix is to be altered by modifying the nucleon propagation "between" virtual scatterings; i.e., we now have

$$(k_f|K_{0\alpha}|k_0)=(k_f|U_{0\alpha}|k_0)+\int_0^\infty \frac{4\pi k^2 dk}{(2\pi)^3} \times(k_f|U_{0\alpha}|k)\frac{1}{(\omega_0-\omega_k)[1+f^2\Delta(\omega_0-\omega_k)]} \times(k|K_{0\alpha}|k_0), \quad (1)$$

where the function Δ is given by Eq. (4) of reference 2 and all symbols have the same meaning as in that reference. At the same time, the "potential" $U_{0\alpha}$ is changed to the following:

$$(k_n|U_{0\alpha}|k_m)=c_\alpha 2\pi\frac{f^2}{\mu^2}\frac{k_n k_m}{(\omega_n\omega_m)^{\frac{1}{2}}} \times\frac{v(k_n)v(k_m)}{(\omega_0-\omega_n-\omega_m)[1+f^2\Delta(\omega_0-\omega_n-\omega_m)]}. \quad (2)$$

That is, nucleon propagation "within" a fundamental virtual scattering is also modified. The two modifications are of the same order. For the problem in question the "average" value of $f^2\Delta$ is roughly -0.3 either "inside" or "outside" a virtual scattering. This may seem large for an allegedly weak coupling situation, but a preliminary investigation indicates that further important corrections to the propagation function are unlikely. For this reason no modification has been made of formula (14) from reference (2), which gives most of the scattering in the (1/2, 1/2) state.

In the following letter, a machine numerical integration of Eq. (1) above for the (3/2, 3/2) state will be described, with $f^2=0.058$ and $\omega_{max}=5.6\mu$. These values of the fundamental parameters were based on a preliminary solution of Eq. (1) by a Fredholm approximation recommended by Gammel.[6] The values were chosen so as to give $\delta_{33}=90°$ near 200 Mev[4,5] while at the same time $\delta_{33}=9°$ at 65 Mev, as reported by the Columbia group.[7]

TABLE I. Theoretical P-wave phase shifts according to the Fredholm approximation.

ω_0/μ	E_{lab}(Mev)	δ_{33}	$\delta_{31}=\delta_{13}$	δ_{11}
1.2	38	+3.7°		
1.3	57	8.0°	−1.0°	−2.3°
1.4	78	14.7°		
1.5	99	24.9°	−2.0°	−4.3°
1.6	122	39.4°		
1.7	144	56.9°	−3.3°	−6.4°
1.8	167	73.2°		
1.9	190	85.8°	−4.8°	−8.4°
2.0	215	94.6°		
2.1	240	99.5°	−6.3°	−10.3°

The detailed results of the Fredholm approximation are given in Table I. The values for δ_{11} were obtained by adding formula (14) of reference 3 to the appropriate Fredholm solution of Eq. (1) above. Since the numerical solution of the equation agrees reasonably well with the Fredholm approximation in the (3/2, 3/2) case, it has been assumed that the Fredholm results for the other P states, where the interaction is weaker, are also accurate.

The author is greatly indebted to J. Gammel for advance communication of his results on the same general problem.

* Supported by the U. S. Office of Naval Research.

[1] G. F. Chew, Phys. Rev. **94**, 1749 (1954).
[2] G. F. Chew, Phys. Rev. **94**, 1755 (1954).
[3] G. F. Chew, Phys. Rev. **89**, 591 (1953).
[4] M. Glicksman, Phys. Rev. (to be published).
[5] DeHoffmann, Metropolis, Alei, and Bethe, Phys. Rev. (to be published).
[6] J. L. Gammel, Phys. Rev. **95**, 209 (1954).
[7] Bodansky, Sachs, and Steinberger, Phys. Rev. **93**, 1367 (1954).

Numerical Calculation of 3/2−3/2 Pion-Nucleon Reaction Matrix and Phase Shifts*

FREDA F. SALZMAN AND JAMES N. SNYDER
Department of Physics, University of Illinois, Urbana, Illinois

(Received May 10, 1954)

THE pion-nucleon reaction matrix $(k'|K_{0\alpha}|k_0)$ given by Eq. (1) of the previous letter, is a solution of the Fredholm integral equation,

$$K_{0\alpha}(k')=U_{0\alpha}(k')+\int_0^\infty dk Y_{0\alpha}(k',k)K_{0\alpha}(k), \quad (1)$$

where the matrix notation has been dropped for convenience, and $Y_{0\alpha}(k',k)$, the kernel, is equal to the coefficient of $K_{0\alpha}(k)$ in the integral as given above. Numerical solutions of (1) were obtained for $\alpha=(3/2, 3/2)$, $f^2=0.058$ and $\omega_{max}=5.6\mu$ by the usual reduction of the integral equation to a system of simultaneous linear algebraic equations given by[1]

$$0=U_0(k_i)+\sum_{j=0}^{N}[a_jY_0(k_i,k_j)-\delta_{ij}]K_0(k_j), \quad 0\leqslant i\leqslant N; \quad (2)$$

where the a_j are the integration coefficients used in approximating the integral by a sum and $K_0(k_j)$ are the $N+1$ unknowns. The system of Eqs. (2) was solved on the Illinois Electronic Digital Computer, with $N=36$.

For $\omega_0<2\mu$ the kernel has a single singularity which occurs at $k=k_0$, and the usual care has to be taken in the numerical approximation of the integral. Straightforward procedures were employed which did not change the form of the system of Eqs. (2). The a_j were chosen to be Simpson coefficients wherever possible.

The scattering phase shifts were obtained from the values of $K_0(k)$ for $k=k_0$. In Table I the values of δ_{33}

TABLE I. The theoretical phase shifts in the (3/2, 3/2) state.

ω_0/μ	δ_{33}
1.24	4.6°
1.43	15.6°
1.72	54.7°
1.91	84.5°
2.01	94.4°

are listed for the particular energies investigated. It is seen that the results of the Fredholm approximation, given in the previous letter, are rather closely reproduced.

The solutions $K_0(k)$ of (2) for $k=k_0$ are the "off-the-energy-shell" elements of the reaction matrix and are required for problems, such as photo-pion production, which involve the pion scattering wave function. The values of $K_0(k)$ are found to be larger than those obtained by the variational method,[2] particularly for high k, where the exact solution remains fairly constant while the approximate one decreases. The difference in behavior of the two solutions for high k accounts for the inaccuracy of the variational approximation for large cutoffs and the consequent underestimation of δ_{33}. The Fredholm approximation proposed by Gammel,[1] on the other hand, does not have this defect.

* Supported by the U. S. Office of Naval Research.

[1] For more details, see J. L. Gammel, Phys. Rev. **95**, 209 (1954).

[2] G. F. Chew, Phys. Rev. **93**, 341 (1954).

Nonlinear Meson Theory of Nuclear Forces

FERDINAND CAP
Institute of Theoretical Physics, University of Innsbruck, Innsbruck, Austria

(Received April 19, 1954)

IT seems to be quite certain that pseudoscalar π mesons are responsible for the nuclear forces. Except for the magnetic moment of the nucleons and the saturation conditions, virtually all known experimental facts of low energy can be well explained by the symmetrical pseudoscalar theory.[1] However, there appear difficulties for high energies and for small distances. Scattering experiments at high energies cannot be explained, nor can the binding energy and the quadrupole moment of of the deuteron be calculated without a cutoff. In spite of the fact that the concept of a "potential of the nuclear forces" can be applied only with certain restrictions at small distances or high energies, it is still possible to describe[2] scattering experiments at high energies by phenomenological static potentials. Here one can use pseudoscalar meson-potentials in the "outer" region and phenomenological potentials in the "interior" region.[3] According to Lévy, Jastrow, and other authors,[4] it is customary to assume the inner potential to be strongly repulsive. However, Yukawa[5] and Banerjee[6] have voiced doubts concerning Jastrow's potential, and furthermore there is a possibility of making the potential finite and attractive or finite and repulsive for $r=0$ by a modification of the field equations of the meson.

As the writer has shown,[7] it seems to be possible by an invariant nonlinear modification of the meson equations to obtain a static potential which connects the interior and exterior region and which is continuous (i.e., not composed of parts). Except for the fact that the new field-theoretical methods of Schwinger, Tomonaga, Dyson, and Feynman still lack a more profound foundation[8] and that they are exposed to strong criticism,[9] there are several reasons for a nonlinear meson theory.[10] For instance, a real multiple production of mesons, today favored by strong arguments,[11] is only possible with a strong interaction, nonlinear in the derivative of the meson field. Furthermore, the decay of the τ meson into three pions, the saturation of the nuclear forces,[12] and the necessity[12] of a $\lambda\varphi^3$ term seem to favor nonlinear equations.

A modification of the meson field equations which leads to a monotonic potential, finite at $r=0$, and which therefore is everywhere attractive for the deuteron problem (symmetrical theory), could be explained physically by a vacuum polarization depending—in the sense of Born[13]—on the meson field strength. The virtual mesons produce a cloud of nucleon pairs surrounding the nucleon. According to Hu,[14] this inhibits the emission of high energy virtual mesons and accordingly removes the divergences. As a matter of fact, a cutoff of the frequencies of linear virtual *PS* mesons, according to the quantum-mechanical l_0 theory,[15] leads to virtually the same potential as the nonlinear classical theory.

The proposed theory can be made[7] unitary or nonunitary. In this note we treat only the unitary form in which the nucleon is—according to Born's electrodynamics—a locus at which the field energy is highly concentrated. Let $\phi=A_{,k}{}^2+\kappa^2A^2$ be the Lagrangian of the neutral linear scalar meson theory; one may put for a nonlinear theory $\mathfrak{L}=\sum_n a_n\phi^n$. Such Lagrangians have already been considered by Russian authors.[16] Following Born, Heisenberg[10] has proposed a Lagrangian $\alpha^{-1}[(1+\alpha\phi)^{\frac{1}{2}}-1]$, but the present writer was able

to show that the static spherical symmetric potential $A(r)$ which belongs to it rises for small distances even more than the Yukawa potential. Therefore the Lagrangians

$$\alpha^{-1}[(1-\alpha A_{,k}{}^2)^{\frac{1}{2}}-1]-\tfrac{1}{2}\kappa^2A^2$$

and

$$\alpha^{-1}[(1-\alpha\phi)^{\frac{1}{2}}-1] \tag{1}$$

were examined, and both of them result in finite potentials at $r=0$. The Lagrangian (1) leads to the differential equation

$$A_{,l,l}-\kappa^2A-A_{,l,l}\alpha(\kappa^2A^2+A_{,k}{}^2)+\alpha A_{,k}A_{,l}A_{,k,l}$$
$$+\alpha\kappa^4A^3+2\alpha\kappa^2AA_{,k}{}^2=0$$

which for large distances (i.e., $\alpha\sim0$) goes over into $(\Box-\kappa^2)A=0$. For static spherical symmetrical cases (pole at rest) this differential equation has a solution $A(r)$ with $A'(0)=0$, so that terms like $(1/r)A'$ remain also finite. In classical approximation the linear pseudoscalar meson field is the dipole solution of the scalar field;[17] the interaction of two nucleons is described by $(\boldsymbol{\sigma}_2\cdot\nabla)(\boldsymbol{\sigma}_1\cdot\nabla)\varphi$, where

$$(\Box-\kappa^2)\varphi=0,$$

$$\varphi=(\boldsymbol{\sigma}_1\cdot\nabla)\frac{e^{-\kappa r}}{r}=|\boldsymbol{\sigma}_1|\frac{d}{dr}\frac{e^{-\kappa r}}{r}\cdot\cos\vartheta.$$

One can therefore in first approximation, by application of the operator $(\boldsymbol{\sigma}_2\cdot\nabla)(\boldsymbol{\sigma}_1\cdot\nabla)$ to the solution $A(r)$ of the scalar nonlinear field (pole), obtain a neutral nonlinear classical meson potential

$$\beta(\boldsymbol{\sigma}_2\cdot\nabla)(\boldsymbol{\sigma}_1\cdot\nabla)A(r)$$
$$=\beta\left(S_{12}\frac{d}{dr}\frac{1}{r}\frac{d}{dr}A'+\boldsymbol{\sigma}_1\cdot\boldsymbol{\sigma}_2\frac{1}{r}A'+\tfrac{1}{3}\boldsymbol{\sigma}_1\cdot\boldsymbol{\sigma}_2\frac{d}{dr}\frac{1}{r}\frac{d}{dr}A'\right), \tag{2}$$

where $S_{12}=(\boldsymbol{\sigma}_1\cdot\mathbf{r})(\boldsymbol{\sigma}_2\cdot\mathbf{r})/r^2-\frac{1}{3}\boldsymbol{\sigma}_1\cdot\boldsymbol{\sigma}_2$ (dipole interaction).

Because the constant α is fixed by the demand that the total energy of the meson field be equal to the self-energy of the nucleon, $Mc^2=938$ Mev, and because, as a consequence of $A(0)$ being finite, no cutoff method has to be applied, β is the only free parameter. κ is already fixed by the mass of the pion. If one puts the potential (2) into the deuteron equation and determines β in such a way that as eigenvalue the binding energy of the deuteron of 2.227 Mev is obtained, then one has, for $\beta=-112$ Mev (a reasonable value in the sense of a potential well depth) and in first very rough approximation, a quadrupole moment of $+5\times10^{-27}$ cm^2 and a 17 percent ^3D admixture. More exact and more extensive calculations, particularly concerning better solutions of the nonlinear differential equation resulting from (1)—and other similar Lagrangians—are in progress. An extensive report will be given later about the results of these calculations.

The author wants to express his sincere gratitude to the European Office, Air Research and Development Command, for the sponsorship of his work.

[1] S. Machida, Progr. Theoret. Phys. Japan **6**, 904 (1951).
[2] R. Jastrow, Phys. Rev. **81**, 165 (1951).
[3] M. Taketani *et al.*, Progr. Theoret. Phys. Japan **6**, 581 (1951); **7**, 45 (1952).
[4] M. M. Lévy, Compt. rend. **234**, 1744 (1952); K. A. Brueckner and F. Low, Phys. Rev. **83**, 461 (1951); R. Jastrow, Phys. Rev. **91**, 749 (1953).
[5] S. Yukawa (private communication).
[6] P. Banerjee, Indian J. Phys. **27**, 173 (1953).
[7] F. Cap, Progr. Theoret. Phys. Japan **10**, 235 (1953).
[8] W. Heisenberg, Leyden Conference, 1953.
[9] H. Steinwedel, Fortschr. Physik **1**, 7 (1953); M. M. Lévy, Phys. Rev. **84**, 441 (1951).
[10] W. Heisenberg, Z. Physik **113**, 61 (1939); **126**, 519 (1949); **133**, 65 (1952).
[11] W. Heisenberg *et al.*, *Kosmische Strahlung* (Springer-Verlag, Berlin, 1953).
[12] L. I. Schiff, Phys. Rev. **84**, 1, 10 (1951); W. Thirring, Z. Naturforsch. **7a**, 63 (1952).
[13] M. Born, Proc. Roy. Soc. (London) **A143**, 410 (1934).
[14] T. M. Hu, Phys. Rev. **80**, 1109 (1951).
[15] A. March, Acta Phys. Austriaca **1**, 19, 137 (1948); further investigations in progress in Innsbruck.
[16] D. Ivanenko and V. Lebedev, Doklady Akad. Nauk. S.S.S.R. **80**, 357 (1951); **88**, 425 (1953).
[17] W. Pauli, *Meson Theory of Nuclear Forces* (Interscience Publishers, Inc., New York, 1946).

O^{14} Decay and the Fermi Coupling Constant in Beta Decay*†

J. B. Gerhart
Palmer Physical Laboratory, Princeton University, Princeton, New Jersey

(Received May 13, 1954)

THE O^{14} positron spectrum has been investigated with a magnetic lens spectrometer and is found to have an allowed shape with end-point energy 1835 ± 8 kev. Remeasurement of the O^{14} half-life leads to a value of 72.1 ± 0.4 sec, about 5 percent lower than reported

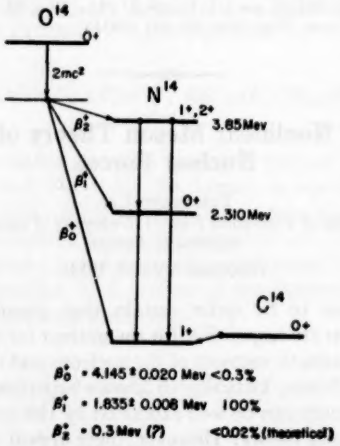

FIG. 1. O^{14} decay scheme.

previously.[1] The ft value for the 1835-kev transition is 3275 ± 75 sec (calculated with the NBS tables[2]). A specific search was made for a ground-state transition (see Fig. 1), but no evidence was found, the percent branching being less than 0.3 percent (corresponding to log ft greater than 7.3).

In general, for allowed transitions, the equation

$$A=ft\left(\left|\int 1\right|^2+R\left|\int \sigma\right|^2\right) \quad (1)$$

is valid, where $R=g_{GT}^2/g_F^2$ and $A=2\pi^3\hbar^7\ln 2/m^5c^4g_F^2$ are constants. R and A are related to the constants B and x introduced by Kofoed-Hansen and Winther[3] as follows:

$$A=B/(1-x); \quad R=x/(1-x). \quad (2)$$

The 1835-kev O^{14} decay is a $0+\rightarrow 0+$ transition,[4] i.e., a pure Fermi transition, so Eq. (1) reduces to $A=ft|\int 1|^2$. Hence one of the beta-decay constants g_F may be determined directly provided the nuclear matrix element $|\int 1|^2$ is known.

In terms of the isotopic spin quantum numbers T and T_z,[5]

$$\left|\int 1\right|^2=T(T+1)-T_zT_z'. \quad (3)$$

For the $O^{14}-N^{14}-C^{14}$ triplet $T=1$, $T_z=-1$, 0, and 1, respectively, and $|\int 1|^2=2$. It is of critical importance to realize that this calculation of the matrix element depends solely on the assumption of charge independence of nuclear forces, an assumption common to all determinations of nuclear matrix elements. It does not, however, require any further assumption about nuclear structure such as is needed to calculate the Gamow-Teller matrix element. There is very considerable experimental evidence for the validity of charge independence, especially in the low-lying levels of light nuclei. Radicati[6] and, more recently, MacDonald[7] have calculated the effects of Coulomb forces and configuration interactions in mixing nuclear states. Their findings indicate that for O^{14} these effects should have only an extremely small effect on the value of $|\int 1|^2$.

In view of these facts, it is assumed here that no uncertainty will be introduced in an evaluation of A because of the nuclear matrix element. Thus $A=6550\pm150$ sec and $g_F=1.374\pm0.016\times10^{-49}$ erg cm^3. This *direct* determination of the Fermi coupling constant is in reasonable agreement with the various attempts which have previously been made to derive it indirectly from shell-model analyses of allowed decays.[2,8]

Though the Fermi matrix element $|\int 1|^2$ can be computed with a high degree of certainty, the calculation of the Gamow-Teller matrix element $|\int \sigma|^2$ is at present most uncertain. The neutron decay ($|\int 1|^2=1$; $|\int \sigma|^2=3$), and none other, provides a case where the calculation of $|\int \sigma|^2$ is well founded and almost certainly correct. With the reported ft value for the neutron[9] and the value of A determined from the O^{14} decay, $R=1.37_{-0.30}{}^{+0.40}$. Almost the entire uncertainty in R is introduced by the large uncertainty in the neutron half-life.

The author is indebted to Professor R. Sherr and Professor M. G. White for many helpful suggestions in the experimental work on O^{14}, and to Dr. I. Talmi and Professor A. S. Wightman for several fruitful discussions of the theoretical aspects of this work.

* This article is based upon a dissertation submitted to Princeton University in partial fulfillment of the requirements for the degree of Doctor of Philosophy.

† This work was supported in part by the U. S. Atomic Energy Commission and the Higgins Scientific Trust Fund.

[1] Sherr, Muether, and White, Phys. Rev. **75**, 282 (1949).
[2] *Tables for the Analysis of Beta Spectra*, National Bureau of Standards Applied Mathematics Series, No. 13 (U. S. Government Printing Office, Washington, 1952).
[3] O. Kofoed-Hansen and A. Winther, Phys. Rev. **86**, 428 (1952).
[4] R. Sherr and J. B. Gerhart, Phys. Rev. **91**, 909 (1953).
[5] E. P. Wigner, Phys. Rev. **56**, 519 (1939).
[6] L. A. Radicati, Proc. Phys. Soc. (London) **A66**, 139 (1953).
[7] W. M. MacDonald, doctoral dissertation, Princeton University, 1954 (unpublished).
[8] See sources cited in reference 4.
[9] J. M. Robson, Phys. Rev. **83**, 349 (1951).

Tensor Forces and the β Decay of C^{14} and O^{14}

B. Jancovici and I. Talmi
Palmer Physical Laboratory, Princeton University, Princeton, New Jersey

(Received May 12, 1954)

THE surprisingly long lifetime[1] ($\log ft=9.03$) of the C^{14} β decay has been known for a long time to be unexplained either by the supermultiplet theory nor by the jj-coupling shell model. Some authors suggested that this high ft value could be explained in intermediate coupling by an "accidental" cancellation of the matrix element involved. Inglis[2] showed that such a cancellation could not occur within a pure p^{-2} configuration if one takes into account central forces and ordinary spin-orbit interaction. Inglis' consideration holds also for a mutual spin-orbit interaction of the type $V_{12}=(\mathbf{s}_1+\mathbf{s}_2)\cdot\mathbf{l}_{12}V(r_{12})$, as in this case the relevant nonvanishing matrix elements of $\sum V_{ij}$ arise only from the interaction of the holes with closed shells, which is an ordinary (single-nucleon) spin-orbit interaction.

We would like to point out that such a cancellation can occur if tensor forces are also considered. In the following, an interaction

$$H=\tfrac{1}{2}(1+P)[V_e e^{-r/r_e}/(r/r_e)+S_{12}V_t e^{-r/r_t}/(r/r_t)] \quad (1)$$

is assumed between the two p holes, and each hole has also a spin orbit interaction $a(\mathbf{l}\cdot\mathbf{s})$ with the residual

nucleus (a is positive for a hole). P is the Majorana exchange operator: $S_{12}=3(\boldsymbol{\sigma}_1\cdot\mathbf{r}_{12})(\boldsymbol{\sigma}_2\cdot\mathbf{r}_{12})/r_{12}^2-(\boldsymbol{\sigma}_1\cdot\boldsymbol{\sigma}_2)$. Harmonic oscillator wave functions are used. The parameter of the well is adjusted so that the mean square radius for the s^4p^{10} configuration be $(3/5)^{\frac{1}{2}}\times1.2\times10^{-13}A^{\frac{1}{3}}$ cm. The energy matrix for the states p^{-2}, $(J,T)=(0,1)$ of C^{14} is found to be,[3] in the LS coupling scheme,

$$\begin{array}{c|cc} & {}^1S_0 & {}^3P_0 \\ {}^1S_0 & (5/4)(I_0+I_2)-(3/2)I_1 & -a\sqrt{2} \\ {}^3P_0 & -a\sqrt{2} & -a \end{array}, \tag{2}$$

and the energy matrix for the states p^{-2}, $(J,T)=(1,0)$ of N^{14} is[3]

$$\begin{array}{c|ccc} & {}^3S_1 & {}^1P_1 & {}^3D_1 \\ {}^3S_1 & (5/4)(I_0+I_2)-(3/2)I_1 & a(2/3)^{\frac{1}{2}} & (3/\sqrt{5})J_1-(\sqrt{5})J_2 \\ {}^1P_1 & a(2/3)^{\frac{1}{2}} & 0 & -\tfrac{1}{2}a(10/3)^{\frac{1}{2}} \\ {}^3D_1 & (3/\sqrt{5})J_1-(\sqrt{5})J_2 & -\tfrac{1}{2}a(10/3)^{\frac{1}{2}} & \tfrac{1}{2}(I_0+I_2)-J_2-\tfrac{3}{2}a \end{array}, \tag{3}$$

where the I and J are the harmonic oscillator radial integrals[4] for the potentials $V_e e^{-r/r_e}/(r/r_e)$ and $V_t e^{-r/r_t}/(r/r_t)$, respectively. These matrices can be diagonalized and determine the wave functions

$$x\psi({}^1S_0)+y\psi({}^3P_0)$$

and

$$\alpha\psi({}^3S_1)+\beta\psi({}^1P_1)+\gamma\psi({}^3D_1)$$

of the ground states of C^{14} and N^{14}. The nuclear β-decay matrix element of the Gamow-Teller operator (the Fermi operator does not contribute) between the states considered is found to be

$$\left|\int\boldsymbol{\sigma}\right|^2=6(x\alpha-y\beta/\sqrt{3})^2. \tag{4}$$

The experimental ft value suggests that (4) is vanishingly small. x and y are both of the same sign,[2] and (4) can vanish only if α and β are of the same sign; this can be achieved only if the $({}^3S_1, {}^3D_1)$ matrix element in (3) is large enough (α and β are of opposite signs if this matrix element is zero[2]), which requires a strong tensor force of short range (so that J_2 be small as compared to J_1).

Such a force can be obtained for example by inserting in (1) the following numerical data[5] which fit also the ground-state data of the deuteron: $r_e=r_t=1.185\times10^{-13}$ cm, $V_e=7.9$ Mev, $V_t=79.6$ Mev. If then a is adjusted to the value $a=2.3$ Mev, (4) practically vanishes, the wave functions being $0.65\psi({}^1S_0)+0.76\psi({}^3P_0)$ for C^{14}, and $0.264\psi({}^3S_1)+0.374\psi({}^1P_1)+0.89\psi({}^3D_1)$ for N^{14}. The value of the magnetic moment of N^{14} computed with this wave function is 0.38, in reasonable agreement with the experimental value[6] of 0.40368. The quadrupole moment of N^{14} is given by

$$Q=[-(1/5)\beta^2+(7/50)\gamma^2+(4\sqrt{5}/25)\alpha\gamma]\langle r^2\rangle. \tag{5}$$

The value obtained with this wave function is $Q=0.011$ barn, in good agreement with the experimental value[7] of 0.01. It should be pointed out that the interaction adopted represents a rather extreme case of a large tensor force compared to the central forces. Moreover, the positions of the energy levels of the excited states computed with the same interaction are unsttisfactory; particularly, the ${}^3D_2$ level is lowered by the tensor force down to 0.15 Mev below the lowest $(J=1)$ level.[8] Thus, it is clear that this model (in which configuration interaction has not been considered) should not be considered as giving a satisfactory explanation. It is, however, interesting to see that tensor forces can play an important role in a possible cancellation of the matrix element (4).

Some indication that the long lifetime of C^{14} is actually caused by an accidental cancellation of the matrix element has been recently found in measurements of the lifetime of the β decay of O^{14} to the ground state of N^{14} (the mirror transition to that of C^{14}). Penning and Schmidt[9] found a 3 percent branching ratio for this decay of O^{14} and quote the value $\log ft=6.7$; more accurate measurements by Gerhart[10] yield a branching ratio not more than 0.3 percent, and $\log ft$ value greater than 7.3. This suggests that in this case the cancellation is partly removed due to the deformation of the wave function of the $(J,T)=(0,1)$ state caused by the additional Coulomb forces present in O^{14}. When this additional Coulomb force is taken into account as a perturbation $-e^2/r$ of the interaction (1) between the two p holes, the matrix element (4) instead of being zero, becomes

$$\left|\int\boldsymbol{\sigma}\right|^2=6[\langle{}^1S_0|e^2/r|{}^1S_0\rangle-\langle{}^3P_0|e^2/r|{}^3P_0\rangle)/(E'-E)]^2x^2\alpha^2, \tag{6}$$

where E' and E are the excitation energies of the two p^{-2}, $(J,T)=(0,1)$ states of C^{14}. $E'-E$ is of the order of magnitude of the experimental first excitation energy[1] of C^{14}, 4.1 Mev, or probably up to twice as much. Using[11]

$$ft=5300\Big/\left|\int\boldsymbol{\sigma}\right|^2, \tag{7}$$

one finds, for O^{14}, $\log ft\sim7.1$, up to 7.7, in fair agreement with the experimental results.

We would like to express our thanks to Professor E. P. Wigner for helpful discussions and suggestions.

[1] F. Ajzenberg and T. Lauritsen, Revs. Modern Phys. **24**, 321 (1952).
[2] D. R. Inglis, Revs. Modern Phys. **25**, 390 (1953).
[3] I. Talmi, Phys. Rev. **89**, 1065 (1953).
[4] I. Talmi, Helv. Phys. Acta **25**, 185 (1952).
[5] H. Feshbach and J. Schwinger, Phys. Rev. **84**, 194 (1951).
[6] W. G. Proctor and F. C. Yu, Phys. Rev. **77**, 716 (1950).
[7] J. Sheridan and W. Gordy, Phys. Rev. **79**, 513 (1950).
[8] This result is in agreement with results independently obtained by T. Regge, Nuovo cimento **11**, 285 (1954).
[9] J. R. Penning and F. H. Schmidt, Phys. Rev. **94**, 779 (1954).
[10] J. B. Gerhart, preceding Letter [Phys. Rev. **95**, 288 (1954)].
[11] A. Winther and O. Kofoed-Hansen, Kgl. Danske Videnskab. Selskab, Mat.-fys. Medd. **27**, 14 (1953).

Magnetic Moment of Os^{189}†

H. R. Loeliger* and L. R. Sarles
Stanford University, Stanford, California
(Received May 10, 1954)

A NUCLEAR induction signal of Os^{189} with a width of 10 gauss, measured between the minima of the differentiated dispersion mode, has been detected in molten OsO_4. The liquid phase of this particular compound was chosen because the Os^{189} nucleus has a large electric quadrupole moment, $Q=(+2.0\pm0.8)\times10^{-24}$ cm^2,[1] and its is therefore necessary to place the nucleus in a symmetric molecular configuration in order to minimize interactions which broaden the resonance line. It is presumed that in our sample, the osmium nucleus is located at the centroid of a tetrahedron having oxygen atoms at its vertices.

The resonant frequency was compared to that of Cl^{35} in pure $TiCl_4$ with the result

$$\nu(Os^{189})/\nu(Cl^{35})=0.791896\pm0.000093. \quad (1)$$

With the spin of Os^{189} assumed to be 3/2,[1] and with the known values of the frequency ratios $\nu(Cl^{35})$ in $TiCl_4$/$\nu(Cl^{35})$ in RbCl,[2] $\nu(Cl^{35})$ in RbCl/$\nu(H^2)$,[3] $\nu(H^2)/\nu(H^1)$,[4] the value of the magnetic moment was found to be, with $\mu(H^1)=2.79268$,[5]

$$\mu(Os^{189})=+0.650655\pm0.000081 \text{ nm}. \quad (2)$$

The positive sign in (2) was verified by comparing the sign of the Os^{189} signal with that of O^{17} in the same compound. Sign comparisons were also made with H^2 and N^{14}. The earlier determination of $\mu(Os^{189})=+0.70\pm0.09$ nm by Murakawa and Suwa[1] is in agreement with the sign and the more precise value of Eq. (2).

In view of the fact that the single-particle shell model[6] predicts that, for the case of a positive magnetic moment, only $p_{1/2}$, $f_{5/2}$, and $h_{9/2}$ states are available between the magic numbers 82 and 126, it seemed to us of interest to check the previous spin determination by an independent method. Accordingly, the heights h and line widths ΔH of Os^{189} and Cl^{37} signals were compared. The reference Cl^{37} signal from a 7.10 molar LiCl solution containing 0.0075 molar $Mn(NO_3)_2$ was used, and care was taken to ascertain that both line shapes represented the nonsaturated slow passage case. If the frequency, the rf field intensity, the Q of the receiver coil, the filling factor, and the sweep field remain unchanged for the measurements of both signals, the application of the phenomenological equations[7] gives

$$I(\text{Os})[I(\text{Os})+1]=I(\text{Cl})[I(\text{Cl})+1] \times\frac{h(\text{Os})}{h(\text{Cl})}\frac{N(\text{Cl})}{N(\text{Os})}\frac{\gamma(\text{Cl})}{\gamma(\text{Os})}\left(\frac{\Delta H(\text{Os})}{\Delta H(\text{Cl})}\right)^2. \quad (3)$$

With the known value of 3/2 for $I(Cl)$,[8] the measured values of the number of nuclei N in each sample, and our experimental results for the other ratios, we find

$$I(Os^{189})=1.45\pm0.13, \quad (4)$$

thus verifying the value 3/2.

Signals were not observable in solidified OsO_4 or in powdered Os metal which has a crystal structure of hexagonal symmetry, presumably because of an unfavorable ratio T_2/T_1.

The authors wish to express their appreciation to Professor F. Bloch for his continued interest in their work.

† Assisted by the joint program of the U. S. Office of Naval Research and U. S. Atomic Energy Commission.
* Now at Physikalisches Institut der Universität, Zürich, Switzerland.
[1] K. Murakawa and S. Suwa, Phys. Rev. **87**, 1048 (1952).
[2] C. D. Jeffries, Phys. Rev. **92**, 1262 (1953).
[3] Walchli, Leyshon, and Scheitlin, Phys. Rev. **85**, 922 (1952).
[4] G. Lindström, Arkiv Fysik **4**, 1 (1951).
[5] Sommer, Thomas, and Hipple, Phys. Rev. **82**, 697 (1952).
[6] M. G. Mayer, Phys. Rev. **78**, 16 (1950); P. F. A. Klinkenberg, Revs. Modern Phys. **24**, 63 (1952).
[7] F. Bloch, Phys. Rev. **70**, 460 (1946).
[8] Townes, Holden, Bardeen, and Merritt, Phys. Rev. **71**, 644 (1947).

Experimental Study of the μ^- Meson Mass and the Vacuum Polarization in Mesonic Atoms*

S. Koslov, V. Fitch, and J. Rainwater
Columbia University, New York, New York
(Received May 17, 1954)

STUDIES of the x-rays emitted in transitions of mesons between atomic orbits about nuclei have been extended[1] to $3D-2P$ and $4F-3D$ transitions in a variety of elements for both π^- and μ^- mesons. Particular attention has been paid to μ^- mesonic transitions having energies below 90 kev, using thin filters between the anticoincidence counter and the NaI crystal of the scintillation spectrometer.[2] Because of the large and rapid change in absorption cross section at the photoelectric "K edge" energy and the precise knowledge of

these energies,[3] it is possible to state whether a particular mesonic x-ray lies above or below the "K edge" of a given filter element and thus place an upper or lower limit on the energy of that transition. Calculated mesonic x-ray energies in this energy range are only slightly affected by readily evaluated nuclear size corrections; other effects,[4] except for the vacuum polarization, are considered negligible. A large number of such transitions have been studied to date. The observed pulse-height spectra contain components of degraded radiation arising from Compton scattering in the meson target and surrounding material and fluorescent radiation from the filter. Thus the upper energy part of the pulse-height distribution is emphasized in the interpretation of the data.

At present, the results of most interest in the determination of the μ^- meson mass and of vacuum polarization effects are the following. For the $2P-1S$ transition in carbon, $Z=77$, 78, 79 filters all behave similarly indicating "K edges" above the mesonic x-ray energy while $Z=74$ has its "K edge" well below the mesonic energy. The $Z=77$ filter indicates that the transition energy is below 76.123 kev. The most significant result was that the phosphorus $3D-2P$ transition energy lies above the $Z=81$ and 82 absorption edges and below the $Z=83$ edge. Corresponding to the $Z=82$ absorption edge we emphasize that the photon energy in this case is greater than 88.065 kev. The $4F-3D$ transition in silicon indicates that the transition energy is above the $Z=47$ and 48 absorption edges and below that for $Z=49$, corresponding to a transition energy greater than 26.713 kev for the $Z=48$ edge.

The lowest-order vacuum polarization effect, as given by the Uehling integral,[5] has been evaluated for these states by two independent approximate methods which agree to within 2 percent. The effect always increases the binding energy. This amounted to 0.40 percent, 0.099 percent, 0.25 percent, 0.103 percent, 0.094 percent, and 0.034 percent for the $1S$ and $2P$ levels in carbon, the $2P$ and $3D$ levels in phosphorus, and the $3D$ and $4F$ levels in silicon, respectively. Table I lists the corresponding upper or lower limits on the μ^- meson mass before and after applying the vacuum polarization correction. The Dirac formula for a point nucleus was used and a nuclear size correction was needed only for the $1S$ level of carbon (decreases binding energy 0.45 percent).

The latest reported value of the μ^- meson mass, measured by independent means,[6] is 206.9±0.2 electron mass units.[7] The stated uncertainty does not include estimates of possible systematic errors which could be of comparable amount. We therefore conclude that an effect of the order of magnitude of the vacuum polarization is necessary for agreement with the lower limit for the meson mass ($3D-2P$ transition in phosphorus with $Z=82$ filter) measured here.

TABLE I. Upper or lower limits on the μ^- meson mass/electron mass without and with vacuum polarization correction.

Transition		Without V_p	With V_p
C: $2P-1S$	less than	209.99	208.95
P: $3D-2P$	greater than	207.67	206.89
Si: $4F-3D$	greater than	206.82	206.47

We wish to thank Professor Norman M. Kroll and Mr. Eyvind Wichmann for helpful discussions on the subject of vacuum polarization.

* This work was performed under the joint program of the U. S. Office of Naval Research and the U. S. Atomic Energy Commission.

[1] Koslov, Fitch, and Rainwater, Bull. Am. Phys. Soc. **29**, No. 4, 37 (1954).
[2] V. Fitch and J. Rainwater, Phys. Rev. **92**, 789 (1953).
[3] Y. Cauchois and H. Hulubei, *Tables De Constantes Selectionnes Longueurs D'Onde Des Emissions X Et Des Discontinuités D'Absorption X* (Hermann et Cie, Paris, 1947). The precision of the K absorption edge energies appears to be better than ±0.07 percent in all cases.
[4] L. N. Cooper and E. M. Henley, Phys. Rev. **92**, 801 (1953).
[5] E. A. Uehling, Phys. Rev. **48**, 55 (1935); R. Serber, Phys. Rev. **48**, 49 (1935).
[6] W. H. Barkas, University of California Radiation Laboratory UCRL-2327, September, 1953 (unpublished).
[7] W. H. Barkas (private communication).

Decay of Sb^{124}

N. H. LAZAR
Physics Division, Oak Ridge National Laboratory, Oak Ridge, Tennessee

(Received May 7, 1954)

THERE is still some disagreement in the literature[1,2] on the interpretation of the decay of Sb^{124}. In an attempt to resolve these difficulties, the gamma radiation following the decay has been investigated in a 3 in.×3 in. NaI(Tl) scintillation spectrometer. The crystal was placed in an aluminum can, 0.005 inch thick, and mounted on a Dumont K-1197 photomultiplier. The data were taken using a 20-channel pulse-height analyzer.[3] Energy calibration was obtained from Cs^{137}, Co^{60}, and Y^{88} gamma rays. The spectrum obtained is shown in Fig. 1. For purposes of subtraction, the Compton distributions from the gamma rays at 2.11, 1.71, and 1.38 Mev were constructed from gamma radiation from Pr^{144} (2.18 Mev), Y^{88} (1.85 Mev), and Na^{24} (1.38 Mev). Relative intensities of the gamma rays (Table I) were determined from the peak areas and experimentally determined peak-to-total efficiency data for this crystal and geometry. Lower-energy gamma rays (<0.6 Mev) were looked for with techniques which eliminated most of the back-scatter peak at pulse height 90, but no indication of other gamma rays was found.

From the intensities and energies of the gamma rays and from the previously reported beta-ray analysis,[1] a consistent decay scheme may be proposed (Fig. 2). The ratio of the sums of the intensities of the gamma

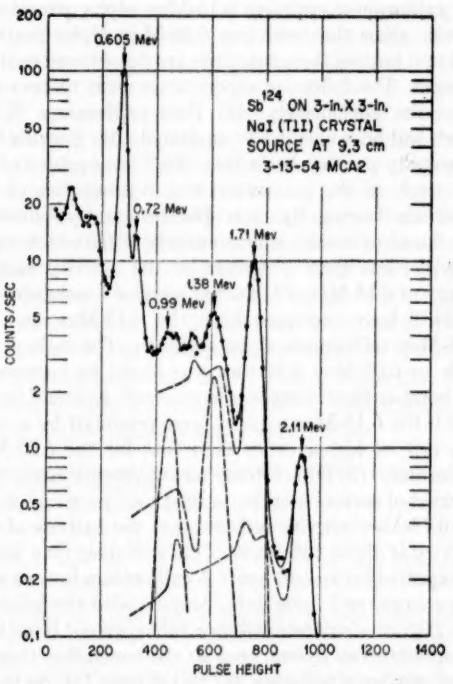

FIG. 1. Pulse-height spectrum from scintillation spectrometer caused by gamma rays following decay of Sb^{124}.

radiation leaving the levels at 2.7 and 2.3 Mev above the ground state was determined as 0.32. From the previous beta-ray analysis, the ratio of intensities of the beta rays feeding these levels is 0.29, indicating the correct placement of the 0.99- and 1.38-Mev gamma rays. From the energy of these gamma rays, the energy of the second excited state is determined.

The coincidence experiment reported by Metzger[2] can now be explained by the coincidence of the 0.72-Mev gamma ray and the Compton electrons from the newly reported gamma rays at 1.38 and 0.99 Mev. The gamma rays of energy 0.99 and 1.38 Mev are exceedingly difficult to observe with NaI crystals of smaller size than were used in this experiment because of the relatively smaller peak intensity for these gamma rays in such detectors and their unfortunate coincidence, energy-wise, with expected effects due to the other gamma rays.

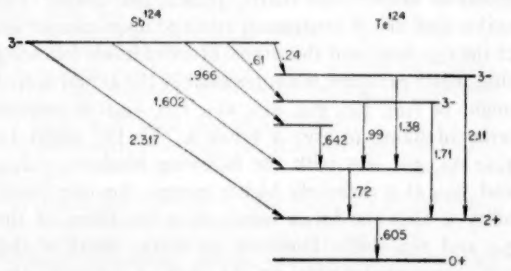

FIG. 2. Proposed decay sheme for Sb^{124}.

TABLE I. Energy and relative intensities of gamma rays in decay of Sb^{124}.

Energy (Mev)	Relative intensity
0.603	1.00
0.99	0.054
1.38	0.062
1.71	0.457
2.11	0.099

It would like to express my appreciation to P. R. Bell for his interest and advice on this subject.

[1] Langer, Lazar, and Moffat, Phys. Rev. **91**, 338 (1953).
[2] E. P. Tomlinson and F. Metzger, Indiana Conference on Nuclear Spectroscopy and the Shell Model, Technical Report, 1953 (unpublished), p. 31.
[3] Kelley, Bell, and Goss, Oak Ridge National Laboratory Report ORNL-1278, 1951 (unpublished).

Evidence for Subshell at $N=152$*

A. GHIORSO, S. G. THOMPSON, G. H. HIGGINS, B. G. HARVEY, AND G. T. SEABORG
Radiation Laboratory and Department of Chemistry, University of California, Berkeley, California

(Received May 13, 1954)

LARGE breaks in the plots of alpha-particle energy *vs* mass number at constant Z give striking evidence[1] for the closing of a major shell at 126 neutrons ($N=126$). We have applied this sensitive criterion to look for the much smaller "subshell" effects which

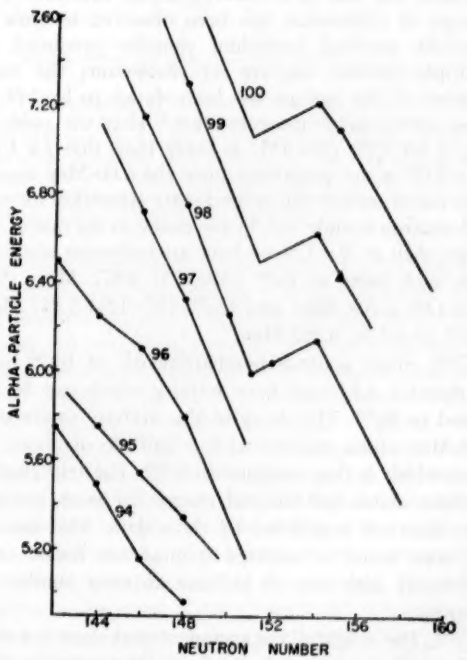

FIG. 1. Plot of alpha energy *vs* mass number.

might be found in the region $N>126$ and find good evidence for a subshell at $N=152$.

The plot of alpha-particle energies[2] *vs* mass number for the isotopes of californium ($Z=98$) hown in Fig. 1s shows a definite break in the region of Cf^{250} to Cf^{252} indicating a subshell at 152 neutrons. This break is of the order of a few percent as large as that corresponding to the major shell at $N=126$ in the analogous curve for polonium.[1]

Since the postulated existence of a subshell at 152 neutrons depends entirely on the mass assignments of the nuclides involved, it appears worth while to review and expand the evidence on which these mass assignments are based.

Cf^{244} and Cf^{246}. These two isotopes of californium have been well established and identified by their respective curium daughters, Cm^{240} and Cm^{242}.

Cf^{248}. This isotope has been produced by He^{++} bombardment of curium containing Cm^{245} as its heaviest constituent. The yield of this activity was consistent with the reaction $Cm^{245}(\alpha,n)Cf^{248}$. The half-life observed agrees very well with that predicted for an even neutron isotope of californium with the alpha energy observed. Additional proof of its even neutron nature is afforded by the fact that this isotope has been found to undergo spontaneous fission with a half-life comparable to that of Cf^{246}.

Cf^{249}. Recent measurements[3] show the alpha spectrum of this nuclide to consist of two prominent alpha groups: 6.00 Mev (10 percent) and 5.82 Mev (90 percent); this is characteristic of many even proton-odd neutron nuclides but not of even-even alpha emitters. This isotope of californium has been observed to grow in carefully purified berkelium samples produced by multiple neutron capture on plutonium; the mass number of this isotope has been shown to be 249 by mass spectrometer measurements.[4] That the point in Fig. 1 for Cf^{249} ($N=151$) is lower than that for Cf^{250} ($N=152$) is not surprising since the 6.00-Mev energy may not represent the ground-state transition for this odd-neutron nuclide and, in any event, in the case of the major shell at $N=126$ we have an analogous situation with such pairs as Po^{209} ($N=125$) 4.877 Mev, Po^{210} ($N=126$) 5.298 Mev, and Em^{211} ($N=125$) 5.847 Mev, Em^{212} ($N=126$) 6.262 Mev.[5]

Cf^{250}. Short neutron bombardments[3] of Bk^{249} have produced a 3.13-hour beta activity which can be assigned to Bk^{250}. The decay of this activity produces a 6.05-Mev alpha emitter with a half-life of about 12 years which is thus assigned to Cf^{250}. The relationship between alpha half-life and energy for even isotopes of californium is satisfied by these data. This isotope has been found to undergo spontaneous fission at a sufficiently high rate to indicate an even number of neutrons.

Cf^{252}. The weight of the argument that there is a subshell at 152 neutrons falls chiefly on the conclusion that the californium emitting 6.15-Mev alpha particles is heavier than that emitting 6.05-Mev alpha particles and that both of these activities are due to even neutron isotopes. The following experiments seem to bear this out quite conclusively. (1) Pure californium (Cf^{249}) which had been chemically separated after growing into a carefully purified berkelium (Bk^{249}) was subjected for one week to the maximum mtr, neutron flux of the Materials Testing Reactor. The resultant californium was found to consist almost entirely of 6.05-Mev alpha activity; less than 2 percent of the activity had an energy of 6.15 Mev. (2) Longer neutron bombardments of Bk^{249} have produced both the 6.15-Mev and the 6.05-Mev californium alpha activities. The ratio of the 6.15- to 6.05-Mev activities was found to increase as the bombardment time was lengthened, as would be the case if the 6.15-Mev activity were produced by a reaction rate of higher order than that for the 6.05-Mev californium. (3) Direct decay measurements[3] made over a period of several months on relatively pure samples of the 6.15-Mev activity indicate that the half-life of this activity is about two years. This is shorter than would be expected for an odd-neutron californium isotope with this energy, and these data, coupled with the information that this isotope exhibits a three percent branching for spontaneous fission, lead to the conclusion that its mass number is probably 252 rather than 251. So far no radioactivity has been found that might be associated with Cf^{251}; this is not surprising since a combination of a high neutron capture cross section and a long alpha half-life as expected for an odd-mass isotope would make it difficult to make such an identification. Recent mass spectrometer measurements[4] on californium isotopes are in agreement with the above assignments of the 6.15- and 6.05-Mev alpha activities to Cf^{252} and Cf^{250}, respectively.

The curve for californium in Fig. 1 is sketched in beyond $N=154$ on the assumption that the behavior is analogous to that for polonium[1] in the region of the major shell at $N=126$. In the same spirit, analogous curves based on a subshell at $N=152$ are sketched in for elements 99 and 100 using the experimental data available.[6] Similar curves for $Z<98$ might also be expected due to closed subshells at Bk^{249}, Cm^{248}, etc.

So definite a subshell at this point does not seem to be predictable from a simple consideration of the shell model of Mayer[7] and Haxel, Jensen, and Suess.[8] The major shell of 126 neutrons is attained upon completion of the $i_{13/2}$ level and the simple order of levels following this, which of course is not necessarily the actual order,[9] might be $i_{11/2}$, $g_{9/2}$, $g_{7/2}$, $d_{5/2}$, $d_{3/2}$, $s_{1/2}$, $j_{15/2}$. A possible order of filling to give a break at $N=152$ might be $g_{9/2}$, $s_{1/2}$, $g_{7/2}$, $d_{5/2}$ with the following levels $i_{11/2}$, $d_{3/2}$, and $j_{15/2}$ at a definitely higher energy. Another possibility is that the break comes after the filling of the $g_{9/2}$ and $j_{15/2}$ shells. However, an energy break of this sort interpreted simply on the basis of subshell com-

pletion in the process of the filling of levels in the simple single-particle shell model may be an oversimplification because this is just the region where the strong surface coupling caused by large spheroidal distortion[10–13] or configuration interaction[14–18] of several nucleons may be important. In this connection one might expect on the basis of either the Bohr-Mottelson[12] strong surface coupling model or the de-Shalit-Goldhaber[15] configuration interaction arguments regarding trends of first excited state energies, that if the nucleon configuration at $N=152$ involves only completely filled levels, the first excited state energies should approach a maximum as is observed in the closing of other shells[19–21]; the experimental evidence so far indicates that this is not the case.[4,22] Thus it seems that the 152-neutron subshell may be of a fundamentally different nature than the major closed shells.

* This work was performed under the auspices of the U. S. Atomic Energy Commission.

[1] Perlman, Ghiorso, and Seaborg, Phys. Rev. **77**, 26 (1950).

[2] The following alpha energies with corresponding references were used: Cf^{244}, 7.15 Mev [Thompson, Street, Ghiorso, and Seaborg, Phys. Rev. **80**, 790 (1950)]; Cf^{246}, 6.75 Mev [Ghiorso, Thompson, Street, and Seaborg, Phys. Rev. **81**, 154 (1951)]; Cf^{248}, 6.26 Mev [E. K. Hulet, Ph.D. thesis, University of California Radiation Laboratory Unclassified Report UCRL-2283, July, 1953 (unpublished)]; Cf^{249}, 6.00 Mev [Ghiorso, Thompson, Choppin, and Harvey, Phys. Rev. **94**, 1081 (1954)]; Cf^{250}, 6.05 Mev [Ghiorso, Thompson, Choppin, and Harvey, Phys. Rev. **94**, 1081 (1954)]; Cf^{252}, 6.15 Mev [Thompson, Ghiorso, Harvey, and Choppin, Phys. Rev. **93**, 908 (1954)].

[3] Ghiorso, Thompson, Choppin, and Harvey, Phys. Rev. **94**, 1081 (1954).

[4] Diamond, Magnusson, Mech, Stevens, Friedman, Studier, Fields, and Huizenga, Phys. Rev. **94**, 1083 (1954) and private communication.

[5] Hollander, Perlman, and Seaborg, Revs. Modern Phys. **25**, 469 (1953).

[6] The following alpha energies with corresponding references were used: 99^{247}, 7.3 Mev [Ghiorso, Rossi, Harvey, and Thompson, Phys. Rev. **93**, 257 (1954)]; and 99^{253}, 6.63 Mev, 100^{254}, 7.22 Mev, 100^{255}, 7.1 Mev [Choppin, Thompson, Ghiorso, and Harvey, Phys. Rev. **94**, 1080 (1954)]; see also Fields, Studier, Mech, Diamond, Friedman, Magnusson, and Huizenga, Phys. Rev. **94**, 209 (1954). The alpha energy for 99^{254} has been calculated from the closed-cycle data involving Bk^{250} and 99^{254} beta energies and the 100^{254} alpha energy [Ghiorso, Thompson, Choppin, and Harvey, Phys. Rev. **94**, 1081 (1954)]; and Choppin, Thompson, Ghiorso, and Harvey, Phys. Rev. **94**, 1080 (1954).

[7] M. G. Mayer, Phys. Rev. **75**, 1969 (1949); **78**, 16, 22 (1950).

[8] Haxel, Jensen, and Suess, Phys. Rev. **75**, 1766 (1949); Z. Physik **128**, 295 (1950).

[9] G. T. Seaborg, Phys. Rev. **92**, 1074 (1953).

[10] J. Rainwater, Phys. Rev. **79**, 432 (1950).

[11] D. L. Hill and J. A. Wheeler, Phys. Rev. **89**, 1102 (1953).

[12] A. Bohr and B. R. Mottelson, Kgl. Danske Videnskab. Selskab Mat-fys. Medd. **27**, No. 16 (1953); Phys. Rev. **89**, 316 (1953); Phys. Rev. **90**, 717 (1953).

[13] K. W. Ford, Phys. Rev. **90**, 29 (1953).

[14] D. Kurath, Phys. Rev. **80**, 98 (1950).

[15] A. de-Shalit and M. Goldhaber, Phys. Rev. **92**, 1211 (1953).

[16] A. R. Edmonds and B. H. Flowers, Proc. Roy. Soc. (London) **A215**, 120 (1952).

[17] I. Talmi, Helv. Phys. Acta **25**, 185 (1952).

[18] B. H. Flowers, Proc. Roy. Soc. (London) **A212**, 248 (1952); **A215**, 398 (1952); Phys. Rev. **86**, 254 (1952); Phil. Mag. (7), **43**, 1330 (1952).

[19] P. Stähelin and P. Preiswerk, Helv. Phys. Acta **24**, 623 (1951).

[20] G. Scharff-Goldhaber, Phys. Rev. **90**, 587 (1953).

[21] F. Asaro and I. Perlman, Phys. Rev. **87**, 393 (1952).

[22] Ghiorso, Thompson, Harvey, and Choppin (unpublished work).

Q Value of Λ^0 Decay

V. A. J. van Lint, G. H. Trilling, R. B. Leighton, and C. D. Anderson
California Institute of Technology, Pasadena, California

(Received May 10, 1954)

MEASUREMENTS of the energy release or Q value in Λ^0 decay have previously been reported.[1] From the photographs obtained in the 48-in. magnet cloud chambers now operating in Pasadena, a set of the most accurately measurable Λ^0 decays have been selected for calculations of Q values.

In order to be selected, a Λ^0 decay was required to have a heavily ionizing positive secondary whose mass was clearly consistent with the proton mass. Furthermore, the estimated probable error in the Q value was required to be less than or equal to ± 5 Mev. These severe restrictions were practical because the design of the cloud chambers enable a large number of decays of very slow Λ^0 particles to be detected. It is possible to photograph decays which occur as close as 0.5 cm to the brass chamber wall and 1 cm to the lead plate above the chamber. Also the large depth of the illuminated region (23 cm) allowed detection of many unstable particles emitted at large angles to the vertical direction. There were 19 cases which satisfied the selection criteria.

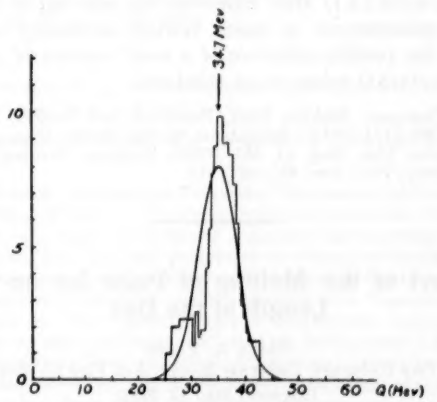

FIG. 1. Distributions of measured Q values for 19 selected cases of Λ^0 decay. Each case is represented in this distribution by a block 5 Mev wide and of a height inversely proportional to the square of the estimated probable error. A case whose estimated probable error is ± 3 Mev is assigned a height of one unit. A Gaussian curve of the same total area corresponding to a probable error of ± 2.5 Mev is shown for comparison.

The Q value of each Λ^0 decay, assuming the only products to be a proton and a π meson, was calculated from the measured momenta of the secondaries and the angle between their initial lines of flight. The errors in the momenta were calculated from the estimated maximum momentum detectable in the chamber. The contribution to the error in the Q value ΔQ arising from errors in measurement of the angle between the tracks was in all cases negligible.

The distribution shown in Fig. 1 was constructed by assigning to each of the 19 cases a "block" 5 Mev wide (centered about the calculated Q value) and a height inversely proportional to the square of the assigned error. A Gaussian curve of the same area and a width corresponding to a probable error of ± 2.5 Mev fits this distribution quite well. The best Q value for the decay $\Lambda^0 \rightarrow p^+ + \pi^-$ is thus indicated to be 34.7 Mev.

The statistical probable error in the mean Q value is calculated to be ± 0.6 Mev. The presence of systematic errors in the calibration of the magnetic field has been considered, and such errors are estimated to contribute possibly ± 0.5 Mev to the error in the Q value. Therefore, the best Q value derived from these data is (34.7 ± 1) Mev.

All the cases from the 48-in. magnet cloud chambers which have been analyzed to date and which clearly have a positive secondary heavier than a π meson are consistent with the decay scheme $\Lambda^0 \rightarrow p^+ + \pi^- + (34.7 \pm 1)$ Mev. However, the selection of cases for measurement is biased toward low-energy cases and the possible existence of a small number of cases with other Q values is not ruled out.

[1] Thompson, Buskirk, Etter, Karzmark, and Rediker, Phys. Rev. **90**, 1122 (1953); Armenteros, Barker Butler, Coates, and Sowerby, Phil. Mag. **44**, 861 (1953); Leighton, Wanlass, and Anderson, Phys. Rev. **89**, 148 (1953).

Effect of the Melting of Polar Ice on the Length of the Day

SERGE A. KORFF
New York University, University Heights, New York 53, New York
(Received May 17, 1954)

THE astronomical standard of time assumes the constancy of the rotation of the earth. There is good evidence today[1] that the rotation of the earth is not constant, and has in it both regular periodic variations and irregular fluctuations of considerable amplitude. It is the purpose of this note to evaluate quantitatively the effect of one possible cause of such fluctuation, namely, the melting of polar ice.

In this computation we shall take the moment of inertia of the earth as 8.1×10^{44} gram cm^2. This figure is obtained by taking the mass of the earth as 5.97×10^{27} grams, and assuming that the density increases linearly toward the center, with a positive discontinuity of about 5 g/cc at the interface between the core and mantle. As a numerical example, to show how little the exact form of density variation matters, we mention that if the earth's density were uniform and equal to its average value, the moment of inertia would be 9.55 of the above units. If we suppose the density d to be a function of radius r and a constant k as $d = d_0 - kr$, where d_0 is the central density, then the moment of inertia is given by

$$I = \int_0^{\pi} \int_0^{R} r^2 \sin^2\theta (d_0 - kr) 2\pi r \sin\theta \cdot r d\theta dr, \qquad (1)$$

which integrates into

$$I = (4\pi R^5/3)[(2d_0 R^2/5) - (kR^3/3)]. \qquad (2)$$

For the core, we take d_0 as 18, k as 2.48×10^{-8} g/cm^4 and the core radius as 3450 km. With these figures, the contribution due to the core is 0.863×10^{44} g cm^2, or about one tenth that of the mantle. The exact values of the density variation with depth k is quite unimportant as is also the absolute value of the central density.

Assuming next that angular momentum is conserved, that small changes occur in the moment of inertia I, and writing ω for the angular velocity, numerically equal to 8.64×10^4 sec/day or 7.25×10^{-5} radian per sec, we have if we neglect the squares of small quantities:

$$dI/I = -d\omega/\omega, \qquad (3)$$

where dI is the change in the moment of inertia and the resulting change in the rotational speed is $d\omega$. Further, the moment of inertia of a thin shell of radius r and mass m is $\frac{2}{3}mr^2$, and a cubic km of ice weighs 10^{15} grams times its specific gravity. Thus a cubic km of ice on the Greenland ice cap, at an average distance of $\frac{1}{6}$ the earth's radius, some 1000 km from the rotational axis, has a moment of inertia of 10^{31} g cm^2.

Suppose next that this ice melts and is spread into a uniform shell about the earth, with a radius r of 6.3×10^8 cm. Then its moment of inertia will be 26×10^{31} g cm^2. Therefore it does not matter, within a few percent, whether the ice was assumed originally in Greenland or nearer the pole of rotation. One cubic kilometer of ice, more or less polar, will therefore cause a change dI/I of 3×10^{-13} if it melts.

The Greenland ice cap is about 1.75×10^6 sq km in area, and the ice is known in many places to average 1 km in thickness, so we have roughly 10^7 cubic km of ice. If the entire surface lowers by as little as 10 cm, then 10^3 cubic km will have melted. Such lowering would cause a change in rotation $d\omega/\omega$ of 3×10^{-10} or about 26 microseconds per day. The abundant geological evidence in the form of nunataks and other glacially eroded formations testifies that the lowering of the Greenland ice cap has, over a period of many years, exceeded our 10-cm figure by substantially more than three orders of magnitude. If the entire Greenland ice cap were to melt, the change would amount to 100 sec/year.

In Antarctica, the latest expedition[2] found the ice to be thicker than previously supposed, and found thicknesses of 2 to 3 km in many places. If we take 2 km as an average, the area being about 15×10^6 km,^{2} the ice volume is 30×10^6 cu km. An average change in Antarctica of 3 cm in the ice level would produce the

same 26-microsecond-per-day change in the rotational period. In point of fact huge tabular icebergs break off and melt, some of which are known to be many square km in extent, so that annual changes of the cited order are to be expected. Clearly too, as the seasons are out of phase, the epoch of accumulation of ice in the north coincides with melting in the south, so the effect will introduce a 6-month periodicity into the astronomical determinations.

Thus we see that the well-known recession of glaciers will result in slowing down the rotation of the earth, by an amount of about 26 microseconds per day per thousand cubic km of ice melted, and that the melting of such thousands of cubic km is an annual event. Superposed on semiannual fluctuations we have a long-time progressive change, which requires some 10^5 cubic km to melt to cause a change of one second per year. Indeed, only one or two tenths of a percent of all the earth's ice need melt to cause a one-second-per-year change in the length of the day.

[1] Dirk Brouwer, Astron. J. **57**, 125 (1952).
[2] G. de Q. Robin, Geograph. J. **119**, 155 (1953).

PHYSICAL REVIEW VOLUME 95, NUMBER 1 JULY 1, 1954

Proceedings of the American Physical Society

Minutes of the 1954 Spring Meeting of the New England Section at Wellesley, Massachusetts on March 20, 1954

THE New England Section of the American Physical Society held its annual Spring Meeting on Saturday, March 20, in Pendleton Hall of Wellesley College, Wellesley, Massachusetts. The morning session was opened with a welcoming address by President Margaret Clapp. There followed four invited papers: "Radio Studies of Clouds in the Milky Way," Bart J. Bok, Harvard; "The Amherst Program: Experience with a Calculus—Physics Course Required of All Students," Arnold Arons, Amherst; "Self-Maintained Oscillations in Fluid Flow," Wesley L. Nyborg, Brown; "The Hall Effect in Ferromagnetics," Robert Karplus, Harvard.

Following lunch, the facilities of the Wellesley College Physics Department were open for inspection. Ten contributed papers were presented at the afternoon session; the abstracts are appended.

W. M. PRESTON
Secretary-Treasurer
New England Section,
Harvard University,
Cambridge, Massachusetts

1. Quantitative Measurements of Radar Echoes from Precipitation. PAULINE M. AUSTIN, *Wellesley College and M. I. T.** (20 minutes).—The general characteristics of radar echoes from precipitation and methods of measuring the average signal strength and the autocorrelation function are discussed. The relation of the intensity of the radar signal to the number, size, shape, and composition of the precipitation particles is pointed out, as well as the dependence of the time variations of the signal upon the motions of the scattering particles. Interpretations and deductions of interest to the meteorologist and precipitation physicist are also considered, such as: measurements of rainfall intensity, observations concerning the growth, melting, and coalescence of snowflakes and indications of wind shear and turbulence.

* Weather Radar Research, under the sponsorship of the Army Signal Corps.

2. A Study of Drop-Size Frequency Distribution in Clouds and Rain.* JOSEPH K. FISH AND SHEPARD BARTNOFF, *Tufts College.*—A study of drop-size frequency distributions in clouds and rain has been undertaken to investigate the functional interrelationship between optical visibility, liquid-water content, radar reflectivity, and precipitation rate. The various methods by which actual drop-size distributions found in nature are obtained from "raw" data will be discussed. These data undergo certain corrections for factors inherent in the collection technique, and then undergoes procedures of statistical analysis from which the above parameters and distributions are then compared with a set of theoretical distributions proposed by Bartnoff and Atlas and also with a set of distributions proposed by Best. The results indicate that in nature there seems to be a preference for certain drop-size frequency distributions.

* This work supported by the Air Force Cambridge Research Center.

3. Observation of Low-Lying States in Nuclei from $(n,n'\gamma)$ Interactions.* JANET B. GUERNSEY† AND CLARK GOODMAN, *M. I. T.*—Previous work[1] has established the NaI scintillation spectrometer as a method of measuring neutron inelastic scattering in elements with first excited states $\gtrsim$800 kev. Problems arise in the extension of this technique to low-lying levels. The rotational states (50 to 500 kev) in very deformed nuclei are of particular interest theoretically.[2] Large internal conversion coefficients and strong self-absorption within the scatterer decrease the detectable gamma flux by orders of magnitude. Inelastic scattering and capture gamma radiation in the NaI produce a large background. Experimental methods of minimizing these difficulties have been explored. The possibility of measuring the internal conversion electrons has been considered.

* Assisted by the joint program of the U. S. Office of Naval Research and the U. S. Atomic Energy Commission.
† On leave from Wellesley College.
[1] R. M. Kiehn and Clark Goodman, Phys. Rev. **93**, 177 (1954).
[2] A. Bohr and B. R. Mottelson, Dan. Mat. Fys. Medd. **27**, No. 16, 158 (1953).

4. Determination of the Thickness of Lithium Targets from the Position of the Geometric Peak.* CHARLES F. DONAGHY† AND CLARK GOODMAN, *M. I. T.*—A study of endoergic reactions of the type (p,n) in the region just above threshold shows that the yield curve in the forward direction is determined by one of five different possible cases. The particular case which occurs is determined by target thickness, counter geometry, and counter position. By proper selection of the solid angle subtended by the counter at the target, the number of possible cases can be limited to at most two for lithium targets up to nearly 40 kev. The character of the yield curve for a given target may be quite different in these two cases. However, the theoretical expression for neutron yield over a small region at the geometric peak is the same for both cases. From this expression has been derived a relation between target thickness and peak position. This method of determining target thickness can be applied to certain other endoergic reactions with little or no modification.

* This work has been assisted by the joint program of the U. S. Office of Naval Research and the U. S. Atomic Energy Commission.
† Enrolled at M. I. T. under the U. S. Naval Postgraduate School System.

5. A Potential Theory Formulation of Radiant Heat Transfer. JEAN I. F. KING, *Geophysics Research Directorate, Air Force Cambridge Research Center.*—The heat flux arising from radiative transfer constitutes an irrotational vector field. Since its curl is everywhere zero, this flux can be represented as the gradient of a radiant heat potential. This potential function is found to be the integral of the radiant source function in all directions about a point multiplied by an exponential attenuation factor. This formulation has the advantage of being independent of the particular coordinate system chosen. All the laws of radiant transfer, such as Schwarzschild's equation, are deducible from this radiant potential. In addition, the radiative cooling at a point becomes a simple function of the second derivative of the Planck intensity. Consequences of the formalism for the calculation of stellar radiative equilibrium configurations will be discussed.

6. Radio-Frequency Mass Spectrometer as a Rocket-Borne Instrument for Atmospheric Composition Studies. WALTER F. SHERIDAN, *Geophysics Research Directorate, Air Force Cambridge Research Center.*—Laboratory studies of the Bennett[1] radio-frequency mass spectrometer as an instrument for determining the composition and other physical phenomena of the upper atmosphere are discussed. Physical form factors recommend this instrument as a rocket-borne device for taking a direct and continuous record of the atmosphere between the altitudes of 100 and 150 km. Observations of the abundance of gases and the degree of dissociation might be telemetered directly to observers on the ground. A brief description of the spectrometer and the associated equipment for laboratory use is given. A critical evaluation of the spectrometer both as a laboratory device and an operational instrument is given.

[1] W. H. Bennett, J. Appl. Phys. **21**, 145 (1950).

7. The Absence of K-Capture in the Decay Scheme of Pb^{205}.* T. T. SUGIHARA,† R. H. HERBER, W. E. BENNETT,‡ AND C. D. CORYELL,§ *Department of Chemistry and Laboratory for Nuclear Science, M. I. T.*—From recent estimates of the age of the earth and the absence of Pb^{205} in natural lead, the upper limit of the half-life of this isotope is set at 6×10^8 years. Extended 15-Mev deuteron bombardment of natural lead failed to produce long-lived electromagnetic activity in the 73-kv region (Tl K x-rays). Exposure of a lead sample enriched to 25.7 percent in Pb^{204} in the thermal-neutron flux of the MTR for a total nvt of 3×10^{20} neutrons/cm^2 similarly failed to give rise to Tl K x-rays or long-lived activity. Thallium K x-ray activity was also absent in the Pb^{204} enriched lead sample exposed to the thermal flux of the Brookhaven pile and counted within four minutes after the end of bombardment. From these data it is concluded that Pb^{205} does not decay by K capture.

* Work supported in part by the U. S. Atomic Energy Commission.
† Now at Department of Chemistry, Clark University.
‡ Now at Department of Chemistry, University of Iowa.
§ Temporary address: Weizmann Institute of Science, Rehovoth, Israel.

8. Replication of Barium Titanate Ceramic Surfaces for Electron Microscopy.* JOHN L. SAMPSON, EDWARD E. ALTSHULER, AND ROBERT W. PERRY, *Tufts College.*—A replication technique which overcomes the difficulties encountered in stripping a Formvar film from the more or less pitted surface of barium titanate ceramic is reported. Polystyrene is used as a bond between the specimen screen and the Formvar film. The Formvar replica film adheres to the specimen more strongly than to the ceramic surface from which it strips without tearing when the screen is lifted. The polystyrene is subsequently dissolved, leaving the Formvar replica on the specimen screen. Inconel wire serves as a good source of metal for shadow-casting, and is in a form that is easier to handle than small metallic pieces.

* This work sponsored by the Office of Ordnance Research of the U. S. Army.

9. Aging of Crushed Silicon and Germanium Powders. SELMA B. BRODY, *University of Connecticut.*—In x-ray diffraction studies of freshly crushed samples, silicon shows surface changes of the kind previously reported[1] for a variety of materials. Germanium does not show these changes, which have been variously interpreted as recrystallization, or as release of strains. Attempts to find evidences of recrystallization by photographing aging crystal fragments in an electron microscope gave negative results.

[1] D. D'Eustachio and S. B. Brody, J. Opt. Soc. Am. **35**, 544 (1954).

10. A Rheological Problem. ALLEN L. KING, *Dartmouth College.*—When a small quantity of dye or other identifiable substance is injected into a tube where a liquid is flowing, it spreads out rapidly near the axis and more slowly near the walls due to the variation of the speed of flow across the tube. At a distance downstream from the point of injection the concentration of dye (or other substance) in a narrow region is measured as a function of time. The concentration at first increases rapidly to a maximum and then decreases rather slowly. This variation can be shown to depend upon the injection time, the distance between the point of injection and the region of measurement, the width of the region of measurement, and the average speed of flow. In fact, the decreasing portion appears to be inversely proportional to a quadratic function of time with constants that depend on the foregoing factors. The equations should be especially valuable in studies of blood flow.

MINUTES OF THE 1954 MEETING OF THE SOUTHEASTERN SECTION

HELD AT KNOXVILLE, TENNESSEE, APRIL 1–3, 1954

THE University of Tennessee in Knoxville was the site of the Twentieth Meeting of the Southeastern Section of the American Physical Society on April 1, 2, and 3, 1954, which was attended by 270 physicists from the universities and other research centers of the area. A program including sixty-six contributed and eight invited research papers was arranged by S. K. Haynes of Vanderbilt University and his committee. The invited papers were:

Shell Effects in Highly Excited Nuclei. HENRY NEWSON, *Duke University.*

Elastic Scattering Angular Distributions and Polarization of Fast Neutrons. HARVEY WILLARD, *ORNL.*

Recent Results from the Study of Cosmic Rays with Nuclear Emulsions. MAURICE M. SHAPIRO, *NRL.*

Research with the Cosmotron. LYLE SMITH, *BNL.*

Recent Advances in Scintillation Spectrometry. P. R. BELL, *ORNL.*

The Application of Infrared Spectroscopy to the Study of Molecular Interactions in Solutions. MARIE-LOUISE JOSIEN, *University of Bordeaux and Fisk University.*

AEC Research Programs and Policies. T. H. JOHNSON, *AEC.*

Research Policies of the National Science Foundation. R. J. SEEGAR, *NSF.*

Professor A. E. Ruark was the dinner speaker on the subject "Physics in the Southland 1934–1954."

The abstracts of the contributed papers appear below. A session devoted to the teaching of physics composed of three invited and seven contributed papers is being reported in the *American Journal of Physics.*

During the meeting the Section elected W. M. Nielsen of Duke University to be its chairman next year. Other officers are M. S. McCay, University of Chattanooga, Vice-Chairman; Dixon Callihan, ORNL, Secretary; R. T. Lagemann, Vanderbilt University, Treasurer; R. C. Williamson of the University of Florida is a member of the Executive Committee. A. H. Nielsen of the University of Tennessee is the retiring chairman. Sixty-nine physicists became members of the Section at the meeting bringing the total to 551.

The 1955 Meeting will be held at the University of Florida on April 7, 8, and 9.

DIXON CALLIHAN
Secretary, Southeastern Section
Box 247, Oak Ridge, Tennessee

1. The Microwave Spectrum and Dipole Moment of Vinylene Carbonate.* GEO. R. SLAYTON, J. W. SIMMONS, AND J. H. GOLDSTEIN, *Emory University.*—The microwave spectrum of vinylene carbonate has been investigated in the region from 19 000 to 32 000 Mc/sec. Eight *R*-branch transitions have been identified and fitted with the following spectroscopic parameters: $a=9346.79$ Mc/sec, $b=4188.46$ Mc/sec, $c=2891.54$ Mc/sec, all ± 0.10 Mc/sec; $\kappa=-0.59818$. The dipole moment of the vapor, as determined from Stark effect studies, is $4.51\pm0.05D$ and lies in the a axis. The molecule has been shown to be planar. The significance of these results will be discussed and a graphical method for determining κ will be described.

* This work was sponsored by the Office of Ordnance Research, U. S. Army.

2. Millimeter Wave Spectrum of Arsine.* ALBERT JACHE, GILBERT BLEVINS, AND WALTER GORDY, *Duke University.*—The 0→1 rotational transition of arsine has been measured at 2.61 mm wavelength, and a B value of 57 476.15±0.1 Mc has been obtained. The nuclear quadrupole coupling of As^{75} was found to be −165.6 Mc, in good agreement with the earlier value[1] −164 obtained for AsH_2D. Similar measurements on AsH_3 are being made.

* Supported by a contract with the United States Air Force.
[1] C. C. Loomis and M. W. P. Strandberg, Phys. Rev. **81**, 798 (1951).

3. Millimeter Wave Spectrum of Phosphine.* CHARLES A. BURRUS,† ALBERT JACHE, AND WALTER GORDY, *Duke University.*—The 0→1 rotational transition of PD_3 has been measured at 2.16-mm wavelength. The observed B value is 69 468.99 Mc. The first rotational line of PH_3 has been found at 1.12-mm wavelength and measured with a cavity wavemeter only. It will be more precisely measured with a frequency standard, and the data, combined with that of PD_3, will be used for calculation of the structure of the molecule.

* Supported by a contract with the United States Air Force.
† Shell Company Fellow.

4. Centrifugal Distortion in the Methyl Halides.* JOHN COX, W. J. ORVILLE THOMAS,† AND WALTER GORDY, *Duke University.*—The extension of the workable millimeter wave region[1] has made possible measurements of high J transitions in the methyl halides, where centrifugal distortion displacements of rotational lines amount to many megacycles. High J transitions of these substances have been measured for a more accurate evaluation of the distortion constants. The new D_J value for CH_3Cl^{35}, 18.0±0.5 kc, is in good agreement with the value of 18.4 Mc, theoretically predicted by Chang and Dennison.[2] Earlier measurements[3] on lower J transitions gave $D_J=26.4$ kc.

* Supported by a contract with the United States Air Force.
† On leave from the University of Wales, Aberystwyth, Wales.
[1] W. C. King and W. Gordy, Phys. Rev. **90**, 319 (1953).
[2] Tsu-Shen Chang and D. M. Dennison, J. Chem. Phys. **21**, 1293 (1953).
[3] J. W. Simmons and W. E. Anderson, Phys. Rev. **80**, 338 (1950).

5. The Near Ultraviolet Absorption Spectrum of 1,2,4-Trifluorobenzene.* K. NARAHARI RAO,† *Duke University.* (Introduced by H. Sponer).—The vapor absorption spectrum of 1,2,4-trifluorobenzene has been investigated in the 2600 region using a 3-m reflection grating spectrograph in an Eagle mounting. The 0,0 band is assigned the wave number 37126. Prominent bands on the short wavelength side of the 0,0 band are found to involve the excited state frequencies 146, 272, 334, 429, 538, 698, 746, 843, 903, 982, 1274, 1369, and 1445 (in cm^{-1}). Of these, the vibrations belonging to 698, 746, 1274, and 1369 are found in progressions and combinations. Temperature dependent bands on the long wavelength side of the 0,0 band are found to involve the ground state frequencies of 162, 319, 387, 444, 584, 735, 787, 860, 971, 1081, 1322, 1468, and 1515 (in cm^{-1}). A comparison will be made

with the absorption spectra of other substituted benzenes containing fluorine atoms.

* Supported by the U. S. Office of Naval Research.
† At present at Department of Physics, University of Tennessee, Knoxville, Tenn.

6. An Infrared Spectroscopic Study of the Influence of Molecular Structure upon ν(NH), ν(CO), and $\nu(CH_2)$ in Benzopyrroles and their Analogs. NELSON FUSON, MARIE-LOUISE JOSIEN, AND ESSIE M. SHELTON, *Fisk University.*—Studies have recently been made of the electronic structure of compound series such as pyrrole, indole, carbazole;[1] cyclopentadiene, indene, fluorene;[2] and cyclopentadienone, indone, fluorenone.[3] An infrared study[4] of the variation in the NH, CO, and CH_2 frequencies shows that for a series of compounds in which the rings are in a linear array $\nu(CH_2)$ increases while ν(NH) and ν(CO) decrease with increasing size of the molecule. The "angle effect"[5] is also present. Comparisons with the ultraviolet spectra of these molecules[6] and with the infrared spectra of quinones[5] will be given.

[1] Longuet-Higgens and Coulson, Trans. Faraday Soc. **43**, 87 (1947); Berthier and Pullman, Compt. rend. **226**, 1725 (1948).
[2] Pullman and Bertier, Bull. Soc. Chim. France **15**, 551 (1948).
[3] Bertier, Pullman, and Pontis, J. chim. Phys. **49**, 367 (1952).
[4] M. L. Josien and N. Fuson, Compt. rend. **246**, 1879, 1958 and 2062 (1953).
[5] Josien, Fuson, Lebas, and Gregory, J. Chem. Phys. **21**, 331 (1953).
[6] Orchin and Friedel, J. Am. Chem. Soc. **71**, 3002 (1949); Clemo and Felton, J. Chem. Soc. 1952, 1658; Felton, *ibid.*, 1668.

7. Molecular Association in Perfluoroalkyl Carboxylic Acids. J. R. LAWSON AND M. B. TOWNS, *Tennessee A. & I. State University.*—Molecular association of trifluoroacetic, perfluoropropionic, and heptafluorobutyric acids in carbon tetrachloride solutions has been investigated by means of infrared spectroscopy. The equilibrium between monomeric and associated molecules has been studied by observing the effects of changes in concentration upon the intensities of the absorption bands arising from the OH and C=O stretching vibrational modes within the carboxylic group.

8. The Infrared Spectrum of σ_2 for $B^{10}F_3$ and $B^{11}F_3$.*† ALVIN H. NIELSEN, *Department of Physics, The University of Tennessee.*—The infrared grating spectra of σ_2 for $B^{10}F_3$ and $B^{11}F_3$ have been re-examined from 650 to 750 K. Two samples of BF_3, one composed of 93.4 percent $B^{10}F_3$ and 6.6 percent of $B^{11}F_3$; and the other of the normal abundance ratio 20 percent $B^{10}F_3$ and 80 percent $B^{11}F_3$ were secured for the investigation. Complete resolution of the rotational fine structure of this parallel-type band was achieved. The following constants were obtained by means of the usual sort of rotational analysis: For $B^{10}F_3$, $\sigma_0 = 718.23$ K, $B_0 = 0.3527_2$ K, $B(v_2=1) = 0.3528_8$ K, $Dj = 13.72 \times 10^{-7}$ K. For $B^{11}F_3$, $\sigma_0 = 691.45$ K and the rotational constants are the same for the two isotopic species.

* This work was supported in part by the U. S. Army Office of Ordnance Research.
† This work was supported in part by the K-25 Laboratories, operated by Carbide and Carbon Chemicals Company, a Division of Union Carbide and Carbon Chemicals Corporation, Oak Ridge, Tennessee.

9. The Infrared Spectrum of Allene-d_2.* WILLIAM H. FLETCHER AND W. E. SHULER, *University of Tennessee.* (Introduced by Alvin H. Nielsen.)—The infrared spectrum of allene-d_2 has been observed from 2μ to 35μ with LiF, CaF_2, NaCl, KBr, and CsBr prisms. Twelve of the fourteen infrared-active fundamentals have been identified and the observed overtones have been satisfactorily assigned. Some of the bands have been observed with a grating spectrometer and the moments of inertia have been calculated.

* This work has been supported by the Research Corporation and by the Office of Ordnance Research, U. S. Army.

10. Vibrational Spectra of the Pentafluorides of Antimony, Arsenic, and Bromine. LAWRENCE K. AKERS AND ERNEST A. JONES, *Vanderbilt University.*—The infrared spectra of gaseous AsF_5, BrF_5, and SbF_5 have been obtained in the region from 2 to 25 microns and the Raman spectra of AsF_5 and SbF_5 have been obtained in the liquid state. The BrF_5 and SbF_5 compounds were obtained from commercially available sources, while the AsF_5 was prepared by passing fluorine over arsenic in an evacuated copper apparatus.

An assignment of the observed infrared bands and Raman lines as fundamentals, overtones, and combinations will be presented together with a suggested structural assignment on the basis of observed data.

11. The Intensity of Infrared Absorption Bands in Methylene Chloride. JOSEPH W. STRALEY, *Dept. of Physics, University of North Carolina.*—The intensities of four vibrational absorption bands of methylene chloride have been measured. These bands are those conventionally designated as ν_6 and ν_7 of symmetry class B_1, and ν_8 and ν_9 of symmetry class B_2. The results have been used to calculate how the dipole moment of these molecules varies during the vibration. These calculations enable one to determine the behavior of the individual bond moments during the vibration. The values of $\partial\mu/\partial r$ determined in this manner have been considered in relation to those determined recently for other molecules. A comparison of intensities observed in solution and in the vapor state has been made.

12. Potential Constants for Carbonyl Fluoride. R. J. LOVELL AND E. A. JONES, *Vanderbilt University.*—A normal coordinate treatment of the planar XYZ_2 molecule was undertaken to explain the results of several spectroscopic studies available in our laboratory. Results of this investigation have been first applied to COF_2 where it was found that a modified valence force potential function of the form

$$2V = k_1(\Delta d_1^2 + \Delta d_2^2) + k^3\Delta d_3^2 + k_r d_1^2\Delta_r^2 + k_B d_1^2(\Delta\beta_1^2 + \Delta\beta_2^2) + kD_{FO}^2 + k_d d_1^2\Delta\partial^2$$

described the molecule. The term D_{FO}

$$= \frac{\Delta d_1(d_1 - d_3\cos\beta) + \Delta d_3(d_3 - d_1\cos\beta) + d_1 d_3 \sin\beta\Delta\beta}{d_{FO}}$$

was introduced to represent the interaction between the oxygen and fluorine atoms. k_1 and k_3 are the C-F and C=O stretching constants; k_B and $k\gamma$ are the O-C-F and F-C-F angle deformation constants; k_d is the out-of-planar angle constant; and k the interaction constant. $d_1 = d_2$ and d_3 are the C-F and C=O equilibrium bond distances; β and γ are the O-C-F and F-C-F equilibrium angles; and d_{FO} is the radical distance between the fluorine and oxygen atoms. The values obtained for these constants are in 10^5 dynes/cm: $k_1 = 4.83834$; $k_3 = 14.38706$; $k_B = 1.31042$; $k\gamma = 2.86763$; $k_d = 0.33383$; and $k = 5.25724$. The validity of this form of potential function for COF_2 is shown by the agreement of the calculated and experimental frequencies.

13. Vibrational Analysis of Polypeptide Chains. W. E. DEEDS, *University of Tennessee.* (Introduced by Alvin H. Nielsen.)—A normal coordinate analysis has been completed for polypeptide chains in the planar and helical configurations,[1] using the multiple origin method and modified valence coordinates.[2] Amino groups were assumed to have lumped parameters, but not point masses. The normal modes are standing waves of various forms and lengths. The normal frequencies have been calculated using force constants from other molecules and are plotted as functions of the quantized amplitude phase difference between adjacent repeating units. More accurate force constants can be calculated when high resolution spectra are available. All band sets should be both infrared and Raman active with intensity patterns as previously predicted,[3] and the positions of the infrared intensity

maxima indicate the number of residues per turn of the helix. The spectra can also indicate the average "straight" length of chain and the relationship of neighboring chains. Work is under way to determine the precise effects of various amino acid groups, and these results may be reported if time permits.

[1] L. Pauling and R. B. Corey, J. Am. Chem. Soc. **72**, 5349 (1950).
[2] W. E. Deeds, Ph.D. Dissertation, Ohio State University, 1951. Phys. Rev. **82**, 131 (1951); **85**, 160 (1952).

14. Photoelectric Measurement of Reversal Temperature.* HEDWIG KOHN AND EINAR HINNOV, *Duke University*.—A convenient photoelectric technique has been worked out for determining spectral line reversal temperatures. In the conventional optical setup a rotating sector is placed between the background radiator and the source of the spectral lines, such as a flame. At a given wavelength, readings of the photocurrent are taken for various openings of the sector, with and without the flame in the path of the rays. The plots of the readings *versus* the percent transmission of the sector can easily be shown to be straight lines. Their point of intersection represents the "matching point." Its abscissa relates the flame temperature to the known brightness temperature of the background source. The procedure can also be applied when the reversal temperature exceeds the brightness temperature of the background source. Reversal (excitation) temperatures have been measured for a number of resonance lines (Li, Na, Sr, Cu) excited in an acetylene-compressed air flame (Lundegardh type). Distinct, though not large differences were observed. To study the nature of these differences the reversal temperatures have been mapped in three mutually perpendicular directions.

* Supported by the U. S. Office of Naval Research.

15. Intensity Measurements of Resonance Lines in a Flame Source.* EINAR HINNOV AND HEDWIG KOHN, *Duke University*.—The intensity-density relation of spectral lines excited in an acetylene-compressed air flame (Lundegardh type) has been studied by photoelectric photometry. Previous measurements by H. Kohn in collaboration with students at Wellesley College had revealed significant differences in the shapes of the intensity-density curves for the resonance lines of various elements. The shapes of such curves can be affected by the inhomogeneity of the source. Essentially they are determined by the shape factor of the lines. By comparing measured intensity-density curves with the theoretical curves of growth for various values of the ratio damping half-width to Doppler half-width conclusions can be drawn with regard to the optical cross sections of the respective atoms. To aid the interpretation the line intensities have been mapped in three mutually perpendicular directions and the "line absorption" has been measured. The present investigation deals with the singlet resonance line of Sr and the Cu resonance doublet. The concentrations of the salt solutions fed into the flame ranged from four to five powers of ten.

* Supported by the U. S. Office of Naval Research.

16. The Molar Polarization, Dipole Moment, and Nonideality of Trichloroheptafluorobutane Vapor.* D. W. MAGNUSON, *K-25 Technical Division, Oak Ridge*.—Dielectric constant measurements, using a microwave technique, were made at several temperatures and many pressures. The plot of the parameter $(\epsilon-1)/(\epsilon+2)\,P$. *vs* P. is used to calculate the molar polarization at zero pressure and the nonideality parameter in the gas law $P(1+AP)=RT/V$. These results are given in the following table. The limit of error is the 95 percent confidence level.

Temperature T(°C)	*Molar polarization* P_M (cc)	*Nonideality* A (atm^{-1})
70.9	52.55 ±0.22	0.089 ±0.014
71.0	52.38 ±0.16	0.097 ±0.010
97.8	51.62 ±0.08	0.0581±0.0025
98.7	51.66 ±0.11	0.0556±0.0032
98.9	51.55 ±0.10	0.0585±0.0029
135.4	50.473±0.046	0.0372±0.0011
135.4	50.507±0.057	0.0385±0.0014

The molar polarization is given by the equation $P_M=39.75+4.395\times10^3/\tau$, and the dipole moment is $(0.85\pm0.08)\times10^{-18}$ esu cm. The author is indebted to the Hooker Electrochemical Company for the sample of trichloroheptafluorobutane.

* This document is based on work performed for the U. S. Atomic Energy Commission by Carbide and Carbon Chemicals Company, A Division of Union Carbide and Carbon Corporation, at Oak Ridge, Tennessee.

17. Further Study of the Po-Be Neutron Spectrum.* B. J. WINNEMORE, H. GURSKY, D. A. COWAN, AND C. D. CURTIS, *Vanderbilt University*.—The Ranger,[1] a device used to count particles of a selected type and energy, has been used in the study of the energy spectrum of the neutrons from Po-Be source. This study was meant to supplement and refine the data reported on previously.[2]

The range resolution was determined to be about 0.3 Mev, and individual points were determined to within several percent. The spectrum was measured from 2.8 to 9.45 Mev with particular attention being paid to the region of the spectrum around 5.0 Mev where a sharp peak had previously been reported.[2] This study shows no such peak, but only a broad maximum in that region. The appearance of the peak in the previous study has been attributed to a mechanical failure in the Ranger itself, which has been corrected. Other broad maxima appear at 3.4, 5.9, 7.7, and 9.5 Mev, results which are consistent with other studies.

* Work supported by U. S. Atomic Energy Commission contract.
[1] D. L. Hill, U. S. Atomic Energy Commission Report AECD-1945 (Rev.), 1948.
[2] Gursky, Winnemore, and Cowan, Phys. Rev. **91**, 209 (1953).

18. Cross Section for Excitation of Pb^{207m} by Inelastic Neutron Scattering. P. H. STELSON AND E. C. CAMPBELL, *Oak Ridge National Laboratory*.—The cross section for the excitation of the 0.82-sec isomeric state of Pb^{207} by inelastic neutron scattering has been measured for neutron energies up to 3.1 Mev using the Li(p,n) source. The lowest neutron energy for which excitation is observed is 1.6 Mev. This is in agreement with the level scheme for Pb^{207} based on other data.[1,2] For the first 600 kev above threshold the cross section rises approximately linearly, attaining a value of 40 millibarns at 2.2 Mev. It then increases more rapidly and has a value of 140 millibarns at 3.1 Mev. The procedure used to determine the absolute cross section will be discussed. It is estimated that the absolute values are accurate to ±50 percent. The shape and absolute cross section for excitation of the isomeric state is calculated in the region close to the threshold by use of the statistical theory of reactions. The theoretical prediction agrees reasonably well with the measured curve.

[1] Goldhaber and Hill, Revs. Modern Phys. **24**, 179 (1952).
[2] F. K. McGowan and E. C. Campbell, Phys. Rev. **92**, 523 (1953).

19. The Inelastic Scattering of D-D Neutrons by Fe and Cu.* L. A. RAYBURN, D. L. LAFFERTY, AND T. M. HAHN, *University of Kentucky*.—Monoenergetic neutrons from the $H^3(d,n)He^3$ reaction produced by the University of Kentucky 120-kv accelerator were used to bombard scatterers of Fe and Cu in the form of rings surrounding a gamma-ray spectrometer. The spectrometer consisted of a NaI(Tl) crystal mounted on a DuMont 6292 photomultiplier tube. The pulses from the spectrometer were analyzed with a single channel pulse-height analyzer. The gamma-ray spectrum obtained by

subtracting the background counting rate from the counting rate with scatterer in place will be presented. An analysis of the Fe spectrum yields gamma rays with energies of 0.462, 0.675, 0.851, 0.892, 0.989, 1.098, 1.24, 1.40, 1.59, 1.70, 1.78, 2.10, 2.21, and 2.66 Mev. An analysis of the Cu spectrum yields gamma rays with energies of 0.965, 1.110, 1.57, 1.91, 2.42, and 2.58 Mev.

* Sponsored by the Office of Ordnance Research, U. S. Army.

20. Neutron Scattering. J. W. CURE AND G. S. HURST, *Oak Ridge National Laboratory.* (Introduced by Elda E. Anderson.)—Since scattered radiation which reaches the point of measurement is one of the major problems of dosimetry, an experiment was designed to determine the variation in neutron dose at a point in air with the distance between the source and detector, and with the height of the source and detector above a concrete slab. When a frustrum of paraffin was placed between the source and detector, only the scattered neutrons contributed to the dose. To reduce extraneous scattering material to a minimum, the detector and source were supported five feet below a steel bar which was suspended from two scaffolds, forty feet apart and fifty-five feet high. The neutron source was $Po^{210}B$ (mean energy 2.6 Mev) and the counter was a proportional counter, ethylene-polyethylene type, with a pulse integrator for measuring the tissue dose. It was found that the inverse square law predicts the dose for distances up to 1.5 meters between the source and detector, and if the source, detector, etc. are 1.5 meters from the walls, floors, etc., the dose contribution at the detector due to scattered neutrons will be less than 5 percent.

21. Demonstration of Neutron Spin from Bloch-Alvarez-Type Experiment. C. P. STANFORD, T. E. STEPHENSON, AND S. BERNSTEIN, *Oak Ridge National Laboratory.*—The Rabi[1]-type magnetic resonance experiment which was used by Alvarez[2] and Bloch for the measurement of the gyromagnetic ratio of the neutron has been extended so as to give a demonstration of the neutron spin. Two magnetized single crystals of magnetite are used in series as neutron beam polarizer and analyzer. They serve also as monochromator. Between these two crystals a constant field H_0 of several hundred oersteds is maintained parallel to the field applied to the magnetite crystals. Transitions between neutron energy levels in the constant field are induced by an oscillating field H_1 perpendicular to H_0. The frequency ω of H_1 is adjusted to satisfy the relation $\omega=(\mu/S)H_0$ where μ/S is the gyromagnetic ratio of the neutron. The neutron spin (1/2) is demonstrated by comparison of the measured transition probability as a function of the amplitude of the oscillating magnetic field to the calculated values based on different assumed values of neutron spin.

[1] Rabi, Zacharias, Millman, and Kusch, Phys. Rev. **53**, 318 (1938).
[2] L. W. Alvarez and F. Bloch, Phys. Rev. **57**, 111 (1940).

22. Activation of Al and Se^{80} by p-Neutron Capture in the Kilovolt Region.* R. H. ROHRER,† *Duke University and Oak Ridge National Laboratory,* H. W. NEWSON, J. H. GIBBONS, P. CAP, *Duke University.*—A neutron cross-section resonance at 6.4±0.5 kev has been detected in aluminum by transmission and by activation measurements using monoenergetic neutrons from the Li(p,n) reaction.[1] The peaks of the total and capture cross sections at resonance were estimated to be 88 b and $\geqslant$12 b, respectively, and the total resonance width was estimated to be ~12 ev. These agree with approximate theoretical predictions if an angular momentum quantum number of $l=1$ is assumed for the incident neutrons. A study of the production of the 58-min and 18-min isomeric states in Se^{81} by both pile beam and Li(p,n) neutrons indicates that the activation of both levels is due, in part, to the 3-kev and 6-kev resonances observed in total cross-section measurements.[2] A further contribution to the 58-min state appears to be due to a p resonance at an energy greater than 3 kev.

* Work supported by the U. S. Atomic Energy Commission.
† At O.R.N.L. as Research Participant from Emory University.
[1] J. H. Gibbons, Phys. Rev. **94**, 773 (1954).
[2] Newson, Williamson, Toller, and Nichols, Phys. Rev. **94**, 774 (1954).

23. On the Theory of Nuclear Reactions with a Radioactive Product. T. A. WELTON, *Oak Ridge National Laboratory.* (Introduced by Arthur H. Snell.)—Recently a number of nuclear reactions have been observed at this laboratory and elsewhere,[1,2] in which a compound nucleus, initially formed by a monoenergetic beam, decays into a first stable particle (A) and a short-lived unstable nucleus (N). This unstable nucleus then decays into two final stable products (B and C). In each case the energy spectrum of A has been observed to contain a strongly peaked component corresponding to the nearly definite energy of the unstable product N. The width of this peaked spectrum then corresponds to the range of energies possessed by N. A general solution of the spectrum problem has been attempted along the lines of the Wigner-Eisenbud theory of resonance reactions. Preliminary results for a simple model show the qualitatively expected (and previously assumed[1]) correspondence between the spectrum shape and the energy variation of the cross section for the scattering of B by C. This correspondence, which seems to hold in general, will be stated more fully.

[1] P. B. Treacy, Phil. Mag. **44**, 325 (1953).
[2] C. D. Moak, University of Tennessee, thesis (1954).

24. $Li^6(d,t)$ Reaction. R. L. MACKLIN AND H. E. BANTA, *Oak Ridge National Laboratory.*—The cross section for the reaction $Li^6(d,t)$ has been measured by collecting and beta counting the tritium produced by the reaction at various energies of bombardment. Deuterons from the 2-Mev and 5-Mev Oak Ridge Van de Graaff generators were used, giving an energy range from 0.4 to 4.2 Mev. The cross section varies between 50 and 300 millibarns. Some information on the forward-backward asymmetry of the reaction can be deduced from the experiment.

25. Excitation Function for the Reaction $Be^9(N^{14})F^{18}He^5$. H. L. REYNOLDS AND A. ZUCKER, *Oak Ridge National Laboratory.* (Introduced by Robert S. Livingston.)—Using the 29-Mev deflected nitrogen beam of the ORNL 63-inch cyclotron the absolute cross section for the reaction $Be^9(N^{14})F^{18}He^5$ as a function of incident nitrogen energy has been determined. Beryllium targets were placed on a 12-position target holder which rotated rapidly through the beam. Appropriate nickel absorbing foils were placed before each target to degrade the nitrogen energy to the desired value. One target hole was left open and the current passing through was collected in a Faraday cup to give the number of particles striking each target. The bombardment time was approximately 30 minutes after which the F^{18} activity in each target was determined with a calibrated end-window Geiger counter. The yield curve obtained was differentiated to obtain an excitation function. The cross section is fairly flat from 20 to 29 Mev and has a value of approximately 2×10^{-28} cm^2. At 10 Mev the cross section has dropped to approximately 10^{-27} cm^2.

26. Angular Distribution of 12-Mev Gamma Rays from the Reaction B^{11} (p,γ) C^{12}.* H. H. GIVIN, G. K. FARNEY, B. D. KERN, AND T. M. HAHN, *University of Kentucky.*—Using a thin boron target, the angular distribution of the 12-Mev gamma rays emitted from C^{12} following the proton bombardment of boron has been obtained at proton energies up to 2 Mev. The gamma-ray energy spectrum was obtained with a scintillation spectrometer at each angular position of the detector for selected values of the protion energy. The results of the measurements will be described and discussed.

* Sponsored by the Office of Ordnance Research, U. S. Army.

27. (p,n) Reactions on As, Y, Nb, and Rh.* REID PATTERSON, *Duke University.*—Protons of 4.25 Mev were used to bombard 40-kev targets of As, Y, Nb, and Rh. Ilford C-2 200 micron emulsions were placed 15 cm from the targets at 0° and 90°. Recoil proton tracks in the processed emulsion were measured under a binocular microscope at 900× oil immersion. After proper corrections were applied, histograms of relative neutron intensity *vs* neutron energy were plotted. Two well-resolved peaks were found in Nb at 0° and 90° with energy shift consistent with mass 93 nucleus. *Q* values are -1.27 ± 0.04 Mev and -2.73 ± 0.04 Mev with relative intensity 3:4, respectively. Four much weaker and doubtful peaks occur. Measurements were taken only at 0° for As, Y, and Rh. Two well-resolved peaks in Y give *Q* values -1.73 ± 0.04 Mev and -2.54 ± 0.04 Mev with relative intensity 7:5, respectively. Two weaker peaks occur. Rh shows four peaks of nearly equal intensity with *Q* values -1.53, -2.01, -2.64, and -2.98 Mev and a weaker peak with *Q* value -3.26 Mev. The peaks in As are poorly resolved. The ground-state peak is consistent with a threshold of 1.70 Mev. The level spacing increases in the neighborhood of neutron number 50.

* Work supported by U. S. Atomic Energy Commission.

28. Recent Progress in Fission Fragment Angular Distribution Measurements. B. L. COHEN, D. J. COOMBE, AND B. L. FERRELL, *Oak Ridge National Laboratory.* (Introduced by Robert S. Livingston.)—The previously reported[1] measurements of angular distributions of fragments from thorium fission induced by 22-Mev protons from the internal circulating beam of the ORNL 86-inch cyclotron have been extended to similar studies of U^{238} and U^{235} fission. As in the case of thorium fission, the angular distributions are symmetric about 90° with maxima in the forward and backward directions, and the anisotropy is greater for asymmetric than for symmetric fission. The magnitude of the anisotropy for symmetric fission is about the same (~10 percent) for the three cases, but for asymmetric fission, the anisotropies are less for the uranium isotopes. Preliminary measurements with protons of 17 and 13 Mev indicate that the angular distributions are quite insensitive to the incident energy. Recent changes and extensions in the experimental techniques will be discussed. Preliminary results for proton induced fission in U^{233} will also be reported.

[1] Cohen, Jones, McCormick, and Ferrell, Phys. Rev. **94**, 758 (1954).

29. Intensities of the Radiations from Hf^{175}. A. O. BURFORD, J. F. PERKINS, AND S. K. HAYNES, *Vanderbilt University.*—For Hf^{175} the electron spectrum and the photoelectron spectrum from Au radiators have been studied in a magnetic lens spectrometer. Conversion lines of the previously reported 430.5, 342.3, 318, 228, 113, and 89 kev transitions were found. The $K/L+M$ ratios for the 342.3 and 228 kev transitions (4.94 ± 0.5 and 2 ± 0.5) agree approximately with Burson.[1] For the 89-kev transition K/L is 6.0 ± 0.7 (double that of Burson) and the K conversion coefficient is equal to or less than 34 times the K conversion coefficient of the 342.3-kev transition. The above information combined with two preliminary values of the K conversion coefficient of the 342.3-kev transition[2] strongly indicates that both transitions are almost entirely M1 with possibly a small amount of E2. Tentative spin and parity assignments are ground state of Lu^{175} 7/2+, 113 kev uncertain, 342.3-kev level 5/2+, 431-kev level 3/2+. When an accurate value of the conversion coefficient of the 342.3-kev transition is available, the Auger electron intensity will indicate to what extent capture transitions direct to the ground state occur.

[1] S. B. Burson and W. C. Rutledge ANL-4746 (1951).
[2] F. K. McGowan and R. J. Kerr (private communications).

30. Discrete Electron Energy Losses in Thin Foils. A. W. BLACKSTOCK,* R. D. BIRKHOFF, AND M. SLATER, *Oak Ridge National Laboratory.*—Discrete energy losses for 45-kev electrons passing through thin foils have been measured using an accelerator and spectrometer of unique design. The instrument consists of three parts: an accelerating tube; a decelerating tube, the potential of which is derived from the same voltage source that supplies the accelerator and in which the electrons lose most of their energy; and an electrostatic analyzer which analyzes the remaining energy (0.2 percent) of the beam. Electrons which lose energy in a foil placed between the accelerator and decelerator may still enter the Faraday cage collector when the potentials applied to the accelerator, decelerator, or analyzer are varied. The resolution is about one part in 25 000. Measurements in aluminum foils 5 to 20μ g/cm^2 thick yield discrete losses separated by 16.0 ± 0.6 ev. These agree substantially with measurements made by Lang[1] and others by different methods. Agreement with the plasma oscillation theory of Pines and Bohm[2] is obtained if the number of free electrons per atom in aluminum is taken as 3.07.

* Oak Ridge Graduate Fellow from North Carolina State College.
[1] W. Lang, Optik **3**, 233 (1948).
[2] D. Pines and D. Bohm, Phys. Rev. **85**, 338 (1952).

31. Electron Capture and Loss Cross Sections for Protons. P. M. STIER, C. F. BARNETT, AND G. E. EVANS, *Oak Ridge National Laboratory.* (Introduced by Arthur H. Snell.)—Electron capture and loss cross sections have been determined for protons passing through various gases in the energy range 20 to 250 kev. The ion beam from the Cockcroft-Walton accelerator passed through a differentially pumped gas cell, in which part of the beam was neutralized by charge exchange. The charged component of the emergent beam was removed by electrostatic deflection, leaving a beam of fast atoms. These fast atoms passed through a second differentially pumped charge exchange chamber. An electrostatic field within this chamber was provided to remove all positive ions formed by electron loss collisions. The intensity of the atomic beam varies as $I=I_0\exp(-n\sigma_1 l)$, where I_0 is the incident atom beam, n the gas density, l the chamber length, and σ_1 the cross section for electron loss. Electron capture cross sections can then be calculated from the previously measured[1] ratio of loss to capture cross sections. Preliminary results, showing good agreement with published results for hydrogen[2] and air,[3] as well as results for helium, nitrogen, neon, and argon will be presented.

[1] Stier, Barnet, and Evans, Phys. Rev. **93**, 926 (1954).
[2] J. H. Montague, Phys. Rev. **81**, 1026 (1951).
[3] H. Kanner, Phys. Rev. **84**, 1211 (1951).

32. The w Value in Electron Volts for 5-Mev Alpha Particles in Gases and Gas Mixtures. T. E. BORTNER AND G. S. HURST, *Oak Ridge National Laboratory.*—The average number of ion pairs formed by Pu^{239} alpha particles in various gases and gas mixtures has been measured. This value expressed in electron volts is designated as w. A parallel plate ionization chamber was filled to a pressure such that the alpha particles lost all their energy in the sensitive volume. The rate of voltage change on an accurately calibrated condenser was measured by means of a potentiometer using an ac operated electrometer as a null indicator. The necessity of gas purification is shown by the spread of w for helium. With no purification, the w value was 30 ev, but when purified the value increased to 46 ev. The methods of gas purification are described and the w values of some fifteen gases and gas mixtures will be presented in tabular form. The effect of contaminating gases in argon and helium is shown graphically.

33. Measurements of Ionization Produced by 5-Mev Alpha Particles in Argon Mixtures. CHARLES E. MELTON, *Oak Ridge*

National Laboratory. (Introduced by Russell Baldock.)—Since it is known that impurities in some of the noble gases greatly reduce the value of w (the average energy required to produce an ion pair), a systematic study of one of them, argon, was conducted by adding to it other gases in measured percentages and observing their effect on the w value. These gases were added in quantities of from 0 to 100 percent in order to determine the percent at which a maximum effect occurred. An uncollimated Pu^{239} alpha source was placed in the center of a large parallel plate ionization chamber, and the ionization produced was measured by means of an accurately calibrated capacitor, a stable high-voltage supply, a vibrating reed electrometer, and a potentiometer. The capacitor and potentiometer were connected in series across the ionization chamber; the change in potential across the capacitor and hence the rate of ionization was determined with the potentiometer by use of a vibrating reed electrometer as a null indicator. Sixteen of the eighteen cases investigated produced increases in ionization varying from 2 to 23 percent when added to argon. The maximum ionization occurred when the percent of the impurity was between 0.1 and 5 percent.

34. Energy Per Ion Pair for Recoil Atoms in Methane. W. G. Stone and Lewis W. Cochran, *Oak Ridge National Laboratory.*—The value of w, the average energy loss per ion pair produced, has been measured for methane, using the recoil atoms resulting from the alpha decay of thorium C and thorium C′. The recoil source, collected on a silvered mica backing, was mounted in the wall of a proportional counter filled with purified methane to a pressure of one to two centimeters of mercury. The heights of the pulses due to the recoil atoms were measured by means of a single channel differential analyzer. Calibration of the proportional counter was accomplished by using a collimated plutonium alpha source. From the data of Hirshfelder and Magee[1] the energy loss in the active volume of the counter by the plutonium alphas was determined and a comparison of relative pulse heights gave the number of ion pairs formed by the recoil atoms. The values of w obtained were 137 and 126 ev/ion pair for the recoil atoms of thorium C and thorium C′ decay, respectively.

[1] J. O. Hirshfelder and J. L. Magee, Phys. Rev. **73**, 207 (1948).

35. A Proportional Counter for Auger Electrons.* Ernest D. Graves and H. C. Thomas, *Mississippi State College.*—The detection of Auger electrons is extremely difficult because of the inability of these particles to penetrate the windows of most counters. The identification of Auger electrons by absorption methods is complicated because the accompanying low-energy x-rays will have about the same range as the Auger electrons, and also because the counting efficiency for these x-rays can often become quite large. In order to make detection and identification of Auger electrons more positive, a proportional counter was constructed. A radioactive sample could be placed within the sensitive volume, thus eliminating window absorption of low-energy particles. The construction, performance, and proposed uses of this counter will be discussed.

* Supported in part by a Frederick Gardner Cottrell grant.

36. A Small Current DC Amplifier. Newton Underwood and G. F. Zindler, Jr., *North Carolina State College of Agriculture and Engineering.*—A small current dc amplifier has been built which uses a pentode (CK512AX) as the input tube, followed by another pentode (6AK5) as an output tube. The amplifier has a readily usable maximum sensitivity of 10^{-13} ampere full scale. With care, a full-scale sensitivity of 10^{-15} ampere can be obtained. The output span of the amplifier is ±1 volt and is stable within ±5 millivolts over a period of 12 hours on the 10^{-13} ampere range. The input grid operates at ground potential. Over-all 100 percent negative feedback is used as well as transient negative and positive feedback. The amplifier is ac operated, and is capable of driving a 0.1-ma recorder.

37. The Low-Momentum End of the Spectrum of Heavy Primary Cosmic Rays.* R. A. Ellis, Jr.,† M. B. Gottlieb, and J. A. Van Allen, *State University of Iowa.* (Introduced by J. R. Lawson.)—Measurements of the intensity of heavy primary cosmic-ray nuclei have been made above the atmosphere by means of the new Iowa Balloon-launched rocket ("rockoon") technique at geomagnetic latitudes $\lambda = 56°$, 76°, 86°. The measuring instrument was a thin-walled, pulse-ionization chamber of 15-cm diameter. The observed data, in conjunction with geomagnetic theory, demonstrate a complete or nearly complete absence of primary heavy nuclei of $z \geqslant 6$ having a magnetic rigidity less than 1.5×10^9 volts (p/mc < 0.8), the result being the most significant for the C,N,O group. It is noted that this spectral cutoff occurs at closely the same magnetic rigidity, and distinctly not at the same velocity, as the previously reported cutoff in the spectra of primary protons and α particles.

* Assisted by joint program of the U. S. Office of Naval Research, the U. S. Atomic Energy Commission, and the Navy Bureau of Aeronautics; and by the Research Corporation.

† Present address: Department of Physics, Tennessee Agricultural and Industrial State University, Nashville, Tennessee.

38. High-Intensity Beam of Low-Energy Protons in the ORNL 86-Inch Cyclotron. F. L. Green and J. A. Martin, *Oak Ridge National Laboratory.* (Introduced by Robert S. Livingston.)—Recent operational experiments with the ORNL 86-inch cyclotron have produced 29.5 milliamperes of 1-Mev protons collected on an internal water-cooled aluminum target at a radius of 25 inches. In order to accelerate these protons to 1 Mev, the magnetic field was lowered to one-third of the 22-Mev proton resonance value so that third half-cycles of the fixed rf oscillator could be used. By adjusting the magnetic field to resonance, protons were also accelerated on fifth half-cycles and seventh half-cycles. Ion transport efficiency (the ratio of target current to total ion current accepted by the dees during the rf cycle times 100) of over 50 percent has been indicated for third half-cycle acceleration. An ion transport efficiency of 17.6 percent has been previously reported[1] for acceleration of protons to 22 Mev.

[1] A. L. Boch and E. D. Hudson, Phys. Rev. **91**, 224 (1953).

39. Magnetic Spectrometer for Recoil Spectrometry. Arthur H. Snell and Frances Pleasonton, *Oak Ridge National Laboratory.*—A 180-degree beta-ray spectrometer magnet has been modified and adapted for use in measuring the momenta of ions of low energy such as might result from beta recoil in a low-pressure gas source. Wedge-shaped poles are used, and with the source and detector well outside of the magnetic field, appropriate oblique incidence and exit enable fringe-field "vertical" focusing and the usual horizontal focusing to produce a stigmatic image after a total deflection of 96.5 degrees. The transmission is about 0.001, the radius of curvature is 17.1 cm, the focal length is 27.4 cm, the object and the double-focused image are, respectively, 41.3 cm and 40.0 cm outside of the pole edges at angles, respectively, 46.5, and 11.5 degrees from the normals to the pole edges, and on the same side as the center of curvature. Using ion sources with 1/16 and 1/2 inch diameter apertures, 10 ev-argon 40 ions have been focused with a resolution of 3 and 4 percent full width at half-maximum in momentum; at least half of this width is attributable to momentum spread from the source. An "object" 1/2 inch in diameter is stigmatically focused to an image 7/16 inch wide and 5/8 inch high.

40. General Relations in a Fluid Convection Theory: I. Similarity Theory for Flow Onset. F. T. ROGERS, JR., *University of South Carolina.*—Conventional similiarity theory has been applied to the problem of conditions obtaining at the onset of convective flow of a fluid in a porous medium and heated from below. The problem is summarized in reference[1] for a nonstatic thermal environment and for a temperature-dependent viscosity. Similarity theory is found to require that the conditions at onset be given by a functional relation between four dimensionless quantities, provided the fluid and medium are of infinite horizontal extent; in the notation of reference,[1] $\nu BD = \nu\beta_c D \cdot f(D/\tau, \nu\beta_c D, E^2D^2)$. This result is consistent with all formulas that have reported and based upon analytical methods. But it exhibits and emphasizes more clearly the status of E^2D^2, which characterizes the supposed repetitive structure of flow.

[1] F. T. Rogers, Jr., J. Appl. Phys. **24**, 877 (1953).

41. Normal Coordinates in the Nuclear Photoeffect.* YU-CHANG HSIEH AND INGRAM BLOCH, *Vanderbilt University.*—If nucleons interact by ordinary Hooke's law forces, one can treat a nucleus as a collection of noninteracting normal-mode oscillators.[1] The oscillators can be so chosen that only one of them has a nonvanishing electric dipole matrix element between the ground state and any excited state of the nucleus; this oscillator corresponds to the *n vs p* vibration discussed by various authors,[2] and becomes singly excited by a photon according to first-order perturbation theory. Presumably the oscillators interact in such a way as to lead to subsequent fission or ejection of a particle. The integrated cross section is given by

$$\int \sigma dE = (\pi e^2 h/mc)(NZ/A) \text{ Mev-barn.}$$

The observed dependence of resonant energy on atomic weight suggests that the Hooke's law forces are many-body forces, in that the force constants depend on how many nucleons are present.

* Assisted by the U. S. Army Office of Ordnance Research.
[1] I. Bloch and Y. C. Hsieh, Phys. Rev. **91**, 240(A) (1953).
[2] M. Goldhaber and E. Teller, Phys. Rev. **74**, 1046 (1948); Ferentz, Gell-Mann, and Pines, Phys. Rev. **92**, 836(L) (1953).

42. Resolution of Four-Dimensional Vector Fields and Tensor Fields. N. L. BALAZS, *Department of Physics, University of Alabama.* (Introduced by Arthur E. Ruark.)—It is common knowledge that a three-dimensional vector field (subject to certain conditions) can be represented uniquely as the sum of an irrotational and a solenoidal vector field. In this note we attempt to generalise this theorem for vector fields and certain tensor fields defined in four-dimensional Euclidean and pseudo-Euclidean spaces [with a signature $(^+, ^+, ^+, ^-)$]. As a matter of fact some of the results can immediately be extended to n-dimensional spaces. It seems, however, the theorem cannot be generalized to general Riemannian spaces. The results are applied to the four potential field satisfying the Maxwell-Lorentz equations; the equations of Dirac's new electrodynamics. They are also applied to the tensor of the electromagnetic field in the presence of charges and poles. The implications are briefly discussed.

43. Some General Properties of Solutions in Dirac's New Electrodynamics. N. L. BALAZS, *Department of Physics, University of Alabama.* (Introduced by Arthur E. Ruark.)—The fifth-field variable, λ, in Dirac's new electrodynamics is related to the charge density. The known solutions of this theory refer to situations where no charges are present, λ being zero. We show here that if λ is finite in a domain D in space vanishing outside it, and the solutions are static or strictly periodic in time and nowhere singular, then, if they exist, they must have the following properties. If $\lambda > 0$ in D the field cannot be purely electrostatic; if $\lambda < 0$ in D the field cannot be purely magnetic. If $\lambda = 0$ the field cannot be purely electric or magnetic, quite naturally, since then Dirac's theory is equivalent to that of Maxwell as far as the electric and magnetic fields are concerned.

44. Electrodynamic Equations Symmetrical in Respect to Charges and Poles; with Remarks on Monopoles. ARTHUR E. RUARK, *University of Alabama.*—The idea of symmetrizing the Maxwell equations by including magnetic poles is old, but not fully developed. We divide the total field into a part due to charges and another due to poles. The latter has a scalar magnetic potential and a vector potential whose curl contributes to E. The system is invariant. Hence, it is not necessary, classically, to use a singular vector potential to describe poles. At first it appears plausible that a Dirac monopole should have a classical radius equal to the electron radius. This assumption amounts to *mass quantization*, the pole mass being $(137/2)^2$ times electron mass. Alternatively: the pole should have an electric moment of $(1/4\pi)$ (pole strength) times (Compton wavelength of pole). Making this moment one Bohr magneton, the pole mass becomes (137/2) times electron mass. However, a completely symmetrical situation in which the monopole strength is equal to the electron charge will be presented for comparative purposes; inasmuch as the Dirac monopole theory, while attractive, is not *certainly* known to correspond to the facts of nature.

45. Interior Value Problems. A. V. MASKET, *The University of North Carolina.*—Conversely to the customary boundary value problem, we have considered the general problem of finding the values of a function on the boundary of a region from known values in the interior. Solutions can be found for familiar problems in wave propagation, heat conduction, and potential theory having symmetry. Wave propagation in two dimensions and the question of uniqueness remain as difficulties. The operational Laplace transform has been employed.

46. Spatial Distribution of Energy Dissipation by a Bremsstrahlung Spectrum. DAVID T. GOLDMAN AND HENRY BRYSK, *Vanderbilt University.* (Introduced by I. Bloch.)—For x-ray dissipation, it is the energy lost by ionizing secondary radiation that is measured experimentally (and gauges biological effects). Close to the entering surface, the x-ray and secondary distributions differ (the x-rays traverse a finite volume of material before making a collision) and the "transition curve" for the latter is found empirically, as well as heuristically, to follow crudely a difference of exponentials. A detailed pilot calculation, in very good agreement with experiment, is being published by the second author, using the techniques of Spencer and Fano and a modification of the Lewis electron diffusion equation. The present work has explored the simplifications that can be made for the bremsstrahlung spectrum from a betatron beam, utilizing knowledge of the specific functional forms and magnitudes that enter, and the relative insensitivity of the solution of an integral equation to modifications of the kernal, and exploiting the information available from the more precise previous calculation for step-by-step comparison, and estimation of relative importance of effects. It has been found possible to eliminate the major part of the calculational labor without appreciable loss of accuracy, and to evolve a straightforward and reasonably short computational routine.

47. A Generalization of a Theorem by Pappus. E. E. MAYO, *University of Louisville.*—This paper points out that the integral referred to in the theorem of Pappus was essentially

$$I_{pqr} = \int_B x^p y^q z^r d^m,$$

where $p=q=r=0$ and the integration is extended over the entire body B. We chose to discuss the above integral with p, q, and r all integers greater than or equal to zero, and define B as the body generated by revolving a surface S with parametric representation in $(\alpha\beta)$ about the z axis, which is external to S. Then the above integral reduces to a finite sum of integrals similar to I_{pqr}, but involving only S. Sample cases in which the theorem is used to compute the mass and the radius of gyration of a few simple cases are also presented.

48. Some Thermodynamic Constants of Liquid Hydrogen Fluoride. C. HARRY KNOWLES AND R. T. LAGEMANN, *Vanderbilt University.*—Because of the experimental difficulties, values of many thermodynamic properties for liquid hydrogen fluoride have not been determined. By means of a measurement of the ultrasonic velocity and knowledge of the density and specific heat at constant pressure, it is possible to proceed to the calculation of the adiabatic and isothermal compressibilities, the ratio of specific heats, and the specific heat at constant volume. This has been done over a 35 degree range of temperature just below the boiling point. Use was made of a newly constructed ultrasonic interferometer made of Teflon (polytetrafluoroethylene) which does not react chemically with hydrogen fluoride.

49. Electrical Conductivity of Sulfur. CARROLL K. GORDON, *Biophysics Laboratory, Tulane University.* (Introduced by Robert T. Nieset.)—The electrical conductivity of liquid sulfur has been measured in the range 120°C to 200°C and for samples containing different amounts of hydrocarbon impurity. For all samples the electrical resistance has been found to vary directly as the viscosity. The resistance of a sample containing approximately one part per million hydrocarbon impurity varies from 5.1×10^{10} ohm to 37×10^{10} ohm in the neighborhood of 170°C. At this same temperature the viscosity varies from 5 centipoise to over 50 000 centipoise. The electrical conductivity of this same sample when held in the liquid state and with a voltage across the sulfur for a period of time changes and becomes almost linear as a function of temperature. The conductivity of all samples of greater impurity (over 0.106 percent impurity) varied in the same manner with the viscosity, but the viscosity dependence did not change with time as in the case of the first sample. These results are interpreted to mean that there are two types of conduction taking place in sulfur—one an electronic conduction as indicated by the linear plot of conductivity *vs* temperature; the other is a viscosity dependent electrophoretic conduction in which the migrating particles are the charged hydrocarbon impurities in the sulfur.

50. Self-Diffusion Coefficient of Nitrogen. LLOYD B. DELUCA, *Biophysics Laboratory, Tulane University.*—The self-diffusion coefficient of nitrogen has been measured by observing the diffusion of tracer nitrogen of 7.2 percent N^{16} into tank nitrogen of 0.4 percent N^{15}. A continuous analysis of the increasing 29/28 ratio of the gas in one diffusion bulb was made with a Nier-type mass spectrometer by the null method.[1] The sampling of the bulb was made through a fixed viscous flow leak. The measured value of the self-diffusion coefficient of nitrogen of 0.186 ± 0.006 cm^2 sec^{-1} at 0°C, referred to 760 mm Hg, agrees well with previous work by Winn[2] and essentially agrees with the theoretical value calculated by Hirschfelder[3] based on the assumption that the molecular interaction potential is of the form

$$V(r)=4\epsilon\{-(r_0/r)^6+(r_0/r)^{12}\}.$$

[1] Nier, Ney, and Inghram, Phys. Rev. **70**, 116 (1946).
[2] E. B. Winn, Phys. Rev. **80**, 1024 (1950).
[3] Hirschfelder, Bird, and Spotz, Chem. Revs. **44**, 205 (1949).

51. Measurements of Solvent Volume Changes in a Sugar Factory Using a Radioactive Tracer Technic. JOHN U. HIDALGO, SR., *Tulane University.*—In order to evaluate the unaccountable losses in the Valentine Sugar Mill, several studies were undertaken. The most fruitful of these was a bacteriological assay of the mill juices, demonstrating the presence of the sucrose utilizing Leuconostoc mesenteroides. Sucrose concentrations over the contaminated portions of the mill were constant, and indicated no sucrose defection unless accompanied by a concomitant loss of solvent matrix. An experiment was done to test for solvent volume changes in the mill, using a tracer material, radioactive gold (Au^{198}). The gold, selected because of its biological inertness, was introduced at a steady rate into the first juice collection tank and serial juice samples were taken from several points in the contaminated area and assayed for radioactivity. Data from these measurements confirmed the solvent-loss hypothesis. The experiment was performed during a regular production run and careful accounting of all 760 mc of Au^{198} was a prerequisite for approval by the Food and Drug Administration. In addition, the final sugar had to demonstrate no detectable radioactivity before it could be released for public consumption.

52. Photolysis of Para-Diazo-N, N-Dimethylaniline Zinc Chloride Dihydrate. ALNERT BARIL, JR., *Biophysics Laboratory, Tulane University.*—A determination of the near ultraviolet and visible absorption spectra for an aqueous solution of para-diazo-N, N-dimethylaniline zinc chloride dihydrate has been made as a preliminary to the investigation of the photolysis of para-diazo-N, N-dimethylaniline zinc chloride dihydrate using a Beckman model DU spectrophotometer. A very broad absorption band was found beginning at about 4600A and continuing into the ultraviolet region. Because of the existence of this broad band the quantum efficiency was measured at a wavelength of 3650A. Using a General Electric AH-6 high pressure mercury arc source, filtered to emit a 3650A wave band and a constant volume manometric technique capable of detecting the evolution of one microliter of nitrogen the quantum efficiency for the photolysis of para-diazo-N, N-dimethylaniline zinc chloride dihydrate was found to be 0.969. An evaluation of the photosensitivity of the diazonium compound was obtained from a knowledge of the absorption spectra and quantum efficiency. Once the sensitivity of the salt was determined it was possible to evaluate its usefulness and the adaptability of the diazonium compound in the field of photomechanical reproduction.

53. Seismology in the Southeast. JACK H. WILLIAMS AND C. F. MERCER, *University of South Carolina.*—The Columbia Seismograph Station is a U. S. Coast and Geodetic Survey station located on the grounds of the University of South Carolina and sponsored by the University. It was established in 1930 to be operated by a member of the Physics Department staff, and has been in continuous operation since. The original seismometers were the McComb-Romberg tilt-compensation type. These were of low magnification and long period. The light beam operated on the principal of the optical lever. There was no vertical component. In 1951, one of the components was exchanged for a Sprengnether instrument with much higher magnification. The station was much more effective, but unbalanced. In December, 1953, a modern three-component Wilson-Lamison seismometer station was installed. The instruments have very high magnification and the vertical unit makes it possible to record phases more sharply than before. The station is now one of the most sensitive in the eastern United States. The study of the arrivals of the many complex waves traversing the earth in different ways through many paths gives us most of the information we have about the earth's interior. The paper will deal with these waves and their interpretations.

54. An Approximate Partition Function for Certain Iron Group Salts at Low Temperatures. L. D. ROBERTS AND J. W. T. DABBS, *Oak Ridge National Laboratory.*—For certain paramagnetic salts of the iron group, the predominant interaction in the "spin" Hamiltonian of the magnetic ion is that due to the crystalline electric field. This term will produce an anisotropy in the magnetic thermodynamic properties of the salt, as, for example, in the adiabatic dependence of temperature on magnetic field and entropy. Assuming the Hamiltonian $H=g_1\beta H_1S_1+g_2\beta H_2S_2+g_3\beta H_3S_3+DS_3^2$ where the g_i, H_i, and S_i are components of the spectroscopic splitting factor, magnetic field, and electron spin operator, where β is the Bohr magneton and D is the electric field, splitting coefficient, one may estimate this anisotropy. Assuming the D term large compared to the terms in H and using the interaction representation of Schwinger, one can obtain the partition function Z

$$Z=\sum_{m=-S}^{S}e^{-m^2/\theta}\left(1+\frac{1}{2}\frac{m^2h_3^2}{\theta^2}\right)$$

$$+\frac{1}{2}(h_1^2+h_2^2)\left[\left\{S(S+1)+\frac{1}{4}\right\}\frac{e^{-1/4\theta}}{2\theta^2}\right.$$

$$\left.\sum_{\substack{m=-S\\ m\neq-\frac{1}{2}}}^{S}[S(S+1)-m(m+1)]\left\{\frac{e^{-m^2/\theta}}{\theta(2m+1)}+\frac{e^{-(m+1)^2/\theta}-e^{-m^2/\theta}}{(2m+1)^2}\right\}\right],$$

where m is the magnetic quantum number, $h_1=g_1\beta H_1/D$, and $\Theta=kT/D$. Calculations of the entropy, and $T=T(H)$ at constant entropy will be presented.

55. A Method for Brute Force Polarization of Hydrogen Nuclei. J. W. T. DABBS AND L. D. ROBERTS, *Oak Ridge National Laboratory.*—Certain anisotropic paramagnetic salts containing hydrogen allow adiabatic demagnetization by rotation of a magnetic field H from the direction of large spectroscopic splitting factor g_l to the direction of small splitting factor g_s, at constant H. Starting at an initial temperature T_i, the proton polarization obtained by "brute force" is given by $f_p=1.0\times10^{-7}Hg_l/T_ig_s$ for small polarizations, in an ideal case. Values of H/T_i up to $\sim2\times10^5$ are available using techniques of indirect cooling[1] together with the superconducting "heat switch" for thermal isolation after cooling to T_i and before rotation. $Ce_2Mg_3(NO_3)_{12}\cdot24H_2O$ has a magnetic anisotropy[2] given by $g_l/g_s\approx7$, and for this case, values of f_p in the range 0.055–0.07 are available, taking into account both the electron and proton spin system (Schottky) specific heats, which arise from the Zeeman splittings $\Delta E(\text{electronic})=2g_s\beta SH$ and $\Delta E=(\text{protons})=2\mu_pH$; these are the only important specific heats in the region of interest. Calculations on this basis indicate that proton polarizations of ~6–7 percent probably could be maintained for reasonable times. It is assumed that the ortho-para energy difference is small compared to kT.

[1] Roberts, Bernstein, Dabbs, and Stanford, Phys. Rev. (to be published).
[2] Cooke, Duffus, and Wolf, Phil. Mag. **44**, 623 (1953).

56. Metastable Magnetic States. J. R. LAMARSH AND B. D. KERN, *University of Kentucky.*—On several occasions during the last century it was reported[1] that specially prepared pieces of soft iron are unstable to increases in magnetization due to mechanical shock, heat, and also light. Though these experiments attracted widespread interest at the time, certain of them now appear to have been forgotten. We have repeated briefly some of these experiments and have been able to confirm the existence of several of the early effects. A qualitative explanation of these phenomena in terms of unstable domain structures will be presented along with details of the experimental procedures.

[1] J. H. Hart, Am. J. Sci **10**, 66 (1900) (references to earlier works are contained here).

57. The Specific Heat of $MnCl_2$ at the Temperatures of Liquid Helium. R. B. MURRAY,* *Oak Ridge National Laboratory and University of Tennessee.*—The specific heat of anhydrous $MnCl_2$ has been measured from 1.3° to 4.2°K by the techniques of low-temperature adiabatic calorimetry. The sample was prepared by the dehydration of pure $MnCl_2\cdot4H_2O$ in a dry HCl atmosphere. Specific heat measurements were carried out by isolating the sample from the liquid helium bath and observing the rise in temperature of the sample associated with the input of a measured amount of heat from an electrical heater coil. Sample temperatures were measured with a carbon resistor whose resistance was carefully calibrated against the temperature of the liquid helium bath at the beginning of each experiment. The results of a series of experiments indicate anomalous behavior of the specific heat near 1.9°K, with the specific heat falling smoothly with increasing temperature from this region to 4.2°K. Experiments at temperatures below the region of anomalous behavior show the specific heat falling slowly with decreasing temperature, and suggest further anomalies at even lower temperatures. Experiments below 1.3°K are planned.

* Graduate Fellow of the Oak Ridge Institute of Nuclear Studies.

58. The Relative Secondary Electron Emission for Ions and Atoms. C. F. BARNETT, P. M. STIER, AND G. E. EVANS, *Oak Ridge National Laboratory.* (Introduced by Arthur H. Snell.)—To use secondary electron emission as a quantitative detector for mixtures of ions and atoms, it is necessary to know the relative secondary emission coefficients. An investigation has been made of this emission for a nickel target bombarded with particles in the energy range 20 to 250 kev. The positive ion beam from a Cockcroft-Walton accelerator passed through a differentially pumped gas cell in which part of the beam was neutralized by charge exchange. The emergent beam passed between electrostatic deflection plates and then impinged on a foil thermocouple. Electrodes were provided for efficient collection of the secondary emission from the foil. Comparisons were then made between the emission for atoms and for mixtures of ions and atoms, in terms of the thermocouple response. It was found that within the limits of measurement (3 percent), the ratio of secondary electron emission coefficients is unity for ions and atoms of nitrogen, neon, and argon, in this energy range. The emission for helium and hydrogen atoms is several percent larger than that for the corresponding ion of the same energy.

59. The Effect of Small Strains on the Electrical Resistance of Uranium Wire. E. W. KAMMER, *Mechanics Division, Naval Research Laboratory.*—If a conductor in wire form is subjected to an elastic deformation by applying a tensile stress, a change in electrical resistance is generally observed. This change in resistance is the result of two effects: the altered dimensions of the wire, and the distortion of the crystal lattice spacings which control the characteristic resistivity. An experiment is described which measures the strain effects upon electrical resistance for polycrystalline uranium wire. The ratio of the resistance change to strain $(\Delta R/R)/(\Delta L/L)$, was found to be +3.67 for the available specimens.

60. The Structures and Resistivities of Sputtered Films of the Platinum Metals Before and After Aging by Heating.*† RICHARD B. BELSER AND MARGARET C. CHESTER, *Georgia Institute of Technology.*—Thin films of the six platinum metals, with melting temperatures in the range 1554°C to 2700°C, are very difficult to deposit by commonly accepted evaporation procedures. These metals, however, may be deposited by sputtering in a high-sputtering-rate apparatus developed at the Georgia Institute of Technology. Normal sputtering rates in a residual argon atmosphere have been approximately 375, 250, 200, 100, 50, and 30 angstroms per minute, respectively,

for the metals Pd, Rh, Pt, Ir, Ru, and Os. These rates have been obtained at approximately 20-ma current, 3750 volts, and a vacuum near 3×10^{-3} mm of Hg. Electron micrographs of these films have shown extremely fine-grain initial structure which coarsened somewhat on heating the films in a vacuum to temperatures in the range 450°–600°C. Resistivities initially in the range 2.5–7.5ρ_b for 1000 angstrom films are normally reduced to values of 1.5–2.5ρ_b during this treatment and electron-diffraction patterns have indicated concurrent grain growth. Ruthenium and osmium vary somewhat from the typical behavior presumably due to oxide inclusions in the films formed during the sputtering action.

* Supported by the United States Army Signal Corps.
† Electrodes of osmium and ruthenium were furnished through the courtesy of Baker & Company, Inc., Newark, New Jersey.

61. Solder-Shear Tests to Metal Films Deposited on Glass Substrates by Evaporation and Sputtering.* MARGARET C. CHESTER AND RICHARD B. BELSER, *Georgia Institute of Technology.*—Solder-shear tests of bonds of indium and tin-lead solders to evaporated and sputtered metal films on glass substrates have been conducted. The metal mating surface was a swiveled brass tongue ¼ in.×¼ in. in area. Bonds to evaporated films of Ag, Al, Au, Co, Cr, Cu, Fe, Ni, Ti, and Zr and sputtered films of Ag, Au, Co, Cu, Fe, Ir, Os†, Pd, Pt, Rh, and Ru† were tested. Indium-solder joints were successfully made to all films without a flux, and shear strengths were in the range 250–800 lb per sq in. Fluxes could be used with indium on nickel, iron, platinum, palladium, rhodium, and iridium. Tin-lead solders made joints to nickel, iron, platinum, palladium, rhodium, iridium, ruthenium, and osmium, both with and without fluxes. Without a flux bond strengths in the range 250–1400 lb per sq in. were observed. With common fluxes, resin, "Nokorode," and an acid-type, shear strengths over 2000 lb per sq in. were frequently obtained. Bond strengths to sputtered films of nickel, platinum, and rhodium were consistently excellent.

* Supported by the United States Army Signal Corps.
† Ruthenium and osmium furnished through the courtesy of Baker & Company, Inc.

62. An Electron Microscope and Diffraction Traversing Technique for the Examination of Bimetal Films.* JOHN L. BROWN AND RICHARD B. BELSER, *Georgia Institute of Technology.*—An R.C.A. type emu diffraction stage has been modified to allow a transmission sample to be moved perpendicularly to the electron beam during operation. Thin films of gold and aluminum have been evaporated onto a silicon-monoxide substrate; first, so that one-half the area of the substrate has been coated with gold and the entire area overcoated with aluminum; second, so that the entire area has been coated with gold and one-half overcoated with aluminum. Electron micrographs and diffraction patterns of each sample were taken initially at five different positions across the width of the sample to show the transition from the dual layer to the single layer film. The sample was removed and successively heated to 200°C, 400°C, and 600°C in an infrared vacuum oven. Micrographs and diffraction patterns were taken after each heat treatment. Results of alloying effects are being studied and compared with results by resistivity, x-ray diffraction, and metallographic studies of the same metal pairs. Effects of inversion of position and simultaneous evaporation are under observation for the same metal pairs.

* Supported by the United States Army Signal Corps.

63. Applications of the NaI Gamma-Ray Spectrometer to Blood Volume Determinations. R. H. ROHRER, W. H. CARGILL, AND A. F. DRATZ, *Radioisotope Unit, Atlanta Veterans Administration Hospital and Emory University.*—Blood volumes in human patients are estimated by measuring the dilution of injected Cr^{51} labeled red cells. The ratio of the red cells to the total blood volume is determined by simultaneously measuring the activity due to the Cr^{51} and the activity of I^{131} resulting from a later injection of I^{131} labeled serum albumin in blood samples. The counting rates at the 364-kev iodine photopeak and the 320-kev chromium photopeak from a NaI scintillation detector are separated by a two-channel pulse analyzer system. Quantitative analysis is made by comparing these counts with the counts from control samples; one containing only labeled red cells, and the other containing only iodine labeled albumin. A photopeak resolution at 364 kev of 12 percent energy width at one-half the maximum is sufficient for satisfactory discrimination between the two activities.

64. A New Technic for Visualizing Thyroid Outline Using I^{131} and a Scintillation Counter. VINCENT SPEAR, *Biophysics Laboratory, Tulane University.* (Introduced by John U. Hidalgo.)—A dose of I^{131} is administered orally. Following its absorption the area is mechanically scanned with a gamma-ray detector. A scintillation counter mounted on a gimbel is made to scan the area with a spiral motion at a constant linear speed. Potentiometers on the axes of the gimbel provide position signals to the plates of a cathode-ray oscilloscope. A lead shield with a ¼-in. hole through its center is placed in front of the NaI crystal of the tube so that the tube will fire only when it is pointing directly at the radioactive source —in this case, the I^{131}. The firing of the tube is transmitted as a pulse to intensity modulate a cathode-ray tube. By this means the outline of the thyroid gland is presented on the face of the cathode-ray tube. A long persistence screen is used and several scans of the thyroid area are taken, in order that a time exposure photograph may be taken. The use of a Polaroid Land Camera, with one minute development time, allows the operator to complete the entire operation in less than twenty minutes.

65. A Rotating Sphere Solid Angle Scanner for Gamma Rays. GEORGE R. MENEELY, ROBERT J. KERR, JESSE E. HOFFMAN, AND SHERWOOD K. HAYNES, *Radioisotope Unit of Thayer Veterans Administration Hospital and Vanderbilt University.*—The distribution and intensity of extended gamma-ray sources are represented on an oscilloscope screen by directing the radiation upon a NaI crystal through a collimator scanning a 30° square solid angle. A rotating 3-inch Heavymet sphere with three $\frac{1}{16}$-inch holes 60° apart in the plane of the equator, perpendicular to the axis of rotation and passing through it is rocked through a 30° vertical angle. The sphere is in front of the crystal which is shielded so that most of the rays which reach it must pass through the collimating holes. As the sphere rotates, each hole scans a thirty degree horizontal angle resulting in six sweeps per revolution. As the axis of the sphere rocks back and forth, each horizontal sweep is below or above the preceding one. The orientation of the active hole is transmitted electronically to the deflection plates of the oscilloscope to form a corresponding raster. The oscilloscope beam is intensified by each pulse from the detector to produce a visible and correctly oriented representation of the source. This devise has been used to determine visually and photographically the distribution and intensity of various sources including radioisotopes in human tissues and organs.

66. Use of Scintillation Counters in the Studies on the Luminous Efficiency of Biological Materials. J. G. KEREIAKES AND A. T. KREBS, *Army Medical Research Laboratory, Fort Knox, Kentucky.*—Two principles of scintillian counting are in use at present: The photon tube scintillation counter first applied in 1941 by Krebs,[1] and the photomultiplier scintillation counter introduced in 1944 by Curran and Baker.[2] In recent years both arrangements have been so improved by

the introduction of new phosphors, new photomultipliers, and new photon tubes, that even the low effective luminescence systems found in biological materials can be detected and studied. Preliminary investigations of these systems as well as published data by Debye and Edwards[3] on the fluorescence and phosphorescence of proteins and pure amino acids indicate the need for more systematic studies of factors influencing the luminescence and scintillation properties of biological materials. Some of these factors, such as concentration, pH, O_2 tension, and status of the material has been studied for different amino acids, nucleic acids, enzymes, and vitamins. The results so far obtained will be presented and discussed in detail.

[1] A. T. Krebs, Ann. Physik **39**, 330 (1941).
[2] S. C. Curran, *Luminescence and the Scintillation Counter* (Academic Press, New York, 1953).
[3] P. Debye and S. O. Edwards, Science **116**, 143 (1952).

Minutes of the 1954 Spring Meeting of the New York State Section at Syracuse, April 9 and 10, 1954

THE thirty-first meeting of the New York State Section was held at Syracuse, New York, on April 9 and 10, 1954, with an official registration numbering about 125.

Circumstances which forced cancellation of the planned tours through the General Electric plant at Electronics Park resulted in a substitute program of four excellent papers by members of the Electronics Laboratory staff. Dr. Lloyd DeVore, Head of the Electronics Division, deserves commendation for converting a difficult situation into a very profitable session on Friday afternoon.

An address by Dr. E. U. Condon followed the Section Dinner on Friday evening. Since all efforts to elicit advance information as to a title for the address failed, and since, to the Secretary's knowledge, no formal title ever *was* announced, let it be recorded here merely that the address was a most enjoyable and entertaining one having to do with the dimensions of physical quantities. No doubt many of the audience have since been indulging in a little numerology, at least, to quote the speaker, "in the privacy of their own rooms," if not openly.

The Saturday morning session was devoted to four invited papers, titles of which are listed below. Open House in Steele Hall, the home of Syracuse University's Physics Department, on Saturday afternoon completed the two-day session.

Let it be recorded here also that the success of the meeting was due in no small measure to the efforts of the local committee, Mr. Peter Bergmann, Mr. Herbert Berry, Mr. Nathan Ginsburg, and Mr. W. R. Fredrickson, under the chairmanship of C. H. Bachman—all members of the staff of the Physics Department at Syracuse University.

L. W. Phillips, *Secretary for New York State Section*
The University of Buffalo
Buffalo 14, New York

Invited Papers

Nonmetallic Ferromagnetic Materials. Paul N. Russell, *General Electric Company.*

Color Television (with Demonstrations). I. C. Abrahams, *General Electric Company.*

Recombination Center Density Measurements in Germanium. Donald C. Cronemeyer, *General Electric Company.*

Survey of Germanium and Silicon Devices. I. A. Lesk, *General Electric Company.*

The Role of Physics in Engineering Education. R. J. Seeger, *National Science Foundation.*

Observational Tests in Cosmology. Fred Hoyle, *Cambridge University, England.*

Infrared Absorption in Semiconductors. Melvin Lax, *Syracuse University.*

The Formation of the Photographic Latent Image in the Silver Halides. G. W. Luckey, *Eastman Kodak Company.*

CONTENTS

The Physical Review — Second Series, Volume 95, No. 1 — JULY 1, 1954

Walter M. Elsasser 1
E. T. Hooppendyke and R. D. Birkhoff 6
N. Sternberger and R. V. Pound 8
F. J. Blatt 12
Robert L. Cummerow 16
W. Primak and L. H. Fuchs 22
B. Abeles and S. Meiboom 31
Seymour Mayberg 38
J. Rose Macdonald and John E. Robinson 46
H. R. Lukens and W. C. Dunlap, Jr. 51
P. A. Wolff 56
Luis Marquez 67
Peter D. Johnson and Ferd E. Williams 69
J. J. Gilvarry 73
R. E. Meyerott 78
E. M. Bernstein and H. W. Lewis 89
E. M. Stafforth and S. S. Hanna 95
G. R. Hennig 97
B. Elbek, K. O. Nielsen, and O. B. Nielsen 98
Behadel Saraf 97
E. Russell, Warren E. Taylor, and John N. Cooper 99
J. L. Dick, W. S. Anderson, and J. D. Kurbatov 101
P. S. Baranskaia, J. W. T. Dabbs, and C. P. Stanford 103
S. S. Hanna, E. C. LaVier, and C. M. Class 110
P. F. Zweifel 112
G. E. Boyd 115
E. W. Pringle, W. Turchinetz, and H. W. Taylor 118
James R. Waddell and James H. Roberts 117
R. C. La, W. H. Kelly, and M. L. Wiedenbeck 121
Martin G. Redlich and Eugene P. Wigner 122
John S. Wahl 126
M. L. Perlman and John P. Welker 133
J. Taylor and A. Roberts 137
J. A. Hipple, Jr., M. B. Gottlieb, and J. A. van Allen 147
Clyde W. Touk, Jr., R. B. Leighton, and E. K. Bjørneruud 159
M. M. Block and D. T. King 171
N. Baker and G. Bergmann 174
Shi-Chang Fung and Anthony Turkevich 176
D. Cuclay, T. R. Palfrey, and R. R. Wilson 178
A. J. Hartzler and R. T. Siegel 183
Benjamin A. Bricknor, and V. D. Hopper 193
Lester Winsberg 198
Lester Winsberg 205
John L. Gartland 209
M. A. Rosenthal, C. A. Levinson, and H. M. Mahmoud 217
Kenneth M. Watson 228
H. E. Moses 237
D. M. Chase 243
W. B. Cheston 247
Léon van Hove 249
Hiroshi Kanazawa, Hirotaki Hasegawa, and Pong-Yul Pao 263
J. H. Smith 271

(Continued on cover three)

LANCASTER PRESS, INC., LANCASTER, PA.